Durham University

Durham E-Theses

Dark Matter : No Place for WIMPs

THOMAS WILLIAM JUBB

How to cite:

JUBB, THOMAS WILLIAM (2017) Dark Matter : No Place for WIMPs. Doctoral thesis, Durham University.

Use policy

The full-text may be used and/or reproduced, and given to third parties in any format or medium, without prior permission or charge, for personal research or study, educational, or not-for-profit purposes provided that:

- a full bibliographic reference is made to the original source
- a https://etheses.durham.ac.uk/id/eprint/12369/ is made to the metadata record in Durham E-Theses
- the full-text is not changed in any way

The full-text must not be sold in any format or medium without the formal permission of the copyright holders.

Please consult the full Durham E-Theses policy for further details.

Academic Support Office, The Palatine Centre, Durham University, Stockton Road, Durham, DH1 3LE
e-mail: e-theses.admin@durham.ac.uk Tel: +44 0191 334 6107
https://etheses.durham.ac.uk

Dark Matter : No Place for WIMPs

Thomas W. Jubb

A Thesis presented for the degree of
Doctor of Philosophy

Institute for Particle Physics Phenomenology
Department of Physics
University of Durham
England

August 2017

Dedicated to

Natalie

Dark Matter : No Place for WIMPs

Thomas W. Jubb

Submitted for the degree of Doctor of Philosophy
August 2017

Abstract

The primary goal of this thesis will be to explore the '*model space*' of *Weakly Interacting Massive Particle* (WIMP) *Dark Matter* (DM), using simplified models in order to make some general statements on the allowed parameter space and to guide future detection efforts. The context for this thesis is a time in which many experiments are attempting, either directly or indirectly, to pin down the interactions of DM with the very precisely measured standard model. So far no robust signals have been found.

Depending on your particular tastes, you may hold out for one particular realization of *Beyond the Standard Model* (BSM) physics (e.g. Supersymmetry) and explore its rich phenomenology to ever increasing precision. But as time marches on, with diminishing confidence in discovery despite concerted efforts, you may instead look for ways in which to explore all possible realizations at once, a *bottom-up* approach, to help guide future searches and model building efforts. This is the utility of simplified models.

We will show that much of the parameter space of a neutral thermal WIMP (with arbitrary spin, spanning a complete set of simplified models) is heavily constrained by a combination of indirect/direct searches.

Inevitably, carrying out such a study requires many assumptions, not all of them sound all of the time. To test the robustness of the study we will take an in-depth phenomenological look at a more detailed model, tackling many of the assumptions of simplified models (such as minimal flavour violation and gauge-invariance).

We will take several detours along the way. We will show that the next generation

of direct detections machines will be sensitive detectors for light (sub GeV) new particles in the neutrino sector.

We will also consider how heavy flavour observables might be impacted by the breakdown of the assumption of quark-hadron duality, rather than from genuine new physics.

Declaration

The work in this thesis is based on research carried out at the IPPP, the Department of Physics, Durham, England and is listed in the table below. No part of this thesis has been submitted elsewhere for any other degree or qualification and it is all my own work unless referenced to the contrary in the text.

Title	Ref.	Completed	Chapter
"No Place for Thermal WIMPS"	Unpublished	2013-2015	Chapters 1-5
"Physics from solar neutrinos in dark matter direct detection experiments"	[1]	2015	Chapter 6
"Charming Dark Matter"	[2]	2016-2017	Chapter 7
"On the ultimate precision of meson mixing observables"	[3]	2016	Chapter 8

Copyright © 2017 by Thomas W. Jubb.

"The copyright of this thesis rests with the author. No quotations from it should be published without the author's prior written consent and information derived from it should be acknowledged".

Contents

Abstract iii

Declaration v

1 Dark Matter 1

1.1 The Evidence for Dark Matter . . . 1

1.1.1 Spiral Galaxies . . . 1

1.1.2 Elliptical Galaxies . . . 2

1.1.3 Galaxy Clusters . . . 2

1.1.4 The CMB . . . 5

1.1.5 Big Bang Nucleosynthesis . . . 7

1.2 Relic Density via Thermal Freeze-Out . . . 8

1.2.1 Cosmology Basics . . . 9

1.2.2 Calculation of Relic Density . . . 10

1.2.3 The Boltzmann Equation . . . 12

1.2.4 Effective Degrees of Freedom . . . 16

1.2.5 Thermally Averaged Cross Section . . . 18

1.3 Outline of this Thesis . . . 22

2 Simplified Models of Dark Matter 25

2.1 The Paradigm of Simplified Models . . . 25

2.2 Simplified Models for this Study . . . 29

2.2.1 Fermionic DM Couplings . . . 31

2.2.2 Scalar DM Couplings . . . 33

2.2.3 Vector DM Couplings . . . 34

2.2.4 Standard Model Couplings to the Hidden Sector 36
2.3 Conclusions 37

3 Indirect Detection of Dark Matter 40
3.1 Cosmic Rays 40
3.2 Primary Gamma Rays from Dark Matter 41
3.2.1 Dark Matter Density Profile 44
3.2.2 Prompt Emission 46
3.3 Secondary Gamma Rays from Dark Matter 49
3.3.1 Formalism for Cosmic Ray Propagation 49
3.3.2 Electron propagation 50
3.3.3 Solving the Diffusion Equation 52
3.3.4 Halo Function 54
3.3.5 Energy Losses 58
3.3.6 Bremsstrahlung Losses 59
3.3.7 Inverse Compton Scattering Losses 61
3.3.8 Synchrotron Losses 62
3.3.9 Other Losses 63
3.3.10 Impact of the propagation parameters on the gamma ray flux 63
3.4 Gamma Ray and Other Indirect Constraints 68
3.5 Conclusions 73

4 Direct Detection of Dark Matter 75
4.1 Introduction 75
4.2 Step 1 : EFT Matching 79
4.2.1 Heavy Quark and Gluon Operators 79
4.2.2 EFT Matching : Fermion DM 84
4.2.3 EFT Matching : Vector DM 92
4.2.4 EFT Matching : Scalar DM 96
4.3 Step 2 : Hadronic Matrix Elements 100
4.3.1 Further Discussion of Hadronic Matrix Elements 107
4.3.2 Renormalization Group Running 116

4.4 Step 3 : Non-relativistic Limit . . . 119
4.5 Direct Detection Constraints : Current and Future Experiments . . . 131
4.5.1 Statistical Methods for Direct Detection . . . 139
4.6 Conclusions . . . 143

5 Constraints on Simplified Models 145
5.1 General points . . . 148
5.2 Fermion Dark Matter . . . 154
5.2.1 Neutral scalar mediator (1/2-S, 1/2*-S) . . . 154
5.2.2 Neutral vector mediator (1/2-V) . . . 159
5.2.3 Charged scalar mediator (1/2-$S^{\pm}$, 1/2*-$S^{\pm}$) . . . 164
5.2.4 Charged vector mediator (1/2-$V^{\pm}$, 1/2*-$V^{\pm}$) . . . 168
5.3 Scalar Dark Matter . . . 171
5.3.1 Neutral scalar mediator (0-S, 0*-S) . . . 171
5.3.2 Neutral vector mediator (0*-V) . . . 175
5.3.3 Charged fermion mediator (0-$F^{\pm}$, 0*-$F^{\pm}$) . . . 179
5.4 Vector Dark Matter . . . 181
5.4.1 Neutral scalar mediator (1-S, 1*-S) . . . 181
5.4.2 Neutral vector mediator (1-V, 1*-V) . . . 185
5.4.3 Charged fermion mediator (1-$F^{\pm}$, 1*-$F^{\pm}$) . . . 189
5.5 Conclusions . . . 194

6 Solar Neutrino Constraints from Direct Detection 196
6.1 Neutrinos from the Sun . . . 196
6.2 New Physics in the Neutrino Sector . . . 198
6.3 Neutrino Detection in Direct Detection Experiments . . . 200
6.3.1 Neutrino Interaction Cross Sections . . . 201
6.4 Event Rates for Direct Detection . . . 205
6.5 New Physics in Current Generation Experiments . . . 208
6.6 New Physics in Future Generation Experiments . . . 213
6.7 Conclusions . . . 222

7 Charming Dark Matter 225

7.1 DMFV : The Model . . . 227
7.2 DMFV : Renormaliation and Mass Splitting . . . 231
7.2.1 Particle Widths . . . 231
7.2.2 Renormalization and Mass Splitting . . . 233
7.3 DMFV : Relic Density with Coannihilation and Decay . . . 244
7.3.1 Annihilation and Scattering . . . 250
7.3.2 Boltzmann Equations for DMFV . . . 253
7.4 DMFV : Flavour Bounds . . . 259
7.4.1 Mixing Observables . . . 259
7.4.2 Rare Decays . . . 266
7.5 DMFV : Indirect Detection . . . 271
7.5.1 Tree Level Annihilation . . . 271
7.5.2 Gamma Ray Lines . . . 274
7.6 DMFV : Direct Detection . . . 282
7.6.1 Tree Level . . . 282
7.6.2 Loop Level : Gluonic Operators . . . 287
7.6.3 Loop Level : Photon Penguins . . . 297
7.6.4 Loop Level : Z, h Penguins . . . 308
7.6.5 Constraints . . . 311
7.7 DMFV : Collider Searches . . . 320
7.7.1 EFT Limit . . . 321
7.7.2 Processes for the LHC . . . 324
7.7.3 Analysis : Monojet . . . 327
7.7.4 Analysis : Dijet . . . 331
7.7.5 Analysis : Stop Search . . . 334
7.7.6 Collider Constraints within DMFV . . . 336
7.8 DMFV : Other Bounds . . . 339
7.8.1 Electroweak Precision Observables . . . 339
7.8.2 Higgs Decay . . . 341
7.8.3 Z decay . . . 342

7.8.4 Perturbative Unitarity . . . 343
7.9 DMFV : Summary, Results and Conclusions . . . 344
7.9.1 Summary . . . 344
7.9.2 Results and Conclusions . . . 347

8 Quark-Hadron Duality Violation or : On The Ultimate Precision of Meson Mixing Observables 360
8.1 What is Quark-Hadron Duality Violation? . . . 360
8.1.1 Inclusive Decay Rates . . . 362
8.1.2 Neutral Meson Mixing . . . 364
8.2 Duality Violation in the B_s and B_d Systems . . . 367
8.3 Duality Violation in Lifetime Ratios . . . 372
8.4 Duality Violation in the D^0 System . . . 377
8.5 Summary and Conclusions . . . 380

Appendices 384

A Background Material 385
A.1 Furry's Theorem . . . 385
A.2 CPT Symmetries . . . 387
A.3 Non-relativistic Limit of Fields . . . 388
A.3.1 Fermion Dark Matter . . . 388
A.3.2 Scalar Dark Matter . . . 390
A.3.3 Vector Dark Matter . . . 391
A.4 Helicity Basis for Spinors and Vectors . . . 395
A.5 Perturbtive Unitarity Violations . . . 400
A.6 Conventions . . . 410
A.7 Statistics . . . 411

B Annihilation Cross Sections 415
B.0.1 Fermionic DM . . . 416
B.0.2 Scalar DM . . . 423
B.0.3 Vector DM . . . 426

Bibliography 432

List of Figures

1.1 An example of galaxy rotation curves from [4]. The expected profile from the visible matter and gas in the disks (long-dashed and dotted lines respectively) clearly does not fit the data unless an additional halo of invisible matter (dot-dashed lines) is included to give the total contribution (solid line). 3

1.2 The bullet cluster from [5], the green contours (left and right) map the total mass as inferred from gravitational lensing. The red and blue (right) shows the distribution of X-ray emission from hot gas. . . 5

1.3 The CMB temperature power spectrum from [6]. 6

1.4 The various nuclei formed during BBN, as a function of the baryon fraction $\Omega_b h^2$ (or equivalently the photon to baryon ratio), the measured fractions are indicated by yellow rectangles. The CMB measurement of $\Omega_b h^2$ [6] is indicated by the blue band, and agrees well with the BBN concordance range (the purple band). Figure taken from [7]. 8

1.5 The DM comoving number density ($m_\chi = 500$ GeV). The equilibrium number density is shown as a dashed line, and rapidly drops as the DM transitions from relativistic to non-relativistic ($x \sim 1 - 10$). However the DM does not stay in equilibrium, as the expansion of the universe causes the interactions (annihilation of DM in this case) to cease, thus fixing the number density (the measured value is the dotted line). If the interactions are stronger, then the freeze-out occurs later (higher x) as the annihilation remain efficient for longer. 12

1.6 The effective degrees of freedom $g_*(T) = h_{\rm eff}^2/g_{\rm eff}$ as defined in Eq.(1.2.33). Assuming $h_{\rm eff} = g_{\rm eff}$ gives the red dashed line. The blue lines are taken from [8] and are more accurate; including the full temperature dependence of $h_{\rm eff}$ and also accounting for the QCD phase transition at $T = 150$ MeV (upper line) or 400 MeV (lower line). The actual quantity that appears in the formulae is $\sqrt{g_*}$ and so the approximate curve is sufficiently accurate. At the highest temperatures, all the SM degrees of freedom are coupled to the thermal bath, as the universe cools these decouple at $T \sim m$ until only the photons and neutrinos remain. 19

3.1 Example diagrams for photon line spectra produced by DM annihilation, where the DM couples directly to a fermion $f = l, q$ (lepton or quark), on the left the DM annihilates into two photons, each with energy m_χ in the c.o.m. frame, on the right DM annihilates into a photon plus a particle X, which could be for example a Z boson. The DM-fermion coupling is represented by an effective vertex which includes all the simplified models listed in Chapter 2. The DM is drawn as spin-1/2, but can be spin-0 or spin-1. 43

3.2 The halo function $\mathrm{I}(\lambda_{\rm D})$, for three radii from the GC in the disk ($z = 0$). The dashed lines bound the region between the MAX ($L = 15$ kpc) and MIN ($L = 1$ kpc) parameters, and the solid line is the MED ($L = 4$ kpc) set. 56

3.3 The electron spectrum $\psi_e(E_e, r)$ after propagation, for a DM mass of 10 GeV, for various radial distances from the GC (with $z = 0$) for annihilation purely into electrons, $\bar{\chi}\chi \to e^+e^-$, and $\langle\sigma v\rangle = 3 \times 10^{-26}$ cm^{3}s^{-1}. The error incurred by the MIN/MAX diffusion parameters is shown with dashed lines. 57

3.4 The various contributions to the energy loss rate, $b_T(E_e)$, during propagation as a function of the electron energy. 58

3.5 The number density per unit energy of ISRF photons with parameters from [9, 10], the leftmost peak corresponds to the CMB, the second is IR radiation from dust, the third optical starlight, and the final three UV starlight. 62

3.6 The photon flux from prompt (first row), ICS (second row) and bremsstrahlung (third row) gamma ray emission for DM annihilation to $\bar{u}u$ (top row) $\bar{e}e$ (left middle and left bottom) and $\bar{b}b$ (right middle and right bottom). The fluxes are for the Fermi-LAT 7 degree window centred on the GC, with an annihilation cross section $\langle\sigma v\rangle = 3 \times 10^{-26}$ cm^{3}s^{-1}, and for a range of DM masses. In the case of ICS and bremsstrahlung emission, the shaded region between the dashed lines corresponds to the error incurred by using the MIN and MAX diffusion parameters. The blue data points are the Fermi excess, after background have been removed [11]. 67

3.7 Galactic gamma ray exclusion region (left column, shaded) for a constant value of $\langle\sigma v\rangle$ against DM mass, for DM annihilation into $\bar{e}e$ (top row) and $\bar{q}q$ (middle) and $\bar{b}b$ (bottom) where $q = u, d, s$ (with $m_{\rm DM} > 0.1$ GeV for $\bar{s}s$). We include propagation as described in the text (blue shaded), and give the result with no propagation (green line). These are compared other indirect detection limits from the literature (right column), see text for details. 69

3.8 An example of the ID exclusion limits (hatched region) obtained in the case of DM annihilation into $\bar{e}e$ pairs (top row), $\bar{u}u$ pairs (middle row, equivalent $\bar{d}d$, and $\bar{s}s$ above 100 MeV), and $\bar{b}b$ pairs (bottom row), where the grey shaded region forbids annihilation as $m_\chi < m_b$. The left column is for fermionic DM with a neutral vector mediator (an s-channel annihilation), the right column a spin-1 DM with a charged fermionic mediator (a t-channel annihilation).The excluded region is usually dominated by the Fermi-LAT data for $m_{\rm DM} > \mathcal{O}(1)$ GeV as one would expect from Fig.3.7. Below 1 GeV the Fermi-LAT dat decreases in sensitivity and other data are more constraining. . . 74

4.1 An example of the gluon contribution to DM-nuclear scattering for a spin-1/2 DM candidate coupled to heavy quarks via a *charged* mediator. Gluons may be emitted via both the heavy quarks and mediator in the loops. 80

4.2 An example of the gluon contribution to DM-nuclear scattering for a spin-1/2 DM candidate coupled to heavy quarks via a *neutral* mediator, which couple to nucleons dominantly through a two-gluon operator (left). The only exception to the two-gluon coupling is a neutral vector or tensor mediator, which couples via three gluons due to Furry's theorem (right). 81

4.3 The long distance contribution to χ (coupled to heavy quark Q) scattering with nucleons through gluons can be found by integrating out the heavy mediator $\phi \gg m_Q$, and using the effective operators denoted by a cross in the right diagram. 82

4.4 The neutron form factors, $F_i^{(n,n)}(E_R)$ for the $i = 1 - 15$ operators considered in Fig.4.5, for scattering on a ^{129}Xe nucleus, for a DM mass of 10 GeV (Left) and 1 TeV (Right). The DM velocity is taken to be $v_{\rm min}$. 122

4.5 The differential recoil rate per kg $\cdot$ s (left) and exclusion limits (right, shaded region) for two EFT operators describing the interaction between DM and nucleons; both vector (upper panels) and axial-vector (lower panels) couplings which are roughly equivalent to the conventional "Spin Independent" (SI) and "Spin Dependent" (SD) models respectively. 132

5.1 The regions in the $m_{\rm DM} - m_{\rm MED}$ plane excluded by ID and DD (LUX and CDMSlite) which are hatched and polka-dots respectively. A spin-1/2 Dirac or Majorana DM candidate exchanging a neutral scalar mediator with a pair of SM fermions, $\bar{u}u$ in the upper row, and $\bar{b}b$ in the lower row. The exclusions depend on the value of the coupling (left column: $g_s = g_p$, right column: $g_p = 0$), taken to be $g = 3, 1, 0.5$ (Red, Blue, Green respectively). The allowed regions are for $1 < g \leq 3$ (Red), $0.5 < g \leq 1$ (Blue) and $g \leq 0.5$ (Green), using an MCMC which requires a relic density $\Omega_\chi h^2 \in [0.9, 1.0]$ $\Omega_c h^2$. 158

5.2 The possible configurations of couplings which lead to distinct behaviour of the ID and DD constraints for the models 1/2-V and 1/2*-V ($g_{\chi,v} = 0$ for Majorana DM). The suppression of DD operators is shown in brackets. 161

5.3 As for Fig.5.1 for a spin-1/2 Dirac DM (Majorana DM applies to the right column also) candidate exchanging a neutral vector mediator with a pair of SM fermions, $\bar{u}u$ in the upper row, and $\bar{b}b$ in the lower row. 163

5.4 The annihilation $\bar{\chi}\chi \to \gamma\gamma$ process for various fermion DM EFT operators coupled to fermions with charge Q_f, note that the Wilson coefficients C have mass dimension -2. 167

5.5 As for Fig.5.1 for spin-1/2 DM exchanging a charged scalar mediator, the top (middle) row applies to Dirac (Majorana) DM, to a $\bar{u}u$ final state, and with chiral couplings (right) or scalar couplings (left). The bottom row is for a $\bar{b}b$ final state with chiral couplings for a Dirac (Majorana) DM on the left (right). The grey shaded region for $m_\chi > m_{\rm MED}$ represents unstable DM candidates. 169

5.6 As for Fig.5.1 for a spin-1/2 Dirac (top row) or Majorana DM (bottom row) candidate exchanging a charged vector mediator with a pair of SM fermions, $\bar{u}u$, the left (right) column is for vector (chiral) couplings. The grey shaded region for $m_\chi > m_{\rm MED}$ represents unstable DM candidates which decay 172

5.7 The annihilation $\bar{\chi}\chi \to \gamma\gamma$ process for scalar DM EFT operators coupled to fermions with charge Q_f and coupling C_i. The loop factor $C_0 \equiv C_0(0, 0, S, m_f, m_f, m_f)$ is given by $C_0 = (1/2S)\log(\beta)^2$ and β defined in Eq.(5.2.15). 174

5.8 As for Fig.5.1 for a spin-0 DM candidate exchanging a neutral scalar mediator with a pair of SM fermions, $\bar{u}u$ (top row) or $\bar{b}b$ (bottom row). The left (right) columns are for chiral (pseudo-scalar) couplings. 176

5.9 As for Fig.5.1 for a spin-0 DM candidate exchanging a neutral vector mediator with a pair of SM fermions, $\bar{u}u$ (top row) or $\bar{b}b$ (bottom row). The left (right) columns are for vector (axial-vector) couplings, and in the bottom row the exclusions from ID for couplings of 1.0 and 0.5 are too weak to be shown. 178

5.10 As for Fig.5.1 for a spin-0 DM candidate exchanging a charged fermionic mediator with a pair of SM fermions, $\bar{u}u$ (top row) or $\bar{b}b$ (bottom row). The left (right) columns are for scalar (chiral) couplings. 182

5.11 The annihilation $\bar{\chi}\chi \to \gamma\gamma$ process for various vector DM EFT operators coupled to fermions with charge Q_f and coupling C_i, note that C_i has mass dimension -2. Operators which are velocity suppressed or zero are not listed, and neither are the interference terms. The loop factor C_0 is identical to the one in Tab.5.7. 185

5.12 As for Fig.5.1 for a spin-1 DM candidate exchanging a neutral scalar mediator with a pair of SM fermions, $\bar{u}u$ (left column) or $\bar{b}b$ (right column). The top (bottom) rows are for chiral (pseudo-scalar) couplings. The dotted lines are LHC bounds from [12], see text. Although the MCMC and ID limits are not valid below the mass threshold m_b, the DD constraints are since they are based on loop induced processes. . 186

5.13 As for Fig.5.1 for a spin-1 DM candidate exchanging a neutral vector mediator with a $\bar{u}u$ pair, for the vertex structures $\mathcal{V}_{1,2,3}$, upper left, upper right, and bottom respectively. Collider bounds shown as dotted line and taken from [12]. 190

5.14 As for Fig.5.1 for a complex spin-1 DM candidate exchanging a charged fermionic mediator with a pair of SM fermions, $\bar{u}u$ (top row) or $\bar{b}b$ (bottom row). The left (right) columns are for chiral (vector) couplings. Dotted lines correspond to LHC bounds in the top row, or unitarity bounds in the bottom row. The region to the left of the dotted lines in the bottom row leads to perturbative unitarity violations. The region below the dotted lines in the top row is excluded by LHC data. 193

6.1 Normalizations (with errors) for the theoretical solar neutrino fluxes, taken from the AGSS09-SFII standard solar model [13]. 197

6.2 Energy spectrum of solar neutrinos, with normalizations as in Fig.6.1. 198

6.3 Differential cross sections, per target particle, including the SM contribution for a neutrino energy of $E_\nu = 10$ MeV (^{8}B and pp ν for NR and ER, right and left panel respectively) and recoil $E_R = 1$ keV$_{\rm er,nr}$. The mediator is scalar, pseudoscalar (ϕ) vector or axial-vector (Z'), a coupling $g \equiv g_{\nu,\phi} = g_{e,i}$ where $i = s, p, v, a$ respectively. 206

6.4 Electron $e-\nu$ recoil (left) and nuclear $n-\nu$ recoil (right) integrated rates as a function of the threshold energy E_{th}. Electron recoils are normalised to ^{132}Xe while nuclear recoils are plotted for a variety of target materials. Top row: scalar coupling; middle row: vector; bottom row: axial-vector. coupling. 209

6.5 Electron recoil (left) and nuclear recoil (right) limits. Top: scalar coupling; middle row: vector coupling; lower panels: axial-vector coupling. 215

6.6 Constraints (90% confidence limits) on new physics from the Borexino neutrino detector, calculated using a $\Delta\chi^2$ method. 220

6.7 The expected neutrino event rate (cyan line) in Borexino for the SM (left) and for a benchmark set of parameters in the Z' model (right). The dominant backgrounds (dashed lines) are taken from [14], the signal (solid lines) are separated according to the neutrino source, and the experimental data shown as black dots without the rather small error bars. 221

6.8 The expected neutrino event rate (solid green) in SuperKamiokande for the SM (left) and for a benchmark set of parameters in the Z' model (right). The signal (dashed lines) are separated according to the neutrino source, and the experimental data shown as black dots with error bars with background and efficiencies removed. 222

6.9 Constraints (90% confidence limits) on new physics from the SK III data, calculated using a $\Delta\chi^2$ method. 223

6.10 Projected 90% CL constraints on the B-L model for nuclear recoils (solid lines) and electron recoils (dashed) in the optimistic scenarios for G2 germanium (red), G2 xenon (blue) and future xenon (green). We also show approximate bounds derived from the current SuperCDMS (red line), CDMSlite (brown solid and dashed lines), and LUX data (blue shaded region). Our bounds are overlaid on existing constraints. To translate these bounds to the other possible scenarios, one should keep in mind that some bounds (intermediate grey) only apply when the new mediator couples to leptons. The supernova bound (brown) only applies to couplings to baryons, while B-factory bounds (pink) require both. The fifth force constraint (dark grey) applies in either case. The grey regions, the neutrino scattering bound and the pink region, and the supernova limits are respectively taken from [15–17]. 224

7.1 Feynman rules for the DMFV interaction (Eq.(7.1.2)). 230

7.2 The representation for the relevant symmetries of the particles introduced in the DMFV model. All of the particles are singlets under $SU(2)_L$ and the other flavour symmetries not listed. 230

7.3 The dominant three body decay diagram for the heavy DM flavours. . 233
7.4 The one-loop contribution to the DM self-energy from the DMFV model. 235
7.5 The one-loop contribution to the DM coupling, λ_{ij} (left) and λ^*_{ij} (right), from the DMFV model. 237
7.6 The one-loop contribution to the quark self-energy from the DMFV model. 238
7.7 The one-loop contribution to the charged scalar self-energy from the DMFV model. 240
7.8 RD 'bounds' (the shaded region is *allowed*) for single flavour DM. Since $\Omega h^2 \propto (\langle\sigma v\rangle)^{-1} \propto m_\phi^4/|D_{ii}|^4$, the bounds scale roughly as D_{ii}. . 246
7.9 Top : partial relic densities for a 2-flavour DM model with fixed annihilation cross section, and a varying coannihilation, assuming no decays or scattering. Bottom : the corresponding RD bounds for the case of $\langle\sigma v\rangle_{ij} = \langle\sigma v\rangle_{ii}$, but varying the relative sizes of the annihilations. 248
7.10 The momentum assignments for $2 \to 2$ scattering. 253
7.11 Partial relic densities for a 3-flavour DM model with fixed annihilation cross section, and a varying coannihilation (left) or mass splitting (right) for various benchmark scenarios which serve to illustrate the principle trends associated to coannihilation and decay in the DMFV model. Scattering is assumed to be absent, to illustrate some of the features discussed in the text. 256
7.12 An illustration of thermal freeze out for three DM candidates (red blue green in ascending order of mass), with $m_1 = 200$ GeV and $\Delta m_{2,3} = 10\%, 20\%$ for a fixed annihilation cross section $\langle\sigma v\rangle = 10^{-8}$ GeV^{-2}, without scattering $\langle\sigma v\rangle' = 0$, and varying the annihilation $\Gamma = \Gamma_{31} = \Gamma_{32} = \Gamma_{21}$ showing the effects of a low decay width (no effect) and a large width which can completely wash out the relic abundance of the decaying particles. 257
7.13 The decay width of χ_i into χ_1 (with the hierarchy $m_{\chi_1} < m_{\chi_2} < m_{\chi_3}$) as a function of the mass splitting (as a percentage of m_{χ_1}). 259

7.14 Illustration of the RD bounds for degenerate mass DM (left column) solving the coupled Boltzmann equations, or with mass splitting (right column) calculated with the approximate method of Sec.7.3. The top panels illustrate the partial densities of the three candidates in the first moments after the Big Bang, and serve to illustrate the effects of annihilation, scattering and decay mentioned in the text. The bottom panels show the regions (hatched) for which the DMFV models allows the correct relic abundance. 260

7.15 Neutral meson mixing : loop diagrams contributing to M_{12} for the DMFV model, where the external momentum are assumed to vanish. 262

7.16 Excluded regions (hatched) for which the value of M_{12} from Fig.7.15 exceeds the $+1\sigma$ contour of the experimental result. The bounds are the most constraining possible given the quoted limits on D_{ii}, but can be made arbitrarily small by adjusting the relative values of the D_{ii} (for example with equal values the constraints disappear completely). 265

7.17 The DMFV model contribution to the effective operators governing rare decays of charm quarks, including explicit self-energy corrections to the external quark legs as explained in the text. The γ, Z couple to a lepton pair. 268

7.18 The upper limit on the Wilson coefficients from a D^0 rare decay $D^0 \to \pi\bar{l}l$. These are found from Tab.II of [18], and correspond to the low q^2 bin. 270

7.19 Left : the modulus of the Wilson coefficients of operators from Eq.(7.4.107) for various DM and mediator masses. With $(\lambda\lambda^\dagger)_{12} = 1$, and in the $q^2 = 0$ limit (except for $C'_{10} \propto q^2$ for which $q^2 = 0.04$ GeV^2), note also that $C'_8 = C'_{10}$ and is not plotted. Right : the exclusions from $|C'_9| < 2.1$ varying $(\lambda\lambda^\dagger)_{12}$. 270

7.20 The constraints on $\langle\sigma v\rangle_{\bar{f}f}$ for $f = q = u, d, s$ (left) and $f = b$ (right), the latter is representative of $f = c, t$ for $m_\chi > m_{c,t}$. The constraints are taken from many different sources (dSph, galactic centre, clusters) and targets (gamma rays, radio waves, positron, anti-protons), see text for details. 273

7.21 The ID constraints on the DMFV model, with 'maximal' mixing $\theta_{ij} = \pi/4$ and χ_1 the lightest (left), or for couplings to top quarks only and χ_3 the lightest (right). Bounds are produced on individual final states, and therefore scale with the dominant annihilation channel, somewhat surprisingly the top quark channel gives stronger constraints due to the extremely sensitive γ-ray search by H.E.S.S [19]. 273

7.22 The Feynman diagrams for DM annihilation into two photons $\gamma\gamma$ (left) and γX where $X = Z, h$ (right), we have not drawn the diagrams in which the final state lines are crossed but these must be included in the calculation. A full set of independent four fermion EFT operators are inserted at the cross. 275

7.23 The total cross section for $\bar{\chi}\chi \to \gamma X$ where $X = \gamma, Z, h$ (red blue and green respectively), with a scalar mass of 100 GeV (left) and 1 TeV (right), the DM is assumed for simplicity to couple equally to u, c, t with couplings equal to 1. The Fermi-LAT and H.E.S.S. limits are shown for $\langle\sigma v\rangle_{\gamma\gamma}$ and must be scaled appropriately for the Z, h final states, however this does not drastically alter their size or position. . 276

7.24 The squared matrix elements for the annihilation $\bar{\chi}\chi \to \gamma\gamma$ for various fermion DM EFT operators coupled to fermions with charge Q_f and coupling g, note that g has mass dimension -2. $C_0 \equiv C_0(0, 0, s, m_q, m_q, m_q)$ and $y' = (4Q_f^4 N_c^2 \alpha^2)/(\pi^2)$. 280

7.25 Squared matrix elements for the annihilation $\bar{\chi}\chi \to \gamma Z$ process for various fermionic DM EFT operators, coupled to fermions with charge Q_f. We define $\Lambda_m = \Lambda(s) - \Lambda(m_Z^2)$ and $A = 1 + 2m_Q^2 C_0$ and the constant $y = (Q_f^2 N_c^2 \alpha)/(\pi^3)$. 281

7.26 Squared matrix elements for the annihilation $\bar{\chi}\chi \to \gamma h$ process for various fermionic DM EFT operators, coupled to fermions with charge Q_f. We define $\Lambda_m = \Lambda(s) - \Lambda(m_h^2)$ and the constant $y = (Q_f^2 N_c^2 \alpha y_q^2)/(\pi^3)$. 281

7.27 The divergent loop diagrams responsible for mixing between the quark vector and axial vector currents $(\bar{\chi}\Gamma\chi\bar{q}\Gamma q)$ above the EW scale (top) and below (bottom). The most important aspect is the mixing of high-scale heavy quark currents $q = c, t$ onto light quark vector currents $q' = u, d$, thus enabling a strong scattering cross section with nuclei. 284

7.28 The effect of the RG running from a high scale $\Lambda = m_\phi$ down to the nuclear scattering scale $\mu_N = 1$ GeV, the running is slightly different above (right) and below (left) the EW scale (taken to be m_Z). 285

7.29 The DD bounds for three coupling choices, for a model in which χ_1 couples to u quarks only with strength D_{11}. Bounds for LUX and CMDSlite are solid (dashed), and the filled region shows the allowed parameters which give the correct relic abundance. Constraints are based on the dominant tree level contribution to scattering. 288

7.30 The Feynman diagrams for DM-gluon scattering in the DMFV model denoted (a)-(d) (from left to right). 289

7.31 The Feynman diagrams for DM-photon scattering in the DMFV model, denoted (a), (b) (from left to right). 299

7.32 The Feynman diagrams for DM-nuclear scattering via a single higgs exchange in the DMFV model. On the r.h.s we indicate that we take the EFT limit of the DM-h vertex and then consider the tree-level scattering. 309

7.33 The Feynman diagrams for DM-nuclear scattering via a single Z exchange in the DMFV model. On the r.h.s we indicate that we take the EFT of the DM-Z vertex and then consider the tree-level scattering. 310

7.34 SM couplings to the Z boson, $\mathcal{L} = (e/2s_W c_W) Z_\mu \bar{f}\gamma^\mu (g_{Z,v} - g_{Z,a}\gamma^5) f$. . 311

7.35 The differential scattering rate in recoil energy for DM-nuclear scattering from a xenon (top row, LUX) or a germanium (bottom row, CDMSlite) target. Each of the quark contributions are plotted separately, u, c, t indicated by red, blue and green lines. The rates are also separated according to the way in which they scatter; via quarks at tree level, via two gluon exchange, or via photon exchange (the magnetic monopole, charge-radius and anapole moments are separately plotted). The right column represents a model with very degenerate masses. 313

7.36 The exclusion on σ_{SI} (the standard WIMP-nucleon cross section) for LUX (dashed black line), compared to a likelihood ratio test applied to the method described in the text. 315

7.37 The data for CDMSlite, from Tab.1 of [20] for an exposure of 70.10 kg days. 318

7.38 The exclusion on σ_{SI} (the standard WIMP-nucleon cross section) for CDMSlite (dashed black line), compared to a likelihood ratio test applied to each energy bin (left) or a Poisson probability test (right), see text for details. The shaded bands include the uncertainty on the event counts from Tab.7.37. 319

7.39 ATLAS monojet bounds from [21] (solid lines) for a range of couplings to the up quark. The EFT approximation breaks down beneath the dashed lines (which are the $R_\Lambda = 0.5$ contours with $g \lesssim 4\pi$ from [22]), and so only the shaded regions between the solid and dashed lines can robustly be excluded using the EFT. 323

7.40 The dominant diagrams contributing to the pure monojet process. Each processes scales as $\sigma \propto \alpha'^2 \alpha_s$ where $\alpha' \sim \lambda\lambda^\dagger$ and can become extremely large if $\lambda > 1$. The cross section is dominated by the diagrams containing a heavy ϕ resonance. 327

7.41 Total cross section for the seven signal regions of the ATLAS monojet search [23] (top left) for two DM masses. Comparison to the CMS monojet search (top right) [24]. Also shown is the behaviour of the cross section with D_{33}, the top-quark coupling (bottom). 329

7.42 Exclusion regions (shaded) for the seven signal regions in the ATLAS (left) and CMS (right) monojet analysis, for no mixing ($\theta_{ij} = 0$) and equal couplings $D_{ii} = 2$. The strongest constraint comes from the $E_T > 450$ GeV bin. 330

7.43 The total cross section for the 1,2-jet process (left, right respectively) with varying DM mass and mediator width, the cuts are those for the CMS monojet search with $E_T > 250$ GeV, the corresponding limit is shown in grey. 330

7.44 The dominant processes contributing to the production of on-shell ϕ, which decay $\phi \to q_i \chi_j$ producing a dijet signal. In monojet analyses, this provides a subdominant contribution compared with pure monojet processes (Fig.7.40) in most of the parameter space. 332

7.45 Top : The visible dijet cross section assuming $\epsilon = 100\%$; for three DM masses and for the three signal regions from Tab.7.2 (for both $\sqrt{s} = 8, 13$ TeV, left and right respectively), grey lines correspond to the experimental limits. Bottom : Dijet bounds for the analyses discussed in the text, showing also the region excluded by relic density (shaded) for a benchmark set of parameters. 335

7.46 Left: the visible cross section assuming $\epsilon = 100\%$ for the ATLAS stop search [25]. Dashed grey lines denote the top production threshold. Right : constraint for the three signal regions and for $\epsilon = 50\%$. Since the coupling matrix λ is diagonal ($\theta_{ij} = 0$), the mediator must be heavy $m_\phi > m_{\chi,3} + m_t$. 337

7.47 Credible regions (2σ contours, corresponding to 95% containment) in the $m_\chi - m_\phi$ plane (left column) and $D_{ii} - m_\chi$ (right panels) where D_{ii} is the coupling associated to the DM candidate which may be χ_1 (top row), χ_2 (middle row) or χ_3 (bottom row). Two values of a mass splitting are chosen $2, 15\%$ which are shown with solid and dashed contours respectively. 351

7.48 As for Fig.7.47 but for the $D_{11} - D_{22}$ plane (left) and $D_{11} - D_{33}$ (right), for both $2, 15\%$ mass splitting (dashed shaded, and solid darker shaded respectively). 352

7.49 As for Fig.7.47 but for the $D_{22} - D_{33}$ plane. 353

7.50 Comparison between 2σ contours of the full MCMC scan and two extensions discussed in the text, for a mass splitting of 2% (left) or 15% (right). The top right plot does not include scenario (2) as there is no allowed phase space. 356

8.1 The possible size of duality violations, $\exp(-1/x)$, for several exclusive decay modes of a B meson, we vary the masses $m_b \in [4.18, 4.78]$ GeV and $m_c \in [0.975, 1.67]$ GeV and the hadronic scale $\Lambda \in [0.2, 2.0]$ GeV. In reality Λ is determined through an explicit calculation and the range we select represents the approximate range of values across the different observables. 364

8.2 The function Γ_{12} for the B_q^0 system arises from the *imaginary* part of the one loop diagram formed from the double insertion of the effective Hamiltonian, indicated by the cutting of the internal quark lines. . . 366

8.3 The theoretical predictions (left, [26, 27]) and experimental measurements (right, [28]), for various mixing quantities associated to the B_s and B_d systems. 367

8.4 Theoretical mixing observables for the B_q systems for Model 1 of duality violation. Note that $\Delta\Gamma_q$ is found from the first column multiplied by the ΔM_q of the SM given in Tab.8.3. 368

8.5 The 90% and 95% confidence limits (shaded blue and red respectively) on $\delta_{cc} - \delta_{uc}$ for duality violation Model 2, for the B_s system showing the allowed region stemming from the experimental measurement of $(\Delta\Gamma_s/\Delta M_s)$. The modification factors $a^s_{sl}/a^{s,\mathrm{SM}}_{sl}$ are shown as straight grey lines. 370

8.6 Left : comparison in the size of $\Delta\Gamma_d$ experimental limits (blue) which allows for sizeable contributions on top of the SM result (green). The inclusion of a duality violation *that does not also show up in the B_s system* (yellow) does not exceed the experimental limit, unless the experimental error shrinks in the future (orange). Right : the SM value of $a^{(s,d)}_{sl}$ are well known (black dot), but their experimental values less so (green and blue), with duality violation (red) there are bounds on a^d_{sl}, which can become important if in future the experimental error shrinks (purple). 371

8.7 The diagram leading to the calculation of the lifetime (Γ_B^{-1}) for the B^0_q system arises from the *imaginary* part of the one loop diagram formed from the double insertion of the effective Hamiltonian, indicated by the cutting of the internal quark lines. 372

8.8 Bounds on the duality violating parameter δ, the lifetime ratio of the B_s, B_d mesons varies with δ (red band). The current experimental error band (blue) is compared with two future scenarios outlined in the text in which the error band shrinks (purple), or the central value shifts towards 1 and the error shrinks (green). 376

8.9 The 95% confidence limits on the duality violating parameters δ_{ss}, δ_{sd} for fixed values of δ_{dd} arising from the comparison of $\Delta\Gamma_D$ between theory and experiment for the D^0 system. 380

A.1 The posterior distributions for D_{11}, D_{22} for both uniform and log-uniform priors, showing the credible 68% region (1σ). The log-uniform distribution favours low values compared to the uniform, and this can affect the results significantly. See Sec.7.9 for more details. 414

B.1 Dirac (left) or Majorana (right) annihilation into fermions via a neutral scalar mediator ϕ. . . . 416
B.2 Dirac (left) or Majorana (right) annihilation via a neutral vector mediator V. . . . 417
B.3 Dirac DM exchanging a charged scalar mediator, ϕ. Majorana DM includes an extra u-channel diagram. . . . 418
B.4 Dirac DM exchanging a charged vector mediator, V^μ. Majorana DM includes an extra u-channel diagram. . . . 419
B.5 Majorana DM and charged scalar mediator annihilation involving both t-channel and u-channel 420
B.6 Majorana DM and charged vector mediator, V^μ, annihilation involving both t-channel and u-channel. . . . 422
B.7 Scalar DM exchanging a scalar mediator. . . . 423
B.8 Scalar DM exchanging a neutral vector mediator. . . . 423
B.9 A scalar DM exchanging a charged fermion mediator in the t or u-channel. Complex scalar annihilate via t-channel, real scalar annihilate via both t and u-channels. . . . 424
B.10 Vector DM exchanging a neutral scalar mediator. . . . 426
B.11 Vector DM exchanging a neutral vector mediator. . . . 427
B.12 A vector DM exchanging a charged fermion mediator in the t or u-channel. Complex vector annihilate via t-channel, real vectors annihilate via both t and u-channels. . . . 429

List of Tables

2.1 Operators involving Dirac or Majorana fermion fields of mass dimension ≤ 4. Note that the Dirac equation for free fields may be used to reduce tree level operators, $i\partial\!\!\!/\chi = m\chi$, however couplings with derivatives are not included since they are dimension 4, and thus do not allow any couplings to the mediator or SM fields. 32

2.2 Operators involving real or complex scalar fields of mass dimension ≤ 4. 33

2.3 Operators involving real or complex vector fields of mass dimension ≤ 4, listed by their Lorentz indices. Note that $\partial^\mu B_\mu = 0$ from the Proca equation. 35

2.4 Each of the models considered in this study, along with their interaction Lagrangian with the SM fermions, f, denoted by $\mathrm{S}_{\mathrm{DM}}^{(*)} - \mathrm{S}_{\mathrm{MED}}^{(\pm)}$, where the DM spin $\mathrm{S}_{\mathrm{DM}} \in \{0, 1/2, 1\}$, the mediator spin $\mathrm{S}_{\mathrm{MED}} \in \{\mathrm{S}, \mathrm{F}, \mathrm{V}\}$ (denoting spin-0, spin-1/2 and spin-1 respectively) and a star on the DM spin (or $\pm$ on the mediator spin) indicates a complex DM/mediator field. Factors of $\left[\frac{1}{2}\right]$ applying to the real DM only, keep the Feynman rules consistent between real and complex DM. 38

3.1 The data used to produce ID constraints, their observational window in galactic coordinates, and the energy range of observed photons. In the case of Fermi-LAT data we used the binned data presented in [11], which was extracted from the publicly available Fermi-LAT data. 49

4.1 EFT operators appearing for spin-1/2 DM candidates. The set of heavy quark operators are identical to $\mathcal{O}_{F1-10}$ but with the quark bilinears replaced according to Eqs.(4.2.4)-(4.2.8) and denoted $\mathcal{O}_{GF1-10}$. 93

4.2 EFT operators appearing for Vector DM candidates. The set of heavy quark operators are identical to $\mathcal{O}_{V1-9}$ but with the quark bilinear replaced according to Eqs.(4.2.4)-(4.2.8) by a gluon current, and denoted $\mathcal{O}_{GV1-9}$. Operators $\mathcal{O}_{V5,V6}$ are redundant, but we include them in this list for completeness. The notation $\mathrm{Re}(\partial_\nu \bar{q}\gamma^\mu q) \equiv (\partial_\nu \bar{q})\gamma^\mu q + \bar{q}\gamma^\mu \partial_\nu q$. 97

4.3 EFT operators appearing for scalar DM candidates. The set of heavy quark operators are identical to $\mathcal{O}_{S1-4}$ but with the quark bilinear replaced according to Eqs.(4.2.4)-(4.2.8) and denoted $\mathcal{O}_{GS1-4}$. 100

4.4 The nucleon constants used in this study, all of which appear from nucleon matrix elements of quark or gluon operators. These can be found in [29] following the methods described in the text. 105

4.5 The NR operators considered in this study, along with their P-parity, T-parity, and whether or not they are spin-dependent. A reasonable upper (lower) recoil energy is $E_R \approx 50$ (1) keV, then $|\bar{q}| \approx 0.1$ (0.005) GeV (from $q^2 = 2m_T E_R$); for these energies the exponential suppression factor common to each of the form factors is ≈ 1. The approximate size of the form factors for a DM mass of 10 GeV and recoil energy of 1 keV is shown for two Xe isotopes in LUX. † : The operator $\mathcal{O}_2$ is neglected due to velocity suppression ($v^2 \approx 10^{-6}$), furthermore, it always appears alongside an operator less suppressed contributing to the same form factor. 121

4.6 Non-relativistic limit of fermion bilinears, $\bar{u}(p')\Gamma u(p)$ which are non-zero, and the $\mathcal{CPT}$ symmetries for the relativistic operators in the leftmost column. Any $\mathcal{C}$-odd structures are zero for Majorana particles. 126

4.7 Non-relativistic limit of vector bilinears which are non-zero. Because $B^0 = 0$ many of the operators only have spatial components, for which the replacements are $\mu \to i$, $\nu \to j$. The $\mathcal{C}$-odd structures necessarily vanish for real DM.
†, †† : Using the DM velocity v rather than $v^\perp$ the results are $i\frac{q^2}{2\mu}$ and $-i\frac{q^2}{2\mu}S^i_\chi$ respectively. 127

4.8 Non-relativistic limit of scalar bilinears which are non-zero, to lowest order in q, $v^\perp$.
†: Using the DM velocity v rather than $v^\perp$ the result is $i\frac{q^2}{2\mu}$. 127

4.9 The NR matching from each of the EFT operators in Tab.4.1 to the operators of Tab.4.5. The leading coefficients of the matching are also given, and the dominant contribution across all NR operators is shaded in blue. 128

4.10 As for Fig.4.9, but for the EFT operators in Tab.4.3 and 4.2. Operators $\mathcal{O}^{\rm EFT}_{V3-4}, \mathcal{O}^{\rm EFT}_{V4-4}$ do not match to any of the NR operators we consider. 129

4.11 The matching from the simplified models, listed in Tab.2.4, to the EFT operators from the spin-1/2 DM models, listed in Tab.4.1. Grey shading indicates the matching, the explicit coefficients are given in Sec.4.2.2. 130

4.12 The matching from the simplified models, listed in Tab.2.4, to the EFT operators (in Tab.4.3 and Tab.4.2) from the spin-0 DM models (upper) and spin-1 DM (lower). The matching coefficients can be found in Sec.4.2.4 and Sec.4.2.3. 130

4.13 The non-relativistic operators (columns) for direct detection that are obtained from the simplified models considered in this work (rows), as shown in Tab.2.4, along with their coupling dependence. For reference we have indicated the spin-dependent operators (SD). The full expressions for the NR operators are given in Table 4.5. Operator $\mathcal{O}^{(\rm NR)}_{13}$ has no matching within the models. 134

4.14 The 8 energy bins for PICASSO; their threshold energy, observed rate and error. 137

4.15 Parameters of current generation DD experiments; the energy window in nuclear recoil energy, the material, the exposure, and the total measured events along with their predicted background given by each collaboration. 139

5.1 The simplified models containing a vector field and which may violate unitarity, along with the tree-level $2 \to 2$ scattering processes containing at least one vector field. Assuming all vectors to be longitudinally polarized the leading dependence on S is shown for the dominant $j = 0$ partial wave amplitude squared, in the limit $S \to \infty$. 153

5.2 The allowed regions projected onto each of the parameters $m_{\rm DM}$, $m_{\rm MED}$ and g, for the spin-1/2 DM models with final state $\bar{u}u$, and coupling choices as shown, for a relic abundance $\Omega_\chi h^2 = \Omega_c h^2$. The lighter shading shows the allowed region if $\Omega_\chi h^2 > 0.9\ \Omega_c h^2$. 155

5.3 The possible configurations of couplings which lead to distinct behaviour of the ID and DD constraints for the models 1/2-S and 1/2*-S. The ID are either s-wave ($\langle\sigma v\rangle \propto v^0$) or p-wave suppressed ($\langle\sigma v\rangle \propto v^2$). The dominant operator for DD scattering is shown with any suppression in brackets. 157

5.4 As for Fig.5.2, but for spin-0 DM models with both $\bar{u}u$ and $\bar{b}b$ couplings. 173

5.5 As for Fig.5.2, but for spin-1 DM models with both $\bar{u}u$ and $\bar{b}b$ couplings. 183

5.6 The possible configurations of couplings which lead to distinct behaviour of the ID and DD constraints for the models 1-V and 1*-V, for the vertex structure (from top to bottom) $\mathcal{V}_{1,2,3,}$. The suppressions of each of the NR operators by q or $v^\perp$ is given in brackets. 191

6.1 Parameters of current generation experiments; the energy window is given for both electron equivalent energy and nuclear recoil energy. Also given; the exposure, and the total SM event yield for ER (pp neutrinos) and NR (^8B neutrinos), the numbers in brackets include the efficiency $\epsilon(E_R)$ which has a substantial effect. 212

6.2 Physical properties of idealized G2 (top 3 lines) and future experiments, with the expected total pp and ^8B neutrino events, based on planned masses of similar experiments and an exposure of 5 years. We give nominal and optimistic threshold energies and maxima for the energy windows based on the energy beyond which backgrounds are expected to dominate. 214

7.1 EFT operators in the DMFV model for a DM-quark scattering processes. 295

7.2 Top : Lower limits (at 95% CL) on the visible cross section for the Run 1 ATLAS dijet plus missing E_T search [30], for $\sqrt{s} = 8$ TeV and $\mathcal{L} = 20.3$ fb^{-1} and three signal regions (SR). Bottom : ATLAS dijet search from Run 2 [31]. 333

7.3 The four relevant signal regions from the ATLAS 2014 stop search [25] along with the cuts that are implemented. 336

7.4 Allowed ranges for the parameters used in the MCMC scan, along with the assumed prior likelihood, which is uniform on either a linear or logarithmic scale. 348

7.5 The 1D 1σ credible intervals for all 8 parameters of the MCMC scan. Colors denote the DM flavour (red, green and blue for up, charm and top DM respectively). The two prior choices on D_{ii} and the masses (log-uniform vs uniform) are shown as lines and shaded regions respectively, the modal average of the log-uniform prior choice is shown as a dot. The two mass splitting cases are contained in different panels. 354

7.6 The 1D 1σ credible intervals for the 6 parameters of extended scenario (1) in which the D_{ii} splitting are equal to the $\Delta m/m_\chi$. Colors denote the DM flavour (red, green and blue for up, charm and top DM respectively). The two prior choices on D_{ii} and the masses (log-uniform vs uniform) are shown as lines and shaded regions respectively, the modal average of the log-uniform prior choice is shown as a dot. The two mass splitting cases are contained in different panels. 358

7.7 The 1D 1σ credible intervals for a future scenario (2) in which the SM prediction for D^0 mixing matches the experimental value. Colors denote the DM flavour (red, green and blue for up, charm and top DM respectively). The two prior choices on D_{ii} and the masses (log-uniform vs uniform) are shown as lines and shaded regions respectively, the modal average of the log-uniform prior choice is shown as a dot. The two mass splitting cases are contained in different panels. The log-uniform results for the 15% splitting and up DM is not shown as no allowed parameter space is found. 359

8.1 Values and errors for the various physical parameters used throughout this chapter. The source for these values can be found in the text. We also give the relative contribution of each parameter to the total error on the lifetime ratio $\tau(B_s)/\tau(B_d)$ to compliment the discussion in the text. 383

A.1 $\mathcal{CPT}$ transformations of scalar (ϕ) and vector (B^μ) fields. Internal parity and time symmetries are taken to be $\eta_{P,T} = +1$. The matrices $P = \text{diag}(1, -1, -1, -1)$ and $T = \text{diag}(-1, 1, 1, 1)$. 388

A.2 The simplified models containing a vector field, along with the tree-level $2 \to 2$ scattering processes containing at least one vector field. Assuming all vectors to be longitudinally polarized and restricting to the dominant $J = 0$ partial wave, the leading dependence on S is shown when $S \to \infty$ is the largest scale. 402

Chapter 1

Dark Matter

1.1 The Evidence for Dark Matter

It is widely accepted that *Dark Matter* (DM) is omnipresent in our universe; evidence has been steadily building since the seminal application of the virial theorem to galaxy clusters by Fritz Zwicky in the 30s [32]. We now understand that dark matter is instrumental in cosmology, forming the largest structures from galaxies to their clusters. We will briefly review the observational evidence for the existence of dark matter.

1.1.1 Spiral Galaxies

In rotating spiral galaxies like the Milky Way, the rotation (or 'circular') velocity of stars $v_c(r)$ is radially dependent, and can be derived by simply requiring the gravitational potential to be responsible for the circular orbit (i.e. gravity provides the centripetal force)

$$v_c(r) = \sqrt{\frac{GM(r)}{r}}, \tag{1.1.1}$$

where the mass contained within radius r is given by

$$M(r) = \int \rho(r, \theta, \phi) r^2 \; d\phi \; d\cos\theta \; dr, \tag{1.1.2}$$

and $\rho(r, \theta, \phi)$ is the total matter density. Assuming $\rho(r)$ to be spherically symmetric, $M(r) = 4\pi \int \rho(r) r^2 dr$. It is possible to measure the mass distribution of luminous

matter, infer the circular velocity and compare with direct measurements based on doppler shifts of spectral lines.

It was first noticed in 1970 [33] for the Andromeda galaxy, and confirmed in later studies through the 80s and 90s (see for example [4], replicated in Fig.1.1) that the rotational velocity in the spiral galaxies was too large to be accounted for by the luminous matter alone, and that an extra halo of matter must exist. As shown in Fig.1.1 the rotational velocity is approximately flat at large radii, and from Eq.(1.1.1)-(1.1.2) this implies the DM density $\rho(r) \propto r^{-2}$ in its outer regions.

1.1.2 Elliptical Galaxies

The presence of DM may also be inferred from elliptical galaxies; which are usually a triaxial shape with chaotic stellar motions, compared with the ordered rotation of spiral galaxies. They have a compact central density of stars, and a much more extended density of ionized gas with a roughly uniform temperature T.

The temperature, T, of the gas can be inferred from its X-ray emission, leading to an estimate of the velocity dispersion via $\sigma^2 = k_B T/\mu m_p$, this would be of similar size to the stellar velocity dispersion, σ_*, if the gravitational potential is dominated by the gas and stars. The stellar velocity dispersion may be measured and compared with the assumption $T \propto \sigma_*^2$.

It is found that $T \propto \sigma_*^{1.45}$ in a sample of 27 ellipticals [34], and that this result is consistent with a dominant dark matter halo which increases the gravitational potential felt by the gas, and heats it up.

1.1.3 Galaxy Clusters

The largest observed structures in the universe are galaxy clusters, large gravitationally bound groups of $\mathcal{O}(10^1 - 10^3)$ galaxies. The dominant luminous matter component (around $10-15\%$ compared to a few percent from stars) comes from extremely hot ($T \sim 10^6 - 10^7$ K) X-ray emitting gas [35]; and this provides a handle on the mass of the visible baryonic matter since the X-rays produced by Bremsstrahlung radiation scale $\propto n^2$ where n is the electron number density.

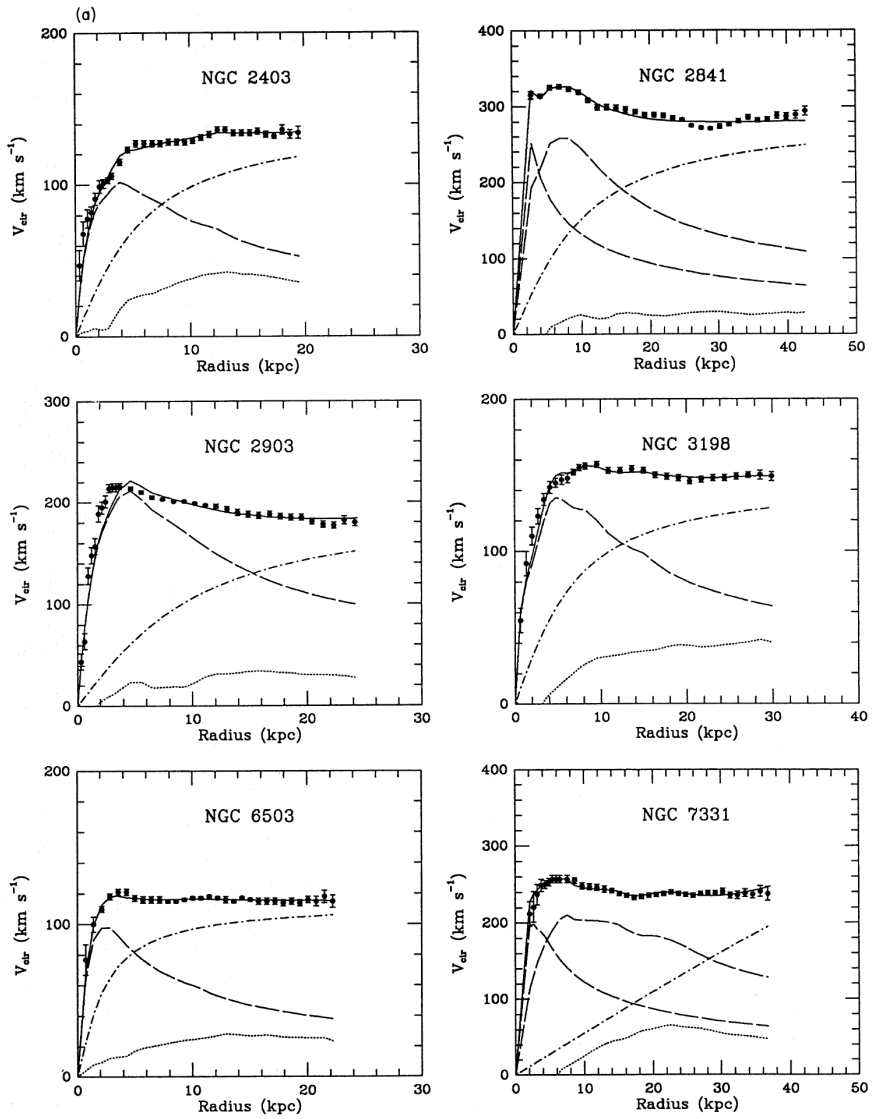

Figure 1.1: An example of galaxy rotation curves from [4]. The expected profile from the visible matter and gas in the disks (long-dashed and dotted lines respectively) clearly does not fit the data unless an additional halo of invisible matter (dot-dashed lines) is included to give the total contribution (solid line).

The velocity of galaxies in the cluster (measured using Doppler shifts) leads to the so called *dynamical mass*, $v(r)^2/2 = GM(r)/r$. This can be compared to the masses of clusters derived by other means, for example using luminosity-mass relations; it was found that the dynamical mass far exceeds the mass inferred from luminosities; without dark matter the clusters would not be gravitationally bound. This was in fact the very first observational hint for dark matter in 1937 [32].

With the theory of general relativity comes a phenomenon which can also be used to measure the mass of galaxy clusters. When light from a bright, distant galaxy travels to earth, it is bent under the gravitational influence of any intervening mass, if a large enough mass (say, a cluster) lies between us and the distant galaxy, the bending of the light can be very distinctive, resulting in very elongated concentric distortions and at the extreme of the effect, a point source of light can be lensed to appear as a perfect annulus (an *Einstein ring*). Effects like this are usually termed *strong lensing* to discriminate them from *weak lensing* which uses statistical information from many lensed galaxies when the effect is much weaker [36].

Ultimately, the mass of the lensing galaxies may be measured, and does not rely on the matter being visible, only that it gravitates. In this way gravitational lensing should include dark matter, and indeed it is observed that the mass inferred from lensing far exceeds that which is measured from X-ray emission. Even the X-ray gas itself demonstrates the existence of DM, since without the large gravitational well provided by the DM, the hot gas would dissipate.

A particularly striking example is given by the *Bullet Cluster*, which is actually the result of a collision between two clusters. The baryonic matter is visible from the X-ray emission, and the total mass is inferred from lensing; the resulting superposition of the data is shown in Fig.1.2 and shows that the baryonic matter (gas) has a smaller separation, as the frictional heating has slowed the gas. On the other hand, the weakly interacting dark matter is not impeded and has moved further apart than the baryonic matter.

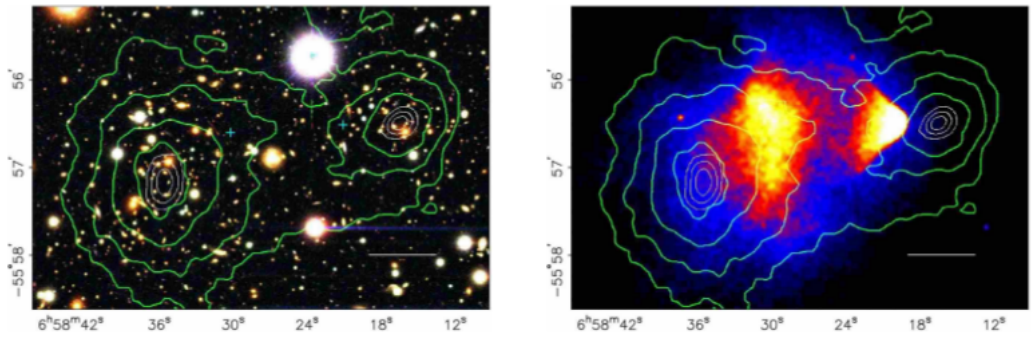

Figure 1.2: The bullet cluster from [5], the green contours (left and right) map the total mass as inferred from gravitational lensing. The red and blue (right) shows the distribution of X-ray emission from hot gas.

1.1.4 The CMB

Evidence for DM arises also at larger scales than the largest visible structures. After the Big Bang, initial density perturbations in the universe evolved according to coupled fluid equations which include the expansion of the universe [37, 38]. The Thomson scattering of photons from electrons left the universe opaque up until the recombination of electrons and ionized matter (at a redshift of around $z \sim 1100$, or $\sim 380,000$ years from the Big Bang), at which point the photons free-stream until their detection today[1]. The cosmological expansion has red-shifted these photons to microwave energies and they are referred to as the *Cosmic Microwave Background* (CMB), hypothesised in 1948 [39] and first discovered in 1964 [40]; recent measurements by Planck have yielded an unprecedented accuracy [41].

The three main components of the universe which dominate its evolution before recombination are dark matter, *baryons* (taken to mean all visible matter) and photons. Before recombination, Thomson scattering keeps baryons and photons tightly coupled, whereas the dark matter couples only gravitationally. The competing effects of the inward collapse of gravity created by baryons and dark matter, with the outward photon pressure permit sound waves in the baryon-photon fluid with a velocity $c_s \sim c/\sqrt{3}$ which is termed *Baryon Acoustic Oscillation* (BAO).

[1] Free streaming occurs if the gravitational potentials are flat, which they almost are. Deviations from this assumption may be caused by any remnant radiation perturbations for example.

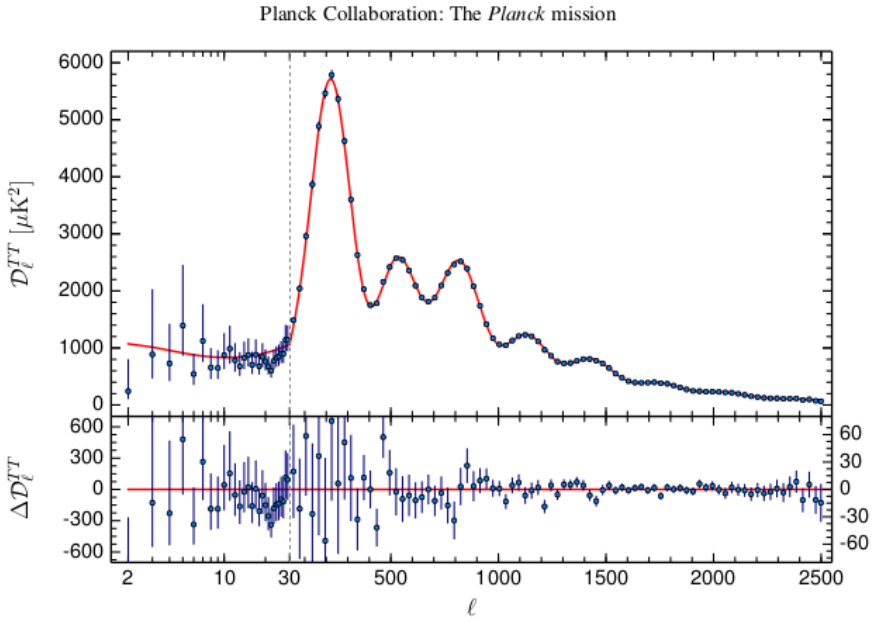

Figure 1.3: The CMB temperature power spectrum from [6].

The resulting spherical sound waves oscillate once they enter the *horizon* (the expanding causal 'edge' of the universe, i.e. the maximum distance travelled by light since the Big Bang), but are frozen in at recombination. For a given perturbation (denoted by its wavenumber, k, in a Fourier decomposition of the true perturbation) if the freeze in occurs at a maximum (minimum) of oscillation, then the resulting overdensity (underdensity) will create a peak in the CMB at angular scales which correspond to k.

The first peak in the CMB is thus formed from a perturbation which enters the horizon and oscillates to its first maximum. Higher peaks of the CMB have spent longer inside the horizon and completed more oscillations. Note that peaks alternate between overdense and underdense perturbations, thus we expect that the peaks corresponding to underdense perturbations are smaller, since due to the gravity of DM and baryons these regions tend to reduce their perturbation, compared with overdensities which will increase. Additionally higher peaks are damped by the photon fluid; high peaks correspond to small distances, which are washed out by the photons which have a finite mean-free path. The density perturbation present at recombination are manifest as tiny temperature fluctuations in the CMB photons, $\Delta T(\theta, \phi)/T$ (with $T = 2.75$), which is then decomposed into spherical harmonics of

multipole order l. The CMB spectrum itself is shown in Fig.1.3 from the Planck mission [6], the location and sizes of the peaks reveal a huge amount of information about our universe. The location of first peak ($l \sim 200$) is an indication of the curvature of the universe, consistent with $k = 0$ (flat). The height of the second peak determines the amount of regular matter in the universe $\sim 5\%$. The third peak can be used to determine the amount of DM, $\sim 26.8\%$, a *relic density* (to be defined shortly) $\Omega_c h^2 = 0.1199 \pm 0.0027$ [6].

1.1.5 Big Bang Nucleosynthesis

Big Bang Nucleosynthesis (BBN) is the study of how light elements formed from the primordial plasma of the Big Bang. At the time of the Big Bang, the universe is extremely hot and dense and any complex nuclei which are formed are immediately destroyed by high energy photons. However, below $z \lesssim 10^8$ (roughly a few minutes after the Big Bang)[2], nuclei may be formed.

First, neutrons and protons form at $T \gg 1$ MeV and the number densities are kept in equilibrium by the weak force, below $T \lesssim 1$ MeV the small mass difference between the two nucleons means equilibrium is no longer maintained and the neutrons freeze-out and roughly 85% decay to protons. Next, deuterium forms ($T \sim 0.1$ MeV) via $n + p \to D + \gamma$ followed by helium and lithium [42–44], reaction rates are too low to produce heavier elements (which are produced ultimately by stars and in supernova).

Theoretical studies into BBN began in 1940 [45] showing that these primordial abundances depend sensitively on the baryon-to-photon ratio $\eta = n_b/n_\gamma$, which itself gives the baryon fraction of the universe $\Omega_b h^2$. The measurement of these primordial elements (hydrogen, helium, deuterium D and lithium ^{7}Li) [46] shows remarkable agreement[3] with the theoretical prediction if the baryon fraction is $\Omega_b h^2 \approx 0.022$. The situation is summarized in Fig.1.4.

[2] In standard cosmology one can track the age of the universe by time t, scale factor a, redshift z, or temperature of the thermal bath T.

[3] With the exception of the measured Lithium abundance, which currently is not consistent with the others, see [47] for a recent review.

Comparing the inferred baryon fraction $\Omega_b h^2 \approx 2.2\%$ to the independently measured total matter fraction $\Omega_m h^2 \approx 14\%$ [6] gives strong evidence of a non-baryonic component of the universe, dark matter.

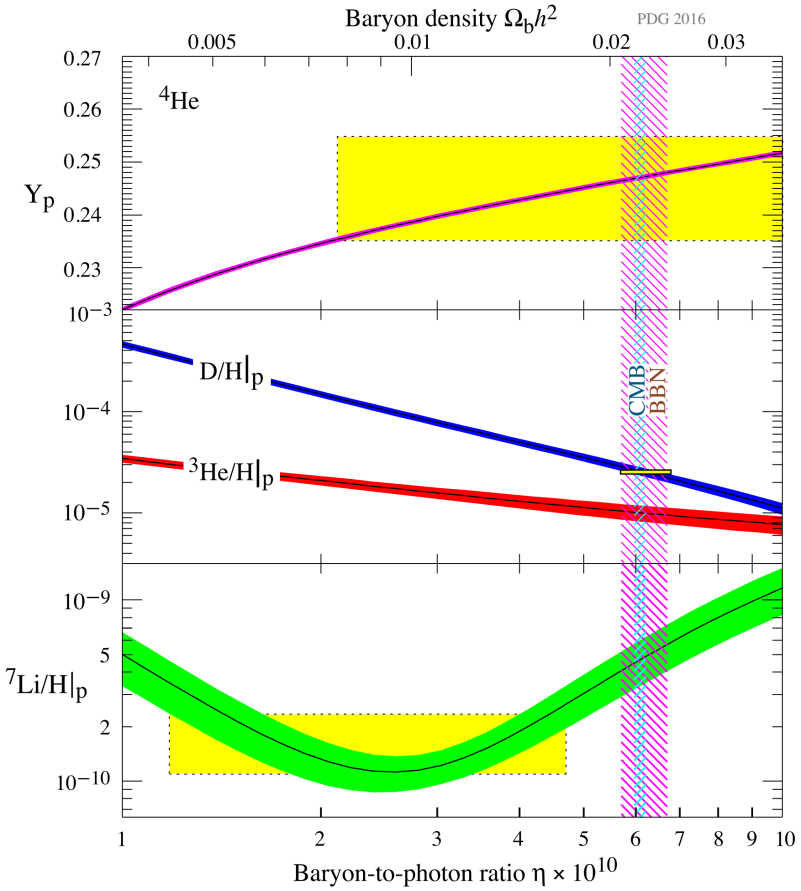

Figure 1.4: The various nuclei formed during BBN, as a function of the baryon fraction $\Omega_b h^2$ (or equivalently the photon to baryon ratio), the measured fractions are indicated by yellow rectangles. The CMB measurement of $\Omega_b h^2$ [6] is indicated by the blue band, and agrees well with the BBN concordance range (the purple band). Figure taken from [7].

1.2 Relic Density via Thermal Freeze-Out

We now turn to the question of how dark matter obtained its currently measured density. The most popular method is *thermal freeze-out*, where we remain agnostic to the creation of dark matter at the Big Bang and simply require it to be in thermal equilibrium initially. It also is required to interact with the particles of the standard

model, and the observed relic density provides a constraint on the nature and size of these interactions.

There are alternative mechanisms which generate the relic density, see for example [48]. Thermal freeze-in is closely related to freeze-out, but instead of being in equilibrium the DM has very weak interactions and cannot reach thermal equilibrium in the early universe before the expansion freezes the number density. In this case we would find $\Omega h^2 \propto \langle \sigma v \rangle$ (the latter quantifies the size of the interactions and will be explained in detail in the following section). The DM could also have such small interactions that it cannot be produced thermally at any stage, this *non-thermal* DM would have a relic abundance equal to the abundance that it was produced with.

We will now explain how to calculate the relic density through a freeze-out mechanism, as this calculation underpins a ubiquitous constraint on the DM parameter space throughout this thesis.

1.2.1 Cosmology Basics

We review some basic facts about cosmology which will be useful in what follows. The starting point for cosmology is the Friedman-Robertson-Walker (FRW) metric used to describe the evolution of the universe [4],

$$ds^2 = -dt^2 + a(t)^2 \left(dx^2 + x^2 d\theta^2 + x^2 \sin\theta^2 d\phi^2 \right) \ , \tag{1.2.3}$$

where x is the *comoving* radial coordinate (i.e. a particle which expands with the metric above sits at fixed comoving distance), and $a(t)$ is the *scale factor* which describes the expansion of the universe at time t, it is conventionally equal to 1 at present day, t_0.

The scale factor is related to the redshift via $1 + z = a(t)^{-1}$. The expansion rate of the universe, or Hubble rate, is given by $H(t) = \dot{a}/a$. The universe is composed of various fluids each with the usual fluid parameters of density and pressure evolving

[4] This is the FRW metric for a flat (curvature $k = 0$), homogeneous and isotropic universe. We will make this assumption, which is consistent with the measurement by Planck [6].

according to,

$$\dot{\rho} + 3H(t)(P + \rho) = 0 \ . \tag{1.2.4}$$

For cold non-relativistic matter (i.e. dark matter), $P = 0$, and thus $\rho \propto a^{-3}$. For relativistic radiation $P = \rho/3$, and $\rho \propto a^{-4}$. For vacuum energy $P = -\rho$, and $\rho = \text{const}$.

The Friedman equation for a universe of curvature k reads,

$$H^2 = \frac{8\pi G\rho}{3} - \frac{k}{a^2} \ . \tag{1.2.5}$$

The *critical density* ρ_c is defined as the density required for a spatially flat ($k = 0$) universe,

$$\rho_c \equiv \frac{8\pi G}{3H^2} \ , \tag{1.2.6}$$

then the dimensionless *density parameter* is defined as $\Omega \equiv \rho/\rho_c$, and the various components of the universe should add up to the critical density,

$$\Omega_m + \Omega_r + \Omega_\Lambda = 1 \ , \tag{1.2.7}$$

where $\Omega_{r,0} \sim 0$ is the radiation, $\Omega_{m,0} \sim 0.3$ is the cold matter (both baryonic and dark matter) and $\Omega_{\Lambda,0} \sim 0.7$ is dark energy. The subscript 0 indicates that these quantities are the present day values.

Each of the components evolves over the history of the universe. The universe was initially radiation dominated (after a period of inflation), by a combination of photons and neutrinos. At a redshift $z_{eq} \sim 3 \times 10^3$ the matter and radiation densities become equal, after that the universe becomes matter dominated and this continues to the present day. We are currently entering a phase of vacuum energy domination which began at $z \sim 0.7$.

1.2.2 Calculation of Relic Density

All the observational evidence for dark matter (DM) presented in the previous section relies on the gravitational influence of DM with itself and with baryonic matter and radiation. Of course there is no *a priori* reason to suspect that it should interact

through any of the forces of the Standard Model (SM), however we should hope that it does. Under the assumption that this is the case; then the couplings between DM and the SM particles influence its cosmological evolution.

The DM candidate, χ, may self-annihilate or decay, and in thermal equilibrium these processes balance the production of dark matter from the thermal bath of SM particles,

$$\text{Ann.} \ : \ \bar{\chi}\,\chi \leftrightarrow \overline{\text{SM}}\ \text{SM}\ , \tag{1.2.8}$$

$$\text{Dec.} \ : \ \chi \leftrightarrow \sum \ \text{SM}\ . \tag{1.2.9}$$

The measured abundance of DM in the universe today, $\Omega h^2 = 0.1199$, is an important quantity to be explained by any DM model. A DM particle which interacts with nothing would simply be diluted by the expansion of the universe, maintaining a fixed comoving number density, equal to its initial value. On the other hand, a massive particle which remains strongly coupled to the thermal bath would have no abundance today, having rapidly annihilated or decayed away once it became non-relativistic.

If the DM couples to the SM and we wish it to achieve the measured relic density, then the true picture of its evolution is somewhere between these two extremes. A DM candidate which interacts with the SM can undergo a process known as *thermal freeze-out*, obtaining a fixed value of Ωh^2 dependent upon the strength of its interactions.

The basic picture of thermal freeze-out is as follows (depicted in Fig.1.5): DM is assumed to be in thermal equilibrium in the very early universe, sharing a common temperature with the thermal bath of SM particles coupled by their interactions[5]. Therefore the DM initially maintains an equilibrium distribution. As the universe expands the number density is diluted, but equilibrium is maintained up until the point at which the interaction time, $(n\sigma v)^{-1}$[6] of the DM is roughly the same size

[5]It is further assumed that the DM is stable (it does not need to be absolutely stable, a weaker requirement is that its lifetime $\tau > t_0$ the age of the universe). The initial abundance of particle and anti-particle should also be equal, but this will be the case if the DM is in thermal equilibrium.

[6]For DM number density n, cross section σ and velocity v.

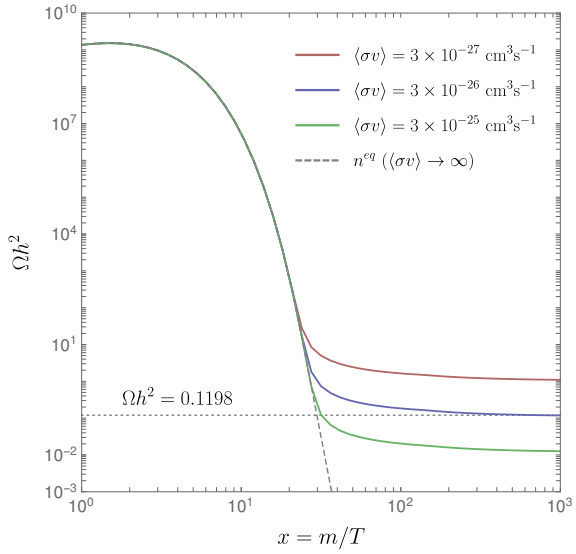

Figure 1.5: The DM comoving number density ($m_\chi = 500$ GeV). The equilibrium number density is shown as a dashed line, and rapidly drops as the DM transitions from relativistic to non-relativistic ($x \sim 1 - 10$). However the DM does not stay in equilibrium, as the expansion of the universe causes the interactions (annihilation of DM in this case) to cease, thus fixing the number density (the measured value is the dotted line). If the interactions are stronger, then the freeze-out occurs later (higher x) as the annihilation remain efficient for longer.

as the expansion time $H(t)^{-1}$. The DM then decouples from the thermal bath, and its comoving number density is *frozen in* to a fixed value, since no interactions are capable of reducing the number density. The relic density is very sensitive to the interaction rate, a large cross section leads to a later decoupling, and the equilibrium number density is a steeply falling function of temperature once the DM becomes non-relativistic (at $T < m_\chi$).

1.2.3 The Boltzmann Equation

Freeze-out is a non-equilibrium process dealing with coupled fluids and is therefore mathematically described by an appropriate Boltzmann equation. The derivation of this from a few basic assumptions can be found in cosmology textbooks [37, 38].

Following these references, we arrive at a simple form for the Boltzmann equation

for a massive DM particle which annihilates into pairs of SM particles,

$$\frac{\partial n}{\partial t} + 3H(t)n = -\langle\sigma v\rangle \left(n^2 - (n^{\rm eq})^2\right) , \tag{1.2.10}$$

where $n \equiv n(t)$ is the average DM number density and $n^{\rm eq}$ is the DM number density assuming thermal equilibrium, $H(t)$ is the Hubble parameter and $\langle\sigma v\rangle$ is the *thermally averaged annihilation cross section* (see Sec.1.2.5), summed over all kinematically allowed final states X,

$$\langle\sigma v\rangle = \left[\frac{1}{2}\right] \sum_{i,j,k,l} \langle\sigma v\rangle_{\chi_i\bar{\chi}_j \to X_k X_l} , \tag{1.2.11}$$

which allows co-annihilations if $i \neq j$ [49], the factor of $1/2$ is present only for non self-conjugate particles. However we will work under the assumption of a single DM candidate χ ($i = j = 1$). Since $H(t) = \dot{a}/a$, where $a(t)$ is the expansion parameter, we can rewrite Eq.(1.2.10)

$$\frac{\partial(na^3)}{\partial t} = -\langle\sigma v\rangle \left(a^3 n^2 - a^3 (n^{\rm eq})^2\right) . \tag{1.2.12}$$

It is useful to change variables to $Y(t) = n(t)/s$, the ratio of the DM number density to entropy density, s (and $s \propto a^{-3}$), which leads to ,

$$\frac{dY}{dt} = -s\langle\sigma v\rangle \left(Y^2 - Y_{eq}^2\right) , \tag{1.2.13}$$

then using the following result for the variable $x \equiv m/T$

$$\frac{dx}{dt} = -\frac{dT}{dt}\frac{m}{T^2} = -\frac{x^2}{m}\frac{dT}{dt} = Hx , \tag{1.2.14}$$

since $T \propto a^{-1}$ (we are assuming freeze out occurs in the radiation dominated era), then we can change the time variable in Eq.(1.2.13) to a temperature variable via the dimensionless variable x and the Boltzmann equation is written

$$\frac{dY}{dx} = \frac{dY}{dt}\frac{dt}{dx} = -\frac{s}{Hx}\langle\sigma v\rangle \left(Y^2 - Y_{eq}^2\right) . \tag{1.2.15}$$

We can parameterize the energy density and entropy as

$$\rho = g_{\rm eff}(T)\frac{\pi^2}{30}T^4, \quad s = h_{\rm eff}(T)\frac{2\pi^2}{45}T^3 , \tag{1.2.16}$$

where $g_{\text{eff}}, h_{\text{eff}}$ are the effective energy density and entropy degrees of freedom (see Sec.1.2.4). The Hubble parameter may be written

$$H = \sqrt{\frac{8}{3}\pi G\rho}\ . \tag{1.2.17}$$

Then Eq.(1.2.15) becomes,

$$\frac{dY}{dx} = -\frac{m_\chi \pi}{x^2}\sqrt{\frac{g_*(x)}{45G}}\,\langle\sigma v\rangle\,(Y^2 - Y_{eq}^2)\ , \tag{1.2.18}$$

where we define $\sqrt{g_*(T)} \equiv h_{\text{eff}}(T)/\sqrt{g_{\text{eff}}(T)}$. To find the DM density in the universe today, i.e. its 'frozen out' density, the DM must *freeze out* at some temperature $T = T_F$ ($x = x_F$). In the limit $x \gg x_F$ (i.e. long after freeze-out), the equilibrium yield Y_{eq} is negligible due to an exponential suppression,

$$\begin{aligned} Y_{eq}(x) = \frac{n_{eq}}{s} &= \frac{45 g_i}{4\pi^4}\frac{x^2 K_2(x)}{h_{\text{eff}}(T)} \\ &\approx \frac{45}{4\sqrt{2}\pi^{3.5}} x^{\frac{3}{2}} e^{-x}, \end{aligned}$$

this form for Y_{eq} can be found from the Boltzmann equation by setting $n = n_{eq}$.

Following [8], the Boltzmann equation Eq.(1.2.18), is written in terms of $\Delta = Y - Y_{eq}$,

$$\frac{d\Delta}{dx} + \frac{dY_{eq}}{dx} = -\frac{m}{x^2}\sqrt{\frac{g_*(x)\pi}{45G}}\,\langle\sigma v\rangle\,(\Delta^2 + 2\Delta Y_{eq})\ , \tag{1.2.19}$$

neglecting the x derivative of Δ (the true DM density tracks its equilibrium value well while interactions are efficient) the freeze out temperature T_F may be defined as the point at which $\Delta = \delta Y_{eq}$, with δ some number $\delta \approx \mathcal{O}(1)$, which leads to,

$$\left.\frac{dY_{eq}}{dx}\right|_{x=x_F} = -\frac{m}{x_F^2}\sqrt{\frac{g_*(x_F)\pi}{45G}}\,\langle\sigma v\rangle\,\delta(\delta+2)Y_{eq}(x_F)^2\ . \tag{1.2.20}$$

Note that $\langle\sigma v\rangle$ is also a function of x_F through any velocity dependence. Inserting Y_{eq} into the above equation leads to an equation for x_F only,

$$\sqrt{\frac{g_*(x_F)\pi}{45G}}\frac{45g}{4\pi^4} m_\chi\,\langle\sigma v\rangle\,\delta(\delta+2) = \frac{K_1(x_F)}{K_2(x_F)^2}, \tag{1.2.21}$$

which, given the asymptotic form of the modified Bessel functions of the second kind,

$$K_1(x) = K_2(x) \approx \sqrt{\frac{\pi}{2}}\frac{e^{-x}}{\sqrt{x}} \quad (x \to \infty) \ ,$$

leads to the approximate result for non-relativistic particles

$$e^{x_F} = \sqrt{\frac{45 g_*(x_F)}{8G}}\frac{m_\chi \delta(\delta+2)\langle\sigma v\rangle}{2\pi^3\sqrt{x_F}} \ . \tag{1.2.22}$$

Solving Eq.(1.2.22) numerically gives x_F. After freeze-out, the DM density scales as a^{-3} diluted only by the expansion. Thus Y_{eq} rapidly drops to zero as $(x \gg x_F)$ and can be neglected, allowing Eq.(1.2.15) to be integrated

$$\int \frac{dY}{Y^2} = -\int \frac{m_\chi \pi}{x^2}\sqrt{\frac{g_*(x)}{45G}}\langle\sigma v\rangle \ dx \ , \tag{1.2.23}$$

where the integral runs from freeze out, $x = x_F$, $Y = Y(x_F)$ to the present day $x = \infty$, $Y = Y_\infty$ we have,

$$-\frac{1}{Y_\infty} + \frac{1}{Y(x_F)} = -m_\chi\sqrt{\frac{\pi^2}{45G}}\int_{x_F}^{\infty}\frac{\sqrt{g_*(x)}\langle\sigma v\rangle}{x^2}\ dx \ .$$

The yield at freeze out is much larger than at the present day $Y(x_F) \gg Y_\infty$ and we can let $1/Y(x_F) \approx 0$, $\langle\sigma v\rangle \approx$ const, and $g_*(T) = g_*$

$$\frac{1}{Y_\infty} = m_\chi\sqrt{\frac{\pi^2}{45G}}\int_{x_F}^{\infty}\frac{\sqrt{g_*(x)}}{x^2}\langle\sigma v\rangle \ dx \approx \sqrt{g_*}\frac{m_\chi\langle\sigma v\rangle}{x_F}\sqrt{\frac{\pi^2}{45G}} \ , \tag{1.2.24}$$

under the approximation that both $\langle\sigma v\rangle$ and g_* are independent of x. Once a value of x_F is established, Eq.(1.2.24) gives the present day yield. From this we find the number density, and thus mass density $\rho_0 = m_\chi Y_\infty s$. The relic density is calculated from

$$\Omega h^2 = \frac{\rho_0}{\rho_{c,0}}h^2 = \frac{m_\chi s_0 Y_\infty h^2}{\rho_c} \ . \tag{1.2.25}$$

The present day entropy density is $s_0 = h_{\text{eff}}(T_0)\frac{2\pi^2}{45}T_0^3 \approx 35\ \text{K}^3$, and the present day critical density $\rho_{c,0} = 3h^2/(8\pi G)$ leading to,

$$\Omega h^2 = \frac{h_{\text{eff}}(T_0)}{g_*(T_F)}\frac{16\pi^3}{9}\frac{T_0^3 x_F}{\langle\sigma v\rangle}\sqrt{\frac{G^3}{5}} \ . \tag{1.2.26}$$

Eq.(1.2.26) is a central result, allowing the calculation of the DM relic density from a general particle physics model (which determines $\langle\sigma v\rangle$). It provides the well known scaling $\Omega h^2 \propto 1/\langle\sigma v\rangle$, since large cross sections lead to a DM which decouples later, allowing its number density to drop further before freeze-out.

We will now elaborate the discussion to a few of the important quantities that enter into the calculation.

1.2.4 Effective Degrees of Freedom

The solution to a Boltzmann equation always produces a *phase space function*, $f(\theta_i)$, that describes the fluid, and which depends on some kinematical variables θ_i (for example position and momentum), and which has the interpretation of the fractional number of particles with variables in the range $\theta_i + d\theta_i$. A relativistic particle has six degrees of freedom from its position $\mathbf{r}$ and momentum $\mathbf{p}$, in equilibrium the solutions to the Boltzmann equation in vacuum yield the familiar Fermi-Dirac (FD) and Bose-Einstein (BE) distributions,

$$f_{\rm eq}(\mathbf{r},\mathbf{p}) = \frac{1}{e^{\beta E} \pm 1} \ , \tag{1.2.27}$$

where the $+$ is the FD, and $-$ is the BE distribution describing fermions and bosons respectively. If the particles are non-relativistic then $E \approx m$ and $\beta = (k_B T)^{-1} \gg m$, then the exponential dominates in the above expression and both distributions approximate to the Boltzmann distribution $f(\mathbf{p}) = e^{-\beta E}$, with $E(\mathbf{p}) = \sqrt{m^2 + |\mathbf{p}|^2}$.

All thermodynamic quantities can be found once the phase space distribution is known. A particular quantity O, for example density or pressure, is found in the usual way as the expectation value, integrated over all states,

$$\langle\mathcal{O}\rangle = \int \frac{d^3\mathbf{p}}{(2\pi)^3}\mathcal{O}(\mathbf{p})f(\mathbf{p}) \ . \tag{1.2.28}$$

In particular number density, energy density, and pressure are given by,

$$n \equiv \langle 1 \rangle = g \int \frac{d^3\mathbf{p}}{(2\pi)^3} f(\mathbf{p}) \ , \tag{1.2.29}$$

$$\rho \equiv \langle E \rangle = g \int \frac{d^3\mathbf{p}}{(2\pi)^3} E f(\mathbf{p}) \ , \tag{1.2.30}$$

$$P = g \int \frac{d^3\mathbf{p}}{(2\pi)^3} \frac{|\mathbf{p}|^2}{3E} f(\mathbf{p}) \ , \tag{1.2.31}$$

where g is the degeneracy of the particle (the number of spin states). For relativistic particles in equilibrium $P = \rho/3$, entropy density $s = (\rho + P)/T = 4\rho/3T$, and from Eq.(1.2.27) we derive,

$$\text{Bosons} \begin{cases} \rho = & g\frac{\pi^2}{30}T^4 \\ n = & g\frac{\zeta(3)}{\pi^2}T^3 \\ s = & g\frac{2\pi^2}{45}T^3 \end{cases} \qquad \text{Fermions} \begin{cases} \rho = & g\frac{7}{8}\frac{\pi^2}{30}T^4 \\ n = & g\frac{3}{4}\frac{\zeta(3)}{\pi^2}T^3 \\ s = & g\frac{7}{8}\frac{2\pi^2}{45}T^3 \end{cases} . \tag{1.2.32}$$

The energy density and entropy may be more generally defined by,

$$\rho = g_{\text{eff}}(T)\frac{\pi^2 T^4}{30} \ ; \ g_{\text{eff}}(T) = \sum_{c,d} g_c(T) + g_d(T),$$
$$s = h_{\text{eff}}(T)\frac{2\pi^2 T^3}{45} \ ; \ h_{\text{eff}}(T) = \sum_{c,d} h_c(T) + g_d(T), \tag{1.2.33}$$

where the sum extends over all particle species (c) which are coupled and therefore in thermal equilibrium sharing a common temperature T, and those which have decoupled (d).

Once a particle decouples at temperature T_{d_i} (its interaction rate drops below the expansion rate of the universe, in exactly the same way that DM freezes out), its temperature T_i will differ from the thermal bath. The decoupled species will nonetheless maintain an equilibrium distribution of temperature T_i which evolves as $T_i \propto a^{-1}, a^{-2}$ for massless and massive particles respectively.

If a particle becomes non-relativistic ($T_i \lesssim m_i$), then its behaviour changes drastically, in particular its number density exponentially decreases. Although not necessarily decoupled, a particle that becomes non-relativistic will no longer contribute to the effective degrees of freedom. It is reasonable also to take $T \sim m_i/20$

for the temperature at which a particular species becomes non-relativistic.

For relativistic particles in thermal equilibrium with common temperature T (i.e. coupled) and internal degrees of freedom[7] g_i,

$$g_{\rm c}(T) = \sum_{\rm bosons} g_i + \frac{7}{8} \sum_{\rm fermions} g_i \ . \tag{1.2.34}$$

We also include any species which decouple at a temperature $T_{d_i} > T$, which modifies the result by a factor $(T_i/T)^4$ to account for the dilution of density,

$$g_{\rm d}(T) = \sum_{\rm bosons} g_i \left(\frac{T_i}{T}\right)^4 + \frac{7}{8} \sum_{\rm fermions} g_i \left(\frac{T_i}{T}\right)^4 \ . \tag{1.2.35}$$

For relativistic particles in thermal equilibrium $P = \rho/3$, then from the definition of entropy density $s = (P + \rho)/T$ we find that $h_{\rm c} = g_{\rm c}$ for the coupled species and so $g_* = \sqrt{g_{\rm eff}}$. However for relativistic decoupled particles we have,

$$h_{\rm d}(T) = \sum_{\rm bosons} g_i \left(\frac{T_i}{T}\right)^3 + \frac{7}{8} \sum_{\rm fermions} g_i \left(\frac{T_i}{T}\right)^3 , \tag{1.2.36}$$

and the scaling behaviour with temperature prevents a simple definition of g_*.

In the Standard Model (SM) before any particles decouple, $g_{\rm eff}(T \gtrsim 300 \text{ GeV}) \approx h_{\rm eff} = 106.75$, below $T \sim 1.0$ MeV the neutrinos are decoupled, but $g_{\rm eff}(T \lesssim 1.0 \text{ MeV}) = 3.38$ remains constant with T since the neutrino temperature tracks the photon temperature $T_\nu = (4/11)^{1/3} T$ (also $h_{\rm eff}(T \lesssim 1.0\text{MeV}) = 3.94$ due to the T^3 temperature dependence). The temperature dependence of $g_*(T)$ is shown in Fig.1.6.

1.2.5 Thermally Averaged Cross Section

The *thermally averaged annihilation cross section*, $\langle \sigma v_{\rm rel} \rangle$, is a central quantity in the calculation of DM relic density, and the interactions of DM in a cosmological setting which may lead to indirect signals for its detection. It can be tricky to

[7] For fermions $g_i = 2$, for spin-1 particles such as the photon $g_i = 3$ and for spin-0 particles $g_i = 1$

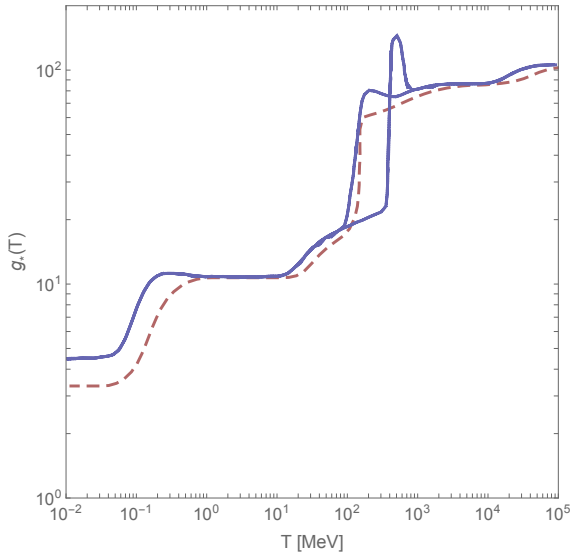

Figure 1.6: The effective degrees of freedom $g_*(T) = h_{\text{eff}}^2/g_{\text{eff}}$ as defined in Eq.(1.2.33). Assuming $h_{\text{eff}} = g_{\text{eff}}$ gives the red dashed line. The blue lines are taken from [8] and are more accurate; including the full temperature dependence of h_{eff} and also accounting for the QCD phase transition at $T = 150$ MeV (upper line) or 400 MeV (lower line). The actual quantity that appears in the formulae is $\sqrt{g_*}$ and so the approximate curve is sufficiently accurate. At the highest temperatures, all the SM degrees of freedom are coupled to the thermal bath, as the universe cools these decouple at $T \sim m$ until only the photons and neutrinos remain.

calculate without making some sensible approximations, we review these briefly now.

We begin by recalling the general formula for the cross section of a $2 \to n$ annihilation,

$$\sigma v_{\rm rel} = \frac{1}{4E_1E_2}\int d\Pi \, \langle |\mathcal{M}|^2 \rangle \ , \tag{1.2.37}$$

where E_1 and E_2 are the fixed energies of the incoming particles with relative velocity $v_{\rm rel} = |\mathbf{v}_1 - \mathbf{v}_2|$, $\langle |\mathcal{M}|^2 \rangle$ is the spin-averaged and squared matrix element of the process, integrated over the Lorentz invariant phase space which is given by,

$$d\Pi = \prod_i^n \frac{d^3\mathbf{p}_i}{(2\pi)^3 2E_i}(2\pi)^4\delta^4\left(p_1 + p_2 - \sum_i^n p_i\right) \ . \tag{1.2.38}$$

For $n = 2$ final state particles with masses $m_{3,4}$ and momentum $p_{3,4}$, and two incoming, identical particles of mass m_χ and momentum $p_{1,2}$ the cross section can be written (in the centre of mass, 'COM' or 'CM', frame),

$$\frac{d\sigma}{d\Omega} = \frac{\langle |\mathcal{M}|^2 \rangle}{64\pi^2 s}\frac{|\mathbf{p}_3|}{|\mathbf{p}_1|} \ . \tag{1.2.39}$$

The differential quantity depends on two independent variables, which are conveniently taken to be the s, t Mandelstam variables. In the centre of mass frame these variables may be expanded in the velocity v of one of the incoming particles,

$$s = 4m_\chi^2(1 + v^2) + \mathcal{O}(v^4), \tag{1.2.40}$$

$$t = (m_f^2 - m_\chi^2) + 2m_\chi \cos\theta v\sqrt{m_\chi^2 - m_f^2} - 2m_\chi^2 v^2 + \mathcal{O}(v^3). \tag{1.2.41}$$

The integration in angles Ω thus yields σv to the desired order in $v = v_{\rm rel}^{\rm (CM)}/2$. One then inserts the thermally averaged value of velocity, $\langle v_{\rm rel}^n \rangle$ to obtain an approximate value of $\langle \sigma v_{\rm rel} \rangle$. For example, in the cosmological context and the calculation of relic density $\langle v^2 \rangle \approx \frac{3}{2x}$ and $\langle v^4 \rangle \approx \frac{15}{8x^2}$ (recall $x = m/T$),

$$\langle \sigma v \rangle = \langle \sigma v \rangle_s + \frac{3}{2x}\langle \sigma v \rangle_p + \frac{15}{8x^2}\langle \sigma v \rangle_d + \cdots \ . \tag{1.2.42}$$

The subscripts on the terms in this expansion indicate the nomenclature; s-wave annihilation has no velocity dependence, p-wave annihilation is proportional to v^2, d-wave to v^4 and so on. Alternatively, in the galactic center at the present day

$v_{\rm rel} \sim 10^{-3}$ (in reality, the radially dependent DM distribution causes a radially dependent velocity, but the approximation of constant velocity will be acceptable for our purposes). For relic density calculations, the cross section is evaluated at freeze-out and thermal averaging of Eq.(1.2.37) may be written as[8]

$$\langle \sigma v_{\rm rel} \rangle = \frac{\int_0^\infty dv_r v_r^2 (\sigma v_r) e^{-v_r^2/4x}}{\int dv_r v_r^2 e^{-v_r^2/4x}} \ . \tag{1.2.44}$$

A typical value for freeze-out is $x_F \sim 20 - 30$, which leads to velocities $v_{\rm rel} \sim c/4$ and thus relativistic corrections may become important. A more rigorous treatment is given in [8]. Eq.(1.2.37) is valid for particles with fixed incoming energies, the thermal averaging arises because the incoming energies are not fixed, but instead are described by the phase space distribution that comes from the solution of the Boltzmann equation. Using the Maxwell-Boltzmann distribution leads to Eq.(1.2.44), using a generic phase space function f modifies Eq.(1.2.37) to

$$\langle \sigma v_{\rm rel} \rangle = \frac{1}{n_1 n_2} \int \frac{d^3\mathbf{p}_1}{E_1} \frac{d^3\mathbf{p}_2}{E_2} f(\mathbf{p}_1) f(\mathbf{p}_2) \int d\Pi \, \langle |\mathcal{M}|^2 \rangle \ , \tag{1.2.45}$$

where $n_i = \int d^3\mathbf{p}_i f(\mathbf{p}_i)$. Since the DM is non-relativistic at decoupling, it is suitable to use the Maxwell-Boltzman distribution, $f(\mathbf{p}) \propto \exp(-E/T)$, rather than Fermi-Dirac or Bose-Einstein. After some algebra this yields an equation,

$$\langle \sigma v_{\rm rel} \rangle = \frac{1}{8 m_\chi^4 T K_2^2(m_\chi/T)} \int_{4m_\chi^2}^\infty \sigma(s - 4m_\chi^2) \sqrt{s} K_1(\sqrt{s}/T) ds \ . \tag{1.2.46}$$

This is especially useful for cross sections near to a resonance (i.e. when the cross section is enhanced at $s = 4m_\chi^2$), resonances are commonly seen in models with s-channel annihilation via a single mediator, and this is one of the contexts in which they appear in this thesis. Mediators with large decay widths have suppressed resonances, and in those cases Eq.(1.2.44) provides a suitable approximation.

[8] The relevant distribution is Maxwell-Boltzmann [50] with relative velocity v_r,

$$f_{\rm MB}(v_r) = \frac{x^{3/2}}{\sqrt{4\pi}} v_r^2 e^{-\frac{v_r^2 x}{4}} \ , \tag{1.2.43}$$

however in reality the distribution is only approximately Maxwell-Boltzmann, due to deviations from spherical symmetry of the DM distribution in the galaxy.

We make one final note, the correct velocity to use in the thermal averaging is known the *Møller velocity* defined by (for two incoming particles of different mass) [8, 50][9]

$$v_{\rm mol} = \frac{\sqrt{(p_1 \cdot p_2)^2 - m_1^2 m_2^2}}{E_1 E_2} \,, \tag{1.2.47}$$

the advantage of this definition is that it is Lorentz covariant, and thus applies in the centre of mass frame and lab frames. The relative velocity (defined in any frame) is $v_{\rm rel} = |v_1 - v_2|$, in the CM frame $v_{\rm rel}^{\rm (CM)} = 2v$ where v is the velocity of one of the particles, whereas in the lab frame $v_{\rm rel}^{\rm (lab)} = v$. On the other hand the Møller velocity is $v_{\rm mol}^{\rm (CM)} = 2v$ and $v_{\rm mol}^{\rm (lab)} = v$ in the CM and lab frame respectively. Thus the relative velocity in the lab and CM frames are equivalent to the Møller velocity.

An additional constraint that occurs for models with thermal freeze-out is the partial wave unitary of the scattering matrix [51], this is model independent and sets $m_\chi \lesssim 100 - 500$ TeV. We will generally not consider such large masses.

1.3 Outline of this Thesis

This thesis is split into three distinct themes, the first body of work covers Chapter 2-5 and covers a broad analysis of dark matter models using the low energy probes of indirect and direct detections. The second theme involves the study of new physics in the neutrino sector, specifically for the future generation of direct detection experiments. The third theme deviates from dark matter, and instead explores the idea of duality violation in the context of heavy flavour physics.

Content summaries can be found at the start of the respective chapters but we provide a very brief summary here also.

[9] or equivalently,

$$v_{\rm mol} = \sqrt{|v_1 - v_2|^2 - |v_1 \times v_2|^2},$$

where $\mathbf{p}_i = \gamma_i m_i v_i$ and $E_i = \gamma_i m_i$ with $\gamma_i = (1 - |v_i|^2)^{-1/2}$.

In Chapter 2 we will provide an introduction to the study of simplified models of dark matter, which provide a very useful framework for comparing constraints on DM models, without the rigour and complexity of theoretically motivated models such as the *Minimal Supersymmetric Standard Model* (MSSM). We will provide a list of assumptions on such models and then a complete list of such models which will be considered in the following four chapters.

In Chapter 3 we will examine indirect detection constraints on simplified models. We provide a detailed description of the calculation for one important such signal, gamma-rays from the galactic centre. We conclude by summarizing the most powerful constraints in the literature.

In Chapter 4 we review and collate in detail the full calculation of direct detection signals of dark matter. We work with the effective field theory limit of the simplified models and give a detailed calculation of the matching procedure between the two. We conclude by analysing a set of relevant *Direct Detection* (DD) experiments and some example bounds.

In Chapter 5 we present the results of applying the bounds from indirect and direct searches to the simplified models and discuss the remaining parameter space which may be explored in future, by collider searches for example.

In Chapter 6 we will build on the work in Chapter 4 and consider the application of DD experiments to neutrino physics, the mediating particles used in simplified models of Dark Matter may in general couple independently to neutrinos, thus giving the possibility of new neutrino interactions with matter that could be detected in the upcoming generation of DD machines. We explore these ideas and present concrete constraints on some general models that can be expected in future.

In Chapter 7 we will investigate a simplified model in depth, tackling each of the assumptions that are made in Chapter 5.

Finally, in Chapter 8 we take a detour from the discussion of Dark Matter to investigate another phenomenon, which arises in heavy flavour physics. There are many precision measurements and also many discrepancies with the SM present in the heavy flavour sector, with so much effort put into explaining these with some

new BSM physics (dark matter among the explanations), we instead investigate the idea that the explanation lies in the methods we use to perform the calculations, perhaps the assumption of duality between the low energy (hadronic) and high energy (quarks and gluons) level is violated by some degree. After a careful analysis we present limits on the size of duality violation that might either explain some discrepancies (for example the lifetime of the neutral charm meson D^0) or else violate some precision measurements (for example the heavy neutral B^0 meson lifetimes).

Chapter 2

Simplified Models of Dark Matter

In this short chapter, we briefly motivate the use of *simplified models* in the framework of dark matter (Sec.2.1), and provide a list of conditions we impose on the models in Sec.2.2. With this in mind, we construct a list of 16 models to consider in this study in Tab.2.4.

2.1 The Paradigm of Simplified Models

In the modern era of experimental particle physics, the search for new physics from a theoretical perspective proceeds in two complementary ways. One may pursue a *top-down* approach, whereby a well motivated concrete model is constructed. Such a model is often sufficiently complex to require many assumptions, to reduce the parameter space to a manageable size and thus direct experimental searches into a narrow enough scope to detect or falsify the model. Examples of 'complete' models include the Minimal Supersymmetric Standard Model (MSSM) [52, 53], Little Higgs models [54], or Universal Extra Dimensions [55] to name only a few.

An alternative approach is *bottom-up*. One tries to remain agnostic as to the correct realisation of the physics, and with a few basic assumptions, builds a simple set of models which capture the relevant phenomenology at detectors, whilst leaving the parameter space sufficiently small to make definite statements about the detectability of the models. In essence, one sacrifices motivation and theoretical

rigour and clarity for a broader approach which simultaneously covers many complete realizations but which stands less chance of missing interesting phenomenology and thus maximizes the utility of the experimental data.

Effective Fields Theories (EFTs) are a common bottom-up approach, these are distinct from simplified models because they contain non-renormalizable operators (those with mass dimension higher than 4), whereas simplified models are UV complete, in the sense that the theory is renormalizable and does not require the addition of any new physics below a sufficiently high scale Λ_{simp}. Then if one matches the simplified model onto an EFT, an operator of mass dimension $n > 4$ is suppressed by some energy scale Λ^{4-n}, this scale parametrizes roughly the energy scale of processes for which the effective theory breaks down, for energies $E < \Lambda$ the EFT gives a good approximate description of the theory but for $E > \Lambda$ there must be some new physics which can no longer be ignored and which invalidates the EFT prediction, and UV completes the model. In simplified models Λ is identified with the mass of a heavy particle.

In simple situations $\Lambda = m_X$ is the mass of some new particle X. A classic example is that of the weak interactions, whose Lagrangian includes the EFT operator responsible for four-lepton interactions

$$\mathcal{O}_{\text{weak}} = G_F \bar{L}\gamma^\mu L \bar{L}\gamma_\mu L \ , \tag{2.1.1}$$

which has mass dimension 6 and is therefore suppressed by two powers of the W-boson mass, $\Lambda^{-2} \equiv m_W^{-2}$. At low energies (for example in β-decay) the above operator describes the process very well. This is not the case for high energy processes, such as very high energy electron-electron scattering (where $s > m_W^2$ with s the centre of mass energy squared) for which one must include the W explicitly.

In simplified models, the DM does not interact directly with the SM, it belongs to the hidden sector which is connected to the SM sector via some mediating sector which in its most simple guise is a single particle. The mediator mass, m_{med}, is generally very large and so an appropriate EFT description follows from integrating

out the mediator. The EFT thus provides a very good description of the theory if the new particles which UV-complete the model are very heavy, or at least heavier than the typical energy scales involved in the process. This is very often true for direct detection since the DM is highly non-relativistic, the momentum exchanges involved in scattering are $q \sim \mathcal{O}(100)$ keV and the EFT remains valid for mediator masses above the GeV scale, similarly in indirect detection through the annihilation of DM the total energy available to the annihilation products is $E \sim 2m_{\rm DM}$ and so the EFT is valid so long as $m_{\rm med} \gg m_{\rm DM}$. EFTs have been widely used for their simplicity and easy application to wide ranges of signals[56, 57]. The EFT approximation can break down if the new physics is at a sufficiently low scale as to become comparable to energy scales of a particular experiment. This would be most pronounced at high-energy collider experiments like the LHC, which is why simplified models recently received so much attention in this context [58–61] (see [62] for an extensive list of references). If the new particles are light (sub-GeV, which we consider in Chapter 6) they will show up at even lower energy detectors.

Therefore, even though one may use EFTs for indirect and direct searches, they cannot be compared with collider searches unless one specifies the UV completion. Simplified models therefore provide the basis for such a comparison. Each UV complete model gives a unique matching to EFT operators for use in low-energy signals.

Another advantage of simplified models is that they are a simple example of many important and ubiquitous phenomenological considerations for the aspiring model builder. Using them emphasises the aspects of the phenomenology that may be applied generally to particular classes of models (for example, all models with a heavy neutral vector mediator coupling to quarks), which may not be elucidated when considering more complete, more rigorous and thus more complex models. They serve to inform the experimental community of the important search regions, without encumbering them with unnecessary details of particular models.

Early attempts at building such a framework began by considering collider

bounds [63, 64], questioning the validity of EFTs and concluding that such an approach can lead to inaccurate results [65–68]. Recently, the models have been developed and applied more broadly, allowing comparison of bounds from all available energy scales [58, 69, 70]. More recently still, the ability for such models to be obtained from UV-complete models without the introduction of important new effects has been called into question [71–74].

In order to lay down the basic ground rules for building simplified models, we borrow from [75] and adhere to the following criteria[1]:

1. **The DM candidate is stable**. This means preventing any DM decay, which can often be achieved by the addition of a $\mathbb{Z}_2$ symmetry under which the DM is charged oppositely to one of its potential decay products. In the models with s-channel annihilation there is no allowed decay; in models with t-channel annihilation we impose that the mediator mass is larger than the DM to prevent a decay DM $\rightarrow$ MED + SM.

2. The Lagrangian contains all terms consistent with Lorentz invariance and renormalizability.

3. Operators from (2) should not violate any exact or accidental symmetries of the SM.

The final point necessarily includes the SM gauge symmetries, the global baryon and lepton number symmetries. The approximate flavour symmetry in the quark sector should also be respected to avoid bounds from precision flavour observables; this restriction can be relaxed using the *minimal flavour violation* (MFV) assumption [76, 77], which allows flavour breaking operators, as long as they are proportional to the quark Yukawa matrices, or CKM matrix since this is the origin of flavour breaking in the SM. MFV is not a necessary requirement, but is commonly implemented

[1] In reality, both (2) and (3) are frequently broken to some extent, the four-scalar (e.g. mediator or DM self-interactions or Higgs couplings) and four-vector operators are generally neglected and MFV and $SU(2)_L$ are explicitly broken in our examples. Both of these represent potential inaccuracies in the model, and we address them for a specific model in Chapter 7.

to avoid bounds from flavour physics on flavour-violating effects, which can be quite strong.

This list is certainly not exhaustive, and as we provide more details of the models we will make many more working assumptions, each of which will be mentioned in this chapter.

2.2 Simplified Models for this Study

Since no direct measurement of DM outside of its gravitational effects has been made, the spin of the DM is unconstrained. The criteria of simplified models then dictates that we consider all possible spins, although we require the spin to be ≤ 1 since all known particles fulfil this criteria. Spin-3/2 DM has been considered in the context of EFTs in [78].

We thus focus on three general types of dark matter particles, namely a spin-0 (which we will refer to as *scalar* or *pseudoscalar*, depending on their coupling structure, and which also may be real or complex), spin-1/2 (fermionic DM may be either *Dirac* or *Majorana*, the fermionic equivalent of a real particle), and finally we may consider a massive spin-1 vector boson (which may be real or complex). This exhausts all possibilities for spin less that 3/2.

Strong constraints exist for DM which is charged under the SM gauge group of $\mathrm{U(1)_Y} \otimes \mathrm{SU(2)_L} \otimes \mathrm{SU(3)_c}$ (hypercharge, weak isospin and color charge), and it is therefore safe to assume that the DM is a gauge singlet. Of course, it is still possible to allow the DM to have a small SM charge, see for example the "milli charged dark matter" class of models [79–83]. In the case of neutral DM, couplings must be to SM gauge singlet fields or field combinations.

In order to couple the DM sector to the SM sector we introduce one further particle which we refer to as a *mediator*, since it mediates an interaction between the

SM and DM. Like the DM, the mediator has arbitrary spin, and we do not impose that it must be neutral under the SM gauge group; however we are dealing with low energy probes in this work (direct and indirect detection, compared with say, LHC signals which could be sensitive to physics above the EW scale), the relevant gauge group below the electroweak scale is $U(1)_{EM} \otimes SU(3)_c$. Using this gauge group simplifies the model building, but it should be noted that above the EW scale an $SU(2)_L$ invariant simplified model should be used which is then matched to our set of models, this may not be trivial and it may not be possible to uniquely match between the models in a 1-1 fashion[2]. This limitation to our approach is analogous to that between our models and the conventional set of EFT operators, and we do caution that as pointed out very recently, the requirement of gauge invariance above EWSB does restrict the parameter space in non-trivial ways [72].

In principle we can construct models with multiple DM candidates and multiple mediators, but we will consider individual models which contain a single DM and single mediator. For each of these DM candidates, we will consider interactions through: a neutral or charged spin-0 scalar (denoted S and $S^{\pm}$ respectively) a neutral or charged spin-1 vector (denoted V or $V^{\pm}$), or finally a charged fermion denoted $F^{\pm}$. We let the DM interact with only one of these mediators at a time, thus avoiding interference terms between different mediators (such interference terms can lead to very different phenomenology; see e.g. [84]). The precise set of available mediators is dictated by the constraints of Lorentz invariance and renormalizability (mass dimension less than or equal to four) in the Lagrangian terms of the simplified model. This leads to 4 spin-0 DM models, 6 spin-1 and 6 spin 1/2 models. These are discussed in more detail in the following sections.

We have in mind the production of the DM relic density through thermal freeze-

[2]The models with neutral mediators can easily be extended to be $SU(2)_L$ invariant (however they necessitate a coupling to both up and down type quarks), however for the charged mediator models it is a little trickier, since for LH fermions the DM or mediator must become an $SU(2)_L$ doublet, and this introduces additional particles to the model.

out as per Chapter 1; this allows for the possibility of either decaying DM (with interactions of the form DM $\rightarrow \sum$SM) or annihilating DM (DM DM $\rightarrow$ SM SM). We will deal with the latter type and with SM being fermions (i.e. leptons and quarks), thus requiring for *processes* like annihilation and scattering that the DM interact with the SM in pairs.

2.2.1 Fermionic DM Couplings

Commonly, DM candidates have spin-1/2, which we denote χ. Many concrete theories like supersymmetry allow for such DM (for example the Majorana neutralino [85] or axino [86, 87] DM). Dirac DM arises in a phenomenological setting in for example, [88, 89].

The basic building block for Lorentz invariant Lagrangian operators is a bilinear $\bar{\psi}_1 \Gamma \psi_2$, where Γ is a matrix in spinor-space, i.e. a 4×4 matrix which can be written as a linear combination of the 16 basis matrices :

$$\Gamma \in \{1, \gamma^5, \gamma^\mu, \gamma^\mu\gamma^5, \sigma^{\mu\nu}\} \ , \tag{2.2.2}$$

where $\sigma^{\mu\nu} = i/2\,[\gamma^\mu, \gamma^\nu]$, these may also be contracted with the Levi-Civita tensor $\epsilon^{\mu\nu\sigma\rho}$ or derivatives. However, neither can give renormalizable theories since the derivative adds a mass dimension and the Levi-Civita tensor has two or more uncontracted indices. Since the fermion bilinear has mass dimension 3, each renormalisable Lagrangian term can only contain a single bilinear (it is not possible to have a fermionic DM and fermionic mediator coupled to SM fermions). These basic buildings blocks are listed in Tab.2.1.

	Dirac Fermion	Majorana Fermion
$\Gamma_\chi^{(i)}$	$\bar{\chi}\chi\ ,\ \ \bar{\chi}i\gamma^5\chi$	$\bar{\chi}\chi\ ,\ \ \bar{\chi}i\gamma^5\chi$
$\Gamma_\chi^{(i),\mu}$	$\bar{\chi}\gamma^\mu\chi\ ,\ \bar{\chi}\gamma^\mu\gamma^5\chi$	$\bar{\chi}\gamma^\mu\gamma^5\chi$
$\Gamma_\chi^{(i),\mu\nu}$	$\bar{\chi}\sigma^{\mu\nu}\chi, \bar{\chi}i\sigma^{\mu\nu}\gamma^5\chi$	$\bar{\chi}i\sigma^{\mu\nu}\gamma^5\chi$

Table 2.1: Operators involving Dirac or Majorana fermion fields of mass dimension ≤ 4. Note that the Dirac equation for free fields may be used to reduce tree level operators, $i\partial\!\!\!/\chi = m\chi$, however couplings with derivatives are not included since they are dimension 4, and thus do not allow any couplings to the mediator or SM fields.

The above bilinears all couple to objects with mass dimension 1, i.e. a scalar or vector boson, except for the tensor bilinear which cannot couple in a renormalizable way[3].

The kinetic and mass terms read,

$$\begin{aligned}\mathcal{L}_{\text{kin}} = &\ \bar{\chi}i\partial\!\!\!/\chi - m_\chi\bar{\chi}\chi + \frac{1}{2}\bar{\chi}_m i\partial\!\!\!/\chi_m - \frac{1}{2}m_{\chi_m}\bar{\chi}_m\chi_m \\ &+ (D^\mu\mathcal{S})^\dagger D_\mu\mathcal{S} - m_{\mathcal{S}}^2\mathcal{S}^\dagger\mathcal{S} - \frac{1}{2}\mathcal{X}^{\dagger,\mu\nu}\mathcal{X}_{\mu\nu} + m_{\mathcal{X}}^2\mathcal{X}^{\dagger,\mu}\mathcal{X}_\mu \\ &+ (\partial^\mu S)^\dagger\partial_\mu S - m_S^2 S^\dagger S - \frac{1}{2}X^{\dagger,\mu\nu}X_{\mu\nu} + m_X^2 X^{\dagger,\mu}X_\mu\ ,\end{aligned} \tag{2.2.3}$$

where we denote the Majorana field with a subscript, the $\mathcal{S}$ and $\mathcal{X}^\mu$ are complex scalar and vector mediator fields charged under the SM gauge group and S, X^μ are the corresponding neutral particles. Eq.(2.2.3) leads to a possible set of interactions for Dirac fields,

$$\begin{aligned}\mathcal{L}_{\text{int}} = &\ \bar{\chi}\left(g_s + ig_p\gamma^5\right)\chi S + \bar{\chi}\gamma^\mu\left(g_v + g_a\gamma^5\right)\chi X_\mu \\ &+ \left(\bar{\chi}\left(g_s' + ig_p'\gamma^5\right)f\mathcal{S}^\dagger + \bar{\chi}\gamma^\mu\left(g_v' + g_a'\gamma^5\right)F\mathcal{X}_\mu^\dagger + \text{h.c.}\right)\ .\end{aligned} \tag{2.2.4}$$

For Majorana fields the terms are identical but with $g_v = g_v' = 0$, the charged mediators couple to SM fermions f and therefore have the same electric and color charges. The couplings $g_{s,p,v,a}$ must all be real, whilst $g'_{s,p,v,a}$ are in general complex.

[3]Except to a tensor field $T^{\mu\nu}$, which we do not consider here. However spin-2 mediators are considered in [90, 91]

Vector mediators X^μ naturally arise for example in kinetic mixing scenarios [80, 92–94], or *gauged B-L* models (for a review see [95]). Although mediator self-interactions are possible S^3, S^4 and $(X^\mu X_\mu)^2, (\mathcal{X}^\mu \mathcal{X}_\mu)^2$ these will not impact the signals considered in this thesis.

2.2.2 Scalar DM Couplings

Spin-0 DM candidates, denoted ϕ if $\phi^\dagger = \phi$ (i.e. a real field) or Φ for a complex field, have received much attention in the literature [96–99]. A good example of a concrete model is the *axion* [100, 101], originally proposed as a solution to the strong CP problem in QCD [102, 103].

The building blocks of Lagrangians involving scalar fields (and their derivatives) are listed below in Tab.2.2 separated into Lorentz scalars, vectors and tensors.

	Real Scalar	Complex Scalar
$\Gamma^{(i)}_{\phi,\Phi}$	$\phi^n,\ n \leq 4$	$\Phi^\dagger\Phi\ , (\Phi^\dagger\Phi)^2\ , \Phi^{(\dagger),n},\ n \leq 4$
$\Gamma^{(i),\mu}_{\phi,\Phi}$	$\phi\partial^\mu\phi$	$\mathrm{Re}(\Phi^\dagger\partial^\mu\Phi)\ ,\ \mathrm{iIm}(\Phi^\dagger\partial^\mu\Phi)$
$\Gamma^{(i),\mu\nu}_{\phi,\Phi}$	$\partial^\mu\partial^\nu\phi\ ,\ \phi\partial^\mu\partial^\nu\phi\ ,\ \partial^\mu\phi\partial^\nu\phi$	$\mathrm{Re/iIm}(\Phi\partial^\mu\partial^\nu\Phi^\dagger)\ ,\ \mathrm{Re/iIm}(\partial^\mu\Phi^\dagger\partial^\nu\Phi)$

Table 2.2: Operators involving real or complex scalar fields of mass dimension ≤ 4.

Other operators of mass dimension 4 or less will reduce to those above from a combination of integration by parts, and the Klein-Gordan equation $\partial^\mu\partial_\mu\phi = m^2\phi$. Operators of mass dimension 4 cannot couple to other particles, those of mass dimension 3 can couple to another scalar (for $\Gamma^{(2)}_\phi$) or a vector (for $\Gamma^{(1),\mu}_\phi$, $\Gamma^{(1,2),\mu}_\Phi$). Those of mass dimension 2 may couple to another operator of dimension 2.

The scalar DM have kinetic and mass terms,

$$\mathcal{L}_{\mathrm{kin}} = \frac{1}{2}\partial_\mu\phi\partial^\mu\phi - \frac{1}{2}m_\phi^2\phi^2 + \partial^\mu\Phi^\dagger\partial_\mu\Phi - m_\Phi^2\Phi^\dagger\Phi\ , \tag{2.2.5}$$

and the renormalizable interaction Lagrangian is,

$$\mathcal{L}_{\text{int}} = g_\chi \Lambda \phi \phi S + i g_\chi \text{Im}(\Phi^\dagger \partial^\mu \Phi) X_\mu + \left(\phi \bar{F}(g_s + i g_p \gamma^5) f + \text{h.c.}\right) + \phi^2 S^2 + \phi^3 S + \Phi^\dagger \Phi S^2 + \phi^2 X^\mu X_\mu + \Phi^\dagger \Phi X^\mu X_\mu \ , \quad (2.2.6)$$

the terms coupling the scalar mediator S contain a scale Λ which is in principle arbitrary, we let $\Lambda = m_\phi$, however this can always be modified by an appropriate rescaling of g_χ. The third term involves only a single DM, and couples to a fermion bilinear which contains an SM fermion, f and a fermionic mediator F (necessarily charged).

Finally, there are three-point (ϕSS, $\phi X^\mu X_\mu$) and four-point interactions between the DM and scalar or vector mediator. In general, when coupled to the SM, such operators lead to scattering and annihilation cross sections which are loop suppressed and we disregard these operators. Above the EW scale terms such as $\Phi^\dagger \Phi H^\dagger H$ may be present, where H is the SM Higgs $\text{SU}(2)_\text{L}$ doublet, a *Higgs portal* model [99, 104, 105] will create the effective operator $(m_q/m_h^2)\Phi^\dagger \Phi \bar{q} q$, suppressed by powers of the Higgs mass. Thus, we are neglecting some important phenomenology which must be left to further studies, there is nothing explicitly wrong with this but it is not in the spirit of simplified models.

2.2.3 Vector DM Couplings

Real or complex vector DM, denoted B^μ and $\mathcal{B}^\mu$ respectively, has received comparatively little attention, perhaps because there are fewer complete models which include them. However such models do exist, for example Minimal Universal Extra Dimensions [106, 107], Randall-Sundrum models [108] or Littlest Higgs[109–111] or as a gauge field [112–114] (see also [115] and references therein). In the context of simplified models these also present the largest set of possible operators, and for expository studies of general phenomenology it is much simpler to work with spin-0 or spin-1/2.

Tab.2.3 lists the relevant operators built from vector fields,

	Real Vector	Complex Vector
$\Gamma^{(i)}_{B,\mathcal{B}}$	$B^\mu B_\mu$	$\mathcal{B}^\mu \mathcal{B}^\dagger_\mu$
	$\partial^\mu (B_\nu B^\nu)$, $B^\nu \partial_\nu B^\mu$	$\partial^\mu(\mathcal{B}^\dagger_\nu \mathcal{B}^\nu)$, $\mathrm{Re}(\mathcal{B}^{\nu,\dagger}\partial_\nu \mathcal{B}^\mu)$, $\mathrm{iIm}(\mathcal{B}^{\nu,\dagger}\partial_\nu \mathcal{B}^\mu)$
$\Gamma^{(i),\mu}_{B,\mathcal{B}}$	B^μ , $\epsilon^{\mu\nu\sigma\rho} B_\nu \partial_\sigma B_\rho$	$\mathcal{B}^{(\dagger),\mu}$, $\mathrm{Re}(\mathcal{B}^{\nu,\dagger}\partial^\mu \mathcal{B}_\nu)$, $\mathrm{iIm}(\mathcal{B}^{\nu,\dagger}\partial^\mu \mathcal{B}_\nu)$
		$\epsilon^{\mu\nu\sigma\rho}\mathrm{Re}(\mathcal{B}^\dagger_\nu \partial_\sigma \mathcal{B}_\rho)$, $\mathrm{i}\epsilon^{\mu\nu\sigma\rho}\mathrm{Im}(\mathcal{B}^\dagger_\nu \partial_\sigma \mathcal{B}_\rho)$
$\Gamma^{(i),\mu\nu}_{B,\mathcal{B}}$	$\partial^\mu B^\nu$, $\partial^\nu B^\mu$	$\partial^\mu \mathcal{B}^\nu$, $\partial^\nu \mathcal{B}^\mu$

Table 2.3: Operators involving real or complex vector fields of mass dimension ≤ 4, listed by their Lorentz indices. Note that $\partial^\mu B_\mu = 0$ from the Proca equation.

The Lorentz vectors which are bilinear in the fields, $\Gamma^{(i),\mu}_{B,\mathcal{B}}$, may couple to a neutral spin-1 mediator X^μ in a renormalizable way, and similarly $\Gamma^{(i)}_{B,\mathcal{B}}$ may couple to a neutral scalar mediator S, however there can be no coupling to a single neutral fermion, instead the fermion F is charged, and the vertex also includes an SM fermion. When contracting with a vector X^μ, $\Gamma^{(2),\mu}_{B}$ and $\Gamma^{(2,5),\mu}_{\mathcal{B}}$ are zero.

The kinetic terms for the massive vector fields are

$$\mathcal{L}_{\mathrm{kin}} = -\frac{1}{4}B^{\mu\nu}B_{\mu\nu} + \frac{1}{2}m_B^2 B^\mu B_\mu - \frac{1}{2}\mathcal{B}^{\dagger,\mu\nu}\mathcal{B}_{\mu\nu} + m_{\mathcal{B}}^2 \mathcal{B}^{\dagger,\mu}\mathcal{B}_\mu, \tag{2.2.7}$$

where $B^{\mu\nu} = \partial^\mu B^\nu - \partial^\nu B^\mu$ is the field strength tensor for B^μ, and similarly for $\mathcal{B}^\mu$.

The renormalizable interaction Lagrangian contains the terms

$$\begin{aligned}
\mathcal{L}_{\mathrm{int}} = {} & g_{BS}\Lambda S B^\mu B_\mu + g_{\mathcal{B}S}\Lambda S \mathcal{B}^\mu \mathcal{B}^\dagger_\mu \\
& + g_{BX,1}\mathrm{Re}\left(B^\nu \partial_\nu B^\mu\right) X_\mu + \left(g_{\mathcal{B}X,1}\mathcal{B}^{\nu,\dagger}\partial_\nu \mathcal{B}^\mu X_\mu + \mathrm{h.c.}\right) \\
& + \epsilon^{\mu\nu\sigma\rho}\left(g_{\mathcal{B}X,3}\mathcal{B}^\dagger_\mu \partial_\nu \mathcal{B}_\sigma + \mathrm{h.c}\right) X_\rho + \epsilon^{\mu\nu\sigma\rho}\left(g_{BX,3}B^\dagger_\mu \partial_\nu B_\sigma + \mathrm{h.c}\right) X_\rho \\
& + i g_{\mathcal{B}X,2}\mathrm{Im}(\mathcal{B}^{\nu,\dagger}\partial_\nu \mathcal{B}^\mu)\mathrm{X}_\mu + \mathrm{ig}_{\mathcal{B}\mathrm{X},2}\mathrm{Im}(\mathcal{B}^{\nu,\dagger}\partial^\mu \mathcal{B}_\nu)\mathrm{X}_\mu \\
& + \left(\bar{F}\gamma^\mu(g^{(f)}_{B,v} + g^{(f)}_{B,a}\gamma^5) f B_\mu + \mathrm{h.c}\right) + \left(\bar{F}\gamma^\mu(g^{(f)}_{\mathcal{B},v} + g^{(f)}_{\mathcal{B},a}\gamma^5) f \mathcal{B}^\dagger_\mu + \mathrm{h.c}\right) ,
\end{aligned} \tag{2.2.8}$$

where Λ is an arbitrary mass scale, and f an SM fermion. Models of this form have been considered in several places [12, 113, 114, 116, 117]. Since we do not consider complex and real vector DM simultaneously we will drop the $\mathcal{B}$ notation, and use B

for both, implicitly referring to complex DM when hermitian conjugation is used.

As with the scalar DM case, four-vector operators may appear $(B_\mu^\dagger B^\mu)(B_\nu^\dagger B^\nu)$, or $(X^\mu X_\mu)(B_\nu^\dagger B^\nu)$, $(S^\dagger S)(B_\nu^\dagger B^\nu)$, but we ignore them since they involve more than one mediator. They generally lead to loop suppressed contributions to signals, however could become relevant for processes in which the tree level contribution is small.

2.2.4 Standard Model Couplings to the Hidden Sector

We have already listed several operators which couple the SM and DM sectors directly, however there are several operators which couple the DM to the mediator, and thus require couplings between the mediator and the SM.

In typical bounds considered in this thesis, detection energies are below the electroweak (EW) scale, and thus the h, $W^\pm, Z, t$ are integrated out of the SM Lagrangian; leaving the leptons $l = e, \mu, \tau, \nu_e, \nu_\mu, \nu_\tau$ and quarks $q = u, d, s, c, b$ [4], along with the photon and gluon fields A^μ and G^μ. The relevant gauge-invariant operators are[5],

$$\begin{aligned}
\Gamma^{(i)}_{\rm SM} &= \bar{l}l \ , \ \bar{q}q \ , \ \bar{l}\gamma^5 l \ , \ \bar{q}\gamma^5 q, \\
\Gamma^{(i),\mu}_{\rm SM} &= \bar{l}\gamma^\mu l \ , \ \bar{q}\gamma^\mu q \ , \ \bar{l}\gamma^\mu\gamma^5 l \ , \ \bar{q}\gamma^\mu\gamma^5 q \ , \ D^\mu, \\
\Gamma^{(i),\mu\nu}_{\rm SM} &= F^{\mu\nu} \ , \ \widetilde{F}^{\mu\nu} \ , \ G^{\mu\nu} \ , \ \widetilde{G}^{\mu\nu} \ , \ \bar{l}\sigma^{\mu\nu} l \ , \ \bar{q}\sigma^{\mu\nu} q \ ,
\end{aligned} \tag{2.2.9}$$

where $F^{\mu\nu} = \partial^\mu A^\nu - \partial^\nu A^\mu$ ($G^{\mu\nu}$) is the photon (gluon) field strength, $\widetilde{F}^{\mu\nu} = (1/2)\epsilon^{\mu\nu\sigma\rho}F_{\sigma\rho}$ its dual field strength, and $D^\mu = \partial^\mu - ieQA^\mu - ig_s G^\mu$ is the covariant derivative for a color triplet fermion with electric charge Q. The tensor field strengths cannot form renormalizable couplings with scalar, fermion or real vector DM, however with complex vector DM the possibility of tree level magnetic and

[4] We will not be considering neutrinos in this study, and the notation f will refer to quarks and leptons (excluding neutrinos). The notation Q will refer to heavy quarks $Q = c, b, t$ and q to either light quarks or all quarks, depending on the context.

[5] Above the EW scale, the relevant fields are left handed quark and lepton doublets, right handed lepton and quark singlets, the higgs doublet H, and hypercharge and $\mathrm{SU}(2)_L$ gauge fields B^μ, $\bar{W}^\mu$

electric dipole moments exists $\mathcal{B}_\mu^\dagger \mathcal{B}_\nu F^{\mu\nu}$ and $\mathcal{B}_\mu^\dagger \mathcal{B}_\nu \widetilde{F}^{\mu\nu}$ respectively.

The couplings between charged mediators and SM fermions have already been listed, the neutral spin-0 and spin-1 mediators couple to the SM as,

$$\mathcal{L}_{\text{int}} = \bar{f}\left(g_{f,s} + ig_{f,p}\gamma^5\right) fS + \bar{f}\gamma^\mu\left(g_{f,v} + g_{f,a}\gamma^5\right) fX_\mu \ , \tag{2.2.10}$$

with $g_{f,i}$ are all real, note that we take $g_{f,(s,p)}$ to be mass independent, but in line with the MFV assumption it is required that they mimic the Yukawa couplings and are thus proportional to the ratio of the fermion mass to some scale (which would be the vev of S) [69], we do not make this assumption but in all of our results it is simple to scale the couplings and recover the Yukawa-like behaviour if required. Combining Eq.(2.2.10) above, with the interaction Lagrangians Eq.(2.2.4), Eq.(2.2.6) and Eq.(2.2.8), we produce a set of models which we will use in our study, and whose Lagrangians are reproduced in Tab.2.4, and each of which are considered independently.

When referring to our models we will use the notation "DM spin - mediator". Unstarred labels on the DM side refer to real DM particles (or Majorana fermion), while in the starred case they are complex (or Dirac fermion). A $\pm$ superscript the mediator on the right hand side means that the particle is charged under the same gauge group as the SM fermions to which it couples.

2.3 Conclusions

The purpose of this chapter is to establish a basis of models of WIMP DM, which can be used to explore the 'model space' of DM. We have done this from the ground up, forming all possible renormalizable and Lorentz invariant interactions between DM and SM fermions, with a single extra mediating field. The spin of the DM and mediator have been left completely arbitrary, and both are allowed to be either real or complex. The conditions of a hermitian Lagrangian, which is Lorentz invariant and renormalizable (mass dimension four) is quite restrictive, and separating models into those with single DM and mediator combinations leads to 16 models. With the

DM	Model	$\mathcal{L}_{\rm int}$ terms
Scalar	0-S, 0*-S	$\left[\frac{1}{2}\right] g_\chi \Lambda \phi^\dagger \phi S + \bar{f}\left(g_s^{(f)} + i g_p^{(q)} \gamma^5\right) f S$
	0*-V	$g_\chi \left(i\phi^\dagger \partial^\mu \phi + \text{h.c.}\right) V_\mu + \bar{f}\gamma^\mu \left(g_v^{(f)} + g_a^{(f)}\gamma^5\right) f V_\mu$
(ϕ)	0-F$^\pm$, 0*-F$^\pm$	$\left(\bar{F}\left(g_s^{(f)} + i g_p^{(f)}\gamma^5\right) f\phi + \text{h.c.}\right)$
Fermion	1/2-S, 1/2*-S	$\left[\frac{1}{2}\right] \bar{\chi}\left(g_{\chi,s} + i g_{\chi,p}\gamma^5\right)\chi S + \bar{f}\left(g_{f,s} + i g_{f,p}\gamma^5\right) f S$
	1/2-V, 1/2*-V	$\left[\frac{1}{2}\right] \bar{\chi}\gamma^\mu \left(g_{\chi,v} + g_{\chi,a}\gamma^5\right)\chi V_\mu + \bar{f}\gamma^\mu \left(g_{f,v} + g_{f,a}\gamma^5\right) f V_\mu$
	1/2-S$^\pm$, 1/2*-S$^\pm$	$\left(\bar{\chi}\left(g_s^{(f)} + g_p^{(f)}\gamma^5\right) f S^\dagger + \text{h.c.}\right)$
(χ)	1/2-V$^\pm$, 1/2*-V$^\pm$	$\left(\bar{\chi}\gamma_\mu \left(g_v^{(f)} + g_a^{(f)}\gamma^5\right) f V^{\dagger,\mu} + \text{h.c.}\right)$
Vector	1-S; 1*-S	$\left[\frac{1}{2}\right] g_\chi \Lambda B_\mu^\dagger B^\mu S + \bar{f}\left(g_s^{(f)} + i g_p^{(f)}\gamma^5\right) f S$
	1-V; 1*-V ($\mathcal{V}_1$)	$\left[\frac{1}{2}\right]\left(g_\chi B_\mu^\dagger \partial^\mu B^\nu + \text{h.c.}\right) V_\nu + \bar{f}\gamma^\mu \left(g_v^{(f)} + g_a^{(f)}\gamma^5\right) f V_\mu$
	1-V; 1*-V ($\mathcal{V}_2$)	$\left[\frac{1}{2}\right]\left(g_\chi B_\mu^\dagger \partial^\nu B^\mu + \text{h.c.}\right) V_\nu + \bar{f}\gamma^\mu \left(g_v^{(f)} + g_a^{(f)}\gamma^5\right) f V_\mu$
	1-V; 1*-V ($\mathcal{V}_3$)	$\left[\frac{1}{2}\right]\left(g_\chi \epsilon^{\mu\nu\sigma\rho} B_\mu^\dagger \partial_\nu B_\sigma + \text{h.c.}\right) V_\rho + \bar{f}\gamma^\mu \left(g_v^{(f)} + g_a^{(f)}\gamma^5\right) f V_\mu$
(B^μ)	1-F$^\pm$, 1*-F$^\pm$	$\left(\bar{F}\gamma^\mu \left(g_v^{(f)} + g_a^{(f)}\gamma^5\right) f B_\mu + \text{h.c.}\right)$

Table 2.4: Each of the models considered in this study, along with their interaction Lagrangian with the SM fermions, f, denoted by $\text{S}_{\rm DM}^{(*)} - \text{S}_{\rm MED}^{(\pm)}$, where the DM spin $\text{S}_{\rm DM} \in \{0, 1/2, 1\}$, the mediator spin $\text{S}_{\rm MED} \in \{\text{S}, \text{F}, \text{V}\}$ (denoting spin-0, spin-1/2 and spin-1 respectively) and a star on the DM spin (or $\pm$ on the mediator spin) indicates a complex DM/mediator field. Factors of $\left[\frac{1}{2}\right]$ applying to the real DM only, keep the Feynman rules consistent between real and complex DM.

conditions set, we will now proceed to consider the indirect and direct constraints that may be set on the parameters of the models.

Chapter 3

Indirect Detection of Dark Matter

In this chapter we examine in moderate detail the methodology of indirect detection (hereafter ID) constraints on DM originating from gamma ray signals from the *Galactic Centre* (GC). We begin by briefly introducing cosmic rays in Sec.3.1, and then outline the calculation of the prompt photon signal from DM annihilation in Sec.3.2. We then consider the emission of secondary photons in Sec.3.3 which involves the calculation of electron transport in the galaxy via a semi-analytical method. We will conclude the chapter in Sec.3.4 by applying these techniques to find the constraints on the DM model parameter space.

3.1 Cosmic Rays

The term *cosmic ray* generally refers to relativistic charged or neutral particles which diffuse through the galaxy, and which when detected at earth can provide information on the astrophysical process by which they are accelerated to energies as high as 10^{21} eV. In this study we use cosmic rays as a probe of DM, a well established branch of study which falls under the umbrella of *indirect detection*, which loosely refers to a group of detection techniques in which the presence of DM would be inferred by interactions which happen outside the boundaries of a terrestrial detector.

Cosmic rays are primarily protons, with a small amount of helium, and even smaller abundances of heavy elements. There is an abundance of electrons and

positrons. *Electromagnetic* (EM) radiation is also present, produced by sources within the galaxy (e.g. stars, pulsars etc.) or from extragalactic sources like the CMB.

Cosmic rays and EM radiation could be produced from DM annihilation or decay within the galaxy. Even if the DM does not couple directly to a particular cosmic ray species there may still be a detectable signal, produced during the hadronization and/or decay of the annihilation/decay products to which the DM does couple. To understand the flux of cosmic rays from DM annihilation or decay one must understand how and where the comsic rays are produced, and how they are transported to their point of detection. These questions are far beyond the scope of this work, and to some extent open questions remain, we will dip into this vast field and use just the particular elements of the theory necessary to describe the contribution from DM.

3.2 Primary Gamma Rays from Dark Matter

Gamma rays, or high-energy photons in general, provide a very good target for the detection of DM. First (and perhaps foremost), high energy photons suffer few energy losses during their propagation from the point of production, leading to a very clean signal.

Several 'smoking gun' gamma ray signatures of DM exist, for example when DM annihilates directly into two photons, or into one photon plus one Z, h for example. These give very distinct spectral lines [118–121] and provide very strong constraints; by kinematics the photon energy is $E_\gamma \approx m_\chi$ if two photons are produced, or $E_\gamma = (s - m_X^2)/2\sqrt{s}$ if a single photon is produced alongside a particle of mass m_X, with the annihilation centre of mass energy $s \sim 4m_\chi^2$.

As an example, we take a spin-1/2 DM, χ, coupled to a neutral pseudoscalar mediator, ϕ, which also couples to electrons (model 1/2-S with $g_{f,s} = g_{\chi,s} = 0$). The

resulting annihilation to two photons is shown in Fig.3.1, and assuming the centre of mass energy $s \approx 4m_\chi^2 \gg 4m_e^2$, then the cross section is [1],

$$\langle \sigma v \rangle_{\gamma\gamma} \approx \frac{\alpha^2 g_{\chi,p}^2 g_{f,p}^2}{4\pi^4} \log^4\left(\frac{m_e}{2m_\chi}\right) \frac{m_e^2}{(m_\phi^2 - 4m_\chi^2)^2} \ , \tag{3.2.1}$$

where $g_{\chi,p}, g_{f,p}$ are the DM-mediator and electron-mediator couplings. m_ϕ is the mass of the mediator, which is integrated out to give the EFT. At $m_\chi = 100$ GeV the limits from line-searches of Fermi-LAT [121] are $\langle \sigma v \rangle_{\gamma\gamma} \lesssim 5.5 \times 10^{-29}$ cm^{3}s^{-1}. The tree-level annihilation cross section into electron positron pairs is given simply by

$$\langle \sigma v \rangle_{\text{ann.}} \approx g_{\chi,p}^2 g_{f,p}^2 \frac{m_\chi^2}{2\pi(m_\phi^2 - 4m_\chi^2)^2} \ , \tag{3.2.2}$$

and thus the one-loop diagram is smaller by a factor $\sim 10^{13}$ at $m_\chi = 100$ GeV, the suppression is extremely large and compensates the stronger limit on $\langle \sigma v \rangle_{\gamma\gamma}$ compared with $\langle \sigma v \rangle_{\text{ann.}} \lesssim 5 \times 10^{-27}$ cm^{3}s^{-1} such that the latter provides the strongest limits on the model parameter m_ϕ. This is not necessarily the case in all models, since the electron final state has a particularly strong bound from tree level annihilation, whereas for example a $\bar{b}b$ final state has bounds on $\langle \sigma v \rangle_{\text{ann.}}$ up to two orders of magnitude weaker at $m_\chi = 100$ GeV. Compare this to the bounds from photon lines which arise from one-loop diagrams, the cross section Eq.(3.2.1) scales with m_f^2 and would be enhanced by $\sim 5-7$ orders of magnitude. Typically $\langle \sigma v \rangle_{\gamma\gamma} \sim (10^{-4} - 10^{-1}) \langle \sigma v \rangle_{\text{ann.}}$.

Several line searches have been performed. Theoretically the line spectrum is a delta function in photon energy, however the finite energy resolution of a particular detector turns this into a Gaussian distribution of width equal to the energy resolution, $\sigma(E)$, which is generally energy dependent. The H.E.S.S. collaboration have performed a search (in the energy range $E \in [0.5, 20]$ TeV with width $\sigma \sim 0.17E$ at $E = 0.5$ TeV, and $\sigma \sim 0.11E$ at $E = 10$ TeV [122]), similarly Fermi-LAT ($E \in [5, 300]$ GeV [123]) set strong constraints. A line search with nearby galaxy

[1] The phase space is given by $\Pi \approx 1/(32\pi^2 m_\chi^2)$, the matrix element should include a loop factor $1/(16\pi^2)$, the extra electron couplings α^2 and a logarithmic factor.

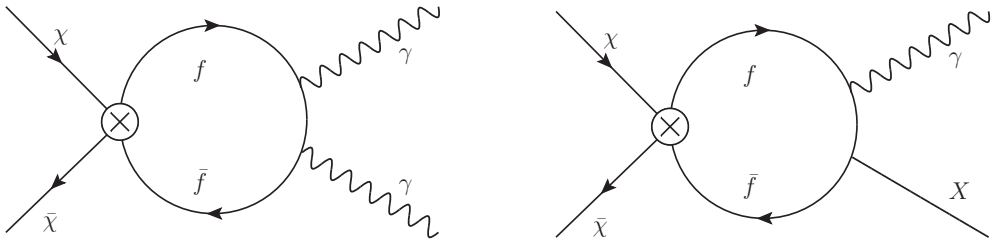

Figure 3.1: Example diagrams for photon line spectra produced by DM annihilation, where the DM couples directly to a fermion $f = l, q$ (lepton or quark), on the left the DM annihilates into two photons, each with energy m_χ in the c.o.m. frame, on the right DM annihilates into a photon plus a particle X, which could be for example a Z boson. The DM-fermion coupling is represented by an effective vertex which includes all the simplified models listed in Chapter 2. The DM is drawn as spin-1/2, but can be spin-0 or spin-1.

clusters as its target has recently been performed [124].

In our models outlined in Chapter 2 we do not consider a direct photon coupling. The full photon energy spectrum has three components; firstly the line spectra we have already seen, for both $\gamma\gamma$ and $X\gamma$ final states ($X = Z, h$) which peak at $E_\gamma = m_\chi$ and $E_\gamma = m_\chi/(1 - m_X^2/4m_\chi^2)$ respectively. Secondly, low energy $E_\gamma/m_\chi \ll 1$ photons are produced during the hadronization and subsequent hadron decays of the annihilation products as an energy *continuum*. Thirdly, *final state radiation* (FSR) of very hard ($E_\gamma/m_\chi \sim 1$) photons from the annihilation products $\bar{f}f$ produces a continuum with $E_\gamma < m_\chi(1 - m_f^2/m_\chi^2)$ [125][2]. The photons which are produced as a *continuum* spectrum at the point of annihilation are called *prompt* photons.

To avoid using different astrophysical targets (for example other galaxies, galaxy clusters or even supernovae) to constrain different DM mass ranges, we will only use the observed galactic diffuse gamma ray emission spectrum. We make use of the fact

[2]In fact, as pointed out in [119] and seen clearly in Fig.3 of [126] the line spectra of photons is always accompanied with a lower energy continuum, however the bounds are significantly weaker when based on this continuum since it has a much lower photon number density. The continuum is enhanced if a single photon is produced along with a Z or h boson and the bounds improve by around an order of magnitude, but are still weaker than the line search.

that for the Milky Way, gamma ray data spans from less than 1 MeV to several TeV. Our ID limits could be further improved by adding data from additional gamma ray sources, such as Dwarf Spheroidal Galaxies (dSph). We do not account for extragalactic (e.g. CMB) emission, which nevertheless is a subdominant component compared with the GC emission [126].

3.2.1 Dark Matter Density Profile

Using only the gravitational influence of galactic DM (so far the only way in which it has been confirmed to interact) makes describing its distribution somewhat difficult, and there are several possible models which fit the data, it is important to include also a model of halo formation [127]. We will assume the density profile is spherically symmetric, however in reality simulations lead to mildly triaxial distributions [128, 129], but the triaxiality is unlikely to make a difference to the results based on the central regions of the galaxy.

The conventional distribution most often used is the Navarro, Frenk and White profile (NFW) [130], which leads to a very sharp peak towards the centre of the galaxy,

$$\rho(r) = \rho_s \frac{r_s}{r}\left(1+\frac{r}{r_s}\right)^{-2} , \tag{3.2.3}$$

where r_s and ρ_s are distance and density parameters fitted to simulation or data. Other profiles such as Einasto assume a less peaked core and appear to provide a good fit to DM only simulations [129, 131, 132],

$$\rho(r) = \rho_s \exp\left[-\frac{2}{\alpha}\left(\frac{r^\alpha}{r_s^\alpha}-1\right)^2\right] , \tag{3.2.4}$$

where $\alpha \sim 0.17$ [126]. A more cored profile (i.e. a much shallower inner profile) is preferred for fitting to galactic rotation curves [133], for example the Burkert profile [134],

$$\rho(r) = \rho_s \left(1+\frac{r}{r_s}\right)^{-1}\left(1+\frac{r^2}{r_s^2}\right)^{-1} . \tag{3.2.5}$$

In principle these various profiles parametrize the uncertainty in the shape of the DM density profile, and this is an important effect, since although these models are of similar radial behaviour near to the earth, they are drastically different towards the centre of the galaxy, where the DM density is highest and where the most gamma rays will be produced.

Many studies of DM density profiles are based on a wide range of spiral galaxies, but since we are focusing on gamma ray emission from the Milky Way alone, which displays a central excess and favours a cuspier profile, we use a modified NFW profile [135]

$$\rho(r) = \rho_s \left(\frac{r}{r_s}\right)^{-\gamma} \left(1 + \left(\frac{r}{r_s}\right)^{\alpha}\right)^{\frac{\gamma-\beta}{\alpha}} , \tag{3.2.6}$$

with $\alpha = 1$, $\beta = 3$ and $\gamma = 1$ for the conventional NFW profile, however a much steeper inner profile $\gamma = 1.2$ appears to fit the Fermi-LAT GeV excess [136], despite being ruled out by DM only simulations [129]. Even steeper profiles are considered for so called *spikes* at the GC. We will conservatively take $\gamma = 1$.

The DM density profile in the very inner regions < 1 kpc of the Milky Way (MW) is unknown, at some point the radial distance from the GC drops below the numerical resolution of the simulations and predictions become uncertain. Additionally, the MW contains a supermassive black hole (SMBH) which dominates the gravitational potential on the $r \sim \mathcal{O}(\text{pc})$ scale. It could be that a density spike is created [137] with $\rho \propto r^{-\gamma}$ and $\gamma > 2$, but others argue that a spike is unlikely since such density spikes are observed in galaxies which undergo dissipative formation whereas those which form via mergers result in SMBH. The SMBH then injects energy into the surrounding material, and washes out the DM spike [138]. Below 0.1 pc, we take a uniform DM density equal to its value at $r = 0.1$ pc, well above the Schwarzchild radius of the SMBH ($\sim 10^{-7}$ pc).

To fix the values of r_s and ρ_s we follow a similar idea as [126]. With the free parameters reduced to two, we can fix their values with two conditions:

1. That the measured DM density at the location of the earth equals $\rho_\odot = 0.36$ GeVcm^{-3} [139] [3]. We take the location of the earth to be $r_E = 8.25$ kpc from the GC and;

2. That the enclosed mass within a radius of 60 kpc equals its measured value $M_{60} = 4.7 \times 10^{11}$ M$_\odot$.

This gives for the NFW profile Eq.(3.2.6), for $\gamma = 1$, $r_s = 17.8$ kpc and $\rho_s = 0.36$ GeVcm^{-3}. For the Einasto profile Eq.(3.2.4) with $\alpha = 0.17$; $r_s = 18.1$ kpc and $\rho_s = 0.083$ GeVcm^{-3} .

3.2.2 Prompt Emission

The gamma ray flux associated with prompt emission is obtained by integrating the photon spectrum which results from the DM annihilation, dN/dE_γ [4], along the *line-of-sight* (l.o.s) distance s and over the solid angle Ω,

$$\frac{d\phi_{\rm prompt}}{dE_\gamma} = \left(\frac{1}{2}\right)\frac{1}{4\pi}\frac{\langle\sigma v\rangle}{2}\left(\frac{\rho_\odot}{m_{DM}}\right)^2\frac{dN}{dE_\gamma}\int_{l.o.s}\left(\frac{\rho(r)}{\rho_\odot}\right)^2 ds\, d\Omega, \tag{3.2.7}$$

where the extra factor of $1/2$ is only necessary if the annihilating particle is complex. The flux is very centrally peaked towards the GC, therefore depending on the size of the angular window, or if we are calculating the flux as a function of angular distance, then accounting for the detector resolution is important. In our case we are integrating the flux over the full angular window, which is much larger than the resolution of the telescopes and thus the resolution can be safely neglected.

The gamma ray flux is thus given by Eq.(3.2.7), where the radial distance from the GC, r, and angular position (θ, ϕ) are related to the line-of-sight by $s \equiv \sqrt{r^2 + r_\odot^2 - 2r\, r_\odot \sin\theta \sin\phi}$, [5] E_γ is the observed photon energy, $\rho_\odot$ the DM energy density at the Sun position, $\rho(r)$ the DM halo profile and $\langle\sigma v\rangle$ the thermally

[3] The value of the local DM density is rather uncertain and takes values in the range $\rho_\odot \sim [0.2, 0.85]$ [140].

[4] These spectra have been computed in [126], using the Pythia monte-carlo simulator.

[5] The two coordinate systems used frequently are the 'Galactic coordinates' s, b, l centered on the earth where s is the l.o.s distance, b (l) is the galactic lattitude (longitude) with respect to the

averaged self-annihilation cross section in the galaxy. The spectra $\frac{dN}{dE_\gamma}$, which include bremsstrahlung processes as well as the hadronization or decay of the final state into photons, are taken from [126] while the DM halo density is assumed to follow a NFW profile given by Eq.(3.2.6).

Eq.(3.2.7) is conventionally written,

$$\frac{d\phi_{\text{prompt}}}{dE_\gamma} = \left(\frac{1}{2}\right) \frac{r_\odot}{4\pi} \frac{\langle\sigma v\rangle}{2} \left(\frac{\rho_\odot}{m_{DM}}\right)^2 \frac{dN}{dE_\gamma} \int J d\Omega, \tag{3.2.11}$$

where the dimensionless *J-factor* is,

$$J = \int_{\text{l.o.s}} \frac{ds}{r_\odot} \left(\frac{\rho(r)}{\rho_\odot}\right)^2. \tag{3.2.12}$$

Notice that in Eq.(3.2.11) the particle physics (i.e. the model dependence) rests entirely in $\langle\sigma v\rangle$. Arguably the spectrum of photons produced in the annihilation to a particular final state, dN/dE_γ contains particle physics and model dependence. However, these are calculated once and for all given a particular final state which makes including them very simple.

We use observations of gamma rays spanning a large energy range, made from data by several collaborations :

1. Fermi-LAT : The *Fermi Large Area Telescope* [141] began operations after launch in 2008 aboard the Fermi satellite, as a successor to EGRET (see below). One of its specific aims is to look for DM in the galaxy.

GC (with coordinates $(r_\odot, 0, 0)$). A second coordinate system exploits the cylindrical symmetry of the diffusion region and is centered on the GC with coordinates (r, z, ϕ), where r (z) is the radial distance (vertical distance) parallel (perpendicular) to the galactic plane and ϕ is the azimuthal angle. The two are related via;

$$s^2 = r^2 + z^2 + r_\odot^2 + 2rr_\odot c_\phi, \tag{3.2.8}$$

$$t_l = rs_\phi/(r_\odot + rc_\phi), \tag{3.2.9}$$

$$t_b = z/\sqrt{r^2 + r_\odot^2 + 2rr_\odot c_\phi}, \tag{3.2.10}$$

where c_X, s_X, t_X are shorthand for $\cos X, \sin X, \tan X$.

2. EGRET : The *Energetic Gamma Ray Experiment Telescope* is a predecessor to the Fermi telescope, aboard NASA's CGRO satellite, and although relatively old (1991-2000 [142]), it is a purpose built gamma ray detector and had an upper energy limit higher than Fermi-LAT.

3. COMPTEL : The *Imaging Compton Telescope* was also aboard the CGRO, it was sensitive to much lower energy photons.

4. INTEGRAL : Launched in 2002, the *International Gamma Ray Astrophysics Laboratory* is currently operational, measuring softer gamma rays $E \lesssim 8$ MeV. See [143] for details.

5. H.E.S.S. : The *High Energy Stereoscopic System* is a ground based telescope array located in Namibia, detecting very high energy gamma rays by means of Cerenkov light from atmospheric showers. At very high photon energies > 300 GeV, H.E.S.S. provides the most constraining GC gamma ray measurement [144] of $\langle \sigma v \rangle \lesssim 5 \times 10^{-25}$ cm^{3}s^{-1}. However at such large DM mass, large cross sections are difficult to obtain within our models.

The relevant parameters to each of these data sets are summarised in Tab.3.1.

In the data used from Fermi-LAT, INTEGRAL, COMPTEL and EGRET the observation window is defined by a square region in galactic latitude and longitude (b, l), centred on the GC. The angular integration is then,

$$\Delta\Omega = 4 \int_{b_{\min}}^{b_{\max}} \int_{l_{\min}}^{l_{\max}} db \; dl \cos b. \tag{3.2.13}$$

In the case of HESS, the observational window is an annulus of inner angle $\theta_{\min} = 0.3^o$ and outer angle $\theta_{\max} = 1.0^o$, where θ is the angle subtended from the vector joining the Sun and GC, in this case the integration is simply given by,

$$\Delta\Omega = 2\pi \int_{\theta_{\min}}^{\theta_{\max}} \sin\theta d\theta \; . \tag{3.2.14}$$

The astrophysical input (density profile) lies entirely in the J-factor, which depends very sensitively on the halo profile used, by up to four orders of magnitude in extreme cases of very cuspy vs. very cored profiles. Nonetheless, it is a matter

	lat. (b)	long. (l)	E (MeV)	ref	$\Delta\Omega$
Fermi-LAT	$0^o \leq \|b\| \leq 3.5^o$	$0^o \leq \|l\| \leq 3.5^o$	$500 - 10^3$	[11]	1.5×10^{-2}
EGRET	$20^o \leq \|b\| \leq 60^o$	$0^o \leq \|l\| \leq 30^o$	$30 - 6000$	[145]	1.1
COMPTEL	$0^o \leq \|b\| \leq 20^o$	$0^o \leq \|l\| \leq 360^o$	$1 - 15$	[146]	4.3
INTEGRAL	$0^o \leq \|b\| \leq 15^o$	$0^o \leq \|l\| \leq 30^o$	$0.02 - 1$	[143]	0.54
	angle (θ)				
H.E.S.S.	$0.3 \leq \theta \leq 1.0^o$		$3 \times 10^5 - 3 \times 10^7$	[144]	8.7×10^{-4}

Table 3.1: The data used to produce ID constraints, their observational window in galactic coordinates, and the energy range of observed photons. In the case of Fermi-LAT data we used the binned data presented in [11], which was extracted from the publicly available Fermi-LAT data.

of simple rescaling of the J-factor to move from a constraint on one halo profile to another.

3.3 Secondary Gamma Rays from Dark Matter

3.3.1 Formalism for Cosmic Ray Propagation

To set the indirect detection limits, one first needs to predict the gamma ray emission expected from each of the DM models considered in this thesis. There are two distinct gamma ray emission mechanisms. One originates from prompt emission (emission of gamma rays directly from the point of annihilation) as discussed in the previous section and the other from cosmic ray (specifically electron/positron) propagation which we now turn to.

We very briefly motivate the macroscopic propagation model used for cosmic rays in the galaxy, details can be found in [147, 148]. Cosmic rays are sufficiently dilute to ignore correlations and consider a one-body phase space with $\psi \equiv \psi(x, p)$ denoting the cosmic ray density with four-position and four-momentum $x = (t, \mathbf{x})$, $p = (E, \mathbf{p})$; a continuity equation for $\psi(x, E)$ can be written as,

$$\partial_t \psi + \partial_E J^0 + \partial_i J^i = Q - D \ , \tag{3.3.15}$$

where Q and D are the source and destruction terms respectively, where Q gives the cosmic rays injected (by supernovae for example) and D are processes which remove them (for example decay). The timelike and spacelike parts of the current J are given by,

$$J^0 = b(\mathbf{x}, E)\psi - D_{EE}(\mathbf{x}, E)\partial_E\psi \ ,$$
$$J^i = V_c^i(\mathbf{x})\psi - K(\mathbf{x}, E)\nabla^i\psi \ , \tag{3.3.16}$$

where $V_c(\mathbf{x})$ parametrizes the stellar wind (which pushes cosmic rays in the $\pm$z-direction away from the disc), $K(\mathbf{x}, E)$ is a diffusion coefficient which parametrizes the microscopic source of diffusion (the scattering of cosmic rays on inhomogeneities in the magnetic field of the galaxy). $b(\mathbf{x}, E)$ parametrizes energy losses, by interaction amongst the various cosmic ray species. Finally $D_{EE}(\mathbf{x}, E)$ corresponds to diffusive reacceleration, the momentum imparted on cosmic rays when the magnetic fields vary with time.

We will only be considering electron/positron propagation. In this case, it is acceptable to assume $D_{EE} = 0$ and $V_c = 0$ [149]. The destruction term can also be neglected since electrons are stable. We will not be modelling backgrounds, and therefore the source term Q injects electrons entirely from the annihilations of DM. Finally, even though all these parameters in principle depend on time, energy and position; we can assume that the time dependence is negligible in all parameters including the cosmic ray density ψ, which is the *steady state approximation*.

3.3.2 Electron propagation

Gamma rays are produced indirectly as a result of cosmic ray propagation additionally to those produced at the point of annihilation/decay (the prompt photons). Here we focus on electron/positron propagation and neglect other cosmic ray species [6]. Such electrons can be pair produced by the DM annihilation directly or originate

[6]For bounds obtained with antiprotons see [150, 151], these bounds are projected to be extremely sensitive, due to the low background of anti-protons. See [152] for electron positron excess

from the decay/hadronisation of other annihilation products. The morphology of the gamma ray flux and energy spectrum that results from these electrons depends on how far the electrons can travel and the amount of energy they can lose, which is fixed by the energy of the electrons at the moment of their injection and the material in the interstellar medium.

To compute the electron spectrum after propagation, $\psi_e \equiv \psi_e(\mathbf{x}, E)$ (or number density per unit energy of electrons at position $\mathbf{x}$ in the galaxy) having units $\mathrm{cm}^{-3}\ \mathrm{GeV}^{-1}$, we solve the diffusion-loss equation from Eq.(3.3.15) and Eq.(3.3.16),

$$\frac{\partial \psi_e}{\partial t} - \nabla(K(\mathbf{x}, E)\nabla\psi_e) - \frac{\partial}{\partial E}(b_T(\mathbf{x}, E)\psi_e) = q(\mathbf{x}, E). \tag{3.3.17}$$

The electrons propagate in both space and energy according to the above equation, and in principle time but we take the steady state approximation,

$$\frac{\partial \psi}{\partial t} = 0. \tag{3.3.18}$$

The second term in Eq.(3.3.17) accounts for spatial diffusion due to the turbulent structure of the galactic magnetic field, and $K(\mathbf{x}, E) = K_0(E/\mathrm{GeV})^\delta$ is the diffusion coefficient, taken to be spatially uniform, but with an energy dependence characterized by δ. The third term describes energy losses, related to the total energy loss rate $b_T(\mathbf{x}, E) \equiv b_T(E)$ also assumed spatially uniform to render the diffusion-loss equation solvable, and measured in $\mathrm{GeV\ s}^{-1}$ (or GeV^2). Finally on the right hand side is the source term responsible for producing the electrons. In our model, DM pair-annihilates to create a fermion anti-fermion pair and leads to a source term,

$$q(r, E_e) = \left(\frac{1}{2}\right) \frac{\langle\sigma v\rangle}{2} \left(\frac{\rho(r)}{m_{\mathrm{DM}}}\right)^2 \left[\frac{dN}{dE_e}\right] , \tag{3.3.19}$$

where $\langle\sigma v\rangle$ is the thermally averaged cross section of DM (with an extra factor of $1/2$ if the DM is a complex field) annihilation into final state $f\bar{f}$ with injection spectrum of electrons dN/dE_e. If the annihilation is directly into e^+e^- then $dN/dE_e = \delta(E_e -$

constraints. Both proton and electron constraints probe locally produced particles. Bounds on neutrinos from Ice-Cube [153] and Super-K [154] produce weaker constraints due to the low detection rate for neutrinos

$m_{\rm DM}$), otherwise it includes the effects of hadronization and decay. $\rho(r)$ is the dark matter density (given in Eq.(3.2.6)) and $m_{\rm DM}$ the dark matter mass. The above source term can be applied to real (Majorana) DM. For complex (Dirac) DM an extra factor of $\frac{1}{2}$ should be included.

Assuming spatially uniform losses, a steady state, and a spatially uniform diffusion coefficient $K(\mathbf{x}, E) \equiv K(E)$, the diffusion equation then reduces to,

$$K(E)\ \nabla^2\ \psi_e\ +\ \frac{\partial}{\partial E}(b_T(E)\ \psi_e)\ +\ q(\mathbf{x}, E)\ = 0, \tag{3.3.20}$$

the diffusion zone is assumed to be an infinite slab of height $2L$, with the galactic plane in the middle. The details of the different steps to solve the diffusion equation are recalled in the next subsection, following [10, 126, 136]. However the solution is essentially given by

$$\psi_e(\mathbf{x}, E) = \frac{\kappa}{b_T(E)} \left(\frac{\rho(r)}{\rho_\odot}\right)^2 \int_E^\infty I(\lambda_D, \mathbf{x}) \frac{dN}{dE}(E_s) dE_s\ , \tag{3.3.21}$$

where $\kappa = \left(\frac{1}{2}\right)(\langle\sigma v\rangle\ /2)(\rho_\odot/m_{DM})^2$, $\lambda_D(E, E_s)$ is the average diffusion distance of the electron, and I is the halo function (defined in Sec.3.3.4) giving the efficiency of the propagation. With ψ_e and the power spectrum (power emitted per unit photon energy E_γ, for a given electron energy E_e) for the dominant sources of photon emission, we can find the total emissivity of particular unit volume in the galaxy,

$$j(E_\gamma, \mathbf{x}) = 2 \int_{E_e^{\rm min}}^{E_e^{\rm max}} P(E_\gamma, E_e, \mathbf{x}) \psi_e(E_e, \mathbf{x})\ dE_e\ , \tag{3.3.22}$$

then we integrate this over the observational window of the experiment, parametrized in terms of the galactic latitude (b), longitude (l) and line of sight (which extends from 0 to the edge of the galactic diffusion zone),

$$E_\gamma^2 \frac{dn}{dE_\gamma} = E_\gamma \int_0^\infty \int_{\rm window} \frac{1}{4\pi s^2} j(E_\gamma, \bar{x}) s^2 ds d\Omega\ . \tag{3.3.23}$$

A factor of E_γ^{-1} is required to provide units of number of photons.

3.3.3 Solving the Diffusion Equation

Using the energy dependence of the diffusion coefficient given below Eq.(3.3.18), one can rewrite Eq.(3.3.20) as,

$$K_0 \epsilon^\delta \nabla^2 \psi_e(\mathbf{x}, \epsilon) + E_0 \frac{\partial}{\partial \epsilon}(b_T(\epsilon)\psi_e(\mathbf{x}, \epsilon)) + q(\mathbf{x}, \epsilon) = 0\ , \tag{3.3.24}$$

where $\epsilon \equiv E/E_0$ and $E_0 \equiv 1$ GeV, one can then solve the diffusion equation for $\widetilde{\psi} = b_T\ \psi_e$ (we will drop the implicit position and energy dependence of b_T, ψ_e and q from now)

$$\frac{K_0\epsilon^\delta}{b_T}\nabla^2\widetilde{\psi} + E_0\frac{\partial}{\partial\epsilon}\widetilde{\psi} + q = 0\ , \tag{3.3.25}$$

and now make the substitution $\tilde{t} = \frac{\epsilon^{\delta-1}}{1-\delta}$, so that $\frac{\partial\tilde{t}}{\partial\epsilon} = -\epsilon^{\delta-2}$, then

$$\frac{\partial\tilde{\psi}}{\partial\tilde{t}} - \frac{K_0\epsilon^2}{E_0 b_T}\nabla^2\tilde{\psi} = \tilde{q}\ , \tag{3.3.26}$$

where $\tilde{q} = \epsilon^{2-\delta}q/E_0$. If we assume $b_T(\epsilon) = b_0E_0^2\epsilon^2$ (the behaviour of the dominant losses at high energy, see Sec.3.3.5), then the factors of ϵ cancel,

$$\frac{\partial\widetilde{\psi}}{\partial\tilde{t}} - A_0\nabla^2\widetilde{\psi} = \tilde{q}, \tag{3.3.27}$$

where $A_0 = K_0/E_0^3b_0$. This is exactly the non-homogeneous diffusion equation for an isotropic media in 3D. This equation has a Green's function $\widetilde{G}(\tilde{t},\mathbf{x};\tilde{t}_s,\mathbf{x}_s)$ which satisfies

$$\frac{\partial\widetilde{G}}{\partial\tilde{t}} - A_0\nabla^2\widetilde{G} = \delta(\mathbf{x}-\mathbf{x}_s)\delta(\tilde{t}-\tilde{t}_s)\ . \tag{3.3.28}$$

For the above equation the Green's functions are explicitly given by,

$$\widetilde{G}(\tilde{t},\mathbf{x};\tilde{t}_s,\mathbf{x}_s) = \theta(\tilde{t})\left(\frac{1}{4\pi A_0\tilde{t}}\right)^{\frac{3}{2}} e^{-\frac{x^2+y^2+z^2}{4A_0\tilde{t}}}, \tag{3.3.29}$$

we can neglect the Heaviside function $\theta(\tilde{t})$, it is satisfied automatically since $\delta < 1$ and $\epsilon > 0$. If we let the halo function be defined by

$$\tilde{I}(E_e,E_s,\mathbf{x}) = \int d\mathbf{x}_s\ \tilde{G}(\tilde{t},\mathbf{x};\tilde{t}_s,\mathbf{x}_s)\left(\frac{\rho(\mathbf{x}_s)}{\rho_\odot}\right)^2, \tag{3.3.30}$$

the electron spectrum can now be written in terms of Green's functions (and we substitute Eq.(3.3.19) for the source term in the second line),

$$\begin{aligned}\tilde{\psi}(\mathbf{x},\tilde{t}) =& \int d\tilde{t}_s\int dx_s\tilde{G}(\tilde{t},\mathbf{x};\tilde{t}_s,\mathbf{x}_s)\tilde{q}(\mathbf{x}_s,E_s)\\ =&\kappa\int dE_s\frac{dN}{dE_s}\tilde{I}(E_e,E_s,\mathbf{x}),\end{aligned} \tag{3.3.31}$$

$$\psi(\mathbf{x},E_e) = \frac{\kappa}{b_T(E_e)}\left(\frac{\rho(r)}{\rho_\odot}\right)^2\int dE_s\frac{dN}{dE_s}I(E_e,E_s,\mathbf{x})\ , \tag{3.3.32}$$

and finally $I = \left(\frac{\rho_\odot}{\rho(\mathbf{x})}\right)^2 \tilde{I}$. We took for simplicity $b(E) \propto E^2$, however we would like to allow a more general energy dependence. This is simple, in Eq.(3.3.25) we introduce the new variable $\tilde{t}$ such that $\frac{\partial E}{\partial t} = \frac{b(E)}{K(E)}$,

$$\tilde{t}(E) = \int_0^E \frac{K(E)}{b_T(E)} dE \ . \tag{3.3.33}$$

Examining the Green's function,

$$\widetilde{G}(\tilde{t}, \mathbf{x}; \tilde{t}_s, \mathbf{x}_s) = \left(\frac{1}{4\pi\Delta\tilde{t}}\right)^{\frac{3}{2}} e^{-\frac{\Delta r^2}{4\Delta\tilde{t}}} \ , \tag{3.3.34}$$

we see that the interpretation of $\Delta\tilde{t}$ is that it is the variance of a Gaussian 'probability' distribution, $4\Delta\tilde{t} \equiv \sigma^2$. The dependent variable is the distance between the source and observer, the standard deviation has the units of length, and we identify it as the diffusion length $\sigma = \lambda_D$,

$$\lambda_D^2 = 4 \int_{E_e}^{E_s} \frac{K(E)}{b(E)} dE \ . \tag{3.3.35}$$

Thus, we have exchanged the variables E_e, E_s for single parameter $\lambda_D(E_e, E_s)$. As a final note, the vertical boundary imposed by the diffusive region at $z = \pm L$ (at which point the electron density is set to zero) requires a modified form of the Green's function, [136, 155],

$$\begin{aligned} &\widetilde{G}_z(z, z_s) = \\ &\frac{1}{L} \sum_{n=1}^{\infty} \left(e^{-\frac{\lambda_D^2 k_n^2}{4}} \sin\left(k_n(L - |z_s|)\right) \sin\left(k_n(L - |z|)\right) \right. \\ &\left. + e^{-\frac{\lambda_D^2 k_n'^2}{4}} \sin\left(k_n'(L - z_s)\right) \sin\left(k_n'(L - z)\right) \right) , \end{aligned} \tag{3.3.36}$$

with $k_n = \frac{(n-1/2)\pi}{L}$, and $k_n' = \frac{n\pi}{L}$. This function can be derived using the *method of images* [156, 157], whereby the source distribution is mirrored in the plane $z = \pm L$. As a rule of thumb, Eq.(3.3.29) can be used if $r \ll L$. We can now discuss the halo function, Eq.(3.3.30), in more detail.

3.3.4 Halo Function

The halo function $I(E_e, E_s, \mathbf{x}) \equiv I(\lambda_D, \mathbf{x})$, given by,

$$I(\lambda_D, \mathbf{x}) = \int d\mathbf{x}_s \widetilde{G}(\lambda_D, \mathbf{x}, \mathbf{x}_s) \left(\frac{\rho(\mathbf{x}_s)}{\rho(\mathbf{x})}\right)^2 , \tag{3.3.37}$$

gives an indication of the efficiency of the propagation. It gives the fraction of electrons at position $\mathbf{x}$ which are retained after propagation over a diffusion length $\lambda_D(E_e, E_s)$, which describes the average distance over which electrons diffuse from a source energy E_s to energy E_e.

The diffusion length λ_D is fixed by the initial and final energies of the electron (E_s and E_e respectively) and is therefore vanishingly small when $E_e \simeq E_s$. Hence all the electrons that have an energy $E_e \simeq E_s$ stay close to where they have been produced (this is just a convoluted way to say that electrons lose energy as they propagate and therefore if they have the same energy that they started with, they have not gone anywhere). This implies that the halo function in Eq.(3.3.37) above be equal to unity. Indeed, since the Green's function are Gaussian functions of width $\sigma = \lambda_D$ (see Eq.(3.3.34)), then as λ_D becomes arbitrarily small, the Green's function approaches a unit sized delta function $\delta^{(3)}(\mathbf{x} - \mathbf{x}_s)$. Feeding this delta function into Eq.(3.3.37) thus leads to

$$I(\lambda_D \to 0) = \int d\mathbf{x}_s \; \delta(\mathbf{x} - \mathbf{x}_s) \left(\frac{\rho(\mathbf{x}_s)}{\rho(\mathbf{x})} \right)^2 = 1 \; . \tag{3.3.38}$$

Due to the Green's function, the halo function will become vanishingly small on distances far beyond the average diffusion distance, i.e. when the electrons have lost all their energy. Hence there are two extreme regimes:

$$\begin{aligned} &\lambda_D \to 0, \quad I(\lambda_D, \mathbf{x}) \to 1, \\ &\lambda_D \to \infty, \quad I(\lambda_D, \mathbf{x}) \to 0. \end{aligned} \tag{3.3.39}$$

$I(\lambda_D) = 1$ indicates that the electrons did not propagate and the point at which $I(\lambda_D) \sim 0$ gives an idea of the distance over which the electrons have lost all their energy. Concretely this means that we do not expect any indirect detection signals from the regions where $I(\lambda_D, \mathbf{x}) = 0$.

It is worth noticing also that the halo function $I(\lambda_D, \mathbf{x})$ can exceed unity, that is, the local density of electrons exceeds what it would otherwise be without any diffusion. This would happen to regions which were close to regions of high electron

density, and in which there is a large amount of diffusion. In the galaxy, this will happen when the electrons produced in the GC manage to travel to $\mathbf{x}$, that is when $\lambda_D \approx r$ (where $r = |\mathbf{x}|$). This case however requires that the diffusion zone be large enough $L \gg r$. Fig.3.2 shows the halo function, $I(\lambda_D)$, for various

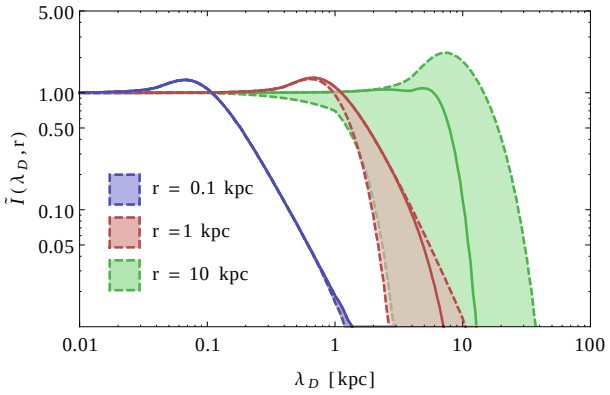

Figure 3.2: The halo function I(λ_D), for three radii from the GC in the disk ($z = 0$). The dashed lines bound the region between the MAX ($L = 15$ kpc) and MIN ($L = 1$ kpc) parameters, and the solid line is the MED ($L = 4$ kpc) set.

radial distances from the GC (and for $z = 0$), for the MAX/MIN/MED parameters, which essentially probe only the half-height of the diffusion zone L (K_0, δ only enter through the definition of λ_D). Close to the GC, all the electrons are produced locally, the vertical boundary then has little effect. Further out, and for $\lambda_D > L$ the vertical boundary can have a large effect, lowering L and thereby confining the electrons into a smaller region increases the peak, and moves it to higher λ_D since the electrons diffuse further radially. Note though that in the full signal $I(\lambda_D)$ is accompanied by a term $(\rho(\mathbf{x})/\rho_\odot)^2$ and regions at $r > r_\odot$ contribute very little to the total flux.

Fig.3.3 shows the propagated electron spectrum for DM annihilations into electrons, for various distances from the GC and for a DM mass of 10 GeV. Very close to the GC, the electrons diffusing from the center have lost little energy and appear as a spike in ψ_e. The buildup of electrons of low energy is due to the bremsstrahlung energy losses, which dominate at low energies and have a $\propto E$ dependence, so the rate of energy loss for low energy particles is much less than that for high energy. Regions close to the GC where the number of electrons is largest, and the density gradient is steepest, are the most sensitive to the diffusion parameters and the cor-

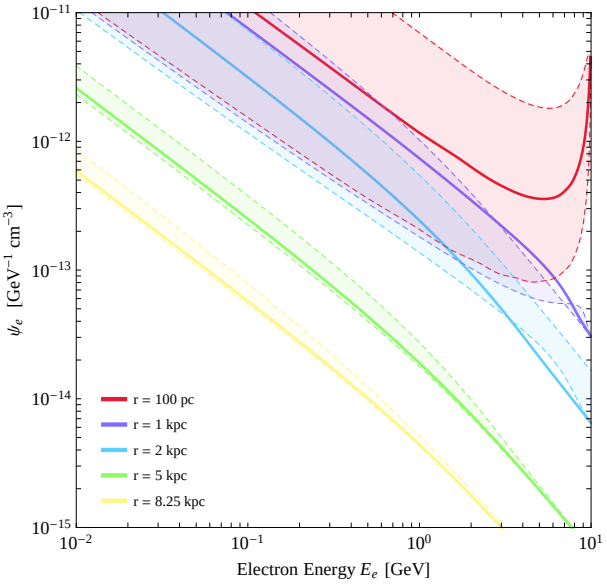

Figure 3.3: The electron spectrum $\psi_e(E_e, r)$ after propagation, for a DM mass of 10 GeV, for various radial distances from the GC (with $z = 0$) for annihilation purely into electrons, $\bar{\chi}\chi \to e^+e^-$, and $\langle\sigma v\rangle = 3 \times 10^{-26}$ cm^{3}s^{-1}. The error incurred by the MIN/MAX diffusion parameters is shown with dashed lines.

responding errors are largest. However, beyond a few kpc from the GC the diffusion parameters have much less effect.

3.3.5 Energy Losses

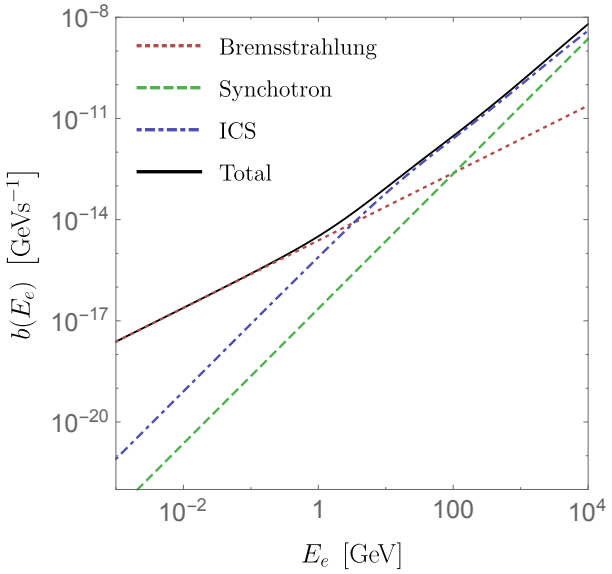

Figure 3.4: The various contributions to the energy loss rate, $b_T(E_e)$, during propagation as a function of the electron energy.

We now briefly collect the various relevant sources of energy loss for galactic electrons and positrons. There are three main sources of energy loss; bremsstrahlung, Inverse Compton Scattering (ICS) and synchrotron. The latter remains subdominant over all energy ranges but we include it anyway. Fig.3.4 shows the energy loss coefficient,

$$b_T(E) = b_{\rm ICS}(E) + b_{\rm Brem}(E) + b_{\rm Sync}(E), \tag{3.3.40}$$

as a function of electron energy. At high energies ICS dominates (since $b_{\rm ICS}(E) \approx E^2$) whereas bremsstrahlung controls the low energy behaviour ($b_{\rm Brem}(E) \approx E$). Due to their behaviour with energy, ICS and synchrotron ($\propto E^2$) tend to steepen the electron spectra $\psi_e(E)$ at low energy, and bremsstrahlung tends to maintain the spectral shape. The expression for each of the losses are as follows [126];

$$b_{\rm ICS}(E) = \frac{4}{3}\frac{\sigma_T}{m_e^3}E^2 U_{\rm ISRF}, \tag{3.3.41}$$

$$b_{\rm Brem}(E) = n\alpha r_0^2 E\left(\frac{4}{3}\phi_1 - \frac{1}{3}\phi_2\right), \tag{3.3.42}$$

$$b_{\rm Sync}(E) = \frac{2\sigma_T B^2}{3\mu_0 m_e^2}E^2, \tag{3.3.43}$$

where $U_{\rm ISRF}$ ('*InterStellar Radiation Field*') is the energy density of the photons in the galaxy, injected from astrophysical sources (see Sec.3.3.8). The energy loss for each component $b_i(E)$ is found from integrating the emission spectrum $P_i(E_\gamma, E_e)$ which appears in Eq.(3.3.22), over the photon energy,

$$b_i(E) \equiv -\frac{dE}{dt} = \int dE_\gamma \; P_i(E_\gamma, E_e) \; . \tag{3.3.44}$$

We now discuss each of these energy loss mechanisms in more detail.

3.3.6 Bremsstrahlung Losses

In classical physics it is known that charged objects radiate when they are accelerated, this process of radiating photons is called *Bremsstrahlung* (roughly 'braking radiation'). In our case this will happen when an electron or positron is accelerated in the Coulomb field of another charged object in the *InterStellar Medium* (ISM); this will mostly be ionized Hydrogen (although electron-electron bremsstrahlung is also possible).

A general expression for the bremsstrahlung cross section between an electron and a charged particle is [158, 159],

$$d\sigma = \frac{dE_\gamma}{E_\gamma} \alpha r_0^2 \frac{1}{E_i^2} \left((E_i^2 + E_f^2)\phi_1 - \frac{2}{3} E_i E_f \phi_2 \right) \; , \tag{3.3.45}$$

where the initial (final) electron energy is E_i (E_f), and by energy conservation $E_i = E_f + E_\gamma$, and $r_0^2 = 3\sigma_T/8\pi$. For a completely ionized target $\phi_1 = \phi_2 = Z^2\phi$ where,

$$\phi = 4 \left(\log \left(\frac{2E_i E_f}{E_\gamma^2} \right) - \frac{1}{2} \right) \; . \tag{3.3.46}$$

However, for a neutral or partially ionized atom, the atomic electrons provide a shielding of the nuclear charge and necessitate the introduction of form factors. Somewhat counterintuitively, very high energy incident electrons suffer maximum screening on atomic targets. In the limit $\Delta = 0$ ($\Delta \propto E_\gamma/E_i$), the ϕ_i are [158],

$$\phi_1^H = 45.79 \; , \tag{3.3.47}$$

$$\phi_2^H = 44.46 \; . \tag{3.3.48}$$

Those for He and H_2 are roughly three and two times the values for H. The composition of the ISM is dominated by neutral atomic and molecular hydrogen [159, 160] (HI and H_2), the density of atomic helium is about $\sim 10\%$ the density of HI; these species are tightly constrained to the disc $z \lesssim 0.2 - 0.5$ kpc, but within the disc extend to high radii $r \lesssim 15$ kpc. In order to derive the semi-analytical solution to the diffusion equation (Eq.(3.3.15) in Sec.3.3) we assumed that the energy losses were spatially homogeneous, we take the number density of HI to be $n_{\rm HI} \sim 1$ cm^{-3} which is suitable for the GC (the subdominant contribution from H^+, He is neglected).

To qualify this assumption we note briefly several points; firstly bremsstrahlung emission dominates over other loss mechanisms for very low energy electrons ($E_e \lesssim 1$ GeV), and is therefore mostly relevant for light DM, and will be a dominant contribution in experiments which are sensitive to low energy photons. The electrons and positrons diffuse very efficiently and so do not venture far from their production point, which is concentrated toward the GC; this means the bulk of the bremsstrahlung emission happens in the GC, and in the GC a homogeneous $n \sim \mathcal{O}(1)$ cm^{-3} is more justified.

The assumption of a homogeneous gas distribution in the galaxy is likely to overproduce bremsstrahlung photons outside of the GC. We will find however that the large majority of the DM parameter space is not in a regime where these photons are the dominant ones.

For a single electron of energy E_e, and target of density $n_H = n_{\rm HI} + n_{\rm H_2} \sim 3$ cm^{-3}, $n_H d\sigma/dE_\gamma$ gives the number of photons produced per unit energy with a given energy E_γ. Then the energy loss coefficient is simply,

$$b(E_e) = -\frac{dE_e}{dt} = n_H \int dE_\gamma E_\gamma \frac{d\sigma}{dE_\gamma} \ , \tag{3.3.49}$$

where the photon energy $E_\gamma \in [0, E_e]$. The above integral reproduces Eq.(3.3.42), and confirms the familiar $b(E_e) \propto E_e$ dependence. The emission spectrum in

Eq.(3.3.44) may be written,

$$P_{\rm Brem}(E_\gamma, E_e) = \frac{3 n_H \alpha \sigma_T}{8\pi} \left[\left(1 + \left(1 - \frac{E_\gamma}{E_e} \right)^2 \right) \phi_1^H - \frac{2}{3} \left(1 - \frac{E_\gamma}{E_e} \right) \phi_2^H \right] , \quad (3.3.50)$$

with σ_T the Thomson cross section.

3.3.7 Inverse Compton Scattering Losses

Compton scattering is the scattering of electrons by photons. In the ICS process the electrons (produced by heavy DM annihilation) of energy E_e are highly relativistic and give energy to low-energy photons (of energy E_γ) to upscatter them to high energies.

The emission spectrum in Eq.(3.3.44) may be written[161],

$$P_{\rm ICS}(E_\gamma, E_e) = \frac{3\sigma_T}{4\gamma^2} \int_{1/4\gamma^2}^1 dq \left(1 - \frac{1}{4q\gamma^2(1-\widetilde{E}_\gamma)} \right) \frac{dn_{\rm ISRF}(E_\gamma)}{dE_\gamma} \frac{1}{q} \times \left(2q \log q + q + 1 - 2q^2 + \frac{1}{2} \frac{\widetilde{E}_\gamma}{1-\widetilde{E}_\gamma} (1-q) \right) , \quad (3.3.51)$$

where $q = m_e/(\gamma(\gamma m_e - E_\gamma))$, $\widetilde{E}_\gamma = 4\gamma E_\gamma / m_e$, and $n_{\rm ISRF}$ is the number density of the *InterStellar Radiation Field* (ISRF) photons. If the energy of the incoming photon is below the electron mass $E_\gamma \ll m_e$ in the electron rest frame, then we are in the *Thomson* limit and Eq.(3.3.44) is particularly simple,

$$b(E_e) = \frac{4}{3} \sigma_T \gamma^2 \int_0^\infty dE_\gamma E_\gamma \frac{dn_{\rm ISRF}}{dE_\gamma}(E_\gamma) . \quad (3.3.52)$$

Thus the energy loss from ICS scales with E_e^2 (since $\gamma \approx E_e/m_e \gg 1$ is the Lorentz boost factor between the centre of mass frame and the electron's rest frame). Note that the maximum photon energy (in the electron rest frame) is $2\gamma E_{\gamma,\rm max}$.

The ISRF energy density $U_{\rm ISRF}$ is

$$U_{\rm ISRF} = \int \frac{dn_{\rm ISRF}(E, \mathbf{x})}{dE} E dE , \quad (3.3.53)$$

$n_{\rm ISRF}$ comprises CMB photons, IR as well as UV photons, each modelled as a grey-body spectra. The spectral parameters can be found in [9, 10]. The resulting energy spectrum is shown in Fig.3.5.

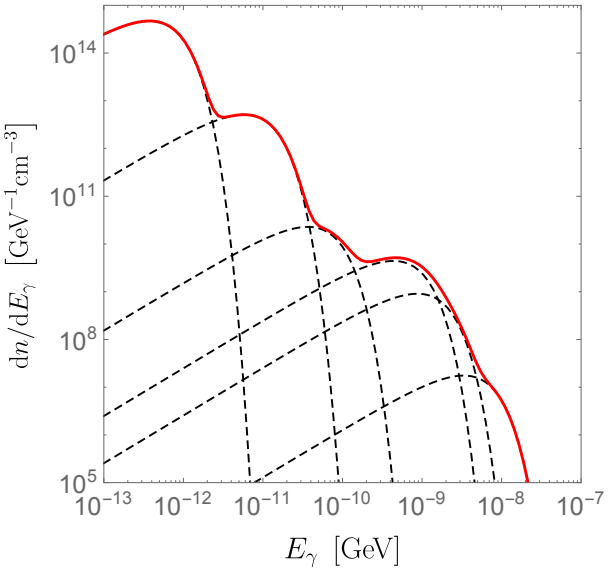

Figure 3.5: The number density per unit energy of ISRF photons with parameters from [9, 10], the leftmost peak corresponds to the CMB, the second is IR radiation from dust, the third optical starlight, and the final three UV starlight.

3.3.8 Synchrotron Losses

Synchrotron emission occurs whenever relativistic electrons are present in a magnetic field, radiating as they spiral around the field lines. Their emission spectrum can be derived from classical arguments [158, 162],

$$P_{\mathrm{Sync}}(E_\gamma, E_e) = \sqrt{3}\frac{e^3 B}{m_e}\frac{E_\gamma}{E_B}\int_{E_\gamma/E_B}^{\infty} K_{5/3}(q)dq, \tag{3.3.54}$$

and $E_B = \frac{3eBE_e^2}{2m_e^3}$. In the limit of highly relativistic electrons, this may be approximately written as,

$$P_{\mathrm{Sync}} \approx \frac{1}{6\pi}\sigma_T B^2 \left(\frac{E_e}{m_e}\right)^2.$$

The spectrum peaks at $E_\gamma \sim E_B$, and so

$$\left(\frac{E_\gamma}{\mathrm{GeV}}\right) \approx 10^{-18}\left(\frac{E_e}{\mathrm{GeV}}\right)^2\left(\frac{B}{\mu\mathrm{G}}\right), \tag{3.3.55}$$

and so even for very heavy DM the photons have very low energy, well outside the gamma ray range of the data we are considering. Nonetheless, the total energy loss rate, $b(E)$, is comparable to that from bremsstrahlung and ICS and thus should be

included in the energy losses.

The synchrotron emission depends on the magnitude of the galactic magnetic field, B, which we must assume to be homogeneous in line with our assumptions. In reality the magnetic field is confined to $z \lesssim 2$ kpc and radially very extended, peaking at around $B_{\rm max} \sim 11$ μG at the GC and dropping to $B_{\rm min} \sim 5$ μG at the Earth's position [163]. However these numbers are quite uncertain, and we conservatively take $B \sim 3$ μG since lower magnetic fields allow greater diffusion of electrons from the GC.

3.3.9 Other Losses

There is also a Coulomb component to the energy loss rate, which depends logarithmically on energy, and an ionization loss component which has a complicated, but approximately logarithmic dependence on electron energy. However, both are negligible for the high energies considered here [164].

3.3.10 Impact of the propagation parameters on the gamma ray flux

Uncertainties in cosmic ray propagation (related to the characteristics of the diffusion zone) are taken into account by considering three sets of values for the K_0, δ, and L parameters, namely MIN, MED and MAX [165–167]. Unless specified otherwise, we assume the MED set of parameters with $K_0 = 0.0112$ kpc^{2}Myr^{-1}, $\delta = 0.7$ and $L = 4$ kpc, the MIN/MAX set are $(L, K_0, \delta)_{\rm MIN} = (1, 0.0016, 0.85)$ and $(L, K_0, \delta)_{\rm MAX} = (15, 0.0765, 0.46)$ in the same units.

The galactic diffusive region is taken to be an radially infinite slab of half height $L = (1, 4, 15)$ kpc for the (MIN, MED, MAX) set. The radial boundary at infinity is not varied (a conventional value of 20 kpc is often taken), and has little or no effect on the result [10], since radial boundary effects tend to be noticeable above $L = 10$ kpc. More importantly the density profile goes as $\rho(r) \propto r^{-3}$ in the outer regions

and the corresponding signal is negligible.

Fig.3.6 shows an example of the flux for several values of $m_{\rm DM}$ for the Fermi-LAT observational window ($7^\circ \times 7^\circ$ centred on the GC), along with the GeV excess data. This assumes $\langle \sigma v \rangle = 3 \times 10^{-26}$ cm^{3}s^{-1} (independent of $m_{\rm DM}$, of course this is not the case when specific models are considered). However, Fig.3.6 shows many features common to all cases. Widening the diffusion zone spreads more of the diffused electrons outside the observational window, and thus decreases the total flux, whilst maintaining the spectral shape, and so the lower dashed line corresponds to the MAX set, and the upper dashed line corresponds to the MIN set. The diffusion error band decreases at the high energy end of the spectra since high energy photons with $E_\gamma \sim m_{\rm DM}$ must be produced from electrons that have diffused very little.

The spectrum of prompt emission from Eq.(3.2.7) is approximately governed by the ratio $(E_\gamma/m_{\rm DM})^2$; the spectrum decreases gently from its peak at $E_\gamma = m_{\rm DM}$, and its peak flux increases quadratically with DM mass (the same is true of bremsstrahlung), since the flux is proportional to $\rho(r)^2$ and $\rho(r) \approx n_{\rm DM}(r) m_{\rm DM}$, and so lowering the DM mass increases the DM number density, and with it the annihilation rate. The energy spectrum of the prompt flux is heavily influenced by the final state, since it is directly proportional to the injection spectrum of photons produced in the annihilation (dN/dE_γ in Eq.(3.2.7)). The $\bar{b}b$ spectrum is softer, arising from pion decay, whereas the $\bar{e}e$ final state also has a strong contribution from initial or final state radiation.

The shape of the bremsstrahlung spectrum (in the lower plots of Fig.3.6) is highly peaked at $E_\gamma \sim m_\chi$, and the dependence on DM mass governed by $\sim m_\chi^{-2}$, giving a particularly large signal for low masses $m_\chi < 10$ GeV. The ICS spectra are in the second row; the peaks of the ISRF photon sources from Fig.3.5 are clearly visible. The highest energy peak is from the CMB photons upscattered to GeV energies. The increase in flux for smaller DM masses is not as extreme as in bremsstrahlung and prompt ($\propto m_\chi^{-2}$) because the emission spectrum P_{ICS} has a dependence on

m_χ which partially cancels the increase from the number density. A very approximate electron spectrum scales as $\psi_e \approx b_T(E)^{-1}$ and $b(E) \propto E^2$, then the emissivity $j \approx \int^{m_\chi} P/b_T(E)$, so that for bremsstrahlung, $P \approx E$ the emissivity has a logarithmic DM mass dependence, whereas for ICS $P \approx E^2$ and there is a linear DM mass dependence, which cancels with the denominator $\rho \propto m_\chi^{-2}$.

As can be seen in Fig.3.6 (which displays the Fermi-LAT excess data), it can often be true that particular combinations of $m_\chi, \langle\sigma v\rangle$ (the later only changes the normalization) can lead to a signal which reproduces the Fermi-LAT gamma ray excess [168], with a cross section which is thermal, these conclusions are highly dependent on the choice of density profile and diffusion model. However, in the majority of cases the shape does not reproduce the data, and instead we can place a constraint on the annihilation cross section. This is done with a simple maximum likelihood analysis, based on the likelihood for a single energy bin E_i,

$$\mathcal{L}_i = \theta\left(\Phi_i^{\rm th} - \Phi_i\right) \exp\left[-\frac{(\Phi_{\rm i}^{\rm th} - \Phi_{\rm i})^2}{2\sigma_{\rm i}^2}\right] + \theta\left(\Phi_{\rm i} - \Phi_{\rm i}^{\rm th}\right), \tag{3.3.56}$$

where Φ_i ($\Phi_i^{\rm th}$) is the measured (predicted) flux in the ith energy bin (and σ^i its error), given by Eq.(3.2.7) and Eq.(3.3.23), and is equivalent to using,

$$\mathcal{L}_i = \exp\left[-\theta\left(\Phi_{\rm i}^{\rm th} - \Phi_{\rm i}\right)\frac{(\Phi_{\rm i}^{\rm th} - \Phi_{\rm i})^2}{2\sigma_{\rm i}^2}\right]. \tag{3.3.57}$$

Then the total likelihood is,

$$\mathcal{L} = \prod_i \mathcal{L}_i \ . \tag{3.3.58}$$

This is normalized to 1 in the event of no signal, and any signal above the measured flux suppresses the likelihood. The test statistic is

$$\mathrm{TS} = -2\ln\left(\frac{\mathcal{L}}{\mathcal{L}_{\rm bck}}\right), \tag{3.3.59}$$

where the background only hypothesis gives simply $\mathcal{L}_{\rm bck} = 1$ since we do not include a background model, making the resulting constraints conservative. To find the 90% *Confidence Level* (CL) in $m_{\rm MED}$ we solve TS = 2.71,

$$\sum_i \theta\left(\Phi_i^{\rm th} - \Phi_i\right)\frac{(\Phi_i^{\rm th} - \Phi_i)^2}{2\sigma_i^2} = \frac{2.71}{2} \ . \tag{3.3.60}$$

If we fix all couplings, and the DM mass, then the theoretical flux is a function of the mediator mass $\phi(m_{\rm MED})$ and this fixes the limit on $m_{\rm MED}$. In Fig.3.7 in the next subsection we will show that the exclusion on $\langle\sigma v\rangle$ (for various channels), including propagation improves the constraint by several orders of magnitude in the case of an electron final state. These electrons are produced directly (rather than as a secondary product as radiation or during hadronization) and thus have a large energy $\sim m_{\rm DM}$ ($m_{\rm DM} > 10$ GeV) and since energy losses into photons scale with E_e^2 (Fig.3.4) the energy loss into photons is efficient in the measured energy range.

Other leptonic final states, i.e. $\bar{\mu}\mu$ and $\bar{\tau}\tau$, the secondary photon flux is much smaller, since in the decay of the leptons only $\sim 1/3$ (1/6) of the total energy of the $\bar{\mu}\mu$ ($\bar{\tau}\tau$) pair is given to electrons, and additionally these electrons have a lower energy causing them to produce fewer photons as they diffuse. The primary photon spectrum is also lower for $\bar{\mu}\mu$ final states since the energy spectrum of the primary photons is softer, however for the $\bar{\tau}\tau$ final state, the energy spectrum of the photons is shifted to higher energies plus a larger fraction of the annihilation energy goes into photons and this may actually increase the primary flux compared with the $\bar{e}e$ final state.

For quark final states, the difference compared with electron final states is, again, that a smaller proportion of the available annihilation energy, $\sim 2m_{\rm DM}$, will go into electrons (a larger proportion of the energy goes into primary photons), and these electrons will be produced with an energy spectrum shifted to lower energy. This makes the secondary photons produced by propagation of electrons a subdominant source of photons, except for very large DM mass (where the electrons are energetic enough to produce photons efficiently during diffusion), or rather small masses (< 5 GeV) where bremsstrahlung emission produces a large flux of low energy photons. However, it is certainly a fair approximation to consider just prompt photons if the final state is purely hadronic.

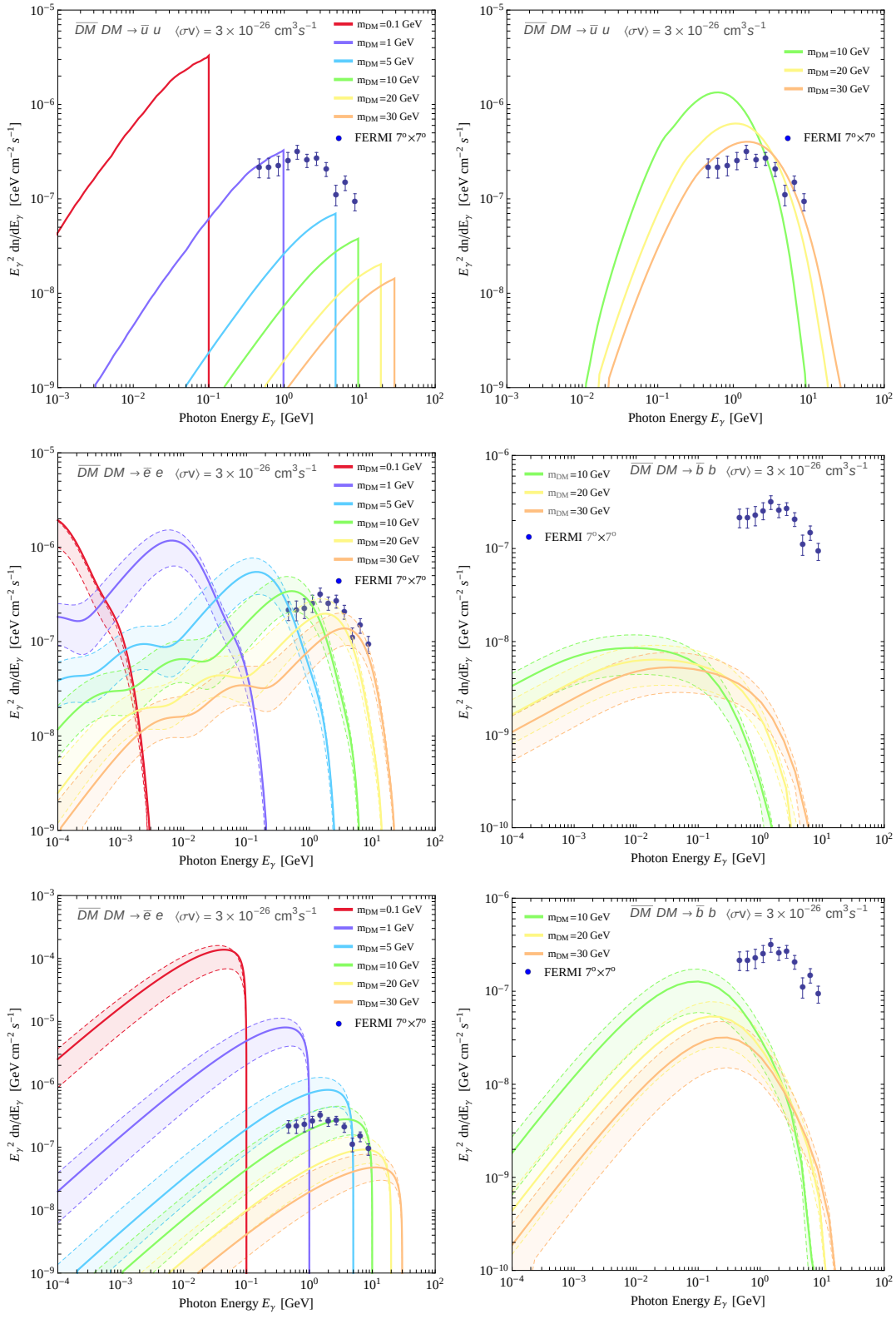

Figure 3.6: The photon flux from prompt (first row), ICS (second row) and bremsstrahlung (third row) gamma ray emission for DM annihilation to $\bar{u}u$ (top row) $\bar{e}e$ (left middle and left bottom) and $\bar{b}b$ (right middle and right bottom). The fluxes are for the Fermi-LAT 7 degree window centred on the GC, with an annihilation cross section $\langle\sigma v\rangle = 3 \times 10^{-26}$ cm^{3}s^{-1}, and for a range of DM masses. In the case of ICS and bremsstrahlung emission, the shaded region between the dashed lines corresponds to the error incurred by using the MIN and MAX diffusion parameters. The blue data points are the Fermi excess, after background have been removed [11].

3.4 Gamma Ray and Other Indirect Constraints

To summarize the relevant discussion so far, DM annihilation to SM particles produces photons directly, but also implies a continuing production of charged particles, leading in turn to a potentially detectable secondary gamma ray signal. The DM halo density in the Milky Way is expected to be strongly peaked towards the centre, making the galactic centre (GC) an ideal target for the detection of DM.

The gamma ray emission from DM annihilations in the GC has essentially two components; prompt emission (Sec.3.2.2) where photons are radiated from charged particles or produced in the decays of hadrons formed from final state quarks. The second component arises from Inverse Compton Scattering (ICS) and bremsstrahlung emission of photons during the propagation of electrons and positrons. The propagation of these particles can be modelled by a steady state diffusion equation which we solve semi-analytically, with energy-losses from ICS, bremsstrahlung and synchrotron radiation.

We set limits by comparing our theoretical estimates of the gamma ray flux expected in each of our models and for each of the SM final states to the Fermi-LAT, EGRET, COMPTEL, INTEGRAL and H.E.S.S. data, see Table.3.1. We establish our 90% CL by finding the value of m_ϕ for each fixed (m_χ, g) pair that yields $-2\ln(\mathcal{L}/\mathcal{L}_{\rm bck}) = 2.71$.

Since we are mostly interested in comparing the ID and direct detection limits, we focus on the gamma ray predictions arising from DM pair annihilation into quarks. However, it is worth remembering that annihilations into lepton pairs lead to stronger ID constraints. This fact is illustrated in Fig.3.7 where we display the exclusion limits that one gets when DM annihilates into electron-positron pairs. As one can see from this figure, all thermal DM candidates which annihilate to electrons and with a mass smaller than a few GeV are essentially ruled out.

For a given model, the results of Fig.3.7 can be translated into limits on the DM

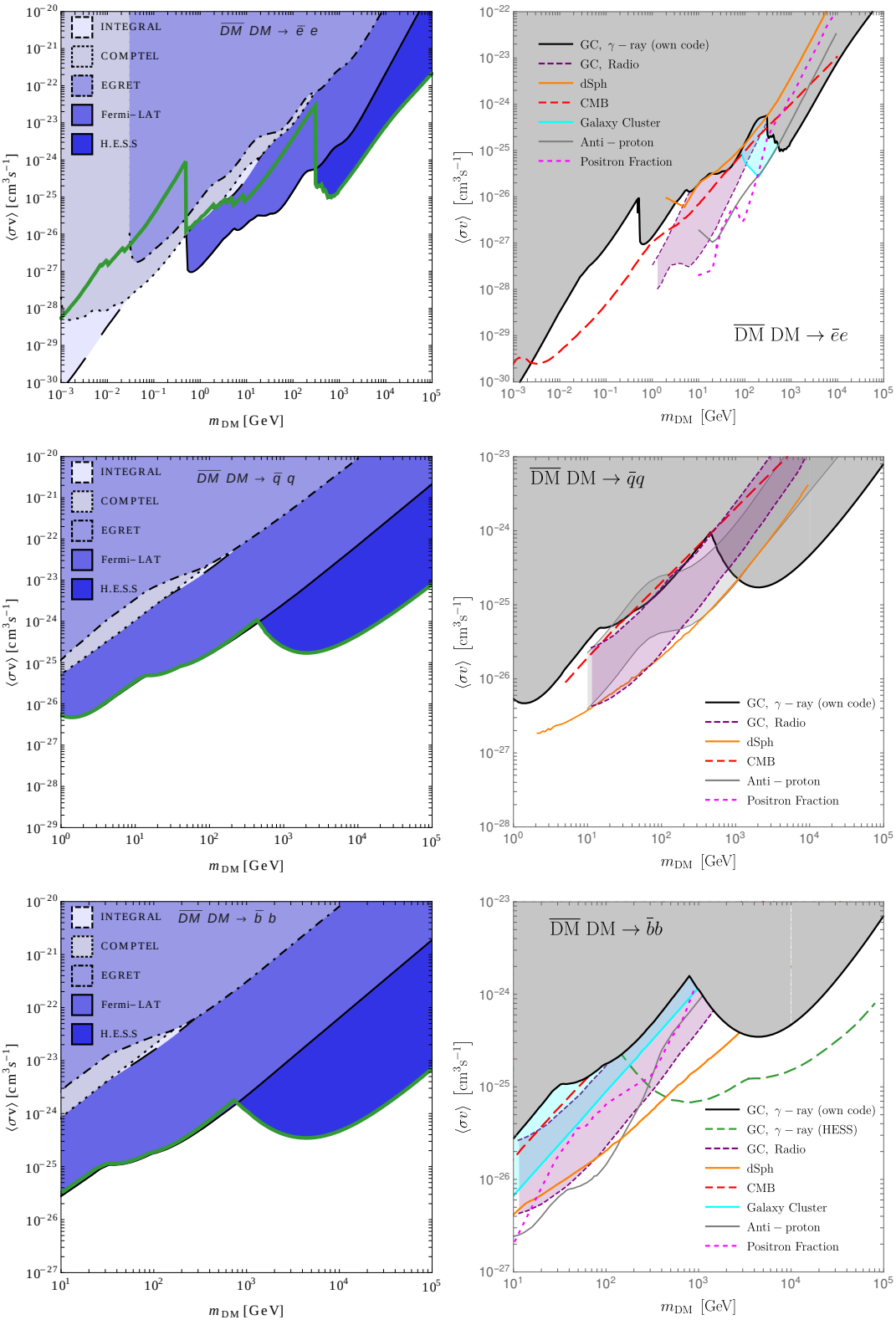

Figure 3.7: Galactic gamma ray exclusion region (left column, shaded) for a constant value of $\langle\sigma v\rangle$ against DM mass, for DM annihilation into $\bar{e}e$ (top row) and $\bar{q}q$ (middle) and $\bar{b}b$ (bottom) where $q = u, d, s$ (with $m_{\rm DM} > 0.1$ GeV for $\bar{s}s$). We include propagation as described in the text (blue shaded), and give the result with no propagation (green line). These are compared other indirect detection limits from the literature (right column), see text for details.

and mediator masses and couplings. Their strength and shape depend on the exact nature of DM as well as the mediator. We show an example in Fig.3.8, for Dirac DM coupled via a spin-1 mediator to a light quark final state ($q = u, d, s$ are treated the same with respect to ID limits for $m_{\rm DM} > m_q$) in the $m_{\rm DM} - m_{\rm MED}$ plane with the couplings set to 1.

The effect of the diffusion parameters (the MIN and MAX set) on the exclusion limit is very small for quark final states, which are mostly dominated by prompt emission, which is not subject to diffusion. Even for leptonic final states the high mass DM signal is dominated by prompt emission and for low masses, it is dominated by bremsstrahlung emission, which peaks at a photon energy $E_\gamma \sim m_\chi$, such that the undiffused electrons dominate the signal.

Gamma ray limits from the GC can exclude DM candidates with masses up to the tens of TeV scale. This is true even if they are coupled to TeV scale mediators, provided that the coupling is sufficiently large (of $\mathcal{O}(1)$).

We also combine our gamma ray constraints with several additional limits from the literature, as shown in Fig.3.8 for the example of light quark ($q\bar{q}$), heavy quark ($b\bar{b}$) and leptonic ($e\bar{e}$) final states. Each signal suffers its own source of uncertainty, but the DM halo profile, and propagation of cosmic rays are frequently the dominant sources of errors. Indirect detection encompasses targets other than the GC, for example galaxy clusters, dSph galaxies, or the CMB. It also includes the detection of particles other than photons, for example electrons or anti-protons. We mention the most powerful constraints only :

1. **Dwarf Spheroidal galaxies** (dSph) of the Milky Way offer an alternative gamma ray target, these galaxies are around $7 - 254$ kpc away with J-factors $J_{\rm ann.} \lesssim 10^{19}$ GeV^2 cm^{-5} sr [169] [7]. The most recent Fermi-LAT data uses a

[7] The notation $J_{\rm ann.}$ distinguishes this quantity from the J defined in Eq.(3.2.12), the difference being that J is dimensionless, and $J_{\rm ann.} = r_\odot \rho_\odot^2 J$.

sample of 25 dSph [170] to provide bounds for all fermionic final states (for $b\bar{b}$ a more recent analysis [171] combines MAGIC to marginally improve the bound), see also [172]. Weaker limits have been set by MAGIC [173], VERITAS [174], HAWC. [175], HESS [176] and DES [177]. The Large Megallanic Cloud (LMC, $s \sim 50$ kpc) or Small Megallanic Cloud (SMC, $s \sim 61$ kpc) which are not included in the dSph surveys already quoted also offer a potential target, the bounds are found most recently in [178, 179] for gamma rays and [180] for radio waves. Although the dSph constraints (the solid orange lines of Fig.3.8) are often more powerful than the GC, to our knowledge, no constraint has been set on light (sub-GeV) DM using dwarf galaxies apart from a pre-Fermi study of Sagittarius [181]. Additionally, for p-wave suppressed annihilation, the lower dispersion velocities of dwarf galaxies imply a large suppression of the annihilation rate with respect to the GC [182].

2. Large scale structure such as **Galaxy clusters** also provide good gamma ray and radio targets, but tend to perform worse than dSphs. Gamma ray bounds have been set by MAGIC [183], HESS [184, 185], VERITAS [186] and Fermi-LAT [187–190] whose most recent study of Virgo [191] seems to be the best. Radio observations also provide similar sized bounds [192], with magnetic fields typically $1 - 10\mu$G. The nearby galaxy **Andromeda** ($s \sim 780$ kpc) has a much higher central field of $50\mu G$, and correspondingly the constraints are much more competitive and can obtain $\langle \sigma v \rangle < 10^{-27}$ [193]. The enhancement of annihilation (or "boost factor") in clusters of galaxies due to substructure is not known with precision and therefore makes the prediction of dark radiation in clusters of galaxies quite uncertain, shown by the shaded cyan region in Fig.3.8.

3. The **Galactic Centre** can be measured in the radio band between 22MHz - 8 GHz and can provide good constraints [194–196], most recently [197] including Planck data (30-70 GHz). The signal arises mainly from synchrotron radiation from electrons and positrons, which in turn depends strongly on the magnetic field at the GC, which is highly uncertain but with a lower limit $B \gtrsim 50\mu G$

[198]. The radio constraints (dashed purple in Fig.3.8) for $\bar{e}e$ and $\bar{b}b$ are taken from [197] who give both a conservative bound, and a *progressive* bound (the more stringent) which includes astrophysical foregrounds (this source of uncertainty dominates over propagation and density profile uncertainties). For the $\bar{q}q$ channel, we use [195], with bands delineating two values of the central magnetic field $B = 10, 100$ μG; and which are of similar strength to [197].

4. **Antiprotons** provide strong constraints for models with quark final states (leptonic channels lead to weak constraints since less primary anti-protons are produced), using the AMS-02 ($E < 450$ GeV, 2015) and PAMELA ($E < 180$ GeV) data. The propagation parameters for anti-protons are not well constrained and lead to sizeable uncertainties on the DM signal, despite a relatively low uncertainty on the background [199]. For the $\bar{b}b, \bar{e}e$ final state see [199], for $\bar{q}q$ see [200] (AMS-02) or [150, 151, 198, 201] (PAMELA).

5. The **positron flux** and **positron fraction** as measured by AMS-02 and PAMELA set extremely powerful constraints for leptonic channels, see for example [202–204]. We use the constraints from [202] based on the AMS-02 data.

6. Other constraints include **neutrino detection** by Ice-Cube [205], and ANTARES [206].

For s-wave cross sections, the GC constraints are competitive (often even subdominant to) the constraints in the list above, and this emphasises the need to consider bounds from various astrophysical targets (both in target location and target particle). We have targeted the GC gamma ray signal because it is ubiquitous across all the models we are considering and thus allows a robust comparison in ID bounds for each simplified model, this somewhat outweighs the potential for slightly stronger bounds to be placed from other targets.

This is particularly true for p-wave suppressed processes, where we have a good handle on the velocity of the DM in the GC [207]. Even though the dSph constraints out-compete the GC for some s-wave annihilation channels, the DM velocity dispersion in dSph is very low $\sigma_v \sim 1-10$ km s^{-1} [182], and these constraints are weakened

compared with the GC (where $\sigma_v \sim 130\ \mathrm{kms}^{-1}$). In many of the searches the p-wave suppression affects the signal in non-trivial ways (e.g. CMB), and specific searches may not have been done.

3.5 Conclusions

We have reviewed and outlined a simple calculation of the gamma ray signal of DM annihilation in the galactic centre, which arises both directly at the point of DM annihilation and as a result of the transport of electrons and positrons through the galaxy, which themselves have been produced by the DM. Although making many approximations along the way, this method is useful as a quick (when compared with the use of purpose-built software such as GalPROP [208] in broad searches with several independent models) and model-independent bound, which spans the full range of WIMP masses GeV $\lesssim m_\chi \lesssim$ TeV. We have compared our bounds to a collection of other ID searches from the literature. GC gamma ray constraints are generally less powerful than the combined literature, and so our catalogue of limits from the literature will be taken forward into later chapters. Nonetheless, having control over the calculation of the signal allows a bound to be placed in scenarios not covered in the literature, such as p-wave suppressed annihilation.

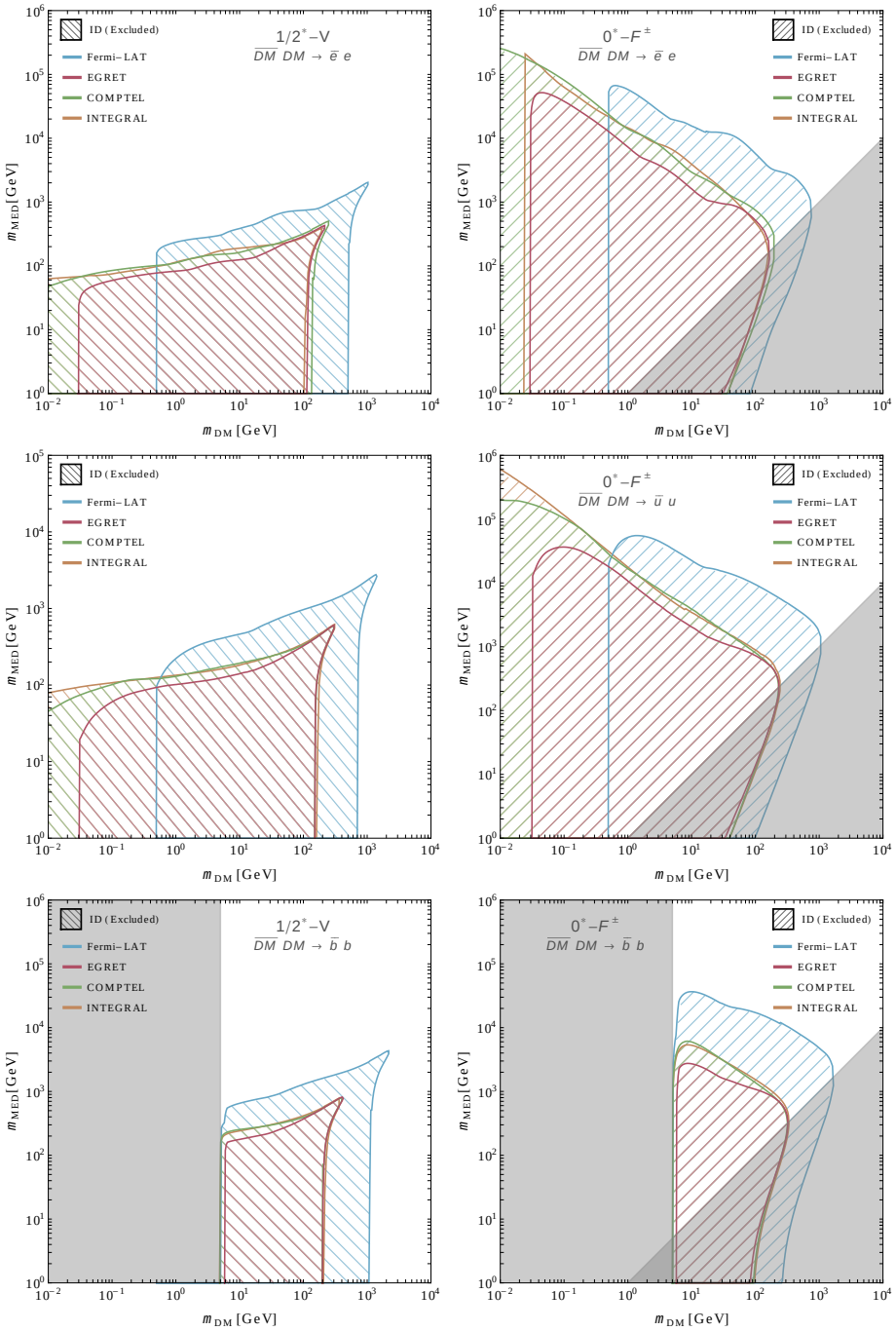

Figure 3.8: An example of the ID exclusion limits (hatched region) obtained in the case of DM annihilation into $\bar{e}e$ pairs (top row), $\bar{u}u$ pairs (middle row, equivalent $\bar{d}d$, and $\bar{s}s$ above 100 MeV), and $\bar{b}b$ pairs (bottom row), where the grey shaded region forbids annihilation as $m_\chi < m_b$. The left column is for fermionic DM with a neutral vector mediator (an s-channel annihilation), the right column a spin-1 DM with a charged fermionic mediator (a t-channel annihilation).The excluded region is usually dominated by the Fermi-LAT data for $m_{\rm DM} > \mathcal{O}(1)$ GeV as one would expect from Fig.3.7. Below 1 GeV the Fermi-LAT dat decreases in sensitivity and other data are more constraining.

Chapter 4

Direct Detection of Dark Matter

In this chapter we review the current and most precise general determination of the dark matter signal in terrestrial based *Direct Detection* (DD) experiments. We will begin with some basics in Sec.4.1, and then proceed through the calculation of the DD dark matter signal with a matching of the full theory (from Chapter 2) to an appropriate EFT in Sec.4.2, then in Sec.4.3 we review the effects of nuclear structure on the event rate, i.e. hadronic matrix elements. Lastly the non-relativistic limit of the EFT is taken in order to match onto nuclear form factors in Sec.4.4. Finally, we show how these calculations translate into constraints on DM models in Sec.4.5, and in doing so summarize the most sensitive and relevant DD experiments of the last few years.

4.1 Introduction

In the previous chapter we saw that if dark matter is a particle, and if it couples to SM fields then we may detect its presence as it annihilates into stable detectable particles such as electrons and photons.

If DM can annihilate, then it should be able to scatter also. As it scatters from electrons and nuclei in a suitable target material, the energy released may be detected. Experiments which aim to do this are usually termed *Direct Detection* experiments. Detecting the energy recoil of a dark matter particle hitting a nucleus

was first described in the 1980s [209] as a means to find evidence for dark matter and as a way to characterise both its mass and the strength of its interactions.

Detection techniques have improved considerably since. Simple kinematics show that detecting recoil energies in the range $E_R \sim 0.1 - 100$ keV (a fair representation of the present day capabilities) requires the DM mass to be in the range $m_\chi \sim 1 - 10^4$ GeV. Current experiments are now sensitive to values of the elastic scattering cross section between a DM particle and a nucleon as small as a few 10^{-45} cm^2 for a DM mass of about 20-30 GeV. Compare this to the gluon-fusion Higgs production followed by decay to two photons $\sigma \sim 10^{-37}$ cm^2, which was used to discover the Higgs.

Confronting theoretical expectations to experimental results is not very straightforward though. There are a few inherent difficulties associated with these calculations. First, to compute DM-nucleon interactions one has to match the full Lagrangian to a set of EFT operators and then use various phenomenological arguments to obtain the DM-nucleon Lagrangian from the DM-quark Lagrangian. These must then be matched to the appropriate non-relativistic (NR) operators which govern elastic scattering at low energies. Finally, one needs to convolve the DM-nucleon matrix element with the appropriate nuclear form factor, which describes the spatial distribution of the nuclear current that the DM couples to.

Two specific form factor parametrisations have been extensively used in the literature so far: the "spin-independent" (SI) and "spin-dependent" (SD) form factors. The former dominates if the DM couples coherently to all nucleons via the identity operator $\mathbf{1}$, and is proportional to the atomic number squared (A^2); whereas the latter is important when the DM couples instead to the nuclear spin J, and goes as $J(J+1)$. These form factors can be approximately computed with nuclear shell models, or parametrized via empirical fits to electron and neutron scattering data.

It was recently pointed out [210, 211] that the DM does not necessarily couple only through these operators, and that the nuclear response should differ as the DM

couples to different currents in the nucleus; in this case a nuclear shell model must be used. By keeping in the terms dependent on the relative DM-target velocity (v) and momentum transfer (q), [211] lists 13 new form factors which could have a direct impact on the DM direct detection signals. Some are dependent on the spin of the nucleus while others are not, thus extending the notion of SI and SD interactions.

The full procedure from beginning (UV complete Lagrangian) to end (the form factors and their coefficients) will be provided in this chapter and we now provide a very terse summary. First, one rewrites the DM-quark Lagrangian as an effective theory by integrating out heavy states, $\mathcal{L}_{\mathrm{DM}-q} = \sum_q C^{(q)}\ \mathcal{O}_q^{\mathrm{EFT}}$, where the $C^{(q)}$ are the Wilson coefficients, depending on the masses and couplings of the particles involved, and $\mathcal{O}_q^{\mathrm{EFT}}$ the effective operator which contains a DM and SM current in the form $\mathcal{O}_q^{\mathrm{EFT}} \equiv \mathcal{J}_{\mathrm{DM}}\mathcal{J}_{\mathrm{SM}}$. $\mathcal{J}$ may carry an explicit Lorentz structure via derivatives (∂_μ) or Dirac matrices (γ^5, γ^μ). This matching must be done case-by-case: we provide each of the $C^{(q)}$'s for the models under consideration in Sec.4.2.

One then assumes that $\mathcal{L}_{\mathrm{DM}-q}$ (at quark level) is structurally equivalent to $\mathcal{L}_{\mathrm{DM}-N} = \sum_N C^{(N)}\ \mathcal{O}_N^{\mathrm{EFT}}$ (at nucleon level), and derive from non-perturbative physics the $C^{(N)}$ coefficients in terms of the $C^{(q)}$ coefficients. This is shown in Sec.4.3. Where they have been computed before, the results that we present are in agreement with the literature (these are mainly summarised in [116, 126]) although we have added several cases that were not covered before, mainly in vector DM scenarios.

Once the $C^{(N)}$ coefficients are fully determined in terms of the masses and couplings, it is relatively easy to identify the couplings to the different form factors and compute the resulting differential cross section at the nucleus level. To do this, one takes a non-relativisitc limit of all the fields and produces a set of coefficients $C_i^{(N)}$ where i is the index of a specific NR operator $\mathcal{O}_i^{(\mathrm{NR})}$ with a corresponding form factor; for example $\mathcal{O}_4^{(\mathrm{NR})} = S_\chi \cdot S_N$ corresponds to the canonical spin-dependent

operator. Once the $C_i^{(N)}$ are found, the squared amplitude for the scattering is,

$$\langle|\mathcal{M}|^2\rangle = \sum_{i=1}^{15} \sum_{N,N'=n,p} \left(\frac{m_T}{m_N}\right)^2 C_i^{(N)}\, C_i^{(N')}\, \mathcal{F}_{i,i}^{(N,N')}, \tag{4.1.1}$$

where $\mathcal{F}_{i,i}^{(N,N')}$ are the different nuclear form factors (as listed in [211, 212]), and m_T, and m_N are the target (nucleus) and nucleon mass respectively. The differential cross section for a particular target nucleus is then given by,

$$\frac{d\sigma}{dE_R} = \frac{1}{32\pi^2 m_\chi^2 m_T} \frac{1}{v^2} \langle|\mathcal{M}|^2\rangle\,, \tag{4.1.2}$$

where m_χ is the DM mass, m_T the mass of the material in the detector, E_R the recoil energy, v the DM velocity.

The technique of simple event counting (the one which we use throughout) is the most widely used; however it is possible to improve the signal-to-background ratio significantly using directional detection [213] or annual modulation [214], and these provide an interesting future search strategy.

It is also possible to consider scattering from electrons, which are either in atomic orbitals (in the case of liquid scintillators) or in a semiconductor crystal (in Germanium crystals in CDMS for example) [215–217]. This requires the involvement of the bound electron wavefunction, since treating the electrons as free particles yields the minimum velocity DM velocity to be $v_{\rm min} \sim \sqrt{m_e E_R/2\mu^2}$ where μ is the DM-electron reduced mass, and due to the smallness of m_e, $v_{\rm min} > v_{\rm esc}$ (the galactic escape velocity) for thresholds above 1 eV and would lead to no observed events.

Correctly accounting for the binding of the electrons alleviates this problem, since then the electron wavefunction can carry large momentum, creating an observable recoil. Even so, the thresholds are still required to be very low, $\mathcal{O}(10)$ eV, and the DM mass $\lesssim 10$ GeV. This provides a subdominant contribution to DD signals unless the DM is *leptophillic*, coupling only to leptons.

4.2 Step 1 : EFT Matching

The first step in calculating the scattering rate is to match the full theory (i.e. a fully renormalizable Lagrangian such as those given in Chapter 2) onto an effective theory in which heavy states are integrated out. This approximation is very good if the heavy states are $\gtrsim \mathcal{O}(10)$ GeV since the scattering energies are so small (the typical direct detection experiment scales are $\ll 1$ GeV). The effective operators are also easier to work with; especially when it comes to finding the hadronic matrix elements necessary to fully describe their scattering.

The effective Lagrangian may be written,

$$\mathcal{L}_{\mathrm{DM-q}} = \sum_i C_i^{(q)} \ \mathcal{O}_q^{\mathrm{EFT}} \ , \tag{4.2.3}$$

where the $C^{(q)}$ are Wilson coefficients and $\mathcal{O}_q^{\mathrm{EFT}}$ the effective operators which contain a DM and SM current in the form $\mathcal{O}_q^{\mathrm{EFT}} \equiv \mathcal{J}_{\mathrm{DM}}\mathcal{J}_{\mathrm{SM},q}$. $\mathcal{J}$ may carry an explicit Lorentz structure via derivatives (∂_μ) or Dirac matrices (γ^5, γ^μ).

4.2.1 Heavy Quark and Gluon Operators

If the DM couples to heavy quarks, denoted $Q = c, b, t$, then a direct coupling to nucleons would be heavily suppressed since the sea quark distributions for c, b, t are extremely small. However at low energies, nucleon mass and spin receive large contributions from gluons. Thus if the DM couples to gluons (which is always possible as a quantum correction, for example via an intermediate loop of heavy quarks) then the cross section may become measurable.

The DD interaction scale ($\mu \sim 1$ GeV) is much lower than the heavy quark mass for $Q = b, t$, and so it is reasonable to integrate the Q out of the theory along with the mediator (this is done at a scale $\mu = m_Q$ and termed *threshold matching*; formally we are matching the full theory including heavy quarks to a one-loop effective theory, at lowest order in the strong coupling g_s). Technically one should integrate out the heaviest particle first, the order does not affect the calculation for neutral

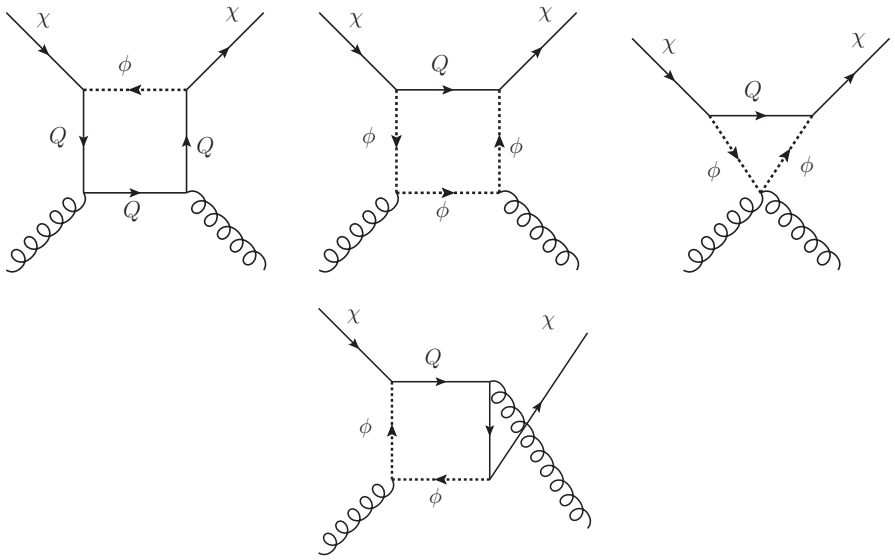

Figure 4.1: An example of the gluon contribution to DM-nuclear scattering for a spin-1/2 DM candidate coupled to heavy quarks via a *charged* mediator. Gluons may be emitted via both the heavy quarks and mediator in the loops.

mediators if we neglect RG running effects and in the charged mediator case both appear in loops and must be integrated out simultaneously. RG running effects are only considered in cases where they dramatically effect the DD signal, and otherwise the running between the mediator and heavy quark scales is not included.

For matching to gluon operators a distinction can be made between models with charged mediators (necessarily charged under $SU(3)_c$ if coupled to heavy quarks, as well as $U(1)_Q$ charge) and those with neutral mediators; charged mediators appear inside the heavy quark loop (as in Fig.4.1), whereas they cannot if they are neutral (Fig.4.2) [1].

[1] In principle the matching between the loop diagrams and the EFT can be done using conventional Feynman rules; however one loses manifest gauge covariance during intermediate steps of the calculation, and therefore for more involved calculations, techniques which preserve it are less arduous. Indeed the background field technique [218] provides a suitable framework for dealing with the neutral mediator case, and the *Feynman-Schwinger* gauge (developed in the same study [218], but used for exactly our purpose more recently [219]) for the charged mediator case.

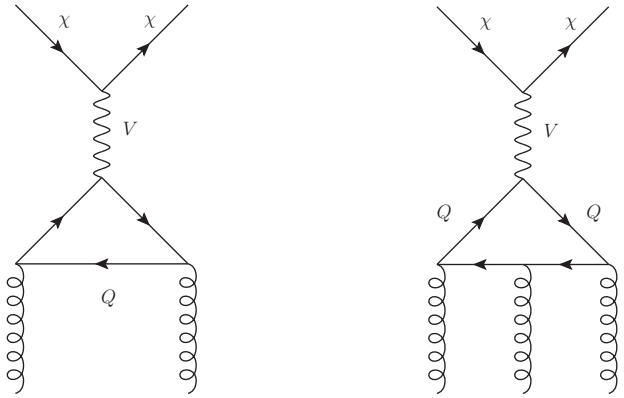

Figure 4.2: An example of the gluon contribution to DM-nuclear scattering for a spin-1/2 DM candidate coupled to heavy quarks via a *neutral* mediator, which couple to nucleons dominantly through a two-gluon operator (left). The only exception to the two-gluon coupling is a neutral vector or tensor mediator, which couples via three gluons due to Furry's theorem (right).

For the charged mediator models, Fig.4.1, the threshold matching of quark Q to the leading gluon operator, $\mathcal{O}_{GX}^{(Q)}$, is dominated by loop momenta of roughly either the heavy quark or mediator mass (rather than just the heavy quark mass as in the neutral mediator models). Assuming $m_{\rm MED} > m_Q$ as is almost always the case, the contributions from momenta $\sim m_{\rm MED}$ (m_Q) are termed *short distance* (*long distance*). The long distance contributions are found with relative ease by integrating out the mediator at tree level (as is done for in each model) and then calculating the gluon contribution using the resulting EFT operators, as depicted in Fig.4.3. Then, just as in the neutral mediated models, the Wilson coefficients are simply $C_{GXi}^{(Q)} \sim C_{Xi}^{(q)}$ where $X = S, F, V$ and with masses and couplings appropriated substituted. Because $\mathcal{O}_{GXi}^{(Q)}$ and $\mathcal{O}_{Xi}^{(q)}$ are assumed to lead to the same nucleon operator $\mathcal{O}_{Xi}^{(N)}$ the contribution to scattering from threshold matching of heavy quarks to gluons and from light quark scattering is of the same form (in terms of E_R dependence and form factors) differing only in overall normalization from hadronic matrix elements. The short distance contribution is less relevant, except if $m_{\rm MED} \lesssim m_Q$ and we mention it only for completeness.

The effective gluon operators are covariant, and are therefore built from the gluon field/dual-field strength ($G^{\mu\nu}$, $\widetilde{G}^{\mu\nu}$) and the covariant derivative (D^μ). For each of

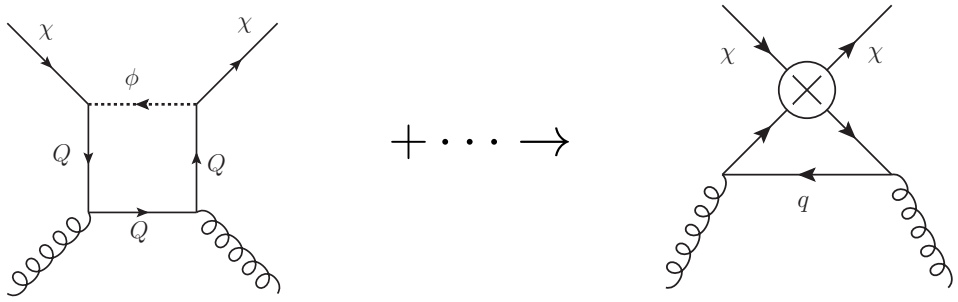

Figure 4.3: The long distance contribution to χ (coupled to heavy quark Q) scattering with nucleons through gluons can be found by integrating out the heavy mediator $\phi \gg m_Q$, and using the effective operators denoted by a cross in the right diagram.

the models, we require only the dominant EFT operator (taking to be leading order in m_Q^{-n} and α_s); charged mediator models consistently lead to a contribution from the operator $\mathcal{J}_{\rm DM}\ G^{\mu\nu}G_{\mu\nu}$, however for neutral mediator models the operators can appear quite obscure at first sight. We simply quote the results (which are also stated in [210] except for the tensor current which can be found in [220]) [2],

[2]The photon and gluon are both vector bosons, and both with flavour diagonal quark couplings. Unsurprisingly, matching the heavy quark currents onto two-photon operators yields almost identical results but with the gluon field strength replaced with the photon's $F^{\mu\nu}$. Differences in the matching arise due to the colour algebra. The two-photon operators are ignored however, since their form factors are much smaller than for the gluons, and the matching is additionally suppressed by $\alpha \ll \alpha_s$ at low energy (see for example [221]). Of course, unlike gluons (whose matching begins at $\mathcal{O}(\alpha_s)$) the photon matching begins at $\mathcal{O}(e)$ allowing single photon exchange, rendering the two-photon operators as subleading.

$$\bar{Q}Q \to \frac{\alpha_s}{12\pi m_Q} G^{\mu\nu}G_{\mu\nu} \equiv \mathcal{G}_S, \tag{4.2.4}$$

$$\bar{Q}i\gamma^5 Q \to \frac{\alpha_s}{16\pi m_Q} \widetilde{G}^{\mu\nu}G_{\mu\nu} \equiv \mathcal{G}_P, \tag{4.2.5}$$

$$\bar{Q}\gamma^\mu\gamma^5 Q \to \frac{\alpha_s}{6\pi m_Q^2}\left(G^{\rho\nu}\partial_\rho \widetilde{G}_{\mu\nu} + 2\widetilde{G}^{\mu\rho}\partial_\nu G^{\nu\rho}\right) \equiv \mathcal{G}_A^\mu, \tag{4.2.6}$$

$$\bar{Q}\gamma^\mu Q \to \frac{g_s^3}{45(4\pi)m_Q^4}\left(5\partial_\alpha \mathrm{Tr}\left[G_{\sigma\tau}\{G^{\sigma\tau}, G_{\alpha\mu}\}\right] - 14\partial_\alpha \mathrm{Tr}\left[G_{\mu\sigma}\{G^{\sigma\tau}, G_{\tau\alpha}\}\right]\right) \equiv \mathcal{G}_V^\mu, \tag{4.2.7}$$

$$\bar{Q}\sigma^{\mu\nu}Q \to \frac{g_s^3}{90(4\pi)m_Q^3}\left(15\mathrm{Tr}\left[\{G_{\mu\nu}, G^{\sigma\rho}\}G_{\sigma\rho}\right] - 32\mathrm{Tr}\left[G_{\mu\sigma}\{G^{\sigma\tau}, G_{\tau\nu}\}\right]\right) \equiv \mathcal{G}_T^{\mu\nu}. \tag{4.2.8}$$

Each of these operators appear for heavy quarks coupled to particular neutral mediators, but as already mentioned for charged mediators, $\mathcal{G}_S$ is always present and dominant. Note that the first three currents (scalar, pseudo-scalar and axial-vector) contain two gluon fields, corresponding to diagrams as in Fig.4.2 (the single gluon diagram is forbidden by gauge symmetry, and color conservation). For vector or tensor currents Furry's theorem forbids the two-gluon case also, and therefore there must be three gluons emitted from the loop, which is why the gluonic operator contains three field strengths (the vector current is also a total derivative as a consequence of its conservation). It is also difficult to derive these via the background field method, perhaps best using Feynman diagrams, as in [220].

We now present a list of the EFT operators, along with their Wilson coefficients, $C_i^{(q,Q)}$, for each model, partitioning into sections according to the spin of the DM, starting with spin-1/2. The gluonic operators are not listed explicitly but they are identical to those with light quarks, denoted $\mathcal{O}_{Xi}$, but using the replacements in Eqs. (4.2.4)-(4.2.8), and will be denoted $\mathcal{O}_{GXi}$.

We make one final note regarding the operators in the EFT. When integrating out the heavy quarks we will not just produce gluonic EFT operators, there will also in principle be contributions from photons (as well as Higgs and Z-boson above the

EW scale). Unlike for gluons, the DM can exchange a single photon with nuclei, and these contributions can be described using multipole moments of the DM. Computing all these various contributions is beyond the scope of this work, however the DD signal should not be considered complete unless these contributions are included. However, the limits on the parameter space of each model would only be affected when both the tree level scattering, and gluon scattering are suppressed. Indeed these situations are uncommon but do occur amongst our models, in these further study would likely present even stronger bounds.

Such studies including *all* DD signals are computationally expensive and only a handful can be found in the literature.

4.2.2 EFT Matching : Fermion DM

The set of EFT operators has the form $\mathcal{O}_F \equiv \bar{\chi}\Gamma_i\chi\ \bar{q}\Gamma_j q$, where

$$\Gamma_i, \Gamma_j \in (1, i\gamma^5, \gamma^\mu, \gamma^\mu\gamma^5, \sigma^{\mu\nu}, i\sigma^{\mu\nu}\gamma^5)$$

are the scalar, pseudo-scalar, vector, axial-vector and tensor structures respectively denoted "S,P,V,A,T,T′ ". In all cases the $i = j$ operators dominate over the $i \neq j$ in the non-relativistic limit.

The operators above are dimension six, dimension seven operators follow the same structure but with the introduction of a derivative in the hermitian form $\mathrm{Re}(\bar{\psi}_1\partial_\mu\psi_2) \equiv \bar{\psi}_1\partial_\mu\psi_2 + \partial_\mu\bar{\psi}_1\psi_2$ or $\mathrm{Im}(\bar{\psi}_1\partial_\mu\psi_2) \equiv \bar{\psi}_1\partial_\mu\psi_2 - \partial_\mu\bar{\psi}_1\psi_2$, which can occur on the DM or quark bilinears. Many of these dimension seven operators are equivalent through integration by parts and the Dirac equation, and due to their extra mass suppression we will neglect them[3]. One exception to this is the inclusion of so called *twist-2* operators, which appear in the Wilsonian OPE of EM currents into terms of fixed twist (defined as dimension - spin)[222], for quarks this operator

[3]The derivatives add a momentum dependence which adds further suppression in the NR limit

is [219, 223, 224]

$$\mathcal{O}_{\mu\nu} = \frac{1}{2}\bar{q}\left(D_\mu\gamma_\nu - D_\nu\gamma_\mu - \frac{1}{2}g_{\mu\nu}\not{D}\right)q \ , \tag{4.2.9}$$

which has dimension four, and thus spin-2 (which requires two Lorentz indices as is the case above), this creates a dimension seven or eight operator when contracted with the DM fields ($\bar{\chi}\gamma^\mu\partial^\nu\chi$, $\bar{\chi}\partial^\mu\partial^\nu\chi$). Since the twist-2 operator contains a $m_q\bar{q}q$ piece, it is mixed with $\bar{\chi}\chi\bar{q}q$, and so including it necessarily alters the Wilson coefficient of the scalar-scalar dimension six operator. We will list these alterations as appropriate.

With the structures $\sigma^{\mu\nu}$ and $i\sigma^{\mu\nu}\gamma^5$ we can build a set of four four-fermion operators, denoted $[X]\,[Y]$ with the square brackets denoting some combination of spinors. These four operators reduce to just two ($[\sigma_{\mu\nu}]\,[\sigma^{\mu\nu}]$ and $[\sigma^{\mu\nu}\gamma^5]\,[\sigma_{\mu\nu}]$) using the identity,

$$\sigma^{\mu\nu}\gamma^5 = \frac{1}{2}\epsilon^{\mu\nu\sigma\rho}\sigma_{\sigma\rho}, \tag{4.2.10}$$

and the contraction of the Levi-Civita tensor [225],

$$\epsilon^{\mu\nu\sigma\rho}\epsilon_{\mu\nu\alpha\beta} = -2(\delta^\mu{}_\alpha\delta^\nu{}_\beta - \delta^\mu{}_\beta\delta^\nu{}_\alpha), \tag{4.2.11}$$

then

$$\left[\sigma^{\mu\nu}\gamma^5\right]\left[\sigma_{\mu\nu}\gamma^5\right] = \left[\sigma^{\mu\nu}\right]\left[\sigma_{\mu\nu}\right] \tag{4.2.12}$$

$$\left[\sigma^{\mu\nu}\gamma^5\right]\left[\sigma_{\mu\nu}\right] = \left[\sigma^{\mu\nu}\right]\left[\sigma_{\mu\nu}\gamma^5\right] \ . \tag{4.2.13}$$

We now present the Wilson coefficients for the dominant EFT operators, for the cases of light quarks and heavy quarks[4]. These operators are listed in Tab.4.1, operators $\mathcal{O}_{F1,F5}$ have unsuppressed (no q or $v^\perp$ dependence as per Sec.4.4) spin-independent interactions and thus dominate the event rate, similarly $\mathcal{O}_{F5,F8}$ have unsuppressed spin-dependent interactions and provide a sub-dominant contribution.

[4]For each $C_{Fi}^{(q)} \neq 0$, there is a corresponding Wilson coefficient for heavy quarks denoted $C_{GFi}^{(Q)}$ corresponding to an operator with the same DM current as $\mathcal{O}_{Fi}^{(q)}$ but with the heavy quark current replaced according to Eqs.(4.2.4)-(4.2.8). This represents the leading threshold correction to gluons when the heavy quark is integrated out of the theory.

1/2-S, 1/2*-S

This cases applies to both Dirac and Majorana DM

$$C_{F1}^{(q)} = \frac{g_{q,s}\ g_{\chi,s}}{m_{\rm MED}^2},\ \ C_{F4}^{(q)} = \frac{g_{q,p}\ g_{\chi,p}}{m_{\rm MED}^2},$$
$$C_{F2}^{(q)} = \frac{g_{q,s}\ g_{\chi,p}}{m_{\rm MED}^2},\quad C_{F3}^{(q)} = \frac{g_{q,p}\ g_{\chi,s}}{m_{\rm MED}^2}. \tag{4.2.14}$$

A single γ, Z exchange with the nucleus is impossible at 1-loop order. A single h exchange contributes but only for true scalar mediators $g_{q,s} \neq 0$. The contribution is divergent at one-loop order, and thus runs giving a logarithmic term $\log(m_q/\Lambda)$ where Λ is a high scale. The Higgs couples to the partons in the nucleon, then Yukawa couplings for the light quarks heavily suppress the contribution.

1/2-V, 1/2*-V

This case is again the same for Majorana or Dirac DM, except that for Majorana DM the vector operators $C_{F5}^{(q)} = C_{F7}^{(q)} = C_{F9}^{(q)} = C_{F10}^{(q)} = 0$:

$$C_{F5}^{(q)} = \frac{g_{q,v}\ g_{\chi,v}}{m_{\rm MED}^2},\quad C_{F8}^{(q)} = \frac{g_{q,a}\ g_{\chi,a}}{m_{\rm MED}^2},$$
$$C_{F6}^{(q)} = \frac{g_{\chi,a}g_{q,v}}{m_{\rm MED}^2},\quad C_{F7}^{(q)} = \frac{g_{\chi,v}g_{q,a}}{m_{\rm MED}^2}. \tag{4.2.15}$$

Due to the propagator of V, $g^{\mu\nu} - q^\mu q^\nu/(m_{\rm MED}^2)$, the latter term (longitudinal polarization) leads to $\mathcal{O}_{F4}$, but it is suppressed by $m_q^2/m_{\rm MED}^2$.

Contributions from Higgs exchange are zero, however there can be divergent 1-loop contributions to photon and Z exchange (the former requires $g_{q,v} \neq 0$). The photon exchange is non-zero only for Dirac DM and may be described via the kinetic mixing between the photon and vector mediator [226], this leads to an approximate *charge radius* for the DM of,

$$b_\chi = \frac{2g_{\chi,v}g_{q,v}}{m_{\rm MED}^2}\frac{e}{24\pi^2}\sum_q \log\frac{m_q^2}{\Lambda_{\rm EW}^2}. \tag{4.2.16}$$

For the Z-boson, the vector couplings of the Z to the quark give roughly the same contribution as the photon. However since the Z itself should also be integrated out of the theory, the relevant diagram connects to a light quark bilinear, and thus

the amplitude has a factor q^2e^2/m_Z^2 in the low energy limit and compared with the photon contribution is negligible. The axial vector Z coupling gains a contribution $m_q^2e^2/m_Z^2$ for each quark, which can be somewhat larger for heavy quarks, but it also enforces the presence of $\bar{\chi}\gamma^\mu\gamma^5\chi$ (spin-suppressed) DM bilinear.

1/2-S$^\pm$

The Wilson coefficients are [5],

$$\begin{aligned}
C_{F1}^{(q)} &= C_{F4}^{(q)} = \frac{|g_p^{(q)}|^2 - |g_s^{(q)}|^2}{4(m_\chi^2 - m_{\rm MED}^2)} \\
C_{F2}^{(q)} &= C_{F3}^{(q)} = \frac{g_s^{(q)} g_p^{(q),\dagger} + g_p^{(q)} g_s^{(q),\dagger}}{4(m_\chi^2 - m_{\rm MED}^2)} \\
C_{F6}^{(q)} &= \frac{i(g_s^{(q)} g_p^{(q),\dagger} - g_p^{(q)} g_s^{(q),\dagger})}{4(m_\chi^2 - m_{\rm MED}^2)} \\
C_{F8}^{(q)} &= \frac{|g_s^{(q)}|^2 + |g_p^{(q)}|^2}{4(m_\chi^2 - m_{\rm MED}^2)}.
\end{aligned} \tag{4.2.17}$$

We can optionally include the dimension seven twist-2 operator, this modifies the scalar coupling

$$\begin{aligned}
C_{F1}^{(q)} &= \frac{|g_s^{(q)}|^2 - |g_p^{(q)}|^2}{2(m_\chi^2 - m_{\rm MED}^2)} + \frac{m_\chi m_q (|g_s^{(q)}|^2 + |g_p^{(q)}|^2)}{8(m_\chi^2 - m_{\rm MED}^2)^2}, \\
C_{TF1}^{(q)} &= -\frac{m_\chi (|g_s^{(q)}|^2 + |g_p^{(q)}|^2)}{2(m_\chi^2 - m_{\rm MED}^2)}.
\end{aligned} \tag{4.2.18}$$

When matching with Majorana DM, one will frequently find contributions to the amplitude of the operators which are zero in Tab.4.1, proportional to $C \sim m_f m_\chi / m_{\rm MED}^4$. These Wilson coefficients are formally $1/\Lambda^4$ (i.e. dimension-8), due to the inclusion of a derivative in the quark and DM bilinears (and as such allowing the operator to be non-zero) which projects out the mass of the particle in the low-energy limit. It is incorrect to use these Wilson coefficients for the dimension six operators as the hadronic matrix elements would be artificially inflated.

[5] Note that there is a factor of 1/2 in each of the Wilson coefficients in [219], we explicitly include this factor in the operators in Table. 4.1.

For heavy quarks there is an additional *short distance* contribution to C_{GF1} [219][6],

$$C_{GF1}^{(Q,\mathrm{sd})} = \frac{m_\chi m_Q \left(|g_s^{(Q)}|^2 + |g_p^{(Q)}|^2\right)}{8m_{\mathrm{MED}}^2(m_{\mathrm{MED}}^2 - m_\chi^2)}, \tag{4.2.19}$$

which is negligible given the $1/m_{\mathrm{MED}}^4$ suppression, unless $m_Q \gtrsim m_{\mathrm{MED}}$ which is not the case over most of the allowed parameter space.

For loop-level exchanges of Z, h we do not perform the calculation. Since we have assumed all particles are SM singlets, $\mathrm{SU}(2)_L$ is violated unless coupled to RH quarks. Once the SU(2) symmetry is enforced then the h, Z contributions may be safely calculated. Even so, the possible renormalizable interactions between the Higgs and mediator have been neglected, if included these would dominate the Higgs mediated scattering.

Both Z, h exchanges are mass/Yukawa suppressed relative to the photon contribution. Photon couplings are limited to a suppressed anapole moment for Majorana DM [226] however. Results for each of these may be found in Chapter 7 and so we do not reproduce them here.

[6]Calculating this contribution requires evaluation of box diagrams in which the mediator mass dominates the loop momentum (the one depicted on the left of Fig.4.1, the *long distance* contribution) as well as those in which the quark mass dominates (the right of Fig.4.1, the *short distance* contribution). Both contributions are of roughly the same size [223] and therefore one cannot simply use the EFT insertions from Eq.(4.2.17) with an intermediate heavy quark loop. This procedure would effectively set an upper limit of m_ϕ for the loop momentum, and would thus reproduce only the diagrams whose loop momenta are dominated by scales much lower than the mediator mass (the long distance contribution).

1/2*-S$^{\pm}$

The Wilson coefficients include the appearance of all the Lorentz structures $\mathcal{O}_{F1-9}$,

$$\begin{aligned}
C_{F1}^{(q)} &= C_{F4}^{(q)} = 2C_{F9}^{(q)} = \frac{|g_s^{(q)}|^2 - |g_p^{(q)}|^2}{4(m_\chi^2 - m_{\rm MED}^2)}, \\
C_{F2}^{(q)} &= C_{F3}^{(q)} = 2C_{F10}^{(q)} = \frac{g_s^{(q)} g_p^{(q),\dagger} + g_p^{(q)} g_s^{(q),\dagger}}{4(m_\chi^2 - m_{\rm MED}^2)}, \\
C_{F6}^{(q)} &= -C_{F7}^{(q)} = \frac{i\left(g_s^{(q)} g_p^{(q),\dagger} - g_p^{(q)} g_s^{(q),\dagger}\right)}{4(m_\chi^2 - m_{\rm MED}^2)}, \\
C_{F5}^{(q)} &= -C_{F8}^{(q)} = \frac{|g_s^{(q)}|^2 + |g_p^{(q)}|^2}{4(m_\chi^2 - m_{\rm MED}^2)}.
\end{aligned} \tag{4.2.20}$$

The $C_{F1}^{(q)}$ and $C_{F5}^{(q)}$ dominate in the NR limit, and $C_{F5}^{(q)}$ dominates in the event that $g_s = \pm g_p$. With notation as in the previous case the short distance heavy quark contribution is,

$$C_{GF1}^{(Q,{\rm sd})} = \frac{m_\chi m_Q \left(|g_s^{(Q)}|^2 + |g_p^{(Q)}|^2\right)}{8m_{\rm MED}^2(m_{\rm MED}^2 - m_\chi^2)}. \tag{4.2.21}$$

A full consideration of the scattering via γ, Z, h exchange can be found in Chapter 7 and we do not reproduce it here. The photon contribution is substantially larger than for the gluon.

1/2-V$^{\pm}$

A Majorana DM exchanging a charged vector mediator is similar to a charged scalar mediator,

$$
\begin{aligned}
C_{F1}^{(q)} &= \frac{\left(|g_v^{(q)}|^2 - |g_a^{(q)}|^2\right)}{m_\chi^2 - m_{\rm MED}^2}\left(1 - \frac{m_\chi^2}{4m_{\rm MED}^2}\right), \\
C_{F2}^{(q)} &= \frac{i\left(g_v^{(q)} g_a^{(q),\dagger} - g_a^{(q)} g_v^{(q),\dagger}\right)}{m_\chi^2 - m_{\rm MED}^2}\left(1 + \frac{m_\chi^2}{4m_{\rm MED}^2}\right), \\
C_{F3}^{(q)} &= -\frac{i\left(g_v^{(q)} g_a^{(q),\dagger} - g_a^{(q)} g_v^{(q),\dagger}\right)}{m_\chi^2 - m_{\rm MED}^2}\left(1 - \frac{m_\chi^2}{4m_{\rm MED}^2}\right), \\
C_{F4}^{(q)} &= \frac{\left(|g_v^{(q)}|^2 - |g_a^{(q)}|^2\right)}{m_\chi^2 - m_{\rm MED}^2}\left(1 + \frac{m_\chi^2}{4m_{\rm MED}^2}\right), \\
C_{F6}^{(q)} &= \frac{\left(g_v^{(q)} g_a^{(q),\dagger} + g_a^{(q)} g_v^{(q),\dagger}\right)}{2(m_\chi^2 - m_{\rm MED}^2)}\left(1 - \frac{m_\chi^2}{2m_{\rm MED}^2}\right), \\
C_{F8}^{(q)} &= \frac{|g_v^{(q)}|^2 + |g_a^{(q)}|^2}{2(m_\chi^2 - m_{\rm MED}^2)}\left(1 - \frac{m_\chi^2}{2m_{\rm MED}^2}\right),
\end{aligned}
\tag{4.2.22}
$$

the extra multiplicative factors relative to the 1/2-S$^{\pm}$ case come from the vector propagator term $q^\mu q^\nu / m_{\rm MED}^2$, as the momenta contract with gamma matrices and project out the DM mass from spinors, for example $\bar{u}(p')q^\mu\gamma_\mu u(k) = (m_\chi - m_q)\bar{u}(p')u(k)$.

Although the case for a charged scalar mediator has been discussed at length in the literature, primarily because it appears in supersymmetric models where ϕ and χ provide an analogy to squarks and the neutralino, the case of a charged vector has received relatively little attention.

No full calculation of the relevant box diagrams necessary to include the gluonic contribution from heavy quarks has been performed to my knowledge, however it is possible to obtain an approximate result in the limit of heavy mediators by using the EFT from above; this amounts to including diagrams in which the gluons are emitted from fermion lines (i.e. the leftmost diagram of Fig.4.1).

According to the EFT the result is accurate in the limit that $m_q^2/(m_\chi^2 - m_\phi^2) \ll 1$ [223, 224, 227]. To find this '*long distance*' contribution we can apply the Wilson coefficients in Eq.(4.2.22), then the gluon scattering given by a triangle diagram with a single EFT insertion of $\mathcal{O}_{F1}$ since only the scalar operator, $\mathcal{O}_{F1} = (1/2)\bar{\chi}\chi\bar{Q}Q$ can match to the dominant gluon operator $(1/2)\bar{\chi}\chi G^{\mu\nu}G_{\mu\nu}$. Then calculating the loop integral, and matching (for which one can simply use Eq.(4.2.4)) we find,

$$C_{GF1}^{(Q,\mathrm{ld})} = \frac{\left(|g_v^{(Q)}|^2 - |g_a^{(Q)}|^2\right)}{(m_\chi^2 - m_{\mathrm{MED}}^2)}\left(1 - \frac{m_\chi^2}{4m_{\mathrm{MED}}^2}\right). \tag{4.2.23}$$

As with the charged scalar mediator, the Z, h exchange cannot be calculated before first ensuring $\mathrm{SU}(2)_L$ invariance, which is not present in our Lagrangian. The γ coupling is restricted to an anapole moment by symmetries; but we find that this contribution is also zero as the amplitudes for the two diagrams vanish.

1/2*-V$^{\pm}$

The matching is structurally similar to 1/2*-S$^{\pm}$, but as with Majorana DM the vector propagator accounts for the multiplicative terms,

$$
\begin{aligned}
C_{F1}^{(q)} &= \frac{|g_a^{(q)}|^2 - |g_v^{(q)}|^2}{(m_\chi^2 - m_{\rm MED}^2)} \left(1 - \frac{m_\chi^2}{4m_{\rm MED}^2}\right), \\
C_{F2}^{(q)} &= \frac{i\left(g_v^{(q)} g_a^{(q),\dagger} - g_a^{(q)} g_v^{(q),\dagger}\right)}{(m_\chi^2 - m_{\rm MED}^2)} \left(1 + \frac{m_\chi^2}{4m_{\rm MED}^2}\right), \\
C_{F3}^{(q)} &= -\frac{i\left(g_v^{(q)} g_a^{(q),\dagger} - g_a^{(q)} g_v^{(q),\dagger}\right)}{(m_\chi^2 - m_{\rm MED}^2)} \left(1 - \frac{m_\chi^2}{4m_{\rm MED}^2}\right), \\
C_{F4}^{(q)} &= -\frac{|g_a^{(q)}|^2 - |g_v^{(q)}|^2}{(m_\chi^2 - m_{\rm MED}^2)} \left(1 + \frac{m_\chi^2}{4m_{\rm MED}^2}\right), \\
C_{F5}^{(q)} &= \frac{|g_v^{(q)}|^2 + |g_a^{(q)}|^2}{2(m_\chi^2 - m_{\rm MED}^2)} \left(1 + \frac{m_\chi^2}{2m_{\rm MED}^2}\right), \\
C_{F6}^{(q)} &= \frac{g_v^{(q)} g_a^{(q),\dagger} + g_a^{(q)} g_v^{(q),\dagger}}{2(m_\chi^2 - m_{\rm MED}^2)} \left(1 - \frac{m_\chi^2}{2m_{\rm MED}^2}\right), \\
C_{F7}^{(q)} &= \frac{g_v^{(q)} g_a^{(q),\dagger} + g_a^{(q)} g_v^{(q),\dagger}}{2(m_\chi^2 - m_{\rm MED}^2)} \left(1 + \frac{m_\chi^2}{2m_{\rm MED}^2}\right), \\
C_{F8}^{(q)} &= \frac{|g_v^{(q)}|^2 + |g_a^{(q)}|^2}{2(m_\chi^2 - m_{\rm MED}^2)} \left(1 - \frac{m_\chi^2}{2m_{\rm MED}^2}\right), \\
C_{F9}^{(q)} &= \frac{|g_v^{(q)}|^2 - |g_a^{(q)}|^2}{8(m_\chi^2 - m_{\rm MED}^2)} \frac{m_\chi^2}{m_{\rm MED}^2}, \\
C_{F10}^{(q)} &= \frac{i\left(g_v^{(q)} g_a^{(q),\dagger} - g_a^{(q)} g_v^{(q),\dagger}\right)}{8(m_\chi^2 - m_{\rm MED}^2)} \frac{m_\chi^2}{m_{\rm MED}^2}.
\end{aligned}
\tag{4.2.24}
$$

The matching to $C_{GF1}^{(Q)}$ is the same as for Majorana DM. The photon coupling is different since Dirac DM can have a magnetic dipole moment and a charge radius (as well as anapole moment),

$$
\mu_\chi \approx \frac{3m_\chi}{32\pi^2 m_{\rm MED}^2} \left(|g_v^{(q)}|^2 + |g_a^{(q)}|^2\right) + \frac{m_Q}{2\pi^2 m_{\rm MED}^2} \left(|g_a^{(q)}|^2 - |g_v^{(q)}|^2\right). \tag{4.2.25}
$$

4.2.3 EFT Matching : Vector DM

If the DM is a real or complex vector then there are 20 EFT operators to consider; plus the gluonic and twist-2 operators as shown in Tab.4.2. Some operators are zero,

	Dirac	Majorana
$\mathcal{O}_{F1}$	$\bar{\chi}\chi\bar{q}q$	$\frac{1}{2}\bar{\chi}\chi\bar{q}q$
$\mathcal{O}_{F2}$	$\bar{\chi}i\gamma^5\chi\bar{q}q$	$\frac{1}{2}\bar{\chi}i\gamma^5\chi\bar{q}q$
$\mathcal{O}_{F3}$	$\bar{\chi}\chi\bar{q}i\gamma^5 q$	$\frac{1}{2}\bar{\chi}\chi\bar{q}i\gamma^5 q$
$\mathcal{O}_{F4}$	$\bar{\chi}\gamma^5\chi\bar{q}\gamma^5 q$	$\frac{1}{2}\bar{\chi}\gamma^5\chi\bar{q}\gamma^5 q$
$\mathcal{O}_{F5}$	$\bar{\chi}\gamma^\mu\chi\bar{q}\gamma_\mu q$	–
$\mathcal{O}_{F6}$	$\bar{\chi}\gamma^5\gamma^\mu\chi\bar{q}\gamma_\mu q$	$\frac{1}{2}\bar{\chi}\gamma^5\gamma^\mu\chi\bar{q}\gamma_\mu q$
$\mathcal{O}_{F7}$	$\bar{\chi}\gamma^\mu\chi\bar{q}\gamma^5\gamma_\mu q$	–
$\mathcal{O}_{F8}$	$\bar{\chi}\gamma^5\gamma^\mu\chi\bar{q}\gamma^5\gamma_\mu q$	$\frac{1}{2}\bar{\chi}\gamma^5\gamma^\mu\chi\bar{q}\gamma^5\gamma_\mu q$
$\mathcal{O}_{F9}$	$\bar{\chi}\sigma^{\mu\nu}\chi\bar{q}\sigma_{\mu\nu}q$	–
$\mathcal{O}_{F10}$	$\bar{\chi}\sigma^{\mu\nu}\chi\bar{q}i\gamma^5\sigma_{\mu\nu}q$	–
$\mathcal{O}_{TF1}$	$\bar{\chi}i\partial^\mu\gamma^\nu\chi\mathcal{O}^{Tq}_{\mu\nu}$	$\frac{1}{2}\bar{\chi}i\partial^\mu\gamma^\nu\chi\mathcal{O}^{Tq}_{\mu\nu}$
$\mathcal{O}_{TF2}$	$\bar{\chi}\gamma^\mu\gamma^\nu\chi\mathcal{O}^{Tq}_{\mu\nu}$	$\frac{1}{2}\bar{\chi}\gamma^\mu\gamma^\nu\chi\mathcal{O}^{Tq}_{\mu\nu}$
$\mathcal{O}^{(Q)}_{GF1}$	$\frac{\alpha_s}{12\pi m_Q}\bar{\chi}\chi G^{\mu\nu}G_{\mu\nu}$	$\frac{1}{2}\frac{\alpha_s}{12\pi m_Q}\bar{\chi}\chi G^{\mu\nu}G_{\mu\nu}$

Table 4.1: EFT operators appearing for spin-1/2 DM candidates. The set of heavy quark operators are identical to $\mathcal{O}_{F1-10}$ but with the quark bilinears replaced according to Eqs.(4.2.4)-(4.2.8) and denoted $\mathcal{O}_{GF1-10}$.

for example the tensor operator $(B^\dagger_\mu B_\nu + B^\dagger_\nu B_\mu)\bar{q}\sigma^{\mu\nu}q$ is zero due to the antisymmetry of $\sigma^{\mu\nu}$ (equivalently for real vector DM), we must therefore have the antisymmetric combination $i(B^\dagger_\mu B_\nu - B^\dagger_\nu B_\mu)\bar{q}\sigma^{\mu\nu}q = 2iB^\dagger_\mu B_\nu\bar{q}\sigma^{\mu\nu}q$. A deliberate distinction has been made between the real and imaginary components of operators with derivatives; this is because they have different NR limits, and one must be careful as to which of the operators appears (the difference in the Feynman rules amounts to a relative sign between momenta). $\mathcal{O}_{V1,5-2}$ are the only spin-independent operators which are not either velocity or momentum suppressed; similarly $\mathcal{O}_{V9,8}$ are unsuppressed spin-dependent operators.

For vector particles the combination of polarizations appearing in the amplitudes $\varepsilon^i\varepsilon^j$ should be decomposed into the symmetric and antisymmetric parts, the antisymmetric part, $\varepsilon^{[i}\varepsilon^{j]}$, is proportional to the spin of the particle. The symmetric

component, $\varepsilon^{(i}\varepsilon^{j)}$, gives rise to new operators at the NR level, as pointed out in [116], but in practice these are present alongside operators with a larger form factor.

Some degeneracies are present in the operators listed in Tab.4.2. Firstly, $\mathcal{O}_{V5} = 0$ and $\mathcal{O}_{V6}$ is equivalent to $\mathcal{O}_{V2}$ by integration by parts and the Dirac equation;

$$C_{V5}^{(q)} = 0, \tag{4.2.26}$$

$$C_{V2}^{(q)} = -2m_q C_{V6}^{(q)}. \tag{4.2.27}$$

1-S, 1*-S

The DM-mediator coupling depends on a mass scale Λ,

$$C_{V1}^{(q)} = \frac{\Lambda\ g_s^{(q,Q)}\ g_\chi}{m_{\rm MED}^2}, \quad C_{V2}^{(q)} = \frac{\Lambda\ g_p^{(q,Q)}\ g_\chi}{m_{\rm MED}^2}. \tag{4.2.28}$$

The amplitude is heavily suppressed in the case of $g_s = 0$, since $\mathcal{O}_{V2}$ is momentum suppressed (and spin-dependent). The γ, Z cannot mix with the scalar mediator, and so only single Higgs exchange is possible, for $g_s \neq 0$.

1-V, 1*-V

There are in fact three independent vertices combining two DM vectors with a third vector V

$$\mathcal{V}_1 = (gB_\nu^\dagger \partial^\nu B^\mu + \text{h.c.})V_\mu, \tag{4.2.29}$$

$$\mathcal{V}_2 = (gB_\nu^\dagger \partial^\mu B^\nu + \text{h.c.})V_\mu, \tag{4.2.30}$$

$$\mathcal{V}_3 = \epsilon^{\mu\nu\sigma\rho}(gB_\mu^\dagger \partial_\nu B_\sigma + \text{h.c.})V_\rho. \tag{4.2.31}$$

In each case above g may be complex. For $\mathcal{V}_1$,

$$\begin{aligned} C_{V3}^{(q)} &= \frac{g_v^{(q,Q)}\ \mathrm{Re}(g_\chi)}{m_{\rm MED}^2},\ C_{V3-2}^{(q)} = \frac{g_v^{(q,Q)}\ \mathrm{Im}(g_\chi)}{m_{\rm MED}^2}, \\ C_{V4}^{(q)} &= \frac{g_a^{(q,Q)}\ \mathrm{Re}(g_\chi)}{m_{\rm MED}^2},\ C_{V4-2}^{(q)} = \frac{g_a^{(q,Q)}\ \mathrm{Im}(g_\chi)}{m_{\rm MED}^2}. \end{aligned} \tag{4.2.32}$$

For $\mathcal{V}_2$

$$\begin{aligned} C_{V5}^{(q)} &= \frac{g_v^{(q,Q)}\ \mathrm{Re}(g_\chi)}{m_{\rm MED}^2}, C_{V5-2}^{(q)} = \frac{g_v^{(q,Q)}\ \mathrm{Im}(g_\chi)}{m_{\rm MED}^2}, \\ C_{V6}^{(q)} &= \frac{g_a^{(q,Q)}\ \mathrm{Re}(g_\chi)}{m_{\rm MED}^2}, C_{V6-2}^{(q)} = \frac{g_a^{(q,Q)}\ \mathrm{Im}(g_\chi)}{m_{\rm MED}^2}. \end{aligned} \tag{4.2.33}$$

For $\mathcal{V}_3$

$$C_{V7}^{(q)} = \frac{g_v^{(q,Q)}\ \mathrm{Re}(g_\chi)}{m_{\rm MED}^2}, \quad C_{V7-2}^{(q)} = \frac{g_v^{(q,Q)}\ \mathrm{Im}(g_\chi)}{m_{\rm MED}^2},$$
$$C_{V8}^{(q)} = \frac{g_a^{(q,Q)}\ \mathrm{Re}(g_\chi)}{m_{\rm MED}^2}, C_{V8-2}^{(q)} = \frac{g_a^{(q,Q)}\ \mathrm{Im}(g_\chi)}{m_{\rm MED}^2}. \tag{4.2.34}$$

1-F

There is only a single model with vector DM and a charged mediator (including both real or complex DM), for real DM it gives rise to the following Wilson coefficients

$$C_{V1}^{(q)} = \frac{m_{\rm MED}\left(|g_a^{(q)}|^2 - |g_v^{(q)}|^2\right)}{(m_\chi^2 - m_{\rm MED}^2)} + \frac{m_q\left(|g_v^{(q)}|^2 + |g_a^{(q)}|^2\right)}{(m_\chi^2 - m_{\rm MED}^2)},$$
$$C_{V2}^{(q)} = -i\frac{m_{\rm MED}\left(g_v^{(q)} g_a^{(q),\dagger} - g_a^{(q)} g_v^{(q),\dagger}\right)}{(m_\chi^2 - m_{\rm MED}^2)},$$
$$C_{V7}^{(q)} = -\frac{1}{2}C_{V4-4}^{(q)} = \frac{\left(g_a^{(q)} g_v^{(q),\dagger} + g_v^{(q)} g_a^{(q),\dagger}\right)}{(m_\chi^2 - m_{\rm MED}^2)},$$
$$C_{V8}^{(q)} = \frac{1}{2}C_{V3-4}^{(q)} = \frac{\left(|g_v^{(q)}|^2 + |g_a^{(q)}|^2\right)}{(m_\chi^2 - m_{\rm MED}^2)}\ , \tag{4.2.35}$$

the interaction is dominated by $\mathcal{O}_{V1,V8}$, and is suppressed by chiral couplings $g_v^{(q)} = \pm g_a^{(q)}$ by a factor $m_q/m_{\rm MED}$. We can include the twist-2 operator in this case as it is suppressed only by $(m_\chi^2 - m_{\rm MED}^2)^{-2}$, this modifies the coefficient of $\mathcal{O}_{V1}$,

$$C_{V1}^{(q)} = -\frac{m_{\rm MED}^2 m_q\left(|g_v^{(q)}|^2 + |g_a^{(q)}|^2\right)}{2(m_\chi^2 - m_{\rm MED}^2)^2} + \frac{m_{\rm MED}\left(|g_v^{(q)}|^2 - |g_a^{(q)}|^2\right)}{(m_{\rm MED}^2 - m_\chi^2)},$$
$$C_{TV}^{(q)} = -\frac{2\left(|g_v^{(q)}|^2 + |g_a^{(q)}|^2\right)m_\chi^2}{(m_\chi^2 - m_{\rm MED}^2)^2}. \tag{4.2.36}$$

For heavy quarks the long distance contribution is [7]

$$C_{GV1}^{(Q)} = \frac{m_{\rm MED}\left(|g_a^{(Q)}|^2 - |g_v^{(Q)}|^2\right)}{(m_\chi^2 - m_{\rm MED}^2)} + \frac{m_Q\left(|g_v^{(Q)}|^2 + |g_a^{(Q)}|^2\right)}{(m_\chi^2 - m_{\rm MED}^2)}. \tag{4.2.37}$$

In the limit $m_{\rm MED} \to \infty$ we reproduce the results of [229].

[7] The full box diagrams, including the short distance contribution, are evaluated in the Fock-Schwinger gauge in [219, 228].

1*-F

For this case, we do not include the twist-2 operator since it appears with a $(m_\chi^2 - m_{\rm MED}^2)^{-3}$ suppression,

$$C_{V1}^{(q)} = C_{V9}^{(q)} = \frac{m_{\rm MED}\left(|g_a^{(q)}|^2 - |g_v^{(q)}|^2\right)}{(m_\chi^2 - m_{\rm MED}^2)} + \frac{m_q\left(|g_v^{(q)}|^2 + |g_a^{(q)}|^2\right)}{(m_\chi^2 - m_{\rm MED}^2)},$$
$$C_{V2}^{(q)} = -\frac{1}{2}C_{V10}^{(q)} = \frac{im_{\rm MED}\left(g_a^{(q)}g_v^{(q),\dagger} - g_v^{(q)}g_a^{(q),\dagger}\right)}{2(m_\chi^2 - m_{\rm MED}^2)},$$
$$C_{V4-2}^{(q)} = 2C_{V4-4}^{(q)} = -2C_{V6-2}^{(q)} = -2C_{V7}^{(q)} = \frac{\left(g_a^{(q)}g_v^{(q),\dagger} + g_v^{(q)}g_a^{(q),\dagger}\right)}{(m_\chi^2 - m_{\rm MED}^2)},$$
$$C_{V3-2}^{(q)} = 2C_{V3-4}^{(q)} = -2C_{V5-2}^{(q)} = 2C_{V8}^{(q)} = \frac{\left(|g_v^{(q)}|^2 + |g_a^{(q)}|^2\right)}{(m_\chi^2 - m_{\rm MED}^2)}. \quad (4.2.38)$$

Similarly with the real vector case, the dominant $V1$ spin-independent interaction is suppressed by $m_q/m_{\rm MED}$ in the limit $g_v = g_a$; however $\mathcal{O}_{V5-2}$ is also present which leads to a spin-independent interaction with mass dependence $\approx (m_N m_\chi/m_{\rm MED}^2)$, which can become dominant for large m_χ since for $V1$ the mass dependence is $(m_N/m_{\rm MED})^2$. The heavy quarks lead to the same result as for real vector DM.

4.2.4 EFT Matching : Scalar DM

Scalar DM has the most restricted set of EFT operators, only two dimension five and two dimension 6 operators appear in our models (plus four gluonic operators for heavy quarks, and a single dim-7 twist-2 operator). There are no DM spin-dependent couplings for scalar DM, however $\mathcal{O}_{S1,S3}$ provide a dominant spin-independent response. The operator $\phi\partial^\mu\phi\bar{q}\gamma_\mu q = \frac{1}{2}\partial^\mu(\phi^2)\bar{q}\gamma_\mu q$ is redundant since (via integration by parts) this equals a total derivative plus $\partial^\mu(\bar{q}\gamma_\mu q) = -im_q\bar{q}q$.

0-S, 0*-S

This is a t-channel scattering, and the matching is simple for light quarks,

$$C_{S1}^{(q)} = \frac{\Lambda g_\chi g_s^{(q)}}{m_{\rm MED}^2}, \quad C_{S2}^{(q)} = \frac{\Lambda g_\chi g_p^{(q)}}{m_{\rm MED}^2}, \quad C_{S3,S4,TS}^{(q)} = 0, \quad (4.2.39)$$

and applies equally for real or complex DM.

	Real	Complex
$\mathcal{O}_{V1}$	$\frac{1}{2}B^\mu B_\mu \bar{q}q$	$B^\dagger_\mu B^\mu \bar{q}q$
$\mathcal{O}_{V2}$	$\frac{1}{2}B^\mu B_\mu \bar{q}i\gamma^5 q$	$B^\dagger_\mu B^\mu \bar{q}i\gamma^5 q$
$\mathcal{O}_{V3}$	$\frac{1}{2}B^\nu \partial_\nu B_\mu \bar{q}\gamma^\mu q$	$\mathrm{Re}(B^\dagger_\nu \partial^\nu B_\mu)\bar{q}\gamma^\mu q$
$\mathcal{O}_{V3-2}$	–	$i\mathrm{Im}(B^\dagger_\nu \partial^\nu B_\mu)\bar{q}\gamma^\mu q$
$\mathcal{O}_{V3-3}$	–	$\mathrm{Im}(B^\dagger_\nu B_\mu)\mathrm{Im}(\partial^\nu \bar{q}\gamma^\mu q)$
$\mathcal{O}_{V3-4}$	$\frac{i}{2}B^\nu B_\mu \mathrm{Im}(\partial_\nu \bar{q}\gamma^\mu q)$	$i\mathrm{Re}(B^\dagger_\nu B_\mu)\mathrm{Im}(\partial^\nu \bar{q}\gamma^\mu q)$
$\mathcal{O}_{V4}$	$\frac{1}{2}B^\nu \partial_\nu B_\mu \bar{q}\gamma^\mu\gamma^5 q$	$\mathrm{Re}(B^\dagger_\nu \partial^\nu B_\mu)\bar{q}\gamma^\mu\gamma^5 q$
$\mathcal{O}_{V4-2}$	–	$i\mathrm{Im}(B^\dagger_\nu \partial^\nu B_\mu)\bar{q}\gamma^\mu\gamma^5 q$
$\mathcal{O}_{V4-3}$	–	$\mathrm{Im}(B^\dagger_\nu B_\mu)\mathrm{Im}(\partial^\nu \bar{q}\gamma^\mu\gamma^5 q)$
$\mathcal{O}_{V4-4}$	$\frac{i}{2}B^\nu B_\mu \mathrm{Im}(\partial_\nu \bar{q}\gamma^\mu\gamma^5 q)$	$i\mathrm{Re}(B^\dagger_\nu B_\mu)\mathrm{Im}(\partial^\nu \bar{q}\gamma^\mu\gamma^5 q)$
$\mathcal{O}_{V5}$	$\frac{1}{2}B^\mu \partial_\nu B_\mu \bar{q}\gamma^\nu q$	$\mathrm{Re}(B^\dagger_\mu \partial^\nu B_\mu)\bar{q}\gamma^\nu q$
$\mathcal{O}_{V5-2}$	–	$i\mathrm{Im}(B^\dagger_\mu \partial^\nu B_\mu)\bar{q}\gamma^\nu q$
$\mathcal{O}_{V6}$	$\frac{1}{2}B^\mu \partial_\nu B_\mu \bar{q}\gamma^\nu\gamma^5 q$	$\mathrm{Re}(B^\dagger_\mu \partial^\nu B_\mu)\bar{q}\gamma^\nu\gamma^5 q$
$\mathcal{O}_{V6-2}$	–	$i\mathrm{Im}(B^\dagger_\mu \partial^\nu B_\mu)\bar{q}\gamma^\nu\gamma^5 q$
$\mathcal{O}_{V7}$	$\frac{1}{2}\epsilon^{\mu\nu\sigma\rho}B_\mu \partial_\nu B_\sigma \bar{q}\gamma^\rho q$	$\mathrm{Re}(\epsilon^{\mu\nu\sigma\rho}B^\dagger_\nu \partial_\mu B_\sigma)\bar{q}\gamma^\rho q$
$\mathcal{O}_{V7-2}$	–	$i\mathrm{Im}(\epsilon^{\mu\nu\sigma\rho}B^\dagger_\nu \partial_\mu B_\sigma)\bar{q}\gamma^\rho q$
$\mathcal{O}_{V8}$	$\frac{1}{2}\epsilon^{\mu\nu\sigma\rho}B_\mu \partial_\nu B_\sigma \bar{q}\gamma^\rho\gamma^5 q$	$\mathrm{Re}(\epsilon^{\mu\nu\sigma\rho}B^\dagger_\nu \partial_\mu B_\sigma)\bar{q}\gamma^\rho\gamma^5 q$
$\mathcal{O}_{V8-2}$	–	$i\mathrm{Im}(\epsilon^{\mu\nu\sigma\rho}B^\dagger_\nu \partial_\mu B_\sigma)\bar{q}\gamma^\rho\gamma^5 q$
$\mathcal{O}_{V9}$	–	$iB^\dagger_\mu B_\nu \bar{q}\sigma^{\mu\nu}q$
$\mathcal{O}_{V10}$	–	$B^\dagger_\mu B_\nu \bar{q}\sigma^{\mu\nu}\gamma^5 q$
$\mathcal{O}_{TV}$	$\frac{1}{2}\mathcal{O}^{\mu\nu}_{T2,q}B^\rho \partial^\mu \partial^\nu B_\rho$	$\mathcal{O}^{\mu\nu}_{T2,q}B^\rho \partial^\mu \partial^\nu B^\dagger_\rho$
$\mathcal{O}^{(Q)}_{GV1}$	$\frac{\alpha_s}{24\pi m_Q}B^\mu B_\mu G^{\nu\sigma}G_{\nu\sigma}$	$\frac{\alpha_s}{12\pi m_Q}B^\dagger_\mu B^\mu G^{\nu\sigma}G_{\nu\sigma}$

Table 4.2: EFT operators appearing for Vector DM candidates. The set of heavy quark operators are identical to $\mathcal{O}_{V1-9}$ but with the quark bilinear replaced according to Eqs.(4.2.4)-(4.2.8) by a gluon current, and denoted $\mathcal{O}_{GV1-9}$. Operators $\mathcal{O}_{V5,V6}$ are redundant, but we include them in this list for completeness. The notation $\mathrm{Re}(\partial_\nu \bar{q}\gamma^\mu q) \equiv (\partial_\nu \bar{q})\gamma^\mu q + \bar{q}\gamma^\mu \partial_\nu q$.

For γ, Z, h exchange, the arguments are identical to the $1/2 - S$ model, only the Higgs couples and only when $g_{\chi,s} \neq 0$. This contribution is extremely small due to the Yukawa couplings of the light quarks; it can also introduce more model dependence through couplings between the neutral scalar and Higgs.

0*-V

This is a t-channel scattering, and the matching is simple

$$C_{S3}^{(q)} = \frac{g_\chi g_v^{(q)}}{m_{\rm MED}^2}, \quad C_{S4}^{(q)} = \frac{g_\chi g_a^{(q)}}{m_{\rm MED}^2}, \quad C_{S1,S2,T2}^{(q)} = 0, \tag{4.2.40}$$

and exists only for complex scalar DM.

As for the EW sector, h exchange is not possible. For γ, Z exchange the contribution is most easily found by considering the mixing between V and the photon or Z. After integrating out the mediator the relevant Lagrangian is [226]

$$\mathcal{L}_{\rm eff} = \sum_q \frac{2\epsilon^{(q)} g_\chi}{m_{\rm MED}^2} \left(\phi^\dagger \partial^\mu \phi\right) \partial_\mu F^{\mu\nu}, \tag{4.2.41}$$

where ϵ is the coefficient of the kinetic mixing operator and is approximately given by,

$$\epsilon^{(q)} = \frac{g_v^{(q)} N_c Q e}{24\pi^2} \log\left(\frac{m_q^2}{\Lambda_V^2}\right),$$

with $\Lambda_V \sim 1$ TeV a high scale. We will assume the Z-couplings are negligible compared with the photon case (the scattering cross section would go as $\sim m_\chi^2 m_q^2 / m_\phi^2 m_Z^2$)

0-F$^\pm$

The only scalar DM model with a charged (fermionic) mediator gives, for real DM,

$$\begin{aligned} C_{S1}^{(q)} &= \frac{m_{\rm MED}\left(|g_p^{(q)}|^2 - |g_s^{(q)}|^2\right)}{(m_\chi^2 - m_{\rm MED}^2)} - \frac{m_q\left(|g_s^{(q)}|^2 + |g_p^{(q)}|^2\right)}{(m_\chi^2 - m_{\rm MED}^2)}, \\ C_{S2}^{(q)} &= \frac{i m_{\rm MED}\left(g_p^{(q)} g_s^{(q),\dagger} - g_s^{(q)} g_p^{(q),\dagger}\right)}{m_\chi^2 - m_{\rm MED}^2}, \quad C_{S3,S4}^{(q)} = 0. \end{aligned} \tag{4.2.42}$$

We may optionally include the twist-2 operator, since there is a term $\propto (k\cdot p)^2/(m_\chi^2 - m_{\rm MED}^2)$ in the amplitude, this modifies the scalar coupling,

$$C_{S1}^{(q)} = \frac{m_{\rm MED}\left(|g_p^{(q)}|^2 - |g_s^{(q)}|^2\right)}{(m_\chi^2 - m_{\rm MED}^2)} - \frac{m_q(m_\chi^2 - 2m_{\rm MED}^2)\left(|g_s^{(q)}|^2 + |g_p^{(q)}|^2\right)}{2(m_\chi^2 - m_{\rm MED}^2)^2},$$
$$C_{TS}^{(q)} = -\frac{\left(|g_s^{(q)}|^2 + |g_p^{(q)}|^2\right)}{(m_\chi^2 - m_{\rm MED}^2)^2}. \tag{4.2.43}$$

For heavy quark currents, the box diagrams contribute to the scalar gluon operator $\phi^\dagger\phi\mathcal{O}_{GS1}^{(Q)}$, and we limit ourselves to this (the dominant) operator [8],

$$C_{GS1}^{(Q)} = \frac{m_{\rm MED}\left(|g_p^{(Q)}|^2 - |g_s^{(Q)}|^2\right)}{(m_\chi^2 - m_{\rm MED}^2)} - \frac{m_Q\left(|g_s^{(Q)}|^2 + |g_p^{(Q)}|^2\right)}{(m_\chi^2 - m_{\rm MED}^2)}. \tag{4.2.44}$$

Real scalar DM cannot posses any electromagnetic multipole moments (this forbids single on-shell photon exchange). Two photon exchange is possible, but is sub-dominant to the gluon contribution given above. Single h, Z exchange with the nucleus is possible, but can only be calculated fully after producing an $\mathrm{SU}(2)_L$ invariant Lagrangian; the minimum realization of this would be an SU(2) singlet (doublet) charged mediator coupled to q_R (q_L).

0*-F$^\pm$

The complex scalar leads to the appearance of $\mathcal{O}_{S3}$ unlike the real scalar case. The twist-2 operator is neglected due to a $(m_\chi^2 - m_{\rm MED}^2)^{-3}$ suppression,

$$C_{S1}^{(q)} = -\frac{m_q\left(|g_s^{(q)}|^2 + |g_p^{(q)}|^2\right)}{m_\chi^2 - m_{\rm MED}^2} - \frac{m_{\rm MED}\left(|g_s^{(q)}|^2 - |g_p^{(q)}|^2\right)}{m_\chi^2 - m_{\rm MED}^2},$$
$$C_{S2}^{(q)} = \frac{im_{\rm MED}\left(g_p^{(q)}g_s^{(q),\dagger} - g_s^{(q)}g_p^{(q),\dagger}\right)}{(m_\chi^2 - m_{\rm MED}^2)}, \quad C_{S3}^{(q)} = -\frac{\left(|g_s^{(q)}|^2 + |g_p^{(q)}|^2\right)}{2(m_\chi^2 - m_{\rm MED}^2)},$$
$$C_{S4}^{(q)} = -\frac{\left(g_p^{(q)}g_s^{(q),\dagger} + g_s^{(q)}g_p^{(q),\dagger}\right)}{2(m_\chi^2 - m_{\rm MED}^2)}, \tag{4.2.45}$$

the heavy quark matching, $C_{GS1}^{(Q)}$, is the same as for real DM. Complex scalar DM can posses only a single multipole moment, the charge radius (or electric monopole)

[8] See [219] for both the long and short distance contributions. Note that our definition of G_S includes a factor $\alpha_s/(12\pi m_Q)$.

	Real	Complex
$\mathcal{O}_{S1}$	$\frac{1}{2}SS\bar{q}q$	$S^\dagger S\bar{q}q$
$\mathcal{O}_{S2}$	$\frac{1}{2}SS\bar{q}i\gamma^5 q$	$S^\dagger S\bar{q}i\gamma^5 q$
$\mathcal{O}_{S3}$	-	$\frac{1}{2}i(S^\dagger\partial^\mu S - S\partial^\mu S^\dagger)\bar{q}\gamma_\mu q$
$\mathcal{O}_{S4}$	-	$i(S^\dagger\partial^\mu S - S\partial^\mu S^\dagger)\bar{q}\gamma_\mu\gamma^5 q$
$\mathcal{O}_{TS}$	$\frac{1}{2}\mathcal{O}^{\mu\nu}_{\mathrm{T2,q}}S\partial_\mu\partial_\nu S$	$\mathcal{O}^{\mu\nu}_{\mathrm{T2,q}}S^\dagger\partial_\mu\partial_\nu S$
$\mathcal{O}^{(Q)}_{GS1}$	$\frac{\alpha_s}{24\pi m_Q}SSG^{\mu\nu}G_{\mu\nu}$	$\frac{\alpha_s}{12\pi m_Q}S^\dagger SG^{\mu\nu}G_{\mu\nu}$

Table 4.3: EFT operators appearing for scalar DM candidates. The set of heavy quark operators are identical to $\mathcal{O}_{S1-4}$ but with the quark bilinear replaced according to Eqs.(4.2.4)-(4.2.8) and denoted $\mathcal{O}_{GS1-4}$.

b_ϕ,

$$\mathcal{L} = ib_\phi\partial_\mu\phi^\dagger\partial_\nu\phi F^{\mu\nu}, \tag{4.2.46}$$

which is approximately

$$b_\phi = \frac{QN_c e\left(|g_s^{(q)}|^2 + |g_p^{(q)}|^2\right)}{8\pi^2 m_{\mathrm{MED}}^2}\left(1 + \frac{4}{3}\log\left(\frac{m_Q}{m_{\mathrm{MED}}}\right)\right). \tag{4.2.47}$$

This now concludes the matching procedure after the heavy quarks and mediators are integrated out, leaving the light quarks, DM and gluons. We now move onto the next step in the calculation.

4.3 Step 2 : Hadronic Matrix Elements

Now that our models are matched to EFT operators with a simple quark or gluon structure, we can consider the implications of the fact that even though our model is written in terms of fundamental degrees of freedom (i.e. quarks and gluons), at the low energies of DD experiments the DM scatters from nuclei and so in order to be able to calculate the nuclear form factors, we require a Lagrangian in which the nucleons are the fundamental degrees of freedom.

To account for this we must calculate the value of the hadronic matrix elements for each of the EFT operators (from Tab.4.1, 4.2 and 4.3),

$$\langle N|\mathcal{O}^{(\mathrm{EFT})}|N\rangle\,, \tag{4.3.48}$$

where $|N\rangle \equiv |n(k,s), p(k,s)\rangle$ represents a neutron/proton state with momentum k^μ and spin s^μ. All of the EFT operators are written in the factorized form $\mathcal{O}^{(\mathrm{EFT})} = \mathcal{O}_{\mathrm{DM}}\mathcal{O}_{q,G}$ containing a DM bilinear and a quark or gluon bilinear, then the DM bilinear factors out of the hadronic matrix element,

$$\langle N|\,\mathcal{O}_{\mathrm{DM}}\mathcal{O}_{q,G}\,|N\rangle = \mathcal{O}_{\mathrm{DM}}\,\langle N|\,\mathcal{O}_{q,G}\,|N\rangle\,. \tag{4.3.49}$$

Thus we only need to consider matrix elements of quark bilinears of the form $\mathcal{O}^{(q)}_{S,P,V,A,T,T'} \equiv \bar{q}\{1, i\gamma^5, \gamma^\mu, \gamma^\mu\gamma^5, \sigma^{\mu\nu}, i\sigma^{\mu\nu}\gamma^5\}q$, which due to their symmetries, preserve their Lorentz structure at the nucleon level [9],

$$C_i^{(q)}\bar{q}\Gamma^i q \to \langle N|\,C_i^{(q)}\bar{q}\Gamma^i q\,|N\rangle\,\bar{N}\Gamma^i N = C_i^{(N)}\bar{N}\Gamma^i N, \tag{4.3.50}$$

where $N(k,s), \bar{N}(k,s)$ are nucleon spinors, behaving just like quark spinors. The nucleon-level couplings $C_i^{(N)}$ are related to the quark-level Wilson coefficients $C_i^{(q)}$. One way to think about these matrix elements is that each quark bilinear acts as an operator which probes a particular property of the nucleon; for example $i = S$ probes the number density (mass) of both quark and antiquarks, $i = P, A$ probes the spin of quark and antiquark, $i = T, T'$ probes the difference in spin between quark and anti-quark, and finally $i = V$ probes the valence quark number. The

[9] The form of the nucleon bilinear is constrained by symmetries such as $\mathcal{C}, \mathcal{P}, \mathcal{T}$. In reality multiple operators of nucleon bilinears are present (not just those with the same dirac matrix configuration), for example $q^\mu\bar{N}\sigma^{\mu\nu}N$, which contributes to the anomalous magnetic moment, appears alongside $\bar{N}\gamma^\mu N$ [29], however all such operators are suppressed by momentum exchange q^μ and are neglected. The neglected operators would contribute to the momentum dependence of the nucleon form factor $F(q^2)$, and our approximation amounts to taking $F(0)$.

exact correspondance is [230],

$$C_S^{(N)} = \sum_{q=u,d,s} f_{T_q}^{(N)} \frac{m_N}{m_q} C_S^{(q)}, \tag{4.3.51}$$

$$C_P^{(N)} = \sum_{q=u,d,s} f_{5,q}^{(N)} \frac{m_N}{m_q} C_P^{(q)}, \tag{4.3.52}$$

$$C_V^{(N)} = \sum_{q=u,d,s} \mathcal{V}_q^{(N)} C_V^{(q)}, \tag{4.3.53}$$

$$C_A^{(N)} = \sum_{q=u,d,s} \Delta_q^{(N)} C_A^{(q)}, \tag{4.3.54}$$

$$C_T^{(N)} = \sum_{q=u,d,s} \delta_q^{(N)} C_T^{(q)}, \; C_{T'}^{(N)} = \sum_{q=u,d,s} \delta_q^{(N)} C_{T'}^{(q)}, \tag{4.3.55}$$

where f_{T_q} are the expectation values of the mass distributions of valence quarks inside the nucleon, Δ_q (δ_q) are the expectation of the sum (difference) of the quark/anti-quark spin helicity distributions,

$$\Delta_q^{(N)} = \int_0^1 dx(\Delta q(x) + \Delta\bar{q}(x)),$$
$$\delta_q^{(N)} = \int_0^1 dx(\Delta q(x) - \Delta\bar{q}(x)).$$

We define the pseudo-scalar constant $f_{5,q}^{(N)}$ (equivalent to $f_{5q,N}^{(0)}$ in [29]), it is constructed from the SU(3) flavour singlet, triplet and octet form factors $g_A^{0,3,8}$ (which are themselves defined in terms of Δ_q).

As well as light-quark bilinears, the EFT operators may also contain 2-gluon or 3-gluon operators $\mathcal{G}_i$. These originate from heavy quark bilinears $\bar{Q}\Gamma^i Q$, and so the nucleon operators are constrained to have the same symmetry properties and are essentially a rescaled copy of those in Eq.(4.3.51)-(4.3.55):

$$C_{G_S}^{(Q)} \mathcal{G}_S \to C_{G_S}^{(N)} \bar{N} N, \tag{4.3.56}$$

$$C_{G_P}^{(Q)} \mathcal{G}_P \to C_{G_P}^{(N)} \bar{N} i\gamma^5 N, \tag{4.3.57}$$

$$C_{G_V}^{(Q)} \mathcal{G}_V^\mu \to C_{G_V}^{(N)} \bar{N} \gamma^\mu N, \tag{4.3.58}$$

$$C_{G_A}^{(Q)} \mathcal{G}_A^\mu \to C_{G_A}^{(N)} \bar{N} \gamma^\mu \gamma^5 N. \tag{4.3.59}$$

The nucleon couplings are related the gluon distribution in the nucleon,

$$C_{G_S}^{(N)} = \sum_{Q=c,b,t} f_{T_Q}^{(N)} \frac{m_N}{m_Q} C_{G_S}^{(Q)}, \tag{4.3.60}$$

$$C_{G_P}^{(N)} = \sum_{Q=c,b,t} f_{5,Q}^{(N)} \frac{m_N}{m_Q} C_{G_P}^{(Q)}, \;\; f_{5,Q}^{(N)} = \frac{f_{5,G}^{(N)}}{2m_N} \tag{4.3.61}$$

$$C_{G_A}^{(N)} = \sum_{Q=c,b,t} \Delta_Q^{(N)} C_{G_A}^{(Q)}, \tag{4.3.62}$$

$$C_{G_V}^{(N)} = \sum_{Q=c,b,t} \mathcal{V}_Q^{(N)} C_V^{(Q)}. \tag{4.3.63}$$

In the above results, the vector and axial vector constants arise dominantly through RG running effects as we will discuss.

The scalar coupling Eq.(4.3.60) is well known [231] and can be derived using the QCD scale anomaly, which directly relates $f_{T_Q}^{(N)}$ to $f_{T_q}^{(N)}$. However such a relation is not possible in the other cases. The pseudo-scalar coupling often used [230] is derived using a leading color approximation, under the assumption that the axial-vector form factor $g_A^0(q^2) = 0$ for the flavour singlet current. The assumption $g_A^0 = 0$ gains $\frac{1}{N_c}$ corrections and is estimated to be $g_A^0 \approx 0.34 - 0.37$ [232].

The matrix element of the heavy quark vector current can be extracted from [233], but note that the gluonic operator, Eq.(4.2.8), is a total derivative and can be written in the from $\partial_\nu T^{\nu u}$, with $T^{\nu\mu}$ antisymmetric to preserve current conservation. There is thus suppression factor $\partial^\mu \to q^\mu$ contributing to nucleon form factors which we have neglected for the other cases. One may proceed anyway and derive the proton matrix element,

$$\begin{aligned} q^\mu \langle p| T^{\mu\nu} |p\rangle &= \frac{g_s^3}{45(4\pi)m_Q^2} \left(\frac{1}{2} \left(\frac{\alpha_s}{\pi} \right)^3 \frac{5}{18} \left(\frac{3}{2}\xi(3) - \frac{19}{16} \right) \right) \\ &\times \sum_{q=u,d,s} m_q q^\mu \langle p| \bar{q}\sigma^{\mu\nu} q |p\rangle , \\ &\equiv C_V^{(p)} q^\mu \bar{N}\sigma^{\mu\nu} N. \end{aligned}$$

The heavy quark mass is taken as the renormalization scale and $\alpha_s \sim 0.2$, and the

nulceon tensor charge $\delta_q^{(p)} \equiv \langle p|\, \bar{q}\sigma^{\mu\nu} q\, |p\rangle$ is $\delta_u^{(p)} \approx 0.84$, $\delta_d^{(p)} \approx -0.23$ [234],

$$\begin{aligned} C_V^{(N)} &\approx C_V^{(Q)} \frac{\alpha_s^{9/2}}{m_Q^2 \pi^{5/2} 162} \left(\frac{3}{2}\xi(3) - \frac{19}{16}\right) \sum_q m_q \delta_q^{(N)} \\ &\approx 10^{-7} \left(\frac{C_V^{(Q)}}{m_Q^2}\right). \end{aligned}$$

Clearly the contribution to the form factors is negligible, however as we will discuss shortly there is the possibility that the heavy quark vector current mixes with light quark vector currents as the scale is decreased towards $\mu = m_Q$. The interpretation of the vector current matrix element is that it counts the number of quarks minus the number of anti-quarks, this can be done explicitly with the quark *parton density functions* (pdfs) $q(x, Q^2)$ as a function of x, the momentum of the parton as a fraction of the nucleon's momentum, and the momentum transfer Q^2,

$$\mathcal{V}_q^{(N)} = \int_0^1 dx \left(q(x, Q^2) - \bar{q}(x, Q^2)\right).$$

The intrinsic charm and bottom pdf may be found in [235], although the common assumption $Q(x) = \bar{Q}(x)$ gives $\mathcal{V}_Q^{(N)} = 0$.

The divergence of the axial vector heavy quark current can be written [236],

$$\partial_\mu j_{5,\mu}^Q = \frac{\alpha_s}{48\pi m_Q^2} \partial_\mu R^\mu, \tag{4.3.64}$$

where $j_{5,\mu}^Q = \bar{Q}\gamma^\mu\gamma^5 Q$, and,

$$R^\mu = \partial_\mu \left(G^a_{\rho\sigma} \widetilde{G}_a^{\rho\sigma}\right) - 4\left(D_\rho G^{\sigma\rho}\right) \widetilde{G}_{\sigma\mu}, \tag{4.3.65}$$

in the forward scattering limit $\partial_\mu \to q_\mu \to 0$ the first term in R^μ is suppressed with respect to the second, which contributes to the axial form factor $F_A(q^2)$. We can use the QCD equation of motion for the gluon which reads,

$$D_\mu G^{\mu\nu} = g_s \sum_q^{n_f} \bar{q} t^a \gamma^\nu q, \tag{4.3.66}$$

where the sum runs over all the n_f remaining quarks in the theory, and so

$$\frac{\alpha_s}{48\pi m_Q^2} \lim_{q\to 0} \langle N|\, R_\mu\, |N\rangle = -\frac{\alpha_s}{12\pi m_Q^2} \sum_q^{n_f} \langle N|\, g_s \bar{q} \widetilde{G}_{\nu\mu} \gamma^\nu q\, |N\rangle. \tag{4.3.67}$$

	$N = p$	$N = n$
$f_{T_u}^{(N)}$	0.018(6)	0.016(7)
$f_{T_d}^{(N)}$	0.034(12)	0.038(13)
$f_{T_s}^{(N)}$	0.044(8)	0.044(8)
$f_{T_Q}^{(N)}$	0.067(39)	0.067(38)

	$N = p$	$N = n$
$\Delta_u^{(N)}$	0.84(1)	-0.43(1)
$\Delta_d^{(N)}$	-0.43(1)	0.84(1)
$\Delta_s^{(N)}$	-0.057(21)	-0.057(21)
$g_A^{(N,0)}$	0.35(2)	0.35(2)

	$N = p$	$N = n$
$\delta_u^{(N)}$	0.774(66)	-0.233(28)
$\delta_d^{(N)}$	-0.233(28)	0.774(66)
$\delta_s^{(N)}$	-0.05	-0.05
$f^{(2,N)}$	-0.037	-0.013

	$N = p$	$N = n$
$f_{5,u}^{(N)}$	0.42	-0.41
$f_{5,d}^{(N)}$	-0.85	0.86
$f_{5,s}^{(N)}$	-0.0063	-0.45
$f_{5,Q}^{(N)}$	0.14	0.063

	$N = p$	$N = n$
$\mathcal{V}_u^{(N)}$	2	1
$\mathcal{V}_d^{(N)}$	1	2
$\mathcal{V}_s^{(N)}$	0.0	0.0
$\mathcal{V}_b^{(N)}$	0.0072	0.0

Table 4.4: The nucleon constants used in this study, all of which appear from nucleon matrix elements of quark or gluon operators. These can be found in [29] following the methods described in the text.

The operator $\bar{q}\widetilde{G}_{\nu\mu}\gamma^{\nu}q$ has twist-4 (dimension 5 and therefore spin-1). Unsurprisingly then, it's matrix elements are defined as (see [237], p.368),

$$\langle N|\,\bar{Q}g\widetilde{G}_{\mu\nu}\gamma^{\nu}Q\,|N\rangle = 2m_N^2 f_q^{(2,N)} S_\mu \ , \tag{4.3.68}$$

and are proportional to the nucleon spin $S^\mu \equiv \bar{N}\gamma^\mu\gamma^5 N$. Therefore [236],

$$\langle N|\,\frac{\alpha_s}{48\pi m_Q^2}R_\mu\,|N\rangle = \langle N|\,j^Q_{5,\mu}\,|N\rangle = \frac{\alpha_s}{6\pi}\left(\frac{m_N}{m_Q}\right)^2 f^{(2,N)}S_\mu \ . \tag{4.3.69}$$

We have defined $f^{(2,N)} = \sum_{q=u,d,s,\ldots}^{n_f} f_q^{(2)} \approx f_u^{(2,N)} + f_d^{(2,N)}$, which arises as a power correction to the spin distribution function, and is $f^{(2,p)} \approx -0.037$ for protons and $f^{(2,n)} \approx -0.013$ for neutrons [238]. For the charm quark, $\sum_{q=u,d,s} f_q^{(2,N)} = f_S^{(2,N)}$ is the flavour singlet contribution and the expression for Eq.(4.3.62) would be,

$$\Delta_Q^{(N)} = \frac{\alpha_s}{6\pi} f_S^{(2,N)}\left(\frac{m_N}{m_Q}\right)^2 . \tag{4.3.70}$$

$f_S^{(2,N)}$ can be calculated using an instanton method [239], obtaining $f_S^{(2,N)} = 0.01$, or using QCD sum rules [238] $f_S^{(2,N)} = 0.09$. For the bottom quark we may assume the same value for $\sum_{q=u,d,s,c} f_q^{(2,N)} \approx f_S^{(2,N)}$ due to negligible charm contribution, then the coupling is roughly $(m_c/m_b)^2 \sim 0.09$ times smaller (and even more suppressed for the top quark). This calculation thus provides the intrinsic heavy quark contribution to the first moment of the spin structure function $\Delta q(x,\mu)$. The suppression in this case of the effective nucleon coupling is not so harsh as for heavy-quark vector currents, but still significantly lower than the scalar or pseudo-scalar currents.

This very naive treatment gives a rough estimate of the heavy quark contribution to nucleon spin through the dominant operator arising from threshold matching. However, it neglects the RG running and subsequent threshold corrections of other heavy quark flavours (the axial current has an anomalous dimension). We can instead try to find the intrinsic contribution to the nucleon spin, $\Delta_Q^{(N)}$, including these effects which turn out to be much less suppressed and will be discussed shortly.

4.3.1 Further Discussion of Hadronic Matrix Elements

Scalar

The matrix elements of scalar quark currents are written

$$\langle N|\, m_q \bar{q}q \,|N\rangle \equiv m_N f_{T_q}^{(N)} \ . \tag{4.3.71}$$

This is a reasonable result since $\bar{q}q$ acts as a number operator in the nucleon, counting the number of quark q, so then $f_{T_q}^{(N)}$ represents the fractional contribution of quark q to the nucleon mass m_N. The light quark ($q = u, d, s$) scalar matrix elements may be extracted from lattice calculations. The strange quark contribution is the largest.

The trace of the QCD energy momentum tensor is (at leading order in α_s)[231],

$$\theta^{\mu}_{\ \mu} = \sum_{q=1}^{n_f} m_q \bar{q}q + \frac{\beta_0(\alpha_s)}{4\alpha_s} G^a_{\mu\nu} G_a^{\mu\nu}, \tag{4.3.72}$$

valid for $n_f = 6$ quark flavours, the second term arises from the anomaly of the classical QCD scale invariance to NLO order. At energy scales $\mu \lesssim 170$ GeV, the top quark is integrated out and $n_f = 5$. At DD energy scales $\mu \sim 1$ GeV, the $Q = c, b, t$ quarks are all integrated out leaving $n_f = 3$ flavours, and making the replacement in Eq.(4.3.72),

$$m_Q \bar{Q}Q = -\frac{\alpha_s}{12\pi} G^a_{\mu\nu} G_a^{\mu\nu} + \mathcal{O}(m_Q^{-1}), \tag{4.3.73}$$

for the heavy quarks (this is the leading term in the heavy quark expansion) then since $\beta_0(\alpha_s) = -(11 - \frac{2}{3}n_f)\frac{\alpha_s^2}{2\pi}$ ($n_f = 3$ for $\mu < m_c$), taking the nucleon matrix element of Eq.(4.3.72) and letting $\langle \theta^{\mu}_{\ \mu} \rangle_N = m_N$,

$$-\frac{\alpha_s}{12\pi} \langle G^a_{\mu\nu} G_a^{\mu\nu} \rangle_N = \frac{2}{27} m_N \left(\sum_{q=u,d,s} f_{T_q}^{(N)} - 1 \right) \ . \tag{4.3.74}$$

The threshold matching of quark Q scalar current generates the LHS of the above equation and thus defining $\langle m_Q \bar{Q}Q \rangle_N \equiv f_{T_Q}^{(N)} m_N$ we find,

$$f_{T_Q}^{(N)} = \frac{2}{27} \left(1 - \sum_{q=u,d,s} f_{T_q}^{(N)} \right) \ , \tag{4.3.75}$$

then $f_{T_Q}^{(p,n)} \approx 0.07$. This treatment is approximate in several senses, firstly it is NLO accurate in coupling and mass running. Secondly, the threshold matching considers only the generation of $\mathcal{O}_{G_S}$, but the light quark scalar currents are also generated at two-loop level [231].

It is possible to calculate the heavy quark scalar matrix element $\langle m_Q \bar{Q} Q \rangle$ for $Q = c, b, t$ using the matching conditions between the full theory (with $n_f + 1$ flavours) and the theory with the heavy quark integrated out (with n_f flavours denoted by primed quantities). The threshold matching conditions are written as,

$$\langle \mathcal{O}'_i \rangle (\mu) = M_{ji} \langle \mathcal{O}_j \rangle (\mu) + \mathcal{O}(1/m_Q),$$

where the matching takes place at some scale μ_Q which can be taken to be the heavy quark mass $\mu_Q = m_Q$. The above equation shows that when integrating out heavy quarks, multiple operators are generated with matrix elements M_{ij}, where $i, j = Q, q, g$; these can be calculated order by order in α_s using Feynman diagrams. For example, the matrix element M_{Qg} represents a Feynman diagram which connects a $\bar{Q}Q$ current with $G^{\mu\nu}G_{\mu\nu}$ which is a one-loop diagram with two external gluons and one external scalar current, thus M_{Qg} begins at $\mathcal{O}(\alpha_s)$. Both M_{gQ} and M_{qQ} begin at two-loop level and have been calculated to three-loop level in [240], and using Eq.(4.3.72) one can derive

$$\langle m_Q \bar{Q} Q \rangle' / m_N = M_{qQ} \lambda + M_{gQ} \frac{2}{\tilde{\beta}^{(n_f)}} (1 - (1 - \gamma_m^{(n_f)}) \lambda) \ , \tag{4.3.76}$$

where $\lambda m_N = \sum_q^{n_f} \langle m_q \bar{q} q \rangle$, and the explicit n_f dependence is highlighted with superscripts, and which enters $\tilde{\beta} = \beta / g_s$ and γ_m (the anomalous mass dimension) at two-loop order. These expressions depend on $\alpha_s^{(n_f)}(\mu)$, which we must determine at several scales, and thus we need to know the RG evolution and matching conditions for it. The RG running of the strong coupling constant at NLO leads to,

$$\alpha_s^{(n_f),\mathrm{NLO}}(\mu) = \frac{2\pi}{\beta_0 \log(\mu/\Lambda)} \ , \tag{4.3.77}$$

$\alpha_s^{(n_f)}(\mu)$ depends on the asymptotic scale Λ, which is determined using the boundary

condition that the coupling at the Z mass is equal to $\alpha_s^{(5)}(m_Z) = 0.1184$[10] (in the $n_f = 5$ flavour theory since the top quark is much heavier than the Z). This gives a value $\Lambda = 211$ MeV. Thus by use of Eq.(4.3.77), the strong coupling $\alpha_s^{(5)}(\mu)$ is evolved down from a scale $\mu = m_Z$ to $\mu = m_b = 4.18$ GeV for which $\alpha_s^{(5)}(m_b) = 0.2180$; roughly two times larger.

The $n_f = 5$ flavour theory is matched to the $n_f = 4$ theory at a scale $\mu = m_b$, i.e. the b-quark is integrated out of the theory. The matching for the coupling is given at $\mathcal{O}(\alpha^3)$ by [240],

$$\frac{\alpha_s^{(n_f)}(\mu)}{\alpha_s^{(n_f+1)}(\mu)} = 1 - \frac{\alpha_s^{(n_f+1)}(\mu)}{6}\log\left(\frac{\mu^2}{\mu_h^2}\right) + \alpha_s^{(n_f+1)}(\mu)^2\left(\frac{1}{36}\log\left(\frac{\mu^2}{\mu_h^2}\right)^2 - \frac{19}{24}\log\left(\frac{\mu^2}{\mu_h^2}\right) + \frac{11}{72}\right) , \qquad (4.3.78)$$

where μ is the matching scale (taken to be m_b) and μ_h is the mass of the heavy quark evaluated at a scale μ in the $\overline{\text{MS}}$ scheme[11]. Setting $n_f = 4$, $\mu = 4.18$ and $\mu_h = 4.18$ the logs disappear and $\alpha_s^{(4)}(m_b) = 0.2318$. Then repeating the process and evolving down to $\mu = m_c = 1.275$ GeV, $\alpha_s^{(4)}(m_c) = 0.4818$ (with $\Lambda = 354$ MeV), and then matching to the three flavour theory $\alpha_s^{(3)}(m_c) = 0.5975$.

The hadronic matrix element of the heavy quark scalar current, $\langle m_Q\bar{Q}Q\rangle_N$ is given up to $\mathcal{O}(\alpha_s^4)$ (three loop order) in Eq.(39) of [29], for brevity the NLO result is,

$$\langle m_Q\bar{Q}Q\rangle\frac{1}{m_N} = \frac{1}{3\beta_0^{(n_f)}}(2-2\lambda) + \frac{\alpha_s^{(n_f+1)}(\mu_Q)}{\pi}\left(\frac{57}{2} - \frac{321\lambda}{2} + 8n_f\right) ,$$

where $\lambda m_N = \sum_q^{n_f}\langle m_q\bar{q}q\rangle$. The right hand side is precisely $f_{T_Q}^{(N)}$, which may be calculated sequentially for c, b, t. Firstly $f_{T_c}^{(N)}$ in the $n_f = 3$ theory requires $\beta_0^{(3)} = 9/4$, $\alpha_s^{(4)}(m_c) = 0.3981$ and $\lambda = 0.089$ MeV, which gives $f_{T_c}^{(N)} = 0.078$.

[10] To test the equations we can use the two fixed values $\alpha_s^{(5)}(m_Z) = 0.118$ and $\alpha_s^{(4)}(m_\tau) = 0.36$, starting at m_Z and evolving down, including the matching we find good agreement $\alpha_s^{(4)}(m_\tau) = 0.32$.

[11] The $\overline{\text{MS}}$ masses of the b and c quarks are $\bar{m}_b(\bar{m}_b) = 4.18$ and $\bar{m}_c(\bar{m}_c) = 1.275$ GeV [241].

Next, for the b quark in the $n_f = 4$ theory requires $\beta_0^{(4)} = 25/12$, $\alpha_s^{(5)}(m_b) = 0.2266$ and $\lambda = 0.089 + f_{T_c}^{(N)} = 0.162$ MeV, which gives $f_{T_b}^{(N)} = 0.071$. These values show good agreement with the result derived at the start of the section using the energy-momentum tensor.

The values for the u, d contribution come from the observables,

$$\sigma_{\pi N} = \frac{m_u + m_d}{2} \langle \bar{u}u + \bar{d}d \rangle \in [40, 60] \text{ MeV},$$
$$\sigma_{-}^{n,p} = (m_u - m_d) \langle \bar{u}u - \bar{d}d \rangle \in \pm [0, 4] \text{ MeV}.$$

$\sigma_{\pi N}$ can be found from πN scattering data using *Heavy Baryon Chiral Perturbation Theory* (HBChPT) [242, 243], or from lattice QCD calculations (see [244] for a world average), these agree within 2σ and are in the range stated above. Following [245] we take a conservative value of $\sigma_{\pi N} = 50 \pm 15$ MeV to cover the literature. Using the expressions in [29] with the latest values $R_{ud} = m_u/m_d = 0.48 \pm 0.10$ we produce the values and errors stated in Tab.4.4. The strange quark contribution from lattice calculations gives estimates in the range $\sigma_s = m_N f_{Ts}^N \in [40, 50]$ MeV with an average of $\sigma_s = 41.3 \pm 7.7$ MeV [245].

Pseudo-scalar

The nucleon matrix element of the pseudo-scalar operator $\bar{q}i\gamma^5 q$ between nucleon states $\langle N(k')|$ and $|N(k)\rangle$ is parametrized in a similar way to the scalar operator

$$\langle m_q \bar{q} i\gamma^5 q \rangle \equiv m_N f_{5,q}^{(N)} \ . \tag{4.3.79}$$

Note that in [232] (which we follow) the definition is instead $E_q \equiv \langle \bar{q}i\gamma^5 q \rangle$ and so $E_q \equiv m_N/m_q f_{5,q}^{(N)}$. Additionally one defines

$$\sum_{q=u,d,s} \langle \bar{q}i\gamma^5 q \rangle = \kappa \bar{N} i\gamma^5 N \ , \tag{4.3.80}$$

i.e. $\sum_{q=u,d,s} (m_N/m_q) f_{q,5}^{(N)} = \kappa$, where $\kappa(q^2, \mu)$ is a scale dependent quantity.

The pseudo-scalar current matrix elements are related to those for the axial vector through the axial anomaly. The axial vector bilinears are combined into

singlet triplet and octet states under the SU(3) flavour symmetry,

$$\begin{aligned} A^0_\mu &= \bar{q}\gamma^\mu\gamma^5 T^0 q = \bar{u}\gamma^\mu\gamma^5 u + \bar{d}\gamma^\mu\gamma^5 d + \bar{s}\gamma^\mu\gamma^5 s \ , \\ A^8_\mu &= \bar{q}\gamma^\mu\gamma^5 T^8 q = \bar{u}\gamma^\mu\gamma^5 u + \bar{d}\gamma^\mu\gamma^5 d - 2\bar{s}\gamma^\mu\gamma^5 s \ , \\ A^3_\mu &= \bar{q}\gamma^\mu\gamma^5 T^3 q = \bar{u}\gamma^\mu\gamma^5 u - \bar{d}\gamma^\mu\gamma^5 d \ , \end{aligned} \tag{4.3.81}$$

where $q = (u, d, s)$, and T^i are the SU(3) Gell-man matrices. Rearranging Eq.(4.3.81)

$$\begin{aligned} \bar{u}\gamma^\mu\gamma^5 u &= \frac{1}{3}A^0_\mu + \frac{1}{6}A^8_\mu + \frac{1}{2}A^3_\mu, \\ \bar{d}\gamma^\mu\gamma^5 d &= \frac{1}{3}A^0_\mu + \frac{1}{6}A^8_\mu - \frac{1}{2}A^3_\mu, \\ \bar{s}\gamma^\mu\gamma^5 s &= \frac{1}{3}A^0_\mu - \frac{1}{3}A^8_\mu. \end{aligned} \tag{4.3.82}$$

The divergence of the singlet current A^μ_0 is anomalous, but the triplet and octet are not. The axial anomaly equation is

$$\begin{aligned} \sum_q \langle \partial_\mu \bar{q}\gamma^\mu\gamma^5 q\rangle &= 2\sum_q m_q \langle \bar{q} i\gamma^5 q\rangle - \frac{g_s^2 n_f}{32\pi^2}\langle \epsilon^{\mu\nu\sigma\rho} G^a_{\mu\nu} G^a_{\sigma\rho}\rangle \\ &= 2m_N\left(\sum_q f^{(N)}_{5,q} - \frac{g_s^2 n_f}{64\pi^2} f^{(N)}_{G,5}\right), \\ 3m_N F^0 &= 2m_N\left(\sum_q f^{(N)}_{5,q} - n_f f^{(N)}_{G,5}\right), \end{aligned}$$

with the definition $f^{(N)}_{G,5} \equiv \langle(\alpha_s/8\pi)\widetilde{G}^{\mu\nu}G_{\mu\nu}\rangle$. The derivative can be used to reduce the axial current to a pseudo-scalar one ($\partial^\mu \bar{q}\gamma^5\gamma_\mu q \to m_q \bar{q} i\gamma^5 q$). Accounting also for the anomaly, one finds

$$\begin{aligned} \partial^\mu A^0_\mu &= m_u \bar{u} i\gamma^5 u + m_d \bar{d} i\gamma^5 d + m_s \bar{s} i\gamma^5 s + 3\frac{\alpha_s}{8\pi}\widetilde{G}G \ , \\ \partial^\mu A^8_\mu &= m_u \bar{u} i\gamma^5 u + m_d \bar{d} i\gamma^5 d - 2m_s i\bar{s}\gamma^5 s \ , \\ \partial^\mu A^3_\mu &= m_u \bar{u} i\gamma^5 u - m_d \bar{d} i\gamma^5 d \ . \end{aligned} \tag{4.3.83}$$

Then taking nucleon matrix elements, defining $\langle \partial^\mu A^i_\mu\rangle \equiv m_N g^i_A(q^2,\mu)$ to be the *axial form factors*,

$$\begin{aligned} g^{N,0}_A &= \sum_{q=u,d,s} f^{(N)}_{5,q} + \frac{3}{m_N}\left\langle \frac{\alpha_s}{8\pi}\widetilde{G}G\right\rangle, \\ g^{N,8}_A &= f^{(N)}_{5,u} + f^{(N)}_{5,d} - 2f^{(N)}_{5,s}, \\ g^{N,3}_A &= f^{(N)}_{5,u} - f^{(N)}_{5,d}, \end{aligned} \tag{4.3.84}$$

measurements of the axial form factors at $q^2 = 0$ for the proton yield $(g_A^{p,0}, g_A^{p,3}, g_A^{p,8}) \in (0.35 \pm 0.02, 1.27, 0.52 \pm 0.06)$. Lower values for the singlet and octet form factors are extracted from semi-leptonic hyperon decays [29], for which the notation $F_A^{(N,3)}(q^2) \equiv \frac{1}{2} g_A^{N,3}(q^2)$, $F_A^{(N,8)}(q^2) \equiv \frac{1}{2\sqrt{3}} g_A^{N,8}(q^2)$, $F_A^{(N,0)}(q^2) \equiv \frac{1}{3} g_A^{N,0}(q^2)$ is used. From isospin invariance $g_A^{p,0} = g_A^{n,0}$ and $g_A^{p,8} = g_A^{n,8}$, but $g_A^{p,3} = -g_A^{n,3}$ picks up a relative sign, the octet and triplet factors are scale invariant, but the singlet has a mild scale dependence arising from the anomalous piece, which may be neglected. Using the last two equations of Eq.(4.3.84) (plus Eq.(4.3.80)), one can derive the $f_{5,q}(N)$ in terms of the octet and triplet form factors,

$$\begin{aligned}
f_{5,u}^{(N)} \bar{m}^{-1} &= \frac{\kappa}{m_N} + \frac{1}{2}\left(\frac{2}{m_d} + \frac{1}{m_s}\right) g_A^{N,3} + \frac{1}{2}\frac{1}{m_s} g_A^{N,8}, \\
f_{5,d}^{(N)} \bar{m}^{-1} &= \frac{\kappa}{m_N} - \frac{1}{2}\left(\frac{2}{m_u} + \frac{1}{m_s}\right) g_A^{N,3} + \frac{1}{2}\frac{1}{m_s} g_A^{N,8}, \\
f_{5,s}^{(N)} \bar{m}^{-1} &= \frac{\kappa}{m_N} + \frac{1}{2}\left(\frac{1}{m_u} - \frac{1}{m_d}\right) g_A^{N,3} - \frac{1}{2}\left(\frac{1}{m_u} + \frac{1}{m_d}\right) g_A^{N,8},
\end{aligned} \tag{4.3.85}$$

where we define

$$\bar{m} = (m_u^{-1} + m_d^{-1} + m_s^{-1})^{-1}. \tag{4.3.86}$$

Summing together these terms

$$\sum_{q=u,d,s} f_{5,q}^{(N)}\ \bar{m}^{-1} = \frac{3\kappa}{m_N} + \frac{1}{2}\left(\frac{1}{m_d} - \frac{1}{m_u}\right) g_A^{N,3} + \frac{1}{2}\left(-\frac{1}{m_u} - \frac{1}{m_d} + 2\frac{1}{m_s}\right) g_A^{N,8}. \tag{4.3.87}$$

Combining Eq.(4.3.84),(4.3.85),(4.3.87)

$$\begin{aligned}
\left\langle \frac{\alpha_s}{8\pi} \widetilde{G}G \right\rangle = \frac{1}{2}\frac{m_N \bar{m}}{m_u m_d m_s}\Bigg(&\frac{2}{3}\frac{m_u m_d m_s}{\bar{m}} g_A^0 + \frac{1}{3} m_s (m_d - m_u) g_A^3 \\
&+ \frac{1}{3}(m_s(m_u + m_d) - 2 m_u m_d) g_A^8\Bigg) - \kappa \bar{m}\ .
\end{aligned} \tag{4.3.88}$$

We can set $\kappa \sim 0$, which potentially receives $1/N_c$ corrections [232]. Since $m_s \gg m_{u,d}$ and $m_u \sim m_d$, we can approximately find $f_{5,q}^{(N)}$. Indeed $f_{5,d}^{(N)} \sim -\frac{1}{2} g_A^{N,3} \sim -0.64(0.64)$ for protons (neutrons) respectively, $f_{5,u}^{(N)} \sim -f_{5,d}^{(N)}$ and $f_{5,s}^{(N)} \sim -\frac{1}{2} g_A^{N,8} \sim$

-0.26 [12].

For heavy quark pseudo-scalar currents, $m_Q\bar{Q}i\gamma^5 Q$, we use the fact that the threshold matching at $\mathcal{O}(\alpha_s)$ picks up a contribution to a gluon operator (Eq.(4.2.8)), defining

$$\left\langle \frac{\alpha_s}{16\pi}\widetilde{G}G \right\rangle \equiv \frac{1}{2} f_{5,G}^{(N)}. \tag{4.3.90}$$

Then from Eq.(4.3.84) we get

$$\langle \bar{Q}i\gamma^5 Q\rangle \to \left\langle \frac{\alpha_s}{16\pi m_Q}\widetilde{G}G \right\rangle = \frac{f_{5,G}^{(N)}}{2m_Q} \approx \frac{1}{2}\frac{m_N}{m_Q}\frac{1}{3}\left(g_A^{(N,0)} - \sum_{q=u,d,s} f_{5,q}^{(N)} \right), \tag{4.3.91}$$

which gives numerically $f_{5,G}^{(p)} \sim 0.26$ and $f_{5,G}^{(n)} \sim 0.12$.

Axial Vector

We have preempted the matrix elements of the axial currents already in Eq.(4.3.84). We define,

$$\langle \bar{q}\gamma^\mu\gamma^5 q\rangle \equiv \Delta_q^{(N)} S^\mu, \tag{4.3.92}$$

where S^μ is the nucleon spin vector, and so $\Delta_q^{(N)}$ may be interpreted as the fractional contribution to the spin of nucleon N from quark q[13], and it is related to the *axial form factors* $F_A^{(N,q)}(q^2,\mu)$ at zero momentum transfer,

$$F_A^{(N,q)}(0,\mu) = \int_0^1 (\Delta q(x,\mu) - \Delta\bar{q}(x,\mu))dx, \tag{4.3.93}$$

[12] For light quark masses we use the PDG values [246],

$$\begin{aligned} m_u &= 2.3 \pm 0.6 \text{ MeV}, \\ m_d &= 4.8 \pm 0.4 \text{ MeV}, \\ m_s &= 95 \pm 5 \text{ MeV}. \end{aligned} \tag{4.3.89}$$

[13] Due to the axial anomaly this is not precisely true, and contributions from gluons are also included.

for quark helicity distributions Δq and with $F_A^{(N,q)}(q^2,\mu) \equiv \langle \bar{q}\gamma_\mu\gamma^5 q\rangle\, S^\mu$, and thus $\Delta_q^{(N)} \equiv F_A^{(N,q)}(0,\mu)$ are equivalent notations. Using Eq.(4.3.82) with the values of given in the previous section yield; $\Delta_u^{(p)} = 0.84$, $\Delta_d^{(p)} = -0.43$, $\Delta_s^{(p)} = -0.06$. Using the definition above, Eq.(4.3.93), with NNPDF sets yields similar numbers and allows a determination of the scale dependence with amounts to $\lesssim 1\%$ change in $F_A^{(N,q)}$ between $\mu = 1-2$ GeV [29].

Heavy quarks also contribute to the spin with $\Delta_Q^{(N)}$ defined equivalently to light flavours, these contributions are generated at the loop level with renormalization group techniques [247, 248]. They are relevant for the axial charge for quark couplings to the Z[14] (for example in the measurement of the proton axial charge in νp scattering [248]) which is

$$2g_A^{(Z,p)} = \sum_{q=u,c,t} \Delta_q^{(p)} - \sum_{q=d,s,b} \Delta_q^{(p)} \ , \tag{4.3.95}$$

to arrive at the values of $\Delta_Q^{(p)}$ we will briefly review the technique. One begins with the SM at a sufficiently high scale $\mu > m_t$ as above; then the axial current $J_{\mu,5}$ is anomaly free and given by Eq.(4.3.94). One then performs a *heavy quark expansion* (a Wilsonian OPE) to give an EFT expanded in inverse quark mass, m_Q^{-n}, for which Eq.(4.2.7) provides the highest order term. Now that the theory contains $n_f = 5$ flavours the axial current is anomalous, the anomalous dimension describes the RG running down to the scale of the next largest quark $\mu = m_b$ (in doing so logarithms are generated for the axial current made from the remaining quarks), then the procedure is repeated integrating out the b, c quarks.

Thus in the end we are left with the gluonic operator (contributions from threshold matching of each heavy quark, plus a negligible modification to the operator from RG running), *plus* the RG modified light quark current, specifically the singlet

[14]The axial vector Z coupling to quarks depends on their weak isospin,

$$J_{\mu,5}^Z = \sum_q T_3 \bar{q}\gamma^\mu\gamma^5 q, \tag{4.3.94}$$

then one takes the hadronic matrix element of the above.

current g_A^0 (the one that is actually anomalous). As it turns out the latter is the dominant contribution by far since the suppression with quark mass is only logarithmic, and not m_Q^{-2} as for the gluonic operator. The earliest attempt in 1978 [249] gives an estimate of $\Delta_Q \sim 0.05$, then a decade later ~ 0.04 [250], and finally the more recent treatment [247].

The numerical values of Δ_Q at LO are [247, 251],

$$\Delta_t^{(p)} = -\frac{6}{23\pi}\tilde{\alpha}_t \left(\Delta_u^{(p)} + \Delta_d^{(p)} + \Delta_s^{(p)}\right) \approx -0.0087, \tag{4.3.96}$$

$$\Delta_b^{(p)} = -\frac{6}{23\pi}\tilde{\alpha}_b \left(\Delta_u^{(p)} + \Delta_d^{(p)} + \Delta_s^{(p)}\right) \approx -0.0058, \tag{4.3.97}$$

$$\Delta_c^{(p)} = -\frac{6}{27\pi}\tilde{\alpha}_c \left(\Delta_u^{(p)} + \Delta_d^{(p)} + \Delta_s^{(p)}\right) \approx -0.0029, \tag{4.3.98}$$

using $\tilde{\alpha}_c = 0.35$, $\tilde{\alpha}_b = 0.2$, $\tilde{\alpha}_t = 0.1$, at NLO these quantities are modified to $\Delta_c^{(p)} = -0.0099$, $\Delta_b^{(p)} = -0.0064$ and $\Delta_t^{(p)} = -0.0031$. The contribution for heavy quarks is thus only relevant if the light quark couplings are absent. Lastly we can take $\Delta_Q^{(n)} = \Delta_Q^{(p)}$.

Tensor

The tensor charges of nucleons cannot be probed directly as there are no spin-2 particles in the SM, however the charge itself relates to the *transversality* pdf, $h_1(x)$, of quarks which is the difference between the pdfs of the two transversal polarisation states of the quark inside a polarised nucleon target [252],

$$\delta_q = \int_0^1 dx (h_1(x) - \bar{h}_1(x)), \tag{4.3.99}$$

which is therefore the number of transversely polarised valence quarks. These charges have a mild scale dependence,

$$\delta(\mu^2) = \left(\frac{\alpha_s(\mu^2)}{\alpha_s(\mu_0)^2}\right)^{\frac{4}{33-2n_f}} \delta(\mu_0^2), \tag{4.3.100}$$

which amounts to only an $\sim$ 11% correction from $\mu_0 = m_Z$ to $\mu = m_b$ and $n_f = 5$. The tensor charges for $\bar{q}\sigma^{\mu\nu}q$ and $\bar{q}i\sigma^{\mu\nu}\gamma^5 q$ are equivalent via the identity in Eq.(4.2.10). These may be taken from measurements by Hermes, COMPASS and JLab HALL A (for a global analysis see [253] giving $\delta_u = 0.39(7)(11)$ and $\delta_d =$

$-0.22(14)(8)$), or from lattice QCD [254] $\delta_u = 0.774(66)$, $\delta_d = -0.233(28)$, $\delta_s = 0.008(9)$ giving also the strange quark contribution. Alternatively the Dyson Schwinger formalism gives $\delta_u = 0.55(8)$ and $\delta_d = -0.11(2)$ [255–257]. See also [230, 234, 255] for sets of tensor charges which have been used in DD calculations. We quote the lattice values in Tab.4.4 for $\delta_{u,d}$ and the MicrOmegas value for δ_s.

Twist-2

The quark twist-2 operator

$$\mathcal{O}^{(q)}_{\text{Tw}-2} = \frac{1}{2}\bar{q}\left(i\gamma^{\{\mu}D^{\nu\}} - \frac{i}{2}m_q g^{\mu\nu}\right)q, \tag{4.3.101}$$

has hadronic matrix element [29, 223],

$$\langle\mathcal{O}^{(q)}_{\text{Tw}-2}\rangle = \frac{1}{m_N}\left(p^\mu p^\nu - \frac{1}{4}m_N^2 g^{\mu\nu}\right)f^{(N)}_{q,2}, \tag{4.3.102}$$

where $f^{(N)}_{q,2}$ is the first moment of the quark + anti-quark pdf,

$$f^{(N)}_{q,2}(\mu) = \int_0^1 dx\ x\ (q(x,\mu) + \bar{q}(x,\mu)), \tag{4.3.103}$$

which has a fairly strong scale dependence, we use the values quoted in [29] at $\mu = 1$ GeV ($f^{(p)}_{u,2} = 0.404(9)$, $f^{(p)}_{d,2} = 0.217(8)$, $f^{(p)}_{s,2} = 0.024(4)$ and $f^{(p)}_{c,2} = 0.036(1)$, $f^{(p)}_{b,2} = 0.0219(4)$ with the latter two at $\mu = m_W$) based on the MSTW pdf set. The neutron constants are related as usual via isospin symmetry.

4.3.2 Renormalization Group Running

We have used an EFT approach to construct the quark level EFT, and then the nucleon level EFT by finding the nucleon matrix elements. There are several scales in this calculation, first there is the scale μ_{UV} at which the new physics process becomes effective (i.e. the threshold at which the mediator is integrated out, $\mu_{\text{UV}} = m_{\text{MED}}$), this may in general be above the EW scale μ_{EW} (the threshold at which W,Z,h,t are all integrated out) or below, but we assumed $\mu_{\text{UV}} < \mu_{\text{EW}}$ to avoid dealing with chiral fermions. The lowest scale is $\mu_N = 1$ GeV at which the scattering occurs. Between the two scales μ_{UV} and μ_N the parameters of the theory (the operators, Wilson coefficients and quark masses) run with energy, described as usual by the

RG running equation. However this running has been neglected, as we will now explain.

We first note that since the DM is a singlet under the SM gauge group, and that we write each EFT operator as a product of a DM current and SM current $\mathcal{O}^{(\mathrm{EFT})} = J_{\mathrm{DM}} J_{\mathrm{SM}}$; then the DM current does not participate in any RG running at all. We need only consider the quark currents $\bar{q}\Gamma q$.

Consider the evolution under QCD corrections [29]. First the scalar current, or quark mass term, $m_q \bar{q} q$. This is RG invariant when using $\overline{\mathrm{MS}}$ scheme [219], its anomalous dimension is therefore zero and it does not change under RG flow. At leading order the vector, $\bar{q}\gamma^\mu q$, and axial-vector, $\bar{q}\gamma^\mu\gamma^5 q$[15], currents are also conserved and do not run. The pseudo-scalar does not evolve under RG flow, although it does mix with the $\widetilde{G}G$ operator (the scalar current similarly mixes with GG).

For heavy quarks which are integrated out, the vector current can be neglected, since its threshold matching begins at $\mathcal{O}(g_s^3)$ (Sec.4.1) in the strong coupling g_s, in other words a three gluon operator. The scalar (GG) and pseudo-scalar ($G\widetilde{G}$) operators evolve with a factor $\tilde{\beta}(\mu_l)/\tilde{\beta}(\mu_h) \sim 5.9$ and $\alpha_s(\mu_l)/\alpha_s(\mu_h) \sim 5.0$[16] respectively between the low and high scale ($\mu_{l,h}$), where $\beta(\mu)$ is the QCD β-function. The heaviest quark we consider is a b with $m_b \approx 4.2$ GeV, evolving the threshold matched operators down to 1 GeV amounts to a smaller change than quoted above.

Turning away from QCD corrections and considering weak corrections important effects are observed. In the cases where the DM couples only to a heavy quark vector current, $\bar{Q}\gamma^\mu Q$, the threshold matching at $\mu_Q = m_Q$ leads to a signal which is extremely suppressed. However, during the RG flow from $\mu \gg m_Q$ to m_Q (above threshold) the heavy quark vector current mixes under RG flow with $\bar{q}\gamma^\mu q$ light

[15]The $\mathrm{SU}(3)_{\mathrm{flavour}}$ singlet combination of axial currents evolves weakly under RG due to the axial anomaly.

[16]With $\tilde{\beta} = -\beta_0(\alpha_s/4\pi) + \mathcal{O}(\alpha_s^2)$ [29], and $\mu_{l,h} = m_c, m_Z$.

quark vector currents, this then allows a rather strong signal.

The mixing arises from diagrams involving (below the EW scale) a single photon exchange between the heavy quark loop and the light quarks. Such a diagram is not present for axial-vector (or for that matter scalar or pseudo-scalar) heavy quark bilinears, instead, using the Fermi theory neutral current interactions (four fermion interactions) one can still produce the $\bar{q}\gamma^\mu q$ at one-loop, suppressed by G_F.

Thus the only specific example of RG running we need to consider is the operator $C_{F5}^{(Q)}\bar{Q}\gamma^\mu Q$ (with $Q = c, b$) which is evolved from $\mu_h = m_Z \approx 90$ GeV to $\mu_l = m_c, m_b \sim 1,5$ GeV, resulting in $C^{(u)} = 0.0048C^{(b)} - 0.0097C^{(c)}$, and $C^{(d)} = -0.0024C^{(b)} + 0.0048C^{(c)}$ [258]. These results will be applied in the next chapter.

Although we consider couplings to strongly charged particles, it is possible for DM to couple only to leptons and still produce a DD signal. If there is a coupling at or above the EW scale of the form $\bar{l}\gamma^\mu l$, then the RG running of the EFT operator will mix with others of the same symmetries, including naturally $\bar{q}\gamma^\mu q$ [258] which leads to strong DD signals. Such mixing occurs dominantly via diagrams with a single photon exchange. The same mixing can also occur through a Fermi theory four-fermion interaction $J^\mu J_\mu$ which also permits an axial-vector current $\bar{l}\gamma^\mu\gamma^5 l$, however these contributions are very suppressed by G_F [226]. Below the EW scale the W, Z, h, t are all integrated out, then there are no scalar or pseudo-scalar interactions with leptons in the theory, removing any possible RG running at one loop. Then [259] describes a means by which scalar bilinears $\bar{l}l$ may be incorporated, it involves a two-loop process with two external photons. There are no pseudo-scalar interactions in the SM EFT, so it is difficult to imagine where $\bar{l}\gamma^5 l$ bilinears would contribute to nuclear scattering.

4.4 Step 3 : Non-relativistic Limit

We have constructed an EFT in terms of nucleon spinors, accounting for the form factors that parametrize the scattering from nucleons. This would accurately predict scattering rates if the DM scattered from individual nucleons, if it were energetic enough. However, DM is highly non-relativistic and the resulting smallness of the scattering energy makes this approximation poorly justified for nucleons which are bound inside a nucleus.

In the same way that the non-perturbative binding structure of quarks in nucleons leads to the introduction of nucleon form factors, the non-perturbative binding of nucleons inside the nucleus necessitates the introduction of nuclear form factors.

Luckily, a full consideration of nuclear form factors has been performed [211, 260]. This is done using a set of non-relativistic operators (the limit of small DM velocity, $\mathbf{v}$); and so we must understand how to take the non-relativistic limit of our EFT.

Thus, the final step to construct the matrix element is to find the coefficients, $C_i^{(N)}$ of the NR operators. There are 18 linearly independent operators [116, 211, 260] if one restricts to at most one power of each of the DM velocity $\mathbf{v}$, the DM spin $\mathbf{S}_\chi$ and the nuclear spin $\mathbf{S}_N$ [17], although the latter two are imposed automatically for our models,

$$\mathcal{L}_{\rm NR} = \sum_{N=n,p} \sum_{i=1}^{18} C_i^{(N)} \mathcal{O}_i^{(\rm NR)} \ . \tag{4.4.104}$$

[17] We will use the notation $\mathbf{p}$ ($\mathbf{p}'$) and $\mathbf{k}$ ($\mathbf{k}'$) to label the incoming (outgoing) DM and nucleon three-momenta respectively; working in the CM frame $\mathbf{p} = \mu\mathbf{v}$ where $\mathbf{v}$ is the relative lab-frame velocity and $\mu = m_\chi m_N/(m_\chi + m_N)$ is the DM-nucleon reduced mass. Only Galilean invariants may be present, i.e. combinations of momenta and velocity, parametrized by $\mathbf{v} = \mathbf{v}_i - \mathbf{v}_f$ and $\mathbf{q} = \mathbf{p} - \mathbf{p}' = \mathbf{k} - \mathbf{k}'$. Thus there are four independent Galilean vectors, and note that $i\mathbf{q}$ is Hermitian whereas $\mathbf{q}$ alone is not. To see why consider the hermitian conjugate of a generic DM bilinear $(\bar{\psi}(p')\Gamma\psi(p))^\dagger = \pm\bar{\psi}(p)\Gamma\psi(p')$ which is equivalent to $\mathbf{q} \to -\mathbf{q}$. Usually $\mathbf{v}^\perp = \mathbf{v} + \mathbf{q}/2\mu$ is used rather than $\mathbf{v}$ because $\mathbf{v}^\perp \cdot \mathbf{q} = 0$.

We list the $\mathcal{O}_i^{(\mathrm{NR})}$ in Tab.4.5 along with their discrete symmetries. Charge conjugation ($\mathcal{C}$) is not a good symmetry in a non-relativistic theory (see Tab.4.6 rows 1 and 3 for an explicit example), however we can use parity ($\mathcal{P}$) and time-reversal ($\mathcal{T}$) to constrain which operators we expect to appear;

$$\mathcal{T} \quad : \quad (i\mathbf{q}, \mathbf{v}^{\perp}, \mathbf{S}_{\chi}, \mathbf{S}_N) \to (i\mathbf{q}, -\mathbf{v}^{\perp}, -\mathbf{S}_{\chi}, -\mathbf{S}_N), \tag{4.4.105}$$

$$\mathcal{P} \quad : \quad (i\mathbf{q}, \mathbf{v}^{\perp}, \mathbf{S}_{\chi}, \mathbf{S}_N) \to (-i\mathbf{q}, -\mathbf{v}^{\perp}, \mathbf{S}_{\chi}, \mathbf{S}_N)\ . \tag{4.4.106}$$

Recall that $\mathcal{T}$ is anti-unitary, i.e. $\mathcal{T} i \mathcal{T}^{-1} = -i$. Since the product of the symmetries $\mathcal{CPT}$ is conserved in Lorentz invariant theories, knowledge of $\mathcal{PT}$ gives $\mathcal{C}$.

Each operator in Eq.(4.4.104) corresponds to a term in the interaction hamiltonian, once sandwiched between the ingoing/outgoing states this gives an amplitude which can be decomposed into six electroweak response functions (plus an extra two which arise from interference) [211, 260], which can then be grouped according to the original coefficients in Eq.(4.4.104) to create a form-factor $\mathcal{F}_{i,j}^{(N,N')}(q^2, v^2)$ which allows for interference between different NR operators i, j, and between the neutron/proton interactions N, N'. Since the interference between the operators are always subdominant we will restrict to $\mathcal{F}_i^{(N,N')} \equiv \mathcal{F}_{(i,i)}^{(N,N')}$.

The form factors, $\mathcal{F}_i^{(n,n)}(E_R, v)$, are shown as a function of recoil energy in Fig.4.4, and allow a quick judgement of the relative contributions from each NR operator, they are shown for two DM masses (10 GeV and 1 TeV) as some form factors have a DM mass dependence. It is this step in the calculation which elucidates which operators are momentum suppressed ($\mathbf{q}^2$), velocity suppressed ($\mathbf{v}^2, \mathbf{v}^{\perp,2}$), or spin dependent (containing $\mathbf{S}_N$).

To make the transition between the relativistic theory (Tab.4.1, 4.2 and 4.3) we need the expressions for non-relativistic spinors in the case of the nucleons and spin-1/2 DM. These are computed in the Weyl basis, which is defined by,

$$\gamma^{\mu} = \begin{pmatrix} 0 & \sigma^{\mu} \\ \bar{\sigma}^{\mu} & 0 \end{pmatrix}, \quad \gamma^5 = \begin{pmatrix} -1 & 0 \\ 0 & 1 \end{pmatrix}, \tag{4.4.107}$$

$\mathcal{O}^{(\mathrm{NR})}$	$\mathcal{P}$	$\mathcal{T}$	$\mathcal{PT}=\mathcal{C}$		Xe^{130}	Xe^{129}
$\mathcal{O}_1 = \mathbf{1}$	+	+	+	**SI**	10^3	10^3
$\mathcal{O}_2 = \mathbf{v}^\perp \cdot \mathbf{v}^\perp$	+	+	+	**SI**	$\approx 10^{-6}$ †	$\approx 10^{-6}$ †
$\mathcal{O}_3 = \mathbf{S}_N \cdot \left(\frac{i\mathbf{q}}{m_N} \times \mathbf{v}^\perp\right)$	+	+	+	SD	10^{-6}	10^{-6}
$\mathcal{O}_4 = \mathbf{S}_\chi \cdot \mathbf{S}_N$	+	+	+	SD	0	10^{-2}
$\mathcal{O}_5 = \mathbf{S}_\chi \cdot \left(\frac{i\mathbf{q}}{m_N} \times \mathbf{v}^\perp\right)$	+	+	+	**SI**	10^{-6}	10^{-6}
$\mathcal{O}_6 = \left(\mathbf{S}_\chi \cdot \frac{i\mathbf{q}}{m_N}\right)\left(\mathbf{S}_N \cdot \frac{i\mathbf{q}}{m_N}\right)$	+	+	+	SD	0	10^{-9}
$\mathcal{O}_7 = \mathbf{S}_N \cdot \mathbf{v}^\perp$	-	+	-	SD	0	10^{-7}
$\mathcal{O}_8 = \mathbf{S}_\chi \cdot \mathbf{v}^\perp$	-	+	-	**SI**	10^{-3}	10^{-3}
$\mathcal{O}_9 = \mathbf{S}_\chi \cdot \left(\mathbf{S}_N \times \frac{i\mathbf{q}}{m_N}\right)$	-	+	+	SD	0	10^{-5}
$\mathcal{O}_{10} = \frac{i\mathbf{q}}{m_N} \cdot \mathbf{S}_N$	-	-	+	SD	0	10^{-5}
$\mathcal{O}_{11} = \frac{i\mathbf{q}}{m_N} \cdot \mathbf{S}_\chi$	-	-	+	**SI**	10^{-1}	10^{-1}
$\mathcal{O}_{12} = \mathbf{S}_\chi \cdot (\mathbf{S}_N \times \mathbf{v}^\perp)$	-	-	+	SD	10^0	10^0
$\mathcal{O}_{13} = \left(\mathbf{S}_N \cdot \frac{i\mathbf{q}}{m_N}\right)\left(\mathbf{S}_\chi \cdot \mathbf{v}^\perp\right)$	+	-	-	SD	0	10^{-17}
$\mathcal{O}_{14} = \left(\mathbf{S}_\chi \cdot \frac{i\mathbf{q}}{m_N}\right)\left(\mathbf{S}_N \cdot \mathbf{v}^\perp\right)$	+	-	-	SD	0	10^{-17}
$\mathcal{O}_{15} = \left(\mathbf{S}_\chi \cdot \frac{i\mathbf{q}}{m_N}\right)\left(\frac{i\mathbf{q}}{m_N} \cdot \mathbf{S}_N \times \mathbf{v}^\perp\right)$	-	-	+	SD	10^{-7}	10^{-7}
$\mathcal{O}_{17} = i\frac{\mathbf{q}}{m_N} \cdot \mathcal{S} \cdot \mathbf{v}^\perp$	+	-	-	SD	10^{-13}	10^{-13}
$\mathcal{O}_{18} = i\frac{\mathbf{q}}{m_N} \cdot \mathcal{S} \cdot \mathbf{S}_N$	-	-	+	SD	10^{-11}	10^{-11}

Table 4.5: The NR operators considered in this study, along with their P-parity, T-parity, and whether or not they are spin-dependent. A reasonable upper (lower) recoil energy is $E_R \approx 50$ (1) keV, then $|\bar{q}| \approx 0.1$ (0.005) GeV (from $q^2 = 2m_T E_R$); for these energies the exponential suppression factor common to each of the form factors is ≈ 1. The approximate size of the form factors for a DM mass of 10 GeV and recoil energy of 1 keV is shown for two Xe isotopes in LUX.
† : The operator $\mathcal{O}_2$ is neglected due to velocity suppression ($v^2 \approx 10^{-6}$), furthermore, it always appears alongside an operator less suppressed contributing to the same form factor.

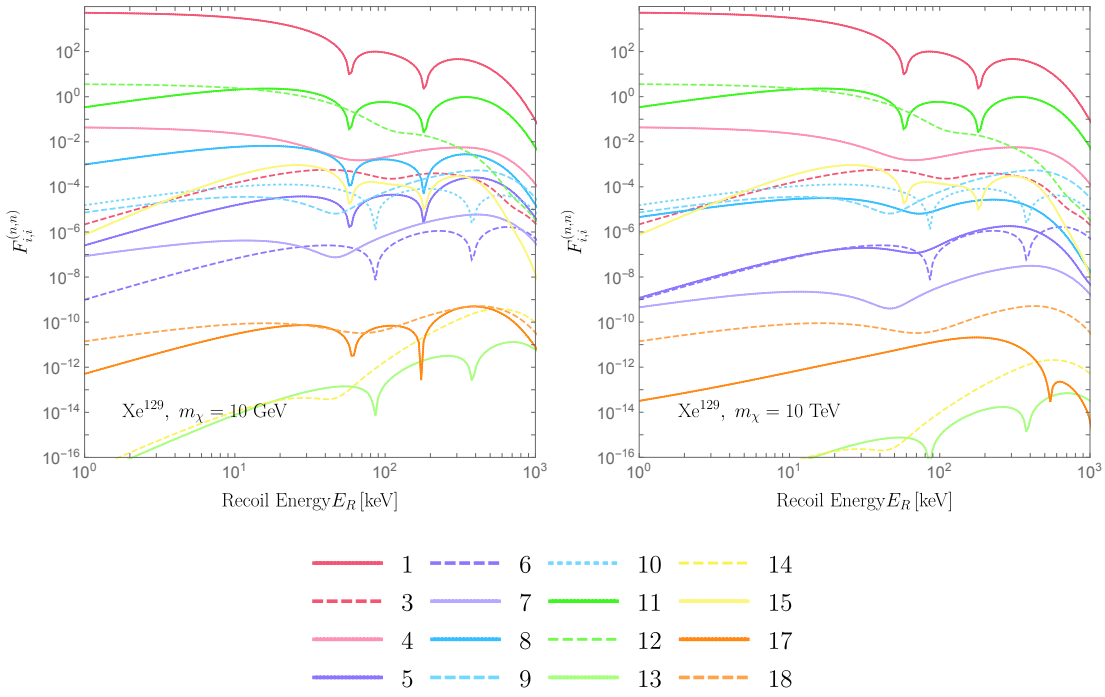

Figure 4.4: The neutron form factors, $F_i^{(n,n)}(E_R)$ for the $i = 1 - 15$ operators considered in Fig.4.5, for scattering on a ^{129}Xe nucleus, for a DM mass of 10 GeV (Left) and 1 TeV (Right). The DM velocity is taken to be $v_{\rm min}$.

where $\sigma^\mu = (1, \overrightarrow{\sigma})$, $\bar{\sigma}^\mu = (1, -\overrightarrow{\sigma})$ and σ^i are the Pauli matrices. The spinors can be written as,

$$u^s(p) = \begin{pmatrix} \sqrt{p \cdot \sigma}\xi^s \\ \sqrt{p \cdot \bar{\sigma}}\xi^s \end{pmatrix}, \quad v^s(p) = \begin{pmatrix} \sqrt{p \cdot \sigma}\eta^s \\ -\sqrt{p \cdot \bar{\sigma}}\eta^s \end{pmatrix}, \tag{4.4.108}$$

where the spin operator is $\hat{S} = \frac{1}{2}\overrightarrow{\sigma}$ and $\xi_1, \eta_1 = (1, 0)$, $\xi_2, \eta_2 = (0, 1)$ are conventionally taken so that the spin is along the z-axis. The spin vector $\hat{S}$ arises from combinations such as $\xi_i^\dagger \overrightarrow{\sigma}_{ij}\xi_j \equiv 2\hat{S}\delta_{ij}$, but we will suppress the spin-conserving delta function which is present in all cases. The various four-momenta $p_i^\mu = (E_i, \mathbf{p}_i)$ for the scattering $\chi(p)q(k) \to \chi(p')q(k')$ are parameterized by the momentum transfer $\mathbf{q} = (\mathbf{p} - \mathbf{p}')$ and the incoming DM velocity $\mathbf{v} = \mathbf{p}/\mu$, with μ the reduced mass of the DM-nucleon pair $\mu = (m_\chi m_N)/(m_\chi + m_N)$. The velocity vector $\mathbf{v}$ may be replaced with the *transverse velocity*,

$$\mathbf{v}^\perp = \frac{\mathbf{1}}{\mathbf{q^2}}\mathbf{q} \times (\mathbf{q} \times \mathbf{v}). \tag{4.4.109}$$

Then $\mathbf{v}^\perp \cdot \mathbf{q} = 0$, which simplifies the kinematics. Since the DM and SM particles (as opposed to anti-particles) always appear, we only need the spinor configuration $\bar{u}(p')\Gamma u(p)$ for DM fermions, and $\bar{u}(k')\Gamma u(k)$ for nucleons.

The following identity is useful,

$$\sqrt{\sigma \cdot p} = \frac{(E + m) - \boldsymbol{\sigma} \cdot \mathbf{p}}{\sqrt{2(E + m)}}, \tag{4.4.110}$$

$$\sqrt{\bar{\sigma} \cdot p} = \frac{(E + m) + \boldsymbol{\sigma} \cdot \mathbf{p}}{\sqrt{2(E + m)}}. \tag{4.4.111}$$

From which we get for arbitrary momenta p_1, p_2

$$\begin{aligned} &\sqrt{(\sigma \cdot p_1)(\bar{\sigma} \cdot p_2)} = \\ &\frac{1}{2}\sqrt{(E_1 + m_1)(E_2 + m_2)}\left(1 + \boldsymbol{\sigma} \cdot \left(\frac{\mathbf{p}_2}{E_2 + m_2} - \frac{\mathbf{p}_1}{E_1 + m_1}\right)\right. \\ &\qquad \left. - \frac{\mathbf{p}_1 \cdot \mathbf{p}_2}{(E_1 + m_1)(E_2 + m_2)} - \frac{i(\mathbf{p}_1 \times \mathbf{p}_2) \cdot \boldsymbol{\sigma}}{(E_1 + m_1)(E_2 + m_2)}\right). \end{aligned}$$

Similar relations can be derived using this one, for example $\sqrt{(\sigma \cdot p_1)(\sigma \cdot p_2)}$ is equivalent under the replacement $\mathbf{p}_2 \to -\mathbf{p}_2$. We also use the relation for Pauli matrices

$\sigma^a\sigma^b = \delta^{ab} + i\varepsilon^{abc}\sigma^c$ with ε^{abc} the totally antisymmetric Levi-Civita tensor in three dimensions.

As an example calculation, the pseudo-scalar DM bilinear is

$$\begin{aligned}\bar{u}(p_2)\gamma^5 u(p_1) &= \left(\xi_2^\dagger\sqrt{p_2\cdot\sigma} \quad \xi_2^\dagger\sqrt{p_2\cdot\bar{\sigma}}\right)\begin{pmatrix}0 & 1\\ -1 & 0\end{pmatrix}\begin{pmatrix}\sqrt{p_1\cdot\sigma}\xi_1\\ \sqrt{p_1\cdot\bar{\sigma}}\xi_1\end{pmatrix}\\ &= -\xi_2^\dagger(\sqrt{(p_2\cdot\bar{\sigma})(p_1\cdot\sigma)} - \sqrt{(p_2\cdot\sigma)(p_1\cdot\bar{\sigma})})\xi_1\\ &\approx \xi_2^\dagger\sqrt{(E_2+m_2)(E_1+m_1)}\left(\boldsymbol{\sigma}\cdot\left(\frac{\mathbf{p}_2}{E_2+m_2} - \frac{\mathbf{p}_1}{E_1+m_1}\right)\right)\xi_1,\end{aligned}$$

then taking the non-relativistic limit $E_i \approx m_i$ and $m_1 = m_2$

$$\begin{aligned}\bar{u}(p_2)\gamma^5 u(p_1) &= \xi_1^\dagger\sqrt{(E_1+m_1)(E_2+m_2)}\left(\boldsymbol{\sigma}\cdot\left(\frac{\mathbf{p}_2}{E_2+m_2} - \frac{\mathbf{p}_1}{E_1+m_1}\right)\right)\xi_2\\ &\approx \xi_1^\dagger\boldsymbol{\sigma}\xi_2\cdot(\mathbf{p}_2-\mathbf{p}_1)\\ &= -2\mathbf{q}\cdot\mathbf{S}_\chi.\end{aligned}$$

For bilinears with γ^μ the identity $\sigma^j\sigma^i\sigma^k p_1^j p_2^k = \sigma^k p_2^k p_1^i + i\epsilon^{jil}\sigma^l\sigma^k p_1^j p_2^k = \sigma^k p_2^k p_1^i + i\epsilon^{jik}p_1^j p_2^k - (\sigma^i p_1\cdot p_2 - \sigma^j p_1^j p_2^i)$ is useful.

The remaining DM bilinears for scattering are given in Tab.4.6. The nucleon bilinears are identical, but with the substitution $(\mathbf{q}, \mathbf{v}^\perp) \to -(\mathbf{q}, \mathbf{v}^\perp)$ and $(S_\chi, m_\chi) \to (S_N, m_N)$. These and similar expressions for other spinor configurations may also be found in [117] with the exception of the $\sigma^{\mu\nu}\gamma^5$ structure. These expressions may be checked via the Gordon identity (and an equivalent identity including a γ^5),

$$\begin{aligned}\bar{\chi}\gamma^\mu\chi &= \frac{i}{2m_\chi}\bar{\chi}\sigma^{\mu\nu}\chi Q_\nu + \frac{1}{2m_\chi}P^\mu\bar{\chi}\chi,\\ \bar{\chi}\sigma^{\mu\nu}\gamma^5\chi Q_\nu &= P^\mu\bar{\chi}i\gamma^5\chi,\end{aligned}$$

where $P^\mu = (p'+p)^\mu = (2m_\chi, 2\mu\mathbf{v}^\perp)$ and $Q^\mu = (p'-p)^\mu = (0, -\mathbf{q})$. Spin-dependence arises in all bilinears, but is subdominant in all but the nucleon $\bar{N}\gamma^i\gamma^5 N$. The least suppressed interactions are $\bar{\chi}\chi$ and $\bar{\chi}\gamma^0\chi$.

We turn now to the NR limit for spin-1 particles. The free dynamics of massive spin-1 DM, B^μ, are governed by the Proca equation,

$$\partial^\mu B_{\mu\nu} - m^2 B^\nu = 0, \tag{4.4.112}$$

where $B^{\mu\nu} = \partial^\mu B^\nu - \partial^\nu B^\mu$ is the field strength of the vector field B; this leads directly to the constraint $\partial^\mu B_\mu = 0$, or in momentum space $p \cdot \varepsilon = 0$ (the time-like polarization $\varepsilon^0 = 0$ since $p^\mu = (m, 0)$ in the rest frame[18]) where ε^i is the polarization three vector. The polarization relates to the spin via [19],

$$i\epsilon_{ijk} S^k_\chi = \varepsilon_i^\dagger \varepsilon_j - \varepsilon_j^\dagger \varepsilon_i, \tag{4.4.113}$$

if we choose $\varepsilon_s^i = \delta_s^i$ as a basis. As well as the above antisymmetric combination of polarizations, for certain models the symmetric combination of ϵ is present (as pointed out in [210]) and leads to new form factors [116]. In the NR limit the only non-zero spin-1 DM bilinears from Tab.4.2 are shown in Tab.4.7, where $\mathcal{S}_{ij} = \varepsilon_i^\dagger \varepsilon_j + \varepsilon_i \varepsilon_j^\dagger$ is the symmetric combination of the polarizations, we also omit the contracted polarizations $\epsilon_1 \cdot \epsilon_2$ which arise when the vector fields are contracted since they contribute 1. Spin-0 DM is trivial to reduce to NR form, since for any scalar fields $\phi \to 1$, these are shown in Tab.4.8.

Finally, similar calculations to the above can be found in [116], but using the Bjorken-Drell normalization of the fields. To map between the two, multiply our results by $1/\sqrt{m}$, $1/\sqrt{m}$, $1/\sqrt{2m}$ for spin-0, spin-1 and spin-1/2 fields of mass m respectively.

In Tab.4.9 we list the matching between each of the relativisitic EFT operators, and the NR operators. Once the coefficients are fixed, inclusion of the form factors

[18] Since we are explicitly breaking Lorentz invariance this argument does not hold, and we should work consistently in the lab frame, this leads to $\varepsilon^0 = (\mathbf{p} \cdot \varepsilon)/m$ which is $\mathcal{O}(q, v^\perp)$ and so can be consistently neglected.

[19] The vector particle lives in the same representation of the Lorentz group as ordinary four-vectors, for which the spin operator is $\hat{S}_i = \frac{1}{2}\epsilon_{ijk} L^{jk}$ where L^{jk} are the spatial components of the generators of the Lorentz group and $(L^{jk})_{lm} = i(\delta^i_l \delta^j_m - \delta^j_l \delta^i_m)$

DM Bilinear		$\mathcal{C}$	$\mathcal{P}$	$\mathcal{T}$	$\mathcal{CPT}$
$\bar{\chi}\chi$	$2m_\chi + i\frac{\mu}{m_\chi} q \cdot (v^\perp \times S_\chi)$	+	+	+	+
$\bar{\chi} i\gamma^5 \chi$	$-2iq \cdot S_\chi$	+	-	-	+
$\bar{\chi}\gamma^0\chi$	$2m_\chi - i\frac{\mu}{m_\chi} q \cdot (v^\perp \times S_\chi)$	-	+	+	-
$\bar{\chi}\gamma^0\gamma^5\chi$	$-4\mu v^\perp \cdot S_\chi$	+	-	+	-
$\bar{\chi}\gamma^i\chi$	$2\mu v^{\perp,i} + 2i\epsilon^{ijk} q_j S_{\chi,k}$	-	-	-	-
$\bar{\chi}\gamma^i\gamma^5\chi$	$-4m_\chi S^i_\chi - i\frac{\mu}{2m_\chi}\epsilon^{ijk} v^\perp_j q_k$	+	+	-	-
$\bar{\chi}\sigma^{0i}\chi$	$iq^i - 4\mu\epsilon^{ijk} v^\perp_j S_{\chi,k}$	-	-	+	+
$\bar{\chi}\sigma^{ij}\chi$	$4m_\chi \epsilon^{ijk} S_{\chi,k}$	-	+	-	+
$\bar{\chi}\sigma^{0i} i\gamma^5\chi$	$-4m_\chi S^i_\chi$	+	+	+	+
$\bar{\chi}\sigma^{ij} i\gamma^5\chi$	$i\epsilon^{ijk} q_k - 4\mu v^{\perp,[i} S^{j]}_\chi$	+	-	-	+

Table 4.6: Non-relativistic limit of fermion bilinears, $\bar{u}(p')\Gamma u(p)$ which are non-zero, and the $\mathcal{CPT}$ symmetries for the relativistic operators in the leftmost column. Any $\mathcal{C}$-odd structures are zero for Majorana particles.

can be done according to [211],

$$\langle |M|^2 \rangle (v^\perp, q) = \sum_{N,N'=n,p} \sum_{i,j=1}^{15} C_i^{(N)} C_j^{(N')} \left(\frac{m_T}{m_N}\right)^2 \left(F_{i,j}^{(N,N')}\right)^2 , \tag{4.4.114}$$

where the possibility of interference between operators is allowed. From the squared spin-averaged matrix element above, the next step is to find the differential cross section with recoil energy E_R,

$$\frac{d\sigma}{dE_R} = \frac{1}{32\pi m_\chi^2 m_T} \frac{1}{v^2} \langle |M|^2 \rangle . \tag{4.4.115}$$

Finally the differential event rate per unit target mass (if n_T is the number of target particles per unit mass),

$$\frac{dR}{dE_R} = \frac{\rho_\odot}{m_\chi} n_T \int d^3v \; f(v) v \frac{d\sigma}{dE_R}, \tag{4.4.116}$$

where $f(v)$ is the DM velocity distribution in the Earth frame, taken as a truncated Maxwell-Boltzmann and for isothermal density profile. The velocity expansion is taken to $\mathcal{O}(v^2)$ and thus has a v^0 and v^2 term, then the velocity integration can be done analytically for the v^0 and v^2 terms as in [230].

DM Bilinear		$\mathcal{C}$	$\mathcal{P}$	$\mathcal{T}$	$\mathcal{CPT}$
$B^\mu B_\mu = B^\mu B_\mu^\dagger$	1	+	+	+	+
$\mathrm{Re}(B^{\mu\dagger} B^\nu)$	$2\mathcal{S}^{ij}$	+	+	+	+
$i\mathrm{Im}(B^{\mu\dagger} B^\nu)$	$\epsilon^{ijk} S_{\chi,k}$	-	+	-	+
$\mathrm{Re}(B^{\mu\dagger} \partial_\mu B^i)$	$\mu\epsilon^{ijk} v_j^\perp S_{\chi,k} - \frac{i}{2} q_j \mathcal{S}^{ji}$	+	-	+	-
$i\mathrm{Im}(B^{\mu\dagger} \partial_\mu B^i)$	$\frac{i}{2}\epsilon^{ijk} q_j S_{\chi,k} + \mu v_j^\perp \mathcal{S}^{ji}$	-	-	-	-
$i\mathrm{Im}(B^{\mu\dagger} \partial_0 B_\mu)$	$2m_\chi$	-	+	+	-
$\mathrm{Re}(B_\mu^\dagger \partial_0 B^\mu)$	$0^\dagger$	+	+	-	-
$i\mathrm{Im}(B^{\mu\dagger} \partial_i B_\mu)$	$2\mu v_i^\perp$	-	-	-	-
$\mathrm{Re}(B_\mu^\dagger \partial_i B^\mu)$	iq_i	+	-	+	-
$\mathrm{Re}(\epsilon^{\mu\nu\sigma 0} B_\mu^\dagger \partial_\nu B_\sigma)$	$-2\mu v^\perp \cdot S_\chi$	+	-	+	-
$\mathrm{Re}(\epsilon^{\mu\nu\sigma i} B_\mu^\dagger \partial_\nu B_\sigma)$	$2m_\chi S_\chi^i$	+	+	-	-
$i\mathrm{Im}(\epsilon^{\mu\nu\sigma 0} B_\mu^\dagger \partial_\nu B_\sigma)$	$iq \cdot S_\chi$	-	-	-	-
$i\mathrm{Im}(\epsilon^{\mu\nu\sigma i} B_\mu^\dagger \partial_\nu B_\sigma)$	$0^{\dagger\dagger}$	-	+	+	-

Table 4.7: Non-relativistic limit of vector bilinears which are non-zero. Because $B^0 = 0$ many of the operators only have spatial components, for which the replacements are $\mu \to i$, $\nu \to j$. The $\mathcal{C}$-odd structures necessarily vanish for real DM.
†, †† : Using the DM velocity v rather than $v^\perp$ the results are $i\frac{q^2}{2\mu}$ and $-i\frac{q^2}{2\mu} S_\chi^i$ respectively.

DM Bilinear		$\mathcal{C}$	$\mathcal{P}$	$\mathcal{T}$	$\mathcal{CPT}$
$\phi^\dagger \phi$	1	+	+	+	+
$\mathrm{Re}(\phi^\dagger \partial_0 \phi)$	$0^\dagger$	+	+	-	-
$i\mathrm{Im}(\phi^\dagger \partial_0 \phi)$	$2m_\chi$	-	+	+	-
$\mathrm{Re}(\phi^\dagger \partial_i \phi)$	iq_i	+	-	+	-
$i\mathrm{Im}(\phi^\dagger \partial_i \phi)$	$2\mu v_i^\perp$	-	-	-	-

Table 4.8: Non-relativistic limit of scalar bilinears which are non-zero, to lowest order in q, $v^\perp$.
†: Using the DM velocity v rather than $v^\perp$ the result is $i\frac{q^2}{2\mu}$.

	$\mathcal{O}_1^{(\mathrm{NR})}$	$\mathcal{O}_2^{(\mathrm{NR})}$	$\mathcal{O}_3^{(\mathrm{NR})}$	$\mathcal{O}_4^{(\mathrm{NR})}$	$\mathcal{O}_5^{(\mathrm{NR})}$	$\mathcal{O}_6^{(\mathrm{NR})}$	$\mathcal{O}_7^{(\mathrm{NR})}$	$\mathcal{O}_8^{(\mathrm{NR})}$	$\mathcal{O}_9^{(\mathrm{NR})}$	$\mathcal{O}_{10}^{(\mathrm{NR})}$	$\mathcal{O}_{11}^{(\mathrm{NR})}$	$\mathcal{O}_{12}^{(\mathrm{NR})}$	$\mathcal{O}_{13}^{(\mathrm{NR})}$	$\mathcal{O}_{14}^{(\mathrm{NR})}$	$\mathcal{O}_{15}^{(\mathrm{NR})}$
$\mathcal{O}_{\mathrm{F1}}^{\mathrm{EFT}} = \bar{\chi}\chi\bar{N}N$	$4m_\chi m_N$		$2m_\chi\mu$	$\mathcal{O}(q^2, v^{\perp,2})$	$\frac{2m_N^2\mu}{m_\chi}$										
$\mathcal{O}_{\mathrm{F2}}^{\mathrm{EFT}} = \bar{\chi}i\gamma^5\chi\bar{N}N$											$-4m_N^2$			$-2\frac{\mu m_N^2}{m_\chi}$	
$\mathcal{O}_{\mathrm{F3}}^{\mathrm{EFT}} = \bar{\chi}\chi\bar{N}i\gamma^5N$										$4m_\chi m_N$					
$\mathcal{O}_{\mathrm{F4}}^{\mathrm{EFT}} = \bar{\chi}i\gamma^5\chi\bar{N}i\gamma^5N$						$-4m_N^2$									
$\mathcal{O}_{\mathrm{F5}}^{\mathrm{EFT}} = \bar{\chi}\gamma^\mu\chi\bar{N}\gamma_\mu N$	$4m_\chi m_N$	$4\mu^2$	$-2m_\chi m_N$	$-4q^2$	$-4m_N^2$	$-4m_N^2$									
$\mathcal{O}_{\mathrm{F6}}^{\mathrm{EFT}} = \bar{\chi}\gamma^\mu\gamma^5\chi\bar{N}\gamma_\mu N$							$-q^2\left(\frac{\mu}{m_\chi}\right)$	$-8m_N m_\chi$	$8m_\chi m_N$						
$\mathcal{O}_{\mathrm{F7}}^{\mathrm{EFT}} = \bar{\chi}\gamma^\mu\chi\bar{N}\gamma_\mu\gamma^5N$							$8m_\chi m_N$	$q^2\left(\frac{\mu}{m_N}\right)$	$8m_N^2$						
$\mathcal{O}_{\mathrm{F8}}^{\mathrm{EFT}} = \bar{\chi}\gamma^\mu\gamma^5\chi\bar{N}\gamma_\mu\gamma^5N$	$\mathcal{O}(q^2, v^{\perp,2})$		$\frac{2m_N^2\mu}{m_\chi}$	$-16m_\chi m_N$	$2m_\chi\mu$										
$\mathcal{O}_{\mathrm{F9}}^{\mathrm{EFT}} = \bar{\chi}\sigma^{\mu\nu}\chi\bar{N}\sigma_{\mu\nu}N$	$-q^2$		$-4\mu m_\chi$	$32m_\chi^2$	$2m_\chi\mu$	$-4\mu m_\chi$									
$\mathcal{O}_{\mathrm{F10}}^{\mathrm{EFT}} = \bar{\chi}\sigma^{\mu\nu}\chi\bar{N}i\gamma^5\sigma_{\mu\nu}N$										$4m_N^2$	$-8m_\chi m_N$	$-16\mu(m_N + 2m_\chi)$			

Table 4.9: The NR matching from each of the EFT operators in Tab.4.1 to the operators of Tab.4.5. The leading coefficients of the matching are also given, and the dominant contribution across all NR operators is shaded in blue.

	$\mathcal{O}_1^{(\mathrm{NR})}$	$\mathcal{O}_2^{(\mathrm{NR})}$	$\mathcal{O}_3^{(\mathrm{NR})}$	$\mathcal{O}_4^{(\mathrm{NR})}$	$\mathcal{O}_5^{(\mathrm{NR})}$	$\mathcal{O}_6^{(\mathrm{NR})}$	$\mathcal{O}_7^{(\mathrm{NR})}$	$\mathcal{O}_8^{(\mathrm{NR})}$	$\mathcal{O}_9^{(\mathrm{NR})}$	$\mathcal{O}_{10}^{(\mathrm{NR})}$	$\mathcal{O}_{11}^{(\mathrm{NR})}$	$\mathcal{O}_{12}^{(\mathrm{NR})}$	$\mathcal{O}_{13}^{(\mathrm{NR})}$	$\mathcal{O}_{14}^{(\mathrm{NR})}$	$\mathcal{O}_{15}^{(\mathrm{NR})}$
$\mathcal{O}_{S1}^{\mathrm{EFT}} = \phi^\dagger\phi\bar{N}N$	$2m_N$		μ												
$\mathcal{O}_{S2}^{\mathrm{EFT}} = \phi^\dagger\phi\bar{N}i\gamma^5 N$										$2m_N$					
$\mathcal{O}_{S3}^{\mathrm{EFT}} = i\mathrm{Im}(\phi^\dagger\partial_\mu\phi)\bar{\mathrm{N}}\gamma^\mu\mathrm{N}$	$4m_\chi m_N$		$-2\mu(m_\chi + 2m_N)$												
$\mathcal{O}_{S4}^{\mathrm{EFT}} = i\mathrm{Im}(\phi^\dagger\partial_\mu\phi)\bar{\mathrm{N}}\gamma^\mu\gamma^5\mathrm{N}$							$8m_\chi m_N$								
$\mathcal{O}_{V1}^{\mathrm{EFT}} = B_\mu^\dagger B^\mu\bar{N}N$	$2m_N$		μ												
$\mathcal{O}_{V2}^{\mathrm{EFT}} = B_\mu^\dagger B^\mu\bar{N}i\gamma^5 N$										$2m_N$					
$\mathcal{O}_{V3}^{\mathrm{EFT}} = \mathrm{Re}(\mathrm{B}_\nu^\dagger\partial^\nu\mathrm{B}_\mu)\bar{\mathrm{N}}\gamma^\mu\mathrm{N}$														$-2\mu m_N$	
$\mathcal{O}_{V3-2}^{\mathrm{EFT}} = i\mathrm{Im}(\mathrm{B}_\nu^\dagger\partial^\nu\mathrm{B}_\mu)\bar{\mathrm{N}}\gamma^\mu\mathrm{N}$				$-q^2$	$m_N\mu$	$-m_N^2$									
$\mathcal{O}_{V3-3}^{\mathrm{EFT}} = \mathrm{Im}(\mathrm{B}^{\mu,\dagger}\mathrm{B}^\nu)\mathrm{Im}(\partial_\mu\bar{\mathrm{N}}\gamma_\nu\mathrm{N})$														$4m_N\mu$	
$\mathcal{O}_{V4}^{\mathrm{EFT}} = \mathrm{Re}(\mathrm{B}_\nu^\dagger\partial^\nu\mathrm{B}_\mu)\bar{\mathrm{N}}\gamma^\mu\gamma^5\mathrm{N}$											$\mathcal{O}(q^2)$	$4m_N\mu$			
$\mathcal{O}_{V4-2}^{\mathrm{EFT}} = i\mathrm{Im}(\mathrm{B}_\nu^\dagger\partial^\nu\mathrm{B}_\mu)\bar{\mathrm{N}}\gamma^\mu\gamma^5\mathrm{N}$								$\mathcal{O}(q^2)$	$2m_N^2$						
$\mathcal{O}_{V4-3}^{\mathrm{EFT}} = \mathrm{Im}(\mathrm{B}^{\mu,\dagger}\mathrm{B}^\nu)\mathrm{Im}(\partial_\mu\bar{\mathrm{N}}\gamma_\nu\gamma^5\mathrm{N})$												$-8\mu m_N$			
$\mathcal{O}_{V5}^{\mathrm{EFT}} = \mathrm{Re}(\mathrm{B}_\nu^\dagger\partial_\mu\mathrm{B}^\nu)\bar{\mathrm{N}}\gamma^\mu\mathrm{N}$	$\mathcal{O}(q^2)$		$\mathcal{O}(q^2)$												
$\mathcal{O}_{V5-2}^{\mathrm{EFT}} = i\mathrm{Im}(\mathrm{B}_\nu^\dagger\partial_\mu\mathrm{B}^\nu)\bar{\mathrm{N}}\gamma^\mu\mathrm{N}$	$4m_\chi m_N$		$-2\mu(m_\chi + 2m_N)$												
$\mathcal{O}_{V6}^{\mathrm{EFT}} = \mathrm{Re}(\mathrm{B}_\nu^\dagger\partial_\mu\mathrm{B}^\nu)\bar{\mathrm{N}}\gamma^\mu\gamma^5\mathrm{N}$							$\mathcal{O}(q^2)$			$4m_N^2$					
$\mathcal{O}_{V6-2}^{\mathrm{EFT}} = i\mathrm{Im}(\mathrm{B}_\nu^\dagger\partial_\mu\mathrm{B}^\nu)\bar{\mathrm{N}}\gamma^\mu\gamma^5\mathrm{N}$							$8m_\chi m_N$								
$\mathcal{O}_{V7}^{\mathrm{EFT}} = \mathrm{Re}(\epsilon^{\mu\nu\sigma\rho}\mathrm{B}_\mu\partial_\nu\mathrm{B}_\sigma)\bar{\mathrm{N}}\gamma_\rho\mathrm{N}$								$4m_\chi m_N$	$4m_\chi m_N$						
$\mathcal{O}_{V7-2}^{\mathrm{EFT}} = i\mathrm{Im}(\epsilon^{\mu\nu\sigma\rho}\mathrm{B}_\mu\partial_\nu\mathrm{B}_\sigma)\bar{\mathrm{N}}\gamma_\rho\mathrm{N}$											$2m_N^2$				
$\mathcal{O}_{V8}^{\mathrm{EFT}} = \mathrm{Re}(\epsilon^{\mu\nu\sigma\rho}\mathrm{B}_\mu\partial_\nu\mathrm{B}_\sigma)\bar{\mathrm{N}}\gamma_\rho\gamma^5\mathrm{N}$				$-8m_\chi m_N$	μm_χ										
$\mathcal{O}_{V8-2}^{\mathrm{EFT}} = i\mathrm{Im}(\epsilon^{\mu\nu\sigma\rho}\mathrm{B}_\mu\partial_\nu\mathrm{B}_\sigma)\bar{\mathrm{N}}\gamma_\rho\gamma^5\mathrm{N}$														$4\mu m_N$	
$\mathcal{O}_{V9}^{\mathrm{EFT}} = iB_\mu^\dagger B_\nu\bar{N}\sigma^{\mu\nu}N$					$4m_N$										
$\mathcal{O}_{V10}^{\mathrm{EFT}} = B_\mu^\dagger B_\nu\bar{N}\sigma^{\mu\nu}\gamma^5 N$											m_N	4μ			

Table 4.10: As for Fig.4.9, but for the EFT operators in Tab.4.3 and 4.2. Operators $\mathcal{O}_{V3-4}^{\mathrm{EFT}}, \mathcal{O}_{V4-4}^{\mathrm{EFT}}$ do not match to any of the NR operators we consider.

Model	F1	F2	F3	F4	F5	F6	F7	F8	F9	F10
1/2*-S	■	■	■	■						
1/2*-V					■	■	■	■		
1/2*-S$^{\pm}$	■	■	■	■	■	■	■	■	■	■
1/2*-V$^{\pm}$	■	■	■	■	■	■	■	■	■	■
1/2-S	■	■	■	■						
1/2-V						■		■		
1/2-S$^{\pm}$	■	■	■	■		■		■		
1/2-V$^{\pm}$	■	■	■	■		■		■		

Table 4.11: The matching from the simplified models, listed in Tab.2.4, to the EFT operators from the spin-1/2 DM models, listed in Tab.4.1. Grey shading indicates the matching, the explicit coefficients are given in Sec.4.2.2.

Model	S1	S2	S3	S4
0-S	■	■		
0-V			■	■
0-F$^{\pm}$	■	■		
0*-F$^{\pm}$	■	■	■	

Model	V1	V2	V3	V3-2	V4	V4-2	V5	V5-2	V6	V6-2	V7	V7-2	V8	V8-2	V9	V10
1-S	■	■														
1*-S	■	■														
1$^{(*)}$-V : $\mathcal{V}_1$			■	■	■	■										
1$^{(*)}$-V : $\mathcal{V}_2$							■	■	■	■						
1$^{(*)}$-V : $\mathcal{V}_3$											■	■	■	■		
1-F$^{\pm}$	■	■									■		■			
1*-F$^{\pm}$	■	■		■		■		■		■	■		■		■	■

Table 4.12: The matching from the simplified models, listed in Tab.2.4, to the EFT operators (in Tab.4.3 and Tab.4.2) from the spin-0 DM models (upper) and spin-1 DM (lower). The matching coefficients can be found in Sec.4.2.4 and Sec.4.2.3.

4.5 Direct Detection Constraints : Current and Future Experiments

The benchmark cross sections in the literature are usually termed *spin-independent* (SI) and *spin-dependent* (SD), which refers to interactions that do or do not depend on the spin of the nucleus with which the DM scatters. This is by no means the full picture (there are in fact at least 18 other coupling structures of which SI and SD are a subset).

We recall the formula for the conventional SI and SD interactions,

$$\frac{dR}{dE_R} = N_T N_\chi \int_{v_{\min}}^{v_{\rm esc}} d\mathbf{v} f(\mathbf{v}) \frac{d\sigma}{dE_R} \ , \tag{4.5.117}$$

where $N_{T,\chi}$ are the numbers of DM and target T, $f(\mathbf{v})$ is the velocity distribution of the DM. The differential cross section is given by

$$\frac{d\sigma_{\rm SI}}{dE_R} = \frac{m_T}{2\mu_T^2}\frac{1}{v^2}\left(\sigma_{\rm SI}F_{\rm SI}^2 + \sigma_{\rm SD}F_{\rm SD}^2\right) \ , \tag{4.5.118}$$

with μ_T the DM-target reduced mass and

$$\sigma_{\rm SI} = \frac{4\mu_T^2}{\pi}\left(Z\sigma_p + (A-Z)\sigma_n\right)^2 \ , \tag{4.5.119}$$

$$\sigma_{\rm SD} = \frac{32\mu_T^2}{\pi}G_F^2\frac{J+1}{J}\left(a_p\langle S_p\rangle + a_n\langle S_n\rangle\right)^2 \ . \tag{4.5.120}$$

We assumed the proton and neutron cross sections are the same, $\sigma_p = \sigma_n$. Thus the overall SI cross sections is $\propto A^2$, a so called coherent enhancement where the interactions with the nucleons add coherently, without interference. On the other hand if the interaction depends on the nuclear spin, there is a lot of interference since nuclear spins are $J \sim \mathcal{O}(1)$ compared with $\mathcal{O}(A)$.

In principle $\langle S_p\rangle$ and $\langle S_n\rangle$ must be calculated using some sophisticated nuclear model; the simple shell model gives a good intuition. In the shell model, nucleons fill up energy shells in pairs (as they are fermions), and any pair of nucleons contributes zero to the nucleus spin. Therefore the spin of the nucleus is carried by an unpaired nucleon, and its value is given by the J quantum number of the shell in which the

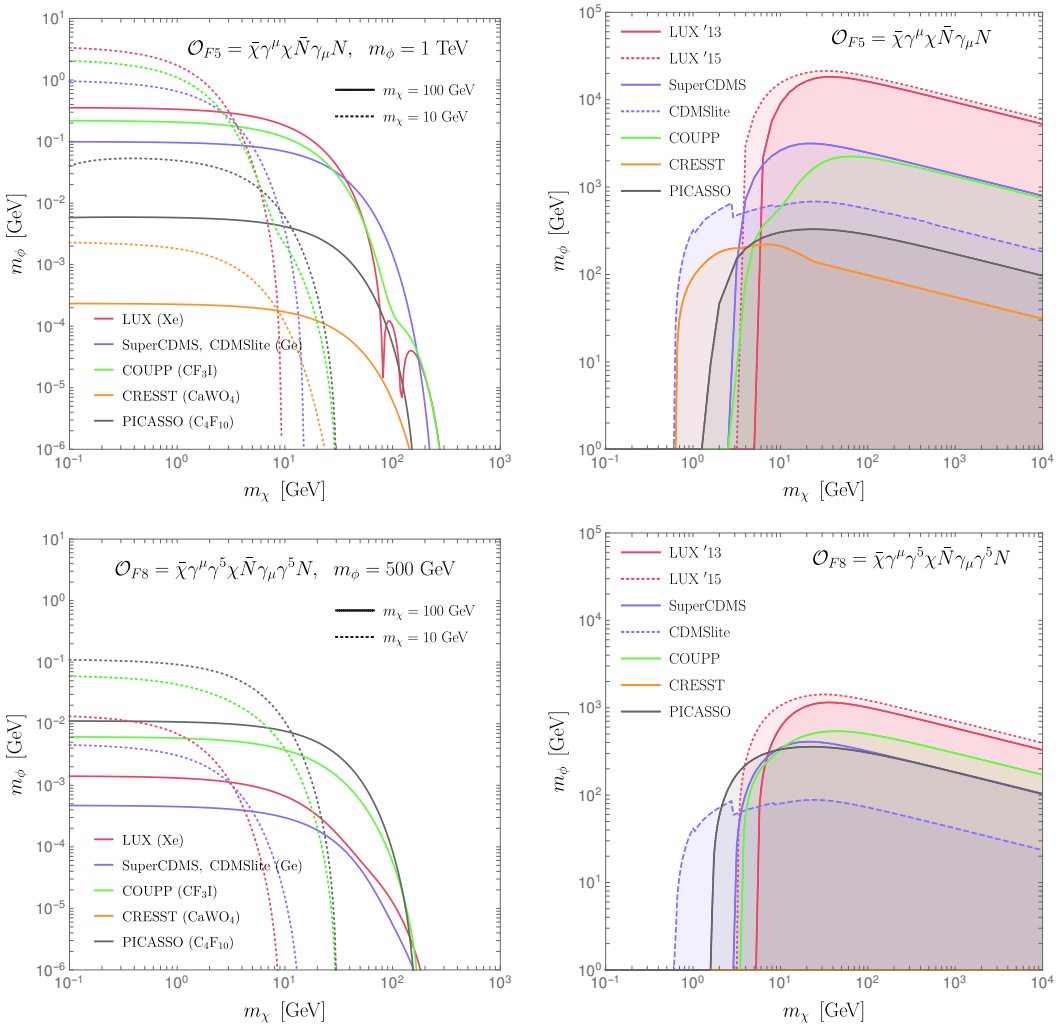

Figure 4.5: The differential recoil rate per kg · s (left) and exclusion limits (right, shaded region) for two EFT operators describing the interaction between DM and nucleons; both vector (upper panels) and axial-vector (lower panels) couplings which are roughly equivalent to the conventional "Spin Independent" (SI) and "Spin Dependent" (SD) models respectively.

unpaired nucleon resides. Thus *even-even* nuclei (those with even numbers of protons and neutrons) are completely insensitive to SD interactions.

Both of these benchmark cross sections translate easily into the fuller picture of simplified models. The SI cross section is approximately equal to an $\bar{\chi}\gamma^\mu\chi\bar{N}\gamma_\mu N$ or $\bar{\chi}\chi\bar{N}N$ effective operator, and SD roughly equal to $\bar{\chi}\gamma^\mu\gamma^5\chi\bar{N}\gamma_\mu\gamma^5 N$.

In the present treatment the event rate is given by Eq.(4.4.116), but with the

differential cross section given as a product of the non-relativistic two-body phase space and the matrix element as in Eq.(4.4.115). The matrix element is matched to the non-relativistic nuclear form factors as in Eq.(4.4.114). Table 4.13 shows how each of the simplified models couples to nuclei in the non-relativistic limit. The NR operators are given explicitly in Table 4.5.

Although counting powers of $\mathbf{q}$ and $\mathbf{v}$ helps to give a rough indication of the suppression of a particular operator compared with $\mathcal{O}_1^{(\mathrm{NR})}$ whose form factor scales as $\sim A^2$, it is not always clear which operators dominate from the counting alone. For example the canonical spin-dependent operator $\mathcal{O}_4^{(\mathrm{NR})} = S_\chi \cdot S_N$ is over an order of magnitude smaller than $\mathcal{O}_{11}^{(\mathrm{NR})} \propto q \cdot S_\chi$ and $\mathcal{O}_{12}^{(\mathrm{NR})} \propto S_\chi \cdot (S_N \times v^\perp)$, at recoil energies around a keV and DM mass 10 GeV.

It is clear that the DM-quark scattering cross section is very sensitive to the coupling choices imposed for a particular model, for example a coupling to γ^μ versus $\gamma^\mu\gamma^5$ can drastically change the scattering cross section, the dominant operators and their coupling dependence is shown in Fig.4.13. Only a few EFT operators can yield the dominant A^2 enhanced scattering: $\bar{\chi}\chi\bar{q}q$, $\bar{\chi}\gamma^\mu\chi\bar{q}\gamma_\mu q$ for spin-1/2 (the latter is not present for Majorana DM), $\phi^\dagger\phi\bar{q}q$ and $i\mathrm{Im}(\phi^\dagger\partial^\mu\phi)\bar{\mathrm{q}}\gamma^\mu\mathrm{q}$ for spin-0, and $B^\dagger_\mu B^\mu\bar{q}q$ and $i\mathrm{Im}(\mathrm{B}^\mu\partial^\nu\mathrm{B}^\dagger_\mu)\bar{\mathrm{q}}\gamma_\nu\mathrm{q}$ for spin-1 DM. This list does not include any operators containing γ^5 since these all lead to spin-dependent interactions in the NR limit.

The observable of interest in DD, the total event count, is given by the integral of Eq.(4.4.116) over recoil energy, and multiplied by the exposure of the detector (a product of its mass and time length, conventionally in kg $\cdot$ day or ton $\cdot$ yr). If the data are binned, then the count for each bin is computed over the energy range of that bin. If the data are un-binned then the integral is over the complete energy range of the data.

From an experimental perspective, there are a few broad detection techniques, for a review as of 2015 see [261]. Noble liquid targets (primarily xenon, as in LUX,

	SI $\mathcal{O}_1^{(\mathrm{NR})}$	SD $\mathcal{O}_4^{(\mathrm{NR})}$	SD $\mathcal{O}_6^{(\mathrm{NR})}$	SD $\mathcal{O}_7^{(\mathrm{NR})}$	SI $\mathcal{O}_8^{(\mathrm{NR})}$	SD $\mathcal{O}_9^{(\mathrm{NR})}$	SD $\mathcal{O}_{10}^{(\mathrm{NR})}$	SI $\mathcal{O}_{11}^{(\mathrm{NR})}$	SD $\mathcal{O}_{12}^{(\mathrm{NR})}$	SD $\mathcal{O}_{14}^{(\mathrm{NR})}$
$1/2^{(*)}$-S	$g_{f,s}g_{\chi,s}$		$g_{f,p}g_{\chi,p}$				$g_{f,p}g_{\chi,s}$	$g_{f,s}g_{\chi,p}$		$g_{f,s}g_{\chi,p}$
1/2*-V	$g_{f,v}g_{\chi,v}$	$g_{f,a}g_{\chi,a}$	$g_{f,v}g_{\chi,v}$	$g_{f,a}g_{\chi,v}$	$g_{f,v}g_{\chi,a}$	$g_{f,a}g_{\chi,v}, g_{f,v}g_{\chi,a}$				
1/2-V		$g_{f,a}g_{\chi,a}$			$g_{f,v}g_{\chi,a}$	$g_{f,v}g_{\chi,a}$				
1/2-$S^{\pm}$	$\lvert g_s^2\rvert - \lvert g_p^2\rvert$	$\lvert g_s^2\rvert + \lvert g_p^2\rvert$	$\lvert g_s^2\rvert - \lvert g_p^2\rvert$		$i(g_s g_p^\dagger - g_p g_s^\dagger)$	$i(g_s g_p^\dagger - g_p g_s^\dagger)$	$(g_s g_p^\dagger + g_p g_s^\dagger)$	$(g_s g_p^\dagger + g_p g_s^\dagger)$		
1/2*-$S^{\pm}$	$\lvert g_s^2\rvert \pm \lvert g_p^2\rvert$	$\lvert g_s^2\rvert \pm \lvert g_p^2\rvert$	$\lvert g_s^2\rvert \pm \lvert g_p^2\rvert$	$i(g_s g_p^\dagger - g_p g_s^\dagger)$	$i(g_s g_p^\dagger - g_p g_s^\dagger)$	$i(g_s g_p^\dagger - g_p g_s^\dagger)$	$(g_s g_p^\dagger + g_p g_s^\dagger)$	$(g_s g_p^\dagger + g_p g_s^\dagger)$		
1/2-$V^{\pm}$	$\lvert g_v^2\rvert - \lvert g_a^2\rvert$	$\lvert g_v^2\rvert + \lvert g_a^2\rvert$	$\lvert g_v^2\rvert - \lvert g_a^2\rvert$		$g_v g_a^\dagger + g_a g_v^\dagger$	$g_v g_a^\dagger + g_a g_v^\dagger$	$i(g_v g_a^\dagger - g_a g_v^\dagger)$	$i(g_v g_a^\dagger - g_a g_v^\dagger)$		
1/2*-$V^{\pm}$	$\lvert g_v^2\rvert \pm \lvert g_a^2\rvert$	$\lvert g_v^2\rvert \pm \lvert g_a^2\rvert$	$\lvert g_v^2\rvert \pm \lvert g_a^2\rvert$	$g_v g_a^\dagger + g_a g_v^\dagger$	$g_v g_a^\dagger + g_a g_v^\dagger$	$g_v g_a^\dagger + g_a g_v^\dagger$	$i(g_v g_a^\dagger - g_a g_v^\dagger)$	$i(g_v g_a^\dagger - g_a g_v^\dagger)$		
$0^{(*)}$-S	$g_\chi g_{f,s}$						$g_\chi g_{f,p}$			
0*-V	$g_\chi g_{f,v}$			$g_\chi g_{f,a}$			$g_\chi g_{f,a}$			
0-$F^{\pm}$	$\lvert g_s\rvert^2 \pm \lvert g_p\rvert^2$						$i(g_p g_s^\dagger - g_s g_p^\dagger)$			
0*-$F^{\pm}$	$\lvert g_s\rvert^2 \pm \lvert g_p\rvert^2$			$g_s g_p^\dagger + g_p g_s^\dagger$			$i(g_p g_s^\dagger - g_s g_p^\dagger)$			
$1^{(*)}$-S	$g_\chi g_{f,s}$						$g_\chi g_{f,p}$			
1-V ($\mathcal{V}_1$)		$\mathrm{Im}(g_\chi)g_v$	$\mathrm{Im}(g_\chi)g_v$			$\mathrm{Im}(g_\chi)g_a$			$\mathrm{Re}(g_\chi)g_a$	$\mathrm{Re}(g_\chi)g_v$
1-V ($\mathcal{V}_2$)	$\mathrm{Im}(g_\chi)g_v$			$\mathrm{Im}(g_\chi)g_a$			$\mathrm{Re}(g_\chi)g_a$			
1-V ($\mathcal{V}_3$)		$\mathrm{Re}(g_\chi)g_a$			$\mathrm{Re}(g_\chi)g_v$	$\mathrm{Re}(g_\chi)g_v$		$\mathrm{Im}(g_\chi)g_v$		$\mathrm{Im}(g_\chi)g_a$
1-$F^{\pm}$	$\lvert g_v\rvert^2 \pm \lvert g_a\rvert^2$	$\lvert g_v\rvert^2 + \lvert g_a\rvert^2$			$g_v g_a^\dagger + g_a g_v^\dagger$	$g_v g_a^\dagger + g_a g_v^\dagger$	$i(g_v g_a^\dagger - g_a g_v^\dagger)$			
1*-$F^{\pm}$	$\lvert g_v\rvert^2 \pm \lvert g_a\rvert^2$	$\lvert g_v\rvert^2 + \lvert g_a\rvert^2$	$\lvert g_v\rvert^2 + \lvert g_a\rvert^2$	$g_a g_v^\dagger + g_v g_a^\dagger$	$g_a g_v^\dagger + g_v g_a^\dagger$	$g_v g_a^\dagger + g_a g_v^\dagger$	$i(g_v g_a^\dagger - g_a g_v^\dagger)$			

Table 4.13: The non-relativistic operators (columns) for direct detection that are obtained from the simplified models considered in this work (rows), as shown in Tab.2.4, along with their coupling dependence. For reference we have indicated the spin-dependent operators (SD). The full expressions for the NR operators are given in Table 4.5. Operator $\mathcal{O}_{13}^{(\mathrm{NR})}$ has no matching within the models.

XENON, and LZ for example, although liquid argon and neon are proposed) rely on the detection of scintillation photons from the excitation by collision, and subsequent de-excitation of the target and also the detection of ionization electrons, which drift to the top of the detection under the influence of an applied electric field. The detection of these two signals allows the separation of electron recoil (ER) and nuclear recoil (NR) events; this enables a significant background reduction, which comes primarily from ER. The DM scattering may contribute to both ER and NR, but is dominated by NR after backgrounds are removed for couplings to quarks. The high density of the noble liquid offers good self-shielding, and the detectors are generally larger in terms of target mass.

Germanium crystals allow the detection of phonons (heat) from collisions with the crystal lattice (for example in CoGENT). These benefit from lower thresholds, lower radioactivity levels and better energy resolution compared with noble liquid scintillators, however the detectors are typically limited in size due to the ability to grow the crystals.

Cryogenic bolometers use the same target crystals, but with the addition of an applied eletcric field are able to measure the charge yield of each event; with this additional signal the ER/NR events can be distinguished and the background reduced. Crystal targets are often germanium (CDMS, CDMSII, SuperCDMS, CDMSlite, EDELWEISS-II) and also silicon (CDMSII), or even calcium tungstate $CaWO_4$ (CRESST, in this case the scintillation signal is measured rather than the charge).

It is necessary to consider several DD experiments, since no single experiment provides the most powerful constraints over the full DM mass range. There are several reasons for this, for example, lighter targets generally allow exclusions of lighter DM compared with heavier targets, this comes from the minimum DM velocity to produce a recoil, $v_{\min} = \sqrt{2m_T E_R/\mu_T^2}$ with energy E_R. In practice this limits the reach of xenon experiments to DM masses $\gtrsim 5$ GeV . However it is generally easier to scale up the mass of certain target materials such as liquid xenon, making such

experiments able to create larger exposures and therefore be more excluding. We now list several experiments that we wish to consider in this study:

1. PICASSO : The *Project In CAnada to Search for Supersymmetric Objects* is located in SNOLAB. The 32 detector modules contain emulsified droplets of C_4F_{10} in a superheated state, a charged particle traversing the droplet which deposits energy above the threshold induces a rapid phase transition which nucleates a bubble in the fluid which then creates an acoustic signal. Varying the temperature of the target varies the energy threshold between 1.7 and 54.8 keV, defining 8 bins. The upper energy of each bin is 92 keV (25^oC). Data has been taken intermittently since late 2008, with an overall exposure of 114.3 kg-days [230] across 10 of the 32 detectors selected for the results. PICASSO is naturally suited to spin-dependent cross sections due to its large proportion of fluorine. Dealing with the background is somewhat convoluted; the 10 detectors each utilize the 8 temperature settings, for each detector the average rate is calculated over the entire temperature range, $\bar{R}_i$, then subtracted from the measured rate at each temperature, finally the data is averaged across the detectors to give 8 data points. The observed rate in energy bin k, $R_k^{\rm obs} = \Delta R_k + \bar{R}$, where $\bar{R} = 14.9$ per kg-day is the average of the average rates $\bar{R}_i$, weighted by their exposures and ΔR are the published data points (from Tab.3 and Fig.5 of [262] respectively), these values are shown in Tab.4.14 below. The measured event rate is linear with temperature, indicative of an α particle induced background, and thus $\bar{R}$ serves as the predicted background rate in each bin. Since the event count is not known, only the rate, we use a simple chi-squared statistic

$$\chi^2(M) = \sum_k \frac{(R_k^{\rm th}(M) + \bar{R} - R_k^{\rm obs})^2}{2\delta R_k^{\rm obs}},$$

the exclusion on M is found such that $\chi^2(M_{\rm exc}) = \chi^2(M_{\rm min}) + \Delta\chi^2$, with $\Delta\chi^2 = 2.71$ for the 90% confidence limit with one degree of freedom. $\chi^2(M_{\rm min})$ is the minimized chi squared. The value of χ^2 for the background only is 1.68, and can generally be reduced by including some DM signal since some of the data fluctuate below the expected background and the DM signal always

$E_{\rm th}$ (keV)	$R^{\rm obs}$ (kg^{-1} day^{-1})	$\delta R^{\rm obs}$ (kg^{-1} day^{-1})
1.7	8.90	42.60
2.9	14.60	0.54
4.1	16.50	14.4
5.8	14.70	1.84
6.9	14.95	0.065
16.3	16.30	2.38
38.8	14.70	0.34
54.8	16.20	6.11

Table 4.14: The 8 energy bins for PICASSO; their threshold energy, observed rate and error.

increases the rate.

2. COUPP : The *Chicagoland Observatory for Underground Particle Physics* is also located in SNOLAB, employing a similar technique of bubble nucleation of 4kg of superheated liquid CF_3I. The data was taken with three nucleation thresholds [263], with varying exposures of $\sim 70-400$ kg-days, $E_{\rm th} = 7.8, 11.0, 15.5$ keV and $MT = 55.8, 70.0, 311.7$ kg-days (including an efficiency cut of 79.1%; there were a total of 13 observed events (2,3,8) and an expectation of 4.5 (0.8,0.7,3.0)).

3. PICO : Formed from a merger between PICASSO and COUPP, PICO is a bubble chamber containing 2.9 kg of C_3F_8. The data consists of four operating temperatures $T = 14.2-11.6^o$ C (or $E_R = 3.2-8.1$ keV), with a total exposure 211.6 kg-days and 12 measured events (see Tab.I of [264]). However these 12 events are spurious and all are removed by applying a cut, while simultaneously retaining $49-63\%$ of the exposure. We will conservatively use 49% with zero observed and zero background events. A subsequent analysis by PICO-60L [265], a CF_3I bubble chamber, obtained 1335 kg-days of exposure, including an overall acceptance of 48.2% due to cuts, no events are observed after cuts, with an expected single-bubble background of 0.5 ± 0.2. The threshold is a continuum between $7-20$ keV (Fig.3 of [265]), with the bulk of the exposure between $10-17$ keV.

4. SuperCDMS : The *Super Cryogenic Dark Matter Search* is also located at the SNOLAB. The 15 detector modules are each a single 0.6 kg germanium crystal, sensitive to both ionization and phonon signatures of energy deposition, the total exposure of 577 kg-days was taken between 2012 and 2013 with 7 of the 15 detectors. A total of 11 events pass the selection criteria, with an expectation of 6.1. It is necessary to include the efficiency curve (red) in Fig.1 of [266] which lies between $10 - 50\%$.

5. CDMSlite : The *CDMS low ionization threshold experiment* uses the same detectors as SuperCDMS, but operated in 'lite' mode, sacrificing the ability to discriminate NR events from ER but obtaining an extremely low threshold of 0.074 keV. The collaboration present the data for *electron-equivalent* energy keV_{ee}, we describe how to convert this to *nuclear recoil* energy keV_{nr} in Sec.6.5. The data is split into 4 energy bins to remove dominant background from ^{71}Ge electron capture. Again, the efficiency must be included (the grey line in Fig.1 of [20])

6. LUX : The *Large Underground Xenon* detector is located in the Stanford underground laboratory, the first data release in 2013 [267] was based on 85.0 days and 118 kg of exposure. An updated analysis of the same data was presented in 2015 [268], but with an extra 10 days and 35 kg of exposure, there are 591 observed events with an expected 589 background (primarily from gamma rays), which reduces to 1 event with expected 1.1 when including the effects of the cuts.

7. CRESST : The *Cryogenic Rare Event Search with Superconducting Thermometers* is located in Gran Sasso, Italy. The detector is based on calcium tungstate $CaWO_4$ crystals cooled to mK temperatures, and measures both phonon and scintillation signals. The recent publication [269] analyses 52.2 kg-days of data with a threshold of 0.307 keV, with a binned spectrum up to 40 keV (Fig.6 of [269]), which we assume to be entirely background.

We summarize the important quantities for each of these experiments in Tab.4.15. The constraints are a 90% confidence limit produced by comparing binned or un-

Experiment	$E_{\rm nr}$ ($\rm keV_{nr}$)	Material	Exposure (kg-days)	ref.	$N_{\rm obs}$	$N_{\rm bck}$
PICASSO	1.7 – 78 *(Binned)*	C_4F_{10}	114.3	[230]	$\sim$ 13500	-
COUPP	7.8 – ∞ *(Binned)*	CF_3I	437.5	[263]	13	4.5
SuperCDMS	1.6 – 10.0	Ge	577	[270]	11	8
LUX 2015	1.1 – 18.6	Xe	1.4×10^4	[268]	591	589
LUX 2013	3.0 – 18.0	Xe	5046	[267]	1	0.64
CDMSlite	0.074 – 20.0 *(Binned)*	Ge	70	[20]	936	-
CRESST	0.307 – 30.0 *(Binned)*	$CaWO_4$	52	[269]	$\sim$ 1000	-

Table 4.15: Parameters of current generation DD experiments; the energy window in nuclear recoil energy, the material, the exposure, and the total measured events along with their predicted background given by each collaboration.

binned event counts (with the exception of PICASSO), and following the procedure laid out in the next section.

This list is by no means complete, for an overview of past present and future experiments see recent reviews [261, 271–274]. Often the PhD Theses of the larger collaborations provide excellent summaries of experimental results.

In principle one should include detector effects to correctly model the DM signal; the most important of which are detector efficiency and resolution. For the LUX data we are using, we have checked that using the detector response given in [267] gives almost identical results in our parameter space to integrating Eq.(4.4.116) between $E_{R,\rm min} = E_{\rm th} = 2$ keV and $E_{R,\rm max} = 30$ keV.

4.5.1 Statistical Methods for Direct Detection

The statistical methods employed to construct the limits on DM models (via the EFT operators) vary between authors. A full statistical treatment is usually left to the experimental collaboration, and is prohibitively complicated for a study which aims to include multiple experiments. Luckily there are several conservative treat-

ments which are routinely employed to give accurate bounds which are within a factor of ~ 2 or better of the published limits (see Sec.7.6.5 where we make an explicit comparison).

One is generally limited to the published data, which ranges from more complete (each individual event is given alongside its energy, and a full background model is included), for which one can obtain better limits, to less complete. For example, the data may be unbinned, and may not have a background model. It is necessary to employ a few different techniques to encompass these situations which we now briefly explain (see [275] for a review).

For situations where we have both a measured event count, $N_k^{\rm obs}$ (binned into energy bins labelled by k) and theoretical background $N_k^{\rm bck}$, we can use the *likelihood ratio test*, a method based on a bayesian hypothesis test between a background only, and background+signal model[20], with likelihoods $\mathcal{L}$, $\mathcal{L}_{\rm bck}$ respectively [230].

The likelihood of observing the data, D, assuming a particular set of parameters $\{\lambda\}$, is denoted $\mathcal{L}(D|\{\lambda\})$. The likelihood of each bin is a Poisson distribution $\text{Poiss}(N^{\rm obs}, N^{\rm th}(\lambda))$ where $N_k^{\rm th}$ are the predicted number of signal events (including background),

$$\mathcal{L}(N^{\rm obs}|\{\lambda\}) = \prod_k \frac{\left(N_k^{\rm th}\right)^{N_k^{\rm obs}}}{N_k^{\rm obs}!} \exp\left[-N_k^{\rm th}\right], \tag{4.5.121}$$

where $N^{\rm th}(\lambda) = N^{\rm DM}(\lambda) + N^{\rm bck}$. The background only model is identical but with $N^{\rm th} = N^{\rm bck}$. Then the test statistic,

$$\text{TS}(\lambda) = -2\log\left(\frac{\mathcal{L}}{\mathcal{L}_{\rm bck}}\right) \approx 2\sum_k \left(N_k^{\rm th} - N_k^{\rm obs}\log\left[\frac{N_k^{\rm th}+N_k^{\rm bck}}{N_k^{\rm bck}}\right]\right), \tag{4.5.122}$$

follows a χ^2 distribution; the cumulative p.d.f of $\chi^2(x)$ represents the probability that we observe the data given the model parameters λ. The value of x such that

[20] DD collaborations often use this method, but with a profile likelihood to include uncertainties is astrophysical and experimental parameters as nuisance parameters (frequentist approach) or by marginalization over priors (bayesian approach)

$\chi^2(x) = C$ (i.e. the $C\%$ confidence limit), depends on the number of parameters $\{\lambda\}$, in our case that is just one, then one can look up that $\chi^2(2.71) = 0.9$, which means that the 90% confidence bounds on λ are given by $\mathrm{TS}(\lambda) = 2.71$.

Note that this method is invariant under a change of variables, this is important for example for PICASSO, whereby only the measured rates are given. But since the observed event numbers all scale with exposure, then the event rates can be used instead of event counts.

This method works as long as we have a good theoretical model of the background sources; if the likelihood of the background only hypothesis is sufficiently small in Eq.(4.5.122), then it may not be possible to find the value $\chi^2 = 2.71$. This is especially true if we do not know the background.

If the background model is unknown (or if the background distribution is known, but not its normalization), then we can use the above method with the *maximum likelihood* as the null hypothesis in place of $\mathcal{L}_{\mathrm{bck}}$.

$$\mathcal{L}_{\mathrm{bck}} \to \mathcal{L}_{\mathrm{max}} = \mathcal{L}(N^{\mathrm{obs}}|\lambda_0) \equiv \mathrm{Max}\left(\mathcal{L}(N^{\mathrm{obs}}|\lambda)\right) \ ,$$

where λ is allowed to vary until a value λ_0 is found which maximizes the likelihood. This leads to a different interpretation, the null hypothesis is essentially the assumption that the measured data are due to a detection of DM, and then this hypothesis is rejected at 90% confidence. This is obviously not the intended interpretation but nonetheless the method produces a conservative bound.

Note that Eq.(4.5.122) is not valid if $N^{\mathrm{th}} = 0$ for all λ. This can happen for example if the DM is light enough that the velocity integral is zero. In such cases we exclude any bins for which the DM will never give a measurable signal.

The most simple experimental situation occurs when only the total number of events is measured (with an expected background), the single data point allows a very simple computation of a 90% confidence limit, we require that the chance

of measuring the observed number of events, $N^{\rm obs}$, given an expected number of events, $\mu = N^{\rm th} + N^{\rm bck}$, is $P(n < N^{\rm obs}|\mu) = 0.1$ (equivalently a certain fraction, 0.9, of a large number of identical experiments would measure more events over the entire spectra than are actually measured). The probability is given by a Poisson distribution,

$$P(n < N^{\rm obs}|\mu) = \sum_{n=0}^{N^{\rm obs}} \frac{\mu^n e^{-\mu}}{n!} = 0.1 \ . \tag{4.5.123}$$

For example, LUX measures 1 event with an expected background of 1.1 and by the application of the above equation we find that $N^{\rm th} > 2.79$ is excluded at 90% confidence (compared with $N^{\rm th} > 2.56$ from Eq.(4.5.122)).

As $N^{\rm obs}$ becomes large Eq.(4.5.123) is numerically intensive, and it is quicker to sum the probabilities of all events with $n > N^{\rm obs}$ by use of the identity,

$$P(n > N^{\rm obs}|\mu) = \sum_{n=N^{\rm obs}}^{\infty} \frac{(\mu)^n}{n!}\exp\left[-\mu\right] = \int_0^{\mu} dt \ \frac{t^{N^{\rm obs}}}{N^{\rm obs}!}\exp\left[-t\right] \ , \tag{4.5.124}$$

which in the limit of large observed events approximates a Gaussian,

$$P(N^{\rm obs} \to \infty|\mu) = \int_{N^{\rm obs}}^{\infty} \frac{1}{\sqrt{2\pi\mu}}\exp\left[-\frac{(t-N^{\rm obs})^2}{2\mu}\right] \ dt \ . \tag{4.5.125}$$

We obtain limits by letting $P(n > N^{\rm obs}|\mu) = 0.9$. This method does not require any information on the background, and thus the limits are conservative. If the background is known then better limits are obtained by letting $\mu = N^{\rm th} + N^{\rm bck}$.

For experiments which measure no events, or individual energy bins with no events which are used to provide constraints, then Eq.(4.5.124) becomes $N^{\rm th} = -\log(1-C)$ where $C = 0.9$ is the confidence level and then $N^{\rm th} = 2.3$.

A popular technique when the background is unknown is the *maximum gap* method [276]. The measured event energies define gaps; energy windows between each pair of events, and the 'maximum gap' is the gap in which the signal would be largest, and thus the chance of not measuring an event in the gap is smallest. This method is ideal for SuperCDMS, which has a low measured event count and

publishes the energy of individual events. It is less useful for CDMSlite for which $N^{\text{obs}} \sim 10^3$ and individual event energies are not published. In this case, one uses a more recent modified method called the *high statistics optimum interval* method [277]. If the background is known, but not its distribution, one can use the Feldman-Cousins method [278].

We use the likelihood ratio test for the LUX data, and the simple Poisson limit for CMDSlite.

4.6 Conclusions

In this chapter, we have explored in depth the direct detection signal arising from DM scattering with quarks (allowing the DM to be spin-0, spin-1/2, spin-1 and both real/complex with all possible single mediators consistent with Lorentz invariance and renormalizability). Such signals are ubiquitous across our simplified models, and the procedure we have reviewed for calculating it can be applied to any model. We have provided several summary tables for this purpose. We have proceeded through the standard calculation of the DD signal, starting with an EFT matching at tree level (and the loop level matching to gluon operators, as is appropriate for heavy quarks coupled to the DM), then considered the hadronic matrix element of each quark/gluon operator that can result. Finally we have performed a NR matching to a set of nuclear form factors. Although many of the results are to be found in the literature, one cannot find a consistent and self-contained 'codex' for the model-independent calculation of the signal.

We have followed this with a brief review of the most sensitive current DD experiments, their results, and a basic statistical treatment that can yield accurate bounds for each of them. The resulting constraints are among the strongest that can be placed on DM models, sometimes by several orders of magnitude, and this warrants the detail in which we have considered them. We have now laid the groundwork for the next chapter, in which we will apply all the constraints to each of the

16 simplified models.

Chapter 5

Constraints on Simplified Models

In previous chapters, we have explored two of the primary search strategies for DM; *indirect detection* (ID, Chapter 3) and *direct detection* (DD, Chapter 4) in a general way which may be applied to all of our simplified models outlined in Chapter 2. We are now ready to provide full constraints on each of the DM and mediator combinations and coupling structures present for each of the simplified models. Our primary motivation is to provide an illustration of what parameter space is available in the global space of possible simplified models.

Each model contains several independent couplings and in most cases, different combinations of non-zero couplings to the DM χ and the SM fermion f give rise to very different constraints. For example if a coupling may be complex in general, then the real and imaginary parts lead to different signals, especially if the operator associated to the coupling contains a derivative. *In all cases we set any non-zero couplings equal to one another* so that the resulting parameter space consists of a single coupling, and the masses of the DM and mediator $\{m_\chi, m_{\rm MED}, g\}$. For each model, we present constraints for a subset of the different coupling combinations (for example axial-vector and vector combinations) in the two-dimensional $\{m_\chi, m_{\rm MED}\}$ plane, illustrating the correlation between these quantities. We then provide for most combinations the effective 90% containment bands for $m_\chi, m_{\rm MED}$ and the nonzero coupling g in Tables 5.2, 5.4 and 5.5.

Additionally, we fix the SM fermions to which the DM couples. We will take the illustrative examples of a coupling to u (which represents a light quark, and is very similar to d, s), b (representing a heavy quark, and approximately equivalent to c, t) and finally e (representative of leptonic couplings e, μ, τ). In the latter case we do not provide complete bounds, as the DD bounds require two-loop calculations and are beyond the scope of this work [259], and results may be found elsewhere [226, 259, 279]. It should be noted however that the ID and DD bounds from leptophillic DM can still be very powerful.

In all of the figures we show the ID bounds with solid lines, where the hatched region beneath the lines is ruled out by Fermi-LAT, INTEGRAL, COMPTEL, EGRET or H.E.S.S. data, along with the myriad of other indirect bounds given in Sec.3.4. DD bounds from the experiments listed in Sec.4.5 (using only LUX at high mass $m_\chi \gtrsim 5$ GeV, and CDMSlite at low mass $0.1 \lesssim m_\chi \lesssim 5$ GeV) are shown with dashed lines with dotted filling to denoted the parameters which are ruled out. In both cases, the relic density is assumed to saturate the measured density: $\Omega_\chi h^2 = \Omega_c h^2 = 0.1198$ [6]. We will actually weaken the relic density constraint so that χ makes up *at least* 90% of the cosmological dark matter (but no more than 100%), conservatively allowing for some other unspecified particles to dominate the relic density. If the relic abundance falls below $\Omega_c h^2$, the local density $\rho_\odot$ must of course be accordingly rescaled[1], not doing so would result in many parameters being excluded which should in fact be allowed.

We provide these bounds for three choices of the nonzero coupling: $g = 0.5, 1.0$ and 3.0 (coloured green, blue and red respectively), the latter almost saturating the perturbative limit for couplings ($g < 4\pi$). From a model-building point of view these couplings may appear rather large, however they are of the right size to give the correct relic density in the MeV-TeV mass range of DM, they also allow for

[1]The signals from ID and DD are proportional to ρ^2 and ρ respectively, and thus scale as $\left(\Omega h^2/0.1198\right)^2$ and $\left(\Omega h^2/0.1198\right)$. Note that collider bounds have no dependence on the DM density since the DM is produced directly in the interaction.

straightforward comparison with collider bounds (e.g. [280]) which frequently use similarly high couplings. When readily available in the literature, collider bounds are shown as dotted lines and discussed within the text.

In addition to these hard bounds, we present the results of a *Markov Chain Monte Carlo* (MCMC) scan in the three-dimensional space of $(m_\chi, m_{\text{MED}}, g)$. We allow the dark matter and mediator masses to vary from 1 GeV to several tens of TeV. We allow for arbitrarily small couplings. The sample points are coloured red, blue and green, corresponding to couplings $1 < g \leq 3$, $0.5 < g \leq 1$ and $g \leq 0.5$ respectively.

Lighter DM candidates, $m_\chi < 1$ GeV, can in principle acquire the observed relic density through annihilations into neutrinos, photons and potentially other SM particles if there is enough phase space. However predicting the associated ID signature is difficult because cosmic ray propagation at low energies is challenging and one does not have good estimates of the cosmic ray spectrum resulting from prompt emission. Additionally since we are considering quark final states, multiple resonances appear for $E < 1$ GeV, and the cross section deviates from the free quark approximation. Since this is beyond the scope of this work, we restrict our analysis to masses larger than 1 GeV.

For the $\bar{b}b$ final state, if $m_\chi < m_b$ then the gamma-ray signal must be generated by diagrams involving loops of quarks, this changes both the ID constraints and the relic density calculation, so we restrict ourselves to tree level annhilation into fermions and do not produce RD and ID bounds below m_b. However, the DD bounds are calculated from loop-diagrams in which the b is virtual, the bounds are valid below $m_\chi < m_b$. In most cases, the upper bound on the DM mass falls below 100 TeV due to the relic abundance requirement. In the cases that survive, one must be careful not to violate the Kamionkowski and Griest unitarity mass bound [51].

In models for which DM annihilates via an s-channel resonance, the cross section peaks at degenerate masses obeying $m_{\text{MED}} = 2m_\chi$, this is visible in the plots as a soft peak caused by the large mediator width $\Gamma = m_{\text{MED}}/3$. Decreasing the width would cause the peak to become more spiky, and we note that this could allow degenerate models to provide the correct relic abundance for very large masses, however as already mentioned this requires a more careful treatment of the relic density calculation [8]. Additionally, if we were including a calculation of collider bounds the width would have to be calculated for each model since the collider signals are very sensitive to the width of s-channel resonances.

5.1 General points

We outline some very general features that apply across all models and allow some rough estimations of the possible size of various constraints.

Relic Density and Indirect Detection

The allowed regions of parameter space are bounded by contours which represent the DM achieving the correct relic density (the upper edges of the coloured regions). When DM annihilations are s-wave, the contours of constant annihilation cross section $\langle\sigma v\rangle \approx 3 \times 10^{-26}$ cm^{3}s^{-1} have the same shape as the ID constraints, since these are based on the same cross section. This makes the ID constraints very efficient at ruling out parameter space. However, the thermally-averaged cross section for p-wave processes is suppressed by $v^2 \sim 10^{-6}$ in the galaxy today (whereas in RD curves, the suppression is much weaker, $v \sim \mathcal{O}(0.1)$ since the velocity of the DM was much larger at earlier cosmological times). This results in much weaker ID constraints.

The thermally averaged cross section is essentially a non-relativistic expansion, and following [117] quantum mechanical arguments may be used to determine whether each model has an s-wave term in $\langle\sigma v\rangle$. An s-wave term ($v = 0$) appears if the two-particle DM state has orbital angular momentum $L = 0$. From the relativistic DM

bilinear term in the Lagrangian one obtains charge ($\mathcal{C}$) and parity ($\mathcal{P}$) conjugation rules; then quantum-mechanically such symmetries are given by $\mathcal{C} = (-1)^{L+S}$ and $\mathcal{P} = (-1)^{L}$ for bosonic DM and $\mathcal{C} = (-1)^{L+S}$ and $\mathcal{P} = (-1)^{L+1}$ for fermionic DM (the difference arises because fermions and anti-fermions have an opposite internal parity, see e.g. [281]). Hence one may determine the values of L and S; given that $S \leq 2$. The only bilinears that can give $L = 0$ are $\bar{\chi} i\gamma^5 \chi$, $\bar{\chi}\gamma^i\chi$, $\bar{\chi}\gamma^0\gamma^5\chi$, $\bar{\chi}\sigma^{0i}\chi$ for fermionic DM, $\phi\phi^\dagger$ for scalar DM, and $B^\dagger_\mu B^\mu$, $i(B^\dagger_i B_j - B_i B^\dagger_j)$, $B^\nu \partial_\nu B^0$ and $\mathrm{Im}(\epsilon^{i0jk} B^\dagger_i \partial_0 B_j)$ for vector DM.

This is a necessary but not sufficient condition to produce an s-wave cross section. For example, conservation of total angular momentum J may still not be possible in an s-wave configuration, leading to a p-wave suppressed annihilation. Similarly there may be a suppression which reduces the s-wave term, which may arise for example from a quark mass insertion required to produce the correct final state helicities.

For each model, we quote simple expressions for the annihilation cross sections for $\bar{\chi}\chi \to \bar{f}f$, which reproduce the true cross section well, independently of the choice of non-zero couplings. To avoid cluttering the expressions the width of the mediator, Γ, is not shown; the width must be implemented for all s-channel resonances, commonly via the *Breit-Wigner* prescription for which the propagator of the resonance in the amplitude is modified,

$$\mathcal{M} \propto \frac{1}{S - m^2} \to \frac{1}{(S - m^2) + im\Gamma}, \tag{5.1.1}$$

then the cross section goes as $((S - m^2) + m^2\Gamma^2)^{-1}$, in place of the singular denominators which appear in our expressions. The expressions also assume the limits $m_q \ll m_\chi, m_{\text{MED}}$. In the MCMC scan, and the figures of this Chapter, we use the true cross section expanded up to p-wave (or d-wave in some cases for numerical stability), and with full mass and width dependence. These results may be found in Appendix B, suitable for numerical implementation.

In specific cases, we also consider the process of DM annihilation into mediator

pairs which is possible if $m_\chi > m_{\rm MED}$ (for all charged mediators this is inconsistent with DM stability); in some cases this has a dramatic effect and in others only a very small correction. The larger effects come from longitudinal modes of vector mediator final states for which strong unitarity constraints are generically also present; and so in these cases the large unconstrained parameter space provided by the cosmological annihilations for $m_\chi > m_{\rm MED}$ is unlikely to be truly 'allowed'. For example, the modification to the model which removes unitarity violation would potentially also remove the dominant terms from the annihilation cross section.

Direct Detection

For DD, the presence of the operator $\mathcal{O}_1^{(\rm NR)}$ in the non-relativistic limit always indicates a strong constraint, and at low momentum transfers one may take $\mathcal{F}_{1,1}^{(N,N)} = N^2$ where N is the nucleon number. Many of the other operators still provide a constraint strong enough to exclude large regions of parameter space. A quick suggestion of which operators can appear can be accomplished using again the $\mathcal{P}$ and $\mathcal{C}$ symmetries and the requirement of $\mathcal{CPT}$ invariance. A contribution from $\mathcal{O}_1^{(\rm NR)}$ is forbidden if an effective operator is odd under $\mathcal{P}$ or $\mathcal{T}$.

The annihilation cross section scales roughly with couplings as g^4, and inversely with mediator mass $m_{\rm MED}^{-n}$ or DM mass m_χ^{-n} in the limit that either dominates the mass scales. The weaker the dependence on either mass the stronger the constraints. A schematic cross section in the limit of heavy masses is $\sigma \sim g^4 m_\chi^n m_{\rm MED}^m / (m_{\rm MED}^{4+l})$ with $4 + l - m - n = 2$.

Perturbative Unitarity

In quantum field theory the S-matrix must be unitary. Violations of unitarity signify the breakdown of the theory (physically the probability of the process occurring exceeds 1), and can be calculated by considering all scattering amplitudes (i.e. the full S-matrix). Unitarity can be checked order-by-order in perturbation theory beginning at tree level.

Very roughly, the amplitude for a $2 \to 2$ scattering ($i \to f$) in the COM frame depends only on a single kinematic variable, the angle θ between the incoming and outgoing momenta. The amplitude can be decomposed into *partial wave* amplitudes T^j (physically, into angular momentum states $j = 0, 1, \cdots$ with fixed initial/final state helicities), with higher order terms being suppressed. Then the *optical theorem* (derived from unitarity of the S-matrix) relates the imaginary part of this amplitude to the total cross section [282], providing an upper limit on the size of the partial wave (see Appendix A.5 for details),

$$\sum_f \beta_i \beta_f |T^j_{i \to f}(S)|^2 \leq 1, \tag{5.1.2}$$

where $S = 4E^2$ is the usual Mandelstam variable and E is the centre of mass energy, and $\beta_{i,f} \sim 1$[2]. The tree level amplitudes each have a single mediator which scales as $1/S$ in the $S \to \infty$ limit, the combination of external fields and vertices must then conspire to give at least a single power of S to lead to any unitarity violations.

Thus, unitarity violations at tree level are present mostly within models which contain massive spin-1 particles due to the longitudinal modes which scale as $\sqrt{S}/m$. Naively, the more vectors present in the process the larger the dependence on S. We therefore restrict unitarity considerations to models containing spin-1 vectors (which are assumed to be longitudinally polarized), which nonetheless are most of the simplified models under study.

There are several ways to use Eq.(5.1.2) to draw conclusions on the simplified models. Ultimately, the existence of unitarity violation signifies a model which must be supplemented with new physics. Nonetheless, the bound usually comes with an explicit scale S (the centre of mass energy) which depends on the parameters of the theory.

This scale has two interpretations: (a) that the effects of the new physics which are added to the theory become relevant at and above this scale (for example, the

[2]For identical particles in the initial state or final state a factor of 1/2 is applied to β.

mass $m \sim S$ for the new states) and the effects on low energy phenomenology is suppressed by $(E_{\text{low}}/S)^n$ with n some positive number, and E_{low} the energy scale of the process. This scale then indicates that signals with $E_{\text{low}} < S$ are safe from large corrections. (b) that at some fixed scale S, the parameters of the theory are constrained so as not to violate unitarity, this can require the masses of the particles to be very large in order to suppress the contributions.

For us (b) will be used to indicate which regions of parameter space violate unitarity at collider energies $\sqrt{S} = 8, 13$ TeV. A summary of results is shown in Tab.5.1 including the scaling behaviour with S for each process within the relevant models. If the scaling goes as S^0 then the energy dependence disappears and instead the constraint is applied directly to the parameters of the model and is valid at any energy scale. Four of the simplified models have processes like this. If the scaling goes as S^n with $n \geq 1$ then the violation of unitarity sets in at the scale S which depends on the parameters of the model, and which becomes lower as n increases; if $n = 2$ the constraints are very strong, and even have the potential to impact low energy phenomenology. There are three models in this category.

In both the 0*-V and 1-S models, the unitarity bound is evaded if the couplings are small enough and the mass heavy enough. In the case of $1 - V$, the bounds are simply too strong and new physics must be added before any robust conclusions can be drawn. It is also possible that large unitarity violations appear for $j = 1, 2, \cdots$ partial waves, or at one-loop level; we have assumed these to be suppressed.

The details of the calculation, including the helicity representations of spin-1/2 and spin-1 particles in contained in Appendix A.5. It is necessary to move beyond the EFT approximation to carry out these calculations, due to the potential dominance of longitudinal modes exchanged through mediating massive vectors. This would only be correctly captured if the EFT was calculated to two mass dimensions higher than the lowest operator, since then the longitudinal modes would match to operators with derivatives.

Model	Process	$\lvert T^0\rvert^2$
0*-V	$\chi\chi^\dagger \to VV, \bar{q}q \to VV$	S^2
	$\chi\chi^\dagger \to \chi\chi^\dagger$	S^0
	$\bar{q}q \to \chi\chi^\dagger$	0
1/2-V, 1/2*-V	$\bar{\chi}\chi \to VV, \bar{q}q \to VV$	S^1
	$\bar{\chi}\chi \to \bar{\chi}\chi, \bar{q}q \to \bar{q}q$	S^0
	$\bar{q}q \to \bar{\chi}\chi$	S^0
1/2-$V^\pm$, 1/2*-$V^\pm$	$\bar{\chi}\chi \to V^\dagger V, \bar{q}q \to V^\dagger V$	S^1
	$\bar{q}q \to \bar{\chi}\chi$	S^0
1-S; 1*-S	$\chi\chi^\dagger \to \chi\chi^\dagger, SS \to \chi\chi^\dagger$	S^2
	$\bar{q}q \to \chi^\dagger\chi$	S^1
1-F, 1*-F	$\bar{q}q \to \chi^\dagger\chi, \bar{F}F \to \chi^\dagger\chi$	S^1
	$\bar{q}q \to \bar{F}F$	S^0
1-V ($\mathcal{V}_{1,2,3}$)	$\chi^\dagger\chi \to \chi^\dagger\chi,\ \chi^\dagger\chi \to VV$	S^3

Table 5.1: The simplified models containing a vector field and which may violate unitarity, along with the tree-level $2 \to 2$ scattering processes containing at least one vector field. Assuming all vectors to be longitudinally polarized the leading dependence on S is shown for the dominant $j = 0$ partial wave amplitude squared, in the limit $S \to \infty$.

A further important application of the principle of unitarity was made in the well known paper by Kamionkowski and Griest [51]. The DM is assumed to be thermal, and thus $\langle\sigma v\rangle = 3 \times 10^{-26}$ cm^3 s^{-1}, if the DM is sufficiently heavy then unitarity is violated, the resulting bound $m_\chi < 300$ TeV is rather weak, however it is model independent (a caveat to this statement is that the assumption of an s-wave annihilation is made, this bound does not apply to velocity suppressed annihilation). Unsurprisingly, since we already implement the constraint that DM is thermal and does not overclose the universe directly, this bound does not actually rule out further parameter space than is already ruled out but it is worth bearing in mind that the thermal DM mass cannot be arbitrarily large.

Finally, before moving on to the results themselves, it is expected that the previous chapters have been read. We will assume familiarity with the notation used in those chapters to avoid large amounts of repetition of definitions.

5.2 Fermion Dark Matter

5.2.1 Neutral scalar mediator (1/2-S, 1/2*-S)

We can treat the spin-1/2 DM exchanging a neutral scalar mediator identically for Dirac and Majorana DM, as the differences in the self annihilation cross section $\langle\sigma v\rangle$ and the elastic scattering cross section $\sigma_{\rm DD}$ are negligible.

For DD, the EFT contains the scalar and pseudo scalar operators $\mathcal{O}_{F1,F4}$ ($\bar{\chi}\chi\bar{q}q$ and $\bar{\chi}i\gamma^5\chi\bar{q}i\gamma^5 q$) as well as the operators $\mathcal{O}_{F2,F3}$ which mix $1, \gamma^5$ couplings. If $g_{\chi,s}, g_{f,s} \neq 0$ the scalar operator $\bar{\chi}\chi\bar{q}q$ provides the only dominant spin-independent contribution to $\mathcal{O}_1^{(\rm NR)}$. The pseudo scalar couplings $g_{\chi,p}, g_{f,p} \neq 0$ cannot provide this contribution because the bilinear $\bar{\chi}i\gamma^5\chi$ is $\mathcal{P}$-odd and $\mathcal{T}$-odd. Pure pseudo scalar couplings ($g_{\chi,p}, g_{f,p} \neq 0$) lead to a strong $(\rm q/m_N)^4$ suppression (going as $\mathcal{O}_6^{(\rm NR)} = i\rm q\cdot S_N$ in the NR limit), significantly weakening the DD bounds. The appearance of this suppression can be deduced since the only $\mathcal{P}$-odd operators in the NR limit are $\rm p\cdot S$ (i.e. $\rm q\cdot S$ or $\rm v^\perp\cdot S$), where $\rm p = \{p, p'\}$ is the either of the incoming/outgoing DM momenta. The $(\rm q/m_N)^4$ factor leads to a $\sim 10^{-12}$ suppression in $\sigma_{\rm DD}$ compared to pure scalar couplings. However, the cross section depends strongly on $m_{\rm MED}$, $\sigma \propto m_{\rm MED}^{-4}$, and so the constraints on $m_{\rm MED}$ are $\sim 10^{12/4} = 10^3$ times smaller.

Due to parity arguments ($\mathcal{P}$-odd bilinears) a mixture of scalar and pseudo scalar couplings $(g_{f,s}, g_{\chi,p})$ or $(g_{f,p}, g_{\chi,s})$ are suppressed in the NR limit going as $\mathcal{O}_{10}^{(\rm NR)}, \mathcal{O}_{11}^{(\rm NR)}$ which again weaken the DD constraint.

This continues to be true for heavy quark couplings to DM, with the EFT operators containing bilinears $\bar{Q}Q$ and $\bar{Q}i\gamma^5 Q$, and which once integrated out of the

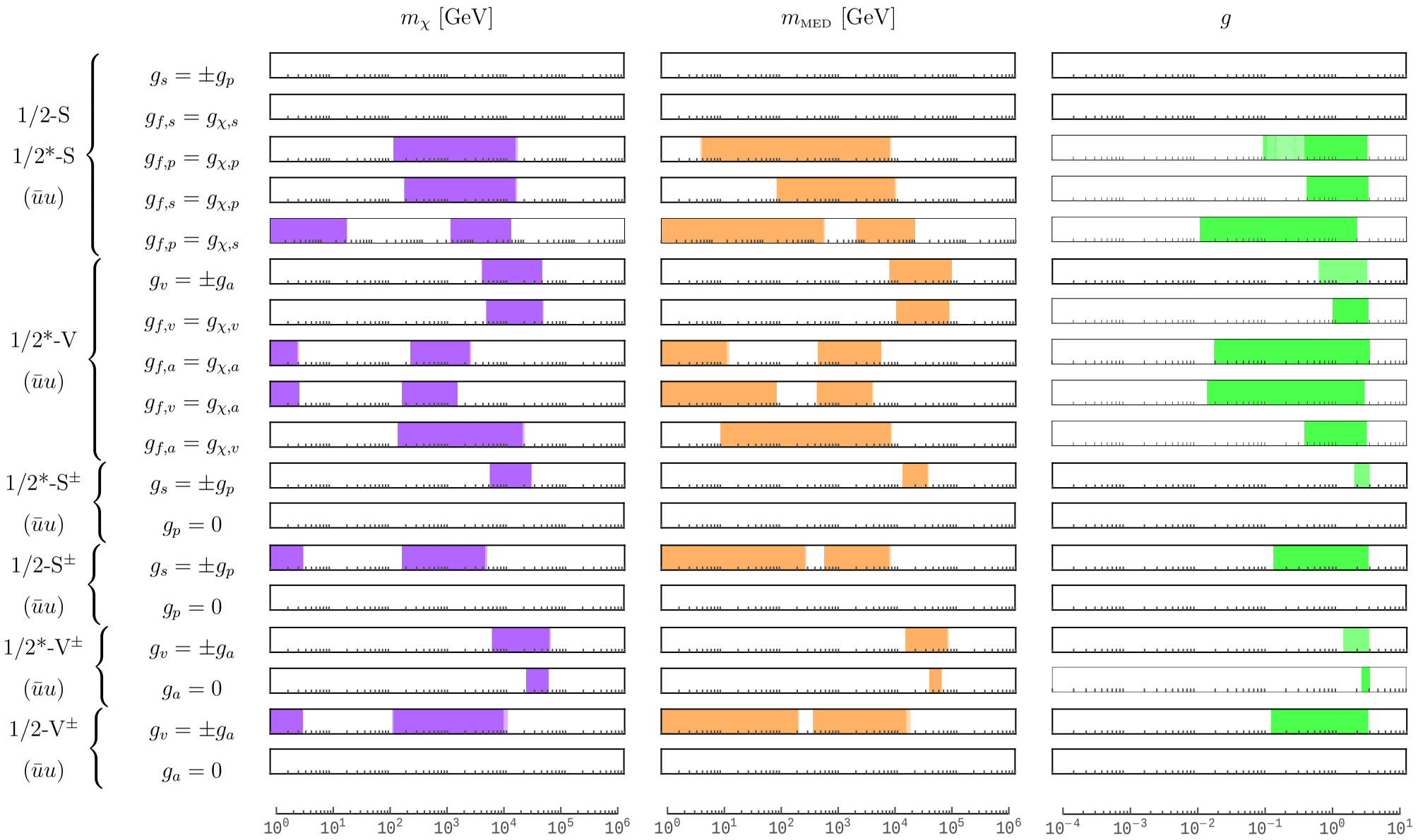

Table 5.2: The allowed regions projected onto each of the parameters $m_{\rm DM}$, $m_{\rm MED}$ and g, for the spin-1/2 DM models with final state $\bar{u}u$, and coupling choices as shown, for a relic abundance $\Omega_\chi h^2 = \Omega_c h^2$. The lighter shading shows the allowed region if $\Omega_\chi h^2 > 0.9\ \Omega_c h^2$.

theory lead to the 'scalar' (and 'pseudo scalar') gluon bilinears $G^{\mu\nu}G_{\mu\nu}$ and $G^{\mu\nu}\widetilde{G}_{\mu\nu}$ respectively, and are suppressed by $f_{T_Q}^{(N)}\left(\frac{m_N}{m_Q}\right)$ and $f_{5,Q}^{(N)}\left(\frac{m_N}{m_Q}\right)$ relative to the light quark scalar and pseudo scalar bilinears, in addition to the NR operator suppression.

The dominant DD cross section is given by Eq.(4.1.1), with the couplings,

$$\begin{aligned}
C_1^{(N)} =& 4g_{\chi,s}\frac{m_\chi m_N}{m_{\rm MED}^2}\left(\sum_{q'=q,Q} f_{T_{q'}}^{(N)} g_{q',s}\frac{m_N}{m_{q'}}\right),\\
C_6^{(N)} =& -4g_{\chi,p}\frac{m_N^2}{m_{\rm MED}^2}\left(\sum_{q'=q,Q} f_{5,q'}^{(N)} g_{q',p}\frac{m_N}{m_{q'}}\right),\\
C_{10}^{(N)} =& 4g_{\chi,s}\frac{m_N m_\chi}{m_{\rm MED}^2}\left(\sum_{q'=q,Q} f_{5,q'}^{(N)} g_{q',p}\frac{m_N}{m_{q'}}\right),\\
C_{11}^{(N)} =& -4g_{\chi,p}\frac{m_N^2}{m_{\rm MED}^2}\left(\sum_{q'=q,Q} f_{T_{q'}}^{(N)} g_{q',s}\frac{m_N}{m_{q'}}\right).
\end{aligned} \tag{5.2.3}$$

The ID constraints for all fermion flavours are strong if the DM pseudo scalar bilinear $g_{\chi,p}\bar{\chi}i\gamma^5\chi$ is present, since this can couple to an $L=0$ (s-wave) state, but $g_{\chi,s}\bar{\chi}\chi$ cannot, so $\langle\sigma v\rangle$ is p-wave suppressed in the event that $g_{\chi,p}=0$. These arguments do not apply to the quark final state and the cross section is proportional to $g_{f,s}^2+g_{f,p}^2$. In the limit $m_f\to 0$:

$$\begin{aligned}
\langle\sigma v\rangle \approx \sum_f \Bigg[&\frac{N_c m_\chi^2}{2\pi(m_{\rm MED}^2-4m_\chi^2)^2} g_{\chi,p}^2(g_{f,s}^2+g_{f,p}^2)\\
&+\frac{N_c v^2 m_\chi^2\left(g_{f,s}^2+g_{f,p}^2\right)}{8\pi(m_{\rm MED}^2-4m_\chi^2)^3}\left(g_{\chi,p}^2(m_{\rm MED}^2+4m_\chi^2)+g_{\chi,s}^2(m_{\rm MED}^2-4m_\chi^2)\right)\Bigg]\\
&+\theta(m_\chi-m_{\rm MED})\frac{g_{\chi,s}^2 g_{\chi,p}^2 m_\chi\sqrt{m_\chi^2-m_{\rm MED}^2}}{2\pi(m_{\rm MED}^2-2m_\chi^2)^2},
\end{aligned} \tag{5.2.4}$$

the third line includes the annihilation to mediators which affects the RD (but not the ID) constraints, and which provides a small correction above the threshold $m_\chi > m_{\rm MED}$. Fig.5.1 (top left) shows the ID and DD bounds for equal 'chiral' couplings ($g_{f,s}=\pm g_{f,p}\equiv g$ and $g_{\chi,s}=\pm g_{\chi,p}\equiv g$) to up-quarks, corresponding to the strongest constraints, and shows that spin-1/2 DM coupled to light quarks is completely excluded for $m_{\rm DM} > 1$ GeV (there is the possibility for degenerate masses with $m_{\rm MED}=2m_\chi$ if the width of the mediator is small $\Gamma \ll m_{\rm MED}/3$, but this requires a more careful treatment of the relic density). The parameter space

is still completely excluded even when coupled only via scalar couplings due to the strength of the DD constraint at low mass, from CDMSlite, despite the p-wave suppression to the ID bound, as shown in Fig.5.1 (top right). The same conclusions can be drawn for the other light quarks, d and s, since they only differ from the u quark case by the nuclear constants $f_{Tq}^{(N)}$, the ID is very similar since $m_\chi, m_{\rm MED} \gg m_q$.

For chiral couplings to b quarks, Fig.5.1 (bottom left), the low mass region $m_\chi < m_b$ is kinematically inaccessible as we are limited to tree level annihilation, however the loop-suppression of the DD constraints lead to an allowed region for high mass DM and mediators. For scalar couplings to b-quarks, the allowed region shrinks because the annihilation is p-wave suppressed and this affects the relic density, as shown in Fig.5.1 (bottom right).

The least excluded model is thus one where the DM couples to the mediator via a scalar coupling (p-wave annihilation), but to the quark via a pseudo-scalar coupling (momentum suppressed scattering). Fig.5.1 is sufficient to illustrate the general behaviour of the constraints, and in Tab.5.3 we qualitatively compare the strength of the constraints for different coupling choice, with the allowed range of each parameters summarized in Tab.5.2.

Non-zero Couplings	ID	DD
$(g_{\chi,p}, g_{\chi,s}, g_{f,s}, g_{f,p})$	s-wave	$\mathcal{O}_1^{(\rm NR)}$
$(g_{\chi,p}, g_{f,p})$	s-wave	$\mathcal{O}_6^{(\rm NR)}$ $((q/m_N)^2)$
$(g_{\chi,s}, g_{f,s})$	p-wave	$\mathcal{O}_1^{(\rm NR)}$
$(g_{\chi,s}, g_{f,p})$	p-wave	$\mathcal{O}_{10}^{(\rm NR)}$ (q/m_N)
$(g_{\chi,p}, g_{f,s})$	s-wave	$\mathcal{O}_{11}^{(\rm NR)}$ (q/m_N)

Table 5.3: The possible configurations of couplings which lead to distinct behaviour of the ID and DD constraints for the models 1/2-S and 1/2*-S. The ID are either s-wave ($\langle\sigma v\rangle \propto v^0$) or p-wave suppressed ($\langle\sigma v\rangle \propto v^2$). The dominant operator for DD scattering is shown with any suppression in brackets.

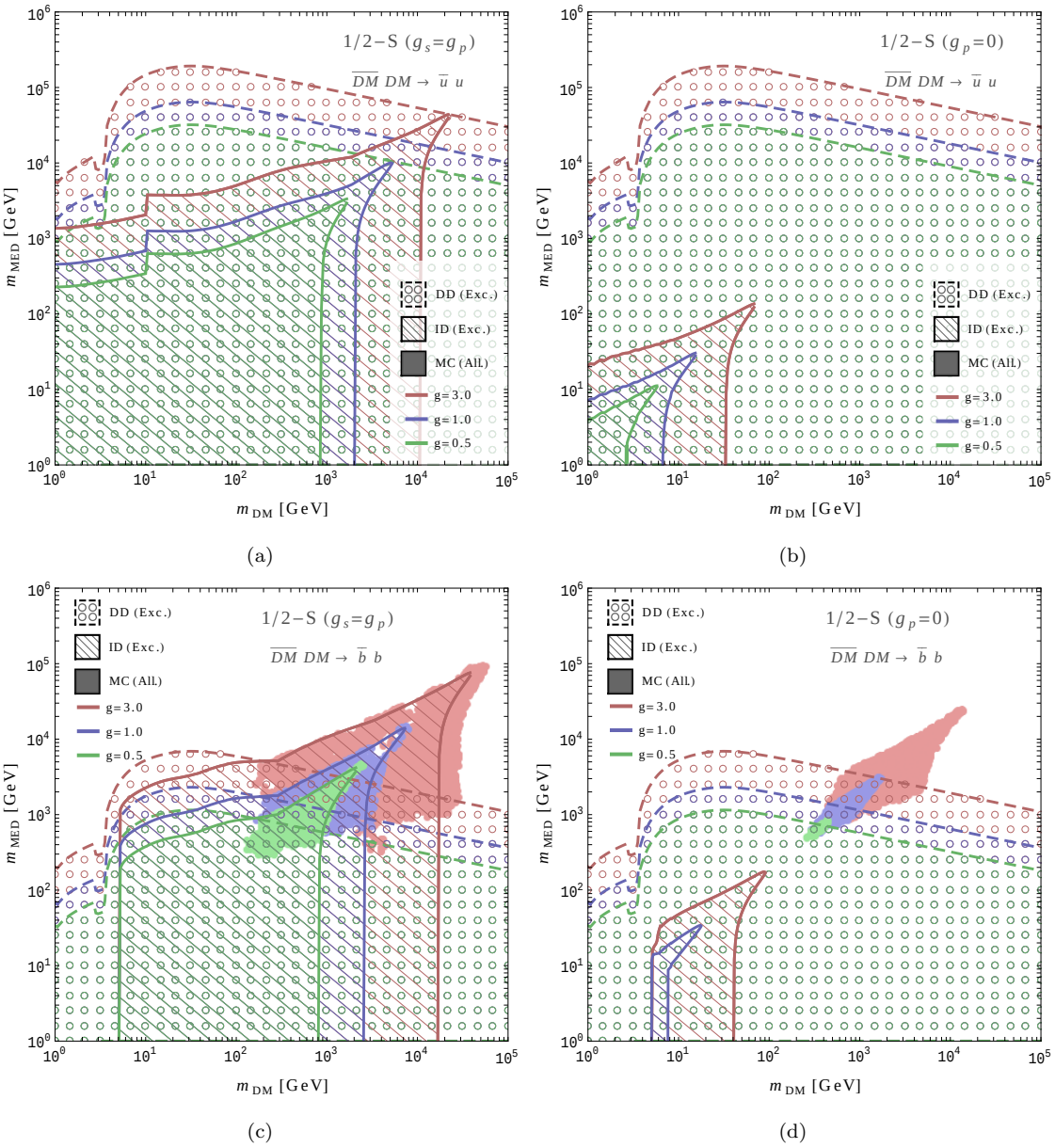

Figure 5.1: The regions in the $m_{\rm DM} - m_{\rm MED}$ plane excluded by ID and DD (LUX and CDMSlite) which are hatched and polka-dots respectively. A spin-1/2 Dirac or Majorana DM candidate exchanging a neutral scalar mediator with a pair of SM fermions, $\bar{u}u$ in the upper row, and $\bar{b}b$ in the lower row. The exclusions depend on the value of the coupling (left column: $g_s = g_p$, right column: $g_p = 0$), taken to be $g = 3, 1, 0.5$ (Red, Blue, Green respectively). The allowed regions are for $1 < g \leq 3$ (Red), $0.5 < g \leq 1$ (Blue) and $g \leq 0.5$ (Green), using an MCMC which requires a relic density $\Omega_\chi h^2 \in [0.9, 1.0]$ $\Omega_c h^2$.

Gamma Ray Line: Since the $\bar{\chi}\chi$ bilinear cannot couple to an s-wave state, then the cross section into two photons $\langle\sigma v\rangle_{\gamma\gamma}$ is p-wave suppressed unless $g_{\chi,p} \neq 0$. In the latter case, the cross section is

$$\langle\sigma v\rangle_{\gamma\gamma} = \sum_f \frac{1}{32\pi^2 m_\chi^2} \frac{N_c^2 \alpha^2 g_{\chi,p}^2 m_\chi^4}{\pi^2 (m_\phi^2 - 4m_\chi^2)^2} \times \left(g_{f,s}^2 \left(4 + \log\left(\frac{m_f^2}{4m_\chi^2} \right)^2 \right)^2 + g_{f,p}^2 \log\left(\frac{m_f^2}{4m_\chi^2} \right)^4 \right) . \quad (5.2.5)$$

The resulting constraints are slightly weaker than from $\langle\sigma v\rangle$, for example take $m_\chi = 100$ GeV (and set all couplings to 1), the constraints $\langle\sigma v\rangle_{\gamma\gamma,\text{Fermi}} \lesssim 10^{-28}$ cm^3 s^{-1}, which in the above equation corresponds to $m_\phi \approx 570$ GeV which is around a factor of 2 weaker.

5.2.2 Neutral vector mediator (1/2-V)

We now turn to the case of a neutral vector mediator, which has vector, γ^μ, and/or axial-vector, $\gamma^\mu\gamma^5$, couplings to the DM and the SM fermions. For DD, Dirac DM candidates lead to the operators $\mathcal{O}_{F5,F8}$ ($\bar{\chi}\gamma^\mu\chi\bar{f}\gamma_\mu f$ and $\bar{\chi}\gamma^\mu\gamma^5\chi\bar{q}\gamma_\mu\gamma^5 q$ respectively), as well as $\mathcal{O}_{F6,F7}$ although $\mathcal{O}_{F5,F7}$ are not present for Majorana DM since the bilinear $\bar{\chi}\gamma^\mu\chi = 0$. Of these, only $\mathcal{O}_{F5}$ can produce the dominant spin-independent operator $\mathcal{O}_1^{(\text{NR})}$. About five orders of magnitude smaller are the form factors for $\mathcal{O}_4^{(\text{NR})}$ (arising for the vector and axial-vector quadrilinears $\mathcal{O}_{F5,F8}$) and $\mathcal{O}_8^{(\text{NR})}$ (arising for mixed vector and axial-vector $\mathcal{O}_{F6}$), and finally $\mathcal{O}_{7,9}^{(\text{NR})}$ (arising for $\mathcal{O}_{F7}$), thus it is impossible to heavily suppress the DD constraints for light quark scattering, but a mild suppression occurs if one removes the vector coupling of either the quark or DM bilinear.

For heavy quark (or strange quark) scattering, an axial vector coupling $g_{Q,a}$ leads to a suppressed σ_{DD} by around two orders of magnitude. This comes from the nucleon constants, $\Delta_Q^{(N)}$, which arise dominantly through heavy quark axial currents mixing with the light quark singlet current g_A^0 under RG evolution (with a subdominant contribution through heavy quark threshold matching to gluon operators). For heavy quark vector couplings $g_{Q,v}$, as outlined in Sec.4.3.2, RG running of the Wilson coefficient also dominates the contribution, leading to $C_1^{(N)}$ suppressed by only

a few orders of magnitude. The heavy quark vector current strongly mixes with the light quark equivalents under RG flow above the heavy quark mass scale (the vector current is conserved and so the threshold matching is extremely suppressed, beginning at $\mathcal{O}(g_s^3)$), leading to a nucleon constant for b quarks $\mathcal{V}_b^{(p)} = 0.0072$, $\mathcal{V}_b^{(n)} = 0$[3].

The dominant Wilson coefficients for any coupling choice are given by,

$$\begin{aligned}
C_1^{(N)} =& 4 g_{\chi,v} \frac{m_\chi m_N}{m_{\text{MED}}^2} \left[\sum_{q'=q,Q} \mathcal{V}_{q'}^{(N)} g_{q',v} \right], \\
C_8^{(N)} =& -8 g_{\chi,a} \frac{m_N m_\chi}{m_{\text{MED}}^2} \left[\sum_{q'=q,Q} \mathcal{V}_{q'}^{(N)} g_{q',v} \right], \\
C_4^{(N)} =& -16 g_{\chi,a} \frac{m_\chi m_N}{m_{\text{MED}}^2} \left[\sum_{q'=q,Q} \Delta_{q'}^{(N)} g_{q',a} \right], \\
C_7^{(N)} =& 8 g_{\chi,v} \frac{m_\chi m_N}{m_{\text{MED}}^2} \left[\sum_{q'=q,Q} \Delta_{q'}^{(N)} g_{q',a} \right], \\
C_9^{(N)} =& \frac{m_N}{m_\chi} C_7^{(N)} - C_8^{(N)},
\end{aligned} \tag{5.2.6}$$

the Wilson coefficients above can be found in Sec.4.3.2.

The ID constraints are strong as long as $g_{\chi,v} \neq 0$, since then the cross section is s-wave. If however the DM is Majorana, or Dirac with $g_{\chi,v} = 0$ then the s-wave term is suppressed by $(m_q/m_\chi)^2$ (due to a helicity suppression) and proportional to only the axial coupling to quarks. For light quarks the mass suppression will be large, enough for the s-wave to be of the same order as, or subdominant to, the p-wave term, and this necessitates the inclusion of the d-wave expansion for numerical stability around the resonant region $2m_\chi = m_{\text{MED}}$, and considerably suppresses the

[3]This result makes sense from an RG running perspective; for consistency we should run down from the EW scale, below which the mixing occurs via photon exchange and so should only be non-zero for scattering with charged particles. We do not have mixing between heavy/light quark axial vector currents for the same reason, but we would find mixing above the EW scale due to the axial Z coupling, however for consistency we ignore this.

Non-zero Couplings	ID	DD
$(g_{\chi,a}, g_{\chi,v}, g_{f,v}, g_{f,a})$	s-wave	$\mathcal{O}_1^{(\mathrm{NR})}$
$(g_{\chi,a}, g_{f,a})$	s-wave ($\propto m_q^2$)	$\mathcal{O}_4^{(\mathrm{NR})}$
$(g_{\chi,v}, g_{f,v})$	s-wave	$\mathcal{O}_1^{(\mathrm{NR})}$
$(g_{\chi,v}, g_{f,a})$	s-wave	$\mathcal{O}_{7,9}^{(\mathrm{NR})}(v, q)$
$(g_{\chi,a}, g_{f,v})$	p-wave	$\mathcal{O}_8^{(\mathrm{NR})}(v)$

Figure 5.2: The possible configurations of couplings which lead to distinct behaviour of the ID and DD constraints for the models 1/2-V and 1/2*-V ($g_{\chi,v} = 0$ for Majorana DM). The suppression of DD operators is shown in brackets.

constraints

$$\begin{aligned}\langle\sigma v\rangle = &\sum_f \left[\frac{N_c}{2\pi}\left(\frac{2m_\chi^2 g_{\chi,v}^2\left(g_{f,a}^2+g_{f,v}^2\right)}{(m_{\mathrm{MED}}^2-4m_\chi^2)^2}+g_{\chi,a}^2 g_{f,a}^2\frac{m_q^2}{m_{\mathrm{MED}}^4}\right)\right.\\ &\left.+\frac{N_c v^2 m_\chi^2 g_{\chi,a}^2}{6\pi(m_{\mathrm{MED}}^2-4m_\chi^2)^2}\left(g_{f,v}^2+g_{f,a}^2\right)\right]\\ &+\theta(m_\chi-m_{\mathrm{MED}})\frac{(m_\chi^2-m_{\mathrm{MED}}^2)^{3/2}}{4\pi m_\chi m_{\mathrm{MED}}^2(m_{\mathrm{MED}}^2-2m_\chi^2)^2}\left[(g_{\chi,v}^2+g_{\chi,a}^2)^2(2m_\chi^2-m_{\mathrm{MED}}^2)\right.\\ &\left.-2(g_{\chi,v}^2-g_{\chi,a}^2)^2(m_\chi^2-m_{\mathrm{MED}}^2)\right]. \qquad (5.2.7)\end{aligned}$$

Thus the most strongly excluded scenario occurs for vector couplings $(g_{\chi,v}, g_{f,v}) \neq 0$. The least excluded scenario occurs if only the axial DM coupling, and vector quark couplings are present $(g_{\chi,a}, g_{f,s}) \neq 0$.

The bulk of the ID constraints from the literature are based on the assumption of an s-wave cross section; if $g_{\chi,v} = 0$ the helicity suppression competes with the velocity suppression of the p-wave term and both are around the same size for light quarks. The s-wave constraints still dominate over most of the parameter space except for a region at $m_\chi \sim 10 - 100$ GeV, where the resonance enhances the p-wave contribution, but suppresses the s-wave contribution (which goes as $(m_\phi^2 - 4m_\chi^2)^2/((m_\phi^2 - 4m_\chi^2)^2 + \Gamma^2 m_\phi^2)$, see Eq.(2.0.7) in Appendix B), the resulting constraints look a bit jagged.

To illustrate this model the two scenarios ($g_{\chi,v} = \pm g_{\chi,a} = g_{f,v} = \pm g_{f,a}$) and ($g_{\chi,a}, g_{f,a}$) are shown in Fig.5.3, in (a) and (b) respectively. (c),(d) are the same as (a),(b) but for a $\bar{b}b$ final state. The DD constraints are generally more powerful than ID for light quark final states, but the opposite is true for heavy quark final states. Fig.5.3 (c) shows that a lighter mediator is possible for a $\bar{b}b$ final state compared with $\bar{u}u$, due to the suppression of the DD constraint; the combination of DD and ID require large couplings $g \gtrsim 0.1$. A summary of the allowed parameters for these scenarios and the others from Fig.5.2 are shown in Tab.5.2.

LHC Bounds : A popular search avenue for DM at colliders is monojet searches plus missing energy, $\bar{q}q \to \bar{\chi}\chi j$, since this process is well measured and is fairly universal within EFT's for DM. Constraints are made on Λ, the heavy scale suppressing the EFT operator which is $\Lambda \sim m_{\text{MED}}$ in our case. Below $m_\chi \lesssim 100$ GeV [4] the collider constraints on Λ are uniform since $\sqrt{s} \gg m_\chi$, above this scale the constraints rapidly decrease since the COM energy is insufficient to produce a DM pair. The constraints are around $\Lambda < 1$ TeV scale for both vector and axial-vector couplings, enough to rule out some of the parameter space at low DM mass.

Perturbative Unitarity : As pointed out in [72] and confirmed in our calculation, this model requires a careful look at perturbative unitarity on self-scattering processes $\bar{f}f \to \bar{f}f$ and $\bar{\chi}\chi \to \bar{\chi}\chi$ exchanging the new mediator in the s-channel and leading to constraints,

$$m_f \lesssim \sqrt{\frac{\pi}{2}} \frac{m_{\text{MED}}}{g_{f,a}} \ , \tag{5.2.8}$$

$$m_\chi \lesssim \sqrt{\frac{\pi}{2}} \frac{m_{\text{MED}}}{g_{\chi,a}} \ . \tag{5.2.9}$$

For couplings to light quarks u, d, s, the first constraint sets a weak lower limit on the mediator mass of $m_{\text{MED}} \gtrsim (1-10)\ g_{f,a}$ MeV. For couplings to b quarks $m_{\text{MED}} \gtrsim 6\ g_{f,a}$ GeV is more constraining.

[4] See for example [283].

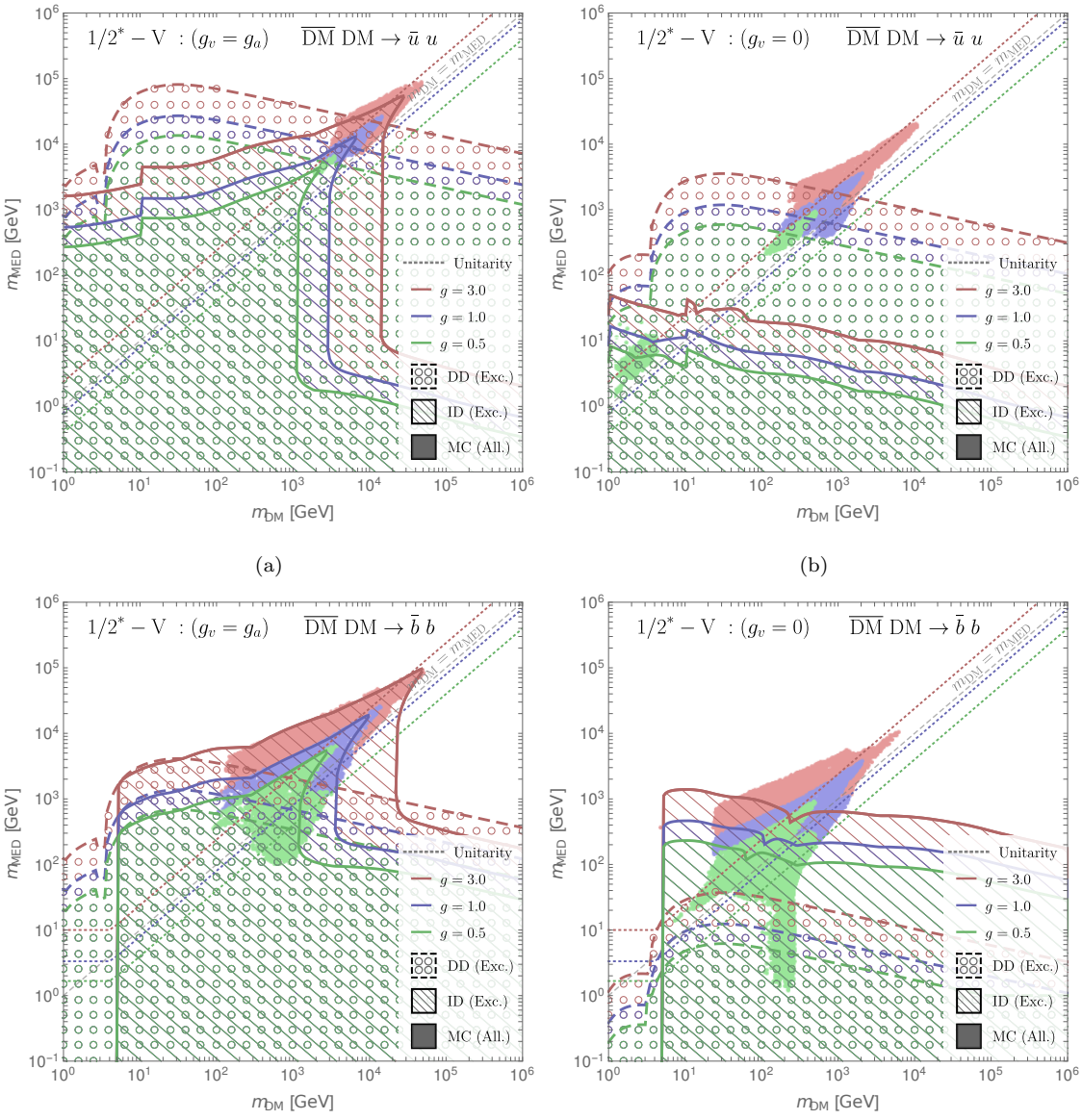

Figure 5.3: As for Fig.5.1 for a spin-1/2 Dirac DM (Majorana DM applies to the right column also) candidate exchanging a neutral vector mediator with a pair of SM fermions, $\bar{u}u$ in the upper row, and $\bar{b}b$ in the lower row.

The latter bound affects a large proportion of the parameter space as can be seen in Fig.5.3, and arises from the longitudinal mode of the spin-1 mediator (in the high energy limit this dominates over the transverse polarizations). In a gauge theory this would correspond to the Goldstone boson of the gauge boson. Since the bound does not depend on an energy scale for the process, it cannot be evaded with the introduction of new physics at some high scale, and thus acts as a genuine constraint on the theory, and as such we include it as a hard limit in the MCMC.

Gamma Ray Lines : If fermion vector couplings are present, $g_{f,v}$, the $\bar{\chi}\chi \to \gamma\gamma$ cross section is zero due to Furry's theorem. In the initial state, to produce an s-wave cross section requires $\bar{\chi}\gamma^i\chi$ or $\bar{\chi}\gamma^0\gamma^5\chi$ (i.e. vector or axial vector couplings, $g_{\chi,a}, g_{\chi,v}$), but it turns out that only $g_{\chi,a}$ gives a non-zero cross section,

$$\langle\sigma v\rangle_{\gamma\gamma} = \sum_f \frac{1}{32\pi^2 m_\chi^2} \frac{8N_c^2\alpha^2 g_{\chi,a}^2 g_{f,a}^2 m_\chi^4}{\pi^2(m_{\rm MED}^2 - 4m_\chi^2)^2} \left(\log\left(\frac{m_f^2}{4m_\chi^2}\right)\right)^2 . \tag{5.2.10}$$

As with the neutral scalar mediated model, the constraint is slightly weaker than from DM annihilation into fermions.

5.2.3 Charged scalar mediator (1/2-S$^\pm$, 1/2*-S$^\pm$)

We now address the first model which contains a mediator which is both EM and colour charged, with these quantum numbers identical to those of the quarks that they couple to. We begin with a word of caution: it should be kept in mind that new charged states are very highly constrained up to masses of $\lesssim$ TeV. Although searches for such particles are normally done in the context of a supersymmetric model, they should apply to generic charged mediators with very little modification. New charged scalars behave very similarly to squarks and are subject to strict n-jet constraints. Squarks coupled to light quarks are constrained $m_{\tilde{q}} > 850$ GeV [30], whereas a coupling to b quarks places strong limits in the squark-neutralino mass plane, restricting the squark mass to 100 GeV $\lesssim m_{\tilde{b}} \lesssim$ 620 GeV, with a limit of $m_{\tilde{\chi}^0} > 100$ GeV at the low end $m_{\tilde{\chi}^0} > 300$ GeV on the high-squark mass end [284]. Once embedded in a full supersymmetric model, these constraints become

even stronger; see e.g. [285] and references therein.

In principle the couplings are complex, we will assume they are real for simplicity, but this does not change the dominant behaviour of any of the equations presented.

For DD, due to a Fierz transformation that is applied to the spinors, all of the fermionic quadrilinears, $\mathcal{O}_{F1-9}$, appear. Thus we may limit ourselves to the quadrilinears which lead to the dominant $\mathcal{O}_1^{(\mathrm{NR})}$ operator, that is, $\mathcal{O}_{F1,F5}$. The coefficient of $\mathcal{O}_{F1}$ is $\propto (|g_s|^2 - |g_p|^2)$ and thus vanishes for chiral couplings $g_s = \pm g_p$, however $\mathcal{O}_{F5}$ is proportional to the combination $(|g_s|^2 + |g_p|^2)$ and does not vanish unless the DM is coupled only to a combination of s, c, b, t quarks (although in that case, RG running generates a contribution to the $\bar{u}\gamma^\mu u, \bar{d}\gamma^\mu d$ operators, see Sec.5.2.2), then the dominant operator would be $\mathcal{O}_4^{(\mathrm{NR})} = S_\chi \cdot S_N$ (where $S_{\chi,N}$ are the DM and nucleon spins). Since $\mathcal{O}_1^{(\mathrm{NR})}$ is always present for Dirac DM, the constraints are always strong (the scalar quadrilinear $\mathcal{O}_{F1}$ gains a factor $(m_N/m_q)^2$ relative to the vector $\mathcal{O}_{F5}$ in the cross section, and so chiral couplings do reduce the constraints),

$$C_1^{(N)} = \frac{m_N m_\chi}{(m_\chi^2 - m_{\mathrm{MED}}^2)} \sum_{q'=q,Q} \left[f_{T_Q}^{(N)} \left(|g_s^{(q')}|^2 - |g_p^{(q')}|^2 \right) \frac{m_N}{m_{q'}} + \mathcal{V}_{q'}^{(N)} \left(|g_s^{(q')}|^2 + |g_p^{(q')}|^2 \right) \right], \tag{5.2.11}$$

the heavy quark contribution to $\mathcal{V}_Q^{(N)}$ arises from RG running effects. For Majorana DM, by choosing chiral couplings it is possible to remove the dominant contribution from the scalar operator (since unlike for Dirac DM $\mathcal{O}_{F5}$ is not present), the subdominant contribution is from a twist-2 operator, proportional to $(|g_s|^2 + |g_p|^2)$ but suppressed by $m_\chi m_q/(m_\chi^2 - 2m_{\mathrm{MED}}^2)$ (which is still larger than the axial-vector operator, $\mathcal{O}_{F8} \to \mathcal{O}_4^{(\mathrm{NR})}$, by $\sim m_\chi/m_N$),

$$C_1^{(N)} = \frac{m_N m_\chi}{(m_\chi^2 - m_{\mathrm{MED}}^2)} \sum_{q'=q,Q} f_{T_{q'}}^{(N)} \left[\left(|g_s^{(q')}|^2 - |g_p^{(q')}|^2 \right) \frac{2m_N}{m_{q'}} + \left(|g_s^{(q')}|^2 + |g_p^{(q')}|^2 \right) \frac{m_N m_\chi}{2(m_\chi^2 - m_{\mathrm{MED}}^2)} \right]. \tag{5.2.12}$$

For ID, and Dirac DM the leading contribution to $\langle \sigma v \rangle$ is s-wave and proportional to $m_\chi(|g_s|^2 + |g_p|^2)$ (there is a subleading piece proportional to $m_f(|g_s|^2 - |g_s|^2)$),

and so the constraints remain of uniform strength for any choice of couplings since we always have $m_\chi > m_f$,

$$\langle \sigma v \rangle = \sum_f \frac{N_c m_\chi^2}{8\pi (m_\chi^2 + m_{\rm MED}^2)^2} \left(|g_s^{(f)}|^2 + |g_p^{(f)}|^2 \right)^2 . \tag{5.2.13}$$

However, if the DM is Majorana then the leading s-wave piece is $\propto m_\chi(|g_s|^2 - |g_p|^2)$ (and the subleading $\propto m_f(|g_s|^2 + |g_p|^2)$), consequently the s-wave term is m_f/m_χ suppressed for chiral couplings, this is a result of a helicity suppression from the effective operator $\bar{\chi}\gamma^\mu\gamma^5\chi\bar{q}\gamma_\mu\gamma^5$ (explained in Sec.5.2.4),

$$\langle \sigma v \rangle = \sum_f \frac{N_c}{8\pi (m_\chi^2 + m_{\rm MED}^2)^2} \left(m_\chi(|g_s^{(f)}|^2 - |g_p^{(f)}|^2) + m_f(|g_s^{(f)}|^2 + |g_p^{(f)}|^2) \right)^2 . \tag{5.2.14}$$

As shown in Fig.5.5 (a) and (b) for Dirac DM, the constraints are strong enough to exclude all models in the mass window $m_{\chi,\phi} > 1$ GeV. This true for pure scalar couplings but for chiral couplings a small window opens at larger masses. For Majorana DM the model is also totally excluded for purely scalar or pseudo-scalar couplings, Fig.5.5 (c) (as this case is equivalent to Dirac DM), however for chiral couplings (Fig.5.5 (d)) the suppressions of both ID and DD lead to a large allowed region. For heavy quark chiral couplings, there is a region of allowed parameters $m_\chi, m_{\rm MED} > 100$ GeV requiring large couplings, as shown in Fig.5.5 (e), due to the suppression of DD constraints. Any other choice of couplings yields the same conclusion. For non-chiral couplings Majorana DM also reproduces this result; however for chiral couplings, the suppression of ID is much weaker than in the light quark case. In fact the s-wave piece of $\langle \sigma v \rangle$ still dominates and so the allowed RD region is suppressed along with the ID constraint, leading to less available parameter space, as shown in Fig.5.5 (f). These results are summarized in Fig.5.2.

Gamma Ray Lines : When dealing with charged mediators, the $\bar{\chi}\chi \to \gamma\gamma$ process involves the calculation of box diagrams with internal fermions and mediators. The photons may be emitted both fermions and mediators in the loop.
Ignoring the photon emission from the scalar ϕ for the moment, we can calculate the

	EFT operator	$\langle\sigma v\rangle_{\gamma\gamma}$
V-V ($F5$)	$\bar{\chi}\gamma^\mu\chi\bar{f}\gamma_\mu f$	0 (Furry's theorem)
A-V ($F6$)	$\bar{\chi}\gamma^\mu\gamma^5\chi\bar{f}\gamma_\mu f$	0 (Furry's theorem)
V-A ($F7$)	$\bar{\chi}\gamma^\mu\chi\bar{f}\gamma_\mu\gamma^5 f$	0
A-A ($F8$)	$\bar{\chi}\gamma^\mu\gamma^5\chi\bar{f}\gamma_\mu\gamma^5 f$	$\frac{2Q_f^4N_c^2C_{F8}^2\alpha^2 s}{\pi^4}\left(1+\frac{m_f^2}{s}\log(\beta)^2\right)^2$
S-S ($F1$)	$\bar{\chi}\chi\bar{f}f$	$\frac{Q_f^4N_c^2C_{F1}^2\alpha^2m_f^2(s-4m_\chi^2)}{128\pi^4m_\chi^2}\left(4+\left(\frac{4m_f^2}{s}-1\right)\log(\beta)^2\right)^2$
P-S ($F2$)	$\bar{\chi}i\gamma^5\chi\bar{f}f$	$\frac{Q_f^4N_c^2C_{F2}^2\alpha^2m_f^2 s}{128\pi^4m_\chi^2}\left(4+\left(\frac{4m_f^2}{s}-1\right)\log(\beta)^2\right)^2$
S-P ($F3$)	$\bar{\chi}\chi\bar{f}i\gamma^5 f$	$\frac{Q_f^4N_c^2C_{F3}^2\alpha^2m_f^2(4m_\chi^2-s)}{128\pi^4m_\chi^2}\log(\beta)^4$
P-P ($F4$)	$\bar{\chi}i\gamma^5\chi\bar{f}i\gamma^5 f$	$\frac{Q_f^4N_c^2C_{F4}^2\alpha^2m_f^2 s}{128\pi^4m_\chi^2}\log(\beta)^4$

Figure 5.4: The annihilation $\bar{\chi}\chi\to\gamma\gamma$ process for various fermion DM EFT operators coupled to fermions with charge Q_f, note that the Wilson coefficients C have mass dimension -2.

remaining diagrams by simply taking the EFT limit[5] (integrating the mediator out as is done for the DD calculation). Then the $\bar{\chi}\chi\to\gamma\gamma$ process is a triangle diagram with a single insertion of a four-fermion operator (see Fig.3.1). The resulting cross sections are shown in Tab.5.4 where,

$$\beta=\frac{-\sqrt{s}+\sqrt{s+4m_f^2}}{\sqrt{s}+\sqrt{s+4m_f^2}}. \tag{5.2.15}$$

Most of the EFT operators lead to very small or zero cross section. The largest cross section is 'A-A', pure axial vector couplings, but even in this case the bounds are weaker than from annihilation into fermions.

A possible caveat is for the case of Majorana DM, for which the operator $\mathcal{O}_{F8}$ appears unsuppressed in the EFT, and the annihilation into fermions is helicity suppressed in the chiral limit. The gamma ray constraints become more excluding since the helicity suppression applies only to $\bar{f}f$ final states, we incorporate the bounds into Fig.5.5.

[5] See for example [118].

We consider just the axial vector EFT operator, then the cross section is given by the 'A-A' row of Tab.5.4 with,

$$C_{F8}^{(q)} \equiv \frac{\left(|g_s^{(q)}|^2 + |g_p^{(q)}|^2\right)}{2(m_\chi^2 + m_\phi^2)} \,, \tag{5.2.16}$$

the above matching differs from the one used for DD since the latter was derived under the assumption $\epsilon = 2k \cdot p/(m_\chi^2 - m_\phi^2) \ll 1$ with k and p the initial state momentum. In the annihilation process $k \cdot p \approx m_\chi^2$ and thus the EFT for DD is not valid if $m_\chi \gg m_\phi$ (although it remains valid if $m_\phi \gg m_\chi$); instead the EFT should be derived under the assumption that $v \to 0$ as in the expression above.

5.2.4 Charged vector mediator (1/2-V$^\pm$, 1/2*-V$^\pm$)

The charged vector mediator leads to roughly the same DD constraints as with the charged scalar, however the EFT operators pick up extra multiplicative factors $\sim (m_\chi/m_{\rm MED})^n$ from the longitudinal modes of the vector. But since for DM stability $m_\chi < m_{\rm MED}$, these factors tend to have little effect. Then just as with the charged scalars, chiral couplings suppress the $\mathcal{O}_{F1}$ operator, but leave the $\mathcal{O}_{F5}$ which reduces to the dominant $\mathcal{O}_1^{(\rm NR)}$ operator in the NR limit. For Majorana DM $\mathcal{O}_{F5}$ is not present, since $\bar\chi\gamma^\mu\chi = 0$, and chiral couplings lead to the dominant operator $\mathcal{O}_{F8} \propto \mathcal{O}_4^{(\rm NR)} = S_\chi \cdot S_N$ in the NR limit. Thus the Dirac DM can be summarized by:

$$\begin{aligned} C_1^{(N)} &= \frac{4m_N m_\chi}{m_\chi^2 - m_{\rm MED}^2}\left(1 - \frac{m_\chi^2}{4m_{\rm MED}^2}\right)\left[\sum_{q,Q} f_{T_{q,Q}}^{(N)}(|g_v^{(q,Q)}|^2 - |g_a^{(q,Q)}|^2)\frac{m_N}{m_{q,Q}}\right] \\ &\quad + \frac{2m_N m_\chi}{m_\chi^2 - m_{\rm MED}^2}\left(1 + \frac{m_\chi^2}{2m_{\rm MED}^2}\right)\left[\sum_{q,Q} \mathcal{V}_{q,Q}^{(N)}(|g_v^{(q,Q)}|^2 + |g_a^{(q,Q)}|^2)\right], \\ C_4^{(N)} &= \frac{8m_\chi m_N}{(m_\chi^2 - m_{\rm MED}^2)}\left(1 - \frac{m_\chi^2}{2m_{\rm MED}^2}\right)\left[\sum_{q,Q} \Delta_{q,Q}^{(N)}(|g_v^{(q,Q)}|^2 + |g_a^{(q,Q)}|^2)\right]. \end{aligned} \tag{5.2.17}$$

The Majorana case is the same but without the contribution from $\mathcal{V}_q^{(N)}$. In the Dirac DM case, the annihilation cross section $\langle\sigma v\rangle$ is s-wave dominated in both the chiral and non-chiral limits, since just as for DD there is always an operator in the EFT which has a velocity independent NR limit

$$\langle\sigma v\rangle \approx \sum_f \frac{N_c m_\chi^2}{8\pi(m_{\rm MED}^2 + m_\chi^2)^2}\left((|g_a^{(f)}|^2 + |g_v^{(f)}|^2)^2\left(2 + \frac{m_\chi^2}{m_{\rm MED}^2}\right)^2 + 2(|g_v^{(f)}|^2 - |g_a^{(f)}|^2)^2\right). \tag{5.2.18}$$

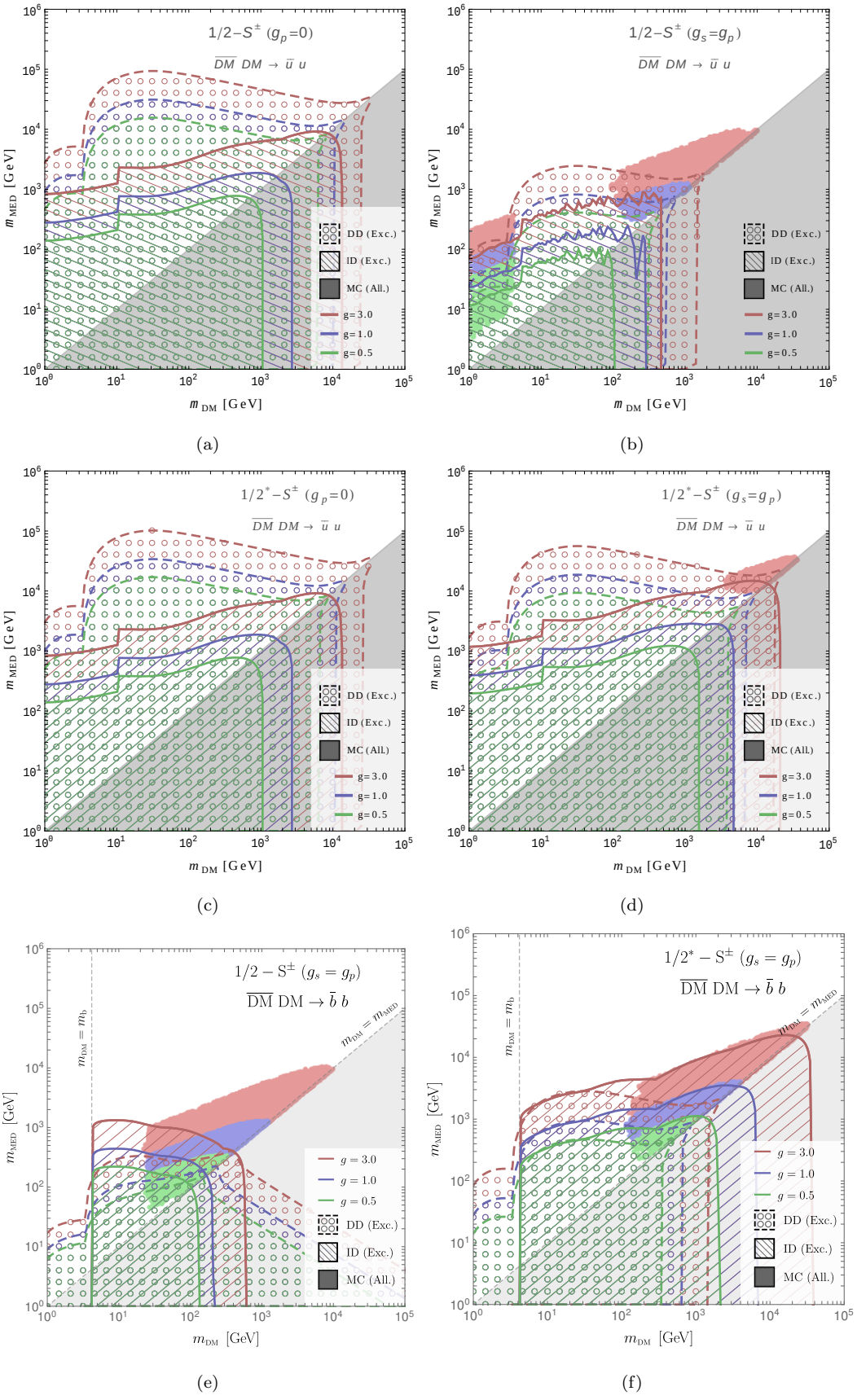

Figure 5.5: As for Fig.5.1 for spin-1/2 DM exchanging a charged scalar mediator, the top (middle) row applies to Dirac (Majorana) DM, to a $\bar{u}u$ final state, and with chiral couplings (right) or scalar couplings (left). The bottom row is for a $\bar{b}b$ final state with chiral couplings for a Dirac (Majorana) DM on the left (right). The grey shaded region for $m_\chi > m_{\rm MED}$ represents unstable DM candidates.

For Majorana DM, chiral couplings lead to an $(m_q/m_{\rm MED})^2$ suppressed s-wave cross section, in which limit the p-wave term is of similar order or larger. This is best explained using the EFT, where the only nonzero operator in the chiral limit, proportional to $(|g_v|^2 + |g_a|^2)$, is $\bar{\chi}\gamma^\mu\gamma^5\chi\bar{q}\gamma_\mu\gamma^5 q$ which allows an s-wave state $L = 0, S = 0$ through the time-like component of the axial-vector DM bilinear. For the state $S = L = 0$, $J = 0$ and hence $J_z = 0$. Assuming the quarks are massless, then chirality and helicity are equivalent. If the outgoing quark and anti-quark travel along the $\pm z$ direction then they cannot be in a $J_z = 0$ state (with their spins in opposite directions, i.e. with equal helicities), since the bilinear only allows the chiralities $\bar{\chi}_L\gamma^\mu\gamma^5\chi_L$, $\bar{\chi}_R\gamma^\mu\gamma^5\chi_R$ (recall that $\bar{\chi}_L$ is a RH state). For massive quarks it is possible to reverse the helicity of one of the particles, at the expense of a factor m_q from a mass insertion into an outgoing fermion leg. The annihilation cross section for Majorana DM is,

$$\begin{aligned}\langle\sigma v\rangle = \sum_f \Bigg[& \frac{N_c}{8\pi m_{\rm MED}^4 (m_\chi^2 + m_{\rm MED}^2)^2} \Bigg(m_\chi^2 (|g_a^{(f)}|^2 - |g_v^{(f)}|^2)^2 (m_\chi^2 + 4m_{\rm MED}^2)^2 \\ & + m_q^2 (|g_a^{(f)}|^2 + |g_v^{(f)}|^2)^2 (2m_{\rm MED}^2 + m_\chi^2)^2 \Bigg) \\ & + \frac{4N_c (|g_v^{(f)}|^2 + |g_a^{(f)}|^2)^2 v^2 m_\chi^2 m_{\rm MED}^2 (m_{\rm MED}^2 + 3m_\chi^2)}{3\pi (m_\chi^2 + m_{\rm MED}^2)^4} \Bigg] ,\end{aligned} \tag{5.2.19}$$

the helicity suppressed s-wave term $\sim (m_q/m_\chi)^2$ is comparable to the p-wave suppression $\sim 2/3\ v^2$ for light quarks; this often leads to a larger p-wave signal in gamma-rays from the GC.

Perturbative Unitarity : The process $q\bar{q} \to \chi\bar{\chi}$, via a t-channel vector exchange, leads to an energy independent unitarity bound,

$$m_V \gtrsim m_\chi \left(\left(\frac{|g_a|}{4\pi} \right)^2 + \left(\frac{|g_v|}{4\pi} \right)^2 \right)^{1/2} \tag{5.2.20}$$

which is redundant when one imposes DM stability which requires $m_V > m_\chi$. However, the process $\chi\bar{\chi} \to V^\dagger V$ leads to violations for energies,

$$E \gtrsim \frac{m_V^2}{m_\chi} \left(\left(\frac{|g_a|}{4\pi} \right)^2 + \left(\frac{|g_v|}{4\pi} \right)^2 \right)^{-1} \tag{5.2.21}$$

which for $g_a = g_v \sim 1$, and $m_V = m_\chi \sim 1$ TeV requires $E \lesssim 1$ TeV. Violations of unitarity would be large at collider energies and the model could become a poor approximation of a complete theory with regard to collider bounds.

Summary : Chiral couplings lead to the suppression of both ID and DD signals if the DM is Majorana and thus is the least excluded scenario, leaving significant free parameter space as shown in Fig.5.6 (d). This emphasises the role that choices of couplings can have on the results, since pure vector (or chiral) couplings to Dirac DM leads to an almost complete exclusion of all thermal DM candidates, as in Fig.5.6 (a) and (b). The allowed regions are summarized in Fig.5.2.

5.3 Scalar Dark Matter

5.3.1 Neutral scalar mediator (0-S, 0*-S)

We begin with the simplest scalar DM model; coupling to a neutral scalar mediator. The DD cross section is fairly simple, matching only the EFT operators $\mathcal{O}_{S1} = \phi\phi\bar{N}N$ and $\mathcal{O}_{S2} = \phi\phi\bar{N}i\gamma^5 N$; the latter is largely suppressed due to a $(q/m_N)^4$ momentum suppression in $\sigma_{\rm DD}$ from $\mathcal{O}_{10}^{(\rm NR)}$. Heavy quarks match to the same operators, with a suppression from loop factors and nuclear constants. Thus the cross section is dominated by the SI scattering from $\mathcal{O}_{S1}$,

$$C_1^{(N)} = \frac{2g_\chi \Lambda m_N}{m_{\rm MED}^2}\left[\sum_{q'=q,Q} f_{T_{q'}}^{(N)} g_s^{(q')} \frac{m_N}{m_{q'}}\right], \tag{5.3.22}$$

$$C_{10}^{(N)} = \frac{2g_\chi \Lambda m_N}{m_{\rm MED}^2}\left[\sum_{q'=q,Q} f_{5,q'}^{(N)} g_p^{(q')} \frac{m_N}{m_{q'}}\right]. \tag{5.3.23}$$

The scale Λ gives the DM-mediator vertex the correct mass dimension; we take $\Lambda = m_\chi$. The DD limits are strong if $g_s^{(q,Q)}$ is present, but much weaker if only $g_p^{(q,Q)}$ is present.

For ID, the dominant s-wave term in $\langle\sigma v\rangle$ is proportional to $g_s^2 + g_p^2$, and thus there is no choice of couplings which weakens the ID constraint. The appearance of an s-wave term is trivial from the initial state ϕ^2 or $\phi^\dagger\phi$ since both are $\mathbf{1}$ in the NR

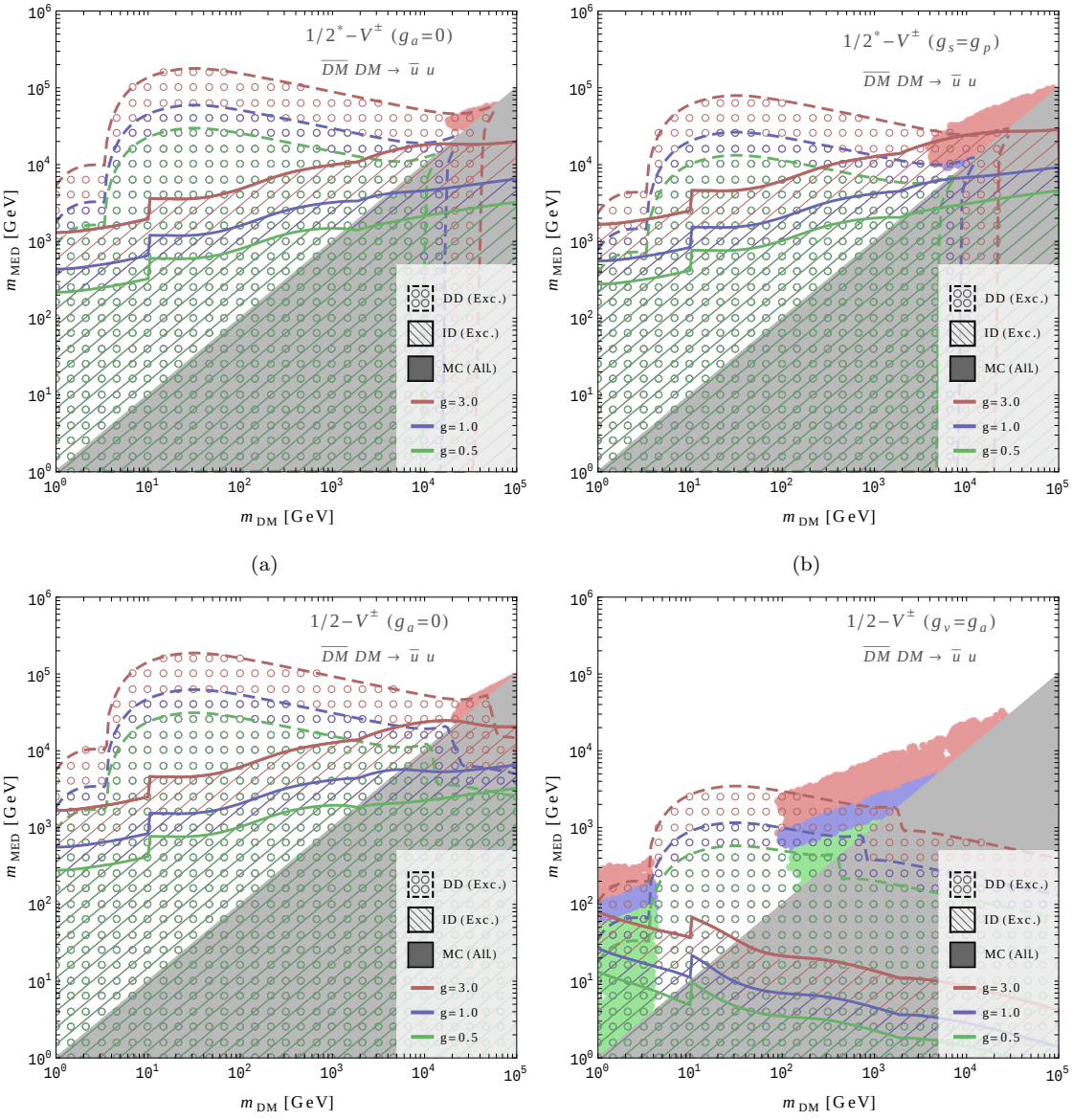

Figure 5.6: As for Fig.5.1 for a spin-1/2 Dirac (top row) or Majorana DM (bottom row) candidate exchanging a charged vector mediator with a pair of SM fermions, $\bar{u}u$, the left (right) column is for vector (chiral) couplings. The grey shaded region for $m_\chi > m_{\rm MED}$ represents unstable DM candidates which decay

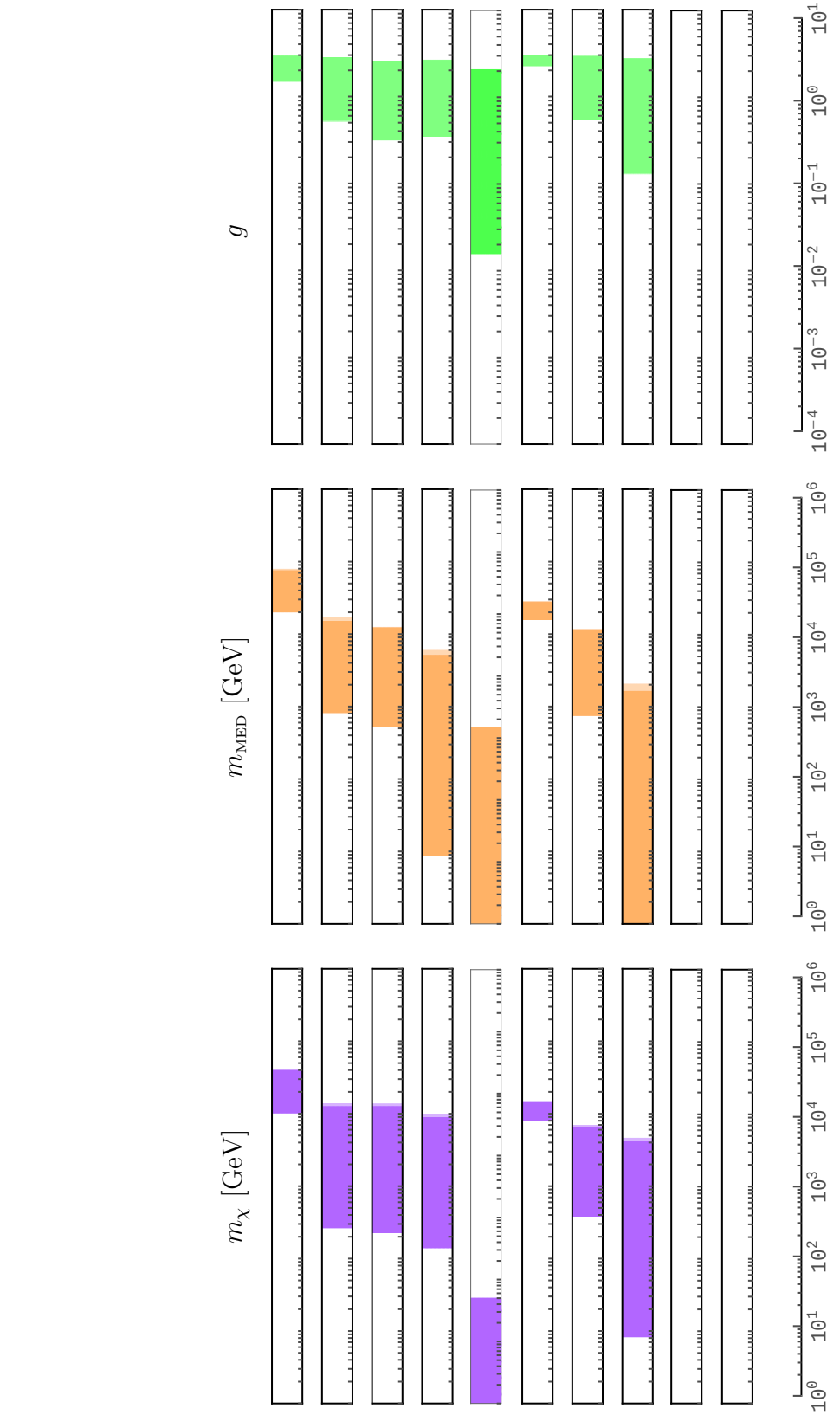

Table 5.4: As for Fig.5.2, but for spin-0 DM models with both $\bar{u}u$ and $\bar{b}b$ couplings.

	EFT operator	$\langle\sigma v\rangle_{\gamma\gamma}$
S1	$\phi^\dagger\phi\bar{f}f$	$\frac{Q_f^2 N_c^2 \alpha^2 C_{S1}^2 m_f^2}{16\pi^4 m_\chi^2}\left[2+(4m_f^2-S)C_0\right]^2$
S2	$\phi^\dagger\phi\bar{f}i\gamma^5 f$	$\frac{Q_f^2 N_c^2 \alpha^2 C_{S2}^2 m_f^2 S^2}{16\pi^4 m_\chi^2}\left[C_0\right]^2$
S3	$i\mathrm{Im}(\phi^\dagger\partial^\mu\phi)\bar{f}\gamma_\mu f$	0 (Furry's theorem)
S4	$i\mathrm{Im}(\phi^\dagger\partial^\mu\phi)\bar{f}\gamma_\mu\gamma^5 f$	$\mathcal{O}(v^2)$

Figure 5.7: The annihilation $\bar{\chi}\chi \to \gamma\gamma$ process for scalar DM EFT operators coupled to fermions with charge Q_f and coupling C_i. The loop factor $C_0 \equiv C_0(0,0,S,m_f,m_f,m_f)$ is given by $C_0 = (1/2S)\log(\beta)^2$ and β defined in Eq.(5.2.15).

limit,

$$\langle\sigma v\rangle = \sum_f \left[\frac{N_c\Lambda^2 g_\chi^2\left(g_s^{(f),2}+g_p^{(f),2}\right)}{4\pi(m_{\rm MED}^2-4m_\chi^2)^2}\right] + \theta(m_\chi - m_{\rm MED})\frac{g_\chi^4\sqrt{m_\chi^2-m_{\rm MED}^2}}{16\pi m_\chi^3(m_{\rm MED}^2-2m_\chi^2)^2}, \tag{5.3.24}$$

the second term arises from DM annihilation to mediator pairs, only affecting the RD bounds, and only slightly increasing the cross section for $m_\chi > m_{\rm MED}$. Gamma-ray line signals are fermion mass suppressed (see Fig.5.7) and subdominant to the tree level ID constraints.

We do not include any collider constraints for this model[6]. Overall, for scalar couplings to light quarks the DD constraint is the dominant source of exclusion above $m_\chi = 1$ GeV, excluding almost all thermal candidates, as shown in Fig.5.8(a). Weakening the DD constraints by around one order of magnitude by setting $g_s = 0$ allows candidates with large couplings $g \gtrsim 0.1$ and large masses $m_\chi, m_{\rm MED} \gtrsim 500$ GeV, Fig.5.8(b). Couplings to heavy quarks lead to a larger allowed region, since the contribution to $C_1^{(N)}$ is suppressed by $\sim 10^{-3}$, and the contribution to $C_{10}^{(N)}$ by

[6]Extracting LHC bounds is difficult for a purely $\bar{u}u$ coupling to DM, since it is usually assumed that DM couples in a flavour diagonal way. Conventionally $\Lambda = m_q$ in analogy to Higgs couplings, then the Wilson coefficients of the relevant EFT operators ($\mathcal{O}_{S1,S2}$) are $\propto m_q/m_\phi^2$ and thus dominated by heavy quarks.

$\sim 10^{-5}$. This leaves the DD constraints very weak (they still exclude small mediator masses), and the ID constraints dominant, excluding small DM masses together with small couplings. This leads to the allowed region favouring both large masses and couplings as shown in Fig.5.8 (c) and (d). These exclusions are summarized in Tab.5.4

5.3.2 Neutral vector mediator (0*-V)

The DD cross section is simple for t-channel scattering via a neutral vector mediator, leading to only the $\mathcal{O}_{S3} = i\text{Im}(\phi^\dagger\partial^\mu\phi)\bar{q}\gamma_\mu q$ and $\mathcal{O}_{S4} = i\text{Im}(\phi^\dagger\partial^\mu\phi)\bar{q}\gamma_\mu\gamma^5 q$ operators; $\mathcal{O}_{S3}$ (from vector quark couplings) leads to the dominant contribution from the SI operator $\mathcal{O}_1^{(\text{NR})}$, and $\mathcal{O}_{S4}$ (from axial-vector quark couplings) leads to $\mathcal{O}_7^{(\text{NR})}$ which is velocity suppressed $\sim v^2$. Thus a large suppression occurs if the couplings are purely axial-vector to the quarks. The Wilson coefficients are:

$$C_1^{(N)} = 4g_\chi \frac{m_\chi m_N}{m_{\text{MED}}^2}\left[\sum_{q'=q,Q} \mathcal{V}_{q'}^{(N)} g_v^{(q')}\right], \tag{5.3.25}$$

$$C_7^{(N)} = 8g_\chi \frac{m_\chi m_N}{m_{\text{MED}}^2}\left[\sum_{q'=q,Q} \Delta_{q'}^{(N)} g_a^{(q')}\right]. \tag{5.3.26}$$

For heavy quarks, the vector current $\propto g_v^{(Q)}$ does not contribute through threshold matching (as already mentioned in Sec.5.2.2), instead it contributes via RG mixing with the light quark vector currents, resulting in an overall suppression of the latter by $\mathcal{V}_Q^{(N)}$. The heavy quark axial-vector current does however contribute due to both a threshold matching and subsequent RG mixing (the latter is the dominant effect, see Sec.4.3.1), picking up a further suppression at the NR level.

For ID, the cross section is purely p-wave. The leading term in $\langle\sigma v\rangle$ is proportional to $(g_v^2 + g_a^2)$ and is thus consistently weak for all values of the couplings,

$$\begin{aligned}\langle\sigma v\rangle = &\sum_f \frac{g_\chi^2 N_c m_\chi^2 v^2}{6\pi(m_{\text{MED}}^2 - 4m_\chi^2)^2}\left(g_a^{(f),2} + g_v^{(f),2}\right) \\ &+ \theta(m_\chi - m_{\text{MED}})\frac{g_\chi^4 m_\chi (m_\chi^2 - m_{\text{MED}}^2)^{5/2}}{\pi m_{\text{MED}}^4 (m_{\text{MED}}^2 - 2m_\chi^2)^2},\end{aligned} \tag{5.3.27}$$

this is due to the initial state bilinear $i\text{Im}(\phi^\dagger\partial^i\phi)$ which is odd under parity $\partial^i \to -\partial^i$ and therefore since $\mathcal{P} = (-1)^L$, L cannot be zero (the timelike piece of the bilinear

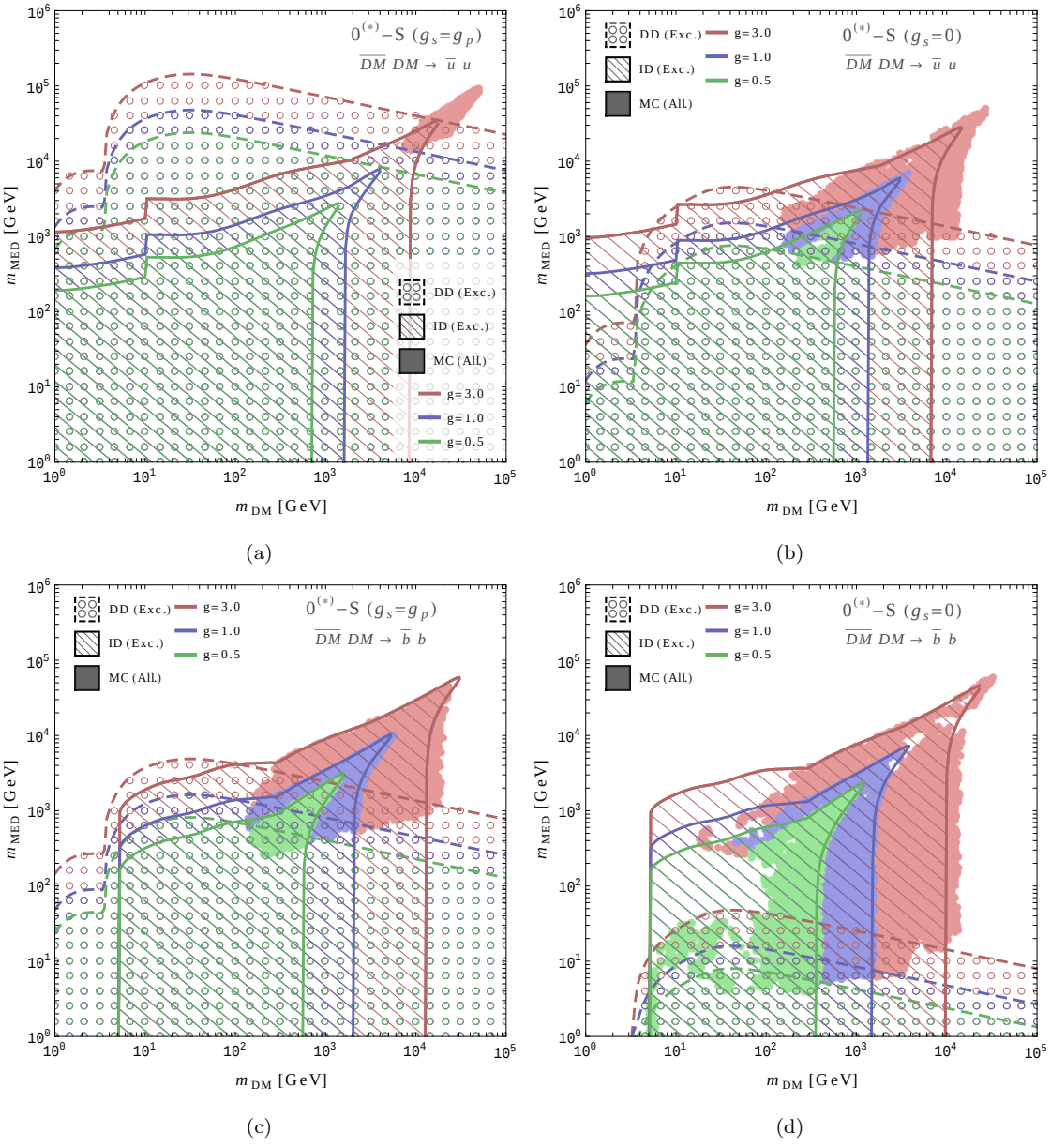

Figure 5.8: As for Fig.5.1 for a spin-0 DM candidate exchanging a neutral scalar mediator with a pair of SM fermions, $\bar{u}u$ (top row) or $\bar{b}b$ (bottom row). The left (right) columns are for chiral (pseudo-scalar) couplings.

vanishes, since its $(\mathcal{C}, \mathcal{P})$ symmetries are $(-,+)$ which forbids a $J = 0$ state, which is inconsistent with the requirement that the operator is a scalar under rotations).

The second term in Eq.(5.3.27) only applies to the relic density calculation, and is the contribution from annihilation into mediator pairs when $m_\chi > m_{\rm MED}$; since a DM is exchanged in the t-channel, the initial state operator is not the same as annihilation to fermion pairs and does not suffer the p-wave suppression. The annihilation rate is huge, due to the longitudinal polarization of the vector, which scales as $\sqrt{S}/m_{\rm MED} \sim m_\chi/m_{\rm MED}$. The cross section goes as $\sigma \sim (1/m_\chi^2)(m_\chi/m_{\rm MED})^4$ and thus increases with m_χ. This makes virtually the entire region $m_\chi > m_{\rm MED}$ 'super-allowed', but forces the couplings to be extremely small to suppress the large annihilation to mediators.

Perturbative Unitarity : Due to the presence of a neutral vector particle, unitarity violation can occur when the vector is exchanged in the s-channel as a consequence of the longitudinal polarization modes. If the vector couples to $\bar{q}\gamma^\mu\gamma^5 q$ then the bounds from $q\bar{q} \to q\bar{q}$ become independent of the energy scale (and are identical to Eq.(5.2.9)). The DM self scattering $\chi^\dagger\chi \to \chi^\dagger\chi$ leads to a bound $g_\chi \lesssim \sqrt{4\pi}$ (which is automatically included by our restriction of all couplings to $g < 3$), and the process $\chi^\dagger\chi \to VV$ leads to a limit on the energy of,

$$E \gtrsim \frac{1}{5} m_V \left(\frac{g_\chi}{4\pi}\right)^{-1}, \tag{5.3.28}$$

which for $g_\chi = 1$ and $m_V \sim 1$ TeV leaves $E \gtrsim 2.5$ TeV and thus the collider signals would be sensitive to any new physics which corrects the unitarity violation, unless the coupling $g_\chi \lesssim 0.25$.

LHC bounds : Bounds for operators $\mathcal{O}_{S3,S4}$ exist in the literature [283] for mono-jet and mono-photon signatures, assuming flavour diagonal coupling and so include couplings to all quark flavours. However, due to the high momentum transfers involved, the pdfs for the quarks in the proton are dominated by the light quarks (and unlike for the neutral scalar mediator, the EFT limit is not suppressed $\propto m_q^2$); thus these bounds are applicable to the light quark final state and are plotted in

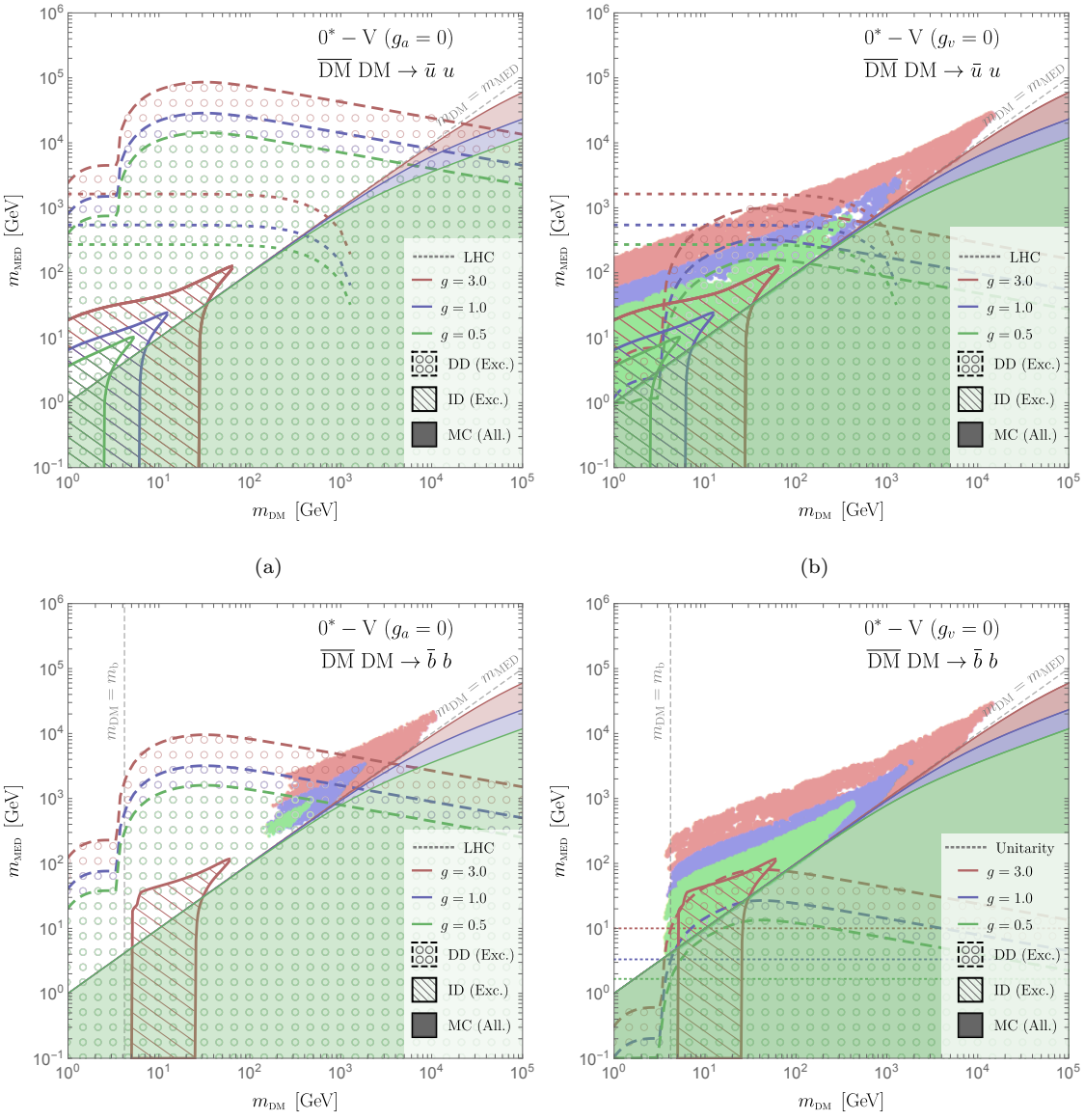

Figure 5.9: As for Fig.5.1 for a spin-0 DM candidate exchanging a neutral vector mediator with a pair of SM fermions, $\bar{u}u$ (top row) or $\bar{b}b$ (bottom row). The left (right) columns are for vector (axial-vector) couplings, and in the bottom row the exclusions from ID for couplings of 1.0 and 0.5 are too weak to be shown.

Fig.5.9. However, since the EFT approximation is made the bounds are not reliable for $m_\phi \lesssim m_\chi$, and they are not included in the MCMC. These bounds are likely to rule out a lot of additional parameter space for purely axial vector couplings (Fig.5.9 (b)).

Gamma-ray lines : The tree level annihilation into fermion final states $\langle \sigma v \rangle_{\bar{f}f}$ is p-wave suppressed by $\sim 10^{-5}$, which is a smaller than a generic loop suppression ($1/(16\pi^2)$ [7]). One might then be tempted to invoke gamma ray line constraints from the one-loop processes $\phi^\dagger\phi \to \gamma\gamma, \gamma h, \gamma Z$. These involve the same s-channel annihilation of the DM into a virtual mediator as for tree level; the DM-Mediator vertex leads to the factor $(p - p')^\mu \sim (0, 2m_\chi \mathrm{v})$ (with p, p' the incoming momenta of the DM pair). Thus the gamma ray line processes are also velocity suppressed (or zero if only g_v is present due to Furry's theorem).

Fig.5.9 gives a summary of these results. For light quarks, with a vector coupling, g_v, the DD bounds are strong enough to rule out the model (Fig.5.9 (a)) for $m_\chi < m_{\mathrm{MED}}$. Replacing the vector with an axial vector causes a suppression of DD, and the parameter space opens up (Fig.5.9 (b)), it is still likely that collider constraints can rule out the range $m_{\mathrm{DM}} \gtrsim \mathcal{O}(100)$ GeV. For heavy quarks and axial-vector mediator both ID and DD are suppressed (5.9 (c), (d)).

5.3.3 Charged fermion mediator (0-F$^\pm$, 0*-F$^\pm$)

This case was first proposed as a theory of light dark matter in the non-chiral case, since the annihilation cross section is independent of the DM mass in the low m_χ limit [96]. The caveat mentioned in Sec.5.2.3 applies, with strict collider constraints forcing the charged mediator to $m_{\mathrm{MED}} > 100$ GeV. With our assumptions on the mediator width, this model is entirely excluded for light and heavy quark (c, b) states by ID and DD signals alone.

[7] Or more accurately $\alpha/(16\pi^2) \sim 5 \times 10^{-5}$.

After integrating out the mediator the dominant EFT operator is $\mathcal{O}_{S1}$, with the same Wilson coefficient for both real and complex DM;

$$C_1^{(N)} = \frac{2m_N^2}{m_\chi^2 - m_{\text{MED}}^2} \sum_{q'=q,Q} f_{T_{q'}}^{(N)} \left(\left(|g_s^{(q')}|^2 + |g_p^{(q')}|^2 \right) + \frac{m_{\text{MED}}}{m_{q'}} \left(|g_s^{(q')}|^2 - |g_p^{(q')}|^2 \right) \right) \tag{5.3.29}$$

For chiral couplings $g_s = \pm i g_p$ the cross section is suppressed by $\approx (m_q/m_{\text{MED}})^2$. For complex scalar DM, an additional contribution from the EFT operator $\mathcal{O}_{S3}$ is present which does not become suppressed in the chiral limit and which contributes;

$$C_1^{(N)} = \frac{2m_N m_\chi}{(m_\chi^2 - m_{\text{MED}}^2)} \left(\sum_{q'=q,Q} \mathcal{V}_{q'}^{(N)} \left(|g_s^{(q')}|^2 + |g_p^{(q')}|^2 \right) \right), \tag{5.3.30}$$

which is $\sim m_N/m_\chi$ times the contribution from $\mathcal{O}_{S1}$ in the chiral limit. It is thus not possible to remove the contribution to $\mathcal{O}_1^{(\text{NR})}$ entirely, but it can be suppressed by choosing chiral couplings.

For ID, and real or complex scalar DM, the dominant s-wave contribution to $\langle \sigma v \rangle$ is suppressed by $(m_f/m_{\text{MED}})^2$ for chiral couplings $g_s = \pm i g_p$, but still remains dominant over the p-wave term. The s-wave term arises purely from the $\phi^\dagger \phi \bar{q} q$ operator;

$$\langle \sigma v \rangle = \frac{N_c}{4\pi (m_{\text{MED}}^2 + m_\chi^2)^2} \sum_f \left| (g_p^{(f)})^2 (m_{\text{MED}} - m_f) + (g_s^{(f)})^2 (m_f + m_{\text{MED}}) \right|^2. \tag{5.3.31}$$

If the couplings are not chiral, then the cross section scales as $m_{\text{MED}}^2/(m_\chi^2 + m_{\text{MED}}^2)^2$ the powers of mediator mass in the numerator weaken the overall dependence on m_{MED} as $m_{\text{MED}} \gg m_\chi$. This has the effect of improving the constraints at low DM mass. It simultaneously favours much heavier mediators for the correct RD. This same behaviour is replicated for DD, and we are able to exclude extraordinarily large mediator masses ($m_{\text{MED}} < 10^8$ GeV), although no thermal DM candidate would be found with such a heavy mediator. Fig.5.10 (a) and (c) shows the configuration ($g_s \neq 0$) for $\bar{u}u$ (equivalent to $\bar{d}d$ and $\bar{s}s$) and $\bar{b}b$ final states respectively. Fig.5.10 (b) and (d) is the same but with chiral couplings ($g_s = \pm i g_p$). These are plotted for

complex scalar DM, but real scalar DM leads to very similar plots as the dominant terms in the ID and DD cross section are the same. Thermal candidates are still ruled out even with chiral couplings, since the RD and ID constraints are suppressed because $\langle\sigma v\rangle$ is still s-wave dominated. Thus, surviving light DM candidates of [96] must be of non-thermal origin.

5.4 Vector Dark Matter

5.4.1 Neutral scalar mediator (1-S, 1*-S)

The neutral scalar mediator leads to an s-channel annihilation and u-channel scattering. The EFT matching for the model leads only to the 'scalar' and 'pseudo-scalar' operators $\mathcal{O}_{V1,V2}$ ($B^\mu B^\dagger_\mu \bar{q} q$ and $B^\mu B^\dagger_\mu \bar{q} i\gamma^5 q$ respectively). The former dominates as it leads to $\mathcal{O}_1^{(\mathrm{NR})}$, which produces the dominant coherent spin-independent interaction. For heavy quarks, threshold matching (integrating out the Q) generates $B^\mu B_\mu G^{\mu\nu} G_{\mu\nu}$ if $g_{q,s}$ is present, which produces a contribution to $\mathcal{O}_1^{(\mathrm{NR})}$ and dominates the scattering,

$$C_1^{(N)} = \frac{g_\chi \Lambda m_N}{m_{\mathrm{MED}}^2}\left[\sum_{q'=q,Q} f_{T_{q'}}^{(N)} g_s^{(q')} \frac{m_N}{m_{q'}}\right], \tag{5.4.32}$$

where Λ is a mass scale associated to the DM-mediator coupling and we take $\Lambda = m_\chi$. If only the pseudo-scalar quark coupling is present then the matching is heavily suppressed to $\mathcal{O}_{10}^{(\mathrm{NR})}$,

$$C_{10}^{(N)} = \frac{g_\chi \Lambda m_N}{m_{\mathrm{MED}}^2}\left[\sum_{q'=q,Q} f_{5,q'}^{(N)} g_p^{(q')} \frac{m_N}{m_{q'}}\right], \tag{5.4.33}$$

the suppression arises because the pseudo-scalar bilinear is a scalar with respect to rotations, and with odd parity, thus in the NR limit it can only contain dot-products involving a single spin-vector (i.e. $\mathrm{p}\cdot S_\chi$ or $\mathrm{p}'\cdot S_\chi$ with p, p' the incoming/outgoing DM momentum), both of which contain a suppression. This is equally true for both real and complex vector DM.

The ID cross section is s-wave, and the dominant piece is proportional to $(g_s^2+g_p^2)$, thus it remains of uniform strength for any choice of couplings. This is because the

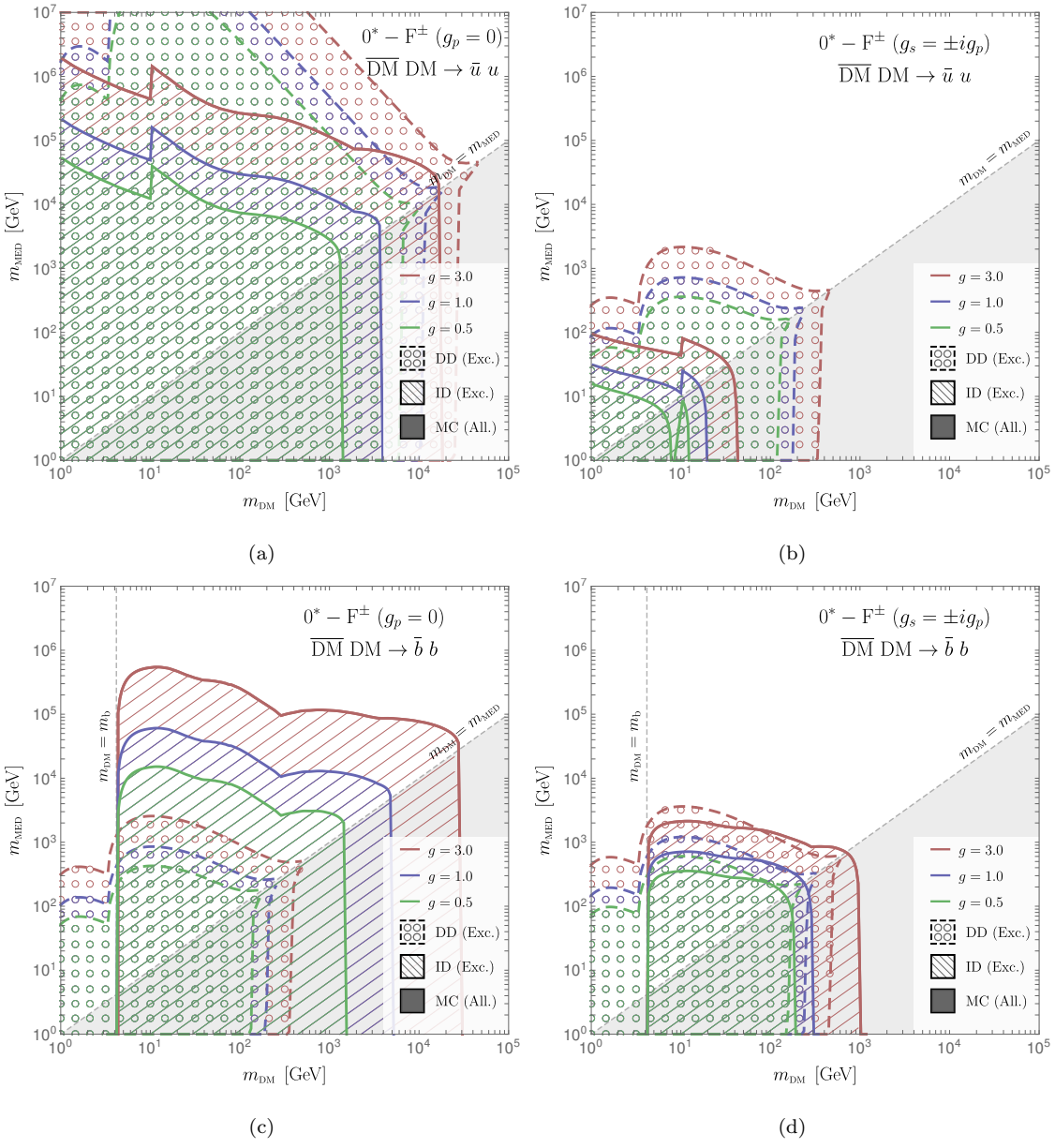

Figure 5.10: As for Fig.5.1 for a spin-0 DM candidate exchanging a charged fermionic mediator with a pair of SM fermions, $\bar{u}u$ (top row) or $\bar{b}b$ (bottom row). The left (right) columns are for scalar (chiral) couplings.

Table 5.5: As for Fig.5.2, but for spin-1 DM models with both $\bar{u}u$ and $\bar{b}b$ couplings.

bilinear $B^\mu B_\mu$ appears in the initial state, which is even under charge and parity, and so allows an $S = 0, L = 0$ s-wave state with $J = 0$. The final state $\bar{q}q$ and $\bar{q}\gamma^5 q$ also have $J = 0$ and can couple to the initial state,

$$\langle \sigma v \rangle = \sum_f \frac{N_c g_\chi^2 \Lambda^2}{12\pi (m_{\rm MED}^2 - 4m_\chi^2)^2} \left(g_s^{(f),2} + g_p^{(f),2} \right) + \theta(m_\chi - m_{\rm MED}) \frac{g_\chi^4 (m_{\rm MED}^4 - 4m_{\rm MED}^2 m_\chi^2 + 6m_\chi^4)\sqrt{m_\chi^2 - m_{\rm MED}^2}}{144\pi m_\chi^7 (m_{\rm MED}^2 - 2m_\chi^2)^2}, \quad (5.4.34)$$

the annihilation to mediators in the second line provides a small correction to the RD calculation. Gamma-ray cross sections are fermion mass suppressed (Fig.5.11) for this model and do not provide significant constraints.

Finally we add the collider constraints from [12], based on the $\sqrt{s} = 8$ TeV LHC run, and for DM couplings to light quarks (shown as dotted lines in the plots). The bounds are based on the same EFT operators that appear in the DD treatment (Sec.4.2.3) and are extremely strong below $m_\chi \lesssim 1$ TeV, outperforming both ID and DD limits (which nonetheless have already ruled out models with the correct relic density), but decrease sharply with increasing DM mass and quickly drop below the DD and ID limits. Additionally, the bounds stop at the point at which the EFT approximation is no longer valid ~ 1 TeV. We do not include the bounds in the MCMC, however it is clear that some of the parameter space would be ruled out by them.

Perturbative Unitarity : The dominant violations of unitarity arise from the processes $\chi\chi \to \chi\chi$ and $SS \to \chi^\dagger\chi$ and appear for energies exceeding,

$$E \gtrsim \frac{m_\chi}{10} \left(\frac{g_\chi}{4\pi} \right)^{-1} \quad (5.4.35)$$

for a 100 GeV DM, $g_\chi \lesssim 0.01$ to avoid unitarity violations at LHC energies. These violations must be corrected before a reliable comparison to collider bounds can be made.

Fig.5.12 shows the constraints for light and heavy quark channels. From these it is clear that if the scalar coupling $g_s^{(q)}$ is present, then light quark final states

	EFT operator	$\langle\sigma v\rangle_{\gamma\gamma}$
V1	$B^\dagger_\mu B^\mu \bar{f} f$	$\frac{Q_f^2 N_c^2 \alpha^2 C_{V1}^2 m_f^2}{144\pi^4 m_\chi^2}\left(12 - 4\frac{S}{m_\chi^2} + \frac{S^2}{m_\chi^4}\right)\left[-2 + (S-4m_f^2)C_0\right]^2$
V2	$B^\dagger_\mu B^\mu \bar{f} i\gamma^5 f$	$\frac{Q_f^2 N_c^2 \alpha^2 C_{V2}^2 m_f^2}{144\pi^4 m_\chi^2}\left(12 - 4\frac{S}{m_\chi^2} + \frac{S^2}{m_\chi^4}\right)\lvert C_0\rvert^2$
V4	$\mathrm{Re}(B^\dagger_\nu \partial_\nu B^\mu)\bar{f}\gamma_\mu\gamma^5 f$	$\frac{Q_f^2 N_c^2 \alpha^2 C_{V4}^2 S^2 (S-4m_\chi^2)^2}{144\pi^4 m_\chi^6}\left[1 + 2m_f^2 C_0\right]^2$
V6	$\mathrm{Re}(B^\dagger_\nu \partial_\mu B^\nu)\bar{f}\gamma_\mu\gamma^5 f$	$\frac{Q_f^2 N_c^2 \alpha^2 C_{V6}^2 S^2}{144\pi^4 m_\chi^2}\left(12 - 4\frac{S}{m_\chi^2} + \frac{S^2}{m_\chi^4}\right)\left[1 + 2m_f^2 C_0\right]^2$

Figure 5.11: The annihilation $\bar{\chi}\chi \to \gamma\gamma$ process for various vector DM EFT operators coupled to fermions with charge Q_f and coupling C_i, note that C_i has mass dimension -2. Operators which are velocity suppressed or zero are not listed, and neither are the interference terms. The loop factor C_0 is identical to the one in Tab.5.7.

are completely excluded (Fig.5.12 (a)), and heavy quark final states are constrained to high masses and couplings (Fig.5.12 (b)). Removing g_s leaves the pseudo scalar coupling, suppressing the constraints and opening up the parameter space (Fig.5.12 (c,d). These results are summarized in Tab.5.5.

5.4.2 Neutral vector mediator (1-V, 1*-V)

Due to the Lorentz indices on both mediator and DM, there are three independent renormalizable coupling structures, which we denote $\mathcal{V}_{1,2,3}$, where two vectors B^μ are the DM, and the third is the mediator V^μ,

$$\mathcal{V}_1 = (g_\chi B^\dagger_\nu \partial^\nu B^\mu + \text{h.c.})V_\mu, \tag{5.4.36}$$

$$\mathcal{V}_2 = (g_\chi B^\dagger_\nu \partial^\mu B^\nu + \text{h.c.})V_\mu, \tag{5.4.37}$$

$$\mathcal{V}_3 = \epsilon^{\mu\nu\sigma\rho}(g_\chi B^\dagger_\mu \partial_\nu B_\sigma + \text{h.c.})V_\rho. \tag{5.4.38}$$

In each case the coupling g_χ may be complex. $\mathcal{V}_2$ with a real coupling results in a total derivative plus the operator $B^\mu B_\mu \partial^\nu \bar{q}\gamma_\nu\gamma^5 q$ in the EFT limit, which has an s-wave annihilation cross section, proportional to only g_a (in fact, g_v is totally absent from the cross section due to a cancellation at the amplitude level). If any of the couplings are purely imaginary, then the DM must be complex.

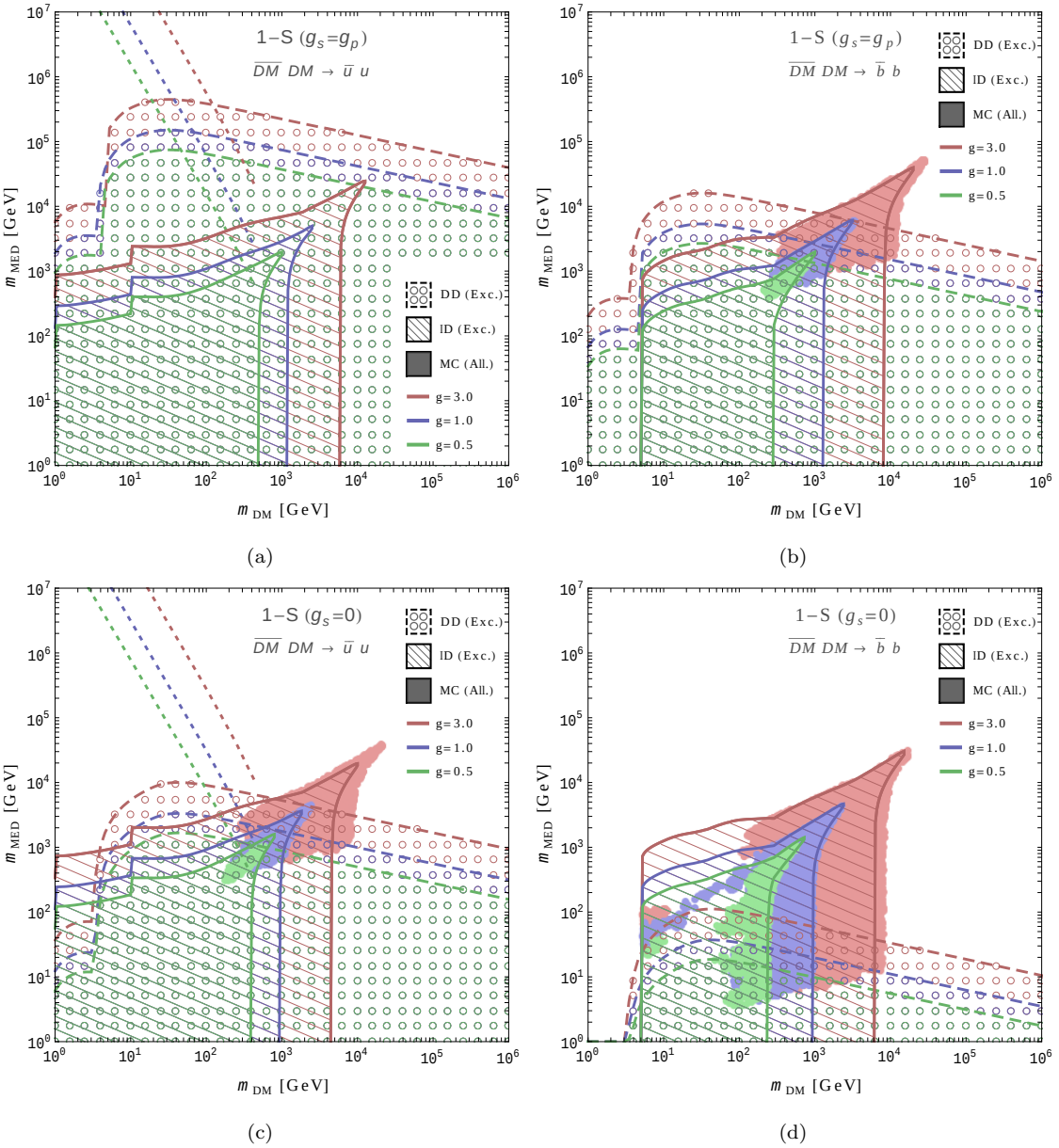

Figure 5.12: As for Fig.5.1 for a spin-1 DM candidate exchanging a neutral scalar mediator with a pair of SM fermions, $\bar{u}u$ (left column) or $\bar{b}b$ (right column). The top (bottom) rows are for chiral (pseudo-scalar) couplings. The dotted lines are LHC bounds from [12], see text. Although the MCMC and ID limits are not valid below the mass threshold m_b, the DD constraints are since they are based on loop induced processes.

Each of the three vertex structures leads to a different DD cross section. Firstly for $\mathcal{V}_1$; a real DM coupling with either a vector or axial-vector quark coupling leads to a very suppressed cross section ($\mathcal{O}_{14}^{(\mathrm{NR})}$ and $\mathcal{O}_{12}^{(\mathrm{NR})}$ respectively). An imaginary g_χ with a vector quark coupling g_v gives a dominant contribution to $\mathcal{O}_5^{(\mathrm{NR})}$ (plus a q^2 suppressed contribution to $\mathcal{O}_4^{(\mathrm{NR})}$), and with an axial-vector coupling to $\mathcal{O}_9^{(\mathrm{NR})}$.

For $\mathcal{V}_2$, if the couplings are real, then there is a non-zero DD cross section only if the quark coupling is axial-vector like, and then it is suppressed to $\mathcal{O}_{10}^{(\mathrm{NR})}$. However for imaginary couplings a vector quark coupling leads to a dominant $\mathcal{O}_1^{(\mathrm{NR})}$ interaction (or $\mathcal{O}_7^{(\mathrm{NR})}$ for axial-vector, which is strongly suppressed).

For $\mathcal{V}_3$, real couplings lead to $\mathcal{O}_{11,14}^{(\mathrm{NR})}$ for vector and axial-vector couplings respectively. Imaginary DM couplings and vector quark coupling lead to $4m_\chi m_N(\mathcal{O}_9^{(\mathrm{NR})} + \mathcal{O}_8^{(\mathrm{NR})})$, which is dominated by $\mathcal{O}_8^{(\mathrm{NR})}$. Imaginary DM couplings with axial-vector quark couplings lead to $\mathcal{O}_{4,5}^{(\mathrm{NR})}$, but dominated by $\mathcal{O}_4^{(\mathrm{NR})}$.

Thus there is a large variety of cross section for models containing a triple vector coupling, and in each there can be large differences depending on choices of couplings. This is summarized in Tab.5.6 for light quarks. For heavy quark couplings g_v, the RG mixing between the EFT operator and the equivalent ones for light-quarks leads to a sizeable contribution. Heavy quark g_a couplings lead to a suppressed scattering according to Eq.(4.3.62). The Wilson coefficients can be found from the tables in Sec.4.2.3.

For ID, the vertex $\mathcal{V}_1$ leads to the same annihilation cross section in the low velocity limit for real or imaginary couplings, which is always p-wave, despite the fact that $B^\nu \partial_\nu B^0$ can couple to an $L = 0, S = 0$ state, because $B^0 \to 0$ in the NR

limit,

$$\langle\sigma v\rangle_{\mathcal{V}_1} \approx \sum_f \frac{m_\chi^2(\mathrm{Re}(g_\chi)^2+2\mathrm{Im}(g_\chi)^2)N_c v^2}{27\pi(m_{\rm MED}^2-4m_\chi^2)^2}\left(g_v^{(f),2}+g_a^{(f),2}\right) + \theta(m_\chi-m_{\rm MED})\frac{(3\mathrm{Re}(g_\chi)^2+\mathrm{Im}(g_\chi)^2)^2\sqrt{m_\chi^2-m_{\rm MED}^2}m_\chi^5}{4\pi m_{\rm MED}^4(m_{\rm MED}^2-2m_\chi^2)^2}. \quad (5.4.39)$$

$\mathcal{V}_2$ allows imaginary couplings, and in the low velocity limits reproduces the result for $\mathcal{V}_1$, since $B^\mu\partial^0 B_\mu$ couples to no (L,S) states and $\mathrm{Im}(B^\mu\partial^i B_\mu)$ picks up a velocity dependence from the derivative. As mentioned, $\mathcal{V}_2$ with real couplings couples to only the axial-vector quark bilinear but leads to an m_f^2 suppressed s-wave cross section,

$$\langle\sigma v\rangle_{\mathcal{V}_2} \approx \sum_f \left[\mathrm{Re}(g_\chi)^2 g_a^{(f),2}N_c\frac{m_f^2}{6\pi m_\phi^4}+\frac{\mathrm{Im}(g_\chi)^2N_c v^2 m_\chi^2}{9\pi(m_{\rm MED}^2-4m_\chi^2)^2}\left(g_v^{(f),2}+g_a^{(f),2}\right)\right] + \theta(m_\chi-m_{\rm MED})\frac{6\mathrm{Im}(g_\chi)^4(m_\chi^2-m_{\rm MED}^2)^{5/2}m_\chi}{\pi m_{\rm MED}^4(m_{\rm MED}^2-2m_\chi^2)^2}. \quad (5.4.40)$$

The vertex structure $\mathcal{V}_3$ also allows an unsuppressed s-wave piece proportional to g_v^2 or g_a^2 if the DM coupling is imaginary, i.e. $\mathrm{Im}(\epsilon^{\mu\nu\sigma\rho}B_\mu^\dagger\partial_\nu B_\sigma)$. Consider the 3-vector component $\mathrm{Im}(\epsilon^{i0jk}B_i^\dagger\partial_0 B_j)$ which due to its charge and parity (-,+) it permits the $L=0, S=1$ state. This $J=1$ initial state can couple to the $J=1$ final state three vectors $\bar{q}\gamma^i q$, $\bar{q}\gamma^i\gamma^5 q$ and leads to,

$$\langle\sigma v\rangle_{\mathcal{V}_3} \approx \sum_f \left[\frac{2N_c m_\chi^2\mathrm{Im}(g_\chi)^2}{3\pi(m_{\rm MED}^2-4m_\chi^2)^2}\left(g_v^{(f),2}+g_a^{(f),2}\right)+\frac{\mathrm{Re}(g_\chi)^2 g_a^{(f),2}N_c v^2 m_f^2}{3\pi m_\phi^4}\right] + \theta(m_\chi-m_{\rm MED})\left[\frac{\mathrm{Re}(g_\chi)^4 m_\chi^2}{2\pi m_{\rm MED}^4}+\frac{\mathrm{Re}(g_\chi)^2\mathrm{Im}(g_\chi)^2}{16m_{\rm MED}^2}+\frac{29\mathrm{Im}(g_\chi)^4}{128m_\chi^2}\right]. \quad (5.4.41)$$

Real couplings in $\mathcal{V}_3$, $\mathrm{Re}(\epsilon^{\mu\nu\sigma\rho}B_\mu^\dagger\partial_\nu B_\sigma)X_\rho$, have the charge symmetry $\mathcal{C}=+$. An s-wave term cannot arise from the component $\mathrm{Re}(\epsilon^{i0jk}B_i^\dagger\partial_0 B_j)X_0$, for which $\mathcal{P}=+$ (since L and S are then both even and with $J=1$, $L\neq 0$). Alternatively, the derivative picks up the term $p_1^0-p_2^0\approx 0$ in the NR limit. This leaves the component $\mathrm{Re}(\epsilon^{ikj0}B_i^\dagger\partial_k B_j)$ with $\mathcal{P}=-,\mathcal{C}=+$ and therefore $L=1$ which is velocity dependent, in fact it cannot couple to the vector bilinear, $\bar{q}\gamma^0 q$ which permits no L,S states, at all. Thus if the DM coupling is real then the axial-vector piece is p-wave, and the vector piece d-wave.

In all three cases, the annihilation of DM to mediator pairs above the threshold $m_\chi > m_{\rm MED}$ is huge, due to the dominant longitudinal polarization of the mediators (this was discussed for model 0-V). This creates a huge allowed region which require small couplings, for which there are no constraints and therefore we do not apply the MCMC there and simply highlight the region in the plots. Even worse, the longitudinal modes of the vectors lead to enormous perturbative unitarity violations in processes such as $\chi^\dagger\chi \to \chi^\dagger\chi$ and $\chi^\dagger\chi \to VV$ (see Tab.5.1), which require new physics even at the energies of indirect constraints ($E \sim m_\chi$). Therefore one should be hesitant about using the simplified model, and should at least check the effects of the new physics on the bounds we have presented.

Gamma ray constraints can be derived from Fig.5.11, and are only sizeable for operators $\mathcal{O}_{V4,6}$, which arise from vertex $\mathcal{V}_{1,2}$ coupling to axial-vector mediators.

To avoid cluttering the discussion we will restrict ourselves to considering each of the three vertices, assuming all couplings are present and equal, ie that $g_\chi = g + ig$, $g_v = g_a = g$, as this provides the dominant behaviour of ID and DD in each case, and presents thus the smallest allowed parameter space, allowing future experiments the opportunity to exclude these models entirely. These are plotted in Fig.5.13, and show that ruling out such models is in some cases difficult but in some cases possible through collider constraints .The projection of the allowed regions onto each of the parameter ranges is shown in Tab.5.5.

5.4.3 Charged fermion mediator (1-F$^\pm$, 1*-F$^\pm$)

We conclude the list of models with a vector DM exchanging a charged fermionic. In the case of complex vector DM, there is only a single diagram (u-channel for our Lagrangian) for DD scattering, and it generates a large subset of the vector DM EFT operators. The dominant ones are $\mathcal{O}_{V1} = B^\mu B^\dagger_\mu \bar{q}q$ and $\mathcal{O}_{V5-2} = i\mathrm{Im}(B^\dagger_\mu \partial^\nu B^\mu)\bar{q}\gamma_\nu q$ since they lead to $\mathcal{O}_1^{(\rm NR)}$. The latter dominates by a factor m_χ/m_N, and thus the DD constraints remain strong even in the chiral limit whereby $\mathcal{O}_{V1}$ is suppressed by

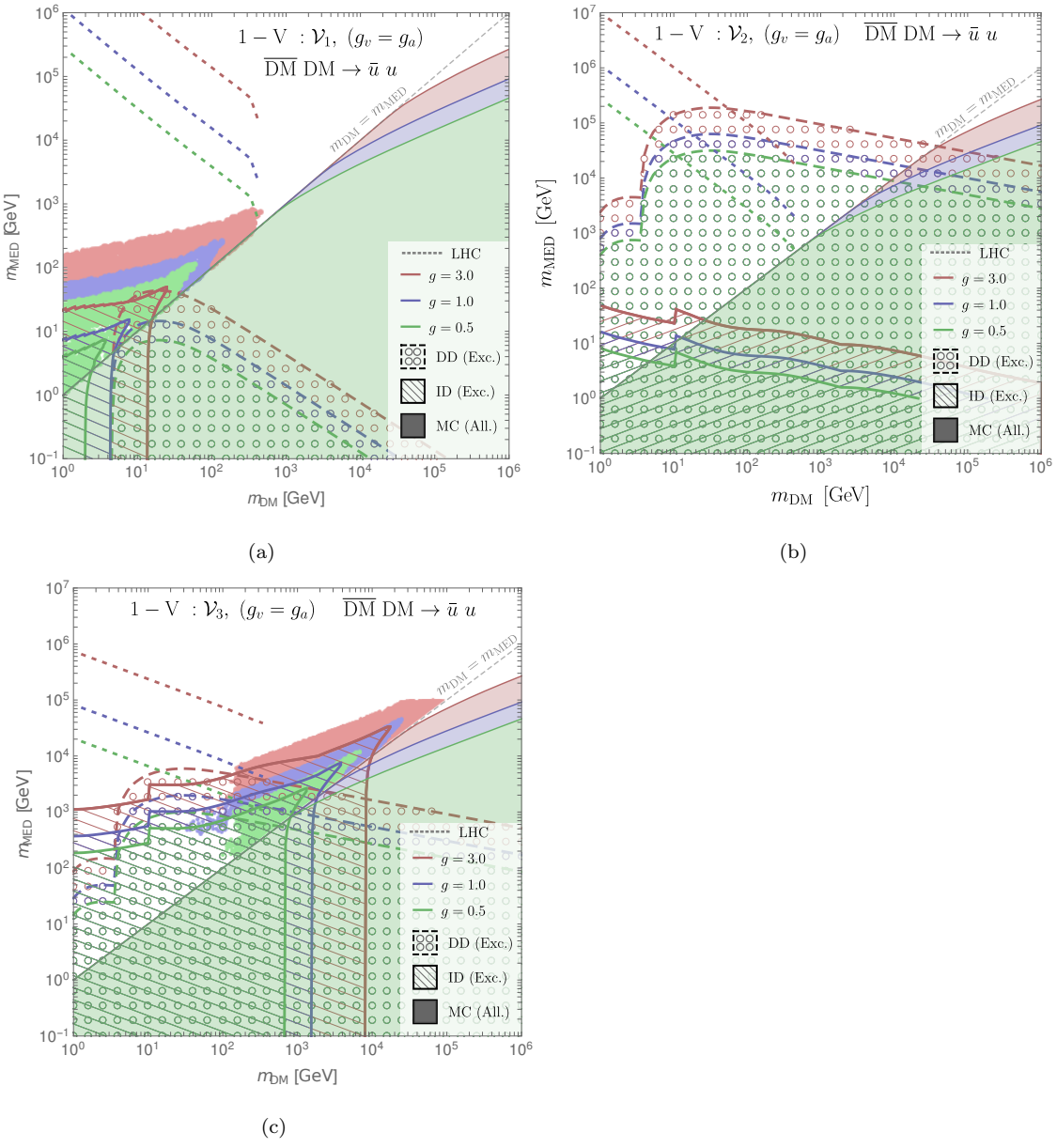

Figure 5.13: As for Fig.5.1 for a spin-1 DM candidate exchanging a neutral vector mediator with a $\bar{u}u$ pair, for the vertex structures $\mathcal{V}_{1,2,3}$, upper left, upper right, and bottom respectively. Collider bounds shown as dotted line and taken from [12].

Non-zero Coup.	ID	DD
$\mathrm{Re}(g_\chi), g_v^{(f)}$	p-wave	$\mathcal{O}_{14}^{(\mathrm{NR})}$ $(q, v^\perp)$
$\mathrm{Re}(g_\chi), g_a^{(f)}$	p-wave	$\mathcal{O}_{12}^{(\mathrm{NR})}$ $(v^\perp)$
$\mathrm{Im}(g_\chi), g_v^{(f)}$	p-wave	$\mathcal{O}_{5}^{(\mathrm{NR})}$ $(q, v^\perp)$
$\mathrm{Im}(g_\chi), g_a^{(f)}$	p-wave	$\mathcal{O}_{9}^{(\mathrm{NR})}$ (q)

Non-zero Coup.	ID	DD
$\mathrm{Re}(g_\chi), g_v^{(f)}$	p-wave	≈ 0
$\mathrm{Re}(g_\chi), g_a^{(f)}$	s-wave (m_f^2)	$\mathcal{O}_{10}^{(\mathrm{NR})}$ (q)
$\mathrm{Im}(g_\chi), g_v^{(f)}$	p-wave	$\mathcal{O}_{1}^{(\mathrm{NR})}$ (1)
$\mathrm{Im}(g_\chi), g_a^{(f)}$	p-wave	$\mathcal{O}_{7}^{(\mathrm{NR})}$ $(v^\perp)$

Non-zero Coup.	ID	DD
$\mathrm{Re}(g_\chi), g_v^{(f)}$	d-wave	$\mathcal{O}_{11}^{(\mathrm{NR})}$ (q)
$\mathrm{Re}(g_\chi), g_a^{(f)}$	p-wave	$\mathcal{O}_{14}^{(\mathrm{NR})}$ $(q, v^\perp)$
$\mathrm{Im}(g_\chi), g_v^{(f)}$	s-wave	$\mathcal{O}_{8}^{(\mathrm{NR})}$ $(v^\perp)$
$\mathrm{Im}(g_\chi), g_a^{(f)}$	s-wave	$\mathcal{O}_{4}^{(\mathrm{NR})}$ (1)

Table 5.6: The possible configurations of couplings which lead to distinct behaviour of the ID and DD constraints for the models 1-V and 1*-V, for the vertex structure (from top to bottom) $\mathcal{V}_{1,2,3,}$. The suppressions of each of the NR operators by q or $v^\perp$ is given in brackets.

m_q/m_{MED}. For the complex vector:

$$C_1^{(N)} = \frac{2m_N^2}{(m_\chi^2 - m_{\mathrm{MED}}^2)} \sum_{q'=q,Q} \left(f_{T_{q'}}^{(N)} \left(|g_a^{(q')}|^2 - |g_v^{(q')}|^2 \right) \frac{m_{\mathrm{MED}}}{m_{q'}} + f_{T_{q'}}^{(N)} \left(|g_v^{(q')}|^2 + |g_a^{(q')}|^2 \right) + 2\mathcal{V}_{q'}^{(N)} \left(|g_v^{(q')}|^2 + |g_a^{(q')}|^2 \right) \frac{m_\chi}{m_N} \right). \tag{5.4.42}$$

If the DM is real, then $\mathcal{O}_{V5-2}$ is absent and choosing chiral couplings one can suppress the contribution to $\mathcal{O}_1^{(\mathrm{NR})}$ by m_q/m_{MED},

$$C_1^{(N)} = \frac{2m_N^2}{(m_\chi^2 - m_{\mathrm{MED}}^2)} \sum_{q'=q,Q} f_{T_{q'}}^{(N)} \left(\left(|g_v^{(q')}|^2 - |g_a^{(q')}|^2 \right) \frac{m_{\mathrm{MED}}}{m_{q'}} + \left(|g_v^{(q')}|^2 + |g_a^{(q')}|^2 \right) \right). \tag{5.4.43}$$

For heavy quarks the constraints are suppressed with respect to the light quarks due to the heavy quark loop by $\approx 0.1 m_q/m_{\mathrm{MED}}$. For ID, any choice of couplings retains an unsuppressed s-wave contribution to $\langle \sigma v \rangle$, for complex and real DM respectively,

$$\langle \sigma v \rangle \approx \sum_f \frac{N_c \left(\left(|g_v^{(f)}|^2 - |g_a^{(f)}|^2 \right)^2 (4m_\chi^2 + 5m_{\mathrm{MED}}^2) + 32 m_\chi^2 |g_a^{(f)}|^2 |g_v^{(f)}|^2 \right)}{36\pi (m_\chi^2 + m_{\mathrm{MED}}^2)^2}, \tag{5.4.44}$$

$$\langle \sigma v \rangle \approx \sum_f \frac{N_c \left(\left(|g_v^{(f)}|^2 - |g_a^{(f)}|^2 \right)^2 (4m_\chi^2 + 3m_{\mathrm{MED}}^2) + 32 m_\chi^2 |g_a^{(f)}|^2 |g_v^{(f)}|^2 \right)}{9\pi (m_\chi^2 + m_{\mathrm{MED}}^2)^2}. \tag{5.4.45}$$

For chiral couplings $g_v = \pm g_a$ the cross section scales as $\langle\sigma v\rangle \propto m_\chi^2/(m_\chi^2 + m_{\rm MED}^2)^2$. For non-chiral couplings, however, we find $\langle\sigma v\rangle \propto m_{\rm MED}^2/(m_\chi^2 + m_{\rm MED}^2)^2$ which weakens the dependence on $m_{\rm MED}$ and strengthens the constraints. This is the same behaviour as for DD, since in the EFT the scalar operator (which dominates nuclear scattering) is also the operator which provides the s-wave contribution to $\langle\sigma v\rangle$. Since the constraints are fairly similar between real and complex DM, we show the complex case only in Fig.5.14. Models coupling to light quarks are ruled out due to the strength of the DD and ID constraints in both the chiral and non-chiral limits (Fig.5.14 (a) and (b)). Models coupling to heavy quarks can produce thermal DM candidates if the masses and couplings are large enough; the DD constraints are suppressed but the ID limits are still strong, as shown in Fig.5.14 (c) and (d). Finally the allowed regions are projected onto each of the parameter dimensions and shown in Tab.5.5.

Perturbative Unitarity : The process $\bar{q}q \to \bar{F}F$ leads to an energy independent bound of,

$$m_\chi \gtrsim m_{\rm MED}\left(\left(\frac{|g_a|}{4\pi}\right)^2 - \left(\frac{|g_v|}{4\pi}\right)^2\right)^{1/2} + m_q\left(\left(\frac{|g_a|}{4\pi}\right)^2 + \left(\frac{|g_v|}{4\pi}\right)^2\right)^{1/2}, \quad (5.4.46)$$

taking the largest allowed couplings, and including the stability of the DM, we require masses $0.3 m_{\rm MED} \lesssim m_\chi \lesssim m_{\rm MED}$ which certainly impacts the allowed parameter space, unless the couplings are chiral in which case the result is suppressed by $(m_q/m_{\rm MED})$. The bounds are displayed in Fig.5.14 but are not implemented into the MCMC.

LHC Bounds : The dominant collider bounds come from couplings to $\mathcal{O}_{\rm V1,V2,V5-2,V9}$[12]. If the DM is complex and $g_v \neq g_a$ then all four operators are present. If the couplings are chiral, $g_v = g_a$, then the contribution to $\mathcal{O}_{V1}$ is suppressed by $m_q/m_{\rm MED}$ but the contribution to $\mathcal{O}_{V5-2}$ remains. These are shown for illustration in Fig.5.14 as dotted lines.

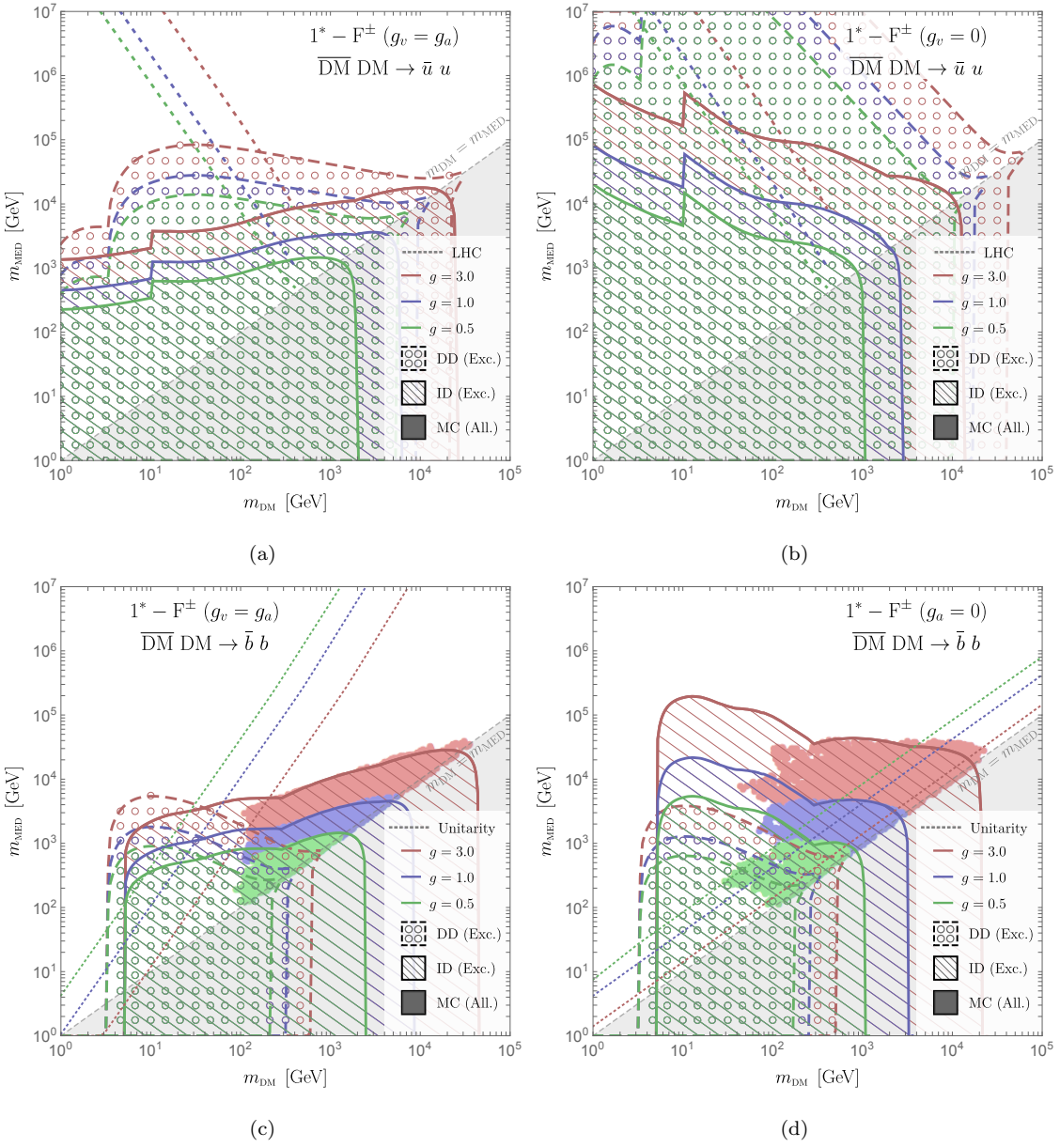

Figure 5.14: As for Fig.5.1 for a complex spin-1 DM candidate exchanging a charged fermionic mediator with a pair of SM fermions, $\bar{u}u$ (top row) or $\bar{b}b$ (bottom row). The left (right) columns are for chiral (vector) couplings. Dotted lines correspond to LHC bounds in the top row, or unitarity bounds in the bottom row. The region to the left of the dotted lines in the bottom row leads to perturbative unitarity violations. The region below the dotted lines in the top row is excluded by LHC data.

5.5 Conclusions

The task of the preceding chapters is a simple one, to consider how constrained the parameter space of a WIMP DM is. This chapter quantifies that question; we have produced a list of 16 UV complete simplified models which introduce a mediator to connect the DM field to the SM fermions (Chapter 2). Subject to these assumptions we have then explored the constraints on each model in detail, focussing on quark (rather than lepton) couplings since these lead to the cleanest DD signals. A WIMP must be produced thermally with the correct relic density (according to Chapter 1 Sec.1.2.5), it also must evade a large literature of indirect searches (outlined in Chapter 3), as well as gamma-ray line searches, and even more powerful direct searches (outlined in Chapter 4). Although usually dominated by tree level, Both ID and DD limits are calculated to the one-loop level as necessary.

Amongst the various constraints there is one conspicuous absence. We have avoided a complete calculation of collider bounds; (although we have added illustrative constraints for some models) this is sensible for models which are not $SU(2)_L$ gauge invariant and which may violate perturbative unitarity, both of which are more likely to be manifest at high energies. We have calculated the dominant violations of unitarity for the relevant models (those with vector fields), and considered where this would lead to a model which is 'too simplified'.

It is clear that there is as much variation in constraints in the particular choice of couplings within a model, as there is between the models themselves. For each model, and each choice of couplings, we have performed an MCMC scan over the masses and coupling. It is difficult to summarise this into a single conclusion, and our aim was not to. Instead, we have provided summarised plots of allowed regions, finding that some models are ruled out entirely, and some evade almost all the constraints. These results are of use to any model builders, to give them a cursory idea of how constrained a model might be.

Naturally, such a study will make several approximations. In Chapter 7, we will

test the accuracy of the results presented here by tackling each of these assumptions for the model 1/2-$S^{\pm}$.

Chapter 6

Solar Neutrino Constraints from Direct Detection

Direct detection of DM is a rapidly evolving field, and the next generation of experiments are soon to begin operation with unprecedented sensitivity to DM-SM scattering, so much so that they will hit the *neutrino floor* whereby neutrino scattering presents a background. In this study, we will demonstrate that this sensitivity allows for the measurement of neutrinos which will improve the precision of neutrino fluxes, and provide very robust and powerful constraints on generic new physics which couples to the neutrino sector.

6.1 Neutrinos from the Sun

Experimental studies of solar neutrinos began in 1968 [286] with the measurement of the total flux by Ray Davis Jr, a third of what was expected by the Standard Solar Model (SSM) at the time [287]. In the subsequent decades the theoretical and experimental predictions have vastly improved and the discrepancy resolved, indeed we now know that neutrinos have mass [288], and that this mass causes them to oscillate into a mixture of the three neutrino flavours, which can have dramatic effects in matter (the MSW effect) [289–292].

To understand the origin of neutrinos in the Sun, Fig.6.1 shows the normaliza-

tions and errors of the various solar neutrino fluxes, and Fig.6.2 shows their energy spectra. Neutrinos are predominantly produced through the pp-chain which is responsible for fusing Hydrogen in the Sun (and stars of similar mass),

$$p \ + \ p \ \rightarrow d + e^{+} + \nu_{e} \ . \tag{6.1.1}$$

These neutrinos are very low energy ($E_\nu \lesssim 400$ keV) and the remaining $\sim 10\%$ of neutrinos produced via other reactions have higher energies. Deuterium is also produced via $p+e^{-}+p \rightarrow d+\nu_e$ (the *pep* neutrinos), which is kinematically less probable than Eq.(6.1.1), and which also produces mono-energetic neutrinos ($E_\nu \sim 1.4$ MeV). The deuterium fuse to produce ^{3}He, and these fuse to produce ^{4}He. A small amount of neutrinos are produced by $^3\mathrm{He} + \mathrm{p} \rightarrow ^4\mathrm{He} + \mathrm{e}^{+} + \nu_\mathrm{e}$ (the *hep* neutrinos). Two Helium isotopes may fuse to produce ^{7}Be, which may then produce neutrinos via electron capture $^7\mathrm{Be} + \mathrm{e}^{-} \rightarrow ^7\mathrm{Li} + \nu_\mathrm{e}$ which results in two line spectra at 0.86 MeV and 0.38 MeV in the ratio $9:1$. The ^{7}Be may form ^{8}B by combining with a proton, and the ^{8}B subsequently decays to produce the *boron-8* neutrinos $^8\mathrm{B} \rightarrow ^8\mathrm{Be}+\mathrm{e}^{+}+\nu_\mathrm{e}$ with $E_\nu \lesssim 15$ MeV.

Hydrogen fusion may also take place via the *CNO cycle*, which accounts for only 1% of fusion in the Sun, but is more important in heavier stars. This mechanism gives rise to the so-called ^{13}N, ^{15}O, ^{17}F neutrinos with energies $E_\nu \lesssim 1$ MeV.

Flux Source	Flux ($\mathrm{cm}^2\mathrm{s}^{-1}$)	Error (%)
pp	6.03×10^{10}	0.6
pep	1.47×10^{8}	1.2
hep	8.31×10^{3}	30
^{7}Be	4.56×10^{9}	7.0
^8B	4.59×10^{6}	14
^{13}N	2.17×10^{8}	14
^{15}O	1.56×10^{8}	15
^{17}F	3.40×10^{6}	16

Figure 6.1: Normalizations (with errors) for the theoretical solar neutrino fluxes, taken from the AGSS09-SFII standard solar model [13].

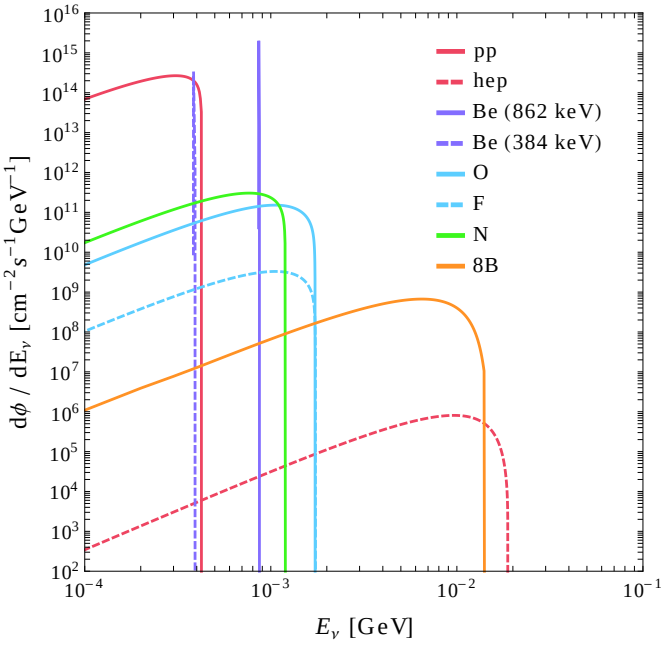

Figure 6.2: Energy spectrum of solar neutrinos, with normalizations as in Fig.6.1.

At the present time only four of these contributions to the solar neutrino flux have been measured, the ^{8}B , *pp*, *pep*, and ^{7}Be. The latter three have all been measured by the Borexino Collaboration [14, 293], and the ^8B by the *Sudbury Neutrino Observatory* (SNO) [294].

The neutrino energies that an experiment is sensitive to depend strongly on the mass of the target particles from which the neutrinos scatter. In this way, DD experiments, which are tailored to nuclear recoils (and possibly electron recoils), offer a tantalizing prospect to measure both solar neutrino-nuclear scattering and the unmeasured *CNO* neutrinos for the first time.

6.2 New Physics in the Neutrino Sector

Many regard the neutrino sector as a likely place in which we might encounter physics *beyond the standard model* (BSM). The neutrino masses themselves are not strictly BSM, since one can accommodate for them in the same way as for other fermions by the addition of a singlet, right handed ν_R, but why are they so small?

Much experimental effort is yet to come, pinning down among other things the exact fermionic nature of neutrinos (whether Dirac or Majorana fields), a measurement of the Dirac CP phase, the mass hierarchy, and a more precise determination of their mixing angles.

By now, a plethora of models exist which introduce new physics in the neutrino sector [295]. However, since this is a phenomenological study, with the reasonably narrow scope of DD and neutrino detectors, we do not intend to build a detailed and complete model. Instead, since we wish to have an observable signal inside terrestrial experiments we simply require that the lepton sector is coupled with the new physics (leading to neutrino-electron scattering), or that the quark sector is coupled also (leading to neutrino-nucleus scattering).

In order to keep the theory renormalizable, any new couplings in the Lagrangian must have mass dimension < 4. This makes a direct coupling between neutrinos and electrons or quarks which also preserves the SM gauge symmetries impossible, and we must introduce at least one new particle to the theory. Since the SM contains left-handed neutrinos only, one immediately constructs the Lagrangian,

$$\begin{aligned}\mathcal{L}_{\text{np}} = &-\frac{1}{4}\mathcal{Z}^{\mu\nu}\mathcal{Z}_{\mu\nu} + m_{Z'}Z'^{\mu}Z'_{\mu} + g_{\nu,Z'}\bar{\nu}_L\gamma^{\mu}\nu_L Z'_{\mu} \\ &+ Z'_{\mu}\left(g_{l,v}\bar{l}\gamma^{\mu}l + g_{l,a}\bar{l}\gamma^{\mu}\gamma^5 l\right) \\ &+ Z'_{\mu}\left(g_{q,v}\bar{q}\gamma^{\mu}q + g_{q,a}\bar{q}\gamma^{\mu}\gamma^5 q\right) \ , \end{aligned} \tag{6.2.2}$$

where $l = e, \mu, \tau$ and $\mathcal{Z}^{\mu\nu} \equiv \partial^{\mu}Z'^{\nu} - \partial^{\nu}Z'^{\mu}$ is the field strength of the Z'. The mediator Z' is similar in its couplings to a SM Z boson, hence the notation. It is sometimes also denoted a *dark photon*. When $g_{l,a} = 0$ ($g_{l,v} = 0$) the particle is known as a *vector* (*axial vector*) *mediator*.

In principle we can allow couplings to a spin-0 boson, ϕ, however since $\bar{\nu}_L\nu_L = \bar{\nu}_L\gamma^5\nu_L = 0$, we must also introduce an inert right-handed neutrino ν_R in order to have viable couplings;

$$\begin{aligned}\mathcal{L}_{\rm np} &= \partial^\mu \phi^\dagger \partial_\mu \phi + m_\phi^2 \phi^\dagger \phi \\ &+ g_{\nu,\phi} \left(\bar{\nu}_L \nu_R \phi + \text{h.c.}\right) + \phi \left(g_{l,s} \bar{l}\ l + i g_{l,p} \bar{l} \gamma^5 l\right) \\ &+ \phi \left(g_{q,s} \bar{q}\ q + i g_{q,p} \bar{q} \gamma^5 q\right)\ , \end{aligned} \tag{6.2.3}$$

where $g_{l,s} = 0$ ($g_{l,p} = 0$) the particle is known as a *scalar* (*pseudo-scalar*) *mediator*.

Eq.(6.2.2) and Eq.(6.2.3) represents the simplified models we will be using for the rest of the study, but note that a final possibility which we do not consider here is a spin-2, or tensor, mediator, T, which would introduce a neutrino coupling $\bar{\nu}_L \sigma_{\mu\nu} \nu_L T^{\mu\nu}$.

6.3 Neutrino Detection in Direct Detection Experiments

Direct Detection (DD) experiments are primarily designed to look for weakly interacting dark matter. The technology for DD has been steadily improving since the pioneering paper by Goodman and Witten [209] in 1985. They all share similar principles, in that they attempt to measure the small amount of energy release ($\sim \mathcal{O}(1)$ keV) when a DM particle scatters from either an electron or nuclei (referred to as *electron recoil* and *nuclear recoil*), this may be through a phonon and ionization signal in the case of CDMS [270], or through scintillation in the case of XENON, LUX [267, 296], and plenty of other detections mechanisms exist.

The primary obstacle to such a search is the expected number of signal events, which can be as low as one per year. A vast background reduction must be achieved in order to stand a chance, and so most DD experiments are built far underground, extremely radio pure, with shielding and fiducial volume cuts to reduce background from radioactive materials.

However, one can never shield an experiment from neutrinos. In general, neutrinos do not provide a background simply because they are too low energy and scatter so rarely. This may not be so in the current era of DD technology, as was first noticed as early as 1985 [297–299]. The irreducible neutrino background is now referred to as the *neutrino floor*. It was noticed recently that the neutrino spectra can even mimic a DM candidate with a mass of around 6 GeV [300], although directional detection techniques may help to break the degeneracy, since neutrinos originate primarily from the Sun, whereas the DM flux is homogeneous in the vicinity of the earth to a good approximation.

As the reader may have anticipated, we do not wish to view neutrinos as a background to the search for DM, but instead pose the question of how well such neutrinos may be measured. The motivations for considering this question are twofold,

1. A detection of neutrinos scattering from nuclei, often referred to as *coherent neutrino scattering*, is a long standing theoretical prediction (1974) [301, 302], but is yet to be experimentally measured. Thus, DD would provide the first verification of this important prediction.

2. If new physics is lurking in the neutrino sector, then DD machines provide an excellent place to detect this new physics. At the very least, it is important to quantify how new physics would manifest itself, and the extent to which bounds may be placed.

6.3.1 Neutrino Interaction Cross Sections

We briefly review some approximate formulae for neutrino scattering in both the SM, and with the additions of Lagrangians Eq.(6.2.2) and Eq.(6.2.3).

Neutrino-Electron Scattering (SM)

In the case of electron scattering, the cross section is lepton-flavour dependent; all neutrino flavours scatter via a t-channel neutral-current diagram, but ν_e scatters

also via an s-channel charged-current diagram.

$$\left.\frac{d\sigma_{\rm SM}}{dE_R}\right|_{\mu,\tau} = -\frac{m_e G_F^2}{2\pi E_\nu^2}\left(-{E_\nu}^2\left(8{s_W}^4 - 4{s_W}^2 + 1\right) + 8E_\nu E_R {s_W}^4\right. \tag{6.3.4}$$
$$\left. +2E_R {s_W}^2\left(-2E_R {s_W}^2 + 2m_e {s_W}^2 - m_e\right)\right) \ ,$$
$$\left.\frac{d\sigma_{\rm SM}}{dE_R}\right|_{e} = -\frac{m_e G_F^2}{2\pi E_\nu^2}\left(-{E_\nu}^2\left(8{s_W}^4 + 4{s_W}^2 + 1\right) + 8E_\nu E_R {s_W}^4\right. \tag{6.3.5}$$
$$\left. +2E_R {s_W}^2\left(-2E_R {s_W}^2 + 2m_e {s_W}^2 + m_e\right)\right) \ ,$$

where E_R and E_ν are the energies of the recoiling electron and incoming neutrino respectively. Since $E_R/E_\nu \ll 1$ these expressions may be simplified,

$$\left.\frac{d\sigma_{\rm SM}}{dE_R}\right|_{\mu,\tau} \approx \frac{G_F^2 m_e}{2\pi}(8s_W^4 - 4s_W^2 + 1) \ , \tag{6.3.6}$$
$$\left.\frac{d\sigma_{\rm SM}}{dE_R}\right|_{e} \approx \frac{G_F^2 m_e}{2\pi}(8s_W^4 + 4s_W^2 + 1) \ , \tag{6.3.7}$$

and the differential cross section is approximately constant with energy.

Neutrino-Electron Scattering (BSM)

The interaction with the spin-0 mediator ϕ, Eq.(6.3.8), gives rise to a lepton-flavour independent cross section,

$$\left.\frac{d\sigma_{\rm BSM}}{dE_R}\right|_{e,\mu,\tau} \approx \frac{g_{\nu,\phi}^2 m_e E_R}{2\pi E_\nu^2}\frac{(2g_{l,s}^2 m_e + g_{l,p}^2 E_R)}{(2m_e E_R + m_\phi^2)^2} \ , \tag{6.3.8}$$

since $m_e \gg E_R$. For a spin-1 mediator Z', there are also interference terms with the SM neutral-current diagram (this interference term also introduces a flavour dependence of the interaction),

$$\begin{aligned}\left.\frac{d\sigma_{\rm BSM}}{dE_R}\right|_{e,\mu,\tau} &= \frac{g_{\nu,Z'}^2 m_e}{2\pi E_\nu^2\left(2E_R m_e + m_{Z'}^2\right)^2}\left(2(2E_\nu^2 + E_R^2 - 2E_R E_\nu)\left(g_{l,a}^2 + g_{l,v}^2\right)\right. \\ &\quad \left. -4(E_R^2 - 2E_\nu E_R)g_{l,a}g_{l,v} + 2E_R m_e\left(g_{l,a}^2 - g_{l,v}^2\right)\right) \\ &\approx \frac{2g_{\nu,Z'}^2 m_e}{\pi\left(2E_R m_e + {m_{Z'}}^2\right)^2}\left({g_{l,a}}^2 + {g_{l,v}}^2\right) \ .\end{aligned} \tag{6.3.9}$$

The cross terms (necessarily flavour dependent) are,

$$\begin{aligned}\left.\frac{d\sigma_{Z-Z'}}{dE_R}\right|_e &= \frac{1}{4\pi E_\nu^2}\frac{\sqrt{2}m_e g_{\nu,Z'}G_F}{(2E_R m_e + m_{Z'}^2)}\left(2(g_{l,v}+g_{l,a})\left(E_\nu^2(1+2s_W^2) - m_e E_R s_W^2\right)\right.\\ &\left.+(g_{l,v}-g_{l,a})\left(E_R m_e(1+2s_W^2) - 4s_W^2(E_\nu - E_R)^2\right)\right)\\ &\approx \frac{\sqrt{2}m_e g_{\nu,Z'}G_F}{2\pi(2E_R m_e + m_{Z'}^2)}(g_{l,v}+g_{l,a}(1+4s_W^2))\ , \qquad (6.3.10)\\ \left.\frac{d\sigma_{Z-Z'}}{dE_R}\right|_{\mu,\tau} &= -\frac{1}{4\pi E_\nu^2}\frac{\sqrt{2}m_l g_{\nu,Z'}G_F}{(2E_R m_l + m_{Z'}^2)}\left(2(g_{l,a}+g_{l,v})\left(E_\nu^2(1-2s_W^2) + m_l E_R s_W^2\right)\right.\\ &\left.+(g_{l,a}-g_{l,v})\left(E_R m_l(1-2s_W^2) + 4s_W^2(E_\nu - E_R)^2\right)\right)\\ &\approx -\frac{\sqrt{2}m_l g_{\nu,Z'}G_F}{2\pi(2E_R m_l + m_{Z'})}\left(g_{l,a}+g_{l,v}\left(1-4{s_W}^2\right)\right)\ . \qquad (6.3.11)\end{aligned}$$

We see from Eq.(6.3.9) that the case of a vector or axial vector coupling are identical. This degeneracy is broken by the cross terms in Eq.(6.3.11), however these are subdominant, and in the end we expect axial vector and vector interactions to be indistinguishable in electron recoils.

Neutrino-Nucleus Scattering (SM)

Neutrino scattering from nuclei is considerably more complicated than electron scattering, because the bound-state structure of the nucleus must be accounted for. At the quark level, we have introduced the Lagrangians in Eq.(6.2.2) and Eq.(6.2.3), however since the energy of the scattering is so low (or equivalently, the Compton wavelength of the neutrino so large), quarks are not the relevant degrees of freedom, instead the neutrino scatters from nucleons.

In order to account for the scattering from nucleons, one must take the hadronic matrix elements of the quark Lagrangian, which introduces nucleonic form factors, and replaces quark spinors with nucleon spinors. This procedure is covered in Chapter 4, Sec.4.3.

The Lagrangian is now written in terms of nucleon currents $\bar{N}\Gamma N$ where $\Gamma = \{1, i\gamma^5, \gamma^\mu, \gamma^\mu\gamma^5\}$ gives the spinor structure of the interaction, but the bound state structure of the nucleons within the nucleus must also be accounted for. This in-

troduces a second set of nuclear form factors. In this case, the so called Helm form factor [303] fits the energy dependence of the form factor well, and we simply use a different normalization for each interaction.

Coherent neutrino-nucleus scattering occurs for a scalar or vector coupling (i.e $\bar{N}N$ or $\bar{N}\gamma^\mu N$), in this case the matrix elements of the scatterings with each individual nucleon add coherently (with no relative phase), and so the interaction with the nucleus is $\propto A$ and thus $\sigma \propto A^2$. This is a significant enhancement for heavy nuclei such as Xenon ($A^2 \sim 10^4$).

On the other hand, other interactions such as pseudoscalar and axial vector (i.e $\bar{N}\gamma^5 N$ or $\bar{N}\gamma^\mu\gamma^5 N$) are not coherent. Instead, for an axial vector interaction, the nuclear interaction is sensitive to the nuclear spin $J_{\rm nuc}$, and $\sigma \propto J_{\rm nuc}^2$. In order to find $J_{\rm nuc}$ we use values from a simple shell model, where the nuclear spin is approximately given by the J quantum number of any unpaired nucleon (thus nuclei with even A are completely insensitive to axial vector interactions).

In the SM, the neutrino-nucleus scattering is given by a coherent vector interaction via a Z,

$$\begin{aligned}\left.\frac{d\sigma_{\rm SM}}{dE_R}\right|_{\rm nuc} &= F^2(E_R)\frac{m_n G_F^2}{2\pi}\left(1-\frac{E_R}{E_\nu}+\frac{E_R^2}{2E_\nu^2}-\frac{m_n E_R}{2E_\nu^2}\right)\\ &\approx F^2(E_R)\frac{m_n G_F^2}{2\pi}\left(1-\frac{m_n E_R}{2E_\nu^2}\right)\ ,\end{aligned} \tag{6.3.12}$$

where $F^2(E_R) \equiv A^2 F_{\rm helm}^2(E_R)$ is the form factor squared, and m_n is the mass of the nucleus. There is also an axial vector contribution but it is neglected since $J_{\rm nuc} \ll A$.

Neutrino-Nucleus Scattering (BSM)

For a neutral spin-0 mediator, the interaction is coherent and the cross section is,

$$\left.\frac{d\sigma_{\rm BSM}}{dE_R}\right|_{{\rm nuc},\phi} \approx \frac{9A^2 E_R m_n \left({g_{\nu,s}}^2+{g_{\nu,s}}^2\right)}{4\pi E_\nu^2(2m_n E_R+m_\phi^2)^2}\left(E_R {g_{q,p}}^2+2g_{q,s}^2 m_n\right)\ , \tag{6.3.13}$$

and as with the electron scattering there are no interference terms with the SM. For vector mediator Z',

$$\begin{aligned}\left.\frac{d\sigma_{BSM}}{dE_R}\right|_{\text{nuc},Z'} &= \frac{m_n\left({g_{\nu,v}}^2+{g_{\nu,a}}^2\right)}{2\pi E_\nu^2(2m_nE_R+m_{\text{MED}}^2)^2}\left(9A^2g_{q,v}^2(2E_\nu^2+E_R^2+E_R(m_n-2E_\nu))\right.\\ &\quad\left.+9g_{q,a}^2\langle S\rangle\left(2E_\nu^2+E_R^2+E_R(m_n-2E_\nu)\right)\right)\\ &\quad+\frac{3G_FQ_Wm_n}{2\sqrt{2}\pi E_\nu^2(2m_nE_R+m_{\text{MED}}^2)}\left(g_{q,a}g_{\nu,a}\langle S\rangle E_R(E_R-2E_\nu)\right.\\ &\quad\left.-Ag_{q,v}g_{\nu,v}(2E_\nu^2+E_R^2-E_R(2E_\nu+m_n))\right)\\ &\approx\frac{9g_\nu^2m_n(2E_\nu^2+E_Rm_n)}{\pi E_\nu^2(2m_nE_R+m_{Z'}^2)^2}\left(A^2g_{q,v}^2+g_{q,a}^2\langle S_n\rangle^2\right)\\ &\quad-\frac{3\sqrt{2}g_\nu G_FQ_Wm_n}{4\pi E_\nu^2(2m_nE_R+m_{Z'}^2)}\left(2g_{q,a}\langle S_n\rangle E_RE_\nu+Ag_{q,v}(2E_\nu^2-E_Rm_n)\right)\ ,\end{aligned} \tag{6.3.14}$$

where we have included the interference with the SM and the spin of the nucleus $\langle S\rangle$ (equivalent to J_{nuc}).

6.4 Event Rates for Direct Detection

Now that we have the individual differential cross sections for scattering, $d\sigma/dE_R$, we review the calculation of the total event rate (or 'recoil rate') in a detector. The total recoil rate (per unit energy) is given by,

$$\frac{dR}{dE_R}=\varepsilon\sum_T\frac{1}{m_T}\int_{E_{\nu,\min}}dE_\nu\frac{d\phi}{dE_\nu}\frac{d\sigma_T}{dE_R}\ , \tag{6.4.15}$$

where the sum extends over all targets T (both electron and nuclear) with mass m_T per particle, with an exposure ε (conventionally in kg-days or ton-years). The integral over the incoming neutrino energy runs from the highest accessible energy to its minimum,

$$E_{\nu,\min}=\frac{1}{2}\left(E_R+\sqrt{E_R^2+2m_TE_R}\right)\ . \tag{6.4.16}$$

The incoming neutrino flux spectrum $d\phi/dE_\nu$ is plotted in Fig.6.2, and the differential cross sections for scattering with target T, $d\sigma_T/dE_R$, are given in the previous

section.

The behaviour of the electron recoil cross section, $d\sigma_e/dE_R$, is shown in Fig.6.3, against mediator mass. The dependence is simple and arises from the propagator of the mediator so that,

$$\frac{d\sigma_e}{dE_R} \propto (2m_e E_R + m_{\phi,Z'})^{-2} \ . \tag{6.4.17}$$

From Eq.(6.3.9) the vector and axial vector interactions are approximately degenerate (neglecting the subdominant cross terms of Eq.(6.3.11)), and far larger than both the scalar and pseudo-scalar interactions, Eq.(6.3.8). The SM result is reproduced in the limit of heavy mediators $m_X \gtrsim 100$ MeV. The scattering with ν_e is enhanced compared to $\nu_{\mu,\tau}$.

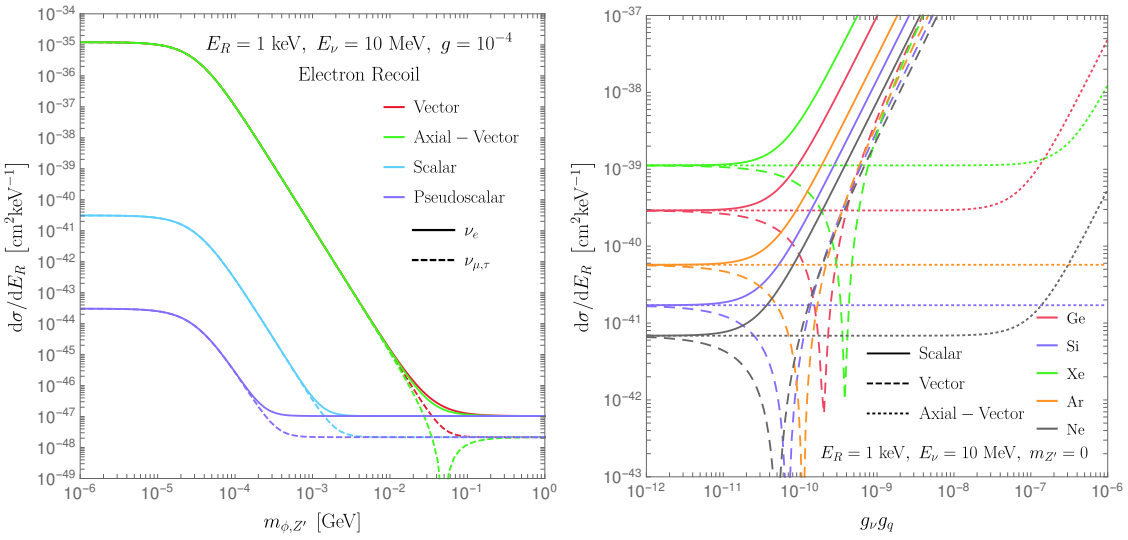

Figure 6.3: Differential cross sections, per target particle, including the SM contribution for a neutrino energy of $E_\nu = 10$ MeV (^{8}B and pp ν for NR and ER, right and left panel respectively) and recoil $E_R = 1$ keV$_{\rm er,nr}$. The mediator is scalar, pseudoscalar (ϕ) vector or axial-vector (Z'), a coupling $g \equiv g_{\nu,\phi} = g_{e,i}$ where $i = s, p, v, a$ respectively.

The behaviour of the scattering rate is similar for nuclear recoils. We show in Fig.6.3 the behaviour of the cross sections for electron nuclear recoil against the coupling combination $g_{\nu,\{\phi,Z'\}} \cdot g_{q,\{s,p,v,a\}}$, for different materials used in DD experi-

ments. The SM result is reproduced in the limit $g \to 0$ or $m_{\phi,Z'} \to \infty$.

The sensitivity from different target materials is fairly simple; the coherence effect $\sigma \propto A^2$ in vector and scalar interactions favours heavier targets. On the other hand, the axial vector interaction is far weaker, as it is not coherent $\sigma \propto \langle S \rangle \sim \mathcal{O}(1)$. In addition, some materials have no isotopes with a non-zero angular momentum and hence are completely insensitive to axial vector interactions.

A useful way to compare different detector set-ups is to consider the total event count, N_{TOT}, against the threshold energy, E_{th}, as shown in Fig.6.4. We consider both ER (left panels) and NR (right panels). Firstly, following Eq.(6.4.16), ER are sensitive to the huge flux of pp neutrinos, since $m_T \sim 0.5$ MeV, $E_R \sim 1 - 100$ keV and so $E_{\nu,\text{min}} \sim 16 - 217$ keV. NR have $m_T \sim 10 - 100$ GeV, $E_R \sim 1 - 100$ keV and $E_{\nu,\text{min}} \sim 2 - 70$ MeV, so they are mainly sensitive to ^8B neutrinos (along with a higher flux of neutrinos from the CNO cycle, if the target mass and/or recoil energy is sufficiently low).

Each representative detector we have chosen contains a different target material. For electronic recoils the material dependence is very weak, essentially scaling with the number of electrons per unit mass of the detector (proportional to Z/A). For the nuclear recoils (right panels of Fig.6.4), the material dependence is more significant. The rightmost curve in each plot comes from the ^8B neutrino spectra, and each material becomes sensitive to the CNO neutrinos at a different energy, since $E_{\nu,\text{min}} \propto \sqrt{m_N} \lesssim 1$ MeV, lower mass targets become sensitive to CNO neutrinos at a higher threshold.

The shape of the ER curves is simpler, for heavy mediators (independent of particular interactions) the cross section is $d\sigma/dE_R \propto (E_R)^n$ with $n \geq 0$, then the threshold has very little effect. For light mediators however, the propagator contributes an $(E_R)^{-2}$ and then $d\sigma/dE_R \propto (E_R)^n$ with $n < 0$, now the event rate is very sensitive to the threshold, the degree of sensitivity depends on the number of

E_R factors in the numerator.

The same is true in the case of NR (right panels), however the trend is more difficult to see. Another difference has been illustrated in the fourth panel; the coupling has been chosen in such a way that the Z-Z' interference term (which is negative) is of similar size to the SM contribution. The event rate is reduced, and this is especially noticeable at very low threshold. This effect is unique to the vector mediator across the models we have chosen.

6.5 New Physics in Current Generation Experiments

We have seen how various detector parameters affect the sensitivity to neutrinos, and shown how this differs for ER and NR. Electron recoils are sensitive to the lowest energy neutrinos, and so decreasing the detector threshold yields no improvement in the SM event count below $E_{\text{th}} \sim 5$ keV since no extra neutrino flux is accessed. Instead, since electron recoils often have larger statistics compared with NR, the detector exposure has the largest effect[1].

For NR, the sensitivity depends on the material chosen (favouring lighter nuclei), the exposure, and the threshold, since a sufficiently low threshold accesses more ^8B neutrinos, and for very light nuclei, neutrinos from the CNO cycle.

It is important to consider two additional detector effects: efficiency and energy resolution. The efficiency $\epsilon(E_R) < 1$ is an energy dependent normalization applied to the event rate, which includes the effects of various cuts applied to the detector to reduce background (for example to remove ER backgrounds). The detector resolution $\sigma(E)$ accounts for the error induced in the inferred energy when counting

[1]Depending on the relative size of the background the sensitivity will scale with the exposure (if the background is zero) or as the square root of the exposure (if the background is large)[271].

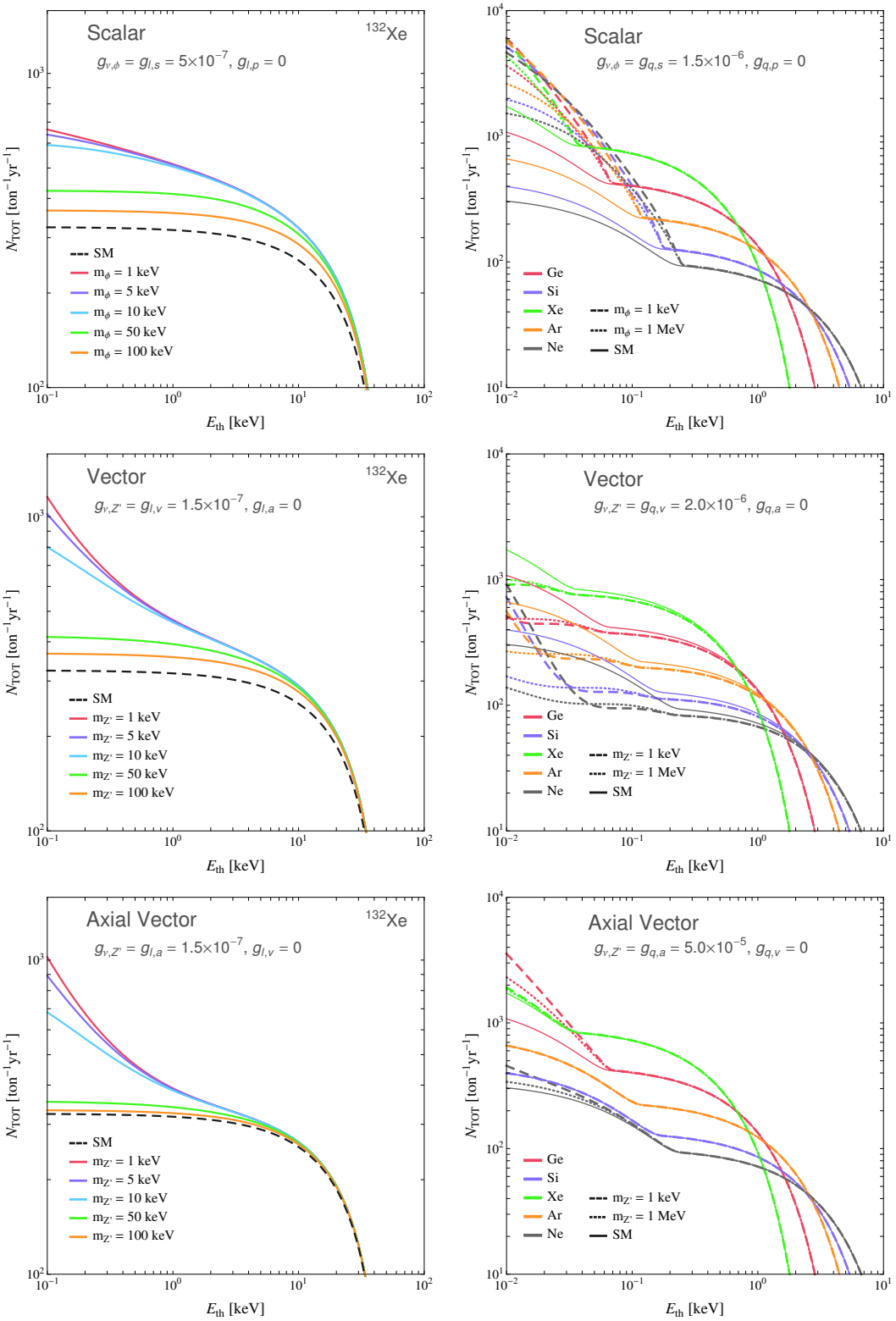

Figure 6.4: Electron $e-\nu$ recoil (left) and nuclear $n-\nu$ recoil (right) integrated rates as a function of the threshold energy E_{th}. Electron recoils are normalised to ^{132}Xe while nuclear recoils are plotted for a variety of target materials. Top row: scalar coupling; middle row: vector; bottom row: axial-vector. coupling.

individual quanta (electrons or photons) which have a natural Poisson distribution (allowing the number of quanta to fluctuate upwards or downwards).

Whilst the efficiency certainly decreases the total event rate, the detector resolution can actually increase the total number of events passing the threshold cut. If the distribution of events is sharply increasing with decreasing recoil energy, then there will be more events which randomly upscatter from below the threshold, than those which downscatter from above the threshold, and thus an overall gain of events.

These effects are included in the following modification of Eq.(6.4.15),

$$\frac{dR}{dE_R} = \epsilon(E_R) \int dE' \frac{dR}{dE'} \frac{1}{\sqrt{2\pi\sigma}} \exp\left[-\frac{(E'-E_R)^2}{2\sigma^2}\right] . \tag{6.5.18}$$

As an illustration of the present status, we consider several important current DD detectors;

1. The LUX collaboration recently updated their results [268], achieving an energy threshold of $E_{\rm th} = 1.1$ keV to nuclear recoils, and an exposure of $1.4 \cdot 10^4$ kg-days. We take the efficiency from Fig.1 of [268], and an energy resolution of $\sigma(E_R) = 0.2{E_R}^{0.6}$, from a fit to Fig.12 of [304].

2. The SuperCDMS collaboration [266] provide data on a WIMP search with an exposure of 577 kg days, and threshold of $E_{\rm th} = 1.6$ keVnr. We take the efficiency from Fig.1 of [266], and neglect the energy resolution since it is very small. In total 11 events were detected. ER events are removed as they constitute a large background, hence SuperCDMS is only sensitive to NR.

3. Finally we consider the very recent results of CDMSlite [20], which achieved an extremely low energy threshold of 0.056 keV to ER, with an exposure of 70 kg-days. In this case spectral information is available as the data are split into four energy bins. We modify the likelihood ratio analysis to include multiple bins (see Sec.4.5.1). Since CDMSlite cannot distinguish ER from NR, we can consider constraints on both ER and NR.

These parameters are summarized in Tab.6.1, along with approximate number of SM events for ER and NR, both with and without the efficiency cut.

The signals from ER and NR inside detectors are usually different, in that they produce different amounts of electrons or photons per unit recoil energy. Thus the signal from the detector actually defines two energy measures, those for an electron recoil of energy $E_{\rm er}$, in units $\text{keV}_{\rm ee}$ and those for a nuclear recoil of energy $E_{\rm nr}$ is units of $\text{keV}_{\rm nr}$. For a given window in $E_{\rm nr}$, the corresponding window in $E_{\rm er}$ is usually at lower energies. We will now provide some approximate formuale for converting between the two.

In SuperCDMS and CDMSlite, the total phonon energy is given by,

$$E_T = E_R + N_{\rm eh} e V_b \ , \tag{6.5.19}$$

where $E_R \equiv E_{\rm nr,er}$ is the recoil energy of either electron or nuclear recoils, $V_b = 69$ V is the voltage across the detector, and $N_{\rm eh}$ is the charge collection, given by $N_{\rm eh} = E_R Y(E_R)/\epsilon_\gamma$, and $1/\epsilon_\gamma = 0.3\ \text{eV}^{-1}$ is the number of charges collected per unit energy. For electron recoils the ionization yield $Y = 1$, whereas for nuclear recoils it parametrises the quenching,

$$Y(E_{\rm nr}) = \frac{kg(\epsilon)}{1 + kg(\epsilon)} \ , \tag{6.5.20}$$

where $k = 0.133 Z^{2/3} A^{-1/2} \sim 0.157$ is the Lindhard factor for Germanium, $\epsilon = 11.5(E_{\rm nr}/\text{keV})\text{Z}^{-7/3}$, and $g(\epsilon) = 3\epsilon^{0.15} + 0.7\epsilon^{0.6} + \epsilon$. In SuperCDMS the energy window $E_{\rm nr} \in [1.6, 10]$ keV is equivalent to $E_{\rm ee} \in [0.3, 2.4]$ keV.

For liquid scintillator experiments such as LUX, the electron recoil and nuclear

Ref.	LUX [268]	SuperCDMS [266]	CDMSlite [20]
$E_R^{(\mathrm{NR})}$ ($\mathrm{keV_{nr}}$)	1.1-25	1.6-10	0.37-63
$E_R^{(\mathrm{ER})}$ ($\mathrm{keV_{ee}}$)	0.17-5.8	0.3-2.4	0.056-20
Exposure (kg·days)	1.4×10^4	577	70
$N_{\mathrm{TOT}}^{(\mathrm{SM,ER})}$ (pp ν)	0.74 (4.9×10^{-5})	0.012 (3.7×10^{-4})	0.013 (6.5×10^{-3})
$N_{\mathrm{TOT}}^{(\mathrm{SM,NR})}$ (^{8}B ν)	2.8 (0.081)	0.098 (0.0091)	0.039 (0.020)
$N^{(\mathrm{obs})}$	-	11	0

Table 6.1: Parameters of current generation experiments; the energy window is given for both electron equivalent energy and nuclear recoil energy. Also given; the exposure, and the total SM event yield for ER (pp neutrinos) and NR (^8B neutrinos), the numbers in brackets include the efficiency $\epsilon(E_R)$ which has a substantial effect.

recoil deposited energies are given by [166, 305] [2],

$$E_{er} = w(n_\gamma + n_e) \ , \tag{6.5.21}$$

$$E_{nr} = w(n_\gamma + n_e)/\mathcal{L} \ . \tag{6.5.22}$$

The *Lindhard factor* $\mathcal{L}$ is the same as the ionization yield in Eq. (6.5.20) and is interpreted as the fraction of nuclear recoil energy transferred to electrons or 'quenching' of the NR signal, generally this is very low $< 20\%$ and most of the recoil energy is lost as heat. We find the electron equivalent energy $E_{er} = \mathcal{L} \times E_{nr}$ using the same Lindhard model as for CMDS.

[2] An 'event' in the detector is characterized by the signals S_1, S_2. The production scintillation photons ($n_\gamma = S_1/g_1$) and ionization electrons ($n_e = S_2/g_2$) from collisions with the liquid xenon requires an average energy of $w = 13.7 \pm 0.2$ eV.

6.6 New Physics in Future Generation Experiments

The next decade will be an exciting time for DD experiments, with the next generation soon to be built and begin data taking. We have created an idealized set of second generation (G2) and future generation (beyond G2) detectors, defined simply by their material, exposure, and threshold. These are listed in Tab.6.2.

Since many of the results are strongly dependent on the energy threshold for nuclear recoil events, we allow for an optimistic threshold as well as a nominal one. Our idealized Ge and Si experiments are representative of SuperCDMS [20], our idealized G2-Xe is similar to LZ [306], with a possible upgrade to Future-Xe, the Future-Ar is similar to DARWIN [307] and finally we explore the possibility of a very light target (Neon) which could have an extremely low threshold if the technology becomes feasible.

The constraints are plotted in the plane $m_{\phi,Z'}$-g. Since we consider each coupling $g_{l,i=\{s,p,v,a\}}$ separately, $g \equiv \sqrt{g_{f,i} g_{\nu,X}}$ where $f = q, l$ and $X = \phi, Z'$. These results are summarized in Fig.6.5.

The first thing to notice is that constraints based on ER tend to be stronger, due to their dominant statistics, since they are sensitive to pp neutrinos. However, despite the fact that nuclear recoils are sensitive to the much lower flux of ^8B neutrinos, the coherent enhancement ($\propto A^2 \sim 10^4$) in the case of vector and scalar mediators does compensate somewhat for the loss of neutrino flux.

The shape of the exclusion limits in Fig.6.5 can be understood again from the propagator $\sigma \propto (2 m_T E_R + m_X^2)^{-2}$; for heavy mediators the event rate scales as $N_{\rm TOT} \propto (g/m_X)^4$, and the constraint is linear in the $\log g - \log m_X$ plane. On the other hand when the mediator is light, the mass can be neglected in the event rate since it appears only in the propagator. Then $N_{\rm TOT} \propto g^4$ the constraint is a plateau

Experiment	ϵ (ton-year)	$E_{th,n}$ (keV)	$E_{th,o}$ (keV)	E_{max} (keV)	$R(pp)$	$R(^8\mathrm{B})$	$R(\mathrm{CNO})$
G2-Ge	0.25	0.35	0.05	50	–	[62 – 85]	[0 – 3]
G2-Si	0.025	0.35	0.05	50	–	[3 – 3]	0
G2-Xe	25	3.0	2.0	30	[2104 – 2167]	[0 – 64]	0
Future-Xe	200	2.0	1.0	30	[17339 – 17846]	[520 – 10094]	0
Future-Ar	150	2.0	1.0	30	[14232 – 14649]	[6638 – 12354]	0
Future-Ne	10	0.15	0.1	30	[1141 – 1143]	[898 – 910]	[21 – 63]

Table 6.2: Physical properties of idealized G2 (top 3 lines) and future experiments, with the expected total *pp* and ^8B neutrino events, based on planned masses of similar experiments and an exposure of 5 years. We give nominal and optimistic threshold energies and maxima for the energy windows based on the energy beyond which backgrounds are expected to dominate.

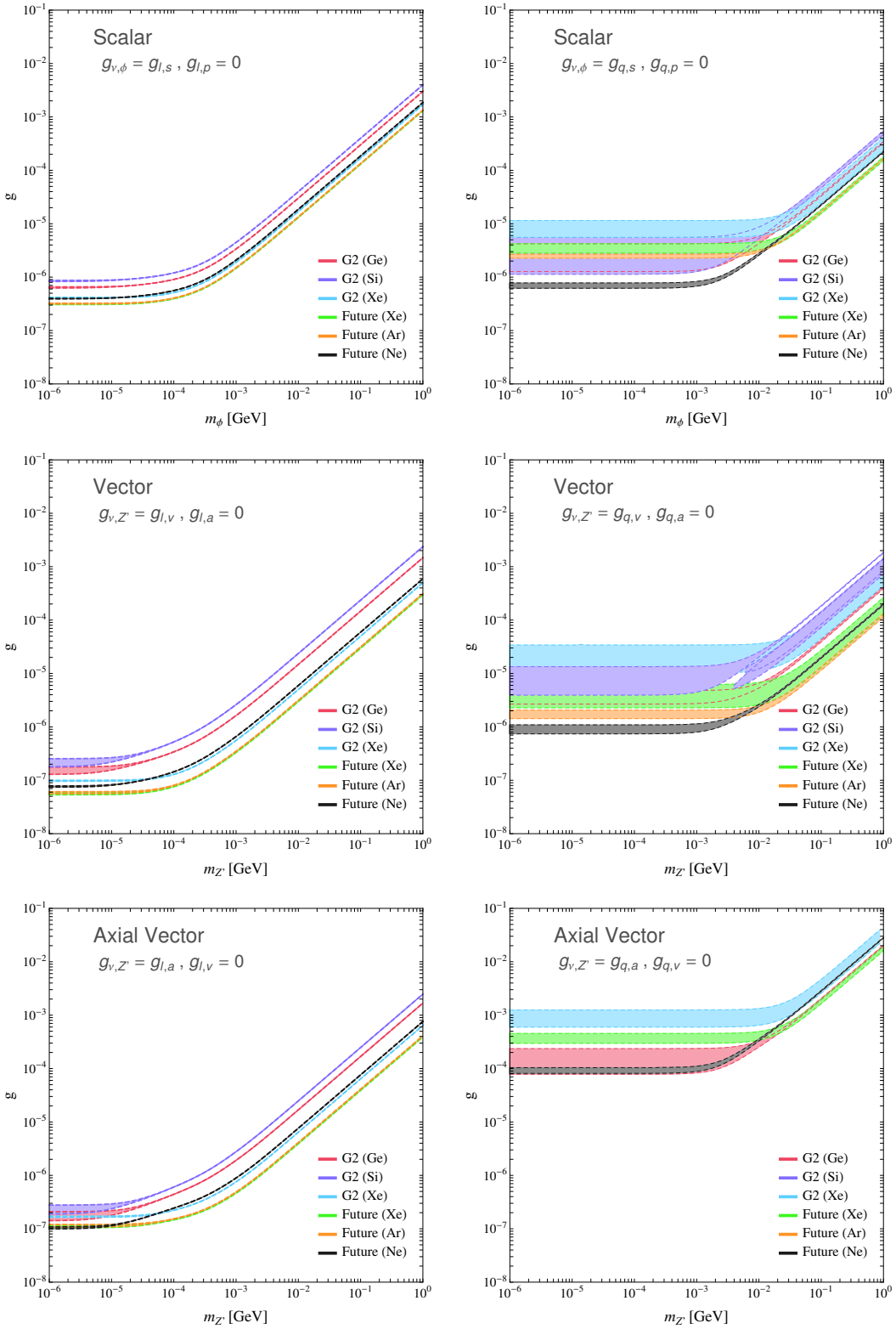

Figure 6.5: Electron recoil (left) and nuclear recoil (right) limits. Top: scalar coupling; middle row: vector coupling; lower panels: axial-vector coupling.

in the $\log g - \log m_X$ plane,

$$m_X \gg \sqrt{2m_T E_R} \quad : \quad N_{\rm TOT} \propto \left(\frac{g}{m_X}\right)^4 , \tag{6.6.23}$$

$$m_X \ll \sqrt{2m_T E_R} \quad : \quad N_{\rm TOT} \propto \left(\frac{g}{\sqrt{m_T E_{\rm th}}}\right)^4 . \tag{6.6.24}$$

The two regions meet at $m^2_{\phi,Z'} \approx 2m_T E_{\rm th}$, and so for electron recoils this occurs at a lower mass. Consequently the NR constraints can be more powerful at higher masses.

Since at low mass $N_{\rm TOT} \propto E_{th}^{-2}$, the depth of the plateau is controlled by the threshold energy of the experiment. In electron recoils there is little sensitivity to decreasing the threshold, because even for moderate threshold values the lowest energy solar neutrinos are already accessible. Since the constraints are controlled by the large statistics of the ER, the most powerful detectors are those with the largest exposure; in this case the large liquid scintillator experiments.

On the other hand, nuclear recoils are extremely sensitive to the threshold choice, and the coloured bands which represents the region between nominal and optimal thresholds is much larger. For many materials, reducing the threshold allows experiments to access CNO neutrinos, and since the event rate rises very steeply with decreasing energy, the detectors with the lowest thresholds tend to lead to more powerful constraints.

One must be careful when considering the vector interaction, as there are certain parameter choices in which the interference between the Z-Z' cancels the contribution from the Z' diagram. This can be seen clearly in the silicon NR (purple band), where a thin strip of parameter space cannot be excluded.

To put these results in context we list a number of other existing constraints from the literature,

1. **Electron or Muon Magnetic Moment**; The anomalous magnetic moment

of the electron or muon, $a_{e,\mu}$[3], is obtained from the one-loop correction to the QED vertex. If a coupling of the new mediator to leptons is present (independent of any neutrino coupling) then it contributes at the one loop level. Formulae for the contribution for each of our models can be found in [308], and this allows us to produce bounds for each model. The bounds are quite strong due to the impressive precision of the measurements [241, 309]

$$a_e^{\text{exp}} = 0.00115965218073(28) \ , \tag{6.6.25}$$

$$a_\mu^{\text{exp}} = 0.00116592091(54) \ . \tag{6.6.26}$$

2. **Solar Constraints** [310]; If the new mediator is spin-1, then mixing with the SM photon can lead to production of Z' in the Sun, particularly resonant production by plasmons for $m_{Z'} \sim 100$ eV, the observed solar luminosity then limits the possible energy loss from Z'. These constraints rely on a tree level kinetic mixing $\epsilon F^{\mu\nu} Z'_{\mu\nu}$ and thus do not require couplings to the lepton or quark sector. Wherever the Z' couples to charged fermions the kinetic mixing operator is generated at 1-loop. The scalar and pseudo scalar mediators cannot mix with the photon and in these cases the constraints are absent.

3. **Atomic Physics** [311]; Electron transitions in atoms can safely be described using non-relativistic (NR) physics, and dominated by a Coulomb potential which can be derived from the NR limit of QED electron-electron scattering,

$$V(r) = \frac{e^2}{4\pi r}\left(1 + \beta e^{-r/\lambda}\right) \ , \tag{6.6.27}$$

β, λ arise from new physics effects and can be searched for in precisely measured electron transitions. In our models $\beta = g_{e,\{s,v\}}/e^2$ and $\lambda = 1/m_X$ with $X = \phi, Z'$. Axial vector and pseudoscalar interactions lead to different r dependence than that considered above, and consequently the bounds apply only to scalar and vector mediators.

[3]This is the deviation of the magnetic moment from its tree level value $a = (g-2)/2$ where the Dirac equation gives $g = 2$, currently the measured anomalous muon magnetic moment deviates from its SM prediction by several σ.

4. **Supernovae** [312]; During a supernova, energy may be lost by the production of Z' (via bremsstrahlung from protons, since the mediators couple to charged particles only) which subsequently escape the explosion. The luminosity of the Z' should not exceed the luminosity in neutrinos (which has been measured from supernova 1987a). Large couplings are not excluded, since the Z' rapidly decays to SM particles which remain in the supernovae, or the Z' itself is trapped. Although derived with kinetic mixing in mind, ultimately these bounds only require a coupling to quarks.

5. **Fixed Target** [313], A1 [314], APEX [315]; In electron-positron colliders, an electron beam dump can produce both ϕ and Z', which are radiated by an electron passing near a proton. The radiated boson may then decay into an electron-positron pair, whose invariant mass produces a resonance feature at the mass of the boson. It should be noted that these constraints are based on formulae which are valid for spin-0 as well as spin-1 bosons, however one should be careful with the high coupling end of the limits [316], since these depend on the total width of the boson, and assume a 100% BR into electrons,

$$g_{\nu,X} g_{e,i} = \frac{\epsilon^2 e^2}{\mathrm{BR}(\mathrm{X} \to \mathrm{e^+ e^-})}, \tag{6.6.28}$$

where $X = \phi, Z'$, and since these limits are based on the formalism of [313], they apply equally well to $i = s, p, v, a$.

6. **Fixed Target** e^+e^- **Collider**: The BaBar experiment [317] produce bounds on the process $e^+e^- \to \gamma Z'$, $Z' \to e^+e^-$, $\mu^+\mu^-$, for which the cross section $\sigma \propto \mathrm{Br}(Z' \to l^+l^-)$ where $l = e, \mu$. We can rescale the given constraints on the kinetic mixing coupling, ϵ by,

$$g_{Z',\nu} g_{e,Z'} = \frac{\sum_l \mathrm{Br}(Z' \to l^+l^-)}{\sum_l \mathrm{Br}(Z' \to l^+l^-)_{\mathrm{kin.}}} e^2\epsilon^2 \ . \tag{6.6.29}$$

where the denominator assumes only the kinetic mixing operator is present, the width can be approximated by

$$\Gamma_{\mathrm{kin.}} = \alpha\chi^2 m_{Z'} \left(3 \cdot \frac{1}{3} + R\frac{1}{3}\right) \ , \tag{6.6.30}$$

$$\Gamma_{Z'} = m_{Z'} \left(3 \cdot g_{l,v}^2 + R g_{q,v}^2 + 3 g_{\nu,Z'}^2\right) . \tag{6.6.31}$$

In kinetic mixing the ν-Z' interaction is highly suppressed since it arises from loop diagrams, in general (as in our models) there may be a tree level contribution. Then we may apply additional bounds from BaBar which are derived in [318] for a mono-photon plus missing energy search f($e^+e^- \to \gamma \not{E}$) where the missing energy comes from the decay of the Z' to light Dark Matter states, but this is equally applicable to neutrino states. The bounds are on g_e and may be converted to our couplings via

$$g_e^2 = g_{e,Z'} g_{\nu,Z'} \mathrm{Br}(Z' \to \nu\bar{\nu}), \tag{6.6.32}$$

since the Z' is assumed to have a 100% branching ratio (BR) into DM. In our models we must take the BR into neutrinos only, and is $Br(Z' \to \nu\bar{\nu}) \sim 1/9{-}1$. Constraints show little variation between a spin-0 or spin-1 mediator.

7. **Borexino** [14, 319] : Borexino is a liquid scintillator neutrino detector located in Gran Sasso, Italy, measuring ER (and thus requiring a coupling to electrons), with a good sensitivity to the recoil energy, along with a published spectrum of backgrounds (mostly from β-decay of radioactive elements). The energy window $E_R \in [165, 590]$ keV is mostly sensitive to ^{7}Be neutrinos, with a small sensitivity to the high energy tail of the pp neutrinos. The fiducial volume (mass) is 86 m^3 (75.5 ton), and the material is roughly 100% 1,2,4-trimethylbenzene (C_9H_{12}, 120.19 g/mol). For the detector resolution we take $\sigma(E) = 0.86\sqrt{E}$ with E in keV, from Chapter 5 of [320] (Eq.(5.138)). In Fig.6.7 we show the expected event rate and background sources for the most recent analysis [14] (408 live days between 2012-2013), for the SM and with a Z'. The predicted rate does not quite match the data since we are using flux normalizations from simulations, whereas Borexino fits the normalization to the data. The resulting constraints for each of the mediators are shown below. These show a significant improvement over previous studies [15] which use earlier data [321], plus do not use spectral information (requiring only an overall increase in the total event yield above the SM of $< 8\%$).

8. **SuperKamiokande III (SK)** [322] : The SK experiment (Japan) is a neu-

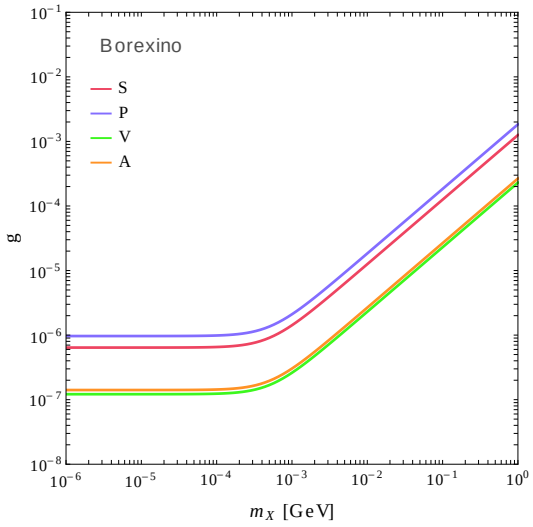

Figure 6.6: Constraints (90% confidence limits) on new physics from the Borexino neutrino detector, calculated using a $\Delta\chi^2$ method.

trino detector, phase III was completed between 2005-2007.[4] We use data from phase III (from Fig.8.6 of [324]), which has been corrected for efficiencies. Comparing theory to data requires including the detector resolution to achieve a sufficient accuracy; this is given by [322],

$$\frac{\sigma(E)}{[\text{MeV}]} = -0.123 + 0.376\sqrt{E} + 0.0349, \tag{6.6.33}$$

as with Borexino, only the electron scattering contributes to the signal, which is shown in Fig.6.8. The resulting exlcusions (below, Fig.6.9) are weaker than those from Borexino by an order of magnitude.

To put these constraints on a solid theoretical footing, we will use the well studied *gauged B-L model* because it is a trivial extension of our simplified model. In the SM there are large flavour symmetries in the quark and lepton sector ($U(5)^4$), which are broken by the mass (Yukawa) terms for the fermions. However there still remains the global $U(1)$ symmetries *Baryon number* (B) and *Lepton number* (L), in which all the quarks are assigned the same B-number (conventionally 1/3) and zero L; and the leptons are assigned the opposite L number to their corresponding neutrinos and zero B charge.

[4] more recent studies have been published since the completion of this work [323]).

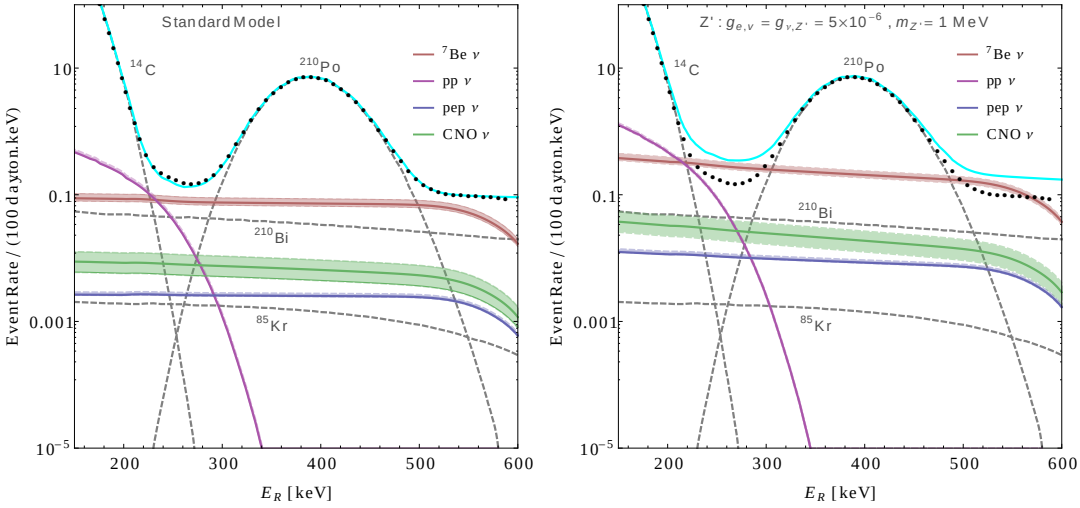

Figure 6.7: The expected neutrino event rate (cyan line) in Borexino for the SM (left) and for a benchmark set of parameters in the Z' model (right). The dominant backgrounds (dashed lines) are taken from [14], the signal (solid lines) are separated according to the neutrino source, and the experimental data shown as black dots without the rather small error bars.

In principle one may gauge these symmetries, however gauging B or L individually introduces anomalies and thus leads to a sick theory. However, the combination B-L is anomaly free and thus can be gauged; leading to the introduction of a new vector gauge boson which couples to the B-L charge and which thus permits the nuclear-ν and electron-ν scattering. The gauge boson is identical to our Z' with couplings to quarks a factor of 3 smaller than to leptons.

Many of the constraints listed above apply to the B-L model, and these are shown in Fig.6.10, alongside the ER and NR constraints for Xe and Ge targets (from Fig.6.5). We also show the current generation DD constraints from Fig.6.5. The constraints are competitive with the existing constraints which detect the neutrino scattering[5], and actually rule out new parameter space at ~ 100 MeV masses.

[5]Note that the Borexino constraints are from Ref.[15] and are weaker than those derived in this section.

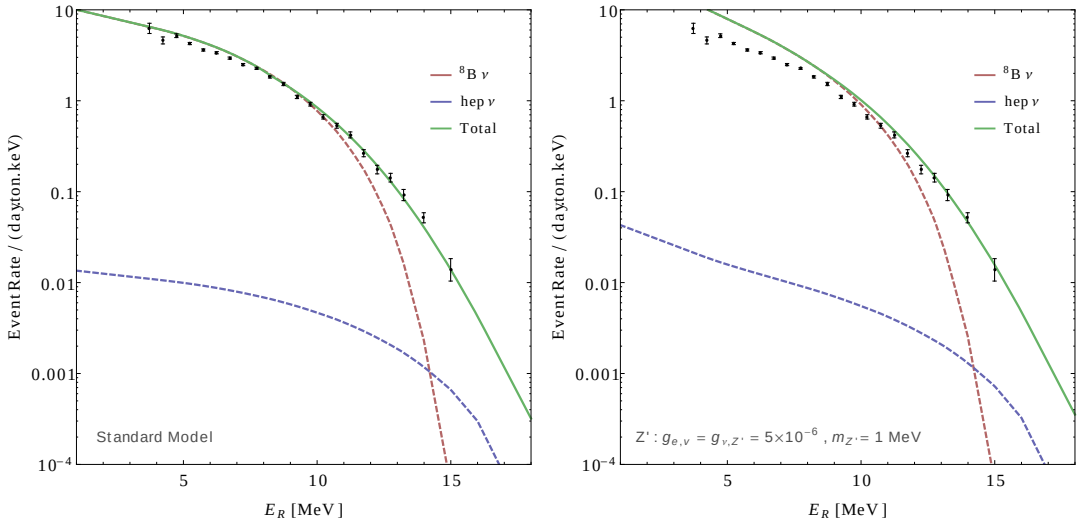

Figure 6.8: The expected neutrino event rate (solid green) in SuperKamiokande for the SM (left) and for a benchmark set of parameters in the Z' model (right). The signal (dashed lines) are separated according to the neutrino source, and the experimental data shown as black dots with error bars with background and efficiencies removed.

6.7 Conclusions

In this study, we have analysed the discovery potential for a broad range of BSM physics which might couple the neutrino sector of the SM to the rest of the fermions (leptons and quarks), by exploiting the scattering of neutrinos in future generation Direct Detection (DD) experiments. We simultaneously analyse the exclusions provided by the current generation of experiments.

Following discussions in Chapter 2, we have used *simplified models* in which we model the new physics as simply as possible (as neutral scalar like and vector like mediators). We have clarified under what conditions each type of new physics is most detectable, or conversely, which of the future experiments is best suited to each case. For example, electronic recoils (ER) provide much greater sensitivity across all experiments at low mass mediators compared with nuclear recoils (NR). This rather general statement emphasises that recording of electronic recoils not only reduces background significantly (its main goal), but allows some powerful constraints to be imposed.

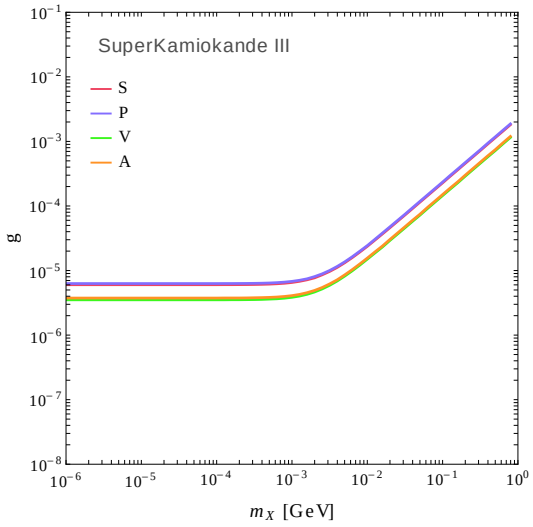

Figure 6.9: Constraints (90% confidence limits) on new physics from the SK III data, calculated using a $\Delta\chi^2$ method.

Fig.6.10 highlights many of these results in a concrete model (gauged B-L), showing the complimentary exclusion regions from the electronic recoil (ER) and nuclear recoil (NR) along with other constraints which can be found in the literature including self-made constraints for current generation DD experiments LUX, SuperCDMS and CDMSlite which we take as representative of the most constraining current DD data.

The future generation, and even current generation DD experiments can uniquely exclude some part of parameter space, and complimentarily exclude others. They have the novel aspect of excluding arbitrarily small mediator masses, unlike many other techniques. This work demonstrates that the neutrino floor, far from being an impenetrable background to limit the search for dark matter, can yield interesting bounds on new physics, and even be used to improve knowledge of the solar neutrino fluxes [1].

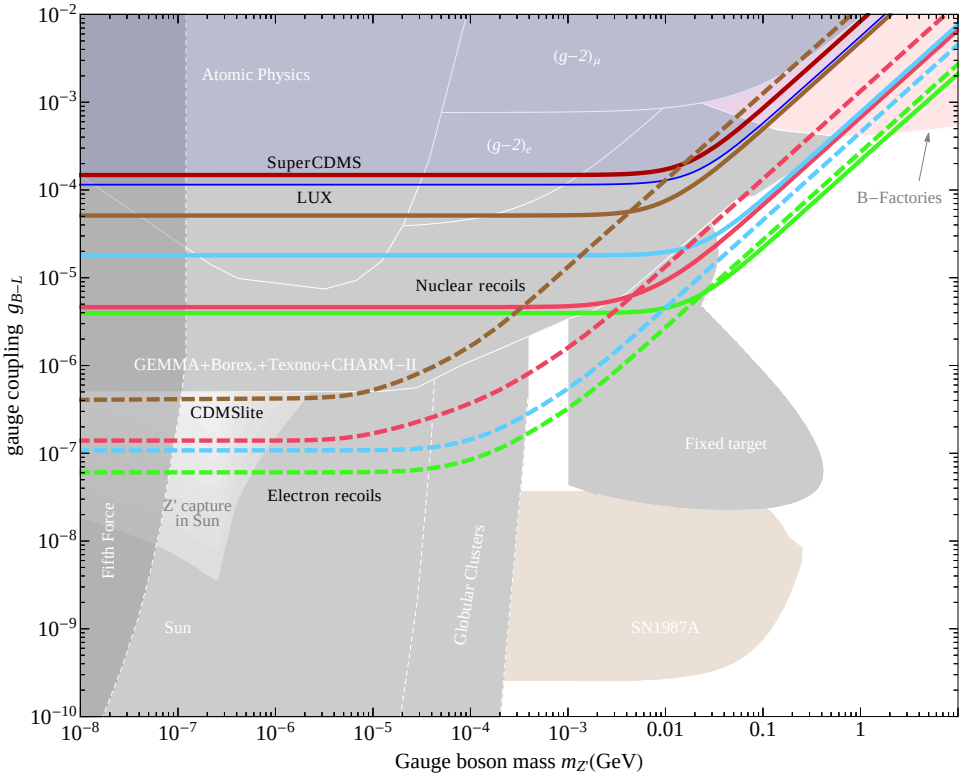

Figure 6.10: Projected 90% CL constraints on the B-L model for nuclear recoils (solid lines) and electron recoils (dashed) in the optimistic scenarios for G2 germanium (red), G2 xenon (blue) and future xenon (green). We also show approximate bounds derived from the current SuperCDMS (red line), CDMSlite (brown solid and dashed lines), and LUX data (blue shaded region). Our bounds are overlaid on existing constraints. To translate these bounds to the other possible scenarios, one should keep in mind that some bounds (intermediate grey) only apply when the new mediator couples to leptons. The supernova bound (brown) only applies to couplings to baryons, while B-factory bounds (pink) require both. The fifth force constraint (dark grey) applies in either case. The grey regions, the neutrino scattering bound and the pink region, and the supernova limits are respectively taken from [15–17].

Chapter 7

Charming Dark Matter

Whereas previous chapters have focussed on breadth of models covering a large group of DM candidates, we now focus more deeply into one particular model (this will be closely related to the model 1/2*-$S^{\pm}$ of Chapter 2).

This chapter will improve on many aspects which were not addressed in the general model analysis of Chapters 2-5. In particular :

- We explore a model which is fully invariant under the SM gauge symmetries, in particular $\mathrm{SU}(2)_L$ meaning that the model is valid above the EW scale.
- The model contains some interesting new phenomenology, including a triplet of DM candidates coupled to the three quark generations. We parametrize the breaking of the SM flavour symmetry explicitly.
- We explore several additional constraints, including gamma ray lines, *electroweak precision observables* (EWPO), decay widths of EW particles, mixing and rare decay flavour bounds and collider bounds. The latter requires the full width of the mediator.

One important aspect that we did not specifically address was the usage of simplified models in which the DM couples only to a single flavour of quark, explicitly breaking the assumption of *minimal flavour violation* (MFV). Given the remarkable agreement between the SM and experimentally measured flavour observables it is

natural for new physics models to enforce the MFV assumption to suppress large NP effects. This assumption limits any quark flavour breaking terms to be at most proportional to the Yukawa couplings, which are responsible for the small violation of the flavour symmetry in the SM. This suppresses *Flavour Changing Neutral Currents* (FCNCs) and avoids strong constraints from rare decays and neutral meson mixing. Nonetheless, many such observables are not reproduced by SM calculations and then allow room for violations of MFV, for example D^0 mixing.

Recent studies of simplified models have begun to go beyond the MFV assumptions. This has been done in the context of down-type couplings [325, 326], leptonic couplings [327], and more recently top-like couplings [328]. There is yet to be a study of up-type couplings. Such models allow a continuous change from the MFV assumption to strong MFV breaking and can quantify the degree of breaking permitted by the flavour constraints.

Our aim in this chapter is to investigate *Dark Minimal Flavour Violation* (DMFV) in the context of up-type couplings, thus extending the work of [326, 328], and to present statistically robust bounds based on a *markov chain monte carlo* (MCMC) approach. By violating the MFV assumption in the up-type quarks we would expect to find constraints from neutral charm meson (D^0) mixing as well as rare decays of the charm meson, as well as strong constraints from direct and indirect detection and collider searches. After outlining the details of the models in Sec.7.1, we will present some important aspects of the model which arise due to the multiplet of DM such as the decay widths and mass splitting generated through RG effects (Sec.7.2), before moving on to a robust calculation of bounds:

- **Relic Density**, Sec.7.3 : We calculate the relic density of all three DM particles, including their widths and coannihilations and by solving the Boltzmann equation explicitly. The discussion supplements Chapter 1.
- **Flavour Constraints**, Sec.7.4 : We provide bounds on the model from D^0 mixing, ensuring that the new physics does not exceed 1σ of the experimental measurement of the mass difference between the heavy and light state of the

D^0. We assess the possibility for constraints on rare decays but find that the NP is essentially unconstrained in the region of interest.

- **Indirect Detection**, Sec.7.5 : We include a large collection of constraints from the literature on the thermally averaged annihilation cross section $\langle \sigma v \rangle$ for annihilation into photons, electrons, protons etc. . We also include a study of gamma ray line searches, generated through loop diagrams, however these do not provide strong bounds.

- **Direct Detection**, Sec.7.6 : We calculate the event rate for the most excluding DD experiments (LUX and CMDSlite) covering the full DM mass range, including all relevant contributions up to one loop order (including gluon, photon, Z and h exchange) and matching to a full set of non-relativistic form factors.

- **Collider Searches**, Sec.7.7 : We perform a robust simulation of the dominant signals for a series of monojet, dijet and stop searches for ATLAS and CMS.

- **Other Constraints**, Sec.7.8 : We compute several other constraints which are not found to be powerful, for example perturbative unitarity for the $2 \to 2$ scattering process between the DM and mediator states, electroweak precision observables (i.e. the constribution of the NP to the Z, W parameters of the SM), Higgs and Z decay widths.

Including the various constraints named above we can carry out an MCMC scan over the parameter space, extending the scans to several possible future scenarios. Results are collected in Sec.7.9.

7.1 DMFV : The Model

The SM (without Yukawa couplings) has a flavour symmetry amongst the quarks, there are no flavour violating effects such as *Flavour Changing Neutral Currents* (FCNC) at tree level. Including the Yuakwa terms, which give the fermions their mass, breaks this symmetry since it mixes LH and RH fields, and thus flavour changing effects are proportional to the quark masses. *Minimal flavour violation* (MFV)

is then the statement that the only flavour symmetry breaking terms in the BSM model are either absent or proportional to the Yukawa terms [329].

In the model of *Dark Minimal Flavour Violation* (DMFV) originally proposed in [325], the SM flavour symmetry is increased by the inclusion of a U(3) symmetry in the dark sector,

$$\mathcal{S}_{\text{flavour}} = \mathrm{U}(3)_{Q_L} \times \mathrm{U}(3)_{u_R} \times \mathrm{U}(3)_{d_R} \times \mathrm{U}(3)_{\chi}, \tag{7.1.1}$$

the $\mathrm{U}(3)_{\chi}$ symmetry is then broken by the inclusion of a single complex 3×3 coupling matrix, λ, which also breaks one of the SM U(3) flavour symmetries. The charges of all the fields are given in Fig.7.2. In the original work $\mathrm{U}(3)_{d_R}$ was broken [325]. In this work we break instead $\mathrm{U}(3)_{u_R}$, and leave the $\mathrm{U}(3)_{Q_L}$ symmetry unbroken to avoid introducing non-trivial transformations for the new fields under $\mathrm{SU}(2)_L$. The interaction Lagrangian reads[1],

$$\mathcal{L}_{\text{int}} = -(\lambda_{ij}\bar{u}_{R,i}\chi_j\phi + \text{h.c.}) \ , \tag{7.1.2}$$

with Feynman rules in Fig.7.1. Using a singular value decomposition λ may be written as,

$$\lambda = U_\lambda D_\lambda V_\lambda, \tag{7.1.3}$$

the 18 free parameters of λ (9 real and 9 complex phases) are accounted for by the diagonal matrix D with real positive entries (3) and the unitary matrices U, V (3 real and 6 complex phases each).

Three of the phases of U (or V) may be removed by a rephasing. Additionally, the $\mathrm{U}(3)_{\chi}$ symmetry produces an invariance under $\chi_i \to U^{\chi}_{ij}\chi_j$ with U^{χ} a unitary matrix, this can be used to completely remove V leaving 6 real parameters and 3 phases,

[1] The kinetic and mass terms are the same as in Eq.(2.2.5),(2.2.3)

$$U_\lambda = \begin{pmatrix} c_{12}c_{13} & s_{12}c_{13}e^{-i\delta_{12}} & s_{13}e^{-i\delta_{13}} \\ -s_{12}c_{23}e^{i\delta_{12}} - c_{12}s_{23}s_{13}e^{i(\delta_{13}-\delta_{23})} & c_{12}c_{23} - s_{12}s_{23}s_{13}e^{i(\delta_{13}-\delta_{12}-\delta_{23})} & s_{23}c_{13}e^{-i\delta_{23}} \\ s_{12}s_{23}e^{i(\delta_{12}+\delta_{23})} - c_{12}c_{23}s_{13}e^{i\delta_{13}} & -c_{12}s_{23}e^{i\delta_{23}} - s_{12}c_{23}s_{13}e^{i(\delta_{13}-\delta_{12})} & c_{23}c_{13} \end{pmatrix}, \tag{7.1.4}$$

$$D_\lambda = \begin{pmatrix} D_{11} & 0 & 0 \\ 0 & D_{22} & 0 \\ 0 & 0 & D_{33} \end{pmatrix} . \tag{7.1.5}$$

The presence of complex couplings ($\delta_{ij} \neq 0$) creates a violation of CP symmetry, this is also permissible in the MFV assumption, so long as the complex phases are flavour-blind[329]. Due to the stringent constraints from electric dipole moments (EDM) in the presence of CP violation we will set $\delta_{ij} = 0$ throughout.

Since D_λ is diagonal, with real positive entries, and U_λ is unitary then,

$$\lambda^\dagger\lambda = (D_\lambda U_\lambda^{-1})(U_\lambda D_\lambda) = (D_\lambda)^2, \tag{7.1.6}$$

is diagonal, however $\lambda\lambda^\dagger$ is not diagonal unless $D_{11} = D_{22} = D_{33}$.

In total we have a 10 dimensional parameter space

$$\{m_{\chi_1}, m_{\chi_2}, m_{\chi_3}, m_\phi, \theta_{12}, \theta_{13}, \theta_{23}, D_{11}, D_{22}, D_{33}\} , \tag{7.1.7}$$

with degenerate DM masses (or relations amongst the masses) this reduces to 8. The masses are unbounded, but for a perturbative theory we require $\lambda_{ij} < 4\pi$ given that θ_{ij} vary between 0 (no mixing) and $\pi/4$ (maximal mixing) this places limits on D_{ii},

$$\theta_{ij} \in [0, \pi/4] , \ D_{ii} < 4\pi, \tag{7.1.8}$$

we will additionally focus on models where $m_\chi, m_\phi \gtrsim 1$ GeV, so that the DM is a conventional WIMP candidate and the mediator is sufficiently heavy to decay to at least the up and charm quarks.

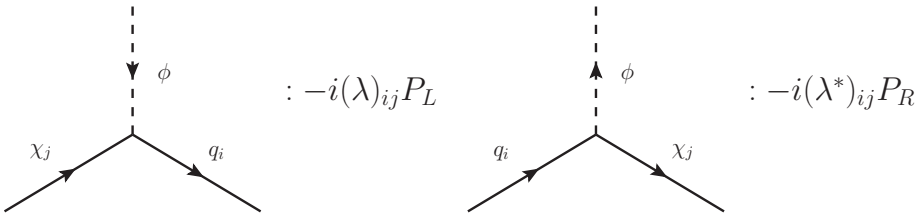

Figure 7.1: Feynman rules for the DMFV interaction (Eq.(7.1.2)).

	$\mathrm{U}(3)_{u_R}$	$\mathrm{U}(3)_\chi$	$\mathrm{SU}(3)_c$	$\mathrm{U}(1)_Q$	$\mathrm{U}(1)_Y$
$u_{R,i}$	**3**	**1**	**3**	2/3	2/3
χ_i	**1**	**3**	**1**	0	0
ϕ	**1**	**1**	**3**	2/3	2/3
λ_{ij}	**3**	$\bar{\mathbf{3}}$	**1**	0	0

Figure 7.2: The representation for the relevant symmetries of the particles introduced in the DMFV model. All of the particles are singlets under $\mathrm{SU}(2)_L$ and the other flavour symmetries not listed.

Although the masses of the DM fields and mediator field are in principle arbitrary free parameters, one must impose $m_{\chi,\min} < m_\phi + m_q$ (with m_q the lightest quark coupled to minimal mass χ) to prevent a tree level decay $m_\chi \to \phi + q$ which would quickly remove the DM relic abundance. In models coupled only to the top $m_\chi \gtrsim 170$ GeV. In models coupled to u, c then $m_\phi \gtrsim m_\chi$. Similarly we must have $m_\phi > m_{\chi,\min} + m_q$, where m_q is the lightest quark to which $m_{\chi,\min}$ couples; this ensures the mediator is prevented from obtaining a relic abundance and itself being a DM candidate.

It can be shown that a residual $\mathbb{Z}_3$ symmetry exists in the model [77, 325], which prevents either χ or ϕ to decay purely into SM particles. This useful symmetry argument ensures the relic DM (the lightest of the three) is completely stable subject to the condition in the previous paragraph. It is possible for the heavier χ fields to decay to the lightest χ (DM), this would only be relevant at cosmologically early times, before thermal freeze out occurs and it will be shown that the rate of such

decays is large enough to erase the relic density of the heaviest two DM.

7.2 DMFV : Renormaliation and Mass Splitting

7.2.1 Particle Widths

It is important to consider the decay widths of the DM and mediator. We ensure that the mediator is unstable and undergoes a two-body decay to at least one of the DM candidates, this is important to prevent a stable ϕ acquiring a relic density, it is also important to have an accurate determination of the width for the collider signals which arise from the on-shell production and decay of the ϕ.

The heavy DM particles may undergo a three body decay into a lighter χ plus a quark anti-quark pair. This is an important effect in the relic density calculation in which 'large' decay widths leave only a single stable relic DM, but 'small' widths may allow the relic density to be distributed across two or three candidates. The resulting relic densities strongly influence direct and indirect signals, and so we seek to quantify the effect of the decay width by including it in the Boltzmann equation which yields the relic density.

The two-body decay width for a particle of mass M (into particles of mass $m_{1,2}$) is given by [330],

$$\Gamma = \frac{|\bar{p}|}{32\pi^2 M^2} \int |\mathcal{M}|^2 d\Omega, \tag{7.2.9}$$

with the outgoing momentum $\bar{p} = \sqrt{(M^2 - (m_1 + m_2)^2)(M^2 - (m_1 - m_2)^2)}/2M$.

Mediator Width

The scalar mediator ϕ may decay to DM-quark pairs, with squared matrix element,

$$\int |\mathcal{M}|^2 d\Omega = -N_c^2 \pi \sum_{ij} \lambda_{ji} \lambda_{ij}^{\dagger} \left(m_{\chi_i}^2 - m_{\phi}^2 + m_{q,j}^2 \right) \ , \tag{7.2.10}$$

and width,

$$\Gamma = \frac{N_c^2 m_\phi}{128\pi} \sum_{ij} \lambda_{ji}\lambda_{ij}^\dagger \left(1 - \delta_{\chi_i}^2 - \delta_{Q,j}^2\right) \left(1 - \delta_{\chi_i}^4 - \delta_{Q,j}^4 + 4\delta_{\chi_i}\delta_{Q,j} + 2\delta_{\chi_i}^2\delta_{Q,j}^2\right)^{1/2} \ , \tag{7.2.11}$$

with $\delta_{\chi_i} = m_{\chi_i}/m_\phi$ and $\delta_{Q,i} = m_{Q,i}/m_\phi$. This implies that $(\Gamma/m_\phi) \lesssim \frac{9}{128\pi}$, which is a very narrow resonance, similar in magnitude to the Z-boson.

The mediator width becomes relevant wherever the mediator is exchanged in the s-channel and can go on-shell. For indirect detection and the relic density calculation the exchange is t-channel, only for direct detection and some collider processes is the mediator exchanged in the s-channel. In the former, the COM energy $S \approx (m_\chi - m_q)^2$, and so for $|m_\chi - m_q| \sim m_\phi$ the mediator can go on shell and the width should be accounted for. This can be done using the *Briet-Wigner prescription* for the s-channel propagator,

$$\frac{i}{S - m_\phi^2} \to \frac{i}{S - m_\phi^2 + i m_\phi \Gamma} \ , \tag{7.2.12}$$

which is a good approximation so long as $\Gamma/m_\phi \ll 1$ [331, 332]. When the width becomes large the Briet-Wigner form of the propagator no longer holds and instead a 'fully kinetic' propagator is used

$$\frac{i}{S - m_\phi^2} \to \frac{i}{S - m_\phi^2 + i\frac{S}{m_\phi}\Gamma(S)} \ . \tag{7.2.13}$$

Dark Matter Width

As we have mentioned, the existence of a $\mathbb{Z}_3$ symmetry in the DMFV model ensures the absolute stability of the lightest DM candidate. However, the heavier candidates may undergo a three body decay, an example diagram is shown in Fig.7.3.

The DM width can be approximated by (where quark masses are neglected)[246]

$$\Gamma_{ij} = \frac{32}{(2\pi)^3 m_i^3} \sum_{lm} |\lambda_{li}\lambda_{mj}^*|^2 \theta(m_i - m_j - m_{q_l} - m_{q_m}) \int_0^{(m_i^2 - m_j^2)} dz \left[\sqrt{2\Delta_-(\Delta_- - \Delta_+)} + \frac{1}{2}(\Delta_+ - 2m_\phi^2) \log\left(\frac{\Delta_+ - 2m_\phi^2 - z - \sqrt{2\Delta_-(\Delta_- - \Delta_+)}}{\Delta_+ - 2m_\phi^2 - z + \sqrt{2\Delta_-(\Delta_- - \Delta_+)}}\right)\right] ,$$

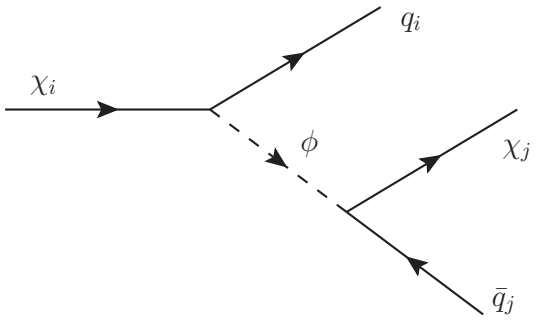

Figure 7.3: The dominant three body decay diagram for the heavy DM flavours.

where $\Delta_\pm \equiv (m_i^2 \pm m_j^2)$. In the limit that $\Delta_- \ll \Delta_+$,

$$\Gamma_{ij} \approx \frac{64\Delta_-^5}{15(2\pi)^3 m_i \Delta_+^4} |D_{ii}|^2 (\lambda\lambda^\dagger)_{jj} \ , \tag{7.2.14}$$

where the sum runs over all kinematically allowed final state quarks. If $m_j = m_i(1+\epsilon)$ with mass splitting $\epsilon < 1$ we can further approximate the decay rate,

$$\Gamma_{ij} \approx m_i \frac{16}{15\pi^3} \frac{\epsilon^5}{(1+\epsilon)^4} |D_{ii}|^2 (\lambda\lambda^\dagger)_{jj} \ . \tag{7.2.15}$$

7.2.2 Renormalization and Mass Splitting

In the Lagrangian Eq.(7.1.2) the DMFV hypothesis imposes a $\mathrm{U}(3)_\chi$ symmetry amongst the DM candidates, in particular for the mass term to be invariant the tree-level masses must be degenerate.

It is possible to keep the symmetry and still split the masses by an operator $\propto \lambda^\dagger\lambda = (D_{ii})^2$; since the $D_{ii} \leq 4\pi$ by perturbativity, this splitting can be made enormous, if the couplings are set differently for each quark generation. The degeneracy may also be broken by hand by directly inserting $\mathrm{U}(3)_\chi$ violating terms or assuming the existence of DMFV breaking terms at a high scale; again the splitting can be made arbitrarily large.

Even if we do not add Lagrangian terms by hand, it is inevitable that we will generate a mass splitting by quantum effects. Any symmetries imposed at tree level are liable to be broken at loop level unless they are gauge symmetries. The resulting

splitting can be most easily found by calculating the one-loop renormalization of the theory via the $\overline{\text{MS}}$ scheme. The masses acquire a scale dependence and run with energy, by assuming that the masses are degenerate at a high scale then they will be split by a possibly large amount at low energies.

The DMFV model introduces parameters m_ϕ, m_{χ_i} and couplings λ_{ij} as well as the associated fields. Each of these must be renormalized, and the quark masses and fields will also receive new contributions. We first briefly recall the primary features of the two most common renormalization schemes.

Renormalization : $\overline{\text{MS}}$ vs On-shell Scheme

We begin with a Lagrangian written in terms of *bare* quantities, including masses m_B, which are divergent at one loop[2]. After renormalization the finite renormalized mass, m_R, replaces it. No matter which renormalization scheme one chooses, the physical mass of the particle should not change. This physical, measurable, mass is also called the *pole mass*, m_P, since it corresponds to the pole in the propagator $(\not{p} - m_P)^{-1}$. To renormalize the mass at one loop one computes the 1PI two-point function $\Sigma_2(\not{p})$, which is schematically $\Sigma_2 = A\not{p} + Bm_R$, where A, B have in general both finite and divergent parts. Including counter terms for the mass and field renormalization, the complete 1PI amplitude is,

$$\Sigma_2(\not{p}) = \not{p} - m_R + \Sigma_2(\not{p}) - (\delta Z + \delta m)m_R + \not{p}\delta Z \ .$$

In the on-shell scheme we choose the counterterms so that the renormalized mass m_R is the pole of the propagator (i.e. the pole mass), this means the counter terms will include finite as well as divergent pieces. Because the physical (pole) mass is m_R, there is no mass running.

Alternatively, we can work in the $\overline{\text{MS}}$ scheme, which is defined by the requirement that the counter terms absorb only the divergent parts of the 1PI amplitude, and thus the propagator would be written $\Sigma_2 = \not{p} - m_R + \Sigma_{2,\text{finite}}(\mu)$, and the physical

[2]A subscript B will be used to denote bare quantities.

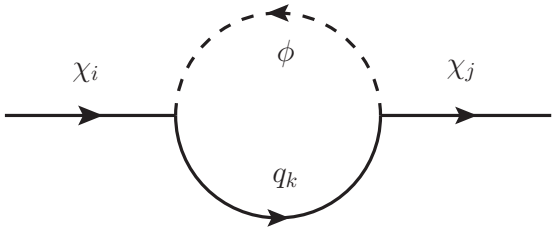

Figure 7.4: The one-loop contribution to the DM self-energy from the DMFV model.

(pole) mass does not coincide with the renormalized mass m_R, there is an extra finite term which has some scale dependence, and thus the mass runs

$$m_{\mathrm{P,on-shell}} = m_R \ ,$$
$$m_{\mathrm{P},\overline{\mathrm{MS}}} = m_R - \Sigma_{2,\mathrm{finite}}(\mu) \ .$$

We now carry out renormalization on the DMFV parameters. For the DM field we will use both schemes as an example, but restrict to $\overline{\mathrm{MS}}$ from then on. Divergences will be calculated using dimensional regularization in $D = 4 - 2\epsilon$ dimensions.

DM Field : (1) On-shell Scheme

Counter-term renormalization proceeds by defining $\chi_i = (Z_\chi^{ij})^{-1/2}\chi_{j,B}$ and $m_i = (Z_{m\chi}^{ij})(Z_\chi^{ij})^{-1}m_{j,B}$ for the renormalized parameters in terms of the bare parameters (denoted with a B) allowing a mixing between the kinetic and mass terms. The renormalized DM Lagrangian is written

$$\mathcal{L} = i\bar{\chi}_i\partial\!\!\!/\chi_i - m_{ii}\bar{\chi}_i\chi_i - i\delta_\chi^{ij}\bar{\chi}_i\partial\!\!\!/\chi_j + \delta_m^{ij}m_{ij}\bar{\chi}_i\chi_j, \tag{7.2.16}$$

where $i, j = 1, 2, 3$ and with,

$$\delta_m^{ij} = (\delta^{ij} - Z_m^{ij}) \ , \ \delta_\chi^{ij} = (\delta^{ij} - Z_\chi^{ij}),$$

these can be found by computing the two-point function for the DM, $i\Sigma^2(\not{p})$ [3], as shown in Fig.7.4 over the k quark flavours

$$\Sigma_{ij}^2(\not{p}) = \frac{N_c}{64\pi^2}\sum_k(\lambda^\dagger)_{jk}\lambda_{ki}\not{p}\left(\left(\frac{1}{\epsilon} + \log\frac{\mu^2}{m_\phi^2}\right) + \text{finite}\right) \ .$$

[3] Equivalent to the standard amplitude but with external spinors stripped away.

The couplings can be simplified using unitarity,

$$\sum_k (\lambda^\dagger)_{ik}\lambda_{kj} = (\lambda^\dagger\lambda)_{ij} = (D^\dagger U^\dagger U D)_{ij} = \delta_{ij}|D_{ii}|^2,$$

where $|D_{ii}|^2$ is the i'th diagonal of D^2 (no summation implied), this therefore ensures the absence of any mass or kinetic term mixing amongst the DM candidates, the off diagonal mass/kinetic terms vanish due to the unitarity of U,

$$\Sigma_i^2(\not{p}) = \frac{N_c}{64\pi^2}|D_{ii}|^2\,\not{p}\left(\frac{1}{\epsilon} + \log\frac{\mu^2}{m_\phi^2}\right) + \text{finite}\ . \tag{7.2.17}$$

The counter terms produce the amplitude $\mathcal{M}_{\text{c.t.}} = \not{p}\delta_\chi^i + m_i\delta_m^i$, and the renormalization conditions are,

$$\Sigma_i^2(-m_i) = 0, \qquad \frac{d}{d\not{p}}\Sigma_i^2(\not{p})\bigg|_{\not{p}=-m_i} = 0. \tag{7.2.18}$$

So then $\delta_m^i = 0$ and $\delta_\chi^i = N_c|D|_{ii}^2/(64\pi^2)$ and thus,

$$Z_\chi^i = 1 + \frac{1}{\epsilon}\frac{N_c}{64\pi^2}|D_{ii}|^2 + \text{finite} + \mathcal{O}(\epsilon^{-2})\ , \tag{7.2.19}$$

$$Z_{m\chi}^i = 1 + \mathcal{O}(\epsilon^{-2})\ . \tag{7.2.20}$$

Now we carry out the mass renormalization in the $\overline{\text{MS}}$ scheme, the masses will be μ dependent and run with energy.

DM Field : (2) $\overline{\text{MS}}$ Scheme

In the $\overline{\text{MS}}$ scheme, the bare mass and field parameters are normalized as,

$$\chi_{B,i} = (Z_\chi^{ij})^{1/2}\chi_j\ , \tag{7.2.21}$$

$$m_{B,i} = Z_m^{ij}m_j\ , \tag{7.2.22}$$

allowing again for a mixing between flavours. Thus the bare Lagrangian becomes

$$\mathcal{L} = iZ_\chi^{ij}\bar{\chi}_i\not{\partial}\chi_j + Z_m^{ij}Z_\chi^{lm}m_{ij}\bar{\chi}_l\chi_m\ , \tag{7.2.23}$$

and where $Z_m^{ij} = \delta^{ij} + \delta_m^{ij}$ and $Z_\chi^{ij} = \delta^{ij} + \delta_\chi^{ij}$ for the counterterms, which will be purely divergent according to the $\overline{\text{MS}}$ prescription. The two point function is identical to Eq.(7.2.17) (we reproduce only the divergent piece and include the counter terms),

$$\Sigma_{ij}^2(\not{p}) = \frac{1}{\epsilon}\frac{N_c}{64\pi^2}|D_{ii}|^2\delta^{ij}\not{p} + \not{p}\delta_\chi^{ij} - m_{ij}(\delta_m^{ij} + \delta_\chi^{ij})\ ,$$

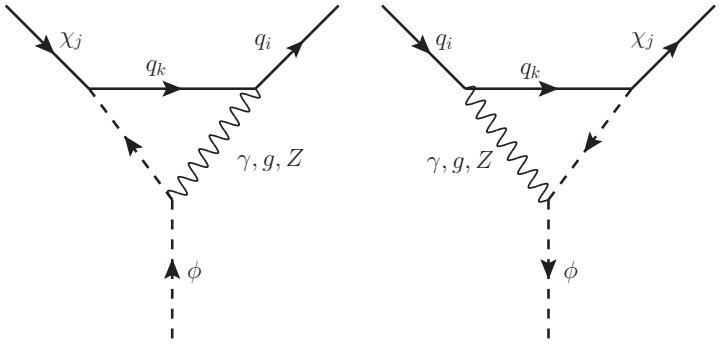

Figure 7.5: The one-loop contribution to the DM coupling, λ_{ij} (left) and λ^*_{ij} (right), from the DMFV model.

because Σ^2_{ij} is diagonal in DM flavours, there is no mixing at one loop and using the same renormalization conditions as for the on-shell scheme Eq.(7.2.18) (but simply absorbing only the pole),

$$Z^i_\chi = 1 - \frac{N_c|D_{ii}|^2}{64\pi^2}\frac{1}{\epsilon} + \mathcal{O}(\epsilon^{-2}) \,, \tag{7.2.24}$$

$$Z^i_m = 1 + \frac{N_c|D_{ii}|^2}{64\pi^2}\frac{1}{\epsilon} + \mathcal{O}(\epsilon^{-2}) \,, \tag{7.2.25}$$

the Z are independent of the mass, and so ultimately depend on scale μ only through the couplings λ_{ij}.

Coupling Renormalization : $\overline{\text{MS}}$ Scheme

To calculate the β-function for couplings λ_{ij} we define the renormalized coupling,

$$\mathcal{L}_{\text{int}} = \lambda_{ij}\bar{q}_{R,i}\chi_j\phi + (Z_{ij} - 1)\lambda_{ij}\bar{q}_{R,i}\chi_j\phi + \text{h.c.}, \tag{7.2.26}$$

defining $\delta_{ij} = Z_{ij} - 1$, then we may calculate the one-loop amputated vertex function $\Gamma^{(1)}(\{p_i\})$ with the renormalization condition of external legs on-shell, $\Gamma^{(1)}(p_i^2 = m_i^2) = -i\lambda_{ij}$.

The diagrams which arise at one loop consist of exchanging vectors $V = g, \gamma, Z$ between the scalar and quark lines, see Fig.7.5, because of this there are no quark-flavour changing diagrams and the matrix Z_{ij} is diagonal in the couplings, i.e. there is no mixing between different λ_{ij}. We work in unitary gauge, in Feynman gauge

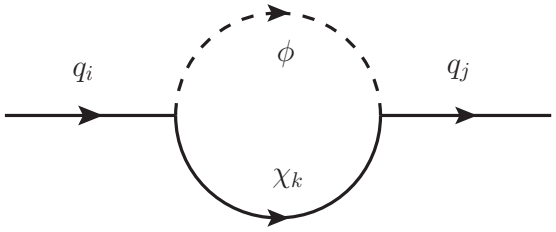

Figure 7.6: The one-loop contribution to the quark self-energy from the DMFV model.

the diagrams should include contributions from goldstone bosons.

The massless internal gauge bosons (γ, g) lead to IR divergences which are present in the matrix element. These IR divergences are independent of the UV divergences of the RG running, and in the end cancel to all orders. To avoid this problem we can give the photon and gluon arbitrary masses, and in the end the UV divergences are mass independent and the limit $m \to 0$ can be taken. The amputated vertex function up to one loop is then,

$$\Gamma(p_i^2 = m_i^2) = -i\lambda_{ij} - i\frac{1}{\epsilon}\delta_{\lambda_{ij}}\lambda_{ij} + \frac{1}{\epsilon}\,\Gamma^{(1)}(p_i^2 = m_i^2)\big|_\epsilon = -i\lambda_{ij}, \tag{7.2.27}$$

with[4],

$$\Gamma^{(1)}(p_i^2 = m_i^2)\big|_\epsilon = -i\lambda_{ij}\left(\frac{Q^2\alpha}{8\pi} + \frac{(N_c-1)\alpha_s}{16\pi} - \frac{Q^2 s_W^2\alpha}{8c_W^2\pi}\right), \tag{7.2.28}$$

which leads to,

$$Z_{ij} = 1 - \frac{1}{\epsilon}\left(\frac{Q^2\alpha}{8\pi}\left(1 - \frac{s_W^2}{c_W^2}\right) + \frac{(N_c-1)\alpha_s}{16\pi}\right)\,. \tag{7.2.29}$$

Note that $s_W^2/c_W^2 \sim 0.3$ and the Z contribution is smaller than for the photon,

$$Z_{ij} = 1 - \frac{1}{\epsilon}\left(\frac{\alpha}{18\pi}\left(1 - \frac{s_W^2}{c_W^2}\right) + \frac{\alpha_s}{8\pi}\right). \tag{7.2.30}$$

Quark Field : $\overline{\text{MS}}$ Scheme

The counter-term Lagrangian reads,

$$\mathcal{L} = i\bar{q}_i\partial\!\!\!/ q_i - m_{q_i}\bar{q}_i q_i + i\delta_q^{ij}\bar{q}_i\partial\!\!\!/ q_j - \delta_{m_q}^{ij} m_{q,ij}\bar{q}_i q_j, \tag{7.2.31}$$

[4]The color factor for the gluon exchange is $(t^a t^a)_{ij} = \frac{1}{2}(N_c - 1)\delta_{ij}$ where i, j are the color indices of the quark and scalar respectively.

where $i = 1, 2, 3$ for $q = u, c, t$. In general, the interactions may mix fields of different flavour since the coupling structure $(\lambda\lambda^\dagger)_{ij}$ appears .

On top of the SM, the quark two-point function, $\Sigma_q(\not{p})$, receives additional contributions from the DMFV model where the DM and ϕ run in the loop as in Fig.7.6, using the same renormalization conditions as for the DM field, we find,

$$\Sigma_q(-m_q)\big|_\epsilon = \frac{1}{64\pi^2}(\lambda\lambda^\dagger)_{ij}, \tag{7.2.32}$$

$$\Sigma'_q(-m_q)\big|_\epsilon = 0, \tag{7.2.33}$$

which leads to Z functions

$$Z_{q,ij} = \delta^{ij} Z^{(\mathrm{SM})}_{q,i} + \frac{1}{\epsilon}\frac{1}{64\pi^2}(\lambda\lambda^\dagger)_{ij}, \tag{7.2.34}$$

$$Z_{m_q,ij} = \delta^{ij} Z^{(\mathrm{SM})}_{m_q,i} - \frac{1}{\epsilon}\frac{1}{64\pi^2}(\lambda\lambda^\dagger)_{ij}, \tag{7.2.35}$$

where the SM Z parameters are [330],

$$Z^{(\mathrm{SM})}_{q,i} = 1 + \frac{1}{\epsilon}\frac{\alpha_s}{4\pi}\frac{13}{3}\ , \tag{7.2.36}$$

$$Z^{(\mathrm{SM})}_{m_q,i} = 1 + \frac{1}{\epsilon}\frac{\alpha_s}{4\pi}\frac{16}{3}\ , \tag{7.2.37}$$

unlike for the DM fields, the coupling combination $\lambda\lambda^\dagger$ is not diagonal and so the renormalization mixes quark flavours.

Scalar Field : $\overline{\mathrm{MS}}$ Scheme

The renormalized scalar field kinetic and mass terms read (with $m^2_{\phi,B} = Z_{m_\phi} m^2_\phi$ and $\phi_B = \sqrt{Z_\phi}\phi$)

$$\mathcal{L}_\phi = \partial^\mu\phi^\dagger\partial_\mu\phi - m^2_\phi\phi^\dagger\phi + (Z_\phi - 1)\partial^\mu\phi^\dagger\partial_\mu\phi - (Z_{m_\phi}Z_\phi - 1)m^2_\phi\phi^\dagger\phi\ , \tag{7.2.38}$$

with $Z_\phi = 1 + \delta_\phi$, $Z_{m_\phi} = 1 + \delta_{m_\phi}$. The scalar field receives more contributions to its one-loop self energy, $\Pi(p^2)$, than the DM due to its charges as shown in Fig.7.7. In unitary gauge :

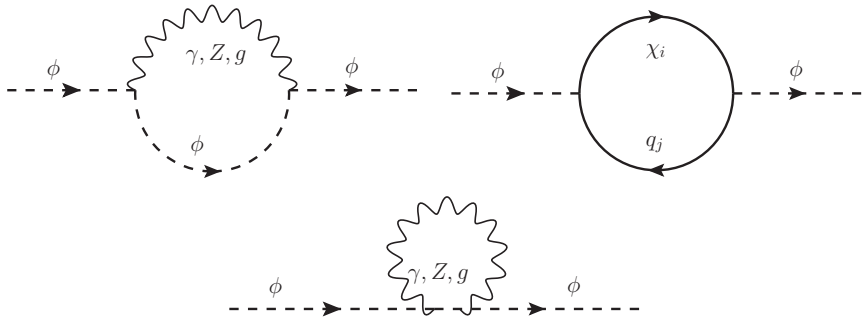

Figure 7.7: The one-loop contribution to the charged scalar self-energy from the DMFV model.

$$\Pi(-m_\phi^2)\big|_\epsilon = m_\phi^2\left(\frac{Q^2\alpha}{4\pi}+\frac{\alpha_s}{3\pi}+\frac{Q^2 s_W^2\alpha}{4c_W^2\pi}\left(\frac{3}{4}+\frac{m_\phi^2}{m_Z^2}+\frac{3}{4}\frac{m_Z^2}{m_\phi^2}\right)\right) - \frac{1}{16\pi^2}\sum_i(2m_{\chi_i}^2+2m_{q,i}^2+m_\phi^2)|D_{ii}|^2-\epsilon m^2(\delta_{m_\phi}+\delta_\phi), \tag{7.2.39}$$

$$\Pi'(-m_\phi^2)\big|_\epsilon = -\frac{2\alpha_s}{3\pi}-\frac{Q^2\alpha}{2\pi}-\frac{Q^2\alpha s_W^2}{\pi c_W^2}\left(\frac{m_\phi^2}{m_Z^2}+\frac{3}{4}\right)+\frac{1}{16\pi^2}\sum_i|D_{ii}|^2+\epsilon\delta_\phi, \tag{7.2.40}$$

where $|D_{ii}|^2 = (\lambda^\dagger\lambda)_{ii} = \sum_j \lambda_{ji}^*\lambda_{ji}$. The mass dependence arises due to the scalar couplings to fermions,

$$Z_\phi = 1+\frac{1}{\epsilon}\left(\frac{Q^2\alpha s_W^2}{\pi c_W^2}\left(\frac{3}{4}+\frac{m_\phi^2}{m_Z^2}\right)+\frac{Q^2\alpha}{2\pi}+\frac{2\alpha_s}{3\pi}-\frac{1}{16\pi^2}\sum_i|D_{ii}|^2\right)+\mathcal{O}(\epsilon^{-2}), \tag{7.2.41}$$

$$Z_{m_\phi} = 1+\frac{1}{\epsilon}\left(-\frac{3Q^2\alpha s_W^2}{4\pi c_W^2}\left(\frac{m_Z^2}{m_\phi^2}\right)-\frac{Q^2\alpha}{4\pi}-\frac{\alpha_s}{3\pi}-\frac{1}{8\pi^2 m_\phi^2}\sum_i(m_{\chi_i}^2+m_{q,i}^2)|D_{ii}|^2\right) + \mathcal{O}(\epsilon^{-2}). \tag{7.2.42}$$

RG Evolution

The fields, masses and couplings are renormalized using the following substitutions,

$$\text{Fields} \begin{cases} \chi_i = (Z_{\chi,i})^{-1/2}\chi_{i,B} \\ q_R = (Z_q)^{-1/2}q_{R,B} \\ \phi = (Z_\phi)^{-1/2}\phi_B \end{cases}, \quad \text{Masses} \begin{cases} m_{\chi,i} = \frac{1}{Z_{m_{\chi,i}}} m_{\chi,i,B} \\ m_q = \frac{1}{Z_{m_q}} m_{q,B} \\ m_\phi^2 = \frac{1}{Z_{m_\phi}} m_{\phi,B}^2 \end{cases}, \tag{7.2.43}$$

$$\text{Coupling} \ : \ \lambda_{ij} = \mu^{-2\epsilon}\frac{\sqrt{Z_{\chi,i}Z_qZ_\phi}}{Z_{\lambda,ij}}\lambda_{ij,B} \equiv \mu^{-2\epsilon}Z_{ij}^{-1}\lambda_{ij,B} \ , \tag{7.2.44}$$

we have seen that $Z_{\chi,i}$ and Z_{ij} are diagonal.

In general, each Z is a function of the renormalized parameters $\{\lambda, m\}$, scale dependence enters through both $\lambda \equiv \lambda(\mu)$ and $m \equiv m(\mu)$. In the $\overline{\text{MS}}$ scheme which is a *mass independent* scheme, the Z depend only on the couplings, which are the source of the scale dependence. The β-function for the couplings, anomalous dimension for fields, and anomalous mass dimension for masses, may be defined as,

$$\beta = \left.\frac{\partial\lambda_{ij}}{\partial\log\mu}\right|_B \ , \ \gamma_m = \frac{1}{m}\left.\frac{\partial m}{\partial\log\mu}\right|_B \ , \ \gamma = \left.\frac{\partial\log Z_F^{1/2}}{\partial\log\mu}\right|_B \ , \tag{7.2.45}$$

where the bare parameters are kept fixed. Each of these depends on the couplings $\{g\} = \{\lambda_{ij}, \alpha, \alpha_s\}$.

Beta Functions

We will assume the form of the renormalized coupling $\lambda_{ij} = \mu^{-2\epsilon}Z_{ij}^{-1}\lambda_{ij,B}$ and suppress the two indices into one (so that $\lambda_i \equiv \lambda_{ij}$), and then,

$$\beta_i = \mu\left(\frac{\partial\lambda_i}{\partial\mu}\right)_{\lambda_{i,B}} = \mu\left(\frac{\partial}{\partial\mu}Z_i^{-1}\mu^{-2\epsilon}\lambda_{i,B}\right)_{\lambda_{i,B}} = -2\lambda_i\epsilon - \frac{\lambda_i}{Z_i}\sum_j \beta_j\frac{\partial Z_i}{\partial\lambda_j} \ , \tag{7.2.46}$$

but $j = i$ is included in the sum on the RHS, so then

$$\beta_i = \lambda_i\left(-2\epsilon - \frac{1}{Z_i}\sum_{j\neq i}\beta_j\frac{\partial Z_i}{\partial\lambda_j}\right)\left(1 + \frac{\lambda_i}{Z_i}\frac{\partial Z_i}{\partial\lambda_i}\right)^{-1} \ , \tag{7.2.47}$$

as we have seen Z_{ij} contains only the α, α_s couplings of the SM from the vertex correction, but acquires a λ_{ij} dependence through the field renormalizations. The

beta function contains at most one power of ϵ, i.e.;

$$\beta_i = \beta_i^{(0)} + \epsilon\beta_i^{(1)} \ , \tag{7.2.48}$$

by equating coefficients of ϵ^n, $n = 0, 1$, in Eq.(7.2.47) we can determine $\beta_i^{(1)} = -2\lambda_i$, and,

$$\beta_i^{(0)}(\lambda_i) = -\lambda_i \sum_j \beta_j^{(1)} \frac{\partial Z_i^{(1)}}{\partial \lambda_j} \ . \tag{7.2.49}$$

We can for simplicity assume that the DMFV model does not affect the QCD or QED beta functions (in reality they are modified at one-loop)[5] and so they run in the conventional SM way, with fixed points $\alpha_s(m_Z^2) = 0.1182$ and $\alpha(m_Z^2) = 1/137$;

$$\alpha_s(\mu^2) = \frac{\alpha_s(\mu_0^2)}{1 - \frac{7}{4\pi}\alpha_s(\mu_0^2)\log\left(\mu^2/\mu_0^2\right)} \ , \tag{7.2.52}$$

$$\alpha(\mu^2) = \frac{\alpha(\mu_0^2)}{1 + \frac{2}{3\pi}\alpha(\mu_0^2)\log\left(\mu^2/\mu_0^2\right)} \ . \tag{7.2.53}$$

If $\beta_i \propto \lambda_{ij} = \beta_0\lambda_{ij}$, for β_0 constant (no μ dependence) we would find

$$\lambda_{ij}(\mu) = \lambda_{ij}(\mu_0)\left(\frac{\mu}{\mu_0}\right)^{\beta_0} \ ,$$

however β_0 depends on α, α_s and so has implicit scale dependence and the correct result is;

$$\lambda_{ij}(\mu^2) = \lambda_{ij}(\mu_0^2)\ \exp\left[-\int_{\log\mu}^{\log\mu_0} \beta_0\ d\log\mu\right] \ . \tag{7.2.54}$$

Eq.(7.2.47) suggests that the beta functions for the six independent parameters of λ form a simultaneous set of equations which must be solved for each of the $\beta_{\lambda_{ij}}$. We will not calculate these results, but instead move on to the mass running which is our main interest for the DMFV model.

[5] To one loop in the SM the QED and QCD beta functions are,

$$\beta_{\rm QCD}(\alpha_s) = -\frac{\alpha_s^2}{4\pi}\left(11 - \frac{2}{3}N_q\right) - \epsilon\frac{\alpha_s}{\pi} \ , \tag{7.2.50}$$

$$\beta_{\rm QED}(\alpha) = \frac{2\alpha^2}{3\pi} - \epsilon\frac{\alpha}{\pi} \ . \tag{7.2.51}$$

Anomalous Mass Dimension

For the anomalous mass dimension assuming $m_i = Z_i^{-1} m_{i,B}$

$$\gamma_m = -\frac{1}{Z_i}\left(\sum_{j\neq i}\frac{\partial X_j}{\partial \log\mu}\frac{\partial Z_i}{\partial X_j}\right)\left(1+\frac{m_i}{Z_i}\frac{\partial Z_i}{\partial m_i}\right)^{-1} , \tag{7.2.55}$$

where X_j are the mass and coupling parameters. Using the ansatz for β (Eq.(7.2.48)) and equating powers of ϵ (γ_m is finite) we get

$$\gamma_m = -\sum_j \beta_j^{(1)}\frac{\partial Z_i}{\partial \lambda_j} . \tag{7.2.56}$$

For the DM masses and using the $\overline{\text{MS}}$-scheme $m_i = (Z_m^i)^{-1} m_{i,B}$ (Eq.(7.2.25)) and thus $X_j \in \{\lambda_{ij}\}$ as the Z are mass independent, and

$$\begin{aligned}
\gamma_m(m_{\chi,i}) &= \sum_{j,k}\left(\lambda_{jk}\frac{\partial Z_{m_\chi,i}}{\partial \lambda_{jk}} + \lambda^*_{jk}\frac{\partial Z_{m_\chi,i}}{\partial \lambda^*_{jk}}\right) \\
&= \frac{N_c}{32\pi^2}\sum_{j,k}\left(\lambda_{jk}\frac{\partial |D_{ii}|^2}{\partial \lambda_{jk}} + \lambda^*_{jk}\frac{\partial |D_{ii}|^2}{\partial \lambda^*_{jk}}\right) \\
&= \frac{N_c}{32\pi^2}\sum_j\left(\lambda_{ji}\lambda^*_{ji} + \lambda^*_{ji}\lambda_{ji}\right) \\
&= \frac{N_c}{16\pi^2}(\lambda^\dagger\lambda)_{ii} ,
\end{aligned} \tag{7.2.57}$$

assuming $\beta(\lambda) = \beta_0\lambda$. We have used the result

$$\frac{\partial |D_{ii}|^2}{\partial \lambda_{jk}} = \delta_{ik}\lambda^*_{ji} , \quad \frac{\partial |D_{ii}|^2}{\partial \lambda^*_{jk}} = \delta_{ik}\lambda_{ji} . \tag{7.2.58}$$

The running of the masses requires the solution of the equation,

$$\gamma_m(\mu) = \frac{\mu}{m(\mu)}\frac{dm(\mu)}{d\mu}, \tag{7.2.59}$$

which is,

$$m(\mu) = m(\mu_0)\exp\left[\int_{\mu_0}^{\mu}\frac{d\mu'}{\mu'}\gamma_m(\mu')\right] . \tag{7.2.60}$$

We will fix the DM mass at a high scale and run it down to an appropriate scale for RD constraints, $\mu \sim m_\chi/25$ (or $\mu_N = 1$ GeV for indirect/direct detection).

Expanding in $(\lambda^\dagger\lambda)/16\pi^2 \ll 1$ we recover the form of the mass in [325],

$$m_i(\mu_N) = m_i(\mu_0)\left(1 + \frac{N_c}{16\pi^2}(\lambda^\dagger\lambda)_{ii}\log\left(\frac{\mu_N}{\mu_0}\right) + \mathcal{O}((\lambda^\dagger\lambda)^2_{ii})\right) \ , \tag{7.2.61}$$

the mass splitting is then given by

$$\begin{aligned}\Delta m_{ij} &= m_\Lambda \frac{N_c}{16\pi^2}\log\left(\frac{\mu_N}{\Lambda}\right)\left(D^2_{ii} - D^2_{jj}\right) \\ &\sim 0.35\left(D^2_{ii} - D^2_{jj}\right) \ ,\end{aligned} \tag{7.2.62}$$

where Λ is a high scale and m_Λ is the universal mass at that scale. The mass differences are completely captured by differences in D_{ii} between two flavours. If the D_{ii} are all equal then we recover the MFV assumption, the degree of MFV violation essentially gives the degree of mass splitting. Given that typically the freeze-out occurs at $T \sim m/25$, the above splitting is reduced to $\sim 0.28(D^2_{ii} - D^2_{jj})$ for a 1 TeV WIMP for the RD calculation, a small change which we ignore in the calculation.

7.3 DMFV : Relic Density with Coannihilation and Decay

The measured relic density (RD) of DM is an extremely important parameter that must be reproduced by any self-respecting DM model. It is currently measured to a very high accuracy by the Planck collaboration [6].

There are many mechanisms by which the DM may acquire the current measured relic density. These may broadly be defined as *thermal* and *non-thermal* production, in other words via equilibrium or non-equilibrium processes. The most common thermal production mechanism is *thermal freeze out* [37, 38], in which the DM is initially in thermal equilibrium, and its number density is depleted by (a) the expansion of the universe and (b) interactions of the DM. The comoving number density (the number density for a unit comoving volume, which expands at the same rate as the universe) is therefore affected only by (b), as the universe evolves eventually the expansion rate exceeds the interaction rate and the interactions stop, thus "freezing

out" the DM density.

In our model we have a fermionic triplet of DM particles, which are neutral but which interact with the SM through a coloured and electrically charged scalar mediator. The dominant interactions which deplete the DM particles are,

$$\begin{aligned} \bar{\chi}_i \chi_i &\to \text{SM} \ , \\ \bar{\chi}_i \chi_j &\to \text{SM} \ , i \neq j \ , \end{aligned} \tag{7.3.63}$$

which occur at tree level, and which are referred to as annihilation, co-annihilation respectively. Freeze out occurs at a temperature $T_f \propto m_{\chi_i}$, and so the heavier DM particles freeze-out first. Then the coannihilation process allows the heavy DM to decay away, if the masses are widely separated this may completely remove the heavy particles.

We can ignore particles which are much heavier than the lightest particle. Heavy particles decouple earlier (since $T_f \sim m_{\chi_i}/25$), and if stable may have a relic density comparable to the lightest DM candidate. However, in scenarios like DMFV these are likely to decay (or coannihilate) to the lightest particle (DM) very quickly (even via loop suppressed processes) before the light DM itself freezes out, and thermal equilibrium of the light DM during the decay of heavier states ensures decays will have no effect on its eventual relic density.

In a scenario with DM which have no coannihilations, scattering or decays (as in Sec.1.2), the partial relic density is simply,

$$(\Omega h^2)_i \propto \frac{1}{\langle \sigma v \rangle_{ii}} \ , \tag{7.3.64}$$

where $\langle \sigma v \rangle_{ii}$ is the thermally averaged annihilation cross section for the process $\chi_i \bar{\chi}_i \to$ SM, from the tree level t-channel exchange of ϕ. This then gives an estimate $\langle \sigma v \rangle_{ii} \sim 3 \times 10^{-26}$ cm^{3}s^{-1} for $\Omega h^2 = 0.1198$. The situation is depicted in Fig.7.8, where we consider single-flavour scenarios in which only one DM particle has a coupling to a single quark flavour.

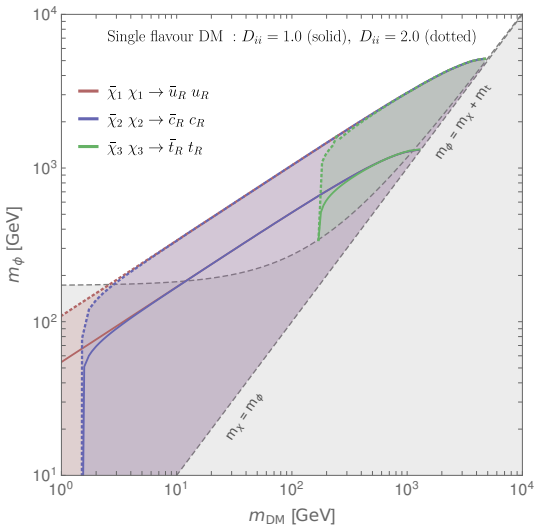

Figure 7.8: RD 'bounds' (the shaded region is *allowed*) for single flavour DM. Since $\Omega h^2 \propto (\langle\sigma v\rangle)^{-1} \propto m_\phi^4/|D_{ii}|^4$, the bounds scale roughly as D_{ii}.

If, however, the DM particles have similar masses the co-annihilation processes can become important and should be taken into account. It was shown in [49] that the thermal freeze out calculation can approximately be treated in exactly the same way as with the single-flavour annihilation process, but with the replacement of $\langle\sigma v\rangle$ by

$$\langle\sigma v\rangle_{\rm eff} = \sum_{i,j} \langle\sigma v\rangle_{ij} \frac{g_i g_j}{g_{\rm eff}^2}(1+\Delta_i)^{3/2}(1+\Delta_j)^{3/2} e^{-x(\Delta_i+\Delta_j)} \equiv a_{\rm eff} + b_{\rm eff} v^2 \ , \quad (7.3.65)$$

$$\langle\sigma v\rangle_{ij} = \sum_{kl} \langle\sigma v\rangle_{\chi_i\bar{\chi}_j \to q_k\bar{q}_l} \equiv a_{ij} + b_{ij} v^2 \ , \quad (7.3.66)$$

where $\Delta_i = (m_i - m_1)/m_1$ (m_1 being the mass of the lightest DM candidate), and g_i are the degrees of freedom (spin, colour, etc.) which is $g_i = 2$ for the DM and quarks (we include the colour d.o.f. of quark in the cross section) and $g_{\rm eff}$ is,

$$g_{\rm eff}(x) = \sum_{i=1}^{N} g_i (1+\Delta_i)^{3/2} e^{-x\Delta_i} \ . \quad (7.3.67)$$

In the limit of degenerate mass fermions $g_{\rm eff} = 2N$, and the factor $g_i g_j/g_{\rm eff}^2 \sim 1/9$. From Eq.(7.3.65) we see that the coannihilation channels only contribute significantly if the masses of the two coannihilating particles are very similar. The Boltzmann suppression ensures that for widely separated masses the coannihilation pro-

cesses are negligible.

The case of 2-flavour DM with equal masses is shown in Fig.7.9, the total relic density can be written approximately as

$$\Omega h^2 \propto \frac{1}{\frac{1}{4}(\langle\sigma v\rangle_{11} + 2\langle\sigma v\rangle_{12} + \langle\sigma v\rangle_{22})} , \tag{7.3.68}$$

which reproduces the correct limit (Eq.(7.3.64)) if $\langle\sigma v\rangle_{12} = 0$ and $\langle\sigma v\rangle_{11} = \langle\sigma v\rangle_{22}$, and also shows that the total relic density is approximately halved with equal sized annihilations/coannihilations. Fig.7.9 also provides the partial densities.

To compute the relic density, one first finds the freeze-out temperature $x_f \equiv m/T_f$ by solving the equation [8, 333, 334],

$$e^{x_f} = \frac{\sqrt{\frac{45}{8}} g_{\rm eff} m_{\chi_1} c M_{\rm pl} \langle\sigma v\rangle_{\rm eff}}{2\pi^3 g_*^{1/2}\sqrt{x_f}} , \tag{7.3.69}$$

for $M_{\rm pl} = G^{-1/2}$ the Planck mass, g_* the number of relativistic d.o.f and $c = 1$ an order 1 number. The relic density itself can then be written [8, 333, 334],

$$\Omega h^2 = 2 \times 1.04 \times 10^9 \frac{x_f}{\sqrt{g^*} M_{\rm pl} (a_{11} I_a + 3 b_{11} I_b / x_f)} , \tag{7.3.70}$$

where a_{11} and b_{11} are the s-wave and p-wave terms of $\langle\sigma v\rangle_{11}$ (the cross section for the relic, plus any particles with degenerate mass) and,

$$\begin{aligned} I_a &= \frac{x_f}{a_{11}} \int_{x_f}^{\infty} x^{-2} a_{\rm eff} dx , \\ I_b &= \frac{2x_f^2}{b_{11}} \int_{x_f}^{\infty} x^{-3} b_{\rm eff} dx . \end{aligned} \tag{7.3.71}$$

If all the DM particles have the same mass then $I_a = I_b = 1$. For the Lagrangian defined in Eq.(7.1.2) the s-wave term of $\langle\sigma v\rangle_{ij}$ is written (for arbitrary masses),

$$\begin{aligned} \langle\sigma v\rangle_{ij} = N_c \sum_{f_1,f_2} |\lambda_{f_1 i} \lambda^*_{f_2 j}|^2 \frac{\sqrt{m_i m_j}\left((m_i+m_j)^4 - (m_{f1}^2 - m_{f2}^2)^2\right)}{64\pi (m_i+m_j)^3 (m_{f2}^2 m_i + m_{f1}^2 m_j - (m_i+m_j)(m_\phi^2 + m_i m_j))^2} \\ \times \sqrt{m_{f1}^4 + (m_{f2}^2 - (m_i+m_j)^2)^2 - 2m_{f1}^2(m_{f2}^2 + (m_i+m_j)^2)}, \end{aligned} \tag{7.3.72}$$

where $m_{f1,f2}$ are the final state fermion masses, $m_{i,j}$ are the initial state DM masses. We include the p-wave term but do not reproduce it here since the expression is

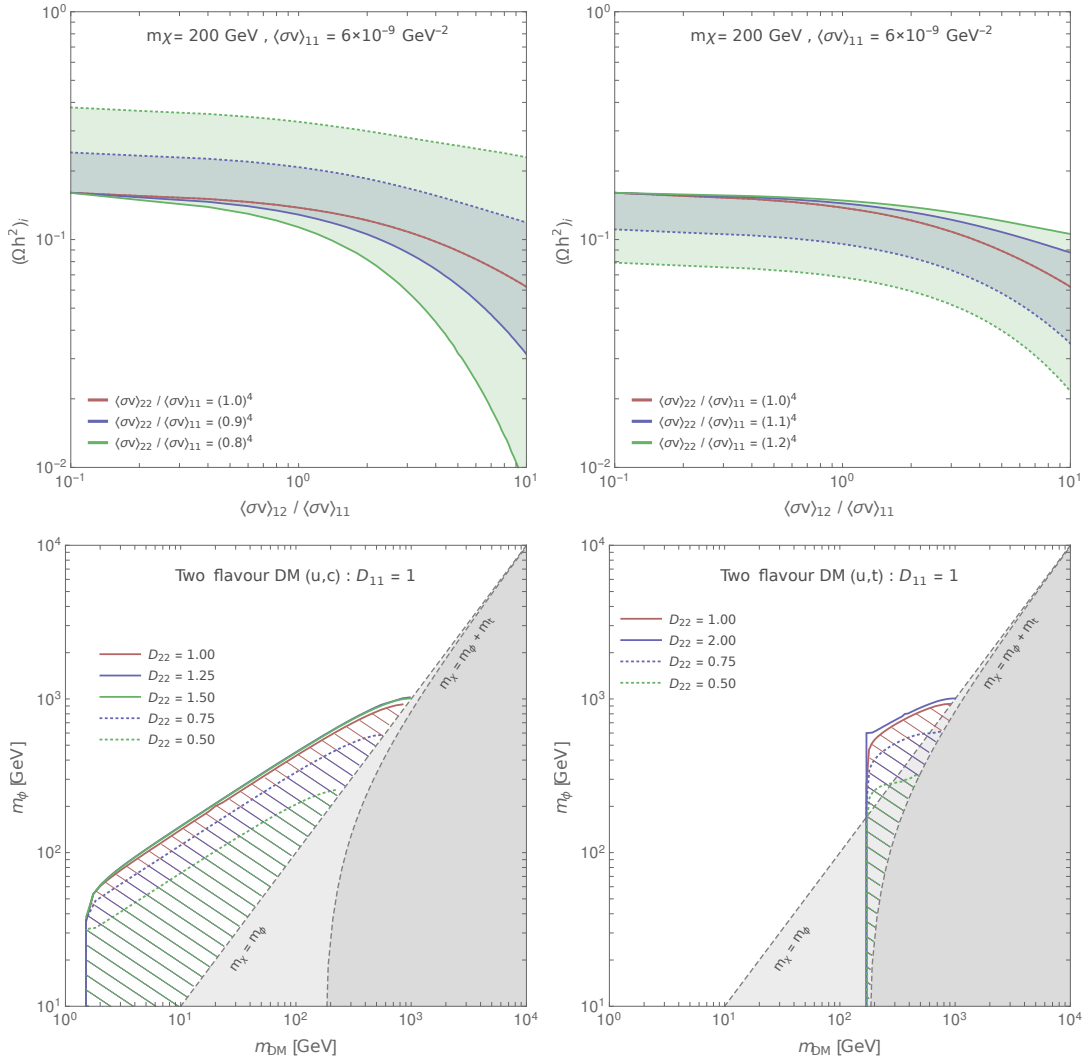

Figure 7.9: Top : partial relic densities for a 2-flavour DM model with fixed annihilation cross section, and a varying coannihilation, assuming no decays or scattering. Bottom : the corresponding RD bounds for the case of $\langle \sigma v \rangle_{ij} = \langle \sigma v \rangle_{ii}$, but varying the relative sizes of the annihilations.

lengthy[6]. If the fermion masses can be neglected then this approximates to,

$$\langle \sigma v \rangle_{ij} \approx |D_{ii}|^2 |D_{jj}|^2 \frac{3(m_i + m_j)\sqrt{m_i m_j}}{64\pi (m_i m_j + m_\phi^2)^2}, \tag{7.3.73}$$

and the annihilation is not very sensitive to the mixing angles.

The most precise measurement of the DM relic density has been made by Planck [6],

$$\Omega h^2 = 0.1198 \pm 0.0015 \ . \tag{7.3.74}$$

Fig.7.9 shows an example of the constraints that this imposes on the DMFV model. In contrast to conventional constraints, the lower the couplings the larger the effect and the more excluded the model. This also means that there is a lower limit on the size of couplings, below which no combination of the other parameters can lead to an allowed model. For example, single flavour DM coupled to u, c (t) and with $m_\phi > 10$ GeV, requires $D_{ii} \gtrsim 0.1$ (0.4).

Assume coannihilations are absent. If the DM are all degenerate in mass, and with equal couplings, then the DM coupled to the c, t effectively just increase the total degrees of freedom of the relic by 2. This causes the freeze out temperature to increase (x_f decreases, see Eq.(7.3.69)) and the DM decouples earlier, but due to the lower cross section the relic density increases compared with a single-flavour scenario.

In the DMFV model the multiplet of N DM are approximately degenerate in mass, and additionally have roughly equal sized annihilation/coannihilation. Then,

$$\langle \sigma v \rangle_{\text{eff}} \approx \frac{1}{N^2} \sum_{i,j}^{N} \langle \sigma v \rangle_{ij} \ \ , N \leq 3 \ . \tag{7.3.75}$$

If the cross sections are all equal ($\langle \sigma v \rangle_{ij} \equiv \sigma$) then $\langle \sigma v \rangle_{\text{eff}} = \sigma$ and $I_{a,b} = 1$, the multiplet act as a single particle but with $g_{\text{eff}} = 2N$ degrees of freedom. The overall

[6] Although conventionally the p-wave term is dropped due to a large velocity suppression as the DM is highly non-relativistic at the present day, this has more of an effect in the early universe where typically $v \sim c$.

change to the relic abundance from a single flavour scenario comes entirely from the lower freeze out temperature, and at most changes the relic abundance by $\sim 5\%$ (depending logarithmically on N). Naively one would expect that with N identical particles the relic density would be N times as large[7]; this is only true when there are no coannihilations, since with coannihilations the overall rate of DM depletion increases.

The larger the coannihilation rate, the larger $\langle\sigma v\rangle_{\text{eff}}$ and consequently the freeze out occurs earlier. The DM is depleted far more by the larger annihilation rate, than compensated for by the earlier freeze-out time. The relic density is thus lowered.

7.3.1 Annihilation and Scattering

We have discussed the process of thermal averaging in Sec.1.2.3, for the case of the cross section. To a sufficient accuracy of $< 10\%$ one can simply calculate the cross section as usual, and expand in the non-relativistic velocity of the annihilating particles using the lab frame. The *thermally averaged decay width* is defined in a very similar way,

$$\langle\Gamma\rangle = \frac{1}{n_i^{(eq)}} \int \Pi_k \frac{d^3p_k}{(2\pi)^3} \frac{1}{2E_k} \sum_{\text{spin}} |\mathcal{M}(\chi_i \to \chi_j X)|^2 \delta^{(4)}(p_1 - p_2 - p_3) e^{-E_1/T} \ , \quad (7.3.76)$$

and it may be approximated by [335],

$$\langle\Gamma\rangle = \Gamma_0 \frac{K_1(x)}{K_2(x)} \ ,$$

where Γ_0 is the zero-temperature decay width (in the decaying particle's rest frame), the Bessel functions $K_1(x) \approx K_2(x)$ in the limit $x \gg 1$ relevant for thermal freeze out of annihilations and so the thermal decay width is given approximately by the normal width of the particle.

[7] Switching off coannihilation, $\langle\sigma v\rangle_{\text{eff}} \approx \sigma/N$, T_f is unchanged and the relic density scales as $\Omega h^2 \propto N$ and so the naive guess is correct.

The differential cross section (a function of s, t Mandelstam variables) is most easily written

$$d\sigma = |\mathcal{M}|^2 d\Pi = \frac{1}{64\pi s|p|^2}|\mathcal{M}|^2 dt \ , \tag{7.3.77}$$

where the limits of integration are

$$t^{(\mathrm{lab})}_{\mathrm{max,min}} = m_1^2 + m_2^2 - \frac{1}{2s}(s + m_1^2 - m_3^2)(s + m_2^2 - m_4^2) \ , \\ \pm 2\sqrt{\frac{s^2 + (m_1^2 - m_3^2)^2}{4s} - \frac{1}{2}(m_1^2 + m_3^2)}\sqrt{\frac{s^2 + (m_2^2 - m_4^2)^2}{4s} - \frac{1}{2}(m_2^2 + m_4^2)} \ . \tag{7.3.78}$$

and finally the velocity expansion is made from s in the lab frame $s^{(\mathrm{lab})} = (m_1 + m_2)^2 + v^2 m_1 m_2$. The momentum/mass assignments are as shown in Fig.7.10. The matrix element for $2 \to 2$ scattering via a t-channel scalar is given by

$$\mathcal{M} = C_\lambda \frac{3(m_1^2 + m_3^2 - t)(m_2^2 + m_4^2 - t)}{4(m_\phi^2 - t)^2} \ , \tag{7.3.79}$$

where C_λ is the appropriate combination of couplings. There are two relevant cross sections; $\langle\sigma v\rangle_{ij}$ denoting $\bar{\chi}_i\chi_j \to \bar{q}_l q_m$, summed over l, m. There are also $\langle\sigma v\rangle'_{ij}$ denoting the scattering process $\chi_i q_l \to \chi_j q_m$ (t-channel) and $\chi_i\bar{q}_l \to \chi_j\bar{q}_m$ (s-channel, with amplitude as in Eq.(7.3.79) but $t \leftrightarrow s$), again summed over l, m. $\langle\sigma v\rangle_{ij}$, $\langle\sigma v\rangle'_{ij}$ differ only in the momentum assignments and give the approximate result (in the

limit of zero quark mass and DM velocity)[8],

$$\begin{aligned}\langle\sigma v\rangle_{ij} &= \frac{3}{64\pi}\sum_{l,m}|\lambda_{li}\lambda^*_{mj}|^2 f_{\rm ann}(m_l,m_m)\\ &\approx D^2_{ii}D^2_{jj}\frac{3m_i^2}{16\pi(m_i^2+m_\phi^2)^2}\ , \end{aligned}\tag{7.3.80}$$

$$\begin{aligned}\langle\sigma v\rangle'_{ij,{\rm t-chan}} &= \frac{3}{64\pi}\sum_{l,m}|\lambda_{li}\lambda^*_{mj}|^2 f_{\rm t}(m_l,m_m)\\ &\approx D^2_{ii}D^2_{jj}\frac{3\epsilon^2 m_i^2}{8\pi(m_i^2+m_\phi^2)^2}\ , \end{aligned}\tag{7.3.81}$$

$$\begin{aligned}\langle\sigma v\rangle'_{ij,{\rm s-chan}} &= \frac{3}{64\pi}\sum_{l,m}|\lambda_{li}\lambda^*_{mj}|^2 f_{\rm s}(m_l,m_m)\\ &\approx D^2_{ii}D^2_{jj}\frac{3\epsilon^2 m_i^2}{8\pi(m_i^2-m_\phi^2)^2}\ , \end{aligned}\tag{7.3.82}$$

where $m_j = (1+\epsilon)m_i$ and the quark masses have been neglected in the approximate expressions, and the scattering process is suppressed relative to annihilation by the mass splitting.

The decay term in the Boltzmann equation is significantly larger than the annihilations, which means decay processes will be effective during freeze-out.

[8] The quark mass dependent functions are,

$$\begin{aligned}f_{\rm t}(m_1,m_2) &= \left((m_2+m_i)^4-(m_1^2-m_j^2)^2\right)\\ &\times\left[((m_i+m_2)^2-(m_1+m_j)^2)(-(m_i+m_2)^2+(m_1-m_j)^2)\right]^{1/2}\\ &\times\left[(m_2+m_i)^2((m_\phi^2+m_im_2)(m_2+m_i)-m_1^2m_2-m_im_j^2)^2\right]^{-1}\ ,\\ f_{\rm s}(m_1,m_2) &= \left((m_1+m_i)^2-(m_2^2-m_j^2)\right)\\ &\times\left[((m_i+m_1)^2-(m_2+m_j)^2)((m_1+m_i)^2-(m_2-m_j)^2)\right]^{1/2}\\ &\times\left[(m_1+m_i)^2(m_\phi^2-(m_1+m_i)^2)^2\right]^{-1}\ ,\\ f_{\rm ann}(m_1,m_2) &= \left((m_i+m_j)^4-(m_1^2-m_2^2)^2\right)\\ &\times\left[((m_i+m_j)^2-(m_1-m_2)^2)((m_i+m_j)^2-(m_1+m_2)^2)\right]^{1/2}\\ &\times\left[(m_i+m_j)^2((m_\phi^2+m_im_j)(m_i+m_j)-m_2^2m_i-m_1^2m_j)^2\right]^{-1}\ .\end{aligned}$$

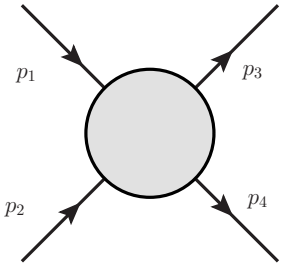

Figure 7.10: The momentum assignments for $2 \to 2$ scattering.

7.3.2 Boltzmann Equations for DMFV

So far, we have outlined a procedure to calculate the total relic density for the DM, Ω_T. This needs refinement for several reasons: firstly, we must be precise about what the DM is. The DM candidate is the lightest of the three χ_i when their mass splitting is large, since the heavier particles freeze-out with a lower abundance and/or rapidly decay to the lighter particles before they leave thermal equilibrium. However, if the mass splitting is small/zero, then, in principle all three χ_i may obtain a stable relic density Ω_i and contribute to the total abundance. This situation would not be correctly captured by the approximate method of the last section, since it implicitly assumes that the heavier states decay before freeze-out.

Finding the partial densities Ω_i is an important consideration when looking at DD and ID signals, which scale as Ω_i and Ω_i^2 respectively, and thus a χ_i with a low partial relic density has suppressed signals and thus the bounds on its parameters should be weakened. Calculating the total relic abundance is possible following [49] and the previous section, or can be accomplished with the MicrOmegas or MadDM codes [335, 336]; however the partial relic densities are not so easy (the two particle case can be handled by MicrOmegas).

The three particles evolve according to a non-linear Boltzmann equation, coupled via the coannihilation, decay and scattering processes. These equations may be

written [49, 335][9]

$$\begin{aligned}\frac{dn_i}{dt} =& -3Hn_i - \sum_j (1+\delta_{ij}) \langle\sigma v\rangle_{ij} (n_i n_j - n_i^{(eq)} n_j^{(eq)}) \\ & - \sum_{j\neq i} \langle\Gamma_{ij}\rangle (n_i - n_i^{(eq)}) + \sum_{j\neq i} \langle\Gamma_{ji}\rangle (n_j - n_j^{(eq)}) \\ & - \sum_{j\neq i} \left(\langle\sigma v'\rangle_{ij} \left(n_i - n_i^{(eq)}\right) n_X - \langle\sigma v'\rangle_{ji} \left(n_j - n_j^{(eq)}\right) n_X \right) , \end{aligned} \tag{7.3.84}$$

where $n_{i,X}$ are the number densities of the DM and quarks respectively, and $n_i^{(eq)}$ are the equilibrium number densities which can be assumed to follow a Maxwell-Boltzmann distribution, and Γ_{ij} represents the decay $\chi_i \to \chi_j + X$. We neglect DM self-interactions $\bar{\chi}_i\chi_j \leftrightarrow \bar{\chi}_k\chi_l$, since such processes are loop suppressed in our model. On the third line are the DM-flavour changing scattering processes, which are enhanced relative to the annihilation due to n_X. We will refer to the lightest of the three DM as m_{χ_1}. Mapping Eq.(7.3.84), into the variables

$$\begin{aligned} Y_i &= \frac{n_i}{s} \ , \ x = \frac{m_{\chi_1}}{T} \ , \\ Z_{ij}^{(\prime)} &= \frac{s(x=1)}{H(x=1)} \langle\sigma v\rangle_{ij}^{(\prime)} = M_{\rm pl} m_{\chi_1} \sqrt{\frac{g_*\pi}{45}} \langle\sigma v\rangle_{ij}^{(\prime)} \ , \\ W_{ij} &= \frac{1}{H(x=1)} \langle\Gamma_{ij}\rangle \ , \end{aligned} \tag{7.3.85}$$

with entropy density s and Hubble parameter H [337],

$$s = \frac{2\pi^2 g_*}{45} T^3 \ , \ H = \sqrt{\frac{4\pi^3 g_*}{45}} \frac{T^2}{M_{\rm pl}}, \tag{7.3.86}$$

then the Boltzmann equation can be written in a simplified form for numerical

[9] To recover the method of the previous section one simply finds the total number density of DM $n' = \sum_i n_i'$, then the scattering and decay terms cancel and one is left with,

$$\frac{dn}{dt} = -3Hn - \sum_{i,j} \langle\sigma v\rangle_{ij} (n_i n_j - n_i^{(eq)} n_j^{(eq)}) \ . \tag{7.3.83}$$

evaluation

$$\begin{aligned}\frac{dY_i}{dx} = &-\frac{1}{x^2}\sum_j \left(Z_{ij}\left(Y_iY_j - Y_i^{(eq)}Y_j^{(eq)}\right)\right)\\ &-\frac{1}{x^2}\sum_{j\neq i}\left(Z'_{ij}\left((Y_i - Y_i^{(eq)}) - (Y_j - Y_j^{(eq)})\right)Y_X^{(eq)}\right)\\ &-\frac{1}{x}\sum_{j\neq i}\left(W_{ij}(Y_i - Y_i^{(eq)}) - W_{ji}(Y_j - Y_j^{(eq)})\right)\,,\end{aligned} \tag{7.3.87}$$

and finally, the equilibrium yield is given by

$$Y_i^{(eq)} = \frac{45}{2\pi^4 g_*}x_i^2 K_2(x_i)\,, \tag{7.3.88}$$

where $x_i \equiv (m_{\chi_i}/m_{\chi_1}) \times x$ in terms of the second Bessel function of the second kind $K_2(x) \approx \sqrt{\frac{\pi}{2}}x^{-1/2}e^{-x}$. The differential equation is solved according to the boundary condition that $Y_i = Y_i^{(eq)}$ at $x = 1$, meaning that before the particle becomes non-relativistic the DM is in thermal equilibrium.

With three DM candidates with similar mass, the equilibrium distributions are the same, which means the number densities of the χ_i are the same right up to freeze out (regardless of their interaction strengths), which can be seen for example in Fig.7.12, right panel.

Without coannihilation scattering or decay, the DM candidates do not communicate with each other, the Boltzmann equations decouple and their relic densities are independent. Then the higher mass DM lead to a higher x_f (higher T_f) which causes an increase in Ωh^2 (Eq.(7.3.70)), although this effect is extremely weak and easily overcome by any changes in the cross section from the increase in mass. Including even extremely small decay widths ($\Gamma \gtrsim 10^{-42}$ GeV) to lighter particles completely removes the relic abundance for the heavy particles by the present day. In the DMFV model we have coannihilations which are of similar size as the standard annihilations, and this dramatically affects the resulting relic densities. Fig.7.11 summarizes the behaviour of the partial relic densities in the three-flavour DM scenario with both coannihilation and mass splitting.

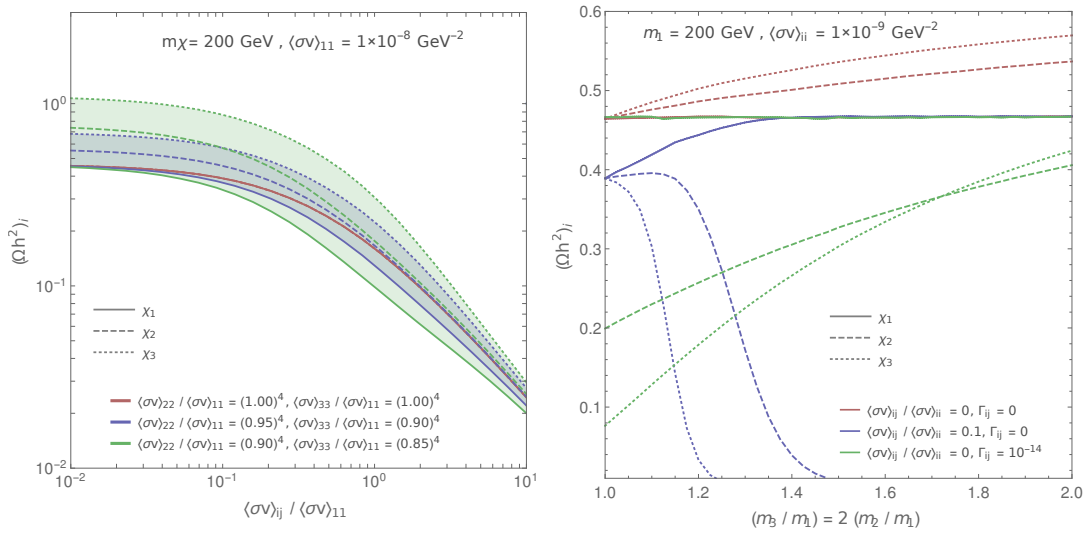

Figure 7.11: Partial relic densities for a 3-flavour DM model with fixed annihilation cross section, and a varying coannihilation (left) or mass splitting (right) for various benchmark scenarios which serve to illustrate the principle trends associated to coannihilation and decay in the DMFV model. Scattering is assumed to be absent, to illustrate some of the features discussed in the text.

Fig.7.12 shows the effect of decay on the partial relic densities of the DM in the absence of scattering. For very small widths (top left panel), the DM decay does not affect the calculation and the freeze-out depends only on annihilation channels, although the heavy particles will eventually decay by the present day. If the width is sufficiently large (bottom right panel), the decay progresses rapidly enough to wash out the relic density of the decaying particles during freeze-out.

From Eq.(7.3.87), the correct relic density corresponds to $Y_i(\infty) = 4.4 \times 10^{-10}$, then the decay term becomes larger than the annihilation at $\Gamma \sim 10^{-12}$ GeV, and this is the approximate scale at which the decays dominate the behaviour. Thus clearly for *'normal'* decay widths such as those in the SM $\Gamma/m \in [10^{-4}, 10^{-1}]$ the decays can safely be assumed to remove the heavier particles completely. This is not the case for our model, since the decay widths are so strongly dependent on the mass splitting, that widths of 10^{-12} or less occur naturally. It follows that the widths should be implemented explicitly to correctly capture the behaviour.

Since $n_X/n_i \sim 10^9$ $(X = u, c, t)$ at freeze-out, the scattering term is sub-

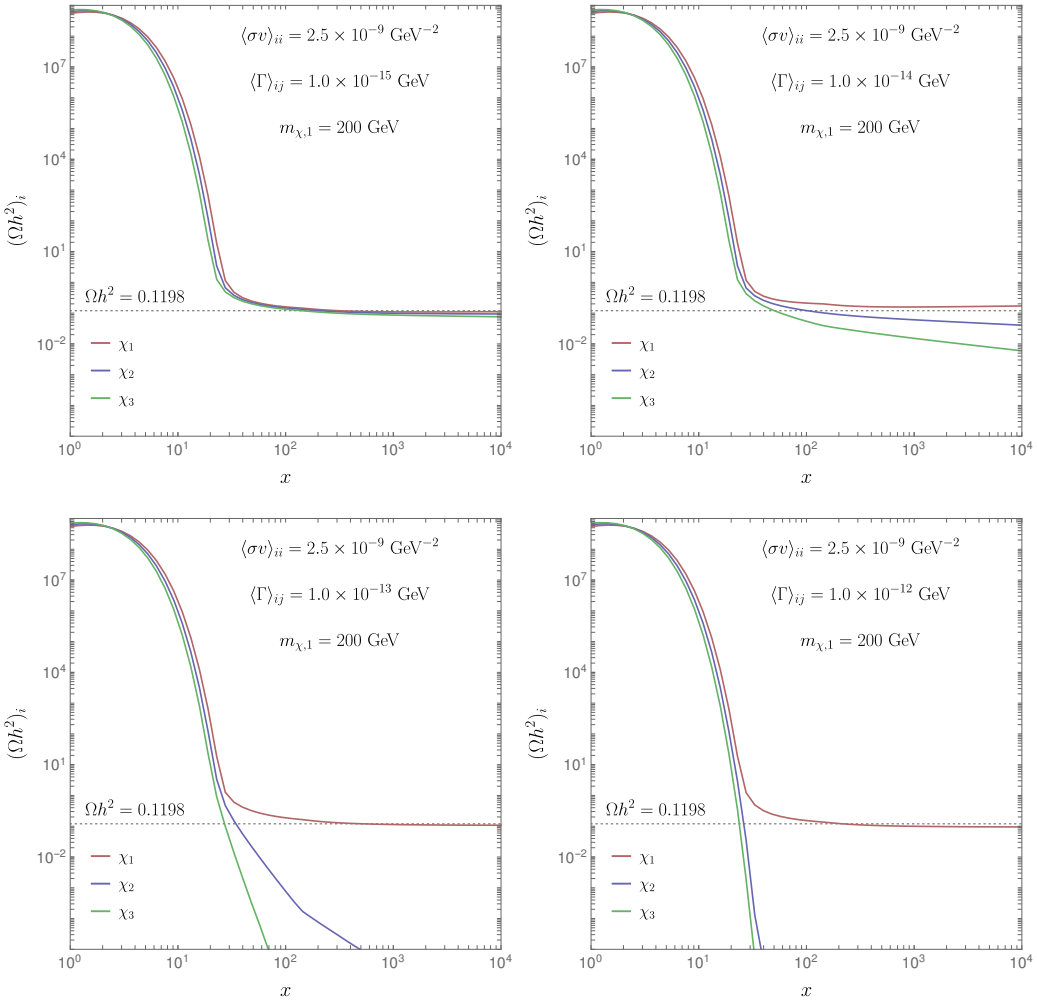

Figure 7.12: An illustration of thermal freeze out for three DM candidates (red blue green in ascending order of mass), with $m_1 = 200$ GeV and $\Delta m_{2,3} = 10\%, 20\%$ for a fixed annihilation cross section $\langle\sigma v\rangle = 10^{-8}$ GeV^{-2}, without scattering $\langle\sigma v\rangle' = 0$, and varying the annihilation $\Gamma = \Gamma_{31} = \Gamma_{32} = \Gamma_{21}$ showing the effects of a low decay width (no effect) and a large width which can completely wash out the relic abundance of the decaying particles.

stantially larger than the annihilation and decay. The high temperatures ensure $\langle\sigma v\rangle'_{ij} \approx \langle\sigma v\rangle'_{ji}$[10] meaning that the DM flavours are kept strongly in thermal equilibrium with each other. However it is the annihilations which still control freeze-out, since the scattering does not alter the total DM number density. Due to the suppression of the decay processes, the scattering does not allow efficient decay until it has itself frozen out. The scattering with t quarks freezes out at $T \sim 30$ GeV, whereas with c, u it is much later, approximately at the QCD transition $T \approx 150$ MeV, given that $m_\chi > 1$ GeV, it is possible that the top quark decays away before DM freeze out, but this doesn't affect the relic abundance.

If we introduce a mass splitting $\Delta m_{2,3} \gtrsim 4.6$ MeV (the threshold for decay to the lightest $\bar{u}u\chi_1$ final state), then $\chi_{2,3}$ decay away during freeze-out even if the width $\Gamma_{2,3}$ is extremely small ($\Gamma \gtrsim 10^{-13}$ GeV). The only relic is the lightest of the three DM. For a 100 GeV DM the degeneracy only needs to be broken by 0.004% to satisfy this condition, therefore it is difficult to imagine a scenario in which the degeneracy remains intact, particularly because a mass splitting is inevitably generated through RG running. To gather an idea of the size of the decays for the DMFV model we refer to Fig.7.13.

To summarize the discussion we can follow two regimes;

1. The masses are truly degenerate, or equivalently a degeneracy which is sufficiently small to prevent decay, i.e. $\Delta m \leq 4.6$ MeV. The scattering is heavily suppressed, but not zero, and still manages to keep the DM in equilibrium until after freeze out. The three DM each obtain an equal relic abundance. Since the mass splitting is a result of flavour-breaking, we must have D_{ii} all equal to preserve the degeneracy, then each DM acquires an identical relic density which must be 1/3 of the measured value.

2. A mass splitting, ϵ, exists; the widths and scattering are $\Gamma_{ij} \propto \epsilon^5$ and $\langle\sigma v\rangle' \propto \epsilon^2$, the latter keep the DM in thermal equilibrium and the former cause the

[10]The average energy of a particle at temperature T is $E \sim 3T = 3m/x$.

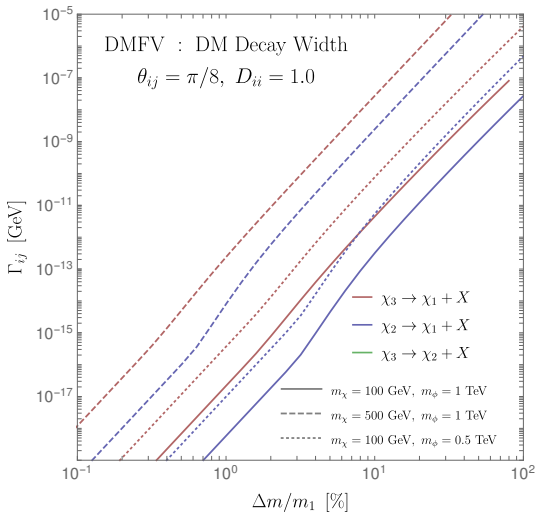

Figure 7.13: The decay width of χ_i into χ_1 (with the hierarchy $m_{\chi_1} < m_{\chi_2} < m_{\chi_3}$) as a function of the mass splitting (as a percentage of m_{χ_1}).

heavier particles to decay. Only the lightest candidate is left, coannihilations may significantly impact the resulting relic abundance and the calculation can be done according to Sec.7.3.

These two cases are summarized in Fig.7.14, comparing the approximate method detailed the previous section to the full Boltzmann equation solution.

7.4 DMFV : Flavour Bounds

7.4.1 Mixing Observables

Since the DMFV introduces couplings to the up type quarks, we would expect new physics effects in the charm sector; specifically the neutral D meson, $D^0 = (\bar{u}c)$ with a mass of $m_{D^0} \sim 1.86$ GeV. Mixing is observed in all neutral meson systems. Theoretically, mixing effects are related to the off diagonal terms of the $D^0 - \bar{D}^0$ mixing matrix Γ_{12} and M_{12} (see Sec.8.1 for a physical definition of these quantities).

These are related to the observable quantities $\Delta\Gamma$ and ΔM which are the decay width and mass differences between the heavy and light mass states of the D^0 meson.

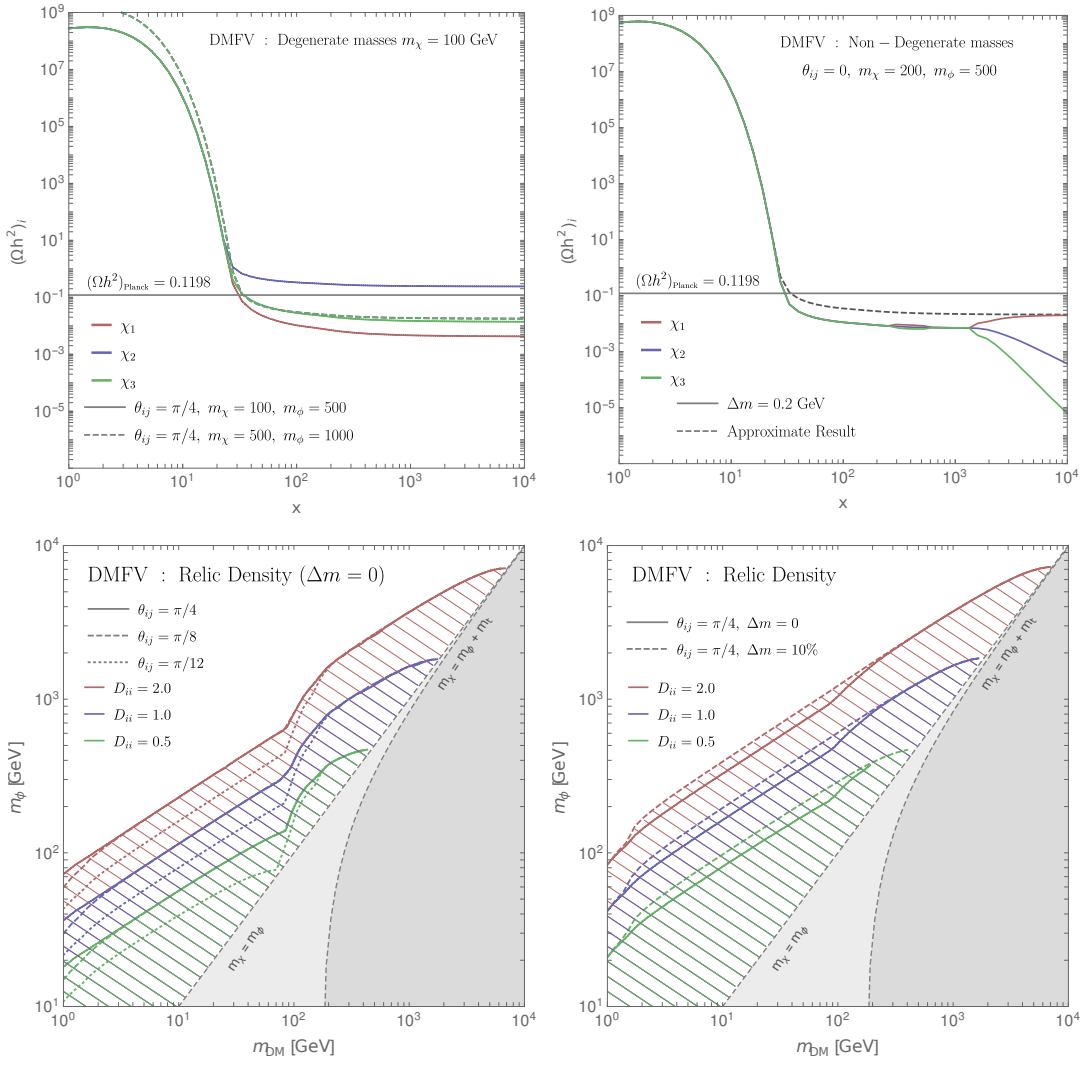

Figure 7.14: Illustration of the RD bounds for degenerate mass DM (left column) solving the coupled Boltzmann equations, or with mass splitting (right column) calculated with the approximate method of Sec.7.3. The top panels illustrate the partial densities of the three candidates in the first moments after the Big Bang, and serve to illustrate the effects of annihilation, scattering and decay mentioned in the text. The bottom panels show the regions (hatched) for which the DMFV models allows the correct relic abundance.

The current experimental measurements are [338],

$$x \equiv \frac{\Delta M}{\Gamma} = (0.63\ ^{+0.19}_{-0.20})\ \% \ , \tag{7.4.89}$$

$$y \equiv \frac{\Delta \Gamma}{2\Gamma} = (0.75 \pm 0.12)\ \% \ . \tag{7.4.90}$$

On the theory side however, things are not so well developed. There are two methods to go about the calculation of mixing parameters – inclusive, where we assume quark-hadron duality and sum quark level diagrams, or exclusive, where individual decay channels that contribute to D_0 mixing are calculated. In the exclusive approach (e.g. [339, 340]), values of x and y on the order of 1% are believed to be possible.

However, a real calculation is hindered by the the fact that the D_0 meson is not sufficiently light to have its decay dominated by a small number of channels. On the inclusive side, we work within the HQE formalism. An early NLO calculation gives $x_{\rm NLO} \approx y_{\rm NLO} \approx 6 \times 10^{-7}$ [341]. As described in that paper, in this calculation physics conspires to cancel relatively large contributions at the first two orders in an expansion in m_s^2/m_c^2, while also a large CKM suppression of the b quark contribution and suppression from chiral symmetry breaking related to $m_d \neq m_s$ further reduce the final result. More recently, a calculation with SU(3) breaking dimension nine contributions in the HQE gives $x \approx 6 \times 10^{-5}, y \approx 8 \times 10^{-6}$ [338] - still missing the experimental results by two or three orders of magnitude.

While there is still a serious question to be answered on whether the HQE is valid for charm system, various calculations [342, 343] have suggested that it could hold with corrections of no more than 50%. It has also recently been suggested [3] that a small breakdown in quark-hadron duality could enhance the value of y by three orders of magnitude to its experimental value.

In light of this, we neglect the SM contribution when calculating our theoretical prediction for ΔM. We convert this to a value of x using the PDG value for the D^0 lifetime.

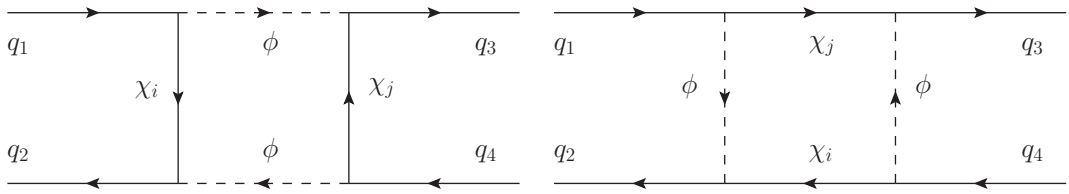

Figure 7.15: Neutral meson mixing : loop diagrams contributing to M_{12} for the DMFV model, where the external momentum are assumed to vanish.

Effective Hamiltonian and M_{12}

The mixing of neutral mesons arises from diagrams as in Fig.7.15 (for both SM and DMFV); M_{12} arises as the dispersive part of the loop integral and is sensitive to heavy internal states (in the SM this is predominantly from internal W, t).

In order to connect the perturbative loop amplitudes to the non-perturbative hadronic physics we need to take hadronic matrix elements. The conventional way to do this is by matching the perturbative amplitudes to an effective four-quark hamiltonian in which the heavy internal states are integrated out. Hadronic matrix elements of this effective Hamiltonian can be taken from lattice calculation.

The effective Hamiltonian is given by,

$$\mathcal{H}_{\text{eff}} = \sum_{i=1,2} C_i \mathcal{O}_i \ ,$$

$$\mathcal{O}_1 = (\bar{u}_a \gamma^\mu (1+\gamma^5) c_a)(\bar{u}_b \gamma_\mu (1+\gamma^5) c_b) \ , \tag{7.4.91}$$

$$\mathcal{O}_2 = (\bar{u}_a \gamma^\mu (1+\gamma^5) c_b)(\bar{u}_a \gamma_\mu (1+\gamma^5) c_b) \ , \tag{7.4.92}$$

where a, b denote colour indices. In order to find the Wilson coefficients C_i we begin by computing the amplitudes in Fig.7.15

$$
\begin{aligned}
i\mathcal{M} &= \int \frac{d^4k}{(2\pi)^4}\ \Bigg[\bar{u}\cdot -i\lambda_{1i}(1-\gamma^5)\frac{i(\not{k}+m_{\chi_i})}{k^2-m_{\chi_i}^2}\cdot -i\lambda_{2i}^*(1+\gamma^5)c \\
&\qquad \times \bar{u}\cdot -i\lambda_{1j}(1-\gamma^5)\frac{i(\not{k}+m_{\chi_j})}{k^2-m_{\chi_j}^2}\cdot -i\lambda_{2j}^*(1+\gamma^5)c\frac{i}{k^2-m_\phi^2}\cdot\frac{i}{k^2-m_\phi^2}\Bigg] \\
&= 4\lambda_{1i}\lambda_{2i}^*\lambda_{1j}\lambda_{2j}^*\left(\bar{u}\gamma_\mu(1+\gamma^5)c\right)\left(\bar{u}\gamma_\nu(1+\gamma^5)c\right)\times\int\frac{d^4k}{(2\pi)^4}\frac{k^\mu k^\nu}{(k^2-m_\phi^2)^2(k^2-m_{\chi_i}^2)(k^2-m_{\chi_j}^2)} \\
&= \lambda_{1i}\lambda_{2i}^*\lambda_{1j}\lambda_{2j}^*\left(\bar{u}\gamma^\mu(1+\gamma^5)c\right)\left(\bar{u}\gamma_\mu(1+\gamma^5)c\right)\times\int\frac{d^4k}{(2\pi)^4}\frac{k^2}{(k^2-m_\phi^2)^2(k^2-m_{\chi_i}^2)(k^2-m_{\chi_j}^2)}\ .
\end{aligned}
$$

After doing the loop integral, we get the following contribution from a single diagram:

$$
\begin{aligned}
i\mathcal{M} &= \frac{i}{(4\pi)^2}\lambda_{1i}\lambda_{2i}^*\lambda_{1j}\lambda_{2j}^*\left(\bar{u}\gamma^\mu(1+\gamma^5)c\right)\left(\bar{u}\gamma_\mu(1+\gamma^5)c\right)\times\frac{1}{(m_{\chi_i}^2-m_{\chi_j}^2)(m_{\chi_i}^2-m_\phi^2)^2(m_{\chi_j}^2-m_\phi^2)^2} \\
&\quad\times\Big[m_\phi^2(m_{\chi_i}^2-m_{\chi_j}^2)(m_{\chi_i}^2-m_\phi^2)(m_{\chi_j}^2-m_\phi^2)+m_{\chi_i}^4m_{\chi_j}^4\ln(m_{\chi_i}^2/m_{\chi_j}^2)+m_{\chi_i}^4m_\phi^4\ln(m_{\chi_i}^2/m_\phi^2) \\
&\qquad -m_{\chi_j}^4m_\phi^4\ln(m_{\chi_j}^2/m_\phi^2)-2m_{\chi_i}^4m_{\chi_j}^2m_\phi^2\ln(m_{\chi_i}^2/m_\phi^2)+2m_{\chi_i}^2m_{\chi_j}^4m_\phi^2\ln(m_{\chi_j}^2/m_\phi^2)\Big]\ .
\end{aligned}
$$

Defining $x_i = m_{\chi_i}^2/m_\phi^2$, we can simplify this to:

$$
\begin{aligned}
i\mathcal{M} &= \frac{i}{(4\pi)^2}\lambda_{1i}\lambda_{2i}^*\lambda_{1j}\lambda_{2j}^*\left(\bar{u}\gamma^\mu(1+\gamma^5)c\right)\left(\bar{u}\gamma_\mu(1+\gamma^5)c\right) \\
&\quad\times\frac{1}{m_\phi^{10}(x_i-x_j)(x_i-1)^2(x_j-1)^2}\times m_\phi^8 \\
&\quad\times\Big[(x_i-x_j)(x_i-1)(x_j-1)+x_i^2x_j^2\ln(x_i/x_j)+x_i^2\ln(x_i)-x_j^2\ln(x_j) \\
&\qquad -2x_i^2x_j\ln(x_i)+2x_ix_j^2\ln(x_j)\Big]\ .
\end{aligned}
$$

Simplifying again we find,

$$
\begin{aligned}
i\mathcal{M} &= \frac{i}{(4\pi)^2}\frac{1}{m_\phi^2}\lambda_{1i}\lambda_{2i}^*\lambda_{1j}\lambda_{2j}^*\left(\bar{u}\gamma^\mu(1+\gamma^5)c\right)\left(\bar{u}\gamma_\mu(1+\gamma^5)c\right) \\
&\quad\times\underbrace{\left[\frac{1}{(1-x_i)(1-x_j)}+\frac{x_i^2\ln x_i}{(x_i-x_j)(1-x_i)^2}-\frac{x_j^2\ln x_j}{(x_i-x_j)(1-x_j)^2}\right]}_{F(x_i,x_j)}, \qquad (7.4.93)
\end{aligned}
$$

where $F(x_i, x_j)$ is the same function as defined in Eq. (C.1) of [325].

We can read off the Wilson coefficients from Eq.(7.4.93),

$$C_1 = \sum_{i,j} \frac{1}{32\pi^2 m_\phi^2} \lambda_{1i}\lambda_{2i}^*\lambda_{1j}\lambda_{2j}^* F(x_i, x_j) \ , \tag{7.4.94}$$

$$C_2 = \sum_{i,j} \frac{1}{32\pi^2 m_\phi^2} \lambda_{1i}\lambda_{2i}^*\lambda_{1j}\lambda_{2j}^* F(x_i, x_j) \ , \tag{7.4.95}$$

hence the effective Hamiltonian, summing over all DM flavours i and j, multiplying by two to account for the second diagram, and dividing by four to account for identical operators, is given by:

$$\mathcal{H}_{\text{eff}}^{\Delta C=2} = \frac{-1}{32\pi^2}\frac{1}{m_{\text{MED}}^2}\left(\bar{u}\gamma^\mu(1+\gamma^5)c\right)\left(\bar{u}\gamma_\mu(1+\gamma^5)c\right)\sum_{i,j}\lambda_{1i}\lambda_{2i}^*\lambda_{1j}\lambda_{2j}^* F(x_i, x_j). \tag{7.4.96}$$

With the Wilson coefficients determined, one must calculate the hadronic matrix elements between meson states, parameterized as,

$$\langle \bar{D}| \mathcal{O}_1 |D\rangle \equiv \frac{8}{3} f_D^2 B_D M_D^2 \ . \tag{7.4.97}$$

The parameter M_{12} is given by

$$M_{12} = \frac{1}{2m_D} C_1 \langle \bar{D}| \mathcal{O}_1 |D\rangle = \frac{-1}{24\pi^2}\frac{1}{m_\phi^2} f_D^2 B_D M_D \sum_{i,j}\lambda_{1i}\lambda_{2i}^*\lambda_{1j}\lambda_{2j}^* F(x_i, x_j), \tag{7.4.98}$$

which may be compared with experiment. Since the SM contributions to ΔM and $\Delta\Gamma$ are poorly known, constraining the BSM contribution by comparison to experiment is not straightforward. One possibility [344] is to require that

$$x_{\text{D}}^{\text{NP}} = \frac{2|M_{12}^{\text{NP}}|}{\Gamma_{\text{D}}} \tag{7.4.99}$$

falls within the 1σ experimental value reported by HFAG, Eq.(7.4.90). This limit would be derived if we assume the NP and SM contributions have roughly the same phase, so that

$$|M_{12}^{\text{NP}} + M_{12}^{\text{SM}}| = |M_{12}^{\text{NP}}| + |M_{12}^{\text{SM}}|, \tag{7.4.100}$$

i.e. they add purely constructively.

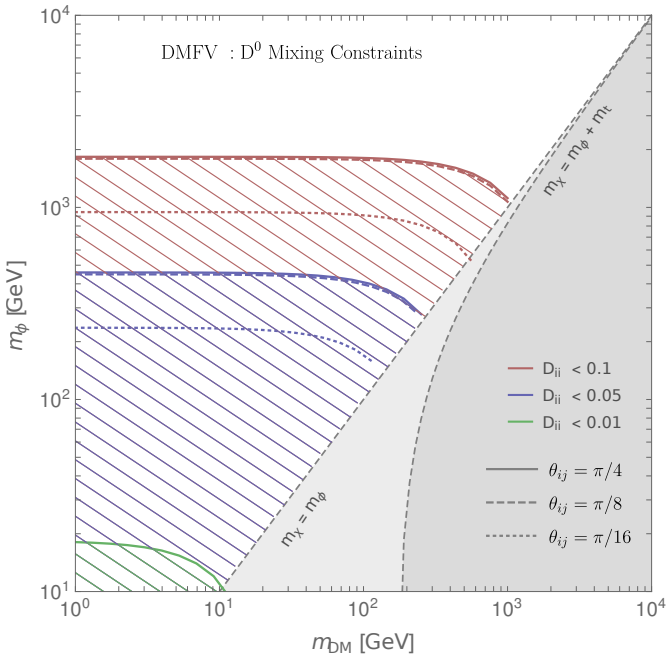

Figure 7.16: Excluded regions (hatched) for which the value of M_{12} from Fig.7.15 exceeds the $+1\sigma$ contour of the experimental result. The bounds are the most constraining possible given the quoted limits on D_{ii}, but can be made arbitrarily small by adjusting the relative values of the D_{ii} (for example with equal values the constraints disappear completely).

Results

The primary result of the previous section is the expression for M_{12}, Eq.(7.4.98). The mass parameters $x_i = m_{\chi_i}/m_\phi \in (0,1)$, the mass dependent function F does not vary strongly $F(x_i, x_j) \in (1/3, 1)$. In the limit $m_{\chi_i} \ll m_\phi$, $F(0,0) = 1$ and $M_{12} \propto ((\lambda\lambda^\dagger)_{12})^2$ and the constraints are primarily sensitive to the value of $(\lambda\lambda^\dagger)_{12}$. The matrix $(\lambda\lambda^\dagger)$ is diagonal if D_{ii} are all equal, or if $\theta_{ij} = 0$ (no mixing between quark flavours) and then the flavour constraints disappear.

Coupling purely to one flavour of quark completely evades the constraints from meson mixing (and this was precisely the way we coupled the DM in the previous chapters). Coupling the same DM candidate to several quarks at once (non zero mixing angles) then introduces the bounds. Even with non-zero mixing the constraints may still be avoided by setting D_{ii} all equal.

Using the upper 1σ value of the experimentally measured x_D leads to bounds as shown in Fig.7.16, these bounds can be very strong and significantly exclude almost all masses $m \gtrsim 1$ TeV for couplings $\lambda \gtrsim 0.1$ unless one fine-tunes the model to remove $(\lambda\lambda^\dagger)_{12}$. The figure also emphasises the interplay between the various parameters is not trivial. For example if $D_{11} \sim D_{22}$ the mixing is suppressed more than if $D_{11} \sim D_{33}$.

This all assumes degenerate DM masses; in practice one can allow for DM masses which are split by some small amount but this does not drastically alter the behaviour. Given the extraordinarily strong bounds from mixing, virtually none of the parameter space allows for DM with the correct relic density unless the model is tuned in a particular way such that $(\lambda\lambda^\dagger)_{12} \approx 0$ due to

1. The mixing angles are zero, $\theta_{ij} = 0$.
2. The D_{ii} are equal to within $\lesssim 1\%$.
3. The D_{ii} are extremely small.

7.4.2 Rare Decays

We consider the semileptonic decay of the neutral D-meson to a lepton pair, $D^0 \to \pi^0 \bar{l}l$, whose short distance (perturbative) contribution comes from the quark level decay $c \to u\bar{l}l$. In the standard model the contribution comes from EW penguin diagrams [345],

$$\mathcal{H}_{\text{eff}}^{(\text{SM})} = -\frac{2G_F}{\sqrt{2}}\frac{\alpha}{4\pi}\frac{A}{s_W^2}\bar{u}\gamma^\mu(1-\gamma^5)c\bar{l}\gamma_\mu l, \tag{7.4.101}$$

with $A \sim 0.065$, the result is both loop and GIM suppressed ($|V_{cb}^* V_{ub}| \sim 1.46 \times 10^{-5}$), and thus we expect this rare decay to have good sensitivity to new physics. In the DMFV model contributions arise at the one-loop level, as photon and Z penguins.

We follow the standard procedure of matching the full theory to the effective

hamiltonian;

$$\mathcal{H}_{\text{eff}} = -\frac{4G_F}{\sqrt{2}} \sum_{i=7,8,9,10,S,P} C_i \mathcal{O}_i, \tag{7.4.102}$$

in which heavy particles are integrated out, and with effective operators [18] [11]

$$\mathcal{O}_7 = -\frac{\alpha}{4\pi}\frac{2m_c^2}{q^2}\bar{u}i\sigma^{\mu\nu}q_\nu P_R c\bar{l}\gamma_\mu l, \tag{7.4.104}$$

$$\mathcal{O}_{11} = -\frac{\alpha}{4\pi}\frac{2m_c^2}{q^2}\bar{u}i\sigma^{\mu\nu}q_\nu P_R c\bar{l}\gamma_\mu\gamma^5 l, \tag{7.4.105}$$

$$\mathcal{O}_9 = \frac{e^2}{(4\pi)^2}\bar{u}\gamma^\mu P_L c\bar{l}\gamma_\mu l \ , \ \mathcal{O}_{10} = \frac{\alpha}{4\pi}\bar{u}\gamma^\mu P_L c\bar{l}\gamma_\mu\gamma^5 l, \tag{7.4.106}$$

$$\mathcal{O}_S = \frac{\alpha}{4\pi}\bar{u}P_R c\bar{l}\gamma^5 l \ , \ \mathcal{O}_P = \frac{\alpha}{4\pi}\bar{u}P_R c\bar{l}\gamma^5 l. \tag{7.4.107}$$

For each operator there is a partner (denoted by a prime) differing only by an opposing projector within the quark bilinear (i.e. $\mathcal{O}'_P$ would be $\bar{u}P_L c\bar{l}\gamma^5 l$). We have added two extra operators $\mathcal{O}_{11}, \mathcal{O}'_{11}$ in order to fully account for all the amplitude structure produced by the Z-penguin diagram, since the Z couples to both vector and axial-vector currents. The following identities are useful,

$$\begin{aligned}\bar{u}i\sigma^{\mu\nu}q_\nu P_R c\bar{l}\gamma_\mu l &= -m_c\bar{u}\gamma^\mu P_L c\bar{l}\gamma_\mu\gamma^5 l + 2\bar{u}P_R c\bar{l}\not{p}_u l,\\ \bar{u}i\sigma^{\mu\nu}q_\nu P_R c\bar{l}\gamma_\mu\gamma^5 l &= -m_c\bar{u}\gamma^\mu P_L c\bar{l}\gamma_\mu\gamma^5 l + 2\bar{u}P_R c\bar{l}\not{p}_u\gamma^5 l + \mathcal{O}(m_l),\end{aligned} \tag{7.4.108}$$

assuming $m_u, m_l = 0$.

the Wilson coefficients $C_i(\mu)$ depend on the renormalization scale μ, and the masses of the particles (we take $m_u \approx 0$, $m_c, m_l \neq 0$) and the momentum exchange through the photon/Z,

$$q^2 = (p_c - p_u)^2 = (p_3 + p_4)^2 \ , \ 0.04 \lesssim q^2 \lesssim 3 \text{ GeV}, \tag{7.4.109}$$

where $p_{3,4}$ are the four-momentum of the lepton and anti-lepton respectively. For the process $D^0 \to \pi^0\bar{l}l$ the maximum value of $q^2_{\text{max}} = (m_D - m_\pi)^2 \sim 3.0$ GeV, well

[11] Including dimension 7 operators we make the replacement,

$$\frac{m_c}{e}\bar{u}\sigma^{\mu\nu}P_R c F_{\mu\nu} = -\frac{m_c}{q^2}\left(2m_c\bar{u}\gamma^\mu c\bar{l}\gamma_\mu l + 4\bar{u}P_R c\bar{l}\not{p}_u l\right). \tag{7.4.103}$$

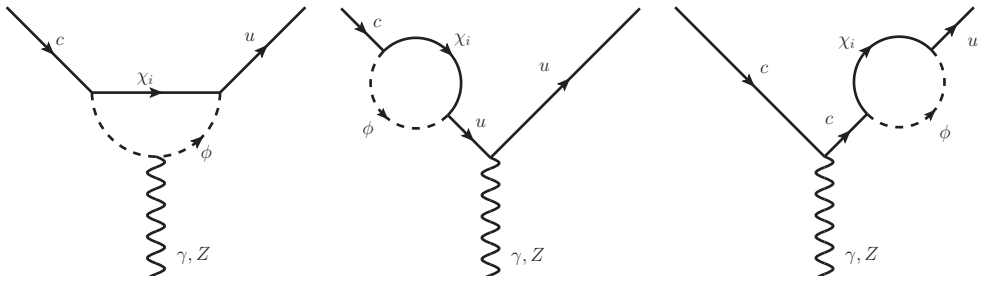

Figure 7.17: The DMFV model contribution to the effective operators governing rare decays of charm quarks, including explicit self-energy corrections to the external quark legs as explained in the text. The γ, Z couple to a lepton pair.

within the perturbative regime, and the minimum value $q^2_{\text{min}} = (2m_l)^2 \lesssim 0.04$ GeV for $l = \mu$.

If m_c is very heavy, or for small momentum exchange then q^2 represents the smallest scale in the problem and we can safely Taylor expand the result. Since we will consider the low energy region, we can simply let $q^2 = 0$ to a good approximation.

To compute the C_i we follow the procedure outlined in [346]. The one loop penguin contribution to the D^0 decay is divergent, and the theory should therefore be renormalized to give a finite result. The external quarks have different flavour, there is no tree level FCNC interaction and so the divergences which appear should cancel against those arising from the flavour violating quark field renormalization, which would appear as an insertion on the external quark legs of the tree level FCNC diagram, as shown in Fig.7.17.

Dealing with the renromalization of the flavour changing self energies requires some extra machinery beyond the scope of this work, and following previous calculations [346] we explicitly include the self energy corrections to the external legs as separate Feynman diagrams, this ensures the cancellation of divergences without performing the renormalization. The self-energy diagrams contribute a finite piece along with the divergences, using a pole mass renormalization scheme would include

these finite pieces in the counter-term, whereas with $\overline{\text{MS}}$ scheme they would be contained in the definition of the renormalized mass $m_{\text{pole}} = m_R + \Sigma_{\text{finite}}$.

The largest wilson coefficients are C_7', C_9' which arise for the photon and Z penguins, although the Z-penguin corrects the results by $\mathcal{O}(1\%)$ and can be neglected. The Z penguin leads to additional contributions to C_8', C_{10}', C_P'. In the limit $q^2 = 0$ the photon penguin contributions are

$$\begin{aligned} C_7'(\mu) =& \frac{\lambda_{ui}\lambda_{ci}^*}{6m_c^6}\Big[m_c^2(m_c^2 - 2(m_\chi^2 - m_\phi^2)) + 2m_c^2(m_\phi^2 - m_\chi^2)\Lambda(m_c^2) + 2m_c^4 m_\phi^2 C_0(m_c^2) \\ &+ ((m_\chi^2 - m_\phi^2)^2 - m_c^2(m_\chi^2 + m_\phi^2))\log\left(\frac{m_\chi^2}{m_\phi^2}\right)\Big], \end{aligned} \tag{7.4.110}$$

$$\begin{aligned} C_9'(\mu) =& \frac{\lambda_{ui}\lambda_{ci}^*}{3m_c^6}\Big[m_c^2(m_c^2 + 12(m_\phi^2 - m_\chi^2)) + 8m_c^2(-m_\chi^2 + m_\phi^2)\Lambda(m_c^2) \\ &+ 2m_c^2(2(m_\chi^2 - m_\phi^2)^2 - m_c^2(m_\chi^2 - 2m_\phi^2))C_0(m_c^2) \\ &+ 4((m_\chi^2 - m_\phi^2)^2 - m_c^2 m_\phi^2)\log\left(\frac{m_\chi^2}{m_\phi^2}\right)\Big], \end{aligned} \tag{7.4.111}$$

where $\Lambda(m^2) \equiv \Lambda(m^2, m_\chi, m_\phi)$ and $C_0(m^2) \equiv C_0(0, 0, m^2, m_\phi, m_\phi, m_\chi)$, the index i refers to the DM and should be summed over using the appropriate masses m_{χ_i}. Due to the hierarchy in scales $q^2 \sim m_c^2 \ll \{m_\chi^2, m_\phi^2\}$ and $m_\phi \gtrsim m_\chi$, we can make the following approximations for the loop functions,

$$\begin{aligned} C_0(s_1^2, s_2^2, s_3^2, m_\phi, m_\phi, m_\chi) &\approx \frac{1}{(m_\chi^2 - m_\phi^2)^2}\left((m_\chi^2 - m_\phi^2) - m_\chi^2\log\left(\frac{m_\chi^2}{m_\phi^2}\right)\right), \\ \Lambda(s^2, m_\chi, m_\phi) &\approx -1 + \frac{1}{2s^2(m_\chi^2 - m_\phi^2)}\log\left(\frac{m_\chi^2}{m_\phi^2}\right)\left[s^2(m_\chi^2 + m_\phi^2) - (m_\chi^2 - m_\phi^2)^2\right], \\ \Lambda(s^2, m_\phi, m_\phi) &\approx -2 + \frac{s^2}{6m_\phi^2}, \end{aligned}$$

where s_i are all assumed to be small $s_i \ll m_\chi, m_\phi$.

In [18] the constraints are placed on $\widetilde{C}_i = V_{ub}V_{cb}^* C_i \approx 5.2 \times 10^{-5} C_i$, for a low and high q^2 region ($q^2 \in [0.0625, 0.276]$ and $q^2 \in [1.56, 4.00]$ GeV^2 respectively).

Since the SM branching ratios for the D^0 decay suffer from a strong GIM cancellation, we would expect strong constraints on the flavour breaking terms of the

C_i	$\lvert C_i^{\max}\rvert$
C_7, C_7'	2.4
C_9, C_9'	2.1
C_P'	3.6
C_{10}	1.4

Figure 7.18: The upper limit on the Wilson coefficients from a D^0 rare decay $D^0 \to \pi\bar{l}l$. These are found from Tab.II of [18], and correspond to the low q^2 bin.

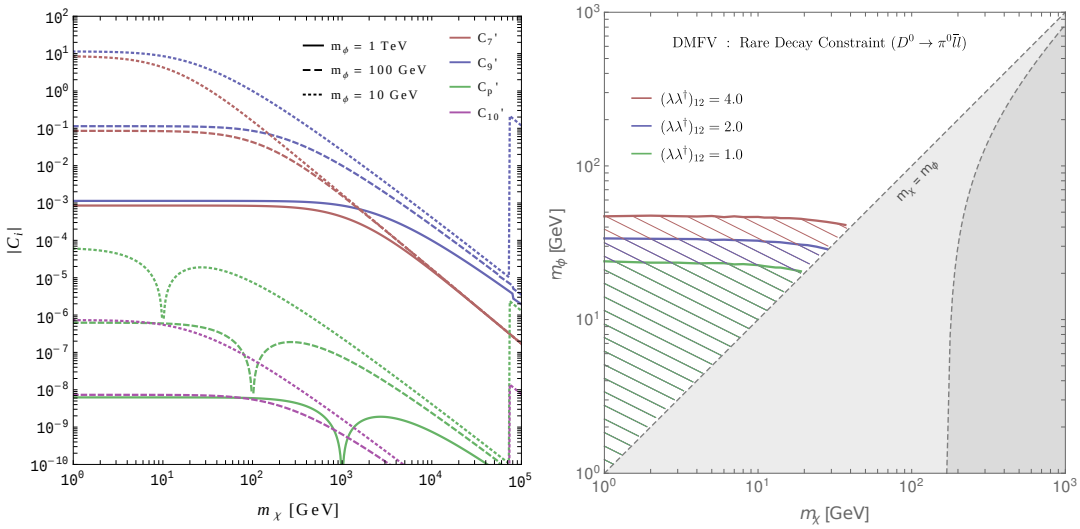

Figure 7.19: Left : the modulus of the Wilson coefficients of operators from Eq.(7.4.107) for various DM and mediator masses. With $(\lambda\lambda^\dagger)_{12} = 1$, and in the $q^2 = 0$ limit (except for $C_{10}' \propto q^2$ for which $q^2 = 0.04$ GeV^2), note also that $C_8' = C_{10}'$ and is not plotted. Right : the exclusions from $|C_9'| < 2.1$ varying $(\lambda\lambda^\dagger)_{12}$.

DMFV model. As with the mixing observables, the rare decay process is a $c \to u$ transition and as such is primarily sensitive to $(\lambda\lambda^\dagger)_{12}$ in the limit of degenerate DM mass. In Fig.7.19 we show the Wilson coefficients $|C_i(m_\chi)|$ for $(\lambda\lambda^\dagger)_{cu} = 1, 2, 4$. The bounds on the individual Wilson coefficients are $|C_i| \lesssim 1-3$ (see Table 7.18) Mediators up to $m_\phi \sim 50$ GeV can be ruled out for couplings $D_{ii} \sim (\lambda\lambda^\dagger)_{12} \sim \mathcal{O}(1)$. These constraints are therefore substantially weaker than from meson mixing observables.

7.5 DMFV : Indirect Detection

7.5.1 Tree Level Annihilation

The dominant annihilation channel for the DM is a tree-level, t-channel exchange of the mediator, producing a quark anti-quark pair (of potentially different flavours) and produces an annihilation cross section

$$\langle \sigma v \rangle_{\bar{\chi}_i \chi_j \to \bar{q}_m q_l} \approx \frac{N_c m_\chi^2}{32\pi (m_\chi^2 + m_\phi^2)^2} \left(\lambda_{li} \lambda_{mj}^*\right)^2 + \mathcal{O}(v^2) \ , \tag{7.5.112}$$

which is dominantly s-wave (the p-wave term can be safely ignored). The ID signals for p-wave processes are suppressed by $v^2 \sim 10^{-6}$ in the galaxy [207], this suppression is always subdominant to the s-wave in the GC, and may be even more severe in other astrophysical targets such as *dwarf spheroidal* (dSph) galaxies [182].

There is a bounty of possible search avenues for this annihilation signal; the energetic quarks will hadronize and decay into stable particles (electrons, protons, photons and the anti-particles, usually referred to as *cosmic rays*), which can be measured directly as they arrive at the earth (in the case of photons especially, which suffer very little energy loss to galactic or inter-galactic material), or indirectly through their influence on cosmic rays (for example photons produced by electrons/protons). We also have great freedom in where to look; generally anywhere where there is a cosmic overdensity of dark matter, close to home in the galactic centre or further afield in *dwarf spheroidal* (dSph) galaxies, galaxy clusters or the CMB.

Underlying all these is Eq.(7.5.112) and so ID constraints are frequently quoted as confidence limits on the thermally averaged annihilation cross section $\langle \sigma v \rangle_{\bar{f}f}$ into fermions of the same flavour, covering a mass range $m_\chi \sim 1$ GeV $-$ 100 TeV. If the DM annihilates into only a single fermion species, these limits can be used directly to place constraints on the model parameters. However in the event that the DM annihilates into different fermions flavours, this is not possible since the ID signal

would look like

$$\sum_{f=u,d,s,\cdots} \langle \sigma v \rangle_{\bar{\chi}\chi \to \bar{f}f} X_f, \tag{7.5.113}$$

where X is some fermion-flavour dependent function, for example the final state radiation pattern from a pair of fermions produced in a single annihilation.

The ID signals from heavy quarks ($q = c, b, t$) are very similar (see [126] Fig.3 and 4), and it is uncommon to find constraints on c, t final states (more common is the b). The primary spectra of electrons, positrons, anti-protons, deuteron and neutrinos are extremely similar between c, b, t quarks, and thus any constraints which look for these particles from DM annihilations will be approximately heavy-flavour independent. The situation is depicted in Fig.7.20. It should be noted that the relative strength of these constraints is not robust, different authors use different halo profiles, different astrophysical parameters and are subject to varying degrees of uncertainty, some significantly larger than others, it is beyond the scope of this work to accommodate all these effects and compare constraints on a like-for-like basis and so what we present should be taken as representative but not precise. We will use the $\bar{b}b$ final state as representative for constraints based on dSph [171] and anti-proton measurements of AMS-02 [199] which dominate other constraints such as those based on other particle targets, such as the positron fraction [202] or neutrinos [205] and also those based on the Galactic Center [19], or galaxy clusters [191].

It would be extremely resource intensive to compute each of the various observables from scratch, and thus be able to include all annihilation channels simultaneously. Instead we will compare the bounds on annihilation to u, c and t couplings *individually* and take the strongest bound. This conservative treatment can still provide strong limits as in Fig.7.21.

An interesting feature of the particular model we are considering is that if the DM is Majorana, the thermally averaged annihilation cross section is helicity suppressed by a factor $(m_q/m_\chi)^2$. This will suppress constraints fairly strongly unless the DM

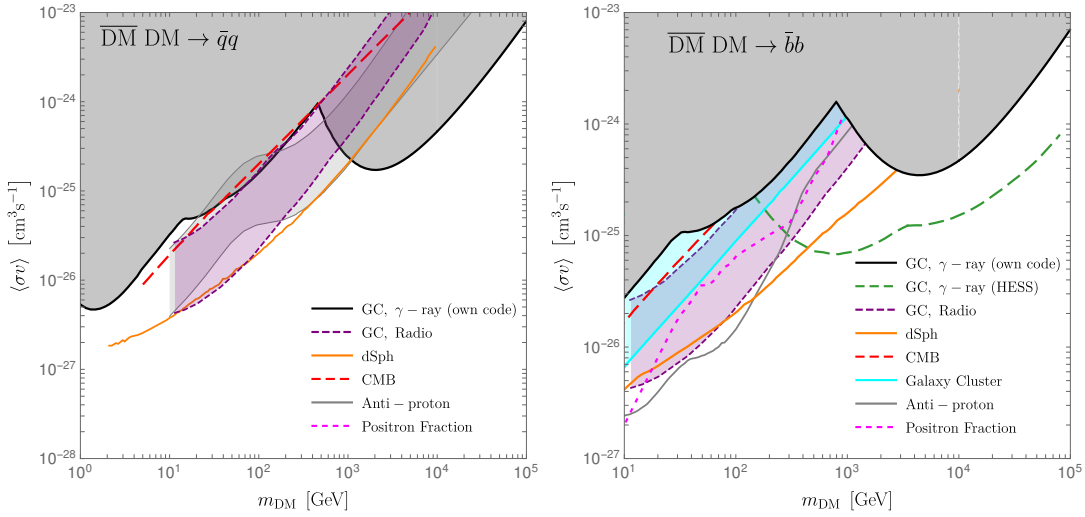

Figure 7.20: The constraints on $\langle\sigma v\rangle_{\bar{f}f}$ for $f = q = u, d, s$ (left) and $f = b$ (right), the latter is representative of $f = c, t$ for $m_\chi > m_{c,t}$. The constraints are taken from many different sources (dSph, galactic centre, clusters) and targets (gamma rays, radio waves, positron, anti-protons), see text for details.

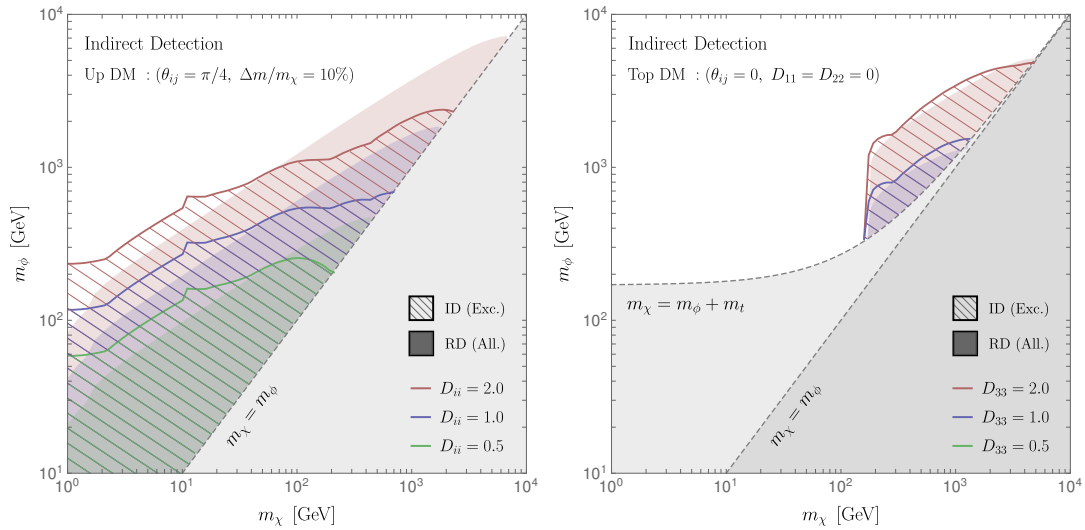

Figure 7.21: The ID constraints on the DMFV model, with 'maximal' mixing $\theta_{ij} = \pi/4$ and χ_1 the lightest (left), or for couplings to top quarks only and χ_3 the lightest (right). Bounds are produced on individual final states, and therefore scale with the dominant annihilation channel, somewhat surprisingly the top quark channel gives stronger constraints due to the extremely sensitive γ-ray search by H.E.S.S [19].

is relatively light and couples strongly to top quarks.

7.5.2 Gamma Ray Lines

The previous section considered the tree level annihilation of dark matter. It is sensible to assume the loop suppressed annihilations are subdominant to the tree level and therefore can be safely ignored, with one exception. The direct production of photons (rather than from the interactions of fermionic final states) leads to the extremely clean signal of a line spectrum, the loop suppression in the cross section is compensated by a significantly stronger limit from detectors.

The process $\bar{\chi}\chi \to \gamma\gamma$ (and also $\bar{\chi}\chi \to \gamma X$ with X some massive particle) leads to a mono-energetic photon signal (smeared by detector resolution effects) and has been analysed by the Fermi-LAT and H.E.S.S. collaborations [122, 123, 347] who produce 95% confidence limits for $\langle\sigma v\rangle_{\bar{\chi}\chi\to\gamma\gamma}$, the thermally averaged annihilation cross section.

The relevant diagrams for annihilation into two photons in our model are box diagrams. Rather than calculate the full result, we first perform the tree level matching described in Sec.7.6.1 by integrating out the mediator. We then use this EFT to calculate the photon production which is now a triangle diagram as shown in Fig.7.22.

From Eq.(7.6.184), with the appropriate values $g_s = 1/2$ and $g_p = -i/2$ for the DMFV model, the EFT contains operators $\mathcal{O}_{F5,6,7,8}$ with equal magnitude coefficients. We list in Tab.7.24 the cross section associated with the insertion of each of the four fermion EFT operators. Then, only a single operator $\mathcal{O}_{F8}$ contributes to the cross section,

$$\langle\sigma v\rangle_{\gamma\gamma} = \frac{\alpha^2 N_c^2 Q_f^4}{1054(m_\chi^2 - m_\phi^2)^2\pi^4} S\left[1 + 2m_f^2 C_0\right]^2 , \tag{7.5.114}$$

where $S \approx 4m_\chi^2$ is the centre of mass energy of the annihilating DM, and C_0 is the

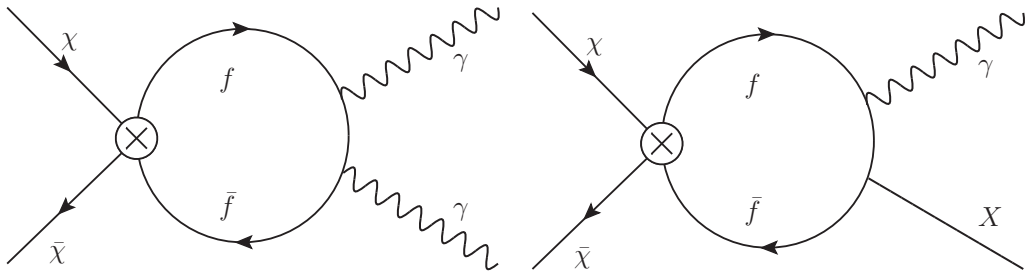

Figure 7.22: The Feynman diagrams for DM annihilation into two photons $\gamma\gamma$ (left) and γX where $X = Z, h$ (right), we have not drawn the diagrams in which the final state lines are crossed but these must be included in the calculation. A full set of independent four fermion EFT operators are inserted at the cross.

scalar integral, where, for $S, m_f > 0$ and $S > m_f$ we have that,

$$C_0 \equiv C_0(0,0,S;m_f,m_f,m_f) = \frac{1}{2S}\left[\log\left|1+\frac{S}{2m_f^2}\left(\sqrt{1-\frac{4m_f^2}{S}}-1\right)\right|+i\pi\right]^2 . \tag{7.5.115}$$

As well as $\gamma\gamma$ final states, there will be γX final states where $X = Z, h$ for example and these also provide constraints (a single gluon or $W^\pm$ emission is prevented by colour or charge conservation respectively). The presence of a massive particle recoiling against the photon shifts the energy to $E_\gamma = m_\chi(1 - m_X^2/4m_\chi^2)$, but still creates a mono-energetic line signature. An example of the cross section is shown in Fig.7.23, which shows that the constraints are slightly weaker than those from tree-level annihilation.

We will present results for the spin averaged squared matrix element $|\langle\mathcal{M}\rangle|^2$ which in general depend on the two Mandelstam variables S and t. The cross section in the c.o.m frame can be derived from the expression,

$$\sigma = \int d\Omega \frac{1}{2E_1 2E_2|v_1 - v_2|}\frac{|p_3|}{16\pi^2 E_{\rm cm}}|\mathcal{M}|^2 \tag{7.5.116}$$

$$= \int d\Omega \frac{1}{\sqrt{S-4m_\chi^2}}\frac{(S-m_X^2)}{64\pi^2 S^{3/2}}|\mathcal{M}|^2 \approx \frac{1}{\sqrt{S-4m_\chi^2}}\frac{(S-m_X^2)}{16S^{3/2}\pi}|\mathcal{M}|^2 , \tag{7.5.117}$$

where $E_1 = E_2 = E_{\rm cm}/2 = \sqrt{s}/2$, $|p_3| = (S - m_X^2)/2\sqrt{S}$ and $|v_1 - v_2| = 2|p_1|/E_1 = 2\sqrt{S-4m_\chi^2}/\sqrt{S}$. In the last line we have taken the approximation of low velocity

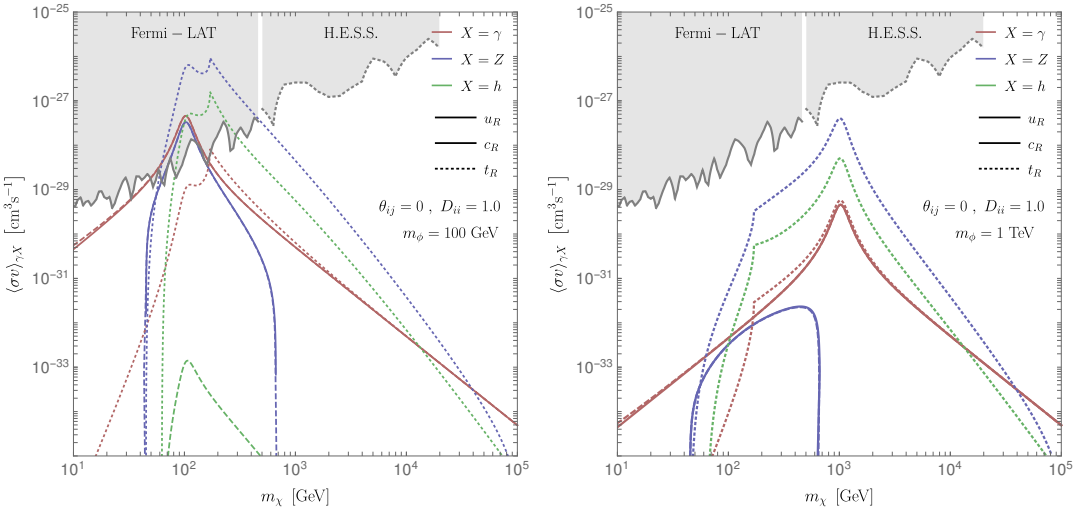

Figure 7.23: The total cross section for $\bar{\chi}\chi \to \gamma X$ where $X = \gamma, Z, h$ (red blue and green respectively), with a scalar mass of 100 GeV (left) and 1 TeV (right), the DM is assumed for simplicity to couple equally to u, c, t with couplings equal to 1. The Fermi-LAT and H.E.S.S. limits are shown for $\langle \sigma v \rangle_{\gamma\gamma}$ and must be scaled appropriately for the Z, h final states, however this does not drastically alter their size or position.

DM in which case the squared matrix element is approximately independent of θ. To see this recall the low velocity limit of the Mandelstam variables,

$$S = 4m_\chi^2 + \mathcal{O}(v^2) \ , \ t = \frac{m_X^2}{2} - m_\chi^2 + \mathcal{O}(v\cos\theta) \ , \tag{7.5.118}$$

and $\cos\theta$ appears velocity suppressed in the matrix element, and this makes implementing the integral is extremely simple, and each of the cross sections take a simple form

$$\langle \sigma v \rangle_{\gamma\gamma} = \frac{1}{8\pi s} |\mathcal{M}|^2_{\gamma\gamma} \ , \tag{7.5.119}$$

$$\langle \sigma v \rangle_{\gamma Z} = \frac{(s - m_Z^2)}{8\pi s^2} |\mathcal{M}|^2_{\gamma Z} \ , \tag{7.5.120}$$

$$\langle \sigma v \rangle_{\gamma h} = \frac{(s - m_h^2)}{8\pi s^2} |\mathcal{M}|^2_{\gamma h} \ . \tag{7.5.121}$$

We now give the analytic expressions for the squared matrix elements.

Two Photon

The matrix element may be written

$$\mathcal{M}^{\mu\nu}_{\gamma\gamma} = \frac{N_c Q_f^2 e^2}{4\pi^2}\left[\Gamma_S^{\mu\nu}(g_{\chi,s}\langle 1\rangle + g_{\chi,p}\langle\gamma^5\rangle) + 2i\Gamma_V^{\mu\nu\sigma}(g_{\chi,v}\langle\gamma_\sigma\rangle + g_{\chi,a}\langle\gamma_\sigma\gamma^5\rangle)\right] , \tag{7.5.122}$$

the functions $\Gamma_{S,V}$ represent the vertex functions for the scalar like ($\mathcal{O}_{F1-4}$) and vector like ($\mathcal{O}_{F5-8}$) EFT operators where the vertex functions are written,

$$\Gamma_S^{\mu\nu} = g_{Q,s} f_2(s) g^{\mu\nu} + g_{Q,s} f_3(s) p_3^\nu p_4^\mu + g_{Q,p} f_4(s)\epsilon^{\mu\nu p_3 p_4} , \tag{7.5.123}$$

$$\Gamma_V^{\mu\nu\sigma} = g_{Q,a} f_1(s)\epsilon^{\mu\nu p_3 p_4}(p_3^\sigma + p_4^\sigma) , \tag{7.5.124}$$

with

$$\begin{aligned} f_1(s) &= \frac{1}{2s}(1 + 2m_q^2 C_0) , \\ f_2(s) &= m_q(2 + (4m_q^2 - s)C_0) , \\ f_3(s) &= \frac{2m_q}{s}(-2 + (s - 4m_q^2)C_0) , \\ f_4(s) &= -2m_q C_0 . \end{aligned} \tag{7.5.125}$$

The two Ward identities $p_3^\mu \mathcal{M}^{\mu\nu} = 0$ and $p_4^\nu \mathcal{M}^{\mu\nu} = 0$ lead to the relation,

$$f_2(s) + \frac{s}{2} f_3(s) = 0 , \tag{7.5.126}$$

which is confirmed in our result. We present the squared matrix element (summed over spins and polarizations) in Table.7.24 for the various EFT operator insertions.

Note that the $\bar{\chi}\chi$ initial state is p-wave suppressed (proportional to $(S - 4m_\chi^2)$), and for small quark masses those with a $\bar{\chi}\gamma^5\chi$ are suppressed by m_q^2, leaving only the operator $\bar{\chi}\gamma^\mu\gamma^5\chi\bar{q}\gamma^\mu\gamma^5 q$ contributing significantly.

Z plus Photon

For the $X = Z$ process, the Z possesses both vector and axial-vector couplings. Furry's theorem still applies for the vector Z coupling and forces the cross section for $\mathcal{O}_{F5,6}$ to depend only on the axial Z coupling, and $\mathcal{O}_{F7,8}$ on the vector Z coupling.

The relevant Lagrangian for DM annihilation to γZ is,

$$\mathcal{L} = \bar{q}\gamma_\mu(g^q_{Z,v} + g^q_{Z,a})qZ^\mu + eQ_f\bar{q}\gamma_\mu q A^\mu + \sum_{i,j} g_{i,j}\bar{\chi}\Gamma_i\chi\bar{q}\Gamma_j q \ . \tag{7.5.127}$$

In [121] (see also [348]) the amplitude for the process $Z'^\sigma \to Z^\mu\gamma^\nu$ is shown, where Z' is a vector boson. Given the form of Eq.(33) of [121] we do not reproduce the expression, however there are two identities (derived from the Schouten identity) which may be employed to reduce the 5 non-zero amplitudes down to 3:

$$\epsilon^{\mu\nu\sigma\rho}p_{4\rho} = \frac{2}{s-m_Z^2}\left(m_Z^2 p_3^\rho\epsilon^{\mu\nu\sigma\rho} + p_4^\mu\epsilon^{\nu\sigma\rho\tau}p_{3\rho}p_{4\tau} + p_4^\sigma\epsilon^{\mu\nu\rho\tau}p_{3\rho}p_{4\tau}\right) \ , \tag{7.5.128}$$

$$\epsilon^{\mu\nu\sigma\rho}p_{3\rho} = \frac{2}{s-m_Z^2}\left(p_3^\nu\epsilon^{\mu\sigma\rho\tau}p_{3\rho}p_{4\tau} - p_3^\sigma\epsilon^{\mu\nu\rho\tau}p_{3\rho}p_{4\tau}\right) \ , \tag{7.5.129}$$

at which point our results agree. The matrix element may be written

$$\mathcal{M}^{\mu\nu}_{\gamma Z} = \frac{N_c Q_f e}{4\pi^2}\left[\Gamma_S^{\mu\nu}(g_{\chi,s}\langle 1\rangle + ig_{\chi,p}\langle\gamma^5\rangle) + i\Gamma_V^{\mu\nu\sigma}(g_{\chi,v}\langle\gamma_\sigma\rangle + g_{\chi,a}\langle\gamma_\sigma\gamma^5\rangle)\right] , \tag{7.5.130}$$

where the vertex functions are

$$\Gamma_S^{\mu\nu} = g_{Z,v}g_{Q,s}f_4(s)\left(\frac{1}{2}(m_Z^2-s)g^{\mu\nu} + p_3^\nu p_4^\mu\right) \ , \tag{7.5.131}$$

$$\Gamma_V^{\mu\nu\sigma} = -f_1(s)\epsilon^{\mu\sigma p_3 p_4}p_3^\nu + \epsilon^{\mu\nu p_3 p_4}\left(f_2(s)p_3^\sigma - f_3(s)p_4^\sigma\right) \ , \tag{7.5.132}$$

with[12]

$$\begin{aligned}
f_1(s) &= \frac{4m_Z^2}{(s-m_Z)^3}\Big[A_f g_A^f\left(s\Lambda(m_Z^2) - s\Lambda(s) + (m_Z^2-s)(1+2m_Q^2C_0)\right) \\
&\quad + B_f g_V^f\left(s\Lambda(m_Z^2) - s\Lambda(s) + (m_Z^2-s)(1+2m_Q^2\frac{s}{m_Z^2}C_0)\right)\Big] \ , \\
f_2(s) &= \frac{2}{(s-m_Z)^3}\Big[A_f g_A^f\left(m_Z^2(m_Z^2+s)(\Lambda(m_Z^2)-\Lambda(s)) + (3m_Z^4 - 4m_Z^2 s + s^2)(1+2m_Q^2C_0)\right) \\
&\quad + B_f g_V^f\Big(m_Z^2(m_Z^2+s)(\Lambda(m_Z^2)-\Lambda(s)) \\
&\quad + (3m_Z^4 - 4m_Z^2 s + s^2)(1+2m_Q^2C_0) + 2(m_Z^2-s)^2C_0\Big)\Big] \ , \\
f_3(s) &= \frac{2}{(m_Z^2-s)^2}\left(A_f g_A^f + B_f g_V^f\right)\left(m_Z^2(\Lambda(m_Z^2)-\Lambda(s)) + (m_Z^2-s)(1+2m_Q^2C_0)\right) \ , \\
f_4(s) &= \frac{2m_q}{(s-m_Z^2)^2}\left(2m_Z^2(\Lambda(m_Z^2)-\Lambda(s)) + (m_Z^2-s)(2+(4m_q^2+m_Z^2-s)C_0)\right)
\end{aligned}$$

[12]The couplings are defined as $A_f = 1/2(g_{LH} + g_{RH})$, $B_f = 1/2(g_{LH} - g_{RH})$, referring to the LH/RH couplings to the Z.

where we define,

$$\Lambda(x) \equiv \Lambda(x, m_Q, m_Q) \ ,$$
$$C_0 \equiv C_0(0, m_Z^2, s, m_Q, m_Q, m_Q) \ . \tag{7.5.133}$$

Using the notation of [121],

$$\begin{aligned} f_1(s) &= B_6^f + \frac{2}{s - m_Z^2} B_2^f - \frac{2m_Z^2}{s - m_Z^2} B_3^f \ , \\ f_2(s) &= B_8^f - \frac{2m_Z^2}{s - m_Z^2} B_3^f + \frac{2}{s - m_Z^2} B_2^f \ , \\ f_3(s) &= B_7^f + B_3^f \ . \end{aligned} \tag{7.5.134}$$

As with the two photon case, the Ward identity $p_3^\mu \mathcal{M}^{\mu\nu} = 0$ is satisfied.

The squared matrix element for each of the four-fermion operators is shown in Tab.7.25. As expected, the operators with a $\bar{\chi}\chi$ initial state are p-wave suppressed (proportional to $(S - 4m_\chi^2)$).

Higgs + Photon

Lastly we focus on the case of DM annihilation $\bar{\chi}\chi \to \gamma h$. The SM Higgs couples to the fermions through the interaction $\mathcal{L} = y_q \bar{q} q h$ with $y_q = m_q/v$ where $v \approx 246$ GeV is the Higgs vev. For t the Higgs coupling is around an order of magnitude larger than that for the Z and γ, for c, b quarks it is around the same size and for light quarks it is much smaller.

Given the full set of EFT operators, only those with a vector-like quark coupling are non-zero (due to Furry's theorem). Additionally the cross section for axial-vector DM couplings is velocity suppressed and therefore only a single operator leads to the $h\gamma$ final state, the vector operator $\bar{\chi}\gamma^\mu\chi\bar{q}\gamma_\mu q$ as shown in Table.7.26.

The matrix element may be written,

$$\mathcal{M}_{\gamma h}^\mu = \frac{N_c Q_f e y_q}{4\pi^2} \left[\Gamma_V^{\mu\sigma} (g_{\chi,v} \langle \gamma_\sigma \rangle + g_{\chi,a} \langle \gamma_\sigma \gamma^5 \rangle) \right] \ , \tag{7.5.135}$$

	EFT operator	$\lvert\mathcal{M}\rvert^2_{\gamma\gamma}$
F1	$\bar{\chi}\chi\bar{f}f$	$2y'g^2_{\chi,s}g^2_{Q,s}m^2_q(s-4m^2_\chi)\left[2-(s-4m^2_q)C_0\right]^2$
F2	$\bar{\chi}i\gamma^5\chi\bar{f}f$	$2y'g^2_{\chi,p}g^2_{Q,s}m^2_q s\left[2-(s-4m^2_q)C_0\right]^2$
F3	$\bar{\chi}\chi\bar{f}i\gamma^5 f$	$6y'g^2_{\chi,s}g^2_{Q,p}m^2_q s^2(s-4m^2_\chi)\lvert C_0\rvert^2$
F4	$\bar{\chi}\gamma^5\chi\bar{f}\gamma^5 f$	$6y'g^2_{\chi,p}g^2_{Q,p}m^2_q s^3\lvert C_0\rvert^2$
F5	$\bar{\chi}\gamma^\mu\chi\bar{f}\gamma_\mu f$	0 (Furry's Theorem)
F6	$\bar{\chi}\gamma^\mu\gamma^5\chi\bar{f}\gamma_\mu f$	0 (Furry's Theorem)
F7	$\bar{\chi}\gamma^\mu\chi\bar{f}\gamma_\mu\gamma^5 f$	0
F8	$\bar{\chi}\gamma^\mu\gamma^5\chi\bar{f}\gamma_\mu\gamma^5 f$	$\frac{3}{2}y'g^2_{\chi,a}g^2_{Q,a}m^2_\chi s\left[1+2m^2_q C_0\right]^2$

Figure 7.24: The squared matrix elements for the annihilation $\bar{\chi}\chi \to \gamma\gamma$ for various fermion DM EFT operators coupled to fermions with charge Q_f and coupling g, note that g has mass dimension -2. $C_0 \equiv C_0(0,0,s,m_q,m_q,m_q)$ and $y' = (4Q_f^4 N_c^2\alpha^2)/(\pi^2)$.

with,

$$\Gamma_V^{\mu\nu\sigma} = g_{Q,v}f_{h,1}(s)\left(\frac{1}{2}(m_h^2-s)g^{\mu\sigma}+p_4^\mu p_3^\sigma\right)\ , \tag{7.5.136}$$

and,

$$f_{h,1}(s) = -\frac{2m_q}{(m_h^2-s)^2}\left[2s(\Lambda(s)-\Lambda(m_h^2))+(m_h^2-s)(-2+(m_h^2-4m_q^2-s)C_0)\right]\ . \tag{7.5.137}$$

As a final note, although the line-like nature of signals generated from processes such as $\bar{\chi}\chi \to \gamma\gamma, \gamma Z, \gamma h$ are spectrally distinct from the smooth continuum emission of photons from fermionic final states; there is still a source of continuum emission which is produced in the line-like processes by final state radiation and decay of the final state particle [119]. However this continuum emission is inevitably subdominant to the primary continuum emission due to loop and coupling suppressions. What it can offer is a constraint at very large DM masses beyond the upper energy reach of the experiment, since the observed photons have a much smaller share of the

	EFT operator	$\lvert\mathcal{M}\rvert^2_{\gamma Z}$
F1	$\bar{\chi}\chi\bar{f}f$	$yg^2_{\chi,s}g^2_{Q,s}g^2_{Z,v}\frac{m_q^2(s-4m_\chi^2)}{4(s-m_Z^2)^2}\left[2m_Z^2\Lambda_m+(s-m_Z^2)(2+(4m_q^2+m_Z^2-s)C_0)\right]^2$
F2	$\bar{\chi}i\gamma^5\chi\bar{f}f$	$yg^2_{\chi,p}g^2_{Q,s}g^2_{Z,v}\frac{m_q^2 s}{4(s-m_Z^2)^2}\left[2m_Z^2\Lambda_m+(s-m_Z^2)(2+(4m_q^2+m_Z^2-s)C_0\right]^2$
F3	$\bar{\chi}\chi\bar{f}i\gamma_5 f$	$\frac{3}{4}yg^2_{\chi,s}g^2_{Q,p}g^2_{Z,v}m_q^2(s-4m_\chi^2)(s-m_Z^2)^2\lvert C_0\rvert^2$
F4	$\bar{\chi}i\gamma^5\chi\bar{f}i\gamma_5 f$	$\frac{3}{4}yg^2_{\chi,p}g^2_{Q,p}g^2_{Z,v}m_q^2 s(s-m_Z^2)^2\lvert C_0\rvert^2$
F5	$\bar{\chi}\gamma^\mu\chi\bar{f}\gamma_\mu f$	$3yg^2_{\chi,v}g^2_{Q,v}g^2_{Z,a}\frac{(8m_\chi^2+m_Z^2)}{4m_Z^2(m_Z^2-4m_\chi^2)^2}\left\lvert 4m_\chi^2m_Z^2\Lambda_m-(4m_\chi^2-m_Z^2)(m_Z^2+8m_\chi^2m_Q^2C_0)\right\rvert^2$
F6	$\bar{\chi}\gamma^\mu\chi\bar{f}\gamma_\mu\gamma^5 f$	$yg^2_{\chi,a}g^2_{Q,v}g^2_{Z,v}\frac{3(8m_\chi^2+m_Z^2)}{4(m_Z^2-4m_\chi^2)^2}\left\lvert 4m_\chi^2\Lambda_m+(4m_\chi^2-m_Z^2)A\right\rvert^2$
F7	$\bar{\chi}\gamma^\mu\gamma^5\chi\bar{f}\gamma_\mu f$	$\frac{yg^2_{\chi,a}g^2_{Q,v}g^2_{Z,a}}{9\pi^3m_Z^2(4m_\chi^2-m_Z^2)^2}\Big[-32m_\chi^6\Big(\lvert A\rvert^2(4m_\chi^2-m_Z^2)^2+m_Z^4\lvert\Lambda_m\rvert^2+m_Z^2\mathrm{Re}(A\Lambda_m^\dagger)(4m_\chi^2-m_Z^2)\Big)+8(4m_\chi^2-m_Z^2)^2\Big[\mathrm{Re}(A)m_\chi^4(4m_\chi^2-m_Z^2)+\mathrm{Re}(\Lambda_m)m_\chi^4m_Z^2+\frac{1}{32}(4m_\chi^2-m_Z^2)^2(3m_Z^3-8m_\chi^2)\Big]\Big]$
F8	$\bar{\chi}\gamma^\mu\gamma^5\chi\bar{f}\gamma_\mu\gamma^5 f$	$\frac{yg^2_{\chi,a}g^2_{Q,a}g^2_{Z,v}}{4\pi^3(4m_\chi^2-m_Z^2)^2}\Big[-32m_\chi^4m_Z^2\Big(4m_\chi^2\lvert\Lambda_m\rvert^2+\mathrm{Re}(\Lambda_mA^\dagger)(4m_\chi^2-m_Z^2)\Big)+\lvert A\rvert^2(4m_\chi^2-m_Z^2)^2\Big(3(4m_\chi^2-m_Z^2)^2-8m_\chi^2m_Z^2\Big)\Big]$

Figure 7.25: Squared matrix elements for the annihilation $\bar{\chi}\chi\to\gamma Z$ process for various fermionic DM EFT operators, coupled to fermions with charge Q_f. We define $\Lambda_m=\Lambda(s)-\Lambda(m_Z^2)$ and $A=1+2m_Q^2C_0$ and the constant $y=(Q_f^2N_c^2\alpha)/(\pi^3)$.

	EFT operator	$\lvert\mathcal{M}\rvert^2_{\gamma h}$
F5	$\bar{\chi}\gamma^\mu\chi\bar{f}\gamma_\mu f$	$2yg^2_{\chi,v}g^2_{Q,v}\frac{m_\chi^2m_q^2}{(m_h^2-4m_\chi^2)^2}\left[-8m_\chi^2\Lambda_m+(4m_\chi^2-m_h^2)(2+(4m_\chi^2-m_h^2+4m_q^2)C_0)\right]^2$

Figure 7.26: Squared matrix elements for the annihilation $\bar{\chi}\chi\to\gamma h$ process for various fermionic DM EFT operators, coupled to fermions with charge Q_f. We define $\Lambda_m=\Lambda(s)-\Lambda(m_h^2)$ and the constant $y=(Q_f^2N_c^2\alpha y_q^2)/(\pi^3)$.

available annihilation energy, on the other hand such large masses $\mathcal{O}(10-100)$ TeV run into difficulties with perturbative unitarity bounds. The continuum is dominantly generated by the decay of the Z, h, which decay similarly to fermions and thus result is a very similar continuum.

7.6 DMFV : Direct Detection

7.6.1 Tree Level

The calculation of the scattering rate in a DD machine is done via an effective theory, whereby heavy states are integrated out. This includes the mediator, the EW particles (W, Z, h) and potentially the c, t quarks. The relevant Feynman diagrams for the scattering of DM with nuclei appears at tree level via the exchange of ϕ if the underlying scattering is with valence (u) or sea quarks (c, t). The ϕ is then integrated out and the theory matched to a set of DM-quark EFT operators.

Only a single four-fermion operator (dimension six) appears in the matching, from a single diagram at tree level with ϕ exchanged in the u-channel. We will limit the scattering amplitudes to those in which the incoming and outgoing DM (and quark) are the same flavour. This avoids the (possibly unknown) computation of the hadronic matrix elements of quark currents $\bar{q}_i \Gamma q_j$ for $i \neq j$. The matching is given by,

$$\mathcal{L}_{\text{EFT}} = C_t^{(ij)}(\mu) \bar{\chi}^i \gamma^\mu P_L \chi^i \bar{q}_R^j \gamma_\mu q_R^j \ , \tag{7.6.138}$$

the vector currents arise due to the Fierz transformation required to bring the quarks and DM into separate bilinears. The Wilson coefficient is

$$C_t^{(ij)}(\mu) = \frac{\lambda_{ji}\lambda_{ji}^*}{2((m_\chi - m_q)^2 - m_\phi^2)} \ . \tag{7.6.139}$$

The scattering with nucleons then proceeds through both vector and axial-vector quark currents. To find their contribution it is necessary to take hadronic matrix elements of the operators, this does not affect the DM bilinear and so this amounts to a computation of $\langle \bar{q}\gamma^\mu q \rangle_N$ and $\langle \bar{q}\gamma^\mu\gamma^5 q \rangle_N$ for $N = n, p$. The latter probes the

spin distribution of quark q in the nucleus, and as such is suppressed relative to the vector current which probes the valence quark content.

The spin contribution of the charm and top quarks are naturally extremely small, and even worse for the conserved vector current they are zero (as is the case for any sea quark). It would appear that the direct detection limits will be extremely weak for charm and top couplings. This however is far from true when one considers the effects of RG running.

The Wilson coefficient Eq.(7.6.139) is generated at the scale of the mediator mass, assumed to be high. The various quark currents coupled to the DM will mix with all the other currents, through loop diagrams which have anomalous dimensions. The scale is first lowered from $\mu = m_\phi$ towards the scale of the Z mass $\mu \sim m_Z$ with mixing through loop diagrams involving the hypercharge boson and Higgs, then a threshold matching is computed as the EW particles are integrated out of the theory. Then the scale is lowered to the nuclear scattering scale $\mu_n \sim 1\text{GeV}$ leading to further mixing with photon and quark mediated loop diagrams. The relevant calculations have been performed in [258] for which the running and mixing are simply computed using a 16×16 matrix and a basis of operators including Eq.(7.6.138),

$$C(\mu_n) \approx \exp\Big[-\gamma^{(0)}_{\text{belowEW}} t_n\Big] \cdot U_{\text{match}} \cdot \exp\Big[-\gamma^{(0)}_{\text{aboveEW}} t_\Lambda\Big] C(\Lambda), \tag{7.6.140}$$

where $\gamma^{(0)}$ is the anomalous dimension matrix, with running of SM couplings neglected (see the Appendices of [258]) both above and below the EW scales. The logarithmic factors $t_\Lambda = \log(\Lambda/m_Z)$ and $t_n = \log(m_Z/\mu_n)$. Finally U_{match} gives the matching at the EW scale; although this primarily just expands the chiral basis (RH and LH fermion couplings) into the Dirac basis (vector and axial-vector couplings).

In particular, the heavy quark vector current $\bar{Q}\gamma^\mu Q$ mixes with the light quark

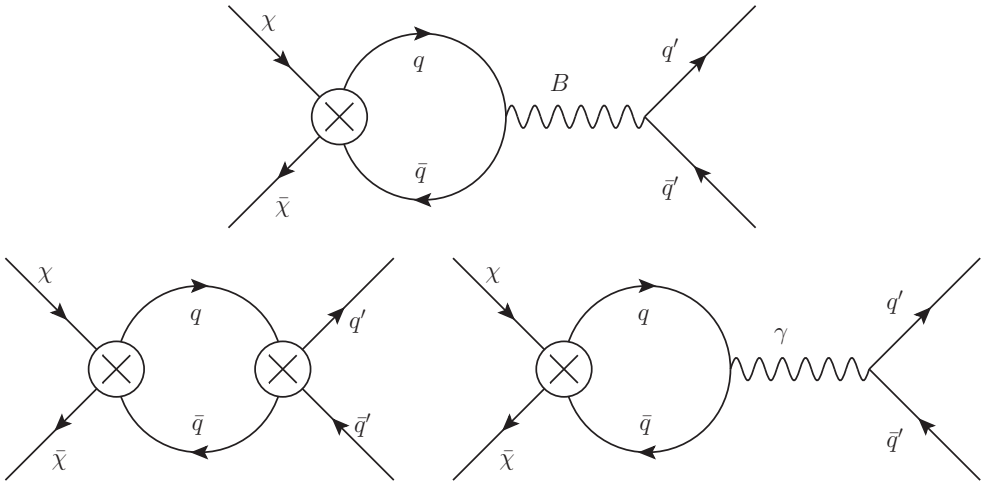

Figure 7.27: The divergent loop diagrams responsible for mixing between the quark vector and axial vector currents ($\bar{\chi}\Gamma\chi\bar{q}\Gamma q$) above the EW scale (top) and below (bottom). The most important aspect is the mixing of high-scale heavy quark currents $q = c, t$ onto light quark vector currents $q' = u, d$, thus enabling a strong scattering cross section with nuclei.

vector current (and vice versa) leading to a replacement;

$$\bar{u}_R\gamma^\mu u_R \to R_{uu}\bar{u}\gamma^\mu u + R_{ud}\bar{d}\gamma^\mu d \ , \tag{7.6.141}$$

$$\bar{c}_R\gamma^\mu c_R \to R_{cu}\bar{u}\gamma^\mu u + R_{cd}\bar{d}\gamma^\mu d \ , \tag{7.6.142}$$

$$\bar{t}_R\gamma^\mu t_R \to R_{tu}\bar{u}\gamma^\mu u + R_{td}\bar{d}\gamma^\mu d \ , \tag{7.6.143}$$

where the high scale is taken to be $\Lambda = m_\phi$. If the mediator $m_\phi < m_Z$ then the EW matching should be neglected, and only the running between m_ϕ and μ_N included. The effect of running is depicted in Fig.7.28, clearly for $m_\phi \gtrsim m_Z$ the mixing is strongest; below this scale the t is integrated out (preventing mixing and requiring a matching to loop induced operators), and the running for the c is slightly weaker. This presents two scenarios in which the DD bounds are weakened:

1. $m_\phi < m_t$ + **top-coupling only** : The top is integrated out of the theory (considered in the next sections), leading to a loop suppressed scattering, which also does not benefit from the mixing. However, this situation violates our assumption of an unstable ϕ and so does not appear in our results unless a coupling to the lighter quarks is present, allowing a ϕ decay channel.

2. $m_\phi < m_Z$ + **charm-coupling only** : If the mediator is sufficiently light and

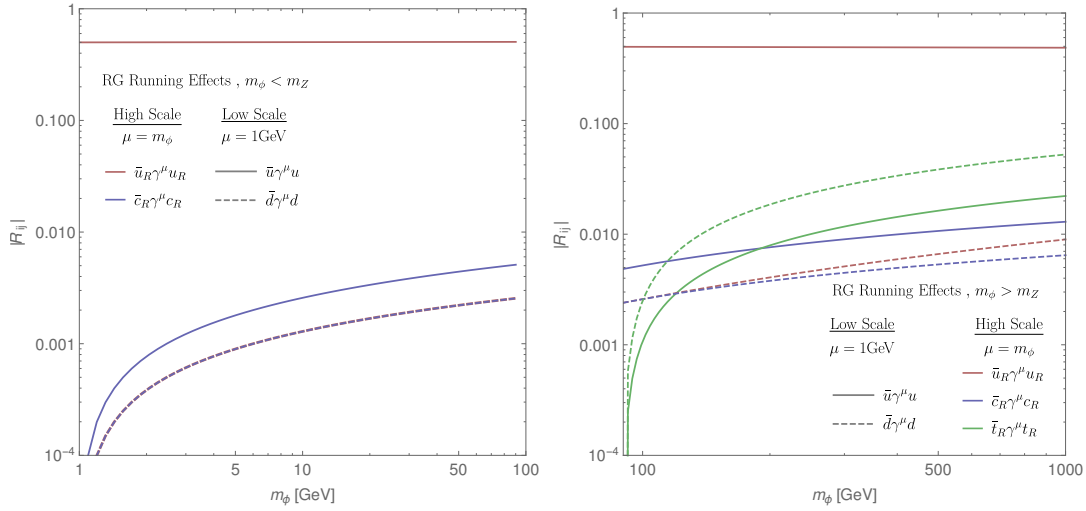

Figure 7.28: The effect of the RG running from a high scale $\Lambda = m_\phi$ down to the nuclear scattering scale $\mu_N = 1$ GeV, the running is slightly different above (right) and below (left) the EW scale (taken to be m_Z).

couples only to charm quarks, then the RG running effect is suppressed by up to $\sim 10^{-3}$ (about the same level as the loop effects). The DD bounds on m_ϕ scale roughly by $10^{-3/2}$ and are therefore significantly weakened.

Generally a null result in DD data requires mediators with large masses, which then induce a mixing of the heavy quark current with suppression, $R_{Q,u}, R_{Q,d} \sim 10^{-2}$, compared with the light quark current. The cross section scales approximately as $\sigma_{\text{heavy}} \sim R_{Qu}^2/m_\phi^4$ and the constraints then decrease by only an order of magnitude, still sufficiently strong to rule out most of the available parameter space.

To match onto a theory which contains nucleons as fundamental degrees of freedom we take hadronic matrix elements of the quark operators. The hadronic matrix elements are extremely simple $\langle\bar{u}\gamma^\mu u\rangle_p = \langle\bar{d}\gamma^\mu d\rangle_n = 2$ and $\langle\bar{u}\gamma^\mu u\rangle_n = \langle\bar{d}\gamma^\mu d\rangle_p = 1$ due to the conserved vector current. Next, the non-relativistic limit of the operators are taken and matched to a set of nuclear form factors; this step justifies our approximation of including only the vector-vector operator $\bar{\chi}\gamma^\mu\chi\bar{q}\gamma_\mu q$, since it is the only one which matches to the largest form factor (which scales as A^2, where A is the atomic number of the target nucleus).

Then, the tree level scattering rate is substantial, even for couplings to the heavy quarks unless the mediator is sufficiently light to prevent the generation of light quark operators through RG running effects, but this requires fine tuning of the mass.

Despite the apparent dominance of the tree level scattering, there are several contributions to scattering which arise at one loop. To present a thorough discussion we will explore these in more detail.

In order to calculate the total event rate in the detector, first one calculates the spin-averaged, squared matrix element for the scattering;

$$\frac{1}{2j_\chi+1}\frac{1}{2j_N+1}\sum_{\text{spin}}|\mathcal{M}|^2=\left(\frac{m_T}{m_N}\right)^2\sum_{i,j}\sum_{N,N'=p,n}C_i^{(N)}C_j^{(N')}F_{ij}^{(N,N')}(v^2,q^2), \tag{7.6.144}$$

where the form factors $F_{ij}^{(N,N')}$ can be found in Appendix A.2 of [211]. The differential cross section is then given by,

$$\frac{d\sigma}{dE_R}=\frac{1}{8\pi m_\chi^2 m_T v^2}\frac{1}{2j_\chi+1}\frac{1}{2j_N+1}\sum|\mathcal{M}|^2. \tag{7.6.145}$$

This is then used to calculate the differential rate,

$$\frac{dR}{dE_R}=N_T n_\chi\int_{v>v_{\min}}\frac{d\sigma}{dE_R}v f_E(v)d^3v, \tag{7.6.146}$$

where the DM number density $n_\chi=\rho_\chi/m_\chi$. The differential rate involves an integral over the velocity vector, weighted by $|\bar{v}|f_E(\bar{v})$, between the minimum velocity and the escape velocity of the galaxy, where f_E is the velocity distribution of the DM, in the Earth's frame and normalized to 1. Since we are not concerned with annual modulation effects, to a good approximation the velocity distribution may be taken as an isotropic Maxwell-Boltzmann. This has the advantage that the integral can be performed analytically.

The cross section according to our prescriptions will in general contain terms proportional to v^n with $n=0,2$ the result for the integrals (termed $\mathcal{J}_0$ and $\mathcal{J}_1$) are

given in Appendix A of [230].

In the DMFV model, at tree level we find

$$C_1^{(p),i} = 4m_i m_N \sum_j (2R_{ju} + R_{jd}) C_t^{(ij)} \ , \tag{7.6.147}$$

$$C_1^{(n),i} = 4m_i m_N \sum_j (2R_{jd} + R_{ju}) C_t^{(ij)} \ , \tag{7.6.148}$$

where R_{Qj} (R_{Qj}) gives the magnitude of the running of operator $\bar{q}_R^j \gamma^\mu q_R^j$ onto $\bar{u}\gamma^\mu u$ ($\bar{d}\gamma^\mu d$). i and j run over the DM and quark flavours respectively.

7.6.2 Loop Level : Gluonic Operators

As well as the tree level scattering of DM, we consider the scattering of the DM with nuclei via its coupling to gluons. To preserve color this requires the exchange of two gluons, arising at the one-loop level as box diagrams. We will use the following Lagrangian to perform the calculation[13];

$$\mathcal{L}_{\text{int}} = \bar{\chi}(g_s + ig_p\gamma^5)F\phi^\dagger + \bar{F}(g_s^\dagger + ig_p^\dagger\gamma^5)\chi\phi \ . \tag{7.6.149}$$

There are four sets of Feyman diagrams as shown in Fig.7.30, which we calculate explicitly using the Mathematica package PackageX [349], and cross checking results using a combination of FeynRules, FeynArts and FormCalc [350–352].

The low energy, zero-momentum transfer limit is taken to simplify the result and match to a small set of EFT operators which are listed in the next section. This calculation has been done several times in the literature [219, 224, 353], however we seek to provide some extra details as in practice using the packages mentioned above the results are difficult to obtain without using some identities.

[13]The factor of i on the γ^5 ensures that the Feynman rule does not change the sign of g_p.

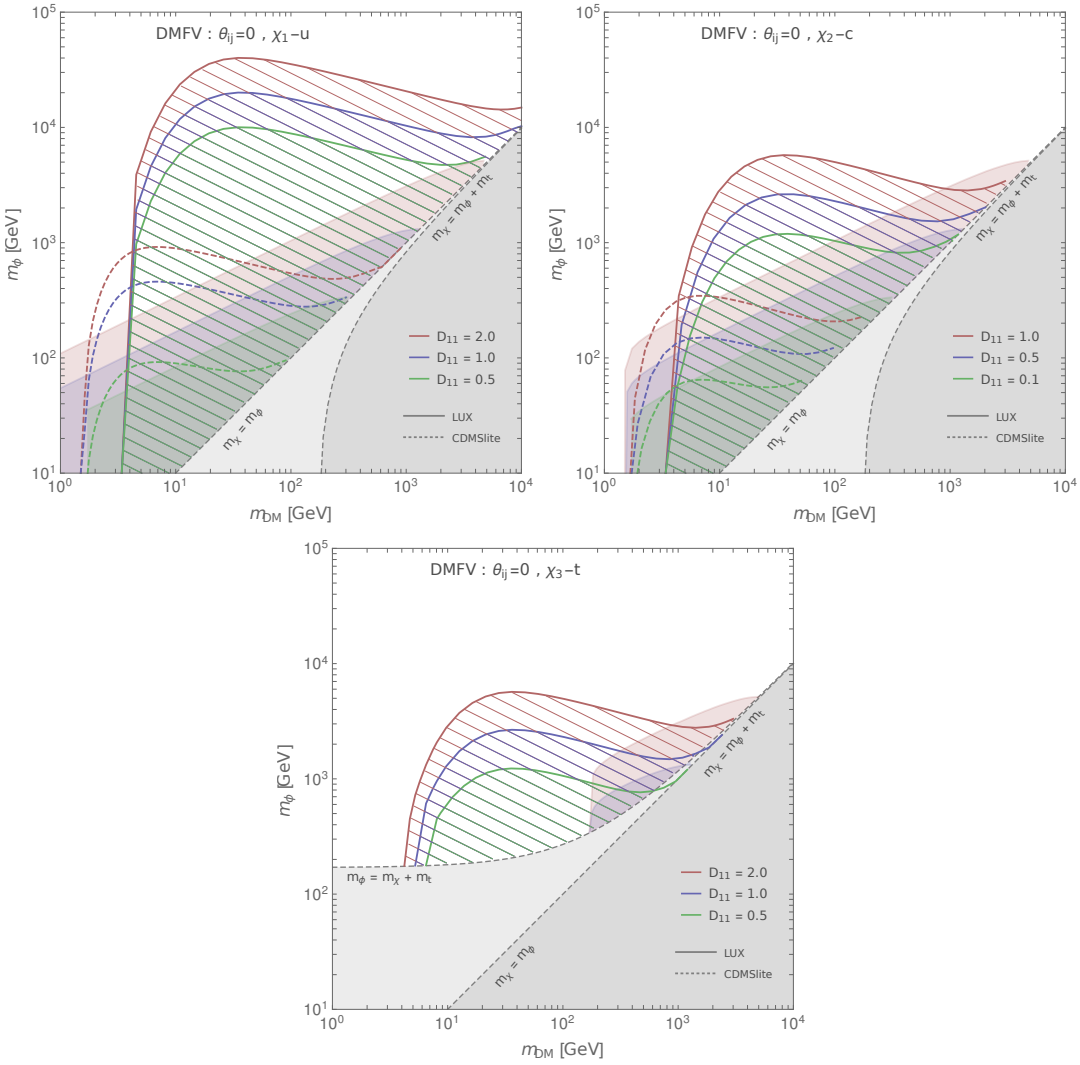

Figure 7.29: The DD bounds for three coupling choices, for a model in which χ_1 couples to u quarks only with strength D_{11}. Bounds for LUX and CMDSlite are solid (dashed), and the filled region shows the allowed parameters which give the correct relic abundance. Constraints are based on the dominant tree level contribution to scattering.

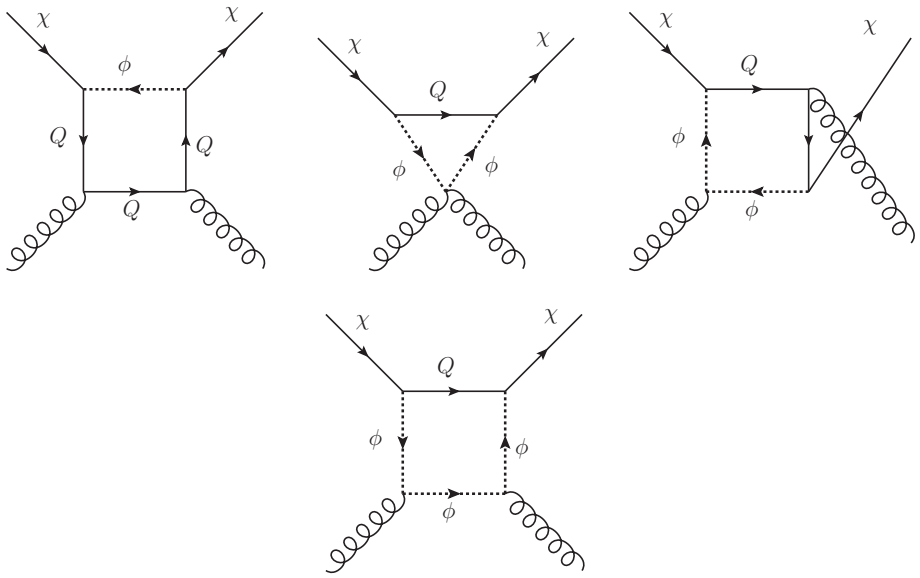

Figure 7.30: The Feynman diagrams for DM-gluon scattering in the DMFV model denoted (a)-(d) (from left to right).

Effective Gluon Operators

We consider in order of mass dimension the operators which lead to DM gluon scattering. These must contain a DM bilinear $\bar{\chi}\Gamma\chi$. The amplitudes for each operator are also shown at $s = u = m_\chi^2$ and $t = 0$ (i.e. the low energy, zero momentum-transfer limit). We will restrict to on-shell gluons for which $\partial^\mu G_{\mu\nu} = 0$ and $\partial^2 G_{\mu\nu} = 0$.

Dimension 4, 5, 6

The only dimension four operator is the DM kinetic term, $\bar{\chi} i \not{\partial} \chi$, which does not have a gluon coupling for color neutral DM. Due to gauge invariance, this remains true to all orders of perturbation theory.

At dim-5 the structure $\bar{\chi}\Gamma\chi$ can only be contracted with $G^{\mu\nu}$, i.e. $\bar{\chi}_i \sigma^{\mu\nu} t^a_{ij} \chi_j G^a_{\mu\nu}$ which is only possible for color charged DM. At dimension 6 we can include a derivative, but still cannot create a color singlet combination.

Dimension 7

At dim-7 it is possible to include two gluon field strengths, with either two or no free indices. The non-zero operators are,

$$\mathcal{O}_{G,s} = \bar{\chi}\chi G^{\mu\nu,a}G^a_{\mu\nu} \ : \ \mathcal{M}^{\mu\nu} = 8\left(q^\mu q^\nu\right)\langle\bar{u}(p')u(p)\rangle\,, \tag{7.6.150}$$

$$\mathcal{O}_{G,s'} = \bar{\chi}\chi \widetilde{G}^{\mu\nu,a}G^a_{\mu\nu} \ : \ \mathcal{M}^{\mu\nu} = 4(q^\sigma Q^\rho)\epsilon^{\sigma\rho\mu\nu}\langle\bar{u}(p')u(p)\rangle\,, \tag{7.6.151}$$

$$\mathcal{O}_{G,p} = \bar{\chi}i\gamma^5\chi \widetilde{G}^{\mu\nu,a}G^a_{\mu\nu} \ : \ \mathcal{M}^{\mu\nu} = 4(q^\sigma Q^\rho)\epsilon^{\sigma\rho\mu\nu}\langle\bar{u}(p')|i\gamma^5|u(p)\rangle\,, \tag{7.6.152}$$

$$\mathcal{O}_{G,p'} = \bar{\chi}i\gamma^5\chi G^{\mu\nu,a}G^a_{\mu\nu} \ : \ \mathcal{M}^{\mu\nu} = 8(q^\mu q^\nu)\langle\bar{u}(p')|i\gamma^5|u(p)\rangle \tag{7.6.153}$$

including both the field strength and its dual $\widetilde{G}^{\mu\nu} \equiv \frac{1}{2}\epsilon^{\mu\nu\sigma\rho}G_{\sigma\rho}$. These operators provide the dominant contribution from the matching.

Dimension 8,9

Many more operators can appear at dimension 8, by the addition of a derivative ∂GG has five lorentz indices and so can only couple to currents with an odd number of lorentz indices,

$$\mathcal{O}_{G,8} = (g\bar{\chi}\gamma^\mu\partial^\nu\chi + g^\dagger\partial^\nu(\bar{\chi})\gamma^\mu\chi)G^{\mu\rho,a}G^a_{\rho\nu} \tag{7.6.154}$$

$$: \ \mathcal{M}^{\mu\nu} = i\mathrm{Im}(g)\langle\bar{u}(p')|\not{Q}|u(p)\rangle\left(q^\mu p^\nu - p^\mu q^\nu\right)\,, \tag{7.6.155}$$

$$\mathcal{O}_{G,8'} = (g\bar{\chi}\gamma^\mu\partial^\nu\gamma^5\chi + g^\dagger\partial^\nu(\bar{\chi})\gamma^\mu\gamma^5\chi)G^{\mu\rho,a}G^a_{\rho\nu} \tag{7.6.156}$$

$$: \ \mathcal{M}^{\mu\nu} = i\mathrm{Im}(g)\langle\bar{u}(p')|\not{Q}\gamma^5|u(p)\rangle\left(q^\mu p^\nu - p^\mu q^\nu\right)\,, \tag{7.6.157}$$

the amplitudes for operators $\bar{\chi}\gamma^\mu\chi G^{\nu\rho,a}\partial_\mu G^a_{\rho\nu}$, $\bar{\chi}\gamma^\mu\gamma^5\chi G^{\nu\rho,a}\partial_\mu G^a_{\rho\nu}$ and $(g\bar{\chi}\gamma^\mu\gamma^5\partial^\nu\chi + g^\dagger\partial^\nu(\bar{\chi})\gamma^\mu\gamma^5\chi)G^{\mu\rho,a}G^a_{\rho\nu}$ are all zero. At dimension 9 a single operator is non-zero for on-shell gluons;

$$\mathcal{O}_{9,1} = \bar{\chi}\sigma^{\mu\nu}\partial^\rho\chi G^{\sigma\nu}\partial_\sigma G^{\mu\rho} \ : \ \mathcal{M} = -4m_\chi\langle\bar{u}_3|\not{Q}|u_1\rangle\left(q^\mu p_1^\nu - p_1^\mu q^\nu\right),$$

which is equivalent to $\mathcal{O}_{G,8}$. The operator $\mathcal{O}_{9,2} = -\bar{\chi}\partial^\mu\partial^\nu\chi G^{\mu\rho}G^{\rho\nu}$ is zero.

We use the Lagrangian laid out in [224] with dim-8,9 terms which do not mix

with the dim-7;

$$\mathcal{L}_{\text{dim}-7} = (B_S + B_D)\bar{\chi}\chi G^{\mu\nu,a}G^a_{\mu\nu} \ , \tag{7.6.158}$$

$$\mathcal{L}_{\text{dim}-8} = 2\left[B_{2S}\bar{\chi}i\partial_\mu\gamma_\nu\chi + \text{h.c.}\right]G^{\mu\rho,a}G_\rho{}^{\nu,a} \ , \tag{7.6.159}$$

$$\mathcal{L}_{\text{dim}-9} = \left[(B_{1D} + B_{1S})\bar{\chi}\partial_\mu\partial_\nu\chi + \text{h.c.}\right]G^{\mu\rho,a}G_\rho{}^{\nu,a} \ , \tag{7.6.160}$$

and then $B_S + B_D = C_{G,s}$, $B_{2S} = C_{G,8}$. The dim-9 operator requires a matching at $\mathcal{O}(t)$ (off shell gluons) and thus we ignore its contribution. We find the dominant contribution,

$$B_D + B_S = \frac{\alpha_s}{12\pi m_\phi^3(1-r^2)\epsilon}\left[1 + \frac{\epsilon}{2r^3(1-r^2)}\left(r^2(-3-2r^2+r^4)\right.\right.$$
$$\left.\left. - 4r^4\log\epsilon + (-3+6r^2+r^4)\log(1-r^2)\right)\right] + \mathcal{O}(\epsilon) \ . \tag{7.6.161}$$

Computing the Feynman diagrams in Fig.7.30, the Wilson coefficients of the dimension 7 operators are as follows (to leading order in the quark mass);

$$C_{G,s} = \frac{\alpha_s}{48\pi m_\phi^3\epsilon}\left[(g_s^2 - g_p^2) + \frac{\epsilon(g_s^2+g_p^2)r(13+8\log\epsilon)}{4}\right] + \mathcal{O}(\epsilon^0) \ ,$$
$$C_{G,s'} = 0 \ ,$$
$$C_{G,p} = \frac{i\alpha_s}{192\pi m_\phi^3\epsilon^2}\left[r(g_s^2+g_p^2) + 3\epsilon(g_s^2-g_p^2)\right] + \mathcal{O}(\epsilon^0) \ ,$$
$$C_{G,p'} = \frac{\alpha_s g_s g_p r}{96\pi m_\phi^3}\left[9 + 8\log\epsilon\right] + \mathcal{O}(\epsilon^0) \ , \tag{7.6.162}$$

where $r \equiv (m_\chi/m_\phi)$ and $\epsilon \equiv (m_Q/m_\phi)$. The dim-8 operators have Wilson coefficients,

$$C_{G,8} = \frac{\alpha_s(g_s^2+g_p^2)}{192\pi m_\phi^4 r^4(1-r^2)^2}\left[r^2 + 3r^4 + (1-2r^2-3r^4)\log(1-r^2) + 4r^4\log\epsilon\right] + \mathcal{O}(\epsilon^1) \ , \tag{7.6.163}$$

$$C_{G,8'} = \frac{2\alpha_s g_s g_p}{192\pi m_\phi^4 r^4(1-r^2)^2}\left[r^2 + 3r^4 + (1-2r^2-3r^4)\log(1-r^2) + 4r^4\log\epsilon\right] + \mathcal{O}(\epsilon^1) \ . \tag{7.6.164}$$

Twist-2 Operator

Rather than classify operators purely on their mass dimension, it can be useful to perform an OPE in the *twist* parameter (dimension minus spin). At lowest order

the dimension 7 operator, $\bar{\chi}\chi G^{\mu\nu}G_{\mu\nu}$, appears, at next order the gluonic *'twist-2'* operator is [219],

$$\mathcal{O}_{\rm Tw2} = \frac{g_G^{(Q,1)}}{\Lambda}\left(i\bar{\chi}\partial^\mu\gamma^\nu\chi + h.c.\right)\mathcal{O}^G_{\mu\nu} - \frac{g_G^{(Q,2)}}{\Lambda^2}\left(\bar{\chi}\partial^\mu\partial^\nu\chi + h.c.\right)\mathcal{O}^G_{\mu\nu}\ , \tag{7.6.165}$$
$$\mathcal{O}^G_{\mu\nu} = G_{\mu\rho}G^{\rho\nu} + \frac{1}{4}g^{\mu\nu}G^{\sigma\rho}G_{\sigma\rho}\ ,$$

which contains dim-8,9 operators defined in Eq.(7.6.160). The twist-2 operator contributes an amplitude (at $t=0$ and $s=m_\chi^2$), [14]

$$\mathcal{M}_{\rm Tw2} = \frac{4g_G^{(Q,1)}}{\Lambda}\bar{u}_3\left[\frac{1}{2}\not{Q}\left(q^\mu p_1^\nu - p_1^\mu q^\nu\right) - m_\chi q^\mu q^\nu\right]u_1 - \frac{4g_G^{(Q,2)}}{\Lambda^2}\left[m_\chi^2\bar{u}_3u_1q^\mu q^\nu\right]\ ,$$

then the twist-2 coupling, Eq.(7.6.165) can be found with the replacements

$$g_G^{(Q,1)} = \Lambda B_{2S}, \tag{7.6.166}$$
$$g_G^{(Q,2)} = \Lambda^2(B_{1D} + B_{1S}), \tag{7.6.167}$$
$$f_G^{(Q)} = (B_S + B_D) - \frac{1}{4}m_\chi B_{2S}, \tag{7.6.168}$$

and for on shell gluons, the only contribution to the twist-2 comes from $g_G^{(Q,1)}$.

[14] In [353] the amplitudes of $g_G^{(Q,\{1,2\})}$ are the same. In order to derive this result it is claimed that $\bar{\chi}\Gamma\gamma^\mu\chi = \bar{\chi}\Gamma i\partial^\mu\chi$, which becomes $\bar{\chi}\Gamma p_1^\mu\chi$, then $Q\cdot p_1 = S - m_\chi^2$ and the amplitudes are the same.

The full amplitudes are

$$\mathcal{M}(g_G^{(1,Q)}) = -4m_\chi q^\mu q^\nu\langle 1\rangle - 2(m_\chi^2 - S)\left(q^\mu\langle\gamma^\nu\rangle - q^\nu\langle\gamma^\mu\rangle\right) + 2\langle\not{Q}\rangle\left(q^\mu p_1^\nu - p_1^\mu q^\nu + (m_\chi^2 - S)g^{\mu\nu}\right),$$
$$\mathcal{M}(g_G^{(2,Q)}) = -4m_\chi^2 q^\mu q^\nu\langle 1\rangle + 4(m_\chi^2 - S)(q^\mu p_1^\nu - p_1^\mu q^\nu)\langle 1\rangle + 2(m_\chi^2 - S)^2 g^{\mu\nu}\langle 1\rangle\,,$$

then using the replacement rule $\gamma^\mu \to p_1^\mu/m_\chi$,

$$\mathcal{M}(g_G^{(1,Q)}) = \left[-4m_\chi q^\mu q^\nu - 4(m_\chi^2 - S)\left(q^\mu p_1^\nu - p_1^\mu q^\nu\right) - 2(m_\chi^2 - S)^2 g^{\mu\nu}\right]\langle 1\rangle\,,$$
$$\mathcal{M}(g_G^{(2,Q)}) = \left[-4m_\chi^2 q^\mu q^\nu + 4(m_\chi^2 - S)(q^\mu p_1^\nu - p_1^\mu q^\nu) + 2(m_\chi^2 - S)^2 g^{\mu\nu}\right]\langle 1\rangle\,.$$

Amplitude of the EFT

We assign momentum as $\chi(p_1)q(p_2) \to \chi(p_3)q(p_4)$, then defining (by eliminating p_3 from overall momentum conservation $p_1 + p_2 = p_3 + p_4$)

$$\begin{aligned} q^\mu &\equiv (p_1 - p_3)^\mu = (p_4 - p_2)^\mu, \\ Q^\mu &\equiv (p_2 + p_4)^\mu, \\ p^\mu &\equiv p_1^\mu \ . \end{aligned} \tag{7.6.169}$$

We express the amplitudes in terms of p, q, Q. We take the $t = (p_1 - p_3)^2 = 0$ (zero momentum transfer) limit, as well as the static limit of the DM ($s = m_\chi^2$). The various scalars are then,

$$\begin{aligned} p \cdot q = 0 \ , \ p \cdot Q = s - m_\chi^2 \ , \ q \cdot Q = 0 \ , \\ p^2 = m_\chi^2 \ , \ q^2 = 0 \ , \ Q^2 = 0 \ . \end{aligned} \tag{7.6.170}$$

The amplitude includes one of the five basis vectors of spinor-space, $\langle \bar{u}(p_3)|\Gamma|u(p_1)\rangle$; $\Gamma = \{1, i\gamma^5, \gamma^\mu, \gamma^\mu\gamma^5, \sigma^{\mu\nu}\}$, as well the various spinor-space scalars in with 0,1,2,4 Lorentz indices $\{1, p_i^\mu, g^{\mu\nu}, \epsilon^{\mu\nu\sigma\rho}\}$.

The polarizations of the gluons can be split from the full amplitude $\mathcal{M} = \mathcal{M}_{\mu\nu}\xi_2^\mu \xi_4^{*,\nu}$ we get $q^\mu = Q^\mu$ and $q^\nu = -Q^\nu$ from transversality of the gluon. The amplitude may be written,

$$\mathcal{M}^{\mu\nu} = \mathcal{M}_S^{\mu\nu} + \mathcal{M}_P^{\mu\nu} + \mathcal{M}_V^{\mu\nu} + \mathcal{M}_A^{\mu\nu} + \mathcal{M}_T^{\mu\nu} \ ,$$

With the contribution from each current being linearly independent from the rest. For scalar and pseudoscalar currents for example,

$$\mathcal{M}_S^{\mu\nu} = \bar{\chi}\chi\Big[s_1 g^{\mu\nu} + s_2 p_1^\mu p_1^\nu + s_3 q^\mu q^\nu + s_4 p_1^\mu q^\nu + s_5 q^\mu p_1^\nu + \epsilon^{\mu\nu\sigma\rho}\left(s_6 q^\sigma Q^\rho + s_7 p_1^\sigma q^\rho + s_8 p_1^\sigma Q^\rho\right)\Big],$$

$$\mathcal{M}_P^{\mu\nu} = \bar{\chi} i\gamma^5 \chi\Big[p_1 g^{\mu\nu} + p_2 p_1^\mu p_1^\nu + p_3 q^\mu q^\nu + p_4 p_1^\mu q^\nu + p_5 q^\mu p_1^\nu + \epsilon^{\mu\nu\sigma\rho}\left(p_6 q^\sigma Q^\rho + p_7 p_1^\sigma q^\rho + p_8 p_1^\sigma Q^\rho\right)\Big].$$

Since the gluons are self-conjugate, the amplitudes must be symmetric under exchange of the gluons, i.e. under $\mu \leftrightarrow \nu$ and $p_2 \leftrightarrow -p_4$ ($Q \to -Q$ and $p, q \to p, q$)

this leads to the constraints,

$$s_4 = s_5 \ , \ s_7 = 0,$$
$$v_7 = v_{11} = v_{12} = 0 \ , \ v_{13} = -v_{14} \ .$$

The amplitude must also satisfy two ward identities, but for QCD the Ward identities are quite involved and depend on the polarizations of the gluons, there will be two such relations and therefore two amplitudes would be removed. Finally hermiticity imposes constraints from the fermions $\mu \leftrightarrow \nu$ and $p_1 \leftrightarrow p_3, p_2 \leftrightarrow p_4$ and $i \to -i$, so that the scalar current has a simple form,

$$\mathcal{M}_S^{\mu\nu} = \bar{\chi}\chi\Big[s_1 g^{\mu\nu} + s_2 q^\mu q^\nu\Big] + \bar{\chi} i\gamma^5\chi\Big[p_1 g^{\mu\nu} + p_2 q^\mu q^\nu\Big] + \bar{\chi}\not{Q}\chi\Big[v(p_1^\mu q^\nu - p_1^\nu q^\mu)\Big].$$

Identities

There are several identities which prove useful for the calculation of the traces of the box diagrams.

The Gordon identity reduces operators with a $\sigma^{\mu\nu}$ via the Dirac equation

$$\langle \sigma^{\mu\nu} q^\mu \xi_i^\nu \rangle = -2im_\chi \langle \not{\xi}_i \rangle + i\,(2p-q)\cdot\xi_i \langle 1 \rangle \,, \tag{7.6.171}$$
$$\langle \sigma^{\mu\nu} q^\mu \xi_i^\nu \gamma^5 \rangle = i\,(2p-q)\cdot\xi_i \langle \gamma^5 \rangle \,, \tag{7.6.172}$$
$$\langle \sigma^{\mu\nu} p^\mu \xi_i^\nu \rangle = -im_\chi \langle \not{\xi}_i \rangle + ip\cdot\xi_i \langle 1 \rangle \,, \tag{7.6.173}$$
$$\langle \sigma^{\mu\nu} p^\mu \xi_i^\nu \gamma^5 \rangle = im_\chi \langle \not{\xi}_i \gamma^5 \rangle + ip\cdot\xi_i \langle 1 \rangle \,, \tag{7.6.174}$$

although operators with $Q^\mu \sigma_{\mu\nu}$ contractions are not reducible in this way. There are several identities related to Levi-Civita tensor derived using the relation

$$\epsilon^{\mu\nu\rho\sigma}\gamma_\sigma\gamma^5 = \frac{1}{2}\left(\sigma^{\mu\nu}\gamma^\rho + \gamma^\rho\sigma^{\mu\nu}\right) \ , \tag{7.6.175}$$

for example,

$$\langle \gamma^\sigma\gamma^5 \rangle \epsilon_{qQ\xi_i\sigma} = -i(2p_1 - q)\cdot\xi_i \langle \not{Q} \rangle \,, \tag{7.6.176}$$
$$\langle \gamma^\sigma\gamma^5 \rangle \epsilon_{p_1Q\xi_i\sigma} = -ip_1\cdot\xi_i \langle \not{Q} \rangle + m_\chi \langle \sigma^{Q\xi_i} \rangle \,, \tag{7.6.177}$$
$$\langle \gamma^\sigma \rangle \epsilon_{qQ\xi_i\sigma} = -i(2p_1 - q)\cdot\xi_i \langle \not{Q}\gamma^5 \rangle + 2m_\chi \langle \sigma^{\epsilon_i Q}\gamma^5 \rangle \,, \tag{7.6.178}$$
$$\langle \gamma^\sigma \rangle \epsilon_{p_1Q\xi_i\sigma} = -ip\cdot\xi_i \langle \not{Q}\gamma^5 \rangle - m_\chi \langle \sigma^{Q\xi_i}\gamma^5 \rangle \tag{7.6.179}$$

and using the Schouten identity one can prove,

$$2\epsilon^{Q\xi_2\xi_4\sigma}\gamma_\sigma\gamma^5 = -\frac{1}{m_\chi}\gamma^5\epsilon^{qQ\xi_2\xi_4} + \frac{1}{m_\chi}\Big[(2p_1-q)\cdot\xi_4\sigma^{Q\xi_2} - (2p_1-q)\cdot\xi_2\sigma^{Q\xi_4}\Big], \tag{7.6.180}$$

and

$$\langle\gamma^\rho\gamma^5\rangle\,\epsilon^{\rho qQ\xi_4}(q\cdot\xi_2) = \langle\gamma^\rho\gamma^5\rangle\,\epsilon^{\rho qQ\xi_2}(q\cdot\xi_4) - m_\chi\,\langle\gamma^5\rangle\,\epsilon^{qQ\xi_2\xi_4}\ , \tag{7.6.181}$$

$$\langle\gamma^\rho\gamma^5\rangle\,\epsilon^{\rho qQ\xi_4}(p\cdot\xi_2) = \langle\gamma^\rho\gamma^5\rangle\,\epsilon^{\rho qQ\xi_2}(p\cdot\xi_4) - 2m_\chi\,\langle\gamma^5\rangle\,\epsilon^{qQ\xi_2\xi_4}\ . \tag{7.6.182}$$

$$\tag{7.6.183}$$

Approximate Result

Since we are working with a general coupling structure $\bar\chi_i(g_s + ig_p\gamma^5)q_j\phi$, we will present the tree level matching for this form. We match to a set of four-fermion operators in Tab.7.1.

	Dirac	Majorana
$\mathcal{O}_{F1}$	$\bar\chi\chi\bar q q$	$\frac{1}{2}\bar\chi\chi\bar q q$
$\mathcal{O}_{F2}$	$\bar\chi i\gamma^5\chi\bar q q$	$\frac{1}{2}\bar\chi i\gamma^5\chi\bar q q$
$\mathcal{O}_{F3}$	$\bar\chi\chi\bar q i\gamma^5 q$	$\frac{1}{2}\bar\chi\chi\bar q i\gamma^5 q$
$\mathcal{O}_{F4}$	$\bar\chi\gamma^5\chi\bar q\gamma^5 q$	$\frac{1}{2}\bar\chi\gamma^5\chi\bar q\gamma^5 q$
$\mathcal{O}_{F5}$	$\bar\chi\gamma^\mu\chi\bar q\gamma_\mu q$	–
$\mathcal{O}_{F6}$	$\bar\chi\gamma^5\gamma^\mu\chi\bar q\gamma_\mu q$	$\frac{1}{2}\bar\chi\gamma^5\gamma^\mu\chi\bar q\gamma_\mu q$
$\mathcal{O}_{F7}$	$\bar\chi\gamma^\mu\chi\bar q\gamma^5\gamma_\mu q$	–
$\mathcal{O}_{F8}$	$\bar\chi\gamma^5\gamma^\mu\chi\bar q\gamma^5\gamma_\mu q$	$\frac{1}{2}\bar\chi\gamma^5\gamma^\mu\chi\bar q\gamma^5\gamma_\mu q$
$\mathcal{O}_{F9}$	$\bar\chi\sigma^{\mu\nu}\chi\bar q\sigma_{\mu\nu} q$	–
$\mathcal{O}_{T1}$	$\bar\chi i\partial^\mu\gamma^\nu\chi\mathcal{O}^{Tq}_{\mu\nu}$	$\bar\chi i\partial^\mu\gamma^\nu\chi\mathcal{O}^{Tq}_{\mu\nu}$
$\mathcal{O}_{T2}$	$\bar\chi\gamma^\mu\gamma^\nu\chi\mathcal{O}^{Tq}_{\mu\nu}$	$\bar\chi\gamma^\mu\gamma^\nu\chi\mathcal{O}^{Tq}_{\mu\nu}$

Table 7.1: EFT operators in the DMFV model for a DM-quark scattering processes.

We will ignore the twist-2 contribution due to the dimensional suppression of

the operators, for the remaining nine operators the Wilson coefficients are;

$$C_{F1}^{(q)} = C_{F4}^{(q)} = -2C_{F9}^{(q)} = \frac{|g_p|^2 - |g_s|^2}{4((m_\chi - m_q)^2 - m_\phi^2)},$$
$$C_{F8}^{(q)} = -C_{F5}^{(q)} = \frac{|g_p|^2 + |g_s|^2}{4((m_\chi - m_q)^2 - m_\phi^2)},$$
$$C_{F2,3}^{(q)} = -\frac{i(g_s g_p^\dagger + g_p g_s^\dagger)}{4((m_\chi - m_q)^2 - m_\phi^2)},$$
$$C_{F6,7}^{(q)} = \frac{i(g_s g_p^\dagger - g_p g_s^\dagger)}{4((m_\chi - m_q)^2 - m_\phi^2)} \ . \tag{7.6.184}$$

For our model the couplings are RH ($g_s = ig_p = \lambda_{ji}$) and note that then $\mathcal{O}_{F1,2,3,4,9}$ each disappear leaving only the vector/axial vector currents $\mathcal{O}_{F5,6,7,8}$ (and thus reproducing Eq.(7.6.138)).

It is possible to obtain an approximate result for each of the gluonic Wilson coefficients $C_{s,s',p,p'}$ by using the four-fermion EFT generated after integrating out the mediator. This then reduces the box diagrams to a triangle diagram with a single EFT insertion as below.

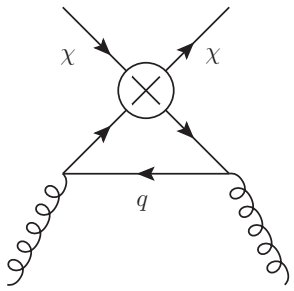

This matches to just dim-7 operators with the following Wilson coefficients if the vertex is scalar $C_{F1,2,3,4}$

$$C_{G,s}^{(q)} = -\frac{1}{8}\left(\frac{\alpha_s C_{F1}^{(q)}}{3m_q\pi}\right) \ , \ C_{G,s'}^{(q)} = -\frac{1}{8}\left(\frac{\alpha_s C_{F3}^{(q)}}{2m_q\pi}\right) \ , \tag{7.6.185}$$
$$C_{G,p}^{(q)} = \frac{1}{8}\left(\frac{\alpha_s C_{F4}^{(q)}}{2m_q\pi}\right) \ , \ C_{G,p'}^{(q)} = \frac{1}{8}\left(\frac{\alpha_s C_{F2}^{(q)}}{3m_q\pi}\right) \ . \tag{7.6.186}$$

or if it is vector $C_{F5,6,7,8}$

$$C_{G,p}^{(q)} = \frac{\alpha_s m_\chi C_{F8}^{(q)}}{12m_q^2\pi} \ , \tag{7.6.187}$$

inserting the Wilson coefficients to the above expression reproduces the leading terms from the calculation of the full loop diagrams, Eq.(7.6.162), except for the $C_{G,p'}$ and second term in $C_{G,s}$. The terms which are not reproduced by the tree level results contain a larger mass suppression (going as r/m_ϕ^3), which suggests they arise from higher dimensional operators; indeed they would be reproduced if we had included a matching to the twist-2 quark operators in the tree level EFT.

Cross Section

We now show how to arrive at the cross section using the gluon EFT of Eq.(7.6.160) and just the scalar operator $\mathcal{O}_{G,s}$. Firstly the hadronic matrix element of the gluonic part of the operator, $G^{\mu\nu,a}G^a_{\mu\nu}$, is taken[15],

$$\langle \frac{\alpha_s}{12\pi} G^{\mu\nu,a}G^a_{\mu\nu}\rangle = -\frac{2}{27} m_N f_{TG}^{(N)},$$

where $\langle\cdots\rangle \equiv \langle \mathcal{N}(k,s)|\cdots|\mathcal{N}(k',s;)\rangle$ represents the nucleon momentum states. The resulting EFT now includes the nucleon spinors, $\mathcal{N}$

$$\mathcal{L} = -\frac{2}{27} m_N f_{TG}^{(N)} C_{G,s}^{(Q)} \left(\bar{\chi}\chi\bar{\mathcal{N}}\mathcal{N}\right) \ , \tag{7.6.188}$$

now we take the NR limit and match the amplitude onto a set of NR operators as defined in [211]. In this case the matching is simple as $\bar{\chi}\chi\bar{\mathcal{N}}\mathcal{N} \overset{\text{n.r.}}{=} 4m_\chi m_N \mathcal{O}_1$, where $\mathcal{O}_1 \equiv 1$ is the identity operator. Thus we find the Wilson coefficient C_1 which may be plugged in Eq.(7.6.146) to give the cross section,

$$C_1^{(N)} = -\frac{8}{27} m_\chi m_N^2 f_{TG}^{(N)} \sum_{Q=c,t} C_{G,s}^{(Q)} \ . \tag{7.6.189}$$

7.6.3 Loop Level : Photon Penguins

DM may scatter with nuclei via photon exchange. Whereas a single gluon exchange is forbidden by color conservation, no such restriction applies to EM charge, and the resulting single photon exchange can be phrased in the language of *electromagnetic multipole moments*. Unlike for the gluon case, the dominant contribution to

[15] The constant $f_{TG}^{(N)} = \left(\sum_q f_{T_q}^{(N)} - 1\right)$ for quarks $q = u, d, s$ and its numerical value can be found in chapter 4.

scattering comes from the exchange of an off-shell photon and hence we will assume $\partial^\mu F_{\mu\nu} \neq 0$.

The possible interactions between the DM and photon are parametrized by the Lagrangian (see for example [354, 355]),

$$\mathcal{L} = \bar{\chi}\gamma^\mu(b_\chi + a_\chi\gamma^5)\chi\partial^\nu F_{\mu\nu} + \frac{\mu_\chi}{2}\bar{\chi}\sigma^{\mu\nu}\chi F_{\mu\nu} + \frac{e_\chi}{2}\bar{\chi}\sigma^{\mu\nu}\chi\widetilde{F}_{\mu\nu} \ , \tag{7.6.190}$$

which are equivalent to various multipole moments in the non-relativistic limit. μ_χ parametrises the magnetic dipole moment (MDM), e_χ the electric dipole moment (EDM), b_χ the charge-radius and a_χ the anapole moment, all of which are real numbers. The MDM and EDM are *static* EM moments, which are non-zero for on-shell photons, whereas the anapole and charge-radius are non-static and require an off-shell photon. The matrix element of Eq.(7.6.190) for Dirac DM is,

$$\begin{aligned}\mathcal{M} = (2m_\chi\mu_\chi - q^2 b_\chi)\,\langle\bar{u}(p')|\not{\xi}\,|u(p)\rangle + q^2 a_\chi\,\langle\bar{u}(p')|\,\gamma^5\not{\xi}\,|u(p)\rangle + 2\mu_\chi\epsilon\cdot p\,\langle\bar{u}(p')|u(p)\rangle \\ + 4e_\chi p\cdot\xi\,\langle\bar{u}(p')|\,\gamma^5\,|u(p)\rangle \ ,\end{aligned} \tag{7.6.191}$$

where p, p' are the incoming and outgoing DM momenta and q^2 is the momentum exchange through the photon (i.e. the amount by which the photon is off-shell) with polarization ξ. For Majorana DM Eq.(7.6.191) only contains a contribution to a_χ. For our model, Dirac DM possesses non-zero μ_χ, b_χ and a_χ (the EDM is CP-odd and would therefore be proportional to δ_{ij}, the CP violating phases of the DMFV model).

The contributing Feynman diagrams are shown in Fig.7.31. Each amplitude contains a factor $Q_f N_c$ from the photon vertex, and color sum. We define $q = p - p'$, then

$$p^2 = p'^2 = m_\chi^2 \ , \ p\cdot p' = m_\chi^2 - \frac{q^2}{2} \ , p\cdot q = -p'\cdot q = \frac{q^2}{2}, \tag{7.6.192}$$

we then expand to first order in q^2 and match to Eq.(7.6.191).

Results : Multipole Moments

We now present the result of the calculation, which is in agreement with the literature (see for example [259, 354, 356, 357]), again using the generalized Lagrangian

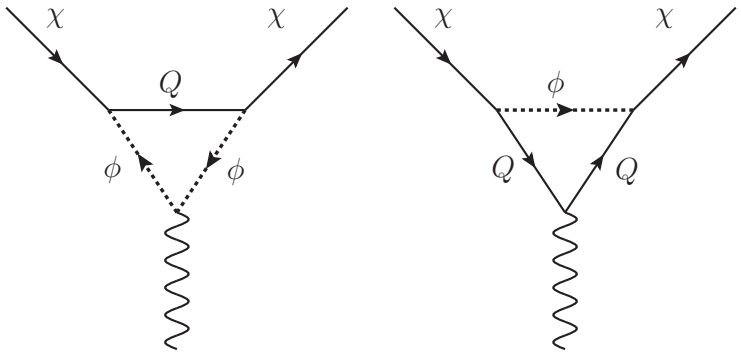

Figure 7.31: The Feynman diagrams for DM-photon scattering in the DMFV model, denoted (a), (b) (from left to right).

Eq.(7.6.149). The two diagrams in Fig.7.31 lead to a charge-radius of,

$$
\begin{aligned}
b_\chi = \frac{Q_f N_c e}{48 m_\phi^2 \pi^2 \Delta^{3/2} \mu^{3/2}} \Bigg[& (|g_s|^2 - |g_p|^2)\sqrt{\epsilon}\Bigg(-2\sqrt{\Delta}\mu(\epsilon-1) + \Delta^{3/2}\log(\epsilon) \\
& - 2(\epsilon-1)(\Delta + \mu(-1-\epsilon+\mu))\log\left(\frac{1+\epsilon-\mu+\sqrt{\Delta}}{2\sqrt{\epsilon}}\right)\Bigg) \\
& + \frac{(|g_s|^2 + |g_p|^2)}{4\sqrt{\mu}}\Bigg(-4\sqrt{\Delta}\mu(4\Delta + \mu + 3\epsilon\mu - \mu^2) - \Delta^{3/2}(8 - 8\epsilon + \mu)\log(\epsilon) \\
& - 2(8\Delta^2 + \Delta\mu(9 + 7\epsilon - 9\mu) + 4\mu^2((\mu-1)^2 - \epsilon(5+\mu))\log\left(\frac{1+\epsilon-\mu+\sqrt{\Delta}}{2\sqrt{\epsilon}}\right)\Bigg)\Bigg] \\
\approx \frac{Q_f N_c e}{48 m_\phi^2 \pi^2 \mu^{3/2}(\mu-1)} \Bigg[& \frac{(|g_p|^2 - |g_s|^2)}{4\sqrt{\mu}}\left(8\mu - 6\mu^2 + (8 - 7\mu + 3\mu^2)\log(1-\mu) - 2\mu^2\log(\epsilon)\right) \\
& + \frac{\sqrt{\epsilon}(|g_s|^2 + |g_p|^2)}{(\mu-1)}\left(2\mu + (2-4\mu)\log(1-\mu) + \mu^2\log(\epsilon)\right)\Bigg] + \mathcal{O}(\epsilon),
\end{aligned}
$$

where $\mu = (m_\chi/m_\phi)^2$, $\epsilon = (m_q/m_\phi)^2$ and $\Delta = \epsilon^2 + (1-\mu)^2 - 2\epsilon(1+\mu)$. For the magnetic dipole moment,

$$\mu_\chi = \frac{Q_f N_c e}{32 m_\phi \pi^2 \sqrt{\Delta}\mu^{3/2}}\Bigg[(|g_s|^2 - |g_p|^2)\left(\sqrt{\Delta\epsilon\mu}\log(\epsilon) + 2\sqrt{\epsilon\mu}(1-\epsilon+\mu)\log\left(\frac{1+\epsilon-\mu+\sqrt{\Delta}}{2\sqrt{\epsilon}}\right)\right) \tag{7.6.193}$$

$$+ (|g_s|^2 + |g_p|^2)\left(-2\mu\sqrt{\Delta} + \sqrt{\Delta}(\epsilon-1)\log(\epsilon) - 2(\Delta + \mu(1+\epsilon-\mu))\log\left(\frac{1+\epsilon-\mu+\sqrt{\Delta}}{2\sqrt{\epsilon}}\right)\right)\Bigg] \tag{7.6.194}$$

$$\approx \frac{-Q_f N_c e}{16 m_\phi \pi^2 \mu^{3/2}}\Bigg[(|g_p|^2 - |g_s|^2)(\mu + \log(1-\mu)) \tag{7.6.195}$$

$$+ \frac{\sqrt{\mu\epsilon}(|g_p|^2 + |g_s|^2)}{(\mu-1)}((1+\mu)\log(1-\mu) - 2\mu\log\epsilon)\Bigg] + \mathcal{O}(\epsilon). \tag{7.6.196}$$

For Majorana DM, both μ_χ and b_χ would be zero. There is a contribution to the anapole moment,

$$a_\chi = \frac{iQ_f N_c e(g_s g_p^\dagger - g_s^\dagger g_p)}{96 m_\phi^2 \pi^2}\frac{1}{\mu\sqrt{\Delta}}\left(-3\sqrt{\Delta}\log(\epsilon) + 2(3\epsilon - \mu - 3)\log\left(\frac{1+\epsilon-\mu+\sqrt{\Delta}}{2\sqrt{\epsilon}}\right)\right)$$

$$\approx \frac{iQ_f N_c e(g_s g_p^\dagger - g_p g_s^\dagger)}{96 m_\phi^2 \pi^2 \mu(\mu-1)}\left((3+\mu)\log(1-\mu) - 2\mu\log\epsilon\right) + \mathcal{O}(\epsilon), \tag{7.6.197}$$

requiring non-chiral complex couplings (note that this expression is identical for Dirac or Majorana DM).

These expressions may be simplified even further (under the assumption $m_q \ll m_\chi \ll m_\phi$),

$$a_\chi = \frac{Q_f N_c e(g_s g_p^\dagger - g_s^\dagger g_p)}{32 m_\phi^2 \pi^2}\left(1 + \frac{4}{3}\log\left(\frac{m_q}{m_\phi}\right)\right), \tag{7.6.198}$$

$$b_\chi = \frac{Q_f N_c e(|g_s|^2 + |g_p|^2)}{32 m_\phi^2 \pi^2}\left(1 + \frac{4}{3}\log\left(\frac{m_q}{m_\phi}\right)\right), \tag{7.6.199}$$

$$\mu_\chi = \frac{Q_f N_c e(|g_s|^2 + |g_p|^2)}{32 m_\phi \pi^2}\frac{m_\chi}{m_\phi}. \tag{7.6.200}$$

Thus for light quarks (or heavy DM and mediator) the magnetic dipole moment is insensitive to the quark mass, however the charge radius and anapole receive logarithmic enhancements for light quarks.

Discussion on Operators

We will now show that a general complex fermion may possess only four independent couplings to the photon. These are the mulitpole moments; electric and magnetic dipoles, charge-radius and anapole moment.

The loop diagrams of Fig.7.31 lead to an effective photon vertex function $\Gamma^\mu(Q,q)$, where we have removed the photon polarization. The most general vertex function includes the momenta $q^\mu = (p_1 - p_3)^\mu$ and $Q^\mu = (p_1 + p_3)^\mu$[16] and the various Dirac structures. It may be written,

$$\begin{aligned}\Gamma^\mu &= \langle \bar{u}_3| \left(s_1 q^\mu + s_2 Q^\mu + p_1 \gamma^5 q^\mu + p_2 \gamma^5 Q^\mu + v_1 \gamma^\mu + a_1 \gamma^\mu \gamma^5 + t_1 \sigma^{\mu\nu} q_\nu + t_2 \sigma^{\mu\nu} Q_\nu \right) |u_1\rangle \,, \\ \Gamma^\mu_\epsilon &= \epsilon^{\mu\nu\sigma\rho} \langle \bar{u}_3| \left(v_2 q^\nu Q^\sigma \gamma^\rho + a_2 q^\nu Q^\sigma \gamma^\rho \gamma^5 + t_3 q^\nu \sigma^{\sigma\rho} + t_4 Q^\nu \sigma^{\sigma\rho} \right) |u_1\rangle \ , \end{aligned} \tag{7.6.201}$$

the transversality of the photon leads to $q^\mu \to 0$ (and thus $s_1 = p_1 = 0$ in the amplitude). The vertex function can be reduced by using the Gordon identity for on-shell DM to eliminate $t_{1,2}$

$$\begin{aligned}\langle q_\nu \sigma^{\nu\mu} \rangle &= 2 i m_\chi \langle \gamma^\mu \rangle - i Q^\mu \langle 1 \rangle \ , \\ \langle Q_\nu \sigma^{\nu\mu} \rangle &= -i q^\mu \langle 1 \rangle \ . \end{aligned} \tag{7.6.202}$$

Using :;

$$\begin{aligned}\xi_\mu p_1^\nu q^\sigma \epsilon^{\mu\nu\sigma\rho} \langle \gamma_\rho \gamma^5 \rangle &= 2 i m_\chi p_1 \cdot \xi \langle 1 \rangle - \frac{i}{2}(t + 4m_\chi^2) \langle \not{\xi} \rangle \ , \\ \xi_\mu p_1^\nu q^\sigma \epsilon^{\mu\nu\sigma\rho} \langle \gamma_\rho \rangle &= \frac{i}{2} t \langle \not{\xi} \gamma^5 \rangle \ , \end{aligned} \tag{7.6.203}$$

we can remove v_2 and a_2[17]. Similar identities will remove $t_{3,4}$. Finally the Ward

[16] The notation p, p' and p_1, p_3 are equivalent, the latter allowing for a shorthand spinor notation $u_i \equiv u(p_i)$.

[17] A note of caution, here we are carrying out a matching to order $\mathcal{O}(q^2)$, to remain consistent we should neglect all terms of order $\mathcal{O}(q^3)$ and higher, and implement any identities up to order $\mathcal{O}(q^2)$. For example, Eq.(7.6.202) can be multiplied by q^2 to give

$$q^2 p_1 \cdot \xi \langle 1 \rangle = m_\chi q^2 \langle \not{\xi} \rangle + \mathcal{O}(q^3) \ , \tag{7.6.204}$$

and also $q^2 Q \cdot \xi \langle \gamma^5 \rangle$ is $\mathcal{O}(q^3)$ and can therefore be neglected.

identity for the photon; $q^\mu \Gamma_\mu = 0$ gives (using $q \cdot Q = 0$),

$$\langle \bar{u}_3 | \left(s_1 q^2 + q^2 p_1 \gamma^5 + 2 m_\chi a_1 \gamma^5 \right) | u_1 \rangle = 0 \ , \tag{7.6.205}$$

so then $s_1 = 0$ and $2m_\chi a_1 = -q^2 p_1$, removing p_1 and leaving 4 couplings;

$$\Gamma^\mu(Q,q) = \langle \bar{u}_3 | \left(s_2 Q^\mu + p_2 \gamma^5 Q^\mu + v_1 \gamma^\mu + a_1 \gamma^\mu \gamma^5 \right) | u_1 \rangle \ . \tag{7.6.206}$$

For a self-conjugate (Majorana) DM, the vertex function should obey a symmetry under exchange of the DM (represented by $p_1 \to -p_3$ and $p_3 \to -p_1$, or $Q \to -Q$), note that the spinors themselves are swapped and swapping them back using the reality of the Majorana field introduces a charge conjugation transformation of the Dirac matrix between the spinors;

$$\langle \bar{u}_1 | \Gamma | u_3 \rangle = \langle \bar{u}_3 | \Gamma' | u_1 \rangle \ ; \ \Gamma' = C^{-1} \Gamma C = \eta_i \Gamma \ , \tag{7.6.207}$$

with $\eta_i = +1$ for $\Gamma = 1, i\gamma^5, \gamma^\mu \gamma^5$ and $\eta = -1$ for $\Gamma = \gamma^\mu, \sigma^{\mu\nu}$. This forces $s_2 = p_2 = v_1 = 0$ leaving only the a_1 coupling which is the anapole moment.

We will now show how these vertex structures appear from the DM-photon Lagrangian. Following the choice of vertex structures in the preceding discussion we consider the vector, axial vector and tensor DM bilinears defined by,

$$\begin{aligned} \mathcal{O}_V^{\mu\nu} &= g_V \bar{\chi} \gamma^\mu \partial^\nu \chi + \text{h.c.}, \\ \mathcal{O}_A^{\mu\nu} &= g_A \bar{\chi} \gamma^\mu \gamma^5 \partial^\nu \chi + \text{h.c.}, \\ \mathcal{O}_T^{\mu\nu} &= g_T \bar{\chi} \sigma^{\mu\nu} \chi, \end{aligned} \tag{7.6.208}$$

where $g_{V,A}$ are in general complex; giving a total of 5 free parameters (one is degenerate as we shall see shortly). To manifest single photon scattering, these contract the photon field strength, $F^{\mu\nu}$ or its dual $\widetilde{F}^{\mu\nu}$ which creates a total of 10 operators (again six of these are degenerate).

Two operators are automatically zero; for real $g_{V,A}$ the derivative can be shifted off the DM bilinear using integration by parts, if the contraction is with the photon dual then $\partial_\nu \widetilde{F}^{\nu\mu} = 0$,

$$\text{Re}(\mathcal{O}_V^{\mu\nu}) \widetilde{F}_{\mu\nu} = 0 \ , \ \text{Re}(\mathcal{O}_A^{\mu\nu}) \widetilde{F}_{\mu\nu} = 0 \ . \tag{7.6.209}$$

Several of the operators are not independent and may be related using identities [18]

$$\left(g\bar{\chi}\gamma^{\mu}\gamma^{5}\partial^{\nu}\chi + \text{h.c.}\right)\widetilde{F}_{\mu\nu} = -i\left(g\bar{\chi}\gamma^{\mu}\partial^{\nu}\chi - g^{\dagger}\partial^{\nu}\bar{\chi}\gamma^{\mu}\chi\right)F_{\mu\nu} - \frac{im}{2}(g-g^{\dagger})\bar{\chi}\sigma^{\mu\nu}\chi F_{\mu\nu}, \tag{7.6.212}$$

which leads to two relations (depending on whether the coupling is real or imaginary),

$$\begin{aligned} i\text{Im}(\mathcal{O}_A^{\mu\nu})\widetilde{F}_{\mu\nu} &= \text{Re}(\mathcal{O}_V^{\mu\nu})F_{\mu\nu} + m\mathcal{O}_T^{\mu\nu}F_{\mu\nu}, \\ \text{Re}(\mathcal{O}_A^{\mu\nu})\widetilde{F}_{\mu\nu} &= -i\text{Im}(\mathcal{O}_V^{\mu\nu})F_{\mu\nu}. \end{aligned} \tag{7.6.213}$$

using the dirac equation for the DM, $i\partial\!\!\!/\chi = m\chi$ and $i\partial_{\nu}\bar{\chi}\gamma^{\nu} = -m\chi$. Similarly,

$$\left(g\bar{\chi}\gamma^{\mu}\partial^{\nu}\chi + \text{h.c.}\right)\widetilde{F}_{\mu\nu} = -i\left(g\bar{\chi}\gamma^{\mu}\gamma^{5}\partial_{\nu}\chi - g^{\dagger}\partial^{\nu}\bar{\chi}\gamma^{\mu}\gamma^{5}\chi\right)F_{\mu\nu} + \frac{m}{2}(g+g^{\dagger})\bar{\chi}\sigma^{\mu\nu}\chi\widetilde{F}_{\mu\nu}, \tag{7.6.214}$$

again, real or imaginary couplings lead to different relations

$$\begin{aligned} i\text{Im}(\mathcal{O}_V^{\mu\nu})\widetilde{F}_{\mu\nu} &= \text{Re}(\mathcal{O}_A^{\mu\nu})F_{\mu\nu}, \\ \text{Re}(\mathcal{O}_V^{\mu\nu})\widetilde{F}_{\mu\nu} &= -i\text{Im}(\mathcal{O}_A^{\mu\nu})F_{\mu\nu} + m\mathcal{O}_T^{\mu\nu}\widetilde{F}_{\mu\nu}. \end{aligned} \tag{7.6.215}$$

Thus we may eliminate six of the ten operators via Eq.(7.6.209),(7.6.213),(7.6.215) leaving four independent; $\text{Re}(\mathcal{O}_V^{\mu\nu})F_{\mu\nu}$ (charge radius), $\text{Re}(\mathcal{O}_A^{\mu\nu})F_{\mu\nu}$ (anapole), $\mathcal{O}_T^{\mu\nu}F_{\mu\nu}$ (magnetic dipole) and $\mathcal{O}_T^{\mu\nu}\widetilde{F}_{\mu\nu}$ (electric dipole).

Contribution to Scattering Cross Section

We now review the general method for converting the analytical expressions for the multipole moments, Eq.(7.6.196)-(7.6.197), into a cross section. Firstly, a non-relativistic limit is taken. The DM momentum (incoming p, outgoing p') are defined

[18] We use the identites [225],

$$i\epsilon^{\mu\nu\sigma\rho}\gamma_{\mu}\gamma^{5} = g^{\nu\sigma}\gamma^{\rho} + g^{\sigma\rho}\gamma^{\nu} - g^{\nu\rho}\gamma^{\sigma} - \gamma^{\nu}\gamma^{\sigma}\gamma^{\rho}, \tag{7.6.210}$$

$$\sigma^{\mu\nu}\gamma^{5} = -\frac{i}{2}\epsilon^{\mu\nu\rho\sigma}\sigma_{\rho\sigma}\ . \tag{7.6.211}$$

in the NR limit as,

$$p^\mu = (m_\chi, \bar{p}) \ , \ p'^\mu = (m_\chi, \bar{p}'), \tag{7.6.216}$$

where $q^0 = 0$, $\bar{q} = \bar{p} - \bar{p}'$ and $Q^0 = 2m_\chi$, $\bar{Q} = \bar{p} + \bar{p}'$, we define $2\bar{p} - \bar{q} \equiv 2\mu v^\perp$ so then

$$\bar{p} = \frac{1}{2}\bar{q} + \mu v^\perp \ , \ \bar{p}' = -\frac{1}{2}\bar{q} + \mu v^\perp \ . \tag{7.6.217}$$

From the plane wave expansion of a Dirac fermion field [330], the derivative operators are $\partial^\mu \chi \to -ip^\mu u(p)$ and $\partial^\mu \bar{\chi} \to ip'^\mu \bar{u}(p')$.

Classically electromagnetism is phrased in terms of E and B fields, in QFT these are packaged into the field strength of the photon $F^{\mu\nu}$ (and its dual $\widetilde{F}^{\mu\nu} = 1/2\epsilon^{\mu\nu\sigma\rho}F_{\sigma\rho}$[19]), in the NR limit these reduce to the classical fields in the following way

$$F^{0i} = E^i \ , \quad \widetilde{F}^{0i} = B^i, \tag{7.6.218}$$

$$F^{ij} = -\epsilon^{ijk}B^k \ , \ \widetilde{F}^{ij} = \epsilon^{ijk}E^k \ , \tag{7.6.219}$$

or alternatively, $B^i = -\frac{1}{2}\epsilon^{ijk}F^{jk}$. Note that $F_{0i} = -F^{0i}$.

The relativistic four-vector relation $\partial^\nu \widetilde{F}_{\mu\nu} = 0$ in the NR limit has a timelike piece, $q \cdot B = 0$, accounting for the absence of magnetic monopoles. The spacelike piece $\partial_0 B^i - \epsilon^{ijk}\partial^j E^k = 0$ gives $q \times E = 0$ when mapping to momentum space, $\bar{q} \to -i\nabla$.

When the matching to the photon EFT is complete one may proceed in two ways;

[19] One must be very careful when dealing with the Levi-Civita tensor. In Minkowski space (with metric $g^{\mu\nu} = g_{\mu\nu} = \text{diag}(+,-,-,-)$) we define the totally antisymmetric Levi-Civita tensor by $\epsilon_{0123} = +1$, this means that $\epsilon^{0123} = -1$; due to the metric we have $\epsilon^{\mu\nu\sigma\rho} = -\epsilon_{\mu\nu\sigma\rho}$ for any $\mu, \nu, \sigma, \rho \in 0, 1, 2, 3$. We may similarly define a 3 dimensional Levi-Civita tensor by $\epsilon_{123} = +1$, then the 3×3 submatrix of the Minkowski LC reduces to the 3D, $\epsilon_{0ijk} = \epsilon_{ijk}$ and $\epsilon^{0ijk} = \epsilon^{ijk}$ but since the reduced metric has negative sign $\eta^{ij} = \eta_{ij} = (-,-,-)$ then we have the relation $\epsilon^{ijk} = -\epsilon_{ijk}$. Making sure all three-vector indices are superscripted avoids errors with the minus signs.

1. To match the result to a DM-quark Lagrangian using diagrams exchanging a photon in the t-channel. Clearly only the $\bar{q}\gamma^\mu q$ current can appear in operators.

2. To consider the vertex function $\Gamma^\mu(q, Q)$ (which represents the DM-photon scattering amplitude without the photon polarisation ξ^μ) coupled to the EM current of the nucleus $J^\mu_{\rm EM}$.

We will use the latter method following [358] closely, and begin by writing the electromagnetic current for protons and neutrons,

$$J^\mu_{\rm EM} = \bar{p}\left(\frac{(k+k')^\mu}{2m_N} + \frac{g_p}{2}\frac{i\sigma^{\mu\nu}q_\nu}{2m_N}\right)p + \bar{n}\left(\frac{g_n}{2}\frac{i\sigma^{\mu\nu}q_\nu}{2m_N}\right)n, \tag{7.6.220}$$

where p, n represent the proton/neutron spinors with incoming momentum k and outgoing momentum k'. Eq.(7.6.220) includes both the charge term for the proton, and the magnetic dipole of the proton and neutron ($g_{n,p}$); this will allow both X-charge and X-dipole type interaction where X is a DM multipole moment. The NR limits are,

$$\begin{aligned} J^0_{\rm EM} &= 2m_N \ , \\ J^i_{\rm EM} &= (k+k')^i - ig_p\epsilon^{ijk}q^j S^k_p - ig_n\epsilon^{ijk}q^j S^k_n \ . \end{aligned}$$

An immediate problem is that the vector component is not Galilean invaraint under $v \to v + \beta$, then,

$$\begin{aligned} (k+k')^i &= -m_N(v^i_{\rm N,in} + v^i_{\rm N,out}) \to (k+k')^i - 2m_N\beta^i, \\ (p+p')^i &= -m_\chi(v^i_{\chi,\rm in} + v^i_{\chi,\rm out}) \to (p+p')^i - 2m_\chi\beta^i, \end{aligned}$$

so then $J^i_{\rm EM} \to J^i_{\rm EM} - \beta^i J^0_{\rm EM}$. Therefore a boost invariant quantity is defined,

$$j_{\rm EM} = J^i_{\rm EM} - \frac{1}{2m_\chi}(p+p')^i J^0_{\rm EM} \ . \tag{7.6.221}$$

The EM current $J^\mu_{\rm EM}$ four vector contains the charge (timelike piece) and three vector current (spacelike piece); along with Maxwells equations $\nabla \cdot E = J^0_{\rm EM}$ and $\nabla \times B = J^i_{\rm EM}$ one may derive (as $\bar{q} \equiv -i\nabla$, and thus $q \cdot J_{\rm EM} = 0$),

$$E = iq^i J^0_{\rm EM}\frac{1}{q^2} \quad , \quad B^i = i\frac{1}{q^2}(q \times J_{\rm EM})^i, \tag{7.6.222}$$

because $J^0_{\rm EM}$ is boost invariant, so is the E field, however the B field is not and one defines a boost invariant version,

$$\mathcal{B}^i = B^i - \frac{1}{2m_\chi}\epsilon^{ijk}E_j(p+p')_k = i\frac{1}{q^2}q\times j_{\rm EM}\ . \tag{7.6.223}$$

From the NR reduction of the relativistic operators we will find that the boost invariant magnetic fields arises naturally, as they should. It is worth anticipating this result however as the algebraic manipulations are not always trivial.

With the NR limit of spinor bilinears from Sec.4.4 combined with Eq.(7.6.219) we can work out the NR limit of the multipole moment operators, for example the magnetic moment operator [20],

$$\begin{aligned}
\bar\chi\sigma^{\mu\nu}\chi F_{\mu\nu} &= -2\bar\chi\sigma^{0i}\chi F_{0i} + \bar\chi\sigma^{ij}\chi F_{ij}\\
&= -2i\bar\chi\gamma^0\gamma^i\chi F_{0i} + i\bar\chi\gamma^{[i}\gamma^{j]}\chi F_{ij}\\
&= -2iE_i\left(q^i + 4i\mu\epsilon^{ijk}v^{\perp,j}S^k\right) - i\epsilon_{ijk}B^k\left(-4im_\chi\epsilon^{ijl}S_l\right)\\
&= -2iq\cdot E - 8m_\chi\left(S\cdot B - \frac{\mu}{m_\chi}S\cdot(E\times v^\perp)\right),
\end{aligned}$$

there is also a charge-radius term $q\cdot E$ which contributes at higher order in q and can thus be ignored, we thus recover the classical magnetic dipole moment operator $S\cdot\mathcal{B}$ in terms of the Lorentz invariant magnetic field. The various multipole moments in the NR limit are,

$$\frac{\mu_\chi}{2}\bar\chi\sigma^{\mu\nu}\chi F_{\mu\nu} \overset{\rm n.r.}{=} -4\mu_\chi m_\chi\left(S\cdot\mathcal{B}\right) + \mathcal{O}(q)\ , \tag{7.6.224}$$

$$b_\chi\bar\chi\gamma^\mu\chi\partial_\nu F^{\mu\nu} \overset{\rm n.r.}{=} 2b_\chi m_\chi\left(iq\cdot E\right) + \mathcal{O}(q,v^\perp)\ , \tag{7.6.225}$$

$$a_\chi\bar\chi\gamma^\mu\gamma^5\chi\partial_\nu F^{\mu\nu} \overset{\rm n.r.}{=} 4a_\chi m_\chi\left(S\cdot iq\times\mathcal{B}\right) = -4m_\chi\left(S\cdot J_{\rm EM}\right)\ . \tag{7.6.226}$$

The NR multipole operators are themselves expressed in terms of $q, v^\perp, S$ using the EM current from Eq.(7.6.220) and the mapping between fields and currents in

[20] Note the definition of $\gamma^{[i}\gamma^{j]} = (1/2)(\gamma^i\gamma^j - \gamma^j\gamma^i)$ includes a factor of $1/2$

Eq.(7.6.222) ;

$$iq \cdot E \to -2m_N \mathcal{O}_1, \tag{7.6.227}$$

$$\mathcal{B} \cdot S \to \frac{g_N m_N^2}{q^2}\mathcal{O}_6 - g_N \mathcal{O}_4 - \frac{2m_N^2}{q^2}\mathcal{O}_5, \tag{7.6.228}$$

$$E \cdot S \to \frac{2m_\chi m_N}{q^2}\mathcal{O}_{11}, \tag{7.6.229}$$

$$S \cdot J_{\rm EM} \to 2m_\chi m_N g_N \mathcal{O}_9 - 4m_\chi m_N Q_N \mathcal{O}_8, \tag{7.6.230}$$

where $N = n, p$, g_N is the gyromagnetic ratio and Q_N is the charge and the operators $\mathcal{O}_i$ are defined in Sec.2.2 of [358].

In order to proceed from the coefficients of the multipole moment operators to the cross section, one may use form factors associated to the mulitpole operators as in [354], or instead perform the full NR reduction of the operators into a basis of standard form factors, as we do :

$$\begin{aligned}
\frac{\mu_\chi}{2}\bar{\chi}\sigma^{\mu\nu}\chi F_{\mu\nu} =& 2m_\chi\mu_\chi\left(\frac{2g_p}{q^2}(m_N^2\mathcal{O}_6 - q^2\mathcal{O}_4) - \frac{4m_N^2}{q^2}\mathcal{O}_5\right)_{\rm p} \\
&+ 2m_\chi\mu_\chi\left(\frac{2g_n}{q^2}(m_N^2\mathcal{O}_6 - q^2\mathcal{O}_4)\right)_{\rm n} \ , \\
b_\chi\bar{\chi}\gamma^\mu\chi\partial^\nu F_{\mu\nu} =& -4m_\chi m_N b_\chi\left(\mathcal{O}_1\right)_{\rm p} \ , \\
a_\chi\bar{\chi}\gamma^\mu\gamma^5\chi\partial^\nu F_{\mu\nu} =& 2m_\chi a_\chi\left(-4m_N\mathcal{O}_8 + 2g_p\mathcal{O}_9\right)_{\rm p} + 2m_\chi a_\chi\left(2g_n\mathcal{O}_9\right)_{\rm n} \ ,
\end{aligned}$$

which are then inserted into Eq.(7.6.146). Then the NR Wilson coefficients can be summarized as:

$$\begin{aligned}
{\rm Charge-radius} \ &: \ C_1^{(p)} = 4m_\chi m_N b_\chi, \\
{\rm MDM} \ &: \ \begin{cases} C_4^{(N)} = 4m_\chi g_N \mu_\chi \\ C_5^{(N)} = \frac{1}{q^2} 8m_\chi m_N^2 \mu_\chi \\ C_6^{(N)} = \frac{1}{q^2} 4m_\chi g_N m_N^2 \mu_\chi \end{cases} \ , \\
{\rm Anapole} \ &: \ \begin{cases} C_8^{(p)} = 8m_\chi m_N a_\chi \\ C_9^{(N)} = 4m_\chi g_N a_\chi \end{cases} \ .
\end{aligned}$$

7.6.4 Loop Level : Z, h Penguins

As well as single photon scattering, the model may posses single Z and single Higgs scattering. It was shown in [354] that both contributions scale as m_q^2, making them important for couplings to the third generation quarks. It was noted that the Higgs contribution is always subdominant.

In the single Higgs exchange, the loop level process leads to the operators $(g_{\chi,h}/v)\bar{\chi}\chi H^\dagger H$ and $g^5_{\chi,h}\bar{\chi}i\gamma^5\chi H^\dagger H$, the latter may be ignored since it leads to a velocity suppressed scattering. We consider the quark-level scattering mediated by the Higgs as shown in Fig.7.32 leading to an amplitude[21]

$$\mathcal{M}_{\chi,h} = \left(\sum_{q=u,c,t} g^{(q)}_{\chi,h}\right)\frac{y_{q'}}{m_h^2}\langle 1\rangle_\chi\langle 1\rangle_{q'} = \left(\sum_{q',q=u,c,t} f^{(N)}_{T_{q'}} g^{(q)}_{\chi,h}\frac{m_N}{vm_h^2}\right)\langle 1\rangle_\chi\langle 1\rangle_N \ , \tag{7.6.231}$$

where $y_q = \sqrt{2}m_q/v$ is the Yukawa coupling and $v^2 = (\sqrt{2}G_F)^{-1}$ the Higgs' vev. In the second expression the hadronic matrix elements have been taken. The DM-higgs coupling is,

$$g^{(q)}_{\chi,h} = \frac{N_c m_\chi \epsilon(g_s g_p^\dagger - g_s^\dagger g_p)}{64\pi^2 v\sqrt{\Delta}\mu^{3/2}}\Bigg[\sqrt{\Delta}(2\mu - (\epsilon-1)\log(\epsilon)) + 2(\Delta + (1+\epsilon-\mu)\log\left(\frac{1+\sqrt{\Delta}+\epsilon-\mu}{2\sqrt{\epsilon}}\right)\Bigg] \ , \tag{7.6.232}$$

with the definitions $\mu = (m_\chi/m_\phi)^2$ and $\epsilon = (m_q/m_\phi)^2$. For the coupling to RH quarks as used here the amplitude is finite, however it is divergent if $(g_s g_p^\dagger + g_p g_s^\dagger) \neq 0$. This matches to the NR coefficient C_1:

$$C_1^{(N)} = 4\frac{m_\chi m_N^2}{vm_h^2} f_Q \sum_{q=u,c,t} g^{(q)}_{\chi,h} \ , \tag{7.6.233}$$

[21] This reproduces the expression of [354] with the replacement

$$\langle 1\rangle_q \to \sum_q \frac{m_N}{m_q} f^{(N)}_{T_q}\langle 1\rangle_N$$

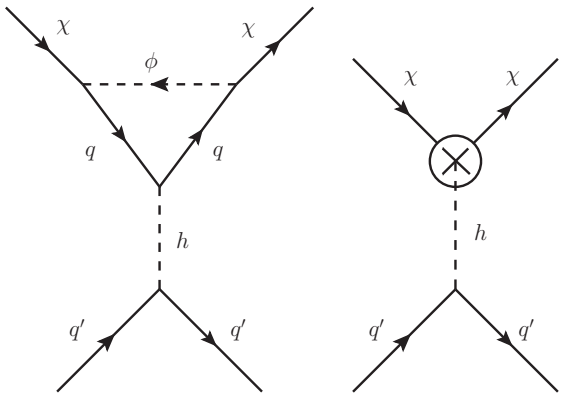

Figure 7.32: The Feynman diagrams for DM-nuclear scattering via a single higgs exchange in the DMFV model. On the r.h.s we indicate that we take the EFT limit of the DM-h vertex and then consider the tree-level scattering.

where $f_Q = \sum_q f_{T_q}^{(N)} \sim 0.09$.

For the Z boson we follow the same procedure, considering the Z-mediated quark scattering as shown in Fig.7.33. The Z has both vector and axial-vector couplings to quarks; however the dominant scattering between the DM and quark currents is vector-vector (the ones involving the axial-vector coupling are velocity or spin suppressed) and leads to an amplitude;

$$\mathcal{M}_Z = \sum_{q=u,c,t} \frac{g_{Z,\text{eft}}^{(q)} g_{Z,v}^{(q')}}{m_Z^2} \langle \gamma_\mu \rangle_\chi \left(g^{\mu\nu} - \frac{1}{m_Z^2} q^\mu q^\nu \right) \langle \gamma_\nu \rangle_{q'} \approx \sum_{q=u,c,t} \frac{g_{Z,\text{eft}}^{(q)} g_{Z,v}^{(q')}}{m_Z^2} \langle \gamma_\mu \rangle_\chi \langle \gamma^\mu \rangle_{q'} \,, \tag{7.6.234}$$

to find the scattering amplitude with nucleons we can make the replacement,

$$g^{(q)} \langle \gamma^\mu \rangle_q \to (2g^{(u)} + g^{(d)}) \langle \gamma^\mu \rangle_p + (2g^{(d)} + g^{(u)}) \langle \gamma^\mu \rangle_n \,, \tag{7.6.235}$$

which effectively takes into account only the valence quarks (due to the fact that the vector current is conserved).

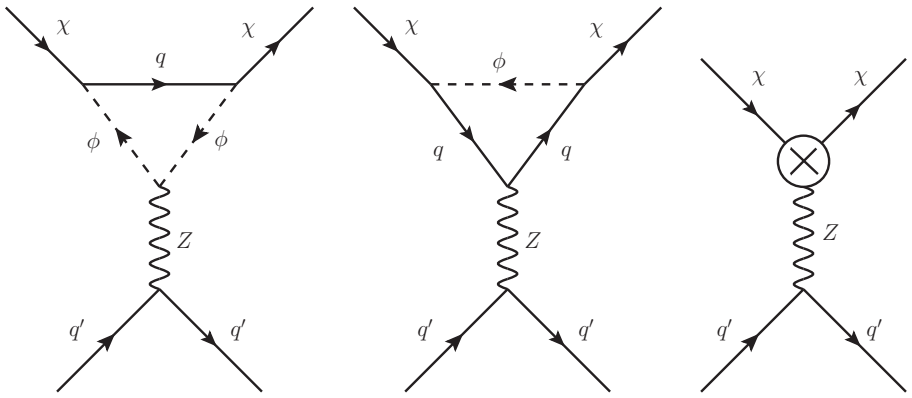

Figure 7.33: The Feynman diagrams for DM-nuclear scattering via a single Z exchange in the DMFV model. On the r.h.s we indicate that we take the EFT of the DM-Z vertex and then consider the tree-level scattering.

The Z boson couples to quarks via,

$$\begin{aligned}\mathcal{L}_{Z-q} &= -\bar{q}\gamma^{\mu}\left(g_{Z,v}+g_{Z,a}\gamma^{5}\right)qZ_{\mu}, \\ g_{Z,v} &= \frac{e}{2s_W c_W}\left(T_3 - Qs_W^2\right), \\ g_{Z,a} &= \frac{e}{2s_W c_W}T_3,\end{aligned} \tag{7.6.236}$$

thus the couplings for up-type quarks are $g_{Z,v} = g_Z\left(1/2 - 4/3s_W^2\right)$ and $g_{Z,a} = g_Z/2$ with $g_Z = -e/2c_W s_W$, these couplings are summarized in Tab.7.34.

We write the effective amplitude for $\bar{\chi}\gamma^{\mu}\chi Z_{\mu}$ in the form,

$$\mathcal{M}^{\mu} = Ap_3^{\nu}\sigma^{\nu\mu} + B\gamma^{\mu} + \left(\text{terms with } \gamma^5\right),$$

making use of the Gordon identity to remove terms $\propto p_3^{\nu}$, then $g_{Z,\text{eft}}^{(q)} = B$. As it turns out, B has no dependence on Q_f through the Z-coupling and depends only on T_3, making the result identical for up and down-type quarks,

$$g_{Z,\text{eft}}^{(q)} = (\lambda_{\alpha q}\lambda_{\alpha q}^{*})\frac{T_3 N_c g_Z}{32\pi^2}\epsilon\left[\log\left(\frac{\mu}{\epsilon}\right) + 2\Delta^{-1/2}(\epsilon - 1 - \mu)\log\left(\frac{-1+\Delta^{1/2}+\epsilon+\mu}{2\sqrt{\epsilon\mu}}\right)\right], \tag{7.6.237}$$

for DM flavour α. For the DMFV model the NR coupling for DM flavour α to the

ψ	$(g_{Z,v}/g_Z) = T_3 - Qs_W^2$	$(g_{Z,a}/g_Z) = T_3$
ν_L	$1/2$	$1/2$
ν_R	0	0
e_L	$-1/2 + s_W^2$	$-1/2$
e_R	s_W^2	0
u_L	$1/2 - 2/3s_W^2$	$1/2$
u_R	$-2/3s_W^2$	0
d_L	$-1/2 + 1/3s_W^2$	$-1/2$
d_R	$1/3s_W^2$	0
proton	$1/2(1 - 4s_W^2)$	$1/2$
neutron	$-1/2$	$-1/2$

Figure 7.34: SM couplings to the Z boson, $\mathcal{L} = (e/2s_W c_W) Z_\mu \bar{f} \gamma^\mu (g_{Z,v} - g_{Z,a}\gamma^5) f$.

operator $\mathcal{O}_1$ reads

$$C_1^{(N)} = 4 m_\chi m_N \sum_{i=u,c,t} \lambda^\dagger_{\alpha i} \lambda_{i\alpha} \frac{\sqrt{2} N_c G_F g_{Z,v}^{(N)}}{64\pi^2} \epsilon_i \Bigg[\log\left(\frac{\mu}{\epsilon_i}\right) + 2\Delta^{-1/2}(\epsilon_i - 1 - \mu) \log\left(\frac{-1 + \Delta^{1/2} + \epsilon_i + \mu}{2\sqrt{\epsilon_i \mu}}\right) \Bigg], \tag{7.6.238}$$

using the relation $(g_Z/m_Z)^2 = \sqrt{2} G_F$, and $g_{Z,v}^{(p)} = 1/2(1 - 4s_W^2)$, $g_{Z,v}^{(n)} = -1/2$.

There are several sources of suppression in this expression, firstly since the process is Z-mediated there is a m_Z^{-2} mass suppression. Secondly, there is a m_f^2 suppression in the case of light quarks (however for tops the reverse is true and this can significantly enhance the scattering). Lastly, for the case of protons there is an accidental suppression from the Z-coupling since $g_p = 1 - 4s_W^2 \sim 0.08$.

7.6.5 Constraints

We have calculated for the DMFV model, the tree level contribution to scattering from u, c, t quarks (the heavy quark scattering arising from RG effects). For the heavy quarks we have computed the leading contribution arising from integrating the quark out of the theory, these result in single γ, Z, h, and two gluon exchange.

The situation is depicted in Fig.7.35, the tree level scattering of u is almost always dominant; next the multipole moments tend to be slightly larger than the tree level scattering from RG mixing. Lastly the gluonic contribution is extremely small. For very degenerate masses ($m_\chi \approx m_\phi$) the relative sizes change considerably, and the loop contributions play a significant role.

Setting Limits

Now we have accumulated the expressions to describe the scattering rate of DM particles with nuclei, including the dominant loop-level contributions, we can produce constraints on the parameters of the model. To do this requires us to connect the theoretical event rate to the experimental data, which is usually a total yield of events over a particular exposure.

Unlike for ID, there is in general no single observable (equivalent to $\langle \sigma v \rangle$) for which one can find constraints once and for all, and then map the constraints onto the parameter space of a particular model. The reason is that each EFT operator leads to a scattering with a unique energy dependence, which is then integrated over.

However, the form factors $F_{i,j}^{(N,N')}(E_R, v)$ (which encapsulate the energy and velocity dependence of the cross section) do in some sense form a complete basis of all the possible energy dependences of the cross section, each cross section being a linear sum with model dependent coefficient. One can then derive a bound on a benchmark model, and simply scale by appropriate functions to translate the bound to other models or other detectors. This is the method employed in [230], for several experiments. We will nonetheless compute our bounds explicitly using the proceeding discussion.

The statistics employed by the experimental groups are often very involved, and require the mapping of the theoretical recoil energy onto the particular experimental observable which is unique to each experiment. A much simplified strategy does not carry out the mapping and instead accounts for the dominant experimental effects

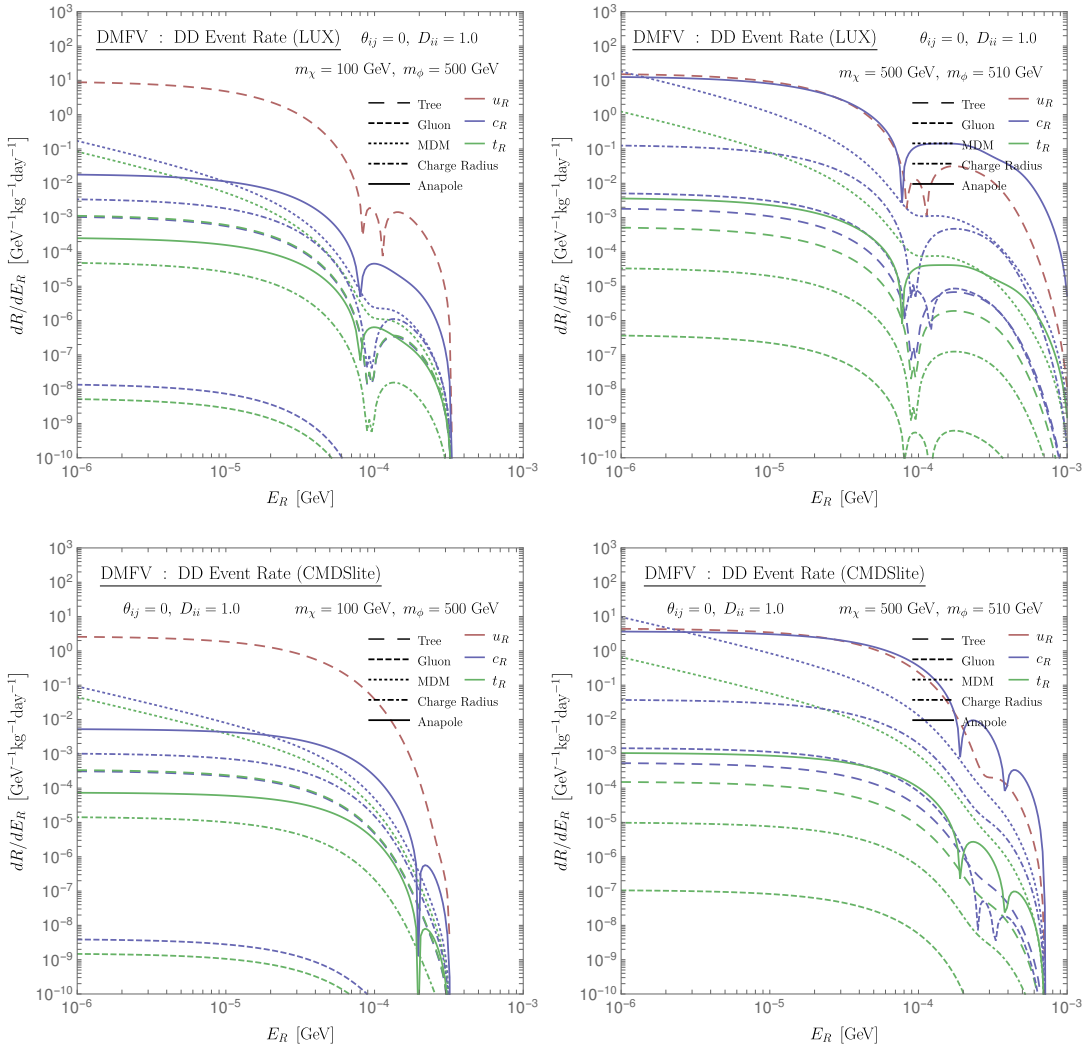

Figure 7.35: The differential scattering rate in recoil energy for DM-nuclear scattering from a xenon (top row, LUX) or a germanium (bottom row, CDMSlite) target. Each of the quark contributions are plotted separately, u, c, t indicated by red, blue and green lines. The rates are also separated according to the way in which they scatter; via quarks at tree level, via two gluon exchange, or via photon exchange (the magnetic monopole, charge-radius and anapole moments are separately plotted). The right column represents a model with very degenerate masses.

of energy resolution and efficiency,

$$N_{\rm TOT} = \int_{E_{R,\rm min}}^{E_{R,\rm max}} dE_R\ \epsilon(E_R) \int_0^\infty dE'\ \frac{dN}{dE'} \frac{1}{\sqrt{2\pi\sigma(E')}} \exp\left(-\frac{(E'-E_R)^2}{2\sigma(E')^2}\right)\ , \tag{7.6.239}$$

where ϵ is the efficiency, $\sigma(E)$ is the energy resolution and dN/dE is the nuclear recoil spectrum of Eq.(7.6.146) multiplied by the exposure.

There are many experimental efforts towards direct detection with a vast range of different target materials. We only need to employ enough of these experiments to yield the dominant constraints at each DM mass; LUX in particular sets the strongest bounds at large DM mass. However at low DM mass, it is experiments like CDMSlite which are able to set the strongest bounds. These experiments are discussed in more detail in chapter 4.

LUX

LUX is a dual-phase liquid scintillation detector. The principle of detection is the measurement of a WIMP-nucleus scattering producing prompt scintillation photons (S_1) and ionization photons (S_2) which are produced as ionized electrons drift to the top of the detector under the applied electric field. The resulting position reconstruction allows a volume fiducialization.

LUX is located in the Stanford underground laboratory, the first data release in 2013 [267] was based on 85.0 days and 118 kg of exposure. An updated analysis of the same data presented in 2015 [268], but with an extra 10 days and 35 kg of exposure (a total of 1.4×10^4 kg days), there are 591 observed events with an expected 589 background (primarily from gamma rays), which reduces to 1 event with expected 1.1 when including the effects of the acceptance cuts (99.81%)[22], the

[22]Fig.4 of [267] shows the same data, the solid red line represents the mean of the NR band created from the neutron calibration source. This motivates an approximation that the WIMP NR band is essentially the same, and so one can multiply the theoretical event rate by 1/2 to include the events below the line, where only a single measured event remains.

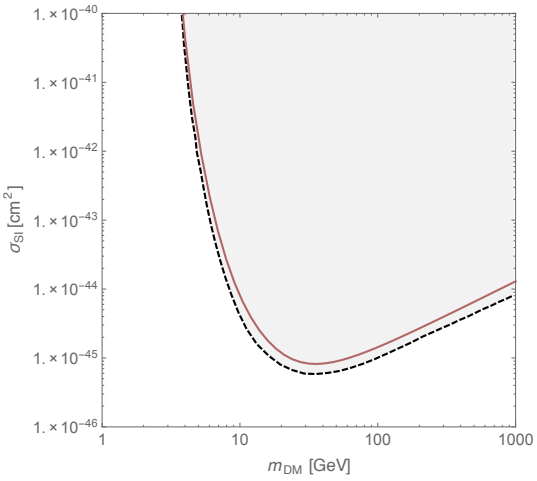

Figure 7.36: The exclusion on σ_{SI} (the standard WIMP-nucleon cross section) for LUX (dashed black line), compared to a likelihood ratio test applied to the method described in the text.

constraints are limited to $m_\chi \gtrsim 4$ GeV due to kinematics, and are shown in Fig.7.36.

The efficiency $\epsilon(E)$ can be read off from the solid black line of Fig.1 in [268]. A further scaling of $97.5 \pm 1.7\%$ is applied on top of the efficiency. We do not include resolution effects, but to understand their size we could assume a Gaussian smearing of width $\sqrt{n}\sigma_{\rm PMT}$, where n is the number of photoelectrons produced in the PMT and $\sigma_{\rm PMT}$ is the PMT resolution in photo electrons (phe). We assume the signal $S2 = 0$ and that $S1 \propto E_R$, using the endpoints of the sensitivity region ($S1 = 2$, $E_R = 1.1$ keV to give the proportionality constant $S1 = 1.8E_R$), then the energy resolution is $\sigma = 0.67\sqrt{E_R}$ assuming $\sigma_{\rm PMT} = 0.5$. Thus the resolution can be significant at the low energy end of the measured spectrum.

Confidence Limits

For situations where we have both a measured event count, $N_k^{\rm obs}$ (binned into energy bins labelled by k) and theoretical background $N_k^{\rm bck}$, we can use the *likelihood ratio test*, a method based on a frequentist hypothesis test between a background only,

and background+signal model[23], with likelihoods $\mathcal{L}$, $\mathcal{L}_{\rm bck}$ respectively [230].

The likelihood of observing the data, D, assuming a particular set of parameters $\{\lambda\}$, is denoted $\mathcal{L}(D|\{\lambda\})$. The likelihood of observation in each bin is a Poisson distribution Poiss($\mathrm{N}^{\rm obs}, \mathrm{N}^{\rm th}(\lambda)$) where $N_k^{\rm th}$ are the predicted number of signal events (including background),

$$\mathcal{L}(N^{\rm obs}|\{\lambda\}) = \prod_k \frac{\left(N_k^{\rm th}\right)^{N_k^{\rm obs}}}{N_k^{\rm obs}!} \exp\left[-\mathrm{N}_{\rm k}^{\rm th}\right], \tag{7.6.240}$$

where $N^{\rm th}(\lambda) = N^{\rm DM}(\lambda) + N^{\rm bck}$. The background only model is identical but with $N^{\rm th} = N^{\rm bck}$. Then the test statistic,

$$\mathrm{TS}(\lambda) = -2\log\left(\frac{\mathcal{L}}{\mathcal{L}_{\rm bck}}\right) \approx 2\sum_{\rm k}\left(\mathrm{N}_{\rm k}^{\rm th} - \mathrm{N}_{\rm k}^{\rm obs}\log\left[\frac{\mathrm{N}_{\rm k}^{\rm th} + \mathrm{N}_{\rm k}^{\rm bck}}{\mathrm{N}_{\rm k}^{\rm bck}}\right]\right), \tag{7.6.241}$$

follows a χ^2 distribution; the cumulative p.d.f of $\chi^2(x)$ represents the probability that we observe the data given the model parameters λ. The value of x such that $\chi^2(x) = C$ (i.e. the $C\%$ confidence limit), depends on the number of parameters $\{\lambda\}$, in our case that is just one, then one can look up that $\chi^2(2.71) = 0.9$, which means that the 90% confidence bounds on λ are given by $\mathrm{TS}(\lambda) = 2.71$.

In other words, if the true value of λ were to be outside the allowed range, then the experiment would have a 90% chance to have detected the DM. In the above, it is implicitly assumed that all parameters included in the theoretical predictions and experimental results are known to perfect accuracy. In reality, many parameters have an uncertainty, and this should have an effect on the confidence limit for which we exclude the models; the less well known the inputs, the less confident we should be and the weaker the bounds.

Including the effects of the uncertainty on parameters can be done using a *profile likelihood ratio test*, we multiply the likelihood in Eq.(7.6.240) with a product

[23] DD collaborations often use this method, but with a profile likelihood to include uncertainties is astrophysical and experimental parameters as nuisance parameters (frequentist approach) or by marginalization over priors (bayesian approach) to give the posterior distribution.

of likelihoods of each parameter which has an uncertainty. Then for the null and signal hypothesis the parameters are varied to maximize the likelihood, aside from this modification the method is the same as before.

In order to check the method, we implement it using the standard differential event rate used by the collaboration themselves (see for example [359]),

$$\frac{dR}{dE_R} = \left(\frac{\rho_\odot}{m_\chi}\right) M N_T \int_{v_{\min}}^{\inf} \frac{\sigma}{dE_r} v f(v) dv, \tag{7.6.242}$$

where M is the mass of the target material and N_T is the total number of target particles per kg,

$$N_T = \sum_{\mathrm{i}} \xi_i \frac{1}{(Z_i m_p + (A - Z_i) m_n)}, \tag{7.6.243}$$

and ξ_i is the abundance of isotope i with proton number Z_i. Then the differential cross section is given by,

$$\frac{d\sigma}{dE_r} = \frac{1}{v^2}\frac{m_N}{2\mu^2}\sigma_{\mathrm{SI}} F_{\mathrm{helm}}(E_R, A)^2 \ , \ \sigma_{\mathrm{SI}} = \sigma_n \left(\frac{\mu}{\mu_n}\right)^2 \frac{1}{f_n^2}\left(f_p Z + (A - Z) f_n\right)^2 = \sigma_n \left(\frac{\mu}{\mu_n}\right)^2 A^2 \ . \tag{7.6.244}$$

Putting this all together,

$$\frac{1}{M}\frac{dR}{dE_R} = \left(\frac{\rho_\odot}{m_\chi}\right) N_T \frac{\sigma_n m_N}{2\mu_n^2} A^2 F_{\mathrm{helm}}^2 \mathcal{J}_0(E_R) \ , \ \mathcal{J}_0 = \int_{v_{\min}}^{\inf} \frac{1}{v} f(v) dv. \tag{7.6.245}$$

CDMSlite

Although the LUX collaboration set the strongest limits for moderate DM masses $m_\chi \gtrsim 5$ GeV, the use of a liquid xenon target makes scattering for $m_\chi \lesssim 5$ GeV kinematically forbidden; in which case detectors with lighter targets are able to set limits (since the minimum accessible recoil energy scales roughly with atomic number A). We include CDMSlite [20], a germanium detector, since their constraints appear to be the strongest currently available for masses $1.6 < m_\chi < 5.5$ GeV, peaking at $\sigma_n < 5 \times 10^{-42}$ cm^2.

The CDMSlite data consists of four energy bins, with energy ranges given in *electron equivalent* energy, which must be converted to nuclear recoil energy as

	$E_{\rm ee}$ [keV]	$E_{\rm nr}$ [keV]	$n_{\rm obs}$
Bin 1	0.056-0.14	0.47-0.82	96^{+48}_{-47}
Bin 2	0.2-1.2	1.13 - 5.49	76 ± 13
Bin 3	1.4 - 10	6.3- 34.9	603 ± 36
Bin 4	11 - 20	37.9 -63.3	189 ± 19

Figure 7.37: The data for CDMSlite, from Tab.1 of [20] for an exposure of 70.10 kg days.

given in Tab.7.37 using the expression [20],

$$E_{\rm nr} = E_{\rm ee}\left(\frac{1+eV_b/\epsilon_\gamma}{1+Y(E_{\rm nr})eV_b/\epsilon_\gamma}\right), \tag{7.6.246}$$

where $V_b = 70$ V is the voltage across the detector, $1/\epsilon_\gamma = 0.3$ eV^{-1} is the number of charges collected per unit energy, and $Y(E)$ is the ionization yield for nuclear recoils (for electron recoils $Y = 1$), which is given by the Lindhard model,

$$Y(E_{\rm nr}) = \frac{kg(\epsilon)}{1+kg(\epsilon)}\ , \tag{7.6.247}$$

where $k = 0.133Z^{2/3}A^{-1/2} \sim 0.157$ is the Lindhard factor for germanium, $\epsilon = 11.5(E_{\rm nr}/{\rm keV}){\rm Z}^{-7/3}$, and $g(\epsilon) = 3\epsilon^{0.15} + 0.7\epsilon^{0.6} + \epsilon$.

The energy resolution is quite small ($\sim 11\%$ at $E_{\rm ee} = 0.16$ keV, dropping to $< 1\%$ at the upper end of the energy range) and can approximately be ignored, however the efficiency includes a fiducial volume cut and is significant, reaching a maximum of 0.5 (see Fig.1 of [20]).

Due to the general behaviour of the signal, the first two energy bins are likely to dominate the constraint, the third and fourth will generally contain less signal events, and also have large backgrounds. For a quick estimate, we can take each energy bin, assume the entire yield is due to some background, and repeat the likelihood method used for LUX, eventually choosing the best constraint from the four energy bins. The result is shown in the left plot of Fig.7.38.

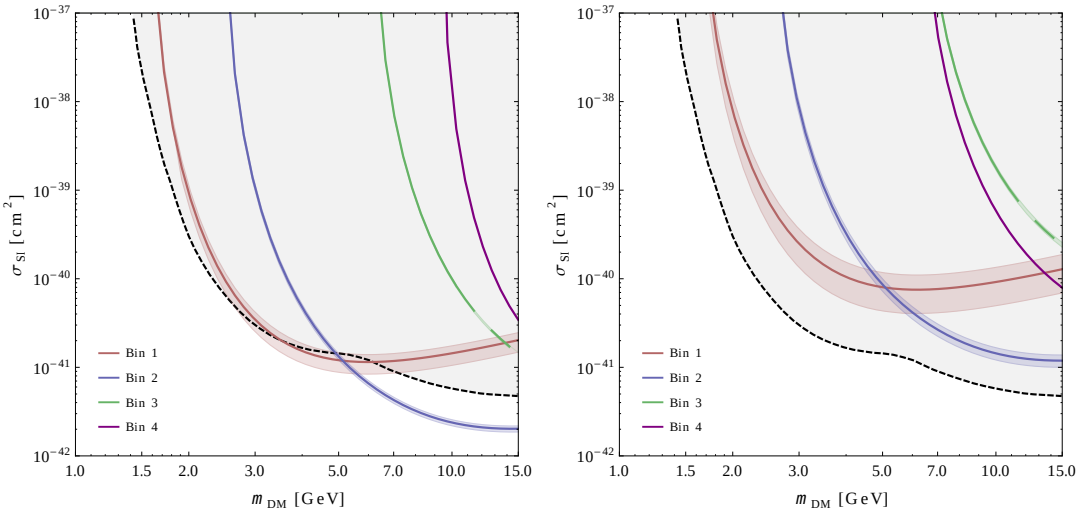

Figure 7.38: The exclusion on σ_{SI} (the standard WIMP-nucleon cross section) for CDMSlite (dashed black line), compared to a likelihood ratio test applied to each energy bin (left) or a Poisson probability test (right), see text for details. The shaded bands include the uncertainty on the event counts from Tab.7.37.

Clearly, assuming that the measured events are all known background is not a conservative treatment as some will be an unknown background. The commonly used conservative statistical method when one does not know the background model is the *optimal interval method* [276, 277].

A more conservative method uses the statement that the 90% confidence limit is such that *there is a probability of 0.9 that if the model were true, then the experiment would have measured more events, n, than have been measured* $n_{\rm obs}$, using the Poisson distribution this probability is,

$$P(n > n_{\rm obs}|\mu) = \sum_{n=n_{\rm obs}}^{\infty} \frac{\mu^n}{n!}\exp(-\mu) \approx \int_{n_{\rm obs}}^{\infty} \frac{1}{\sqrt{2\pi\mu}}\exp\left(-\frac{(t-\mu)^2}{2\mu}\right) dt = 0.9, \tag{7.6.248}$$

the approximation arises in the limit $n_{\rm obs} \gg 1$, this can be further simplified,

$$P(n > n_{\rm obs}|\mu) = \frac{1}{2}\left(\text{Erfc}\left(\frac{n_{\rm obs}-\mu}{\sqrt{2\mu}}\right)\right) = 0.9, \tag{7.6.249}$$

this equation is numerically solvable for μ giving a required signal $\mu = 109^{+51}_{-50}$, 88 ± 14, 635 ± 37 and 207 ± 20 for bins 1 to 4 respectively. Clearly this is conservative since a

large portion of the measured events are background, and the corresponding limits are weaker than those given by the collaboration. The result of this method is shown in the right plot of Fig.7.38.

Both of the previous methods do not make use of the spectral information (i.e. treat the bins effectively as uncorrelated experiments). The best constraint will not necessarily come from a single energy bin, but a range of energies covering multiple bins such that the signal to background ratio is maximized.

7.7 DMFV : Collider Searches

A large number of experimental searches fall under the umbrella of *collider searches*, which generically cover any searches based on collider data, this could be from e^+e^- collisions (LEP), $\bar{p}p$ (Tevatron and its experiments $D0$, CDF) or pp (LHC and its experiments ATLAS and CMS), generally the latter will provide the strongest bounds when DM couples to the quark sector.

A generic and simple analysis of the data simply counts a total number of events passing a set of selection criteria (e.g. an upper limit on p_T), $N_{\rm obs}$, and compares this to an expected number (usually also given by the experimental collaboration) including all SM processes $N_{\rm SM}$. This is then combined with the expected number of events from the DM model, N_χ, and an 90% CL is extracted using a simple χ^2 test. The limit can be made equally well on N_χ or the cross section σ.

For a given signal (e.g. jet plus missing E_T), the expected number of events are calculated from the basic quark/gluon initiated process (the partonic cross section), convoluted with the pdf's of the proton (if using Tevatron or LHC searches) and finally multiplied by an overall efficiency ϵ which is calculated by running a simulation of parton showering, hadronization and detector effects and calculating the ratio of the events which pass the selection cuts to events given by the partonic level cross sections.

This basic technique does yield fairly accurate bounds, however more involved treatments utilize histograms of events with the available data, using both normalization (total event yield) and shape to provide tighter constraints. This requires the use of purpose built event generator codes, and a full understanding of all SM backgrounds and their systematic uncertainties and is generally avoided in broad phenomenological studies of multiple DM models.

As for the searches themselves, there are many. Most popular are mono-X plus large missing E_T searches, in this case a high energy jet, photon, Z, W or other particle is tagged leaving a large missing energy (the dark matter pair). It is a very clear signal, and is easily calculated from a theoretical perspective. Many studies utilized a dark matter EFT which is used for direct detection bounds, since the partonic cross sections are very simple[21, 360, 361]. This allows for very quick computation of the bounds for our model, with matching to the EFT similar to Eq.(7.6.184).

However, by now it is clear that the EFT approach to collider searches is often unreliable. The UV completion (in our case the introduction of the mediator at a scale equal to its mass) of the EFT operator is commonly around the EW scale, $\sim \mathcal{O}(1)$ TeV, which is close to the energy scale of the collisions, this makes the heavy states likely to produce important effects in the process, and indeed the EFT treatment has been shown to give incorrect results when compared with a simple UV completion (see next section). Nonetheless, so long as one is careful about the regions of validity of the EFT, no problems should arise.

7.7.1 EFT Limit

Following [362] and the EFT operators in Table 7.1, operators $\mathcal{O}_{F1-F4}$ lead to weak bounds $\Lambda \lesssim 20$ GeV, $\mathcal{O}_{F5-8}$ give very similar results, $\Lambda \lesssim 300$ GeV, where Λ is the mass suppression scale of the operator. The best constraints however come from the tensor operator $\mathcal{O}_{F9}$. The analysis assumes equal couplings to $q = u, d, s, c$, but due

to the small charm and strange contribution to the proton pdf these results can be approximately applied to the $\chi - u$ couplings.

To provide some simple estimates, we scan over the three DM up-quark couplings taking the EFT operators individually, computing the bound, and selecting the strongest. Since particular operators ($\mathcal{O}_{F9}$) provide substantially stronger bounds, taking the EFT operators individually is likely a good approximation; however if λ_{ij} is such that each quark couples to the DM with roughly equal strength, then stronger bounds would be found by including all the quark flavours simultaneously.

The matching to the EFT operators listed in Tab.7.1 is different that for scattering processes (for the process $\chi_i \bar{\chi}_j \to q_l \bar{q}_m$),

$$C_{F8}^{(q)} = -C_{F5}^{(q)} = -\frac{\lambda_{li}\lambda_{mj}^*}{2m_\phi^2} \ , \ C_{F6,7}^{(q)} = \frac{i\lambda_{li}\lambda_{mj}^*}{2m_\phi^2}, \tag{7.7.250}$$

in which the limit $m_\phi \gg \sqrt{u}$ is taken, with u the usual Mandelstam variable representing the momentum exchange through the mediator. This condition needs careful attention, since it is very easily violated given the large collision energies involved at the LHC.

Following [22], the matching procedure looks schematically like,

$$\frac{g^2}{u - m_\phi^2} \approx -\frac{g^2}{m_\phi^2}\left(1 + \frac{u}{m_\phi^2} + \cdots\right) \equiv \frac{1}{\Lambda^2}, \tag{7.7.251}$$

where Λ sets the mass scale of the EFT operator, on which constraints are based. However, given a bound on Λ it is impossible to know whether $u < m_\phi$ holds (since the coupling g can be arbitrarily small to offset the increase from a degeneracy between u and m_ϕ^2).

One immediate constraint on the validity of the EFT approximation that can be inferred uses the perturbative limit of the coupling $g \leq 4\pi$, giving the limit $u \leq m_\phi^2 \leq (4\pi\Lambda)^2$. The lower the value of g, the stronger the 'bound' becomes and the smaller the region of validity of the EFT. This treatment applies equally

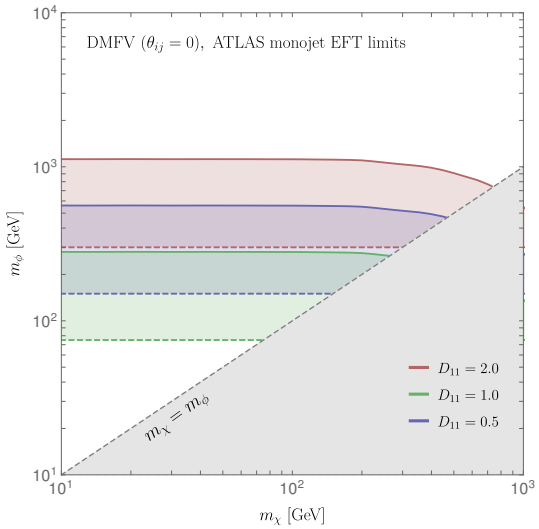

Figure 7.39: ATLAS monojet bounds from [21] (solid lines) for a range of couplings to the up quark. The EFT approximation breaks down beneath the dashed lines (which are the $R_\Lambda = 0.5$ contours with $g \lesssim 4\pi$ from [22]), and so only the shaded regions between the solid and dashed lines can robustly be excluded using the EFT.

well to the direct detection EFT, the difference being that u can be very large at the LHC, but the equivalent kinematic factor for direct detection is extremely small.

In [22] the validity of the EFT approximation is quantified by R_Λ, the ratio between the cross section with the constraint $u < \Lambda^2$ applied, to the total cross section (i.e. the total proportion of the cross section which is valid under the EFT assumption). The lines of $R_\Lambda = 0.50$ are plotted alongside the EFT limits of [362] in Fig.7.39 (the R_Λ contour assumes $|\eta| < 2$ and $p_T < 2$ TeV, the EFT limits assumed the same range of η, but allow $p_T \lesssim 1.2$ TeV). It is worth noting that [22] produce results with the limit $g \lesssim 1$, the bounds become significantly weaker by using $g \lesssim 4\pi$ which then permit a small region of validity as shown in Fig.7.39. The EFT assumption breaks down entirely for $g \lesssim 1$. Thus the EFT approximation cannot be justified in our analysis and we turn to the simulation of the full cross section.

7.7.2 Processes for the LHC

There are several tree-level processes for monojet and dijet searches. Monojet searches veto three-jet events but still allow (one,two)-jet plus missing E_T to which all of the following processes apply;

1. $pp \to \chi\bar{\chi}j$, processes involve both s and t-channel mediator exchange. $q\bar{q}$ initial states require t-channel ϕ and a gluon jet. qg initial states (benefitting from the enhanced gluon pdf) allow for an s-channel ϕ and a quark jet.

2. $pp \to \chi\bar{\chi}jj$ some processes are equivalent to (1) with additional QCD radiation and are thus suppressed by $\sim \alpha_s$. Additional diagrams include processes with two ϕ exchanged in the s-channel, the cross section is dominated by the mediators going on-shell (and subsequently decaying) and therefore can be resonantly enhanced, but off shell production is also included. The former processes must be matched with (1) to avoid the double counting, when for example one of the jets becomes very soft. The latter are not matched since they are of a different order in the couplings.

3. $pp \to \phi^\dagger\phi$. The mediators are produced on-shell and subsequently decay (according to the NWA); this is a 2-jet plus missing E_T process, which nonetheless contributes to the monojet signal. This process is actually double counted in (2) and thus the on-shell phase space region of (2) should be vetoed if these processes are to be generated separately.

4. $pp \to \phi^\dagger\phi j$, if the mediators are on shell then they can contribute to missing energy, so long as they live long enough to escape the detector, however even for extremely small widths of $\Gamma = 1$ eV the average decay length is ~ 0.2 μm. The experimental collaborations veto three or more jets with $p_T > 30$ GeV but this still allows for one or two soft jets to be produced by the decay of the mediators. In this case the contribution should only be significant when $m_\phi \sim m_\chi$ which produces the soft jets. There is also a double counting with (3) which requires a matching.

5. $pp \to \phi^\dagger \chi$ with ϕ on shell. This is double counted with (1), but adding an on-shell veto for the mediator in (1) will correct for this

To include all these processes in MadGraph one must consider separate samples for the on-shell production of two, one or zero mediators, and for the latter two, veto all on-shell phase space for internal mediators to avoid a double counting amongst the samples [363].

Additionally, when using a parton shower the (0,1,2)-jet events must be merged within each sample, to correctly account for the production of jets between the hard matrix elements and parton shower. There is a double counting between the inclusive 1-jet events and inclusive 2-jet events and so on, and merging the two accounts for this. However this statement assumes that the 2-jet process is simply a QCD correction (radiation of a jet) from the 1-jet processes; any 2-jet processes which are not of this type (for example $pp \to \phi^\dagger \phi \to (\chi j)(\bar{\chi} j)$) do not double count and their cross section can simply be added to the total 1-jet cross section.

The processes with two s-channel mediators contribute to the dijet signal (and give the dominant contribution to 2-jet events [364]) are subdominant to the 1-jet events. The simplest way to deal with the $\phi\phi^\dagger$ final states is to use the *narrow width approximation* (NWA),

$$\sigma_{pp\to\bar{\chi}\chi jj} = \sigma_{pp\to\phi^\dagger\phi} \times \mathrm{BR}(\phi \to \bar{\chi} j) \times \mathrm{BR}(\phi^\dagger \to j\chi), \tag{7.7.252}$$

in which the mediator width is assumed to be very small $\Gamma/m_\phi \ll 1$, and the ϕ are produced on shell[363].

In conclusion, to balance accuracy with efficiency we use the following methodology. We calculate the total cross section of the following two samples

1. $pp \to \bar{\chi}\chi j$

2. $pp \to \phi^\dagger \phi \to \bar{\chi}\chi jj$, with ϕ on-shell, using the NWA.

and add them together, without the addition of parton showers (the total inclusive cross section would not be affected anyway) and detector simulations. There is no need to veto any phase space as there is no double counting. The addition of extra jets to process (1) correspond to QCD corrections $\alpha_s \sim 0.1$, plus non QCD corrections which do not require matching (the production of s-channel ϕ) but which can have a large impact since $\lambda_{ij} \gtrsim \alpha_s$ in the regions of interest and (2) represents the dominant contribution to these.

Since the mediator ϕ is an SU(2) singlet, mono-W signals should be suppressed, however models which extend the DMFV to LH fields require ϕ to be an SU(2) doublet and to acquire a coupling to $W^{\pm}$. Even in this case though the electroweak couplings should make such signals (along with mono-photon) negligible compared to QCD coupled processes like monojets and dijets [365].

The cross section for each process $pp \to X$ is found according to

$$\sigma = \sum_{a,b} \int dx_1 dx_2 \left(f_a(x_1) f_b(x_2) + f_a(x_2) f_b(x_1) \right) \hat{\sigma}, \tag{7.7.253}$$

where $\hat{\sigma}$ is the partonic cross section for $ab \to X$ with a, b partons with pdfs $f(x)$, depending on the fraction x of the proton momentum. We will generate results numerically using MadGraph, but it is worth noting that in [22] the appendices give all the relevant analytic formula for the phase space in terms of p_T, η for our model. The matrix elements are given for the EFT, however the simplified model simply gives additional factors $(Q - m_\phi^2)$ from the propagators. The only diagram not accounted for by the EFT would be the internal bremsstrahlung from the mediator.

In the studies we refer to which use the simple cut and count strategy, limits are provided on the *visible cross section* defined as,

$$\sigma_{\text{vis.}} = \sigma \times A \times \epsilon; \tag{7.7.254}$$

the parton level production cross section (Eq.(7.7.253)) times acceptance A times efficiency ϵ. The acceptance arises from the kinematic cuts that are applied to each event, and the efficiency accounts for the detector effects.

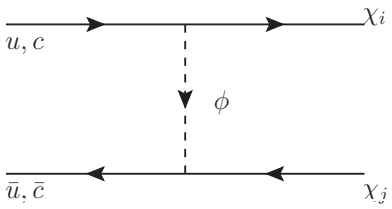

(a) The above diagram must include an emission of a gluon from external legs (ISR, FSR) or internal bremsstrahlung from the mediator. The contribution is roughly equal amongst these emissions.

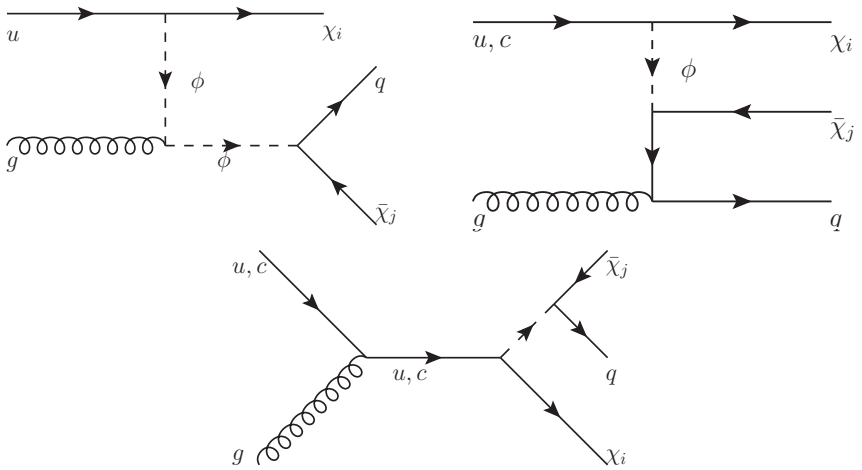

(b) The s-channel ϕ resonance is responsible for (1) and (3) dominating over (2), and the additional enhancement due to the gluon pdf over (a) makes these the overall dominant monojet contribution. For very heavy mediators (1) is suppressed due to the two propagators.

Figure 7.40: The dominant diagrams contributing to the pure monojet process. Each processes scales as $\sigma \propto \alpha'^2 \alpha_s$ where $\alpha' \sim \lambda\lambda^\dagger$ and can become extremely large if $\lambda > 1$. The cross section is dominated by the diagrams containing a heavy ϕ resonance.

7.7.3 Analysis : Monojet

In the DMFV model the monojet plus missing energy signal comes dominantly from the processes listed in Fig.7.40.

The most recent monojet search by ATLAS [23] uses the Run 2 data ($\sqrt{s} = 13$ TeV and $\mathcal{L} = 3.2$ fb^{-1}). The event selection cuts are $|\eta| < 2.4$ and $p_T > 250$ GeV for the leading jet (plus an allowance of up to four jets with $p_T > 30$ GeV and $|\eta| < 2.8$ and an angle $\Delta\phi > 0.4$ between the jet and missing energy vertex), along with a

missing energy cut $E_T > 250, 300, 350, 400, 500, 600, 700$ GeV defining seven signal regions. The efficiency is $\epsilon \sim 100\%$[23].

A similar analysis was performed by CMS [24] with the Run 1 data ($\sqrt{s} = 8$ TeV and $\mathcal{L} = 19.7$ fb^{-1} of integrated luminosity). The dominant event selection criteria are $|\eta| < 2.4$ and $p_T > 110$ GeV for the hardest p_T jet (and $|\eta| < 4.5$, $p_T > 30$ GeV for a possible second jet which must be widely separated from the first jet with $\Delta\phi > 2.5$), leading to bounds $\sigma_{\text{vis}} < 0.0078 - 0.2289$ pb for cuts on $E_T > 250, 300, 350, 400, 450, 500, 550$ GeV defining again seven signal regions.

Fig.7.41 shows the total cross section for a benchmark scenario, along with the ATLAS and CMS constraints in Fig.7.42. The processes which contribute to this signal are shown in Fig.7.40 (single jet processes) and Fig.7.44 (two jet processes).

The width of the mediator has a substantial effect on the cross section (as shown in Fig.7.43); several of the 1-jet and 2-jet processes involve the s-channel exchange of ϕ and are enhanced by the resonance if the width is particularly narrow, which is the case throughout most of the parameter space since we couple the mediator only to the three DM candidates. We ensure that the correct width is implemented for each choice of parameters. This gives the cross section a noticeable peak.

Due to the large missing energy cut, the cross section is insensitive to DM masses below $m_\chi \sim \mathcal{O}(100)$ GeV. Above $m_\chi \sim 1$ TeV, the cross section disappears since the DM is absolutely stable and thus requires at least $s > 4m_\chi^2$ centre of mass energy to produce a pair, and this reaches the energy limit of the beam. The minimum jet p_T requirement further reduces this limit.

For a given DM mass, the upper m_ϕ limit is set by the size of the production cross section for the ϕ times the total branching ratio into jets. The lower limit on m_ϕ is either set by hand by the requirement that $m_\phi \gtrsim \max(m_{\chi_i})$, or may be set by the suppression of the cross section by the mediator's width. For example, if the

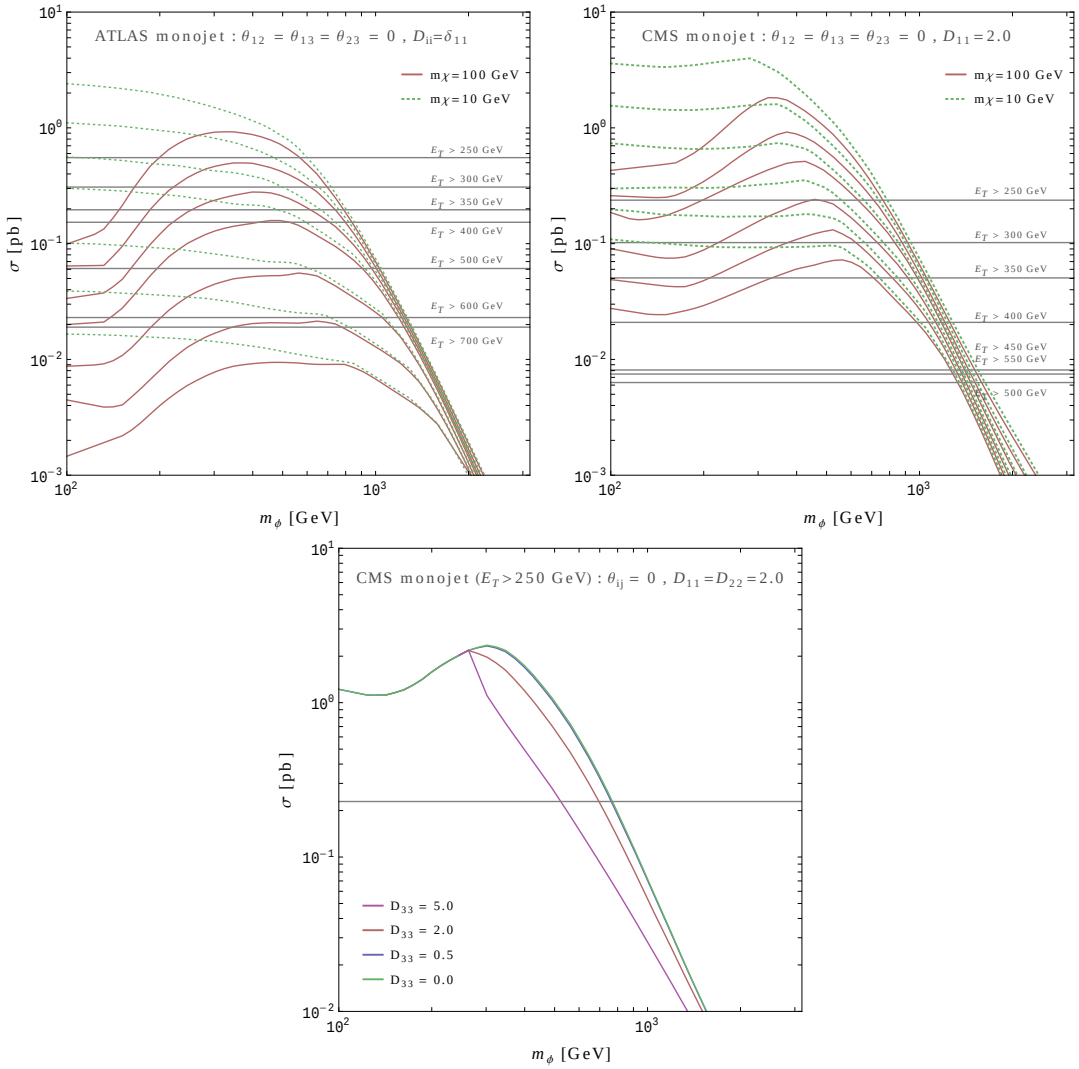

Figure 7.41: Total cross section for the seven signal regions of the ATLAS monojet search [23] (top left) for two DM masses. Comparison to the CMS monojet search (top right) [24]. Also shown is the behaviour of the cross section with D_{33}, the top-quark coupling (bottom).

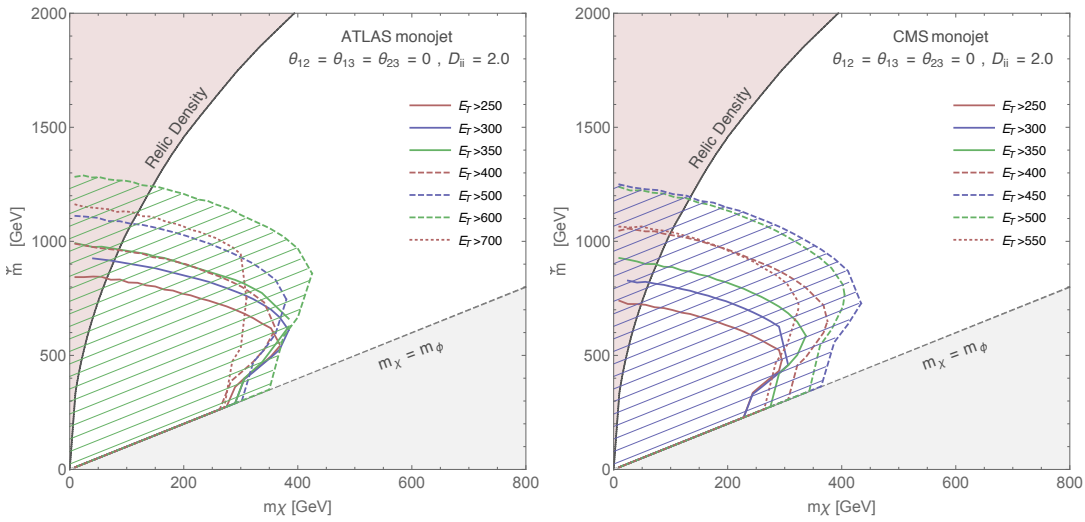

Figure 7.42: Exclusion regions (shaded) for the seven signal regions in the ATLAS (left) and CMS (right) monojet analysis, for no mixing ($\theta_{ij} = 0$) and equal couplings $D_{ii} = 2$. The strongest constraint comes from the $E_T > 450$ GeV bin.

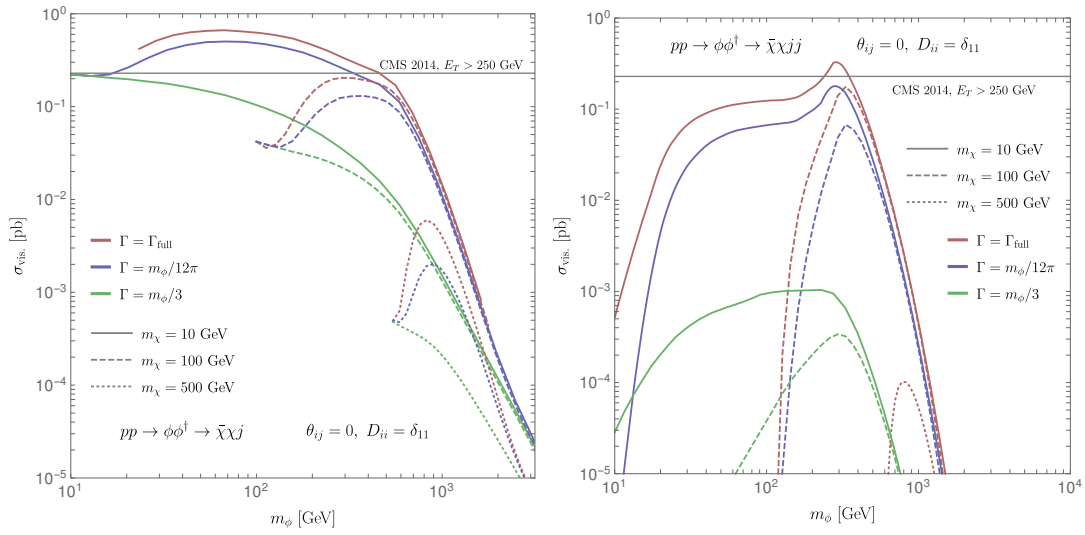

Figure 7.43: The total cross section for the 1,2-jet process (left, right respectively) with varying DM mass and mediator width, the cuts are those for the CMS monojet search with $E_T > 250$ GeV, the corresponding limit is shown in grey.

mediator decays to two or three flavours of DM, then the branching ratio approaches 0 as $m_\phi \to m_\chi$ for the heaviest DM.

The constraints based on monojet analyses are predominantly sensitive to the u, c quark couplings; the $\phi - t$ coupling is neglected (except in the calculation of the ϕ width) since the production of t is followed by the decay $t \to Wb$ producing either three jets (vetoed in the event) or leptons (also vetoed).

The size of the initial state pdf's for the c, t, and the fact that d, s, b do not couple directly to the new particles means that the only initial states to consider are $gg, gu, u\bar{u}$. For pure monojet processes there are no gluon fusion contributions, the gluon bremsstrahlung ($\bar{u}u$ initial state) is subdominant to associated production gu; for which at high m_ϕ the processes with a single on-shell ϕ are dominant, but at low m_ϕ the process with two ϕ are the largest.

The 2-jet contribution to the monojet analysis (Fig.7.44) can be larger than the 1-jet contribution. For example, looking at Fig.7.44 (b) the LH diagram scales as $(\lambda\lambda^\dagger)$ with no α_s suppression at all (compared with the 1-jet processes which have at least one factor of α_s), for large DMFV couplings this diagram will significantly dominate the others for a "narrow" range of masses for which the various p_T, E_T constraints are satisfied.

7.7.4 Analysis : Dijet

In our model there is no tree level contribution to a pure dijet process, as the two jets are always associated with some missing energy carried by the DM. Such searches are usually performed in the context of SUSY. The relevant processes are summarized in Fig.7.44.

A Run 1 search by ATLAS [30] ($\sqrt{s} = 8$ TeV and integrated luminosity $\mathcal{L} = 20.3\ \text{fb}^{-1}$) looks for multiple jets plus missing energy; we restrict to the 2-jet searches which should provide the strongest constraint. The $pp \to \phi\phi \to \bar{\chi}\chi jj$ process pro-

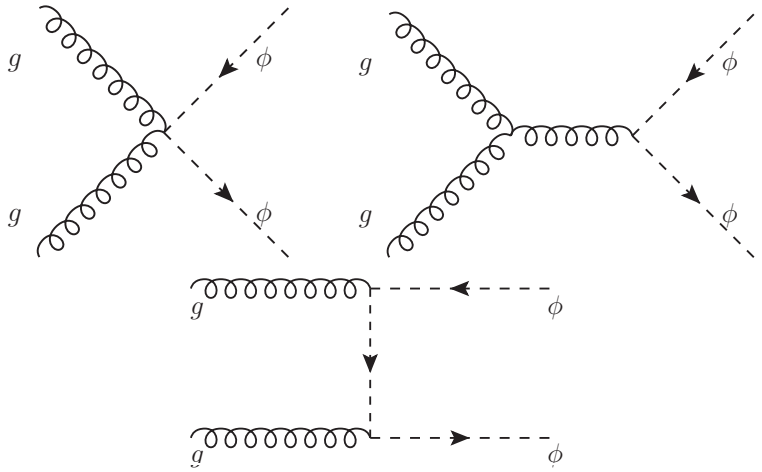

(a) Gluon fusion dijet processes $\sigma \propto \alpha_s^2$.

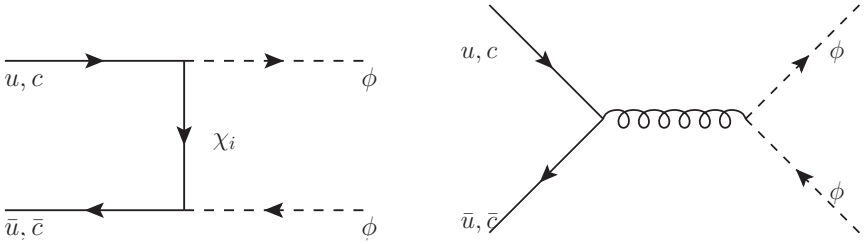

(b) The left (right) process is $\sigma \propto \alpha'^2$ (α_s^2) and so the dominance depends on the size of the new couplings, for couplings which are large enough to be excluded it is usually the LH diagram which dominates.

Figure 7.44: The dominant processes contributing to the production of on-shell ϕ, which decay $\phi \to q_i \chi_j$ producing a dijet signal. In monojet analyses, this provides a subdominant contribution compared with pure monojet processes (Fig.7.40) in most of the parameter space.

SR	N_{obs}	N_{SM}	$N_{\text{n.p.}}$	σ (fb)	σ_{obs} (fb)
tjl	12315	13000 ± 1000	$15 - 704$	$0.78 - 35$	60
tjm	715	760 ± 50	$15 - 59$	$0.75 - 2.9$	4.3
tjt	133	125 ± 10	$22 - 50$	$1.1 - 2.4$	1.9
SR	N_{obs}	N_{SM}	$N_{\text{n.p.}}$	σ (fb)	σ_{obs} (fb)
tjl	263	283 ± 24	$12 - 37$	$3.8 - 12$	16
tjm	191	191 ± 21	$15 - 58$	$4.6 - 18$	15
tjt	26	23 ± 4	$10 - 22$	$3.2 - 6.8$	5.2

Table 7.2: Top : Lower limits (at 95% CL) on the visible cross section for the Run 1 ATLAS dijet plus missing E_T search [30], for $\sqrt{s} = 8$ TeV and $\mathcal{L} = 20.3$ fb^{-1} and three signal regions (SR). Bottom : ATLAS dijet search from Run 2 [31].

vides the dominant contribution to this signal. The results are presented as a total SM background estimate, and a total measured event count; using the same simple event count statistics from Sec.4.5.1 to give the 95% CL we find a limit for the $\pm 1\sigma$ background count and compare this to the observed cross section quoted by the collaboration (Tab.7.2, top rows).

The main selection cuts that are applied are; missing energy $E_t^{\text{miss}} > 160$ GeV, transverse momenta of the two jets $p_{T,(1,2)} > 130, 60$ GeV, azimuthal separation between each of the two jets and the missing momentum $\Delta\phi > 0.4$. The cuts also include a minimum requirement for m_{eff} and $E_T/\sqrt{H_T}$ defined as,

$$H_T = |p_{T,1}| + |p_{T,2}|, \tag{7.7.255}$$

$$m_{\text{eff}} = H_T + E_T, \tag{7.7.256}$$

implemented via Fortran code into MadGraph, the three signal regions are $m_{\text{eff}} > 800, 1200, 1600$ GeV, $E_T/\sqrt{H_T} > 8, 15, 15$ for tjl, tjm, tjt respectively denoting 'loose', 'medium' and 'tight' jet constraints.

In the 2-jet signal we do not need to consider production of a top (or $\bar{t}t$ pair) in the final state, since this will yield a b-jet plus a W which will either decay leptonically (leptons are vetoed) or hadronically (producing 2 additional jets and

contributing to the 3 or 4-jet signal). The $t - \chi$ coupling therefore enters only through the branching ratio of ϕ to the other quark flavours.

We also include a more recent search by ATLAS [31] using Run 2 data ($\sqrt{s} = 13$ TeV and integrated luminosity $\mathcal{L} = 3.2$ fb^{-1}). The constraints from both analyses are included in Fig.7.45, the reduced luminosity of the Run 2 study weakens the bound, but is overcome by the enhancement from the additional CM energy.

7.7.5 Analysis : Stop Search

Lastly, a study in 2014 (Run 1, $\mathcal{L} = 20$ fb^{-1} and $\sqrt{s} = 8$ TeV) by ATLAS [25] considers a set of cuts optimized for the detection of stops, which in our case would be sensitive to the $\phi - t$ coupling D_{33}, dominated by on-shell $\phi\phi^\dagger$ production $pp \to \phi\phi^\dagger \to \bar{t}t\bar{\chi}_i\chi_j$. The signal consists of a lepton in the final state along with four or more jets (originating from a leptonic and hadronic top decay $t \to Wb \to \{\nu_l l, q\bar{q}'\}b$ to a lepton, jets and missing energy). The analysis is performed using a SUSY framework and considering stop decay channels which have no analogy in the DMFV model, for example $\tilde{t} \to b\tilde{\chi}^\pm$ into charginos.

There are four relevant signal regions "`tN_diag`", "`tN_med`", "`tN_high`", "`tN_boost`", each requiring a single lepton with $p_T^l > 25$ GeV, and cuts in Tab.7.3 below [24].

The production of the ϕ pair is dominated by t-channel χ exchange and s-channel gluon exchange; the photon and Z mediated diagrams are neglected. The jet and lepton p_T cuts ensure that the lepton and u, d, s, c, b quark masses can be neglected; assuming also a diagonal CKM matrix the cross section is approximately,

$$\sigma(pp \to 4j + l) \approx 2 \times 2 \times \sigma(pp \to (\bar{b}b)(u\bar{d}) + e^-), \tag{7.7.257}$$

[24] We do not include the cuts on the parameters am_{T2} and m_{T2}^τ. From the published cut flows it can be seen that the effect of these cuts is of the order $\sim 10\%, 2\%$ respectively (although the former cut can have a more pronounced effect $\sim 30\%$ on the "`tN_med`" cut choice).

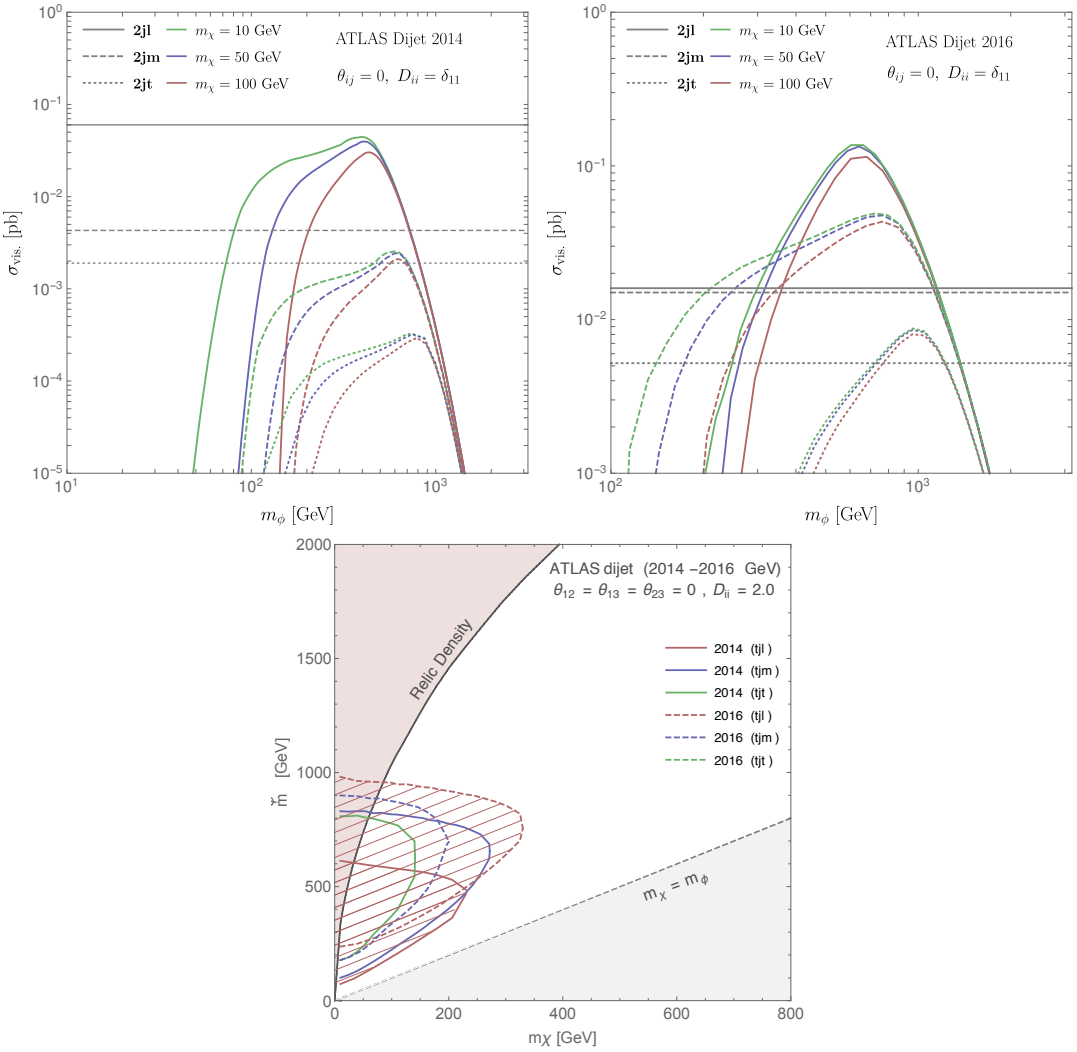

Figure 7.45: Top : The visible dijet cross section assuming $\epsilon = 100\%$; for three DM masses and for the three signal regions from Tab.7.2 (for both $\sqrt{s} = 8, 13$ TeV, left and right respectively), grey lines correspond to the experimental limits. Bottom : Dijet bounds for the analyses discussed in the text, showing also the region excluded by relic density (shaded) for a benchmark set of parameters.

Cut	"tN_diag"	"tN_med"	"tN_high"	"tN_boost"
E_T^{miss} (GeV)	100	200	320	315
$p_{T,i}^{j}$ (GeV)	$(60, 60, 40, 25)$	$(80, 60, 40, 25)$	$(100, 80, 40, 25)$	$(75, 65, 40, 25)$
m_T (GeV)	60	140	200	175
$\Delta R(b, l)$	0.4	0.4	0.4	0.4
$\Delta\phi(j_{1,2}, p_T^{\text{miss}})$	60	140	200	175
Bound σ_{vis} (fb)	$1.8 - 2.9$	0.4	0.3	0.3

Table 7.3: The four relevant signal regions from the ATLAS 2014 stop search [25] along with the cuts that are implemented.

calculated with MadGraph in the narrow width approximation. Although the cross section is predominantly controlled by the size of D_{33}, the light quark couplings D_{11}, D_{22} have a mild affect by reducing the branching ratio $\phi \to \bar{t}\chi_i$ and suppressing the cross section.

At threshold for on-shell top production ($m_\phi = m_t + m_\chi$), if the ϕ couples only to tops then the branching ratio will be 1, meaning that the cross section is essentially just given by the production cross section for $\phi\phi^\dagger$ and hence remains finite; however if even a small coupling to the other quarks exists then the BR rapidly decreases at the threshold.

At the high m_ϕ edge of the exclusion region, the constraint is essentially independent of the DM mass and the cross sections scales with m_ϕ only. Since the top coupling was assumed to be zero in the light squark search, the limits in Fig.7.46 are not comparable to those in Fig.7.41, instead Fig.7.41 is replaced by Fig.7.46 in the event that the ϕ couples predominantly or entirely to the third generation.

7.7.6 Collider Constraints within DMFV

We have now looked at three classes of analysis; monojet searches, dijet searches, and searches optimised for a stop. Within our model we have couplings to u, c, t

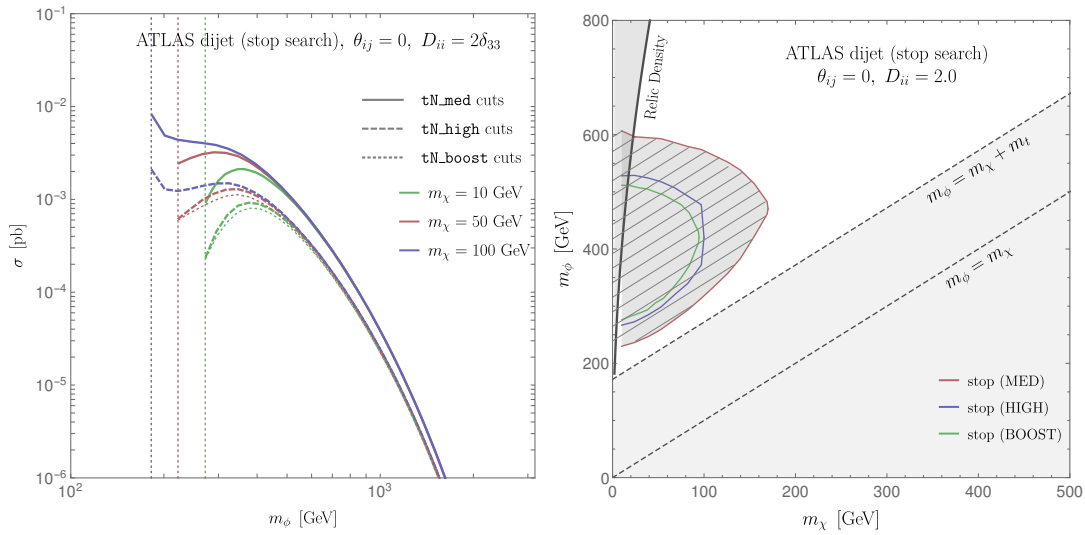

Figure 7.46: Left: the visible cross section assuming $\epsilon = 100\%$ for the ATLAS stop search [25]. Dashed grey lines denote the top production threshold. Right : constraint for the three signal regions and for $\epsilon = 50\%$. Since the coupling matrix λ is diagonal ($\theta_{ij} = 0$), the mediator must be heavy $m_\phi > m_{\chi,3} + m_t$.

(denoted $\lambda_{u,c,t}$) and the relative strengths of these dictate which signals will be dominant.

Compared to λ_u, the monojet and dijet processes are suppressed if only λ_c is non-zero (by pdf's), but generally are enhanced by mixtures of $\lambda_{u,c}$. The coupling λ_t reduces the signals since they come from s-channel ϕ resonances and thus the branching ratio to u, c jets will go as $\mathrm{Br}(\phi \to \chi u, c) \propto (D_{33})^{-2}$ if $D_{11,22} \ll D_{33}$.

The stop search only becomes relevant for large λ_t with $\lambda_t/\lambda_{u,c} \gg 1$. Increasing $\lambda_{u,c}$ suppresses the signal by the branching ratio $\Gamma_\phi \propto (D_{11} + D_{22})^{-2}$ if $D_{11,22} \gg D_{33}$. The sensitivity of the collider searches may be roughly categorized as:

- **Mostly up-type** : The dominant signal will come from the monojet processes which have the least QCD suppression and which require a u in the initial state. Dijet searches are also sensitive but it tends to be the monojet which sets the better constraint.

- **Mostly charm-type** : The monojet processes are enhanced by the presence of

charm coupings, however as the up coupling is reduced the monojet processes become suppressed by the charm pdf by around $\mathcal{O}(10^{-1} - 10^{-2})$. The dijet processes are very similar as for u quarks but the largest contributing diagram is again suppressed by the charm pdf. Both searches provide constraints

- **Mostly top-type :** The monojet signal depends primarily on $\lambda_{u,c}$, only indirectly on λ_t though the widths. λ_t can be probed through stop searches with jet multiplicities of ≥ 4.

Colliders provide very powerful exclusions (up to the TeV scale in mediator mass Fig.7.46,7.45 and 7.42), and are sensitive to all three couplings D_{ii}, although can be significantly weakened by, for example, strong top couplings. The DM is *produced on-shell*, and so the constraints are comparatively weak at high DM mass when compared with searches which depend on the cosmic abundance of DM; on the other hand the fact that the DM is produced in the collider releases any dependence on its relic abundance, thus allowing more powerful constraints on the χ which decay away in the early universe. Sensitivity of colliders to low mass DM is much better than for high mass, whereas the most powerful astrophysical probe (direct detection) cannot detect below the GeV scale due to kinematics, providing a valuable complementarity between collider and astrohpysical searches.

When compared with the most powerful direct detection limits, the collider limits are not as constraining, and this is not likely to change in the future, even with more luminosity and higher energy beams.

It is very difficult for a given parameter choice to determine the strongest bound from colliders amongst the various signals, and one should therefore check all available searches. Due to the interplay between 1,2-jet processes, there is no obvious scaling behaviour of the cross section with the coupling parameters, these factors make implementing collider searches in an MCMC scan extremely difficult/slow as each cross section must be numerically computed at each point in phase space. However, we have checked explicitly that the remaining phase space of the model after

other constraints are applied is not impacted significantly by the collider bounds.

7.8 DMFV : Other Bounds

7.8.1 Electroweak Precision Observables

In our model, since the scalar carries non-zero hypercharge, it can affect various electroweak precision observables (EWPO). For certain kinds of new physics above the weak scale, a simple parameterisation of these effects comes in the form of the Peskin-Takeuchi S, T, U parameters [366, 367]. The S, T, U parameterisation of new physics contributions have the following underlying assumptions:

- That the electroweak gauge group is the standard $(\mathrm{SU}(2)_L \otimes \mathrm{U}(1)_Y)$.
- That the new physics appears at a scale high enough above the weak scale that the corrections can be expanded to first order as a power series in $q^2/\Lambda_{\mathrm{NP}}$, where q^2 is around the weak scale.
- That the new physics has suppressed couplings to light fermions compared to the gauge bosons.

The first of these is obviously true in our model – we have not added any new gauge symmetry. The mass of our new scalar is not a priori above the weak scale, but we will nonetheless find that low masses do not lead to appreciable constraints. The most questionable is the suppressed couplings to light fermions. The photon and Z coupling to ϕ is of the order of 0.1, whereas the coupling to the up quark is of the order of the diagonal elements D_{11}, D_{22}, D_{33}. The light quark coupling could therefore be large, but in much of the parameter space we are within the regime where the Peskin-Takeuchi parameters well describe electroweak corrections.

The S, T, U parameters can be simply thought of in terms of corrections to the Z and W masses, and the Z-γ mixing. They are defined as,

$$\alpha S = 4s_W^2 c_W^2 \left[\frac{A_{ZZ}(m_Z^2) - A_{ZZ}(0)}{m_Z^2} - \frac{\partial A_{\gamma\gamma}}{\partial q^2}|_{q^2=0} - \frac{c_W^2 - S_W^2}{c_W s_W} \frac{\partial A_{\gamma Z}}{\partial q^2}|_{q^2=0} \right] \quad (7.8.258)$$

$$\alpha T = \frac{A_{WW}(0)}{m_W^2} - \frac{A_{ZZ}(0)}{m_Z^2} \quad (7.8.259)$$

$$\alpha U = 4s_W^2 \left[\frac{A_{WW}(m_W^2) - A_{WW}(0)}{m_W^2} - c_W^2 \frac{A_{ZZ}(m_Z^2) - A_{ZZ}(0)}{m_Z^2} - s_W^2 \frac{\partial A_{\gamma\gamma}}{\partial q^2}|_{q^2=0} + 2c_W s_W \frac{\partial A_{\gamma Z}}{\partial q^2}|_{q^2=0} \right] \quad (7.8.260)$$

where the $A(q^2)$ functions come from the two-point correlations functions $\Pi_{XY}^{\mu\nu}(q^2) = A(q^2)g^{\mu\nu} + B(q^2)q^\mu q^\nu$ and q^μ is the four momentum of the incoming/outgoing particle.

Since our new scalar is an SU(2) singlet, the W boson does not couple to it and $A_{WW}(0) = 0$, since $A_{ZZ}(0) = 0$ also, $T = 0$. The expressions for the S and U parameters in our model are

$$S = -U = N_c \frac{2s_W^4}{27\pi} \left(-\frac{16}{3} + 16\frac{m_\phi^2}{m_Z^2} - 6\frac{m_Z^2 - 4m_\phi^2}{m_Z^2} \Lambda(m_Z^2, m_\phi, m_\phi) \right) \quad (7.8.261)$$

where

$$\Lambda(m_Z^2, m_\phi, m_\phi) = \frac{\sqrt{m_Z^2 - 4m_\phi^2}}{m_Z} \log \left(\frac{2m_\phi^2 - 2m_Z^2 + m_Z\sqrt{m_Z^2 - 4m_\phi^2}}{2m_\phi^2} \right) \quad (7.8.262)$$

as long as $m_\phi > m_Z/2$.

The expressions for the contributions from a singlet charged scalar were also calculated in [368], which matches the above result once a factor of N_c is included to account for our scalar being an SU(3) triplet. Since these are good EWPO above the weak scale, we use the calculation of S for scalar masses above 200 GeV. In this region, $|S| \lesssim 10^{-4}$ in comparison the GFITTER group currently gives an experimental limit of $S = 0.05 \pm 0.11$ [369].

7.8.2 Higgs Decay

In our model the corrections to the decay width of the Higgs appear at one loop level, in the process $h \to \phi^\dagger\phi, \bar{\chi}_i\chi_j$. The total SM width is $\Gamma_{\rm SM,tot} = 4.07 \times 10^{-3}$ GeV [246, 370] from which one may derive the bounds,

$$R_I = \frac{\Gamma_{\rm DM}}{\Gamma_{\rm DM} + \Gamma_{\rm SM,tot}} < 0.17 \ . \tag{7.8.263}$$

For decay to DM states the squared matrix element is,

$$|\mathcal{M}|^2_{\bar{\chi}_i\chi} = \frac{9y^2}{1024\pi^4}\frac{m_q^2}{(m_h^2 - 4m_\chi^2)}\Big[2m_\chi^2(\Lambda(m_\chi^2, m_\phi, m_q) - \Lambda(m_h^2, m_q, m_q)) \\ + (m_\chi^2 + m_\phi^2 - m_q^2)\log\frac{m_q^2}{m_\phi^2} + 2m_\chi^2(m_\chi^2 + m_q^2 - m_\phi^2 - \frac{1}{2}m_h^2)C_0\Big]^2 \tag{7.8.264}$$

with $C_0' = C_0(m_h^2, m_\chi^2, m_\chi^2, m_q, m_q, m_\phi)$, this loop suppression is far too large to contribute to the decay width and produce constraints. For decay to mediator states it is[25],

$$|\mathcal{M}|^2_{\phi^\dagger\phi} = \frac{3y^2}{128\pi^4}m_q^2\Big[B_0(m_\phi^2, m_\chi, m_q) + B_0(m_h^2, m_q, m_q) + (m_\chi^2 + m_q^2 - m_\phi^2)C_0'\Big]^2 \tag{7.8.265}$$

with $C_0' = C_0(m_h^2, m_\phi^2, m_\phi^2, m_q, m_q, m_\chi)$. This is a divergent integral, the divergence arises due to a possible tree level coupling of the Higgs to the scalar field, above the EW scale this is, when the Higgs acquires a vev,

$$\mathcal{L} = \lambda_{H,\phi}\phi^\dagger\phi H H^\dagger \ , H = \frac{1}{\sqrt{2}}\begin{pmatrix} 0 \\ v + h \end{pmatrix} \tag{7.8.266}$$

which induces a coupling $\lambda_{H,\phi}v\phi^\dagger\phi h$ and a width,

$$\Gamma = \frac{1}{64\pi^2 m_h^2}v^2\lambda_{H,\phi}^2\sqrt{m_h^2 - 4m_\phi^2} \tag{7.8.267}$$

which using Eq.(7.8.263) rules out the entire kinematically allowed region $m_\phi < m_h/2$ for $\mathcal{O}(1)$ couplings, but below couplings $\lambda_{H,\phi} \sim 0.03$ the bounds on m_ϕ disappear.

[25] There are also diagrams which involve the tree level coupling of ϕ and the SM Z boson, but these are equally suppressed.

We now consider the consequences of the divergent contribution to the $h \to \phi^\dagger\phi$ process. This provides a contribution to the only renormalizable operator between the Higgs and mediator $\mathcal{L} = \lambda_{H,\phi}\phi^\dagger\phi H^\dagger H$; we have set $\lambda_{H,\phi} = 0$ at tree level, if it had been non-zero then its counterterm could absorb the divergence. Thus it is not consistent to let $\lambda_{H,\phi} = 0$, which is not protected by any symmetries. Due to its divergence, $\lambda_{H,\phi} \equiv \lambda_{H,\phi}(\mu)$ runs with energy scale, and so even if we set it equal to zero at some scale, at all other scales the radiative corrections drive it to finite values.

In general, the divergence is proportional to the Yukawa coupling of the quark which runs in the loop, for the u, c this will lead to large suppressions and a very small $\lambda_{H,\phi}$, however the top yukawa $y_t \sim 1$ and this can drive large corrections.

We will assume $\lambda_{H,\phi}(\Lambda) = 0$ at some high scale Λ, and then run down to $\mu = m_\phi$ at which point the mediator is integrated out of the theory. At $\mu = m_\phi$ the EFT operator Eq.(7.8.266) is generated with

$$\lambda_{H,\phi}(m_\phi) = \frac{y_t}{8\pi^2}(\lambda\lambda^\dagger)_{33}\log\left(\frac{\Lambda^2}{m_\phi^2}\right) + \mathcal{O}(y_u, y_c) \tag{7.8.268}$$

solving the Euler-Lagrange equations for ϕ:

$$(p^2 - m_\phi^2)\phi = \lambda_{ij}\bar{u}_{R,i}\chi_j, \;\; (p^2 - m_\phi^2)\phi^\dagger = \lambda^\dagger_{ji}\bar{\chi}_i u_{R,j} \tag{7.8.269}$$

which are used to integrate out the mediator

$$\begin{aligned}\mathcal{L}_{\text{eff}} &= \frac{\lambda_{H,\phi}}{m_\phi^4}\lambda_{ij}\lambda^\dagger_{lm}\bar{u}_{R,i}\chi_j\bar{\chi}_l u_{R,m}H^\dagger H \\ &= \frac{\lambda_{H,\phi}}{m_\phi^4}\lambda_{ij}\lambda^\dagger_{lm}\bar{\chi}_i\gamma^\mu\chi_l\bar{u}_j\gamma_\mu u_m H^\dagger H\end{aligned} \tag{7.8.270}$$

where a Fierz transform is made in the final line. When the Higgs acquires a vev, this leads to the same four-fermion interaction Eq.(7.6.138), but suppressed by $\lambda_{H,\phi}v^2/m_\phi^2$ if $m_\phi \gtrsim v \sim 246$ GeV.

7.8.3 Z decay

The limit on the Z decay to invisible states is [370],

$$R_Z = \frac{\Gamma_{\text{DM}}}{\Gamma_{\text{DM}} + \Gamma_{\text{SM,tot}}} < 0.2$$

with $\Gamma_{\rm SM,tot} = 2.4952 \pm 0.0023$ GeV [246] and arises from loop level processes $Z \to \phi^\dagger\phi, \bar{\chi}_i\chi_j$ for masses $m_\phi < m_Z/2$ and $(m_{\chi i} + m_{\chi j}) < m_Z$. However, since the mediator is given a hypercharge, it picks up a direct coupling to the Z and thus creates a tree level coupling

$$|\mathcal{M}|^2_{\rm tree} = \frac{16\alpha\pi s_W^2}{c_W^2}(m_Z^2 - 4m_\phi^2) \tag{7.8.271}$$

however the resulting width is still far too small to give constraints. Clearly then the loop level decay to DM states will also be too small.

7.8.4 Perturbative Unitarity

Perturbative unitarity derives from the necessary condition on any field theory that the *scattering matrix* (S-matrix) is unitary, that is the probability of any scattering process is less than 1. This must be the case order by order in perturbation theory, and generally the strongest constraints come from the lowest order contribution.

One first makes a partial wave decomposition of the amplitude for a particular process or class of processes, for example we can simply choose all $2 \to 2$ scatterings with initial state i and final state f, this forms a matrix of amplitudes $\mathcal{M}_{if}$. Due to the partial wave decomposition, each process has a specific spin configuration (unlike conventional amplitudes we do not sum over the particle spins). Following [72] a simple bound may be derived on self-scattering processes for which $i = f$,

$$|{\rm Re}(\mathcal{M}_{ii})| \leq \frac{1}{2} \tag{7.8.272}$$

We thus consider the tree level $2 \to 2$ self-scattering processes present within the DMFV model (where the initial state and final state consists of particles and their corresponding anti-particles),

$$1-{\rm loop} \ : \ \bar{\chi}_i\chi_j \to \bar{\chi}_i\chi_j \tag{7.8.273}$$

$${\rm tree} \ : \ \phi\phi^\dagger \to \phi\phi^\dagger \ , \ \bar{\chi}_i\chi_j \to \phi\phi^\dagger \ , \ \bar{q}_iq_j \to \phi\phi^\dagger \ , \ \bar{q}_iq_j \to \bar{q}_iq_j \tag{7.8.274}$$

the DM self-scattering occurs at one loop level and is ignored, the rest occur at tree level.

The Jth partial wave matrix element is given by,

$$\mathcal{M}^J_{if} = \frac{1}{32\pi}\beta_{ij}\int d\cos\theta d^J_{\mu\mu'}\mathcal{M}_{if}(S,\theta), \tag{7.8.275}$$

$d^J_{\mu\mu'}$ are Wigner d-functions, and for $J = 0$ are $d^0_{\mu\mu'} = \delta_{\mu 0}\delta_{\mu' 0}$ where μ, μ' are the total helicities of the initial and final state,

$$\mathcal{M}^0_{if} = \frac{1}{32\pi}\delta_{\mu 0}\delta_{\mu' 0}\int d\cos\theta\mathcal{M}_{if}(S,\theta)\ . \tag{7.8.276}$$

Perturbative unitarity may be violated at low energies in theories which contain massive vector bosons, due to the scaling behaviour of the longitudinal modes $\xi \sim \sqrt{S}/m$. Since the DMFV model does not contain new vectors, there are unlikely to be bounds from unitarity considerations. This turns out to be the case, as we have checked explicitly for all tree level $2 \to 2$ processes involving the fields χ_i, ϕ in our model, where the initial (final) state is a particle anti-particle pair of the same field.

For further details and applications of perturbative unitarity, see Appendix A.5 or Chapter 5.

7.9 DMFV : Summary, Results and Conclusions

7.9.1 Summary

We have explored a simplified model for DM, *dark minimal flavour violation* or DMFV, which as the name suggests is a model which quantifies the degree of quark flavour violation. It does so by the introduction of a triplet of DM candidates χ_i which couple to the RH up-type quarks via a matrix λ parametrized in terms of three mixing angles θ_{ij} (analogous to those of the CKM matrix), and three couplings D_{ii} which give the size of the coupling of χ_i to the three generations of quark.

Despite being a simplified model, DMFV overcomes many of the issues that are commonly faced by models which are over-simplified; it is both SU(2) gauge invariant and UV-complete, and does not lead to any violations of unitary. We have

addressed some theoretical issues by computing the RG running effects, which leads to mass splitting between the χ_i and operator mixing between operators of the low-energy effective theory.

The strategy is simply to understand the allowed parameter space of the model, and so we now summarize the various bounds that we have computed :

- **Relic Abundance :** We have calculated the relic abundance explicitly using the coupled Boltzmann equations including coannihilations, scattering and decay. The relic abundance of the heavy χ is strongly influenced by any mass splitting, since $\langle\Gamma\rangle_{ij} \propto \epsilon^5$ where $m_{\chi_j} = m_{\chi_i}(1+\epsilon)$, and a such a decay (even if extremely suppressed), along with any $\chi_i + X \to \chi_j + Y$ scattering processes, will wash out the relic abundance of the heavier candidates. This in turn prevents indirect and direct detection signals from the heavy particles, which scales as Ω^2 and Ω respectively. Because of this sensitivity we have explicitly performed a one-loop RG running of the DM mass parameters and shown that splittings can be as large as $\sim \mathcal{O}(35\%)$. Signals from colliders and flavour observables include production of real (on-shell) or virtual DM states respectively, and are therefore unaffected by the relic abundance.

- **Collider :** We have checked several ATLAS and CMS analyses (for both Run 1 and Run 2 data of the LHC) including monojet, dijet, and stop searches (the latter is a weaker bound, since it requires a 6-body final state but is included to provide bounds in which the coupling to tops is dominant since then monojet and dijet searches are weak) which have the largest sensitivity to the DMFV model. We have included cuts and efficiencies from the analyses, and performed a simple cut-and-count method to give exclusion limits. The resulting bounds on the mediator are strong $m_\phi \lesssim \mathcal{O}(\text{TeV})$ for $\lambda \sim 2$, but do not extend to high DM mass $m_\chi \lesssim \mathcal{O}(100 - 500\text{GeV})$ which must be pair produced on-shell. One advantage is that very light DM is powerfully excluded. The limits do not have a strong dependence of the size of mixing, or mass splitting, however depend sensitively on the ratios of D_{ii}.

- **Indirect Searches :** We have compiled a list of relevant indirect detections bounds on $\langle\sigma v\rangle$ which can be applied to the model, the tree-level cross section $\bar{\chi}_i\chi_j \to (\bar{u}u, \bar{c}c, \bar{t}t)$ is then compared to these limits. The limits are strong, and very efficient at excluding parameter space since the cross section is the same as for relic density calculation, the latter providing a lower limit on $\langle\sigma v\rangle$ and the former an upper limit. We have also included the loop-suppressed photon line searches for the processes $\bar{\chi}\chi \to \gamma\gamma, \gamma Z, \gamma h$ including limits from Fermi-LAT and HESS, which tend to provide substantially weaker bounds than for the tree level searches.

- **Direct Searches :** We have explored the tree level and one-loop level contribution to nuclear scattering. We have found in particular that a strong RG running effect is present which mixes the quark currents and provides extremely strong bounds which cannot be avoided by coupling predominantly to heavy quarks, unless $m_\phi < m_Z, m_t$ (since the running is strongest above this scale). The loop contributions are small and may be neglected in practice, unless one suppresses the tree level contribution. These bounds do not depend sensitively on the mixing angles or mass splitting per se, but scale as Ω_i, and therefore have no sensitivity to the decaying DM candidates.

- **Flavour Bounds :** We have checked the effect of violating the MFV assumptions through its affect on heavy flavour observables, in particular the rare decays and mixing of the D^0. Underlying these processes is a $c \to u$ transition, and the constraints depend primarily on the size of $(\lambda\lambda^\dagger)_{12}$. The rare decay constraints are weak but the mixing constraints are extremely strong, since in the SM a strong GIM cancellation leaves the mixing parameters very small. To remove the mixing contribution either the mixing angles are zero $\theta_{ij} = 0$, or D_{ii} all equal.

- **Other :** We have computed the DMFV contribution to various observables, which lead to extremely weak bounds; including the electroweak precision observables (EWPO), as well as the Higgs and Z decay widths at one loop. The possibility of violation of perturbative unitary has been checked explicitly

by computing the helicity amplitudes of all tree-level $2 \to 2$ processes.

7.9.2 Results and Conclusions

We have aimed to produce a robust statistical analysis of the eight dimensional parameter space of the DMFV model, using the Bayesian inference tool MultiNest [371, 372] with 5000 live points per scan. We have collected a basic review of the statistical concepts that are used to present the results in Appendix A.7. The motivation for carrying out this analysis is twofold, firstly from a practical standpoint it utilizes very quick and efficient algorithms for scanning a large dimensional parameter space, allowing us to include all parameters in one analysis. Secondly, a rudimentary "hit-or-miss" analysis leaves a large region of parameter space allowed, which is not surprising given the flexibility of 8 free parameters, with a statistical result we can quantify the regions of parameter space which are allowed but very improbable given the errors of the experimental data. For clarity, we represent the allowed parameters as contours containing credible regions, using the method of [373] and the posterior *probability density function* (pdf). The $1, 2\sigma$ contours give an indication of the allowed parameter range, with containment probabilities of $68, 95\%$ respectively.

Regarding the use of priors : We make one note of caution regarding the results; the credible regions depend sensitively on the choice of priors for the parameters. This is not surprising since our constraints allow large regions of parameter space to be equally well allowed, and so the use of priors which bias the parameters to lower values (i.e. log-uniform compared with linearly uniform) is reflected in the final result, which can be up to a factor of $2 - 5$ on the endpoints of the credible region. Nonetheless, we are careful to limit the statements made in the text to those which are independent of the choice of priors. In all figures, unless specified otherwise, the log-uniform priors have been used for the masses and for D_{ii}, as this represents the more conservative choice. The ranges and priors for the parameters of the scan are summarized in Tab.7.4 below.

Parameter	Range	Prior
m_χ [GeV]	$1 - 10^5$	Log-Uniform
m_ϕ [GeV]	$1 - 10^5$	Log-Uniform
θ_{ij}	$0 - \pi/4$	Uniform
D_{ii}	$10^{-2} - 4\pi$	Log-Uniform

Table 7.4: Allowed ranges for the parameters used in the MCMC scan, along with the assumed prior likelihood, which is uniform on either a linear or logarithmic scale.

Our results are summarized in Fig.7.47, 7.48 and 7.49 as $1\sigma, 2\sigma$ contours. We consider three separate samples in which the DM (the lightest χ) is the first, second and third member of the triplet (denoted 'up', 'charm' and 'top' DM and coloured red green and blue respectively). Within each sample we present a low and high mass splitting ($\Delta m/m_\chi = 2\%$ and 15%), which primarily distinguish the effect of coannihilation in the calculation of relic density, but affect all other bounds to some extent as we have explicitly included the mass dependence of each.

Additionally, we produce for each parameter a 1D posterior marginalized over the remaining 7 parameters. From this distribution we find the 1σ credible interval. The results are shown in Fig.7.5, 7.6 and 7.7. Each contains results for both uniform and log-uniform priors on D_{ii}, m_χ and m_ϕ; when the two cases are discrepant by $> 1\sigma$ this is due to an almost flat posterior, and using the 2σ band instead the two would agree.

The masses of the DM and mediator are both required to be in the TeV range,

with upper limits in the hundreds of TeV, see Fig.7.47[26]. The DM and mediator masses are strongly correlated with the D_χ (where D_χ is the coupling D_{ii} associated to the DM), as in Fig.7.47, due to the relic density and mixing bounds which both scale approximately as $(D/m)^4$ in the high mass limit. Masses in the TeV range favours the D_{ii} to be $\mathcal{O}(1)$. The mixing angles are not well constrained in general; $\theta_{ij} = 0$ is favoured, but the full range of angles are usually allowed with $1 - 2\sigma$ credibility.

The D_{ii} themselves can become correlated from the mixing constraints which depend on $(\lambda\lambda^\dagger)_{12}$ which is,

$$(\lambda\lambda^\dagger)_{12} \approx \left(s_{13}s_{23}(D_{22}^2 - D_{11}^2) + s_{12}(D_{33}^2 - D_{11}^2)\right), \tag{7.9.277}$$

and so we see $D_{11} \sim D_{33}$ (and less strongly $D_{11} \sim D_{22}$) to minimise the contribution to D^0 mixing. Because the correlation between D_{22}, D_{33} is less pronounced, the RD bound controls the behaviour and produces an anti-correlation, since the annihilation cross section scales like

$$\langle\sigma v\rangle_{\text{eff}} \propto (D_{11}^2 + D_{22}^2 + D_{33}^2)^2 \sim 3 \times 10^{-26}\ \text{cm}^3\text{s}^{-1}$$

due to coannihilations, as such the trend is most pronounced for small mass splitting. This is seen for example in the range of D_{22} for the small splitting data, Fig.7.48.

In most cases increasing the mass splitting reduces the available parameter space in the masses and couplings of the DM since the coannihilations and annihilations of the heavy particles have a reduced effect on the relic density (scaling with a Boltzmann factor $\exp(-\Delta m)$). This allows less flexibility in the DM parameters whilst

[26]The region $m_\phi \lesssim m_\chi$ is disallowed because the mediator becomes stable, the contours overlap slightly into this region due to the specific kinematic bounds which depend on quark mass m_q,

$$m_\chi < m_\phi + \max(m_q)\ ,$$
$$m_\phi > \min(m_\chi + m_q)\ ,$$

where min/max correspond to the values for which a coupling exists .

opening up the allowed parameters of the heavy particles, since their couplings are out of reach of the astronomical constraints (indirect and direct searches) which are proportional to the relic density of the lightest χ (scaling as Ω^2 and Ω respectively). This effect can be clearly seen in the right panels of Fig.7.47, where the 2% splitting allows much smaller DM couplings compared with the 15% splitting, contrastingly in Fig.7.48 (lower panels) the non DM coupling space opens up with a larger splitting.

Top quark threshold effects are absent in the MCMC scan, due to the high masses ($m_\chi \gtrsim m_t$). Since $m_\chi, m_\phi \gg m_t$ the three quarks are kinematically equivalent, and so the bounds are not strongly dependent on the flavour of DM. The main differences arise due to the quarks SM interactions which impact the DD and ID limits.

As described in Sec.7.7, we have studied collider bounds on our model, but these were not directly incorporated into our MultiNest routine as these bounds are much more computationally intensive than the others. However, as we see from Fig.7.42, 7.45 and 7.46 the collider bounds only rule out sub-TeV scale masses, even at large couplings and so we do not expect that a full likelihood function incorporating the LHC constraints would give significantly different results. As a test, we checked a sample of the points inside our 68% confidence intervals and found only a small minority (of order 1%) that would be excluded by collider data.

Constrained Scenarios

We consider two extensions to previous results:

1. In Sec.7.2.2 we found that the mass splitting which is generated through RG running of the DM self-energy is approximately proportional to D_{ii}^2, this motivates us to consider a scenario in which the couplings D_{ii} are correlated with the masses (thus introducing a coupling splitting $\Delta D_{ii}/D_\chi = 2, 15\%$). The reduced parameter space enforces almost degenerate couplings which leads to two important effects; firstly, it subjects all three χ to the astrophysical con-

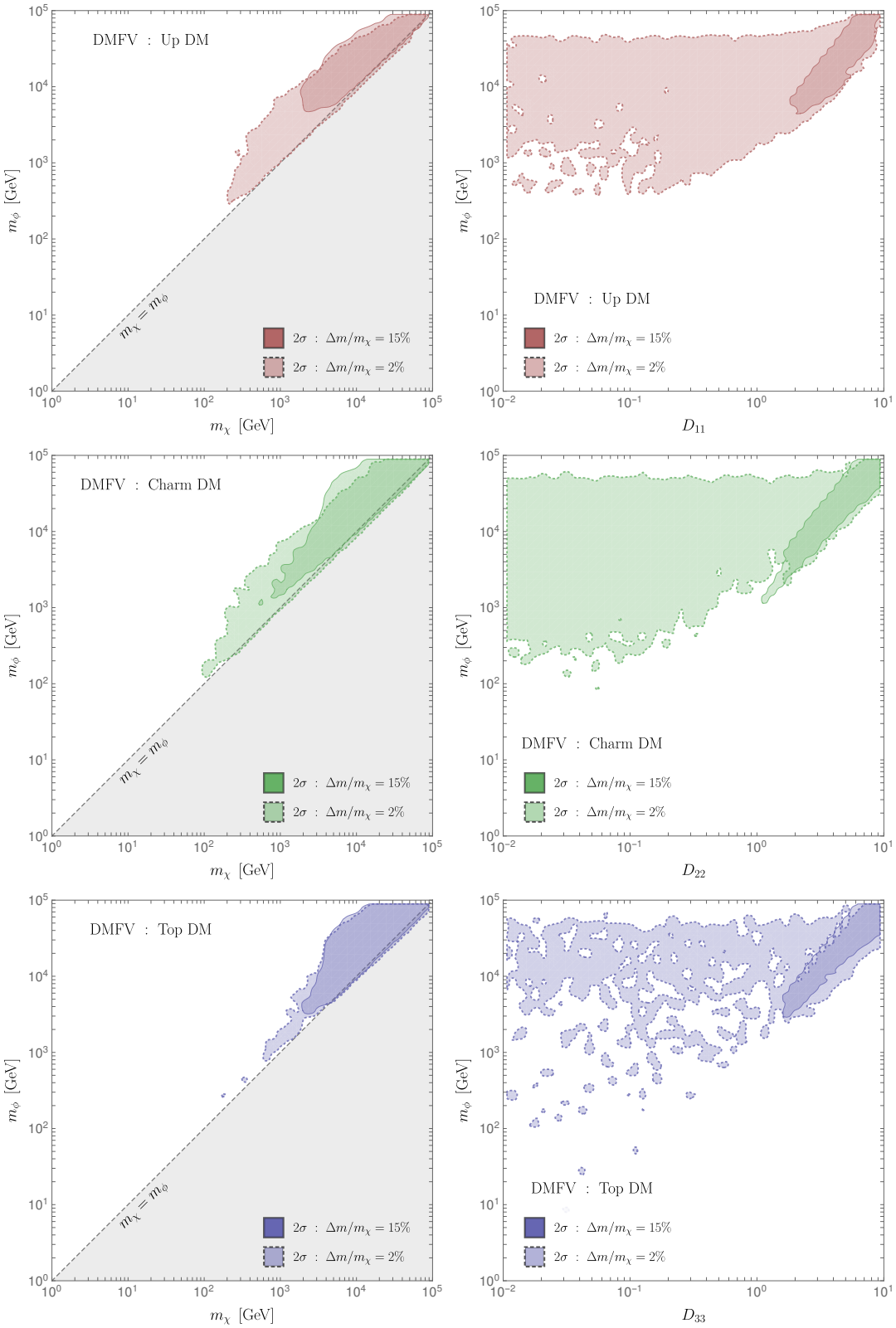

Figure 7.47: Credible regions (2σ contours, corresponding to 95% containment) in the $m_\chi - m_\phi$ plane (left column) and $D_{ii} - m_\chi$ (right panels) where D_{ii} is the coupling associated to the DM candidate which may be χ_1 (top row), χ_2 (middle row) or χ_3 (bottom row). Two values of a mass splitting are chosen $2, 15\%$ which are shown with solid and dashed contours respectively.

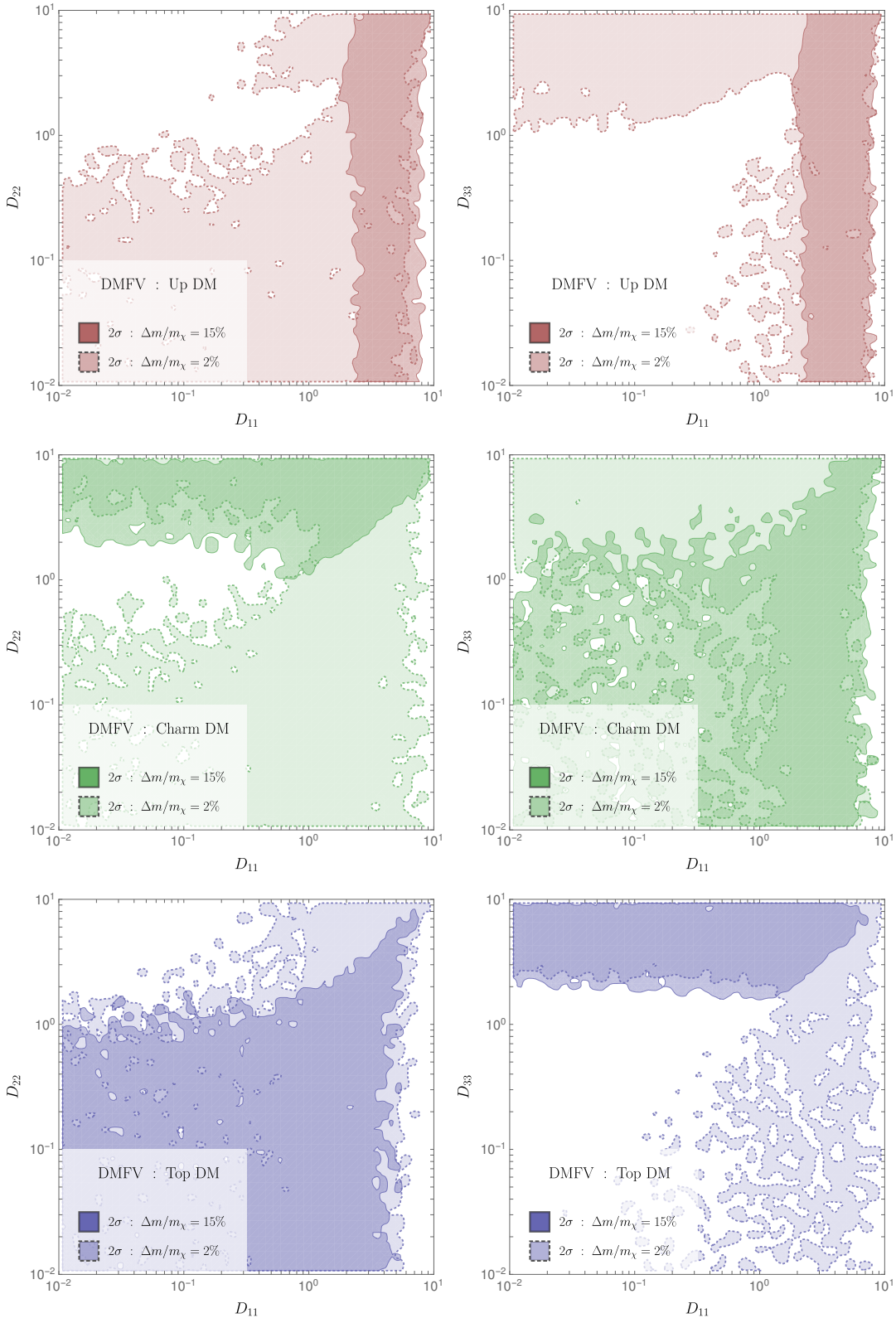

Figure 7.48: As for Fig.7.47 but for the $D_{11} - D_{22}$ plane (left) and $D_{11} - D_{33}$ (right), for both $2, 15\%$ mass splitting (dashed shaded, and solid darker shaded respectively).

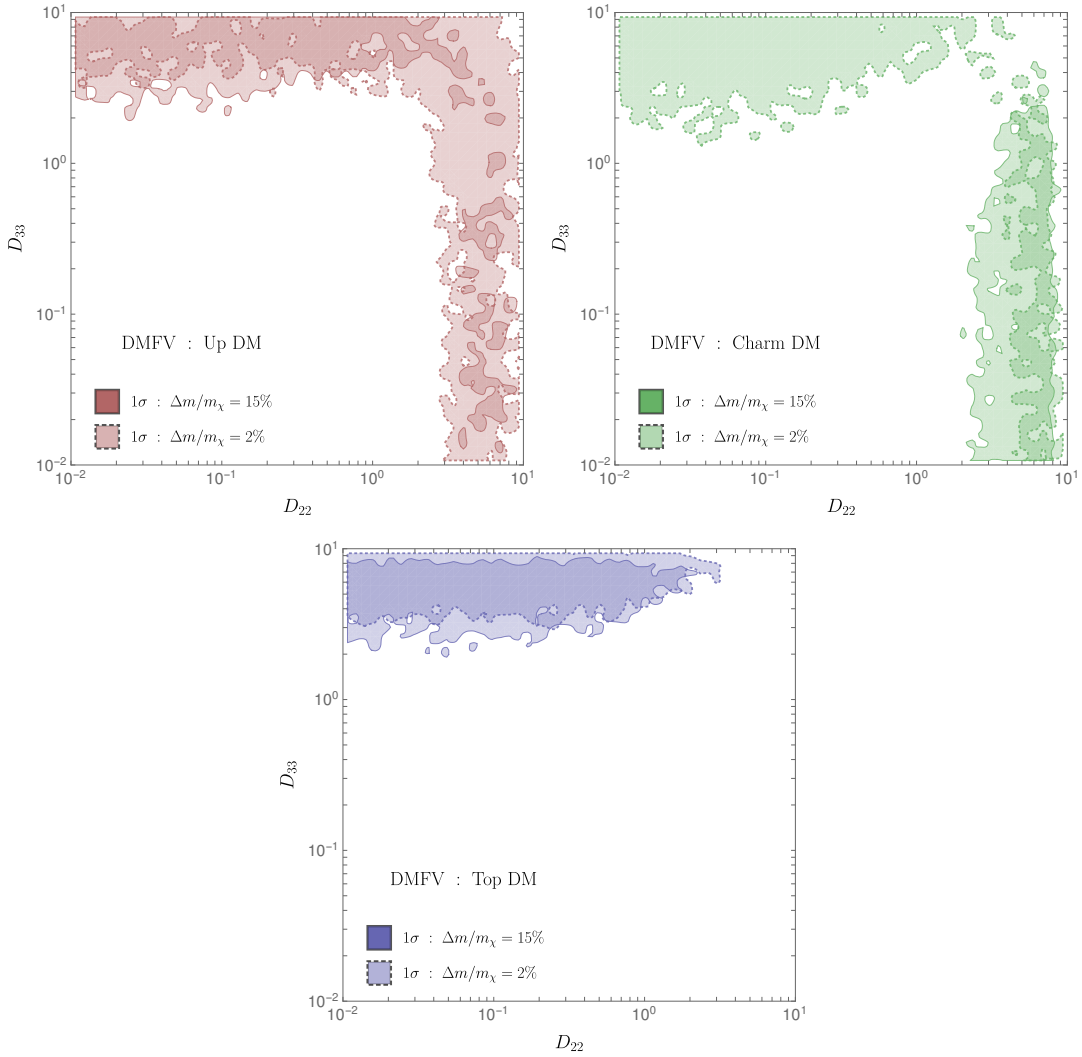

Figure 7.49: As for Fig.7.47 but for the $D_{22} - D_{33}$ plane.

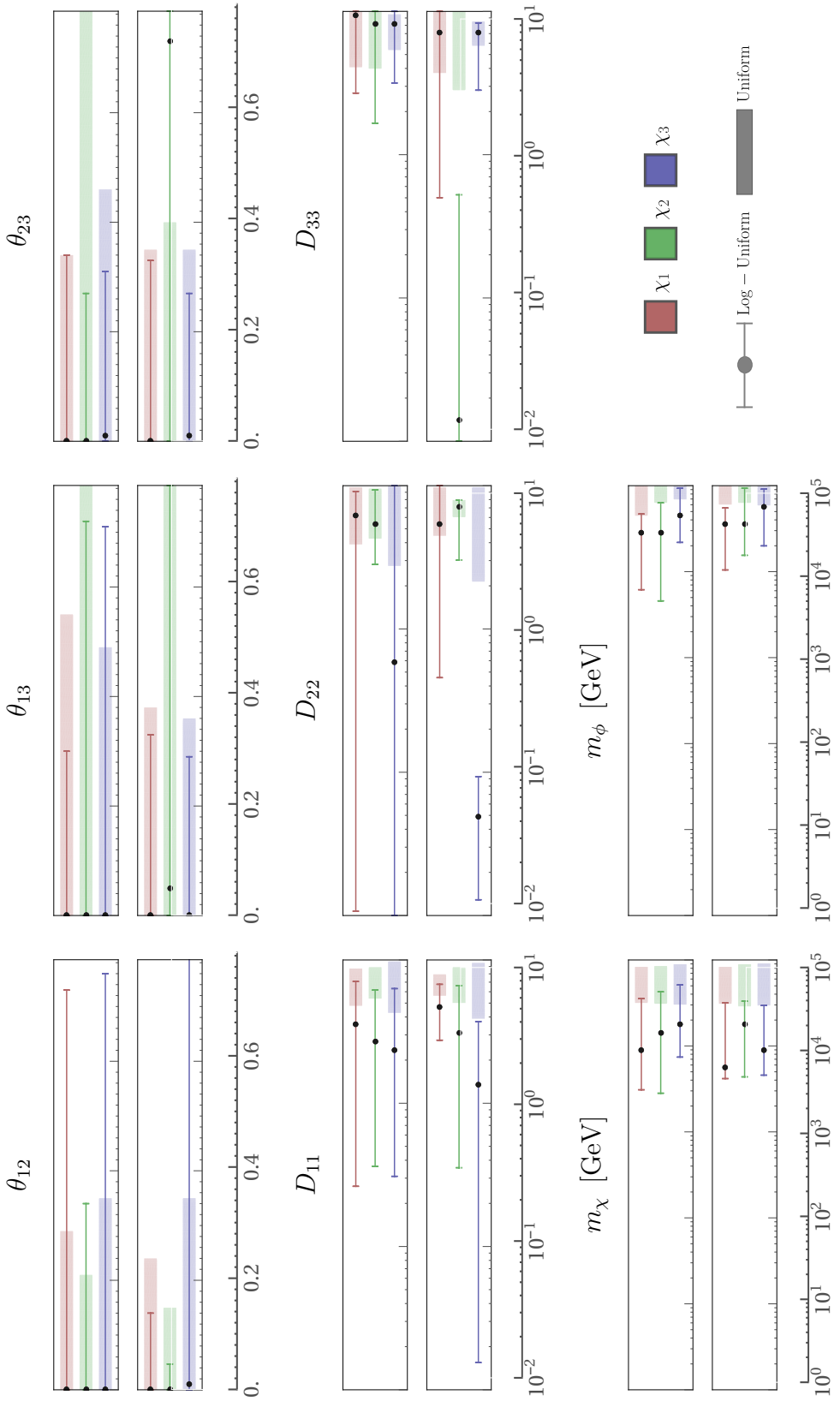

Table 7.5: The 1D 1σ credible intervals for all 8 parameters of the MCMC scan. Colors denote the DM flavour (red, green and blue for up, charm and top DM respectively). The two prior choices on D_{ii} and the masses (log-uniform vs uniform) are shown as lines and shaded regions respectively, the modal average of the log-uniform prior choice is shown as a dot. The two mass splitting cases are contained in different panels.

straints of indirect and direct detection, despite the heavier particles having no relic density. Secondly, because the D_{ii} are equal the mixing effects are naturally small and as a result the mixing angles are much less constrained as they do not need to be small to counteract flavour effects.

This scenario is representative of a model in which MFV is broken only slightly, since the couplings to quark flavours are roughly equal, differing due to the mixing angles and the small differences in the D_{ii}. It is actually only slightly less constrained in both mass and couplings than models in which flavour violation is allowed, which counteracts the naive assumptions that MFV is necessary to protect models from being excluded by flavour observables.

2. When compared with the down-type quark sector, flavour effects do not show up in the precisely measured B meson sector, but instead in the less well constrained D sector. We further weaken the constraint in our conservative treatment in which we assume the SM contribution to D^0 mixing is zero and the experimental value comes entirely from the new physics. This is not entirely unreasonable, since short distance calculations of the observable are known to be very discrepant, nor is it completely reasonable, since long distance calculations are able to bring the SM into good agreement. To cover this caveat we consider a future scenario in which the SM calculation reproduces the experimental number (but the precision of the measurement stays at its current value).

   This is also conservative, since any interference terms between the SM and DMFV amplitude are likely to be large. The constraints on the mixing angles are more pronounced.

We compare the full 9-dim results to constrained scenario (1) and (2) above, in Fig.7.50, and the 1σ intervals in Tab.7.6, 7.7.

Given the current level of data, the model we examine of flavoured DM coupling to up-type quarks has large sections of its parameter space still allowed, so long as large enough masses are considered. Even without collider searches, the lower mass, phenomenologically interesting, regions of parameter space ($m_\chi \lesssim 1$ TeV) are ruled

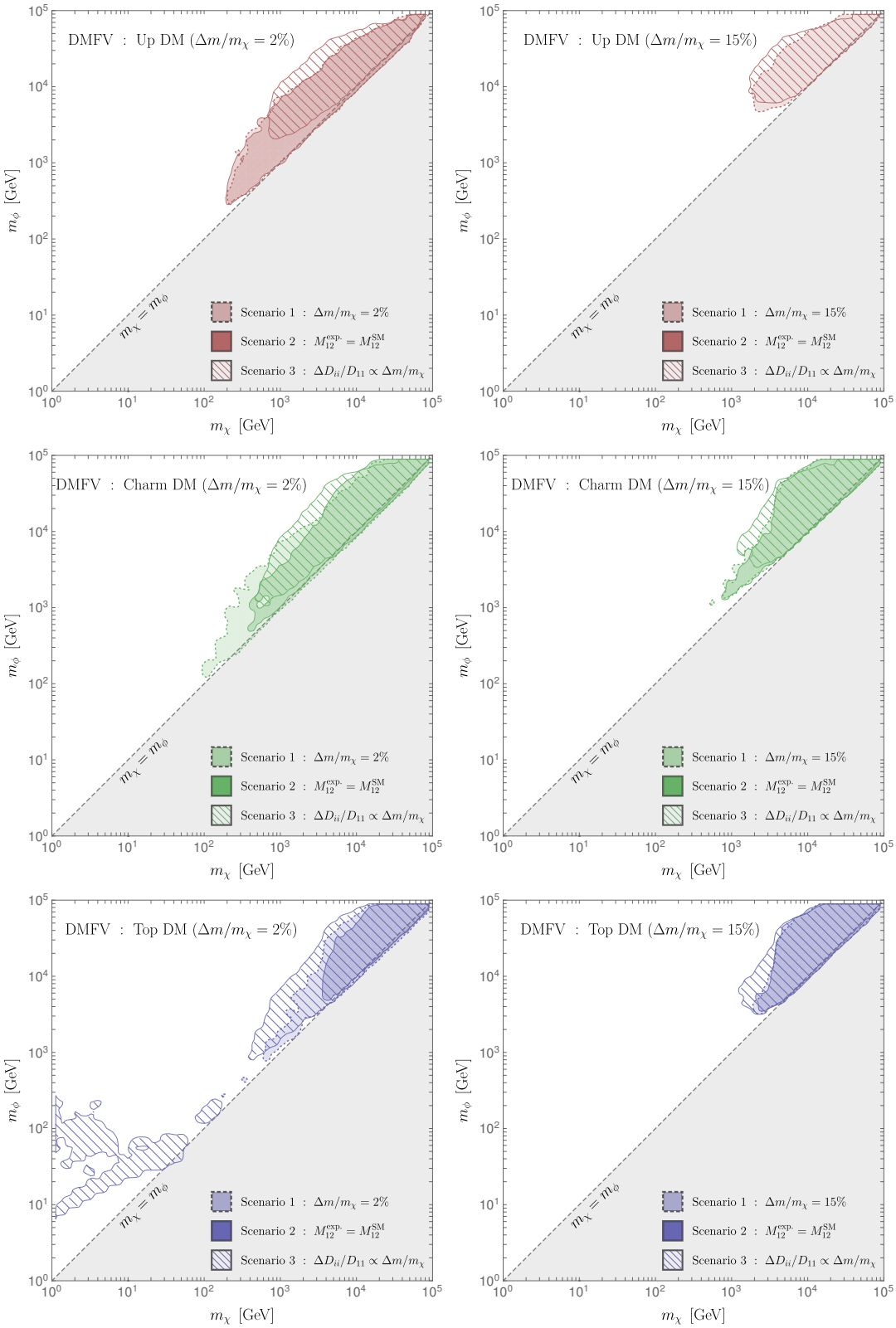

Figure 7.50: Comparison between 2σ contours of the full MCMC scan and two extensions discussed in the text, for a mass splitting of 2% (left) or 15% (right). The top right plot does not include scenario (2) as there is no allowed phase space.

out by flavour, relic density, and direct detection considerations.

The MFV assumption is frequently invoked in simplified models in order to evade potentially large flavour-violating effects. The level of robustness of this assumptions varies considerably between up-type and down-type quarks; for RH down-type quarks strong flavour bounds do ensure that the assumption is a good one[325]. However for couplings to RH up-type quarks we have seen that in fact the flavour bounds are avoided in a large region of MFV-breaking parameter space.

One particular future development could alter this picture however - if a precise theoretical prediction of D-mixing observables could be obtained then either (a) A significant discrepancy requiring new physics is present, or (b) The SM predictions are reproduced with a high precision. The former would motivate the exploration of models which go beyond MFV, and the latter would make the MFV assumption a necessary assumption of the DMFV simplified model if one wants to avoid some fine-tuning.

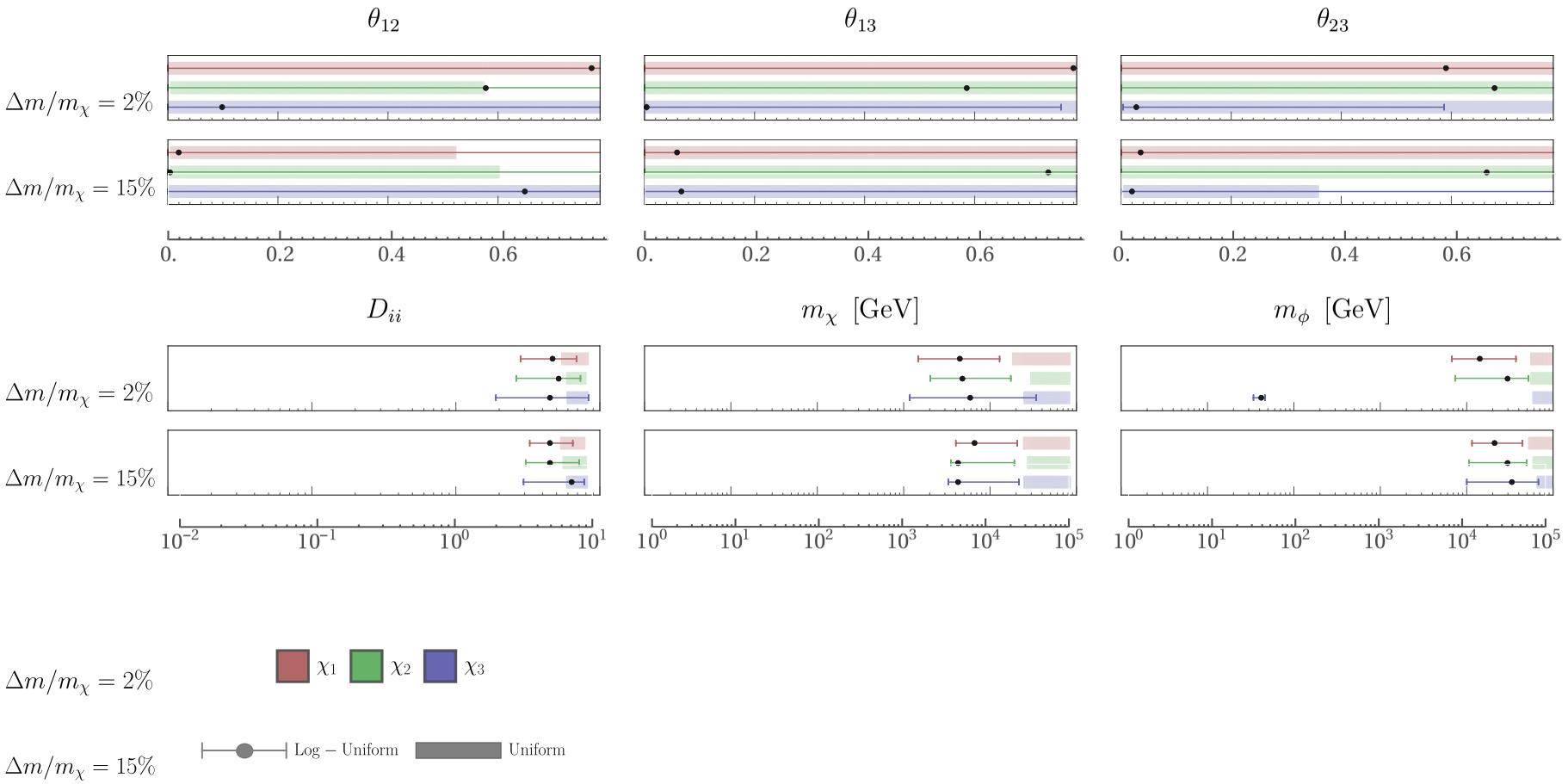

Table 7.6: The 1D 1σ credible intervals for the 6 parameters of extended scenario (1) in which the D_{ii} splitting are equal to the $\Delta m/m_\chi$. Colors denote the DM flavour (red, green and blue for up, charm and top DM respectively). The two prior choices on D_{ii} and the masses (log-uniform vs uniform) are shown as lines and shaded regions respectively, the modal average of the log-uniform prior choice is shown as a dot. The two mass splitting cases are contained in different panels.

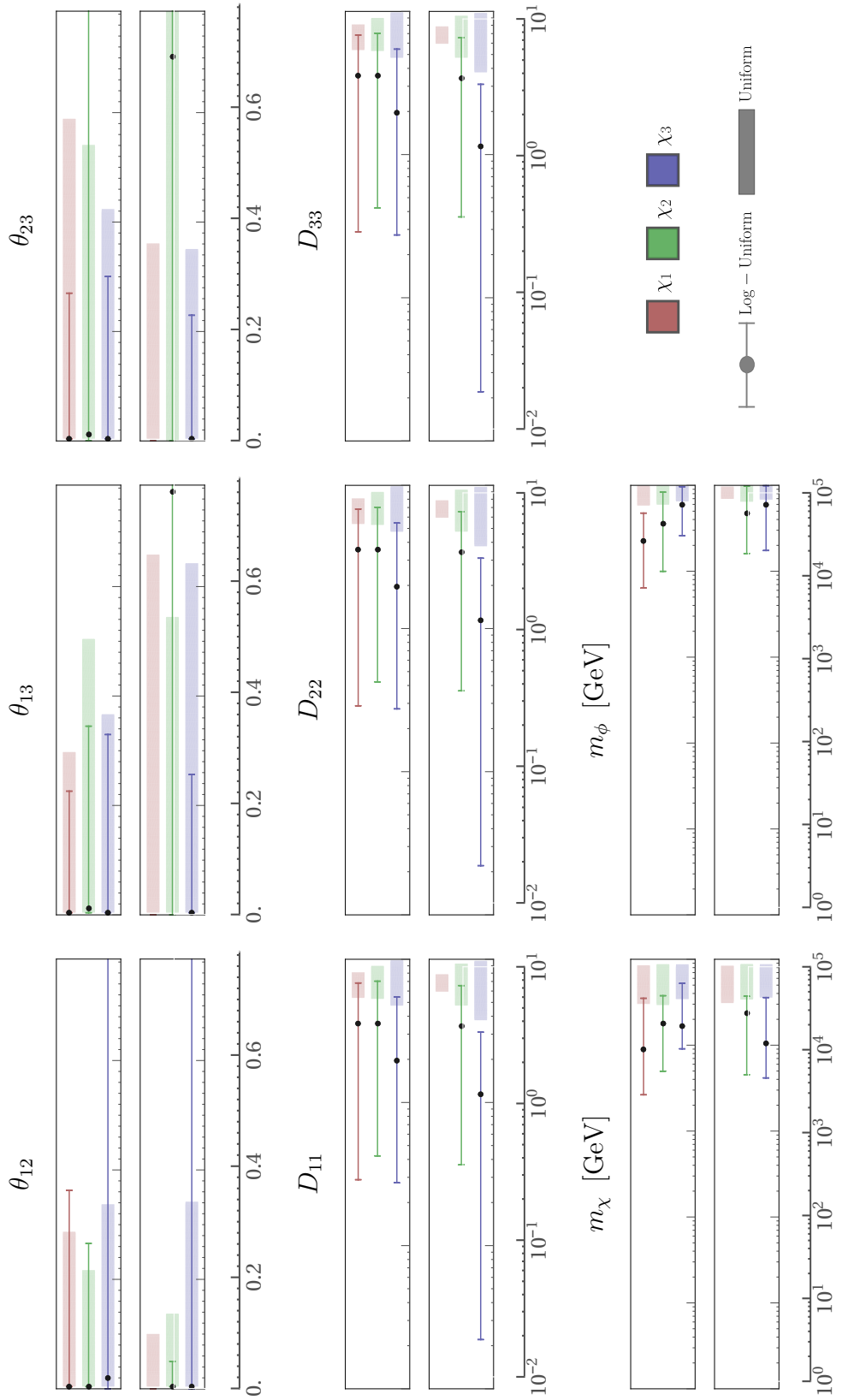

Table 7.7: The 1D 1σ credible intervals for a future scenario (2) in which the SM prediction for D^0 mixing matches the experimental value. Colors denote the DM flavour (red, green and blue for up, charm and top DM respectively). The two prior choices on D_{ii} and the masses (log-uniform vs uniform) are shown as lines and shaded regions respectively, the modal average of the log-uniform prior choice is shown as a dot. The two mass splitting cases are contained in different panels. The log-uniform results for the 15% splitting and up DM is not shown as no allowed parameter space is found.

Chapter 8

Quark-Hadron Duality Violation or : On The Ultimate Precision of Meson Mixing Observables

In this chapter we deviate slightly from constraints on dark matter, for which we have considered constraints coming from heavy flavour observables, and consider an alternative explanation for deviations seen in these observables, the idea of *quark-hadron duality violation*.

We propose a simple model of duality violation, and tightly constrain its possible size using inclusive decay widths and lifetimes for the B_s^0 and B_d^0 mesons, based on the *Heavy Quark Expansion* (HQE). We then observe that a duality violation of around 20% is sufficient to correct the discrepancy between theory and experiment for lifetimes in the D^0 system which we have encountered in Chapter 7.

8.1 What is Quark-Hadron Duality Violation?

In essence, quark-hadron duality is the statement that long-distance, hadronic, processes (necessarily those which are measured experimentally) can be accurately described by theoretical calculations involving only quarks and gluons, the short distance degrees of freedom.

To understand duality in more depth, we briefly review some of the theoretical tools which bridge the gap to theory.

Ultimately we are interested in the decay rates and lifetimes of heavy hadrons H_Q, this is calculated using the optical theorem to relate the decay width, Γ, to the $H_Q \to H_Q$ amplitude, or the *two point correlation function* of H_Q.

We consider the illustrative and simpler example of scalar fields ϕ. The two-point correlation function in position space, $\Pi(x)$, may be written (see for example [330, 374]),

$$\Pi(x) \equiv \langle \Omega | \, \mathcal{T}\{\phi(x)\phi(0)\} \, | \Omega \rangle \, , \tag{8.1.1}$$

where Ω is the fully interacting vacuum, and $\mathcal{T}$ is the usual time-ordering operator. By a complete insertion of states, including the vacuum and multiparticle states one can define the Källén-Lehmann spectral representation,

$$\langle \Omega | \, \mathcal{T}\{\phi(x)\phi(0)\} \, | \Omega \rangle = \int_0^\infty \frac{ds}{2\pi} \rho(s) D_F(x,s),$$

for the physically observable spectral function $\rho(s)$[1]. This is the experimentally measured quantity, $\rho_{\text{exp}}(s)$.

Fourier transforming the two point function to momentum space, the function $\Pi(q)$ has poles at the physical mass $q^2 = m^2$ and at any bounds states. It also contains a branch cut for $q^2 > 4m^2$. The singular structure necessitates the transformation from the Minkowski geometry to the Euclidean domain, $Q^2 = -q^2$. The evaluation of $\Pi(Q)$ at $Q \to \infty$ (the extreme Euclidean domain) is then completed using the *Wilsonian Operator Product Expansion* (OPE) which converts the non-local two-point function into a sum of local operators with singular coefficients.

[1] $\rho(s)$ is a delta function at $s = m^2$ and for any bound states $s < 4m^2$, and is nonzero above the 2 particle threshold $s > 4m^2$.

The OPE will require the trunctation of two independent series. Firstly the sum over local operators is infinite, with each successive term being further suppressed by powers of Q and must be truncated at some order. Secondly, for each local operator, one must calculate its corresponding Wilson coefficient perturbatively (i.e. using Feynman diagrams, whereby higher order terms correspond to QCD corrections) and of course the perturbative expansion must be truncated at some finite order in $\alpha_s(Q)$.

Once $\Pi(Q)$ is calculated, the truncated series is analytically continued, term-by-term, into the Minkowski domain and one may finally arrive at the spectral function $\rho_{\text{theor}}(s)$. Then quark-hadron duality is the statement that $\rho_{\text{theor}}(s) = \rho_{\text{exp}}(s)$ (up to corrections of one order higher in the truncated OPE).

Duality violation can arise from singularities which are not correctly captured by the OPE [375] in the limit $x^2 \to 0$; for example singularities in the limit $x^2 \to -\rho^2$ (or alternatively $\rho^2 \to -\infty$) manifest as $\exp(-Q\rho)$ ($\exp(-Q^2\rho^2)$) in the Euclidean domain and are therefore suppressed and neglected by the OPE, however in the Minkowski domain they oscillate as $\sin(-\sqrt{q^2}\rho)$ ($\sin(-|q^2|\rho^2)$) and are not necessarily small (unless suppressed by powers of $(q^2)^{-n}$ which happens to generally be the case).

8.1.1 Inclusive Decay Rates

The inclusive decay rate of hadron H may be written [376],

$$\Gamma(H \to X) = \frac{1}{2m_H} \sum_X \int d\Pi_X (2\pi)^4 \delta(p_H - p_X) |\langle X| \mathcal{H} |H\rangle|^2, \tag{8.1.2}$$

with phase space Π_X. To simplify this we recall the optical theorem [330],

$$-i\left[\mathcal{M}(a \to b) - \mathcal{M}^*(b \to a)\right] = \sum_X \int d\Pi_X \mathcal{M}^*(b \to X)\mathcal{M}(a \to X), \tag{8.1.3}$$

for the special case of $a = b$ (forward scattering) Eq.(8.1.2) becomes,

$$\Gamma = \frac{1}{2m_H} \langle H| T |H\rangle \ , T = \text{Im}\left(i \int d^4x \mathcal{T}\{\mathcal{H}(x)\mathcal{H}(0)\}\right), \tag{8.1.4}$$

which can now be calculated according to Sec.8.1 using the Wilsonian OPE. Thus we can see that duality violation could be manifest in the lifetimes and decay rates of heavy hadrons. To be more explicit, terms in the OPE of the form $\exp(-Q/\Lambda_{\rm QCD})$ (as we have motivated in the previous sections) are exactly zero when Taylor expanded about the small parameter $(\Lambda_{\rm QCD}/Q)$.

Naively one expects the relevant large mass scale to be $Q^2 = -q^2 \sim -m_b^2$, related to the decay of the free b quark, leading to an expansion parameter $\Lambda_{\rm QCD}/m_b$. However, upon explicit calculation one realises that in fact the correct expansion is $\Lambda_{\rm QCD}/\sqrt{m_i^2 - m_f^2}$ where m_i, m_f are the initial state and final state masses. In Fig.8.1 we give some numerical estimates of the size of duality violation in such terms, the effect can be up to 30% the size of the expansion parameter[2].

The OPE leads to a decay rate which may be written,

$$\Gamma = \Gamma^{(0)} + \left(\frac{\Lambda}{m_b}\right)\Gamma^{(1)} + \left(\frac{\Lambda}{m_b}\right)^2 \Gamma^{(2)} + \cdots , \tag{8.1.5}$$

where each $\Gamma^{(i)}$ are expanded to some order in $\alpha_s(Q)$. We will first consider the B mesons, which are mesons containing a valence b anti-quark. The neutral B^0 mesons are B_s $(\bar{b}s)$, B_d $(\bar{b}d)$, and the charged B mesons are B^+ $(\bar{b}u)$ and B_c^+ $(\bar{b}c)$.

The B mesons decay both semi-leptonically $B \to X l \nu_l$ and hadronically $B \to X_1 X_2$ where X are mesons. The hadronic B decays are primarily due to the $b \to c$ transition, those decaying via the CKM suppressed $b \to u$ transition are known as *rare decays*.

Generally speaking, nonleptonic decays lead to larger duality violations than semileptonic decays since the former tend to have larger corrections [377]. We will

[2]We use the notation $\Lambda_{\rm QCD}$ as a placeholder for some scale in the range $[0.2, 2]$ GeV, and should not be confused with the hadronization scale which is $\sim$ 200 MeV. The stated range of $\Lambda_{\rm QCD}$ comes from explicit calculation of hadronic matrix elements, which come for example from lattice calculations.

Channel	Expansion Parameter x	x	Duality Violation
$b \to c\bar{c}s$	$\frac{\Lambda}{\sqrt{m_b^2-4m_c^2}} \approx \frac{\Lambda}{m_b}\left(1+2\frac{m_c^2}{m_b^2}\right)$	0.054-0.58	$9.4 \cdot 10^{-9} - 0.18$
$b \to c\bar{u}s$	$\frac{\Lambda}{\sqrt{m_b^2-m_c^2}} \approx \frac{\Lambda}{m_b}\left(1+\frac{1}{2}\frac{m_c^2}{m_b^2}\right)$	0.045-0.49	$1.9 \cdot 10^{-10} - 0.13$
$b \to u\bar{u}s$	$\frac{\Lambda}{\sqrt{m_b^2-4m_u^2}} \approx \frac{\Lambda}{m_b}$	0.042-0.48	$4.2 \cdot 10^{-11} - 0.12$

Figure 8.1: The possible size of duality violations, $\exp(-1/x)$, for several exclusive decay modes of a B meson, we vary the masses $m_b \in [4.18, 4.78]$ GeV and $m_c \in [0.975, 1.67]$ GeV and the hadronic scale $\Lambda \in [0.2, 2.0]$ GeV. In reality Λ is determined through an explicit calculation and the range we select represents the approximate range of values across the different observables.

thus focus on the nonleptonic case, and indicate the range in size of possible duality violation in some exclusive decay channels.

8.1.2 Neutral Meson Mixing

The phenomenon of meson mixing is analogous to the mixing of neutrinos in the lepton sector. However, instead of mixing between flavours of neutrinos, the mixing occurs between neutral mesons and their anti-particles (necessarily neutral so that the particle and anti-particle possess the same quantum numbers). The weak interaction mediates the interactions between the neutral mesons.

The description of mixing can be described quantum mechanically using the Schrodinger equation for the two states,

$$i\frac{\partial}{\partial t}\begin{pmatrix} B_q^{(0)} \\ \bar{B}_q^{(0)} \end{pmatrix} = \mathcal{H}\begin{pmatrix} B_q^{(0)} \\ \bar{B}_q^{(0)} \end{pmatrix} = \begin{pmatrix} M_{11} - \frac{i}{2}\Gamma_{11} & M_{12} - \frac{i}{2}\Gamma_{12} \\ M_{21} - \frac{i}{2}\Gamma_{21} & M_{22} - \frac{i}{2}\Gamma_{22} \end{pmatrix}\begin{pmatrix} B_q^{(0)} \\ \bar{B}_q^{(0)} \end{pmatrix}, \tag{8.1.6}$$

where M_{ii}, Γ_{ii} are the masses and decay widths of the meson/anti-meson respectively (note that the meson and anti-meson have identical masses and decay widths in the flavour basis due to CPT invariance). The off diagonal terms arise from processes $b\bar{q} \to \bar{b}q$, which in the SM are box diagrams with virtual W, q. To move from the flavour basis (mesons defined in terms of valence quarks) to the mass basis we diagonalise $\mathcal{H}$. This results in a heavy and light state with masses M_H and M_L respectively.

We define the decay rate and mass differences of the heavy and light states as follows [378],

$$\Delta M = M_H - M_L, \tag{8.1.7}$$

$$\Delta\Gamma = \Gamma_H - \Gamma_L, \tag{8.1.8}$$

which can be written in terms of Γ_{12} and M_{12} as follows,

$$\begin{aligned}\Delta M &= 2|M_{12}|\left(1 - \frac{1}{8}\frac{|\Gamma_{12}|^2}{|M_{12}|^2}\sin(\theta)^2 + \cdots\right)\\ &\approx 2|M_{12}|, \end{aligned}\tag{8.1.9}$$

$$\begin{aligned}\Delta\Gamma &= 2|\Gamma_{12}|\cos\theta\left(1 + \frac{1}{8}\frac{|\Gamma_{12}|^2}{|M_{12}|^2}\sin(\theta)^2 + \cdots\right)\\ &\approx 2|\Gamma_{12}|\cos\theta, \end{aligned}\tag{8.1.10}$$

with $\theta = \arg(-M_{12}/\Gamma_{12})$. To actually calculate M_{12} and Γ_{12} requires the evaluation of loop diagrams for the process $\bar{b}q \to \bar{q}b$, M_{12} given by the real part (aka dispersive part), and Γ_{12} from the imaginary part (aka absorptive part). The primary observables of interest are,

$$\frac{\Delta\Gamma_q}{\Delta M_q} = -\mathrm{Re}\left(\frac{\Gamma_{12}^q}{M_{12}^q}\right), \tag{8.1.11}$$

$$a_{sl}^q = \mathrm{Im}\left(\frac{\Gamma_{12}^q}{M_{12}^q}\right). \tag{8.1.12}$$

The latter is called the *semileptonic asymmetry*, and is experimentally measured for the B_s system (limits can be placed for the B_d system). Additional measurements have been made for ΔM and $\Delta\Gamma$ individually for both B_s and B_d systems.

The actual calculation of Γ_{12} follows the general outline given in Sec.8.1.1, given by the imaginary part of the $B_q \to \overline{B}_q$ scattering diagram as shown in Fig.8.2, and takes the analytic form,

$$\Gamma_{12}^q = \frac{\Lambda^3}{m_b^3}\left(\Gamma_3^{q,(0)} + \frac{\alpha_s}{4\pi}\Gamma_3^{q,(1)} + \cdots\right) + \frac{\Lambda^4}{m_b^4}\left(\Gamma_4^{s,(0)} + \cdots\right) + \cdots, \tag{8.1.13}$$

the series begins at third order in the expansion parameter (Λ/m_b), since the lowest order operator in the OPE is a four quark operator (dimension 6), the next terms

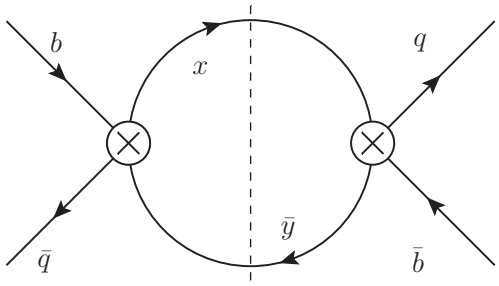

Figure 8.2: The function Γ_{12} for the B_q^0 system arises from the *imaginary* part of the one loop diagram formed from the double insertion of the effective Hamiltonian, indicated by the cutting of the internal quark lines.

in the series are thus dimension 7 and contain extra derivatives. It is sufficient to consider the lowest order, dimension 6, operators which are written as follows[3]

$$\Gamma_{12}^q = -\sum_{x=u,c}\sum_{y=u,c} \lambda_x^q \lambda_y^q \Gamma_{12}^{q,xy}, \tag{8.1.14}$$

where x, y denote the quarks that propagate inside the loop (note that the top quark is integrated out of $\mathcal{H}$ and so does not propagate in the loop), and recall that ultimately these represent the decay $\bar{b} \to qxy$.

The off-diagonal mass M_{12} is given by the same UV diagram that leads to Fig.8.2, but the real part of the loop integral. The imaginary part of the diagram, Γ_{12}, is related to on shell intermediate states (the products of the physical decay), the real part, M_{12} thus relates to the off-shell intermediate states and so the top quark can contribute. In fact, the top quark contribution dominates and we can write,

$$M_{12} = \lambda_t^2 \bar{M}_{12}^q, \tag{8.1.15}$$

for both the B_s and B_d systems. The origin of this simple result lies in the fact that the loop integral results in a dominant mass-independent term, plus a suppressed mass dependent term, the combination of all the intermediate states results in a

[3]The coupling λ denotes the appropriate CKM factors,

$$\lambda_x^q \equiv V_{xq} V_{xb}^*.$$

Observable	SM	Experiment
ΔM_s (ps^{-1})	18.3 ± 2.7	17.757 ± 0.021
$\Delta\Gamma_s$ (ps^{-1})	0.088 ± 0.020	0.082 ± 0.006
a^s_{sl}	$(2.22 \pm 0.27) \cdot 10^{-5}$	$(-750 \pm 410) \cdot 10^{-5}$
$\Delta\Gamma_s/\Delta M_s$	$48.1(1 \pm 0.173) \cdot 10^{-4}$	$46.2(1 \pm 0.073) \cdot 10^{-4}$
ΔM_d (ps^{-1})	0.528 ± 0.078	0.5055 ± 0.0020
$\Delta\Gamma_d$ (ps^{-1})	$(2.61 \pm 0.59) \cdot 10^{-3}$	$0.66(1 \pm 10) \cdot 10^{-3}$
a^d_{sl}	$(-4.7 \pm 0.6) \cdot 10^{-4}$	$(-15 \pm 17) \cdot 10^{-4}$
$\Delta\Gamma_d/\Delta M_d$	$49.4(1 \pm 0.172) \cdot 10^{-4}$	$13(1 \pm 10) \cdot 10^{-4}$

Figure 8.3: The theoretical predictions (left, [26, 27]) and experimental measurements (right, [28]), for various mixing quantities associated to the B_s and B_d systems.

strong GIM suppression of the constant term, the remaining mass dependent term increases with quark mass.

In the SM, M_{12} is calculated at NLO in α_s [379–381], with the dominant uncertainty coming from the lattice parameters. The experimental situation is as follows (see [26]). The decay width and mass differences are measured [28], however $\Delta\Gamma_d$ is poorly constrained, and thus so is $\Delta\Gamma_d/\Delta M_d$, the semileptonic asymmetries are measured but the error bar is large. The situation is summarized in Tab.8.3

8.2 Duality Violation in the B_s and B_d Systems

We have seen that the decay rate difference of neutral B mesons can be related to the decay of a b quark into light quarks $x, y = u, c$ via the quantity $\Gamma_{12}^{q,xy}$ where $q = s, d$ for the $B_{s,d}$ systems. This is where we would expect duality violation to show up and we parametrize it simply by an overall multiplicative factor.

Motivated by the expectation that duality violation should be stronger as the available phase space of the decay becomes smaller, the $x = y = c$ contribution

should produce the largest violation. It thus makes sense to introduce a duality violation which is proportional to the available phase space of the decay $b \to \bar{x}yq$;

$$\text{Model 1} \begin{cases} \Gamma_{12}^{q,cc} \to \Gamma_{12}^{q,cc}(1+4\times\delta) \\ \Gamma_{12}^{q,uc} \to \Gamma_{12}^{q,uc}(1+1\times\delta) \\ \Gamma_{12}^{q,uu} \to \Gamma_{12}^{q,uu}(1+0\times\delta) \end{cases}, \tag{8.2.16}$$

this allows us to place constraints very simply since there is only one free parameter, however we would also like to examine a more general case in which each final state has an independent duality violation

$$\text{Model 2} \begin{cases} \Gamma_{12}^{q,cc} \to \Gamma_{12}^{q,cc}(1+\delta_{cc}) \\ \Gamma_{12}^{q,uc} \to \Gamma_{12}^{q,uc}(1+\delta_{uc}) \\ \Gamma_{12}^{q,uu} \to \Gamma_{12}^{q,uu}(1+\delta_{uu}) \end{cases}, \tag{8.2.17}$$

however, we restrict these to the hierarchy $\delta_{cc} \geq \delta_{uc} \geq \delta_{uu}$ and with all the δs having the same sign.

We may now derive bounds on the δs. For Model 1 we can input the SM parameters and derive the following numerical values for the two mixing observables of Eq.(8.1.12) (Tab.8.4), For model 1 the values are shown in Tab.8.4 as a function

Observable	B_s^0	B_d^0
$\Delta\Gamma_q/\Delta M_q$	$48.1(1+3.95\delta)\cdot 10^{-4}$	$49.5(1+3.76\delta)\cdot 10^{-4}$
$\Delta\Gamma_q$ (ps^{-1})	$88.0(1+3.95\delta)\cdot 10^{-3}$	$2.61(1+3.76\delta)\cdot 10^{-3}$
a_{sl}^q	$2.225(1-22.3\delta)\cdot 10^{-3}$	$-4.74(1-24.5\delta)\cdot 10^{-4}$

Figure 8.4: Theoretical mixing observables for the B_q systems for Model 1 of duality violation. Note that $\Delta\Gamma_q$ is found from the first column multiplied by the ΔM_q of the SM given in Tab.8.3.

of δ, for model 2 the values are,

$$\frac{\Delta\Gamma_s}{\Delta M_s} = 48.1\,(1+0.982\delta_{cc}+0.0187\delta_{uc}-0.000326\delta_{uu})\cdot 10^{-4}, \tag{8.2.18}$$

$$\Delta\Gamma_d = 26.1\,(1+0.852\delta_{cc}+0.350\delta_{uc}-0.202\delta_{uu})\cdot 10^{-4}\ \text{ps}^{-1}, \tag{8.2.19}$$

$$a_{sl}^s = 2.225\,(1-7.75\delta_{cc}+8.67\delta_{uc}+0.0780\delta_{uu})\cdot 10^{-5}, \tag{8.2.20}$$

$$a_{sl}^d = -4.74\,(1-8.52\delta_{cc}+9.60\delta_{uc}-0.0787\delta_{uu})\cdot 10^{-4}. \tag{8.2.21}$$

Using the values of the experimental $\Delta\Gamma_s/\Delta M_s$ from Tab.8.3 we derive a 2σ limit on δ for the B_s meson,

$$\delta \in [-0.06, 0.04]\,. \tag{8.2.22}$$

Therefore the largest duality violation allowed is $-23.3\%, +15.2\%$ in the cc channel. Given this level of violation, we allow values of the semileptonic asymmetry in the range,

$$a^s_{sl} \in [0.34, 5.12] \cdot 10^{-5}, \tag{8.2.23}$$

which is within 2σ of the experimental result. Given the large experimental error it is not completely unreasonable to imagine that an experimental and theoretical agreement of a^s_{sl} could be reached at the same level as for $\Delta\Gamma_s/\Delta M_s$ (i.e. 22%), this would push the limits on δ to the sub percent level.

In the B_d system it is unwise to carry out the same procedure since $\Delta\Gamma_d$ is not experimentally measured, just bounded, and the constraints on δ would be extremely weak. Instead when examining the numerical values of $\Gamma_{12}^{(s,d),xy}$ we find that they are very similar. The hadronic decays of B_s and B_d mesons do not have large phase space differences when compared to the phase space differences caused by different x, y. Thus the duality violation derived from the B_s system should approximate well to the B_d system. This being the case, we derive the range of values for the B_d system from Eq.(8.2.22),

$$a^d_{sl} \in [-11.5, -0.326] \cdot 10^{-4}, \tag{8.2.24}$$

$$\Delta\Gamma_d \in [2.04, 2.98] \cdot 10^{-3}. \tag{8.2.25}$$

The semileptonic asymmetry and $\Delta\Gamma_d$ are both within the large experimental bounds, however if the experimental uncertainty decreases and the central value lies outside the range of Eq.(8.2.25), this could be an indication of new physics effects.

Now moving to Model 2, it is clear from Eq.(8.2.21) that the mixing observables we are considering are insensitive to the uu channel, and we can ignore its contribution. However for $\Delta\Gamma_d$ the uu contribution can be more significant, but we have

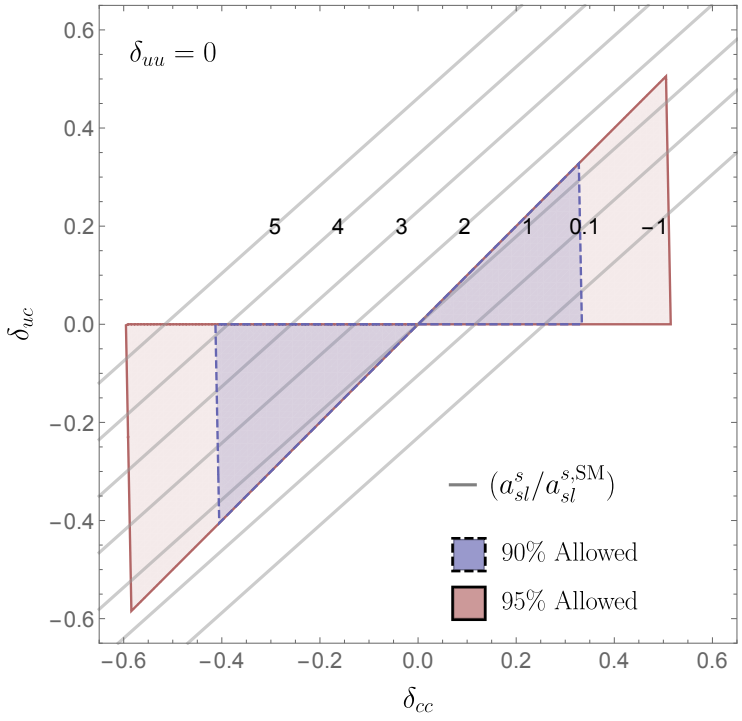

Figure 8.5: The 90% and 95% confidence limits (shaded blue and red respectively) on $\delta_{cc} - \delta_{uc}$ for duality violation Model 2, for the B_s system showing the allowed region stemming from the experimental measurement of $(\Delta\Gamma_s/\Delta M_s)$. The modification factors $a^s_{sl}/a^{s,\mathrm{SM}}_{sl}$ are shown as straight grey lines.

checked that it affects the bounds by no more than 20%.

In Fig.8.5 we show the allowed regions of duality violation in the $\delta_{cc} - \delta_{uc}$ plane. Duality violations are limited to at most $\sim 60\%$ in the cc and uc channels, and even though the semileptonic asymmetry can deviate significantly from its current theoretical level (up to a factor of ~ 5.5) this is not enough to confront the poorly constrained experimental measurement.

Given the forms of a^s_{sl} and a^d_{sl} in Eq.(8.2.21), the maximum (minimum) values occur for $\delta_{uc} = 0$ and $\delta_{cc} < 0$ ($\delta_{uc} > 0$) and these lead to bounds on the observables,

$$a^s_{sl} \in [-2.48, 8.32] \cdot 10^{-5}, \tag{8.2.26}$$

$$a^d_{sl} \in [-19.0, 6.28] \cdot 10^{-4}, \tag{8.2.27}$$

$$\Delta\Gamma_d \in [1.52, 3.45] \cdot 10^{-3}\ \mathrm{ps}^{-1}, \tag{8.2.28}$$

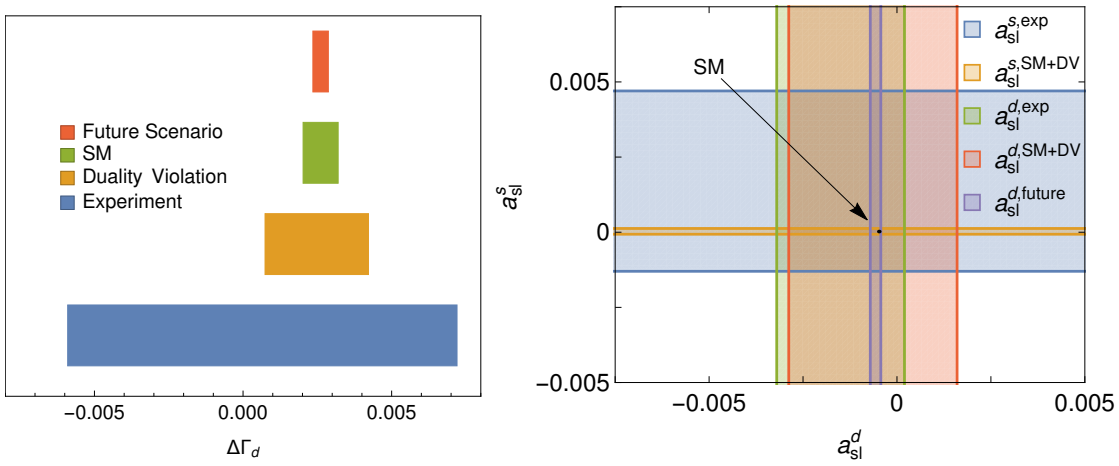

Figure 8.6: Left : comparison in the size of $\Delta\Gamma_d$ experimental limits (blue) which allows for sizeable contributions on top of the SM result (green). The inclusion of a duality violation *that does not also show up in the B_s system* (yellow) does not exceed the experimental limit, unless the experimental error shrinks in the future (orange). Right : the SM value of $a_{sl}^{(s,d)}$ are well known (black dot), but their experimental values less so (green and blue), with duality violation (red) there are bounds on a_{sl}^d, which can become important if in future the experimental error shrinks (purple).

the range of $\Delta\Gamma_d$ is well within the uncertainties of the experimental result, it would take a significant improvement to begin to draw conclusions on duality violations so we turn instead to the semileptonic asymmetries and depict the situation graphically in Fig.8.6 for clarity.

Up to now, we have based our constraints entirely on the measurement of $\Delta\Gamma_s$ in the B_s system, and compared the resulting bounds to analogous observables for B_d, finding bounds from $\Delta\Gamma_d$ only if the experimental uncertainty shrinks, the same conclusion applies to a_{sl}^d. The question arises as to whether there are other data which can be used to tighten these constraints, and we begin with the well measured value of the *lifetime ratio*.

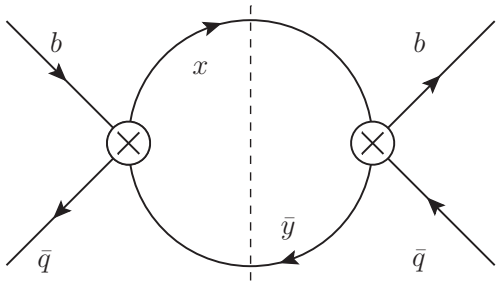

Figure 8.7: The diagram leading to the calculation of the lifetime (Γ_B^{-1}) for the B_q^0 system arises from the *imaginary* part of the one loop diagram formed from the double insertion of the effective Hamiltonian, indicated by the cutting of the internal quark lines.

8.3 Duality Violation in Lifetime Ratios

The decay width (inverse lifetime $\Gamma = 1/\tau$) of a B_q^0 meson may be found using the HQE following Eq.(8.1.4) with the effective Hamiltonian given by [4],

$$\mathcal{L}_{\text{eff}} = \frac{G_F}{\sqrt{2}}\left(\sum_{q=u,c} V_{cq}(C_1 Q_1 + C_2 Q_2) - V_p \sum_{j=3}^{6} C_j Q_j\right),$$

$$Q_2 = (\bar{c}_i b_i)_{V-A}(\bar{d}_j u_j)_{V-A}, \tag{8.3.29}$$

$$Q_1 = (\bar{c}_i b_j)_{V-A}(\bar{d}_j u_i)_{V-A}\ , \tag{8.3.30}$$

where Q_2 appears at tree level from integrating out the W-exchange diagrams, and Q_1 arises from first-order QCD corrections to Q_2 (one loop diagrams with gluon exchange between the quark legs). The rest of the operators Q_{3-6} arise from penguin contributions.

Performing the Wilsonian OPE on Eq.(8.1.4) with a double insertion of Eq.(8.3.29) between external meson states $b\bar{q}$ (shown in Fig.8.7) results in an expansion in inverse powers of the heavy quark scale m_b, which multiply hadronic matrix elements of operators with successively higher dimensions and which scale roughly as Λ_{QCD}^n. The resulting width may be written as [376],

$$\Gamma = \frac{G_F^2 m_b^5}{192\pi^3}|V_{cb}|^2\left[c_3\frac{\langle B|\,\bar{b}b\,|B\rangle}{2m_B} + \frac{c_5}{m_b^2}\frac{\langle B|\,\bar{b}g_s\sigma_{\mu\nu}G^{\mu\nu}b\,|B\rangle}{2m_B} + \sum_{\Gamma}\frac{c_6^q}{m_b^3}\frac{\langle B|\,(\bar{b}q)_\Gamma(q\bar{b})_\Gamma\,|B\rangle}{m_B}\right], \tag{8.3.31}$$

[4] The V-A (S-P) notation refers to the $\gamma^\mu(1-\gamma^5)$ ($(1-\gamma^5)$) structure in the fermion bilinear.

this series is truncated at dimension 6, which generates four-fermion effective operators of the form,

$$Q^q = (\bar{b}q)_{V-A}(\bar{q}b)_{V-A}, \tag{8.3.32}$$

$$Q_S^q = (\bar{b}q)_{S-P}(\bar{q}b)_{S-P}, \tag{8.3.33}$$

$$T^q = (\bar{b}t^a q)_{V-A}(\bar{q}t^a b)_{V-A}, \tag{8.3.34}$$

$$T_S^q = (\bar{b}t^a q)_{S-P}(\bar{q}t^a b)_{S-P}. \tag{8.3.35}$$

The origin of the various terms in Eq.(8.3.31) is as follows; c_3 arises from the double insertion of the four-fermion effective operator, contracted to leave the spectator quark free. The second term c_5 is gluon condensate term, the same diagram as c_3 but with a gluon emitted from an internal line (and coupled to the vacuum). Lastly the dim-6 c_6 contribution arises from a one-loop diagram in which the spectator quark couples to the EFT insertions.

The state of the art for this prediction is NLO for c_3 [382, 383] (for LO see [384]), LO only for c_5 [384], NLO for several of the c_6^q ($q = u, d, s$) [385]. We use the NLO (LO) values $c_3 = 6.88$ (5.29) [376, 386], and the LO value $c_5 = -7.9$.

The non-perturbative matrix elements can be defined as [5],

$$\langle B|\,\bar{b}b\,|B\rangle = 1 - \frac{\mu_\pi^2 - \mu_G^2}{2m_b^2}\ , \tag{8.3.36}$$

$$\langle B|\,\bar{b}g_s\sigma_{\mu\nu}G^{\mu\nu}b\,|B\rangle = \mu_G^2\ , \tag{8.3.37}$$

$$\langle B|\,(\bar{b}q)_\Gamma(q\bar{b})_\Gamma\,|B\rangle = c_\Gamma f_B^2 m_B B_\Gamma\ , \tag{8.3.38}$$

the latter relation covers the various four-fermion structures which appear, and in Eq.(8.3.31) these are absorbed into the definition of the new coefficient $\tilde{c}_6$,

$$\begin{aligned}\tilde{c}_6 =& |V_{ud}|^2\left(F^u B_1 + F_S^u B_2 + G^u\epsilon_1 + G_S^u\epsilon_2\right)\\ &+ |V_{cd}|^2\left(F^c B_1 + F_S^c B_2 + G^c\epsilon_1 + G_S^c\epsilon_2\right).\end{aligned} \tag{8.3.39}$$

[5] These expressions are derived using *Heavy Quark Effective Theory* and are subject to m_b^{-1} corrections.

For explicit expressions for the Fs and Gs see [376].

Inserting the hadronic matrix element definitions Eq.(8.3.38) we may write the decay width as,

$$\Gamma(B_d) = \frac{G_F^2 m_b^5}{192\pi^3}|V_{cb}|^2\left[c_3\left(1-\frac{\mu_\pi^2}{2m_b^2}\right)+c_G\frac{\mu_G^2}{2m_b^2}+\frac{16\pi^2 f_B^2 M_{B_d}}{m_b^3}c_6\right], \tag{8.3.40}$$

the rate is dominated by the $b\to c$ transition, and hence is proportional to V_{cb}^2 (the $b\to u$ transition has instead $V_{ub}\sim 0.4\lambda V_{cb}$, with $\lambda\sim 0.2$).

The difference in decay rates between the B_s^0 and B_d^0 mesons is mildly affected by the dim-3 and dim-5 operators since μ_π and μ_G differ by at most 10% between the two mesons, it is far more strongly affected by the dim-6 operators in which differences arise from CKM elements, the bag parameters and the meson mass.

The lifetime ratio may then be written as,

$$\begin{aligned}\frac{\tau(B_s)}{\tau(B_d)} = 1+\frac{\Gamma_s-\Gamma_d}{\Gamma_s} &= 1+\frac{\mu_\pi^2(B_d)-\mu_\pi^2(B_s)}{2m_b^2}+\frac{c_G}{c_3}\frac{\mu_G^2(B_s)-\mu_G^2(B_d)}{2m_b^2}\\ &+\frac{c_6(B_d)}{c_3}\frac{\langle B_d|\,Q\,|B_d\rangle}{m_b^3 M_B}-\frac{c_6(B_s)}{c_3}\frac{\langle B_s|\,Q\,|B_s\rangle}{m_b^3 M_B}.\end{aligned} \tag{8.3.41}$$

One useful aspect of considering the lifetime ratios as shown above is that several sources of large uncertainty cancel, such as the bag parameters f_B, and only the differences in μ_π^2 and μ_G^2 are needed (and which are small).

This lifetime ratio is found experimentally by HFAG [28] (globally averaged over all measurments) and this can be compared to the numerical value of Eq.(8.3.41) above,

$$\left(\tau(B_s^0)/\tau(B_d^0)\right)_{\text{exp.}} = 0.990\pm 0.004\ , \tag{8.3.42}$$

$$\left(\tau(B_s^0)/\tau(B_d^0)\right)_{\text{theor.}} = 1.0005\pm 0.0011\ , \tag{8.3.43}$$

and thus theory and experiment are discrepant by around $\sim 3\sigma$. We now investigate how much duality violation is required to bring the theory into agreement with

experiment.

Our model of duality violation is based essentially on phase space arguments, such that the phase space of the $c\bar{c}$ intermediate state is larger than the $u\bar{c}$ which is larger than the $u\bar{u}$, and Fig.8.7 makes clear that these arguments should apply equally well to the lifetimes as for Γ_{12}, and the substitutions given in Eq.(8.2.16) and (8.2.17) can be easily implemented given the form of Eq.(8.3.39).

By explicit calculation of the lifetimes of the B_s and B_d mesons it can be shown that the latter is dominated by the $u\bar{c}$ intermediate state, and the former by the $c\bar{c}$. This useful result contradicts the naive expectation that the duality violating effects would roughly cancel in the lifetime ratio.

The theoretical prediction for the lifetime ratios in model 1 and model 2 are,

$$\left(\frac{\tau(B_s^0)}{\tau(B_d^0)}\right)_{\text{Model 1}} = 1 + 0.0005\,(1 - 45.0\delta)\,, \tag{8.3.44}$$

$$\left(\frac{\tau(B_s^0)}{\tau(B_d^0)}\right)_{\text{Model 2}} = 1 + 0.0005\,(1 - 13.4\delta_{cc} + 8.92\delta_{uc})\ . \tag{8.3.45}$$

The experimental measurement (Eq.(8.3.43)) leads to bounds on Model 1,

$$\delta \in [0.13, 0.80]\ , \tag{8.3.46}$$

the fact that this range of values does not allow for zero duality violation is a result of the disagreement between experiment and theory of around 2.5σ. These large allowed values of δ are well outside the range found for $\Delta\Gamma_s$ and would leave theory and experiment discrepant in the B_s sector.

Thus it seems that the discrepancy for the lifetimes ratios cannot be reconciled by duality violation. However, we consider two possible future scenarios;

1. **Scenario 1** : The central value of the experimental measurement does not change, but the error is reduced to 0.001,

$$\left(\frac{\tau(B_s^0)}{\tau(B_d^0)}\right)_{\text{Scen.I}} = 0.990 \pm 0.001\ , \tag{8.3.47}$$

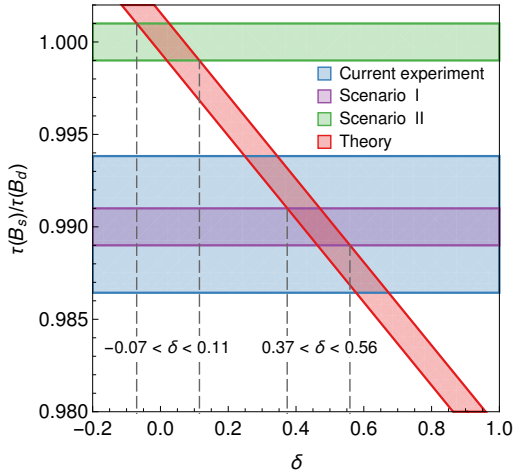

Figure 8.8: Bounds on the duality violating parameter δ, the lifetime ratio of the B_s, B_d mesons varies with δ (red band). The current experimental error band (blue) is compared with two future scenarios outlined in the text in which the error band shrinks (purple), or the central value shifts towards 1 and the error shrinks (green).

then the allowed range of δ shrinks to $\delta \in [0.34, 0.60]$, then duality violation is unable to explain the discrepancy in the lifetime ratios without also creating one in the B_s mixing measurements. We would conclude that some new physics affect is responsible.

2. **Scenario 2** : The central experimental value matches the theoretical one, and the error is simultaneously reduced to 0.001,

$$\left(\frac{\tau(B_s^0)}{\tau(B_d^0)}\right)_{\text{Scen.II}} = 1.000 \pm 0.001 \ , \tag{8.3.48}$$

the range of allowed duality violation now includes zero since there is no requirement to explain a discrepancy $\delta \in [-0.11, 0.15]$. However the bounds on δ are still weaker than found for mixing observables.

These various scenarios are depicted in Fig.8.8. If the experimental errors shrink, then the potential of duality violation to reconcile theory and experiment becomes weaker. If however the measure lifetime ratio shifts towards 1, then duality violation is not required, but the bounds on it are consistent with those found in the B_s system.

Similar conclusions to those above may be drawn for Model 2, since the bounds become even weaker. This is because there is a mild cancellation which occurs

between the $\bar{u}c$ and $\bar{c}c$ intermediate states in the lifetime ratio, this cancellation is less pronounced in Model 1 since the $\bar{c}c$ channel gains a factor of 4 compared with $\bar{u}c$.

There are many parameters which enter into the calculation of the lifetime ratios, not all of them known precisely. To enable our numerical results to be reproduced, and to catalogue the presently known precision of the various hadronic parameters we list the central values, their errors, and their individual contribution to the total error on $\tau(B_s^0)/\tau(B_d^0)$ in Tab.8.1, which appears at the end of the section for clarity.

8.4 Duality Violation in the D^0 System

We have so far focussed on the heavy B^0 meson mixing, however mixing in the D^0 ($\bar{u}c$) sector is presently (as of 2014) measured with a reasonable precision [28],

$$x \equiv (\Delta M/\Gamma) = (0.37 \pm 0.16) \cdot 10^{-2}, \tag{8.4.49}$$

$$y \equiv (\Delta\Gamma/2\Gamma) = (0.66\ ^{+0.07}_{-0.10}) \cdot 10^{-2}, \tag{8.4.50}$$

since experimentally $(\Gamma)^{-1} = \tau(D^0) = 0.4101 \pm 0.0015$ ps (see [246] p.44) we can use the definitions in Eq.(8.4.50) above to give,

$$\Delta M_D = \frac{x}{\tau(D^0)} = 0.00902\ \text{ps}^{-1}, \tag{8.4.51}$$

$$\Delta\Gamma_D = 2\frac{y}{\tau(D^0)} = 0.0322\ \text{ps}^{-1}, \tag{8.4.52}$$

thus the experimental side is well understood and the errors are under control. We now turn to the theory side, as in Sec.8.1.2 we may use the HQE but now for a heavy charm quark rather than heavy bottom quark. As it turns out, this approach produces a prediction for x, y which are orders of magnitude below the experimental measurements ($\Delta M_D \approx (1.4 - 5.3) \cdot 10^{-5}$ ps^{-1} [387], $\Delta\Gamma_D/\Gamma_D \leq$ few $\times\ 0.01$ [388]). There are several possible reasons for this;

(1) Perhaps the HQE breaks down for the charm system, despite its success in the B system. Going to higher orders might then alleviate the issues, since the expansion in m_c^{-n} gives less suppression compared to m_b^{-n}, and it is possible that

the GIM cancellation which is responsible for the smallness of the first order terms in the expansion is lifted in higher orders. To rule this out would require the calculation of the higher order terms. To counter this point one may look at the lifetime ratios of D mesons, and find that for example $\tau(D^+)/\tau(D^0)$ at NLO QCD there is agreement between theory and experiment [343].

(2) A second possibility is that new physics effects dominate the SM contribution, and bounds on potential models can be found in [389].

(3) The third and most relevant possibility is that no new physics is necessary, and the discrepancy is entirely due to a large duality-violating effect. The HQE is a quark level calculation representing the short distance contribution to the mixing observables, however it is possible to calculate x, y using an exclusive (hadron level, and thus long distance) approach [339, 340]. This method reproduces x, y well and thus adds weight to either (2) or (3) as a solution to the problem.

We will thus investigate whether duality violating effects can be responsible for matching theory to experiment within the framework we have established. To do this we must find both Γ_{12} and M_{12} for the D^0 system, the latter is presently not calculated and a calculation of it is beyond our scope. We have access only to Γ_{12} and make use of the theoretical lower bound [3],

$$|\Gamma_{12}| > \frac{1}{2}\Delta\Gamma_D \ , \tag{8.4.53}$$

and then the value of $|\Gamma_{12}|$ which reproduces the experimental data is a conservative lower bound. It can be written as [390],

$$\Gamma_{12} = \lambda_s^2\Gamma_{12}^{ss} + \lambda_s\lambda_d\Gamma_{12}^{sd} + \lambda_d^2\Gamma_{12}^{dd} \ , \tag{8.4.54}$$

where down-type quarks propagate in the loop of the diagram in Fig.8.2 (the heavy internal b-quark does not contribute to the imaginary part of the loop integral). In the above $\lambda_x \equiv V_{cx}V_{ux}^*$. We can eliminate λ_d using CKM unitarity;

$$\lambda_s + \lambda_d + \lambda_b = 0 \ , \tag{8.4.55}$$

this is done so that Γ_{12} displays a hierarchy of CKM factors

$$\Gamma_{12} = \lambda_s^2(\Gamma_{12}^{ss} - 2\Gamma_{12}^{sd} + \Gamma_{12}^{dd}) + 2\lambda_s\lambda_b(\Gamma_{12}^{sd} - \Gamma_{12}^{dd}) - \lambda_b^2\Gamma_{12}^{dd} \ , \tag{8.4.56}$$

which is best shown by the numerical values of the CKM factors;

$$\lambda_s^2 = 4.81733 \cdot 10^{-2} - 3.00433 \cdot 10^{-6} i, \tag{8.4.57}$$

$$2\lambda_s\lambda_b = 2.49872 \cdot 10^{-5} + 5.90908 \cdot 10^{-5} i, \tag{8.4.58}$$

$$\lambda_b^2 = -1.48814 \cdot 10^{-8} + 1.53241 \cdot 10^{-8} i \ . \tag{8.4.59}$$

The result for $\Gamma_{12}^{x,y}$ will include a mass independent contribution, and a piece depending on the ratio $z \equiv (m_s/m_c)^2$ (m_d is assumed to be zero, and the masses $m_x \equiv \overline{m}_x(\overline{m}_x)$ are the $\overline{\text{MS}}$ scheme masses, evaluated at the relevant mass scale). Numerically,

$$\Gamma_{12}^{ss} = 1.8696 - 5.5231z - 13.8143z^2 + \cdots \mathcal{O}(z^3) \ , \tag{8.4.60}$$

$$\Gamma_{12}^{sd} = 1.8696 - 2.7616z - 7.4906z^2 + \cdots \mathcal{O}(z^3) \ , \tag{8.4.61}$$

$$\Gamma_{12}^{dd} = 1.8696 + \cdots \mathcal{O}(z^3) \ , \tag{8.4.62}$$

this result may be found in [390], and includes the dimension 6 and 7, $\Delta C = 1, 2$, operators, with NLO QCD corrections (accounting for a $\sim 26\%$ correction to the LO result). The result is written in a way which clearly shows the GIM mechanism at work. Recalling the simple duality violation models we employ, we will also clearly see how the duality violation lifts the GIM suppression.

For duality violations of Model 1 (identical to Eq.(8.2.16) but for $c \to s$ and $u \to d$) Eq.(8.4.52) becomes,

$$\Delta\Gamma_D = 2\sqrt{1.26523 \cdot 10^{-11} + 1.10168 \cdot 10^{-6}\delta + 0.0297794\delta^2} \ . \tag{8.4.63}$$

For this to match the central experimental value requires a duality violation as low as $\delta = +9.3\%$. As we have seen in the B_s system, if this level of violation were present for $\bar{c}c$ internal quarks it would be excluded, producing an over-estimate of $(\Delta\Gamma_s/\Delta M_s)$.

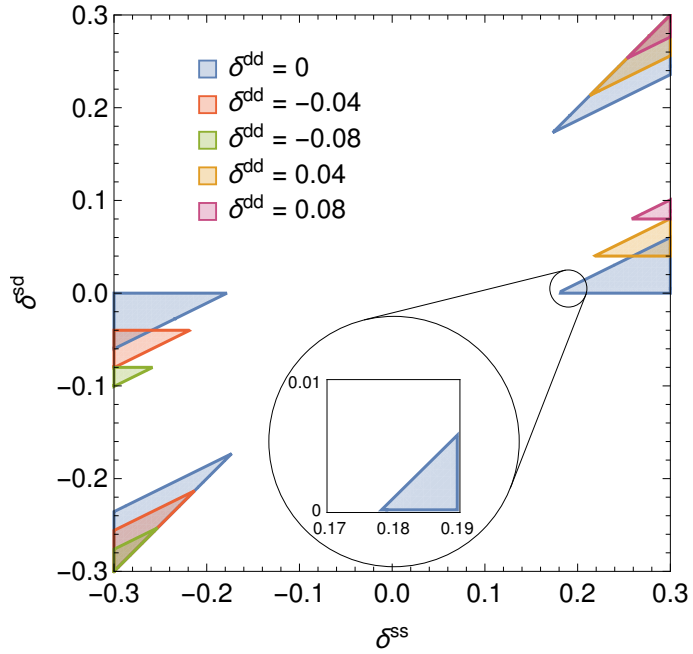

Figure 8.9: The 95% confidence limits on the duality violating parameters δ_{ss}, δ_{sd} for fixed values of δ_{dd} arising from the comparison of $\Delta\Gamma_D$ between theory and experiment for the D^0 system.

For Model 2 (again identical to Eq.(8.2.17) but for $c \to s$ and $u \to d$) Eq.(8.4.52) is used to identify the values of δ_{ss}, δ_{sd} which reproduce the experimental value, with values of $\delta_{dd} = 0, \pm 0.04, \pm 0.08$, and the result is shown in Fig.8.9. Due to cancellations which can occur for specific values of the δs, we can make δ_{ss}, δ_{sd} arbitrarily large, but the minimum possible values are $\delta_{ss} > 0.18$, $\delta_{sd} = 0$. It is interesting to find that such a moderate duality violation of $\sim 20\%$ can produce an agreement between experiment and the inclusive theory calculation.

8.5 Summary and Conclusions

In this work we have explored the possibility of duality violations in heavy meson decays. The study of such effects has a long tradition in flavour physics. Since the direct measurement of $\Delta\Gamma_s$ in 2012 by the LHCb collaboration huge duality violating effects have been excluded by experiment. But there is still space for duality violating effects of the order of 20%. Because of the constantly improving experimental precision in flavour physics it is crucial to consider corrections of the order

of 20% and to investigate whether, and how, such a bound can be improved.

To do so, we introduced a simple parameterisation of duality violating effects, see Eq.(8.2.16),(8.2.17) that relies solely on phase space arguments: the smaller the remaining phase space is in a heavy hadron decay, the larger duality violations might be. In such a model, decay rate differences, $\Delta\Gamma_q$, depend moderately on the duality violating parameter, δ, whereas semi-leptonic asymmetries, a_{sl}, have a strong δ dependence, see Eq.(8.1.12). Currently we get the strongest bound on δ from,

$$\frac{\left(\frac{\Delta\Gamma_s}{\Delta M_s}\right)^{\text{Exp}}}{\left(\frac{\Delta\Gamma_s}{\Delta M_s}\right)^{\text{SM}}} = 0.96 \pm 0.19, \;\; |\delta| \lesssim 0.1 \; . \tag{8.5.64}$$

If the semi-leptonic asymmetries were to agree with a similar precision between experiment and theory then the bound on δ would go down to $|\delta| \lesssim 0.009$. Unfortunately, the semi-leptonic asymmetries have not been observed yet, and we only have experimental limits. The same is true for the decay rate difference $\Delta\Gamma_d$. Thus we use our bounds on δ from $\Delta\Gamma_s$ to determine the maximal possible size of a_{sl}^q and $\Delta\Gamma_d$, if duality is violated. These regions are compared with current experimental ranges in Fig.8.6. Any measurement outside the region allowed by duality violation is a clear signal for new physics. We also show a future scenario in which the duality violation is further constrained by more precise values of $\Delta\Gamma_s$ both in experiment and theory.

Duality violations would also affect the still unsolved problem of the dimuon asymmetry measured by the D0 collaboration, since it depends on a_{sl}^d, a_{sl}^s and $\Delta\Gamma_d$. We found, however, that an agreement between experiment and theory for the dimuon asymmetry would require values of δ in the region of -0.4 to -1.9, which is considerably outside the allowed region found above. Taking only allowed values of δ we find that the theory prediction including duality violation is still an order of magnitude smaller than experiment. Hence duality violation cannot explain the value of the dimuon asymmetry. We have shown that the duality violating parameter δ will also affect the lifetime ratio $\tau(B_s^0)/\tau(B_d^0)$ where we currently have a

deviation of about 2.5 standard deviations between experiment and theory. Looking at the historical development of this ratio depicted in Fig.1 one might be tempted to assume a statistical fluctuation.

Taking the current deviation seriously, it is either a hint for new physics or for a sizeable duality violations of the order of $\delta \sim 0.5$, which is inconsistent with our bounds on δ derived from $\Delta\Gamma_s$. Here a future reduction of the experimental error of $\tau(B_s^0)/\tau(B_d^0)$ will give us valuable insight. We have studied two future scenarios in Fig.8.8, which would either point towards new physics and duality violations or stronger bounds on duality violation. It is very important to note here that the theory prediction has a very strong dependence on almost unknown lattice parameters. In particular, we can see from our error budget for the lifetime ratio in Fig.8.1 that any new calculation of the bag parameters 1,2 would bring large improvements in the theory prediction for $\tau(B_s^0)/\tau(B_d^0)$.

We finally focus on the charm-system, where a naive application of the HQE gives results that are several orders of magnitude below the experimental values. We found the unexpected result that duality violating effects as low as 20% could solve this discrepancy. Such a result might have profound consequences on the applicability of the HQE. As a decisive test we suggest a lattice calculation of the matrix elements arising in the ratio of charm lifetimes. This ratio is free of any GIM cancellation, which are very severe in mixing.

x_i	$\langle x_i \rangle$	$\delta(x_i)$	$\partial\tau/\partial x_i$	Error Budget
$\bar{m}_b(\bar{m}_b)$ [GeV]	4.248	0.05	$+8.08 \times 10^{-4}$	4.00×10^{-5}
$\bar{m}_c(\bar{m}_b)$ [GeV]	0.997	0.01989	$+3.68 \times 10^{-4}$	7.26×10^{-6}
M_{B_d} [GeV]	5.27955	0.00026	$+9.63 \times 10^{-4}$	2.53×10^{-7}
M_{B_s} [GeV]	5.3667	0.0004	-1.36×10^{-3}	5.51×10^{-7}
f_{B_d}	0.1905	0.0042	$+5.36 \times 10^{-2}$	2.26×10^{-4}
f_{B_s}	0.2277	0.0045	-6.46×10^{-2}	2.92×10^{-4}
$\lvert V_{ub}\rvert/\lvert V_{cb}\rvert$	0.0862278	0.00442474	-2.28×10^{-6}	1.02×10^{-8}
$\lvert V_{cb}\rvert$	0.04117	0.00114	$+2.49 \times 10^{-2}$	2.56×10^{-5}
δ_{CKM}	1.17077	0.0378736	-7.33×10^{-7}	2.03×10^{-8}
$\lvert V_{us}\rvert$	0.22548	0.00034	-5.40×10^{-5}	2.76×10^{-8}
B_1	1.1	0.2	$+6.98 \times 10^{-4}$	1.41×10^{-4}
B_2	0.79	0.1	-9.95×10^{-4}	1.01×10^{-4}
ϵ_1	-0.02	0.02	$+3.53 \times 10^{-2}$	7.13×10^{-4}
ϵ_2	0.03	0.01	-5.03×10^{-2}	5.08×10^{-4}
$\mu_\pi^2(B_s) - \mu_\pi^2(B_d)$	0.09	0.01	$+2.31 \times 10^{-2}$	2.34×10^{-4}
$\mu_G^2(B_s)/\mu_G^2(B_d)$	1.07	0.03	$+9.29 \times 10^{-3}$	2.81×10^{-4}
$\mu_G^2(B_d)$	0.35	0.07	$+1.86 \times 10^{-3}$	1.31×10^{-4}
c_3 (NLO)	6.88	0.74	3.02×10^{-4}	2.26×10^{-4}
c_G	-7.9	0.814	-8.23×10^{-5}	6.77×10^{-5}
τ_{B_s} [ps]	1.505×10^{-12}	0.004×10^{-12}	2.18×10^{-16}	1.34×10^{-6}
μ	4.248	$^{+2.124}_{-8.496}$	5.13×10^{-5}	1.77×10^{-4}
G_F [GeV^{-2}]	1.166378×10^{-5}	-	-	-
$\alpha_s(m_Z)$	0.1185	-	-	-
$C_1(m_b)$	-0.240787	-	-	-
$C_2(m_b)$	1.10333	-	-	-
m_W [GeV]	80.385	-	-	-

Table 8.1: Values and errors for the various physical parameters used throughout this chapter. The source for these values can be found in the text. We also give the relative contribution of each parameter to the total error on the lifetime ratio $\tau(B_s)/\tau(B_d)$ to compliment the discussion in the text.

Appendices

Appendix A

Background Material

A.1 Furry's Theorem

Throughout this thesis, Furry's theorem is frequently invoked when working with loop diagrams containing external vector particles. The theorem simply states that *the amplitude for a fermion loop with n external vector emissions is zero if n is odd*, although there are actually more general statements that can be made. To show this, consider a fermion loop with n external legs (for generality we will denote the vertex between the fermions and external bosons, which may be scalar or vector, by Γ_i where $i = 1, \cdots n$ indexes the external particle). There are always two possible diagrams corresponding to the two directions of fermion flow around the loop (these account for the crossing of external legs). In general the trace structure emerging from the loop is an alternating product of vertices, Γ, and Dirac propagators :

$$\mathcal{M}_1 = \mathrm{Tr}\left[\Gamma_1 S_F(p_1)\Gamma_2 \ldots \Gamma_n S_F(p_n)\right], \tag{1.1.1}$$

where we neglect the loop integral and propagator denominators; in the above $S_F(p) = \not{p} + m$ is the usual fermion propagator and p_i is the momentum flowing between point i and $i+1$. The second amplitude is then

$$\mathcal{M}_2 = \mathrm{Tr}\left[S_F(-p_n)\Gamma_n \ldots \Gamma_2 S_F(-p_1)\Gamma_1\right], \tag{1.1.2}$$

we next use the identity (proof below),

$$\mathrm{Tr}\left(\gamma^\mu\gamma^\nu \ldots \gamma^\sigma\gamma^\rho\right) = \mathrm{Tr}\left(\gamma^\rho\gamma^\sigma \ldots \gamma^\nu\gamma^\mu\right), \tag{1.1.3}$$

to reverse the ordering of the second amplitude,

$$\mathcal{M}_2 = \mathrm{Tr}\left[\Gamma_1^* S_F(-p_1)\Gamma_2^* \ldots \Gamma_n^* S_F(-p_n)\right] \tag{1.1.4}$$

and Γ^* is Γ but with the reversed indices. We then use the result

$$S_F(-p_i) = \gamma^5 S_F(p_i)\gamma^5, \tag{1.1.5}$$

to write $\mathcal{M}_2$ in the same form as $\mathcal{M}_1$,

$$\mathcal{M}_2 = \mathrm{Tr}\left[\bar{\Gamma}_1 S_F(p_1)\bar{\Gamma}_2 \ldots \bar{\Gamma}_n S_F(p_n)\right], \tag{1.1.6}$$

but with modified vertices $\bar{\Gamma}_i = \gamma^5\Gamma_i^*\gamma^5$. Because $\bar{\Gamma} = \pm\Gamma$ we can impose selection rules on the loop diagrams. If $\Gamma = +\bar{\Gamma}$ the amplitudes are equal, if $\Gamma = -\bar{\Gamma}$ the the total amplitude is zero if $(-1)^n = 1$.

The Dirac matrices $\Gamma = \{1, i\gamma^5, \gamma^\mu\gamma^5\}$ all obey $\bar{\Gamma} = +\Gamma$; and $\Gamma = \{\gamma^\mu, \sigma^{\mu\nu}\}$ obey $\bar{\Gamma} = -\Gamma$. Therefore Furry's theorem applies equally to vector *and* tensor couplings, and does not depend on the number of axial-vector, pseudoscalar or scalar couplings, nor on the masses of the fermions in the loop.

Proof of Trace Identity

Consider a string of matrices $\Gamma = \gamma^{\mu_1} \ldots \gamma^{\mu_n}$ and take the Hermitian conjugate (recall $\gamma^\mu, \dagger = \gamma^0\gamma^\mu\gamma^0$)

$$\begin{aligned}\Gamma^\dagger &= \gamma^0\gamma^{\mu_n}\gamma^0 \ldots \gamma^0\gamma^{\mu_1}\gamma^0 \\ &= \gamma^0\Gamma^*\gamma^0,\end{aligned} \tag{1.1.7}$$

where Γ^* is defined as above, and when taking the trace the γ^0 cancel. If the string of gamma matrices also contains γ^5, the result includes a factor $(-1)^N$ where N is the number of γ^5, since

$$(\gamma^\mu\gamma^5\gamma^\nu)^\dagger = -\gamma^0\gamma^\nu\gamma^5\gamma^\mu\gamma^0, \tag{1.1.8}$$

however by inserting a factor of i for each γ^5 the result is the same.

A.2 CPT Symmetries

For a recent easy to read review of this topic see [391]. The combined $\mathcal{CPT}$ symmetry is implement by the unitary matrix Θ. The CPT theorem for a field theory states

$$\Theta^\dagger \mathcal{L}(x)\Theta = \mathcal{L}^\dagger(-x) \ , \tag{1.2.9}$$

for a Lagrangian $\mathcal{L}$ in position space. The Lagrangian is assumed to be a Lorentz scalar, but not necessarily Hermitian. In our discussion we have, without loss of generality, ensured operators are hermitian, but not necessarily Lorentz invariant, and the CPT condition for operators $\mathcal{O}$ is

$$\Theta^\dagger \mathcal{O}^{\mu\nu\cdots}(x)\Theta = \pm\mathcal{O}^{\mu\nu\cdots}(x) \ . \tag{1.2.10}$$

First one can construct the $\mathcal{CPT}$ symmetries of Lorentz *covariant* operators, using the general transformation of complex fields,

$$\Theta^\dagger \phi(x)\Theta = \phi^\dagger(-x) \ , \tag{1.2.11}$$

$$\Theta^\dagger \chi(x)\Theta = -\gamma^5(\chi^\dagger)^T(-x) \ , \tag{1.2.12}$$

$$\Theta^\dagger B_\mu(x)\Theta = -B_\mu^\dagger(-x) \ , \tag{1.2.13}$$

for spin-0,1/2,1 fields respectively. Derivatives are invariant under $\mathcal{CPT}$; $\partial^\mu \to \partial^\mu$, as are the Levi-Civita and metric tensors. This then determines the $\mathcal{CPT}$ properties of the various structures, which obey a simple rule; *operators with an even (odd) number of Lorentz indices are even (odd) under* $\mathcal{CPT}$.

The individual symmetries of a fermion field are most simply calculated for field bilinears (see for example [330] or any introductory field theory textbook). A scalar particle has trivial symmetries (all +), for vectors they may be recovered explicitly using the results for polarization vectors $\varepsilon_\mu^\lambda(-\mathbf{p}) = -\varepsilon_\mu^\lambda(\mathbf{p})$ and $\varepsilon_\mu^{-\lambda}(\mathbf{p}) = -\varepsilon_\mu^\lambda(\mathbf{p})$ (which can be shown using a Lorentz transformation from $-\mathbf{p}$ to $\mathbf{p}$). The individual symmetries for scalar and vector bosons are summarized in Tab.A.1.

	$\mathcal{C}$	$\mathcal{P}$	$\mathcal{T}$
$\phi(x)$	$\phi^\dagger(x)$	$\phi(P^\mu{}_\nu x^\nu)$	$\phi(T^\mu{}_\nu x^\nu)$
$B^\mu(x)$	$B^{\mu\dagger}(x)$	$P^\mu{}_\nu B^\nu(P^\mu{}_\nu x^\nu)$	$T^\mu{}_\nu B^\nu(T^\mu{}_\nu x^\nu)$

Table A.1: $\mathcal{CPT}$ transformations of scalar (ϕ) and vector (B^μ) fields. Internal parity and time symmetries are taken to be $\eta_{P,T} = +1$. The matrices $P = \text{diag}(1,-1,-1,-1)$ and $T = \text{diag}(-1,1,1,1)$.

A.3 Non-relativistic Limit of Fields

We briefly recall some details for calculating the non-relativistic limit of the effective operators for fermion, scalar and vector DM.

A.3.1 Fermion Dark Matter

In order to determine the NR operators that appear for operators containing spin-1/2 particles and their derivatives, we recall the standard field theory definitions of Dirac fermion fields in terms of their creation and annihilation operators,

$$\begin{aligned}\chi(x) &= \int \frac{d^3\mathrm{q}}{(2\pi)^3}\frac{1}{\sqrt{2E_\mathrm{q}}}\sum_s \left(u_s(\mathrm{q})a^s_\mathrm{q}e^{-iq\cdot x} + v_s(\mathrm{q})b^{\dagger,s}_\mathrm{q}e^{iq\cdot x}\right)\ ,\\ \bar\chi(x) &= \int \frac{d^3\mathrm{q}}{(2\pi)^3}\frac{1}{\sqrt{2E_\mathrm{q}}}\sum_s \left(\bar u_s(\mathrm{q})a^{\dagger,s}_\mathrm{q}e^{iq\cdot x} + \bar v_s(\mathrm{q})b^s_\mathrm{q}e^{-iq\cdot x}\right)\ ,\end{aligned} \tag{1.3.14}$$

where $a^{s,\dagger}_\mathrm{p}$ ($b^{s,\dagger}_\mathrm{p}$) creates a particle (anti-particle) of momentum p and spin s, and a^s_p (b^s_p) destroys one. Thus acting on the vacuum $\langle 0|\, a^{s,\dagger}_\mathrm{p} = \langle 0|\, b^{s,\dagger}_\mathrm{p} = 0$ and $a^s_\mathrm{p}\,|0\rangle = b^s_\mathrm{p}\,|0\rangle = 0$. The scattering process $\chi(p) \to \chi(p')$ requires the evaluation of the expression

$$\langle\chi(p',s')|\cdots|\chi(p,s)\rangle = \sqrt{2E_\mathrm{p}}\sqrt{2E_{\mathrm{p}'}}\,\langle 0|\, a^{s'}_{\mathrm{p}'}\cdots a^{\dagger,s}_\mathrm{p}\,|0\rangle\,, \tag{1.3.15}$$

by commuting the creation/annihilation operators to annihilate the vacuum, in doing so using the commutation relations[1],

$$\left[a^s_{\rm p}, a^{s'\dagger}_{\rm q}\right] = \delta^{ss'}(2\pi)^3\delta^{(3)}({\rm p}-{\rm q}), \tag{1.3.16}$$

$$\left[b^s_{\rm p}, b^{s'\dagger}_{\rm q}\right] = \delta^{ss'}(2\pi)^3\delta^{(3)}({\rm p}-{\rm q}), \tag{1.3.17}$$

$$\left[a^s_{\rm p}, b^{s'\dagger}_{\rm p}\right] = \left[a^{s\dagger}_{\rm p}, b^{s'}_{\rm p}\right] = 0. \tag{1.3.18}$$

The matrix element is conventionally found from

$$i(2\pi)^4\delta^{(4)}(p-p')\mathcal{M} = \int d^4x \,\langle X(p')|\,\mathcal{O}(x)\,|X(p)\rangle\,, \tag{1.3.19}$$

which produces an amplitude in terms of spinors and Dirac gamma matrices, which can then be reduced to the standard NR form according to Sec.4.4.

Operators containing single derivatives of fermions (such as those in the vector DM EFT) may be written

$$\begin{aligned} R^{\mu\nu} &\equiv {\rm Re}\,(\partial^\nu\bar\chi\gamma^\mu\chi) = (\partial^\nu\bar\chi)\gamma^\mu\chi + \bar\chi\gamma^\mu\partial^\nu\chi, \\ I^{\mu\nu} &\equiv i{\rm Im}\,(\partial^\nu\bar\chi\gamma^\mu\chi) = i(\partial^\nu\bar\chi)\gamma^\mu\chi - \bar\chi\gamma^\mu(i\partial^\nu\chi), \end{aligned} \tag{1.3.20}$$

within the matrix element Eq.(1.3.15) we can make the replacements $\partial^\mu\chi(p,s) \to -ip^\mu u_s({\rm p})$ and $\partial^\mu\bar\chi(p',s') \to ip'^\mu\bar u_{s'}({\rm p}')$. The momenta are defined as,

$$\begin{aligned} p^\mu &= (m_\chi, \frac{1}{2}q^i + \mu v^{\perp,i}), \\ p'^\mu &= (m_\chi, -\frac{1}{2}q^i + \mu v^{\perp,i}), \end{aligned} \tag{1.3.21}$$

see Sec.4.4 footnote 14. Then the NR matrix elements are

$$\begin{aligned} \langle R^{00}\rangle_{i\mathcal{M}} &= \langle R^{0i}\rangle_{i\mathcal{M}} = 0, \\ \langle R^{i0}\rangle_{i\mathcal{M}} &= -iq^i\bar u({\rm p}')\gamma^0 u({\rm p}), \\ \langle R^{ij}\rangle_{i\mathcal{M}} &= -iq^i\bar u({\rm p}')\gamma^j u({\rm p}), \end{aligned}$$

[1] Almost identical expressions hold for other spins, but with a $1, \delta^{\lambda\lambda'}$ in place of $\delta^{ss'}$ for scalar and vector particles respectively.

and

$$\begin{aligned}\langle I^{00}\rangle_{i\mathcal{M}} &= -2m_\chi \bar{u}(\mathrm{p}')\gamma^0 u(\mathrm{p}),\\ \langle I^{0i}\rangle_{i\mathcal{M}} &= -2m_\chi \bar{u}(\mathrm{p}')\gamma^i u(\mathrm{p}),\\ \langle I^{i0}\rangle_{i\mathcal{M}} &= -2\mu v^{\perp,i} \bar{u}(\mathrm{p}')\gamma^0 u(\mathrm{p}),\\ \langle I^{ij}\rangle_{i\mathcal{M}} &= -2\mu v^{\perp,i} \bar{u}(\mathrm{p}')\gamma^j u(\mathrm{p}),\end{aligned}$$

which can be fully reduced using Tab.4.6. For nucleon bilinears one makes the replacement $(q^i, v^{\perp,i}) \to -(q^i, v^{\perp,i})$.

A.3.2 Scalar Dark Matter

A complex scalar field ϕ and its conjugate $\phi^\dagger$ can be written in the standard way in terms of creation/annihilation operators

$$\begin{aligned}\phi(x) &= \int \frac{d^3\mathrm{q}}{(2\pi)^3}\frac{1}{\sqrt{2E_\mathrm{q}}}\left(a_\mathrm{q} e^{-iq\cdot x} + b^\dagger_\mathrm{q} e^{iq\cdot x}\right),\\ \phi^\dagger(x) &= \int \frac{d^3\mathrm{q}}{(2\pi)^3}\frac{1}{\sqrt{2E_\mathrm{q}}}\left(a^\dagger_\mathrm{q} e^{iq\cdot x} + b_\mathrm{q} e^{-iq\cdot x}\right),\end{aligned} \tag{1.3.22}$$

where $E_\mathrm{q} = \sqrt{\mathrm{q}^2 + m^2}$. The scattering process $\phi(p) \to \phi(p')$ comes from the expression,

$$\langle\phi(p')|\cdots|\phi(p)\rangle = \sqrt{2E_\mathrm{p}}\sqrt{2E_{\mathrm{p}'}}\,\langle 0|\, a_{\mathrm{p}'}\cdots a^\dagger_\mathrm{p}\,|0\rangle\,, \tag{1.3.23}$$

inserted into Eq.(1.3.19). Since $(\partial^\mu\phi)^\dagger = \partial^\mu\phi^\dagger$, the scalar vertex with a derivative is written

$$\begin{aligned}g\phi^\dagger\partial^\mu\phi A_\mu + \mathrm{h.c.} &= (g\phi^\dagger\partial^\mu\phi + g^\dagger\phi\partial^\mu\phi^\dagger)A_\mu,\\ &= i\mathrm{Im}(g)\left(\phi^\dagger\partial^\mu\phi - \phi\partial^\mu\phi^\dagger\right)A_\mu + \mathrm{Re}(g)(\phi^\dagger\partial^\mu\phi + \phi\partial^\mu\phi^\dagger)A_\mu\,,\\ &= i\mathrm{Im}(g)\left(\phi^\dagger\partial^\mu\phi - \phi\partial^\mu\phi^\dagger\right)A_\mu\,,\end{aligned} \tag{1.3.24}$$

the last line follows from integration by parts and $\partial^\mu A_\mu = 0$ from the Proca equation, thus the coupling in Eq.(1.3.24) must be purely imaginary. The Feynman rule can be read off noting from Eq.(1.3.22) that ϕ ($\phi^\dagger$) creates an anti-particle (particle) of momentum p or annihilates a particle (anti-particle) of momentum $-p$. For

scattering $\phi(p) \to \phi(p')$ the matrix element for the operator $i\mathrm{Im}(g)\left(\phi^\dagger\partial^\mu\phi - \phi\partial^\mu\phi^\dagger\right)$ (with Feynman rule $i(p+p')^\mu$) is,

$$i\mathrm{Im}(g)((-ip^\mu) - (ip'^\mu)) \to \mathrm{Im}(g)(p+p')^\mu.$$

In the NR limit, ϕ and $\phi^\dagger$ simply reduce to $\mathbf{1}$. Since $(p+p')^\mu = (2m_\chi, 2\mu v^\perp)$, we get for contraction with a vector nucleon bilinear [2] :

$$\begin{aligned}
\langle i(\phi^\dagger\partial_0\phi - \phi\partial_0\phi^\dagger)\bar{N}\gamma^0 N\rangle_{\mathcal{M}} &= 2m_\chi\left(2m_N - i\frac{\mu}{m_N}\epsilon^{ijk}q_i v_j^\perp S_{N,k}\right)\\
&= 4m_\chi m_N\mathcal{O}_1^{(\mathrm{NR})} - 2m_\chi\mu\mathcal{O}_3^{(\mathrm{NR})},\\
\langle i(\phi^\dagger\partial_i\phi - \phi\partial_i\phi^\dagger)\bar{N}\gamma^i N\rangle_{\mathcal{M}} &= 2\mu v_i^\perp\left(-2\mu v^{\perp,i} - 2i\epsilon^{ijk}q_j S_{N,k}\right)\\
&= -4\mu^2\mathcal{O}_2^{(\mathrm{NR})} + 4\mu m_N\mathcal{O}_3^{(\mathrm{NR})},
\end{aligned}$$

where $\partial^\mu = (\partial_0, -\nabla)$. Similarly for the axial-vector nucleon bilinear

$$\begin{aligned}
\langle i(\phi^\dagger\partial_0\phi - \phi\partial_0\phi^\dagger)\bar{N}\gamma^0\gamma^5 N\rangle_{\mathcal{M}} &= 2m_\chi\left(4\mu v^\perp\cdot S_N\right) = 8\mu m_\chi\mathcal{O}_7^{(\mathrm{NR})},\\
\langle i(\phi^\dagger\partial_i\phi - \phi\partial_i\phi^\dagger)\bar{N}\gamma^i\gamma^5 N\rangle_{\mathcal{M}} &= 2\mu v_i^\perp\left(-4m_N S_N^i - i\frac{\mu}{2m_N}\epsilon^{ijk}v_j^\perp q_k\right) = -8\mu m_N\mathcal{O}_7^{(\mathrm{NR})}.
\end{aligned}$$

Then for operators $\mathcal{O}_{S3,S4}$ we find,

$$\langle\mathcal{O}_{S3}\rangle_{\mathcal{M}} \approx 4m_\chi m_N\mathcal{O}_1^{(\mathrm{NR})} + 4m_N^2\mathcal{O}_2^{(\mathrm{NR})} - 2m_\chi m_N\mathcal{O}_3^{(\mathrm{NR})}, \tag{1.3.26}$$

$$\langle\mathcal{O}_{S4}\rangle_{\mathcal{M}} \approx 8m_\chi m_N\mathcal{O}_7^{(\mathrm{NR})}. \tag{1.3.27}$$

A.3.3 Vector Dark Matter

The plane wave expansion of a complex vector field may be written,

$$B_\mu(x) = \int\frac{d^3\mathrm{q}}{(2\pi)^3}\frac{1}{\sqrt{2E_\mathrm{q}}}\sum_\lambda\left(\varepsilon_\mu^\lambda(\mathrm{q})a_\mathrm{q}e^{-iq\cdot x} + \varepsilon_\mu^{\lambda\dagger}(\mathrm{q})b_\mathrm{q}^\dagger e^{iq\cdot x}\right), \tag{1.3.28}$$

$$B_\mu^\dagger(x) = \int\frac{d^3\mathrm{q}}{(2\pi)^3}\frac{1}{\sqrt{2E_\mathrm{q}}}\sum_\lambda\left(\varepsilon_\mu^{\lambda\dagger}(\mathrm{q})a_\mathrm{q}^\dagger e^{iq\cdot x} + \varepsilon_\mu^{\lambda}(\mathrm{q})b_\mathrm{q} e^{-iq\cdot x}\right). \tag{1.3.29}$$

[2] We will use the shorthand $\langle X\rangle_{\mathcal{M}}$ to denote

$$\langle X\rangle_{\mathcal{M}} \equiv -i(2\pi)^3\delta^3(p+k-p'-k')\,\langle\chi(p')N(k')|\,X\,|\chi(p)N(k)\rangle\,, \tag{1.3.25}$$

which is the matrix element $\mathcal{M}$.

For the scattering process $B(p,\lambda) \to B(p',\lambda')$ we require the expression

$$\langle B_\mu(p',\lambda')| \cdots |B_\nu(p,\lambda)\rangle = \sqrt{2E_{\rm p}}\sqrt{2E_{\rm p'}}\,\langle 0|\, a^{\lambda'}_{\rm p'} \cdots a^{\lambda\dagger}_{\rm p}\,|0\rangle\,, \tag{1.3.30}$$

and then the matrix element is found from Eq.(1.3.19).

From the Proca equation $k^\mu \varepsilon^\lambda_\mu = 0$. We choose the polarizations so that $\varepsilon^\lambda_0 = 0$ and $\varepsilon^\lambda_i = \delta^\lambda_i$ and normalize them according to $\varepsilon^\lambda \cdot \epsilon^{\lambda'} = -g^{\lambda\lambda'}$, and also $\varepsilon^\lambda_\mu \varepsilon^\lambda_\nu = g_{\mu\nu}$ with summation on λ implied [3].

The spin three-vector S^k is a matrix in 'polarization space' given by $i\left[S^k\right]^{\lambda\lambda'} = \epsilon^{ijk}\varepsilon_i^{\lambda,\dagger}\varepsilon_j^{\lambda'}$ and hence

$$\varepsilon_i^{\lambda,\dagger}\varepsilon_j^{\lambda'} - \varepsilon_j^{\lambda,\dagger}\varepsilon_i^{\lambda'} = i\epsilon_{ijk}(S^k)^{\lambda\lambda'}\,. \tag{1.3.31}$$

We may also define a linearly independent symmetric combination of polarizations,

$$\varepsilon_i^{\lambda,\dagger}\varepsilon_j^{\lambda'} + \varepsilon_j^{\lambda,\dagger}\varepsilon_i^{\lambda'} \equiv 2(\mathcal{S}_{ij})^{\lambda\lambda'}, \tag{1.3.32}$$

then for example the coupling structure $i(B^\dagger_\mu B_\nu - B^\dagger_\nu B_\mu)$ leads to the operator $i\left(\varepsilon_i^{\lambda,\dagger}\varepsilon_j^{\lambda'} - \varepsilon_j^{\lambda,\dagger}\varepsilon_i^{\lambda'}\right)$, and is therefore purely spin-dependent. The symmetric combination $\mathrm{Re}(B^\dagger_\mu B_\nu)$ is equivalent to Eq.(1.3.32).

There are three vertices with a derivative $\mathcal{V}^\mu_{1,2,3}$ defined in Eqs.(4.2.29)-(4.2.31), we begin with $\mathcal{V}^\mu_1$ which is split into real and imaginary parts,

$$\mathcal{V}^\mu_{1,I} = i\left(B^\nu \partial_\nu B^{\mu,\dagger} - B^\dagger_\nu \partial^\nu B^\mu\right) \tag{1.3.33}$$

[3] We can choose the momentum of the vector pair to be in the ±z-direction. The basis of polarization vectors is conventionally chosen as $\varepsilon^1_\mu = (0,1,0,0)$ and $\varepsilon^2_\mu = (0,0,1,0)$ which represent the *transverse* polarizations, and $\varepsilon^3_\mu = (\mathrm{p}/m, 0, 0, E/m)$ which is the *longitudinal* polarization. It is convenient to choose $\varepsilon^3_\mu = (0,0,0,1)$ in the rest frame of the particle as we have done (equivalent to the longitudinal mode in the limit $v \to 0$).

and leads to the amplitude,

$$\begin{aligned}\langle \mathcal{V}^i_{1,I}\rangle_{\mathcal{M}} &= (p^j \varepsilon^{\lambda'}_j \varepsilon^{\lambda,i,\dagger} + p'^j \varepsilon^{\lambda,\dagger}_j \varepsilon^{\lambda',i}),\\ &= \frac{1}{2}(p+p')_j \varepsilon^{\lambda'\{i,}(\varepsilon^{\lambda j\}})^\dagger - \frac{1}{2}(p-p')_j \varepsilon^{\lambda'[i,}(\varepsilon^{\lambda j]})^\dagger,\\ &= 2\mu \mathcal{S}^{ij} v^\perp_j + \frac{i}{2}\epsilon^{ijk} q_j S_{\chi,k}.\end{aligned}$$

The real equivalent of Eq.(1.3.33) is, $\mathcal{V}^\mu_{1,R} = \left(B^\nu \partial_\nu B^{\mu,\dagger} + B^\dagger_\nu \partial^\nu B^\mu\right)$ and leads to the amplitude,

$$\begin{aligned}\langle \mathcal{V}^i_{1,R}\rangle_{\mathcal{M}} &= i\left(p_j \varepsilon^{\lambda' j,\dagger}\varepsilon^{\lambda i} - p'_j \varepsilon^{\lambda j}\varepsilon^{\lambda' i,\dagger}\right),\\ &= \frac{i}{2}\left((p+p')_j \varepsilon^{\lambda'\dagger,[j}\varepsilon^{\lambda i]} + (p-p')_j \varepsilon^{\lambda',\dagger[j}\varepsilon^{\lambda i]}\right),\\ &= \mu\epsilon^{ijk} v^\perp_j S_{\chi,k} + i q_j \mathcal{S}^{ij},\end{aligned}$$

these can contract with a vector or axial vector nucleon bilinear $\bar{N}\gamma^\mu N$, $\bar{N}\gamma^\mu\gamma^5 N$,

$$\begin{aligned}\langle \mathrm{Re}(B_\nu \partial^\nu B^\dagger_\mu)\bar{N}\gamma^\mu N\rangle_{\mathcal{M}} &= -\left(iq^j \mathcal{S}_{ji}\right)\left(-2\mu v^{\perp,i} - 2i\epsilon^{ilm} q_l S_{N,m}\right)\\ &\quad -\left(\mu\epsilon_{ijk} v^{\perp,j} S^k_\chi\right)\left(-2\mu v^{\perp,i} - 2i\epsilon^{jlm} q_l S_{N,m}\right),\\ &\approx 2\mu m_N\left(\frac{iq}{m_N}\cdot\mathcal{S}\cdot v^\perp\right) + 4\mu m_N (v^\perp\cdot S_N)\left(\frac{iq}{m_N}\cdot S_\chi\right),\\ &= 2\mu m_N \mathcal{O}^{(\mathrm{NR})}_{17} + 4\mu m_N \mathcal{O}^{(\mathrm{NR})}_{14}\ , \qquad (1.3.34)\\ \langle \mathrm{Re}(B_\nu \partial^\nu B^\dagger_\mu)\bar{N}\gamma^\mu\gamma^5 N\rangle_{\mathcal{M}} &= -\left(iq^j \mathcal{S}_{ji}\right)\left(-4m_N S^i_N - i\frac{\mu}{2m_N}\epsilon^{ikl} v^\perp_k q_l\right)\\ &\quad -\left(\mu\epsilon_{ijk} v^{\perp,j} S^k_\chi\right)\left(-4m_N S^i_N - i\frac{\mu}{2m_N}\epsilon^{ilm} v^\perp_l q_m\right),\\ &\approx 4m_N^2\left(\frac{iq}{m_N}\cdot\mathcal{S}\cdot S_N\right) + 4m_N\mu\left(v^\perp\cdot(S_\chi\times S_N)\right),\\ &= 4m_N^2 \mathcal{O}^{(\mathrm{NR})}_{18} + 4\mu m_N \mathcal{O}^{(\mathrm{NR})}_{12}\ . \qquad (1.3.35)\end{aligned}$$

Thus this vertex structure leads to a very suppressed spin-dependent scattering cross section. To check the consistency of this result recall, for example, the $\mathcal{CPT}$ symmetries of $\mathrm{Re}(B^\nu\partial^\nu B^\dagger_i)$ are $(+-+)$ and for $\bar{q}\gamma^i q$ are $(---)$, and so the combined symmetries are $(-+-)$ for Eq.(1.3.34), which are perfectly consistent with the $\mathcal{PT}$ symmetries of the NR operators (see Tab.4.5)[4].

[4] A note of caution: the symmetries of a particular bilinear may not match between relativistic

We now turn to the operator $\mathcal{V}^{\mu}_{2,I} = i(B^{\dagger}_{\mu}\partial^{\nu}B_{\mu} - B^{\mu}\partial^{\nu}B^{\dagger}_{\mu})$,

$$\begin{aligned}\langle \mathcal{V}^{\nu}_{2,I}\rangle_{\mathcal{M}} &= i\left(\varepsilon^{\lambda'\dagger}_{\mu}(-ip_{\nu})\varepsilon^{\lambda,\mu} - \varepsilon^{\lambda,\mu}(ip'_{\nu})\varepsilon^{\lambda'\dagger}_{\mu}\right),\\ &= (p+p')^{\nu}\left(\varepsilon^{\lambda'\dagger}\cdot\varepsilon^{\lambda}\right),\end{aligned} \tag{1.3.36}$$

suppressing the trivial spin-conserving delta function then the axial-vector and vector contractions are,

$$\begin{aligned}\langle i\mathrm{Im}(B^{\dagger}_{\mu}\partial_{\nu}B^{\mu})\bar{N}\gamma^{\nu}N\rangle_{\mathcal{M}} &= 2m_{\chi}\left(2m_N + i\frac{\mu}{m_N}q\cdot v^{\perp}\times S_N\right)\\ &\quad - 2\mu v^{\perp}_i\cdot\left(-2\mu v^{\perp,i} - 2i\epsilon^{ijk}q_j S_{N,k}\right),\\ &= 4m_{\chi}m_N\mathcal{O}^{(\mathrm{NR})}_1 + 4\mu^2\mathcal{O}^{(\mathrm{NR})}_2 - 2\mu m_{\chi}\mathcal{O}^{(\mathrm{NR})}_3 - 4\mu m_N\mathcal{O}^{(\mathrm{NR})}_3,\end{aligned} \tag{1.3.37}$$

$$\begin{aligned}\langle i\mathrm{Im}(B^{\dagger}_{\mu}\partial_{\nu}B^{\mu})\bar{N}\gamma^{\nu}\gamma^5 N\rangle_{\mathcal{M}} &= 2m_{\chi}\left(4\mu v^{\perp}\cdot S_N\right) - 2\mu v^{\perp}_i\left(-4m_N S^i_N - i\frac{\mu}{2m_N}\epsilon^{ijk}v^{\perp}_j q_k\right),\\ &= 8m_{\chi}m_N\mathcal{O}^{(\mathrm{NR})}_7.\end{aligned} \tag{1.3.38}$$

The vertex $\mathcal{V}^{\mu}_{2,R} = (B^{\dagger}_{\mu}\partial^{\nu}B^{\mu} + B^{\mu}\partial^{\nu}B^{\dagger}_{\mu})$ is, $i(p'-p)^{\nu}(\varepsilon^{\lambda'\dagger}\cdot\varepsilon^{\lambda})$ which contracts to give,

$$\langle \mathrm{Re}(B^{\dagger}_{\mu}\partial_{\nu}B^{\mu})\bar{N}\gamma^{\nu}N\rangle_{\mathcal{M}} = -iq_i(-2\mu v^{\perp,i} - 2i\epsilon^{ijk}q_j S_{N,k}) = 0 \tag{1.3.39}$$

$$\langle \mathrm{Re}(B^{\dagger}_{\mu}\partial_{\nu}B^{\mu})\bar{N}\gamma^{\nu}\gamma^5 N\rangle_{\mathcal{M}} = -iq_i\left(-4m_N S^i_N - i\frac{\mu}{2m_N}\epsilon^{ijk}v^{\perp}_j q_k\right) = 4m^2_N\mathcal{O}^{(\mathrm{NR})}_{10} \tag{1.3.40}$$

Finally we consider the vertex $\mathcal{V}^{\rho}_3 = \epsilon^{\mu\nu\sigma\rho}(gB^{\dagger}_{\mu}\partial_{\nu}B_{\sigma} + \mathrm{h.c.})$ with imaginary couplings, $\mathcal{V}^{\rho}_{3,I} \equiv i\epsilon^{\mu\nu\sigma\rho}\mathrm{Im}\left(B^{\dagger}_{\mu}\partial_{\nu}B_{\sigma}\right)$, the amplitude is $\propto (p-p')_{\nu} = (0,q)$, since $\varepsilon^0 \approx 0$ only $\mathcal{V}^0_{3,I}$ is nonzero:

$$\epsilon_{ikj0}\varepsilon^{\lambda,i}(p)\varepsilon^{\lambda'j}(p')(p-p')^k = \epsilon_{ijk}\varepsilon^{\lambda,i}(p)\varepsilon^{\lambda',j}(p')q^k = iq\cdot S_{\chi}, \tag{1.3.41}$$

where we relate the Levi-Civita tensor between four and three dimensions $\epsilon^{0ijk} \equiv \epsilon^{ijk}$. The couplings to vector and axial-vector bilinears (EFT operators $\mathcal{O}_{V7-2,V8-2}$), are

and NR limit if the bilinear is not a Lorentz scalar. Only Lorentz invariant combinations of bilinears will yield matching symmetries between the two regimes. For example, the bilinear $\bar{\chi}\gamma^0\chi \approx 2m_{\chi}$ in the NR limit for scattering; the $\mathcal{T}$ and $\mathcal{C}$ symmetries do not match.

then quite simple

$$\langle i\mathrm{Im}(\epsilon^{\mu\nu\sigma\rho}B_\mu^\dagger\partial_\nu B_\sigma)\bar{N}\gamma_\rho N\rangle_{\mathcal{M}} \approx -2m_N^2\mathcal{O}_{11}^{(\mathrm{NR})}+\mu m_N\mathcal{O}_{15}^{(\mathrm{NR})}, \tag{1.3.42}$$

$$\langle i\mathrm{Im}(\epsilon^{\mu\nu\sigma\rho}B_\mu^\dagger\partial_\nu B_\sigma)\bar{N}\gamma_\rho\gamma^5 N\rangle_{\mathcal{M}} \approx 4\mu m_N\mathcal{O}_{14}^{(\mathrm{NR})}\ , \tag{1.3.43}$$

thus $\mathcal{O}_{V7-2}$ is dominated by $\mathcal{O}_{11}^{(\mathrm{NR})}$ which has only a single q suppression, and $\mathcal{O}_{V8-2}$ is dominated by $\mathcal{O}_{14}^{(\mathrm{NR})}$.

For real couplings in $\mathcal{V}_{3,R}^\rho \equiv \epsilon^{\mu\nu\sigma\rho}\mathrm{Re}\left(B_\mu^\dagger\partial_\nu B_\sigma\right)$ the amplitude is $\propto i(p+p')^\nu = i(2m_\chi, 2\mu v^\perp)$ in the NR limit and thus the non-zero components are,

$$i\epsilon_{i0jk}\varepsilon^{\lambda,i}(p)\varepsilon^{\lambda',j}(p')(p+p')^0 = 2m_\chi S_\chi^k \tag{1.3.44}$$

$$i\epsilon_{ikj0}\varepsilon^{\lambda,i}(p)\varepsilon^{\lambda',j}(p')(p+p')^k = 2i\mu v^k\varepsilon^{\lambda,i}(p)\varepsilon^{\lambda',j}(p')\epsilon^{ijk} = -2\mu(S_\chi\cdot v^\perp) \tag{1.3.45}$$

leading to the NR expansion of EFT operators $\mathcal{O}_{V7,V8}$

$$\begin{aligned}\langle\mathrm{Re}(\epsilon^{\mu\nu\sigma\rho}B_\mu^\dagger\partial_\nu B_\sigma)\bar{N}\gamma_\rho N\rangle_{\mathcal{M}} &= -4\mu m_N(S_\chi\cdot v^\perp)+2m_\chi S_\chi^i\cdot(-2\mu v^{\perp,i}-2i\epsilon^{ijk}q^jS_N^k),\\ &= -4m_\chi m_N\mathcal{O}_8^{(\mathrm{NR})}+4m_\chi m_N\mathcal{O}_9^{(\mathrm{NR})}\end{aligned} \tag{1.3.46}$$

$$\begin{aligned}\langle\mathrm{Re}(\epsilon^{\mu\nu\sigma\rho}B_\mu^\dagger\partial_\nu B_\sigma)\bar{N}\gamma_\rho\gamma^5 N\rangle_{\mathcal{M}} &= -8\mu^2(v^\perp\cdot S_N)(v^\perp\cdot S_\chi)\\ &\quad+2m_\chi S_\chi^i\left(-4m_N S_N^i-i\frac{\mu}{2m_N}\epsilon^{ijk}v^jq^k\right),\\ &= -8\mu^2\mathcal{O}_7^{(\mathrm{NR})}\mathcal{O}_8^{(\mathrm{NR})}-8m_Nm_\chi\mathcal{O}_4^{(\mathrm{NR})}+\mu m_\chi\mathcal{O}_5^{(\mathrm{NR})}\ .\end{aligned} \tag{1.3.47}$$

This concludes our discussion of the NR limit of spin-0,1/2,1 fields for direct detection. When calculating the amplitudes appropriate for perturbative unitarity constraints, the *helicity* basis is required for all the fields (for the scalar field there is no difference, but the field expansions for fermion and vector fields stated previously are for *spin* states), and so we now review the expressions for the states of fixed helicity for fermions and vector bosons.

A.4 Helicity Basis for Spinors and Vectors

In this section we will elaborate on the calculation of partial wave amplitudes which requires the field of the theory to be in helicity eigenstates. For scalar fields this is

trivial, since they only have heliciy 0, but for spin-1/2 and spin-1 fields more detail is required.

We will work with a $2 \to 2$ scattering process, with labels $12 \to 34$, we will assume $m_1 = m_2 \equiv m_i$ and $m_3 = m_4 \equiv m_f$ and the total helicity of the initial/final state will be denoted μ, μ'. The momenta of the incoming/outgoing particles in the COM frame are,

$$\begin{aligned}
p_1^\mu &= \left(\sqrt{S}/2, 0, 0, \sqrt{S - 4m_i^2}\right), \\
p_2^\mu &= \left(\sqrt{S}/2, 0, 0, -\sqrt{S - 4m_i^2}\right), \\
p_3^\mu &= \left(\sqrt{S}/2, \sin\theta\sqrt{S - 4m_f^2}, 0, \cos\theta\sqrt{S - 4m_f^2}\right), \\
p_4^\mu &= \left(\sqrt{S}/2, -\sin\theta\sqrt{S - 4m_f^2}, 0, -\cos\theta\sqrt{S - 4m_f^2}\right),
\end{aligned} \tag{1.4.48}$$

where θ is the scattering angle between the initial and final state.

The polarization of external state vectors are denoted $\xi_\lambda^{\mu,*}(p_i)$ for helicity $\lambda = 0, \pm 1$. Longitudinal polarizations ($\lambda = 0$) are only present for massive vector fields. The polarization vector has four degrees of freedom, but for any massive vector particle we have the Lorentz invariant condition,

$$p^\mu \xi_\mu(p) = 0, \tag{1.4.49}$$

reducing the four free parameters of ξ to three. Explicitly, one can use the rest frame to let $\xi^0 = 0$ and the three remaining ξ^i are split into *transverse* and *longitudinal*

modes which may be written for momenta in the (θ, ϕ) direction as [5],

$$\begin{aligned}
\xi_+^\mu &= \frac{1}{\sqrt{2}}\left(0, -\cos\theta\cos\phi + i\sin\phi, -\cos\theta\sin\phi - i\cos\phi, \sin\theta, 0\right), \\
\xi_-^\mu &= \frac{1}{\sqrt{2}}\left(0, \cos\theta\cos\phi + i\sin\phi, \cos\theta\sin\phi - i\cos\phi, -\sin\theta, 0\right), \\
\xi_L^\mu &= \frac{1}{m}\left(E\cos\theta, E\sin\theta\sin\phi, E\sin\theta\cos\phi, p\right).
\end{aligned} \tag{1.4.50}$$

The subscripts $+/-$ denote the helicity of the transverse states, the helicity of the longitudinal mode is 0. To show this one can use the spin operator $S^i = \epsilon^{ijk}\mathcal{S}_{jk}/2$,

$$(\mathcal{S}_{\sigma\rho})^\mu{}_\nu = i(g_\sigma{}^\mu g_{\rho\nu} - g_\rho{}^\mu g_{\sigma\nu}) \tag{1.4.51}$$

the helicity operator is then $\lambda = \hat{p}\cdot S$ [6]. In the processes considered here the vector are always in back-to-back pairs, since the polarization is a Lorentz vector, one can simply rotate the definitions given above by 180^o to give the polarization of the partner particle. We use the convention that the subscripts of the polarizations refer to the helicity in the *particles own frame*, so that if we make some global definition of helicity (say with p in the z-direction) the $+$ state for the particle moving in $-p$ direction has a negative helicity. Thus, the spin-1 helicity combinations which give $\mu = 0$ are $--$, LL and $++$ where the $\pm, L$ represents the helicity in the particles own frame (according to the definitions above). Similarly, $+L, L-$ $(-L, L+)$ represent the $\mu = 1$ $(\mu = -1)$ states.

For spin-1/2 particles we follow the same convention, defining spinors of definite helicity in the $(\theta, \phi) = (0, 0)$ z-direction and then rotating them into the (θ, ϕ) direction for the partner; this again enforces the convention that a $++$ or $--$ state

[5] Explicitly for vectors in the initial and final state:

$$\xi_{1,L}^\mu = \frac{1}{m_1}\begin{pmatrix} p \\ 0 \\ 0 \\ E \end{pmatrix}, \; \xi_{2,L}^\mu = \frac{1}{m_2}\begin{pmatrix} p \\ 0 \\ 0 \\ -E \end{pmatrix}, \; \xi_{3,L}^\mu = \frac{1}{m_3}\begin{pmatrix} p \\ E\sin\theta \\ 0 \\ E\cos\theta \end{pmatrix}, \; \xi_{4,L}^\mu = \frac{1}{m_4}\begin{pmatrix} p \\ -E\sin\theta \\ 0 \\ -E\cos\theta \end{pmatrix}.$$

[6] For consistency the helicity operator should have eigenvalues $\pm 1/2$ for fermions and $0, \pm 1$ for spin-1 particles.

has total helicity 0 ($+,-$ refer to a physical helicity $\pm 1/2$). Again, this may be checked with the correct spin operator for fermions, $S^i = \epsilon^{ijk}\mathcal{S}_{jk}/2$, with

$$\mathcal{S}^{\mu\nu} = \frac{1}{2}\sigma^{\mu\nu} = \frac{i}{4}\left[\gamma^\mu, \gamma^\nu\right] \ . \tag{1.4.52}$$

The spinors may be written explicitly once one decides whether they are states of definite spin (the conventional choice u_σ, v_σ with $\sigma = \pm 1/2$ along the z-axis), or definite helicity (u_λ, v_λ, $\lambda = \pm 1/2$). The basis choice for the gamma matrices must also be specified (either Dirac or Weyl are the conventional choices, see Sec.A.6).

The four solutions of the Dirac equation are split into two positive energy, $u(p)$, and two negative energy, $v(p)$. We impose the standard normalization (inner product), and spin sum (outer product) relations,

$$\bar{u}_\lambda(p)u_{\lambda'}(p) = 2m\delta_{\lambda\lambda'}, \tag{1.4.53}$$

$$\bar{v}_\lambda(p)v_{\lambda'}(p) = -2m\delta_{\lambda\lambda'}, \tag{1.4.54}$$

and,

$$\sum_\lambda u_\lambda(p)\bar{u}_\lambda(p) = \not{p} + m, \tag{1.4.55}$$

$$\sum_\lambda v_\lambda(p)\bar{v}_\lambda(p) = \not{p} - m. \tag{1.4.56}$$

The *standard representation* of spinors consists of writing spin states in the Dirac basis;

$$u_s(p) = \sqrt{E+m}\begin{pmatrix} \chi_s \\ \frac{\sigma\cdot p}{E+m}\chi_s \end{pmatrix} \ , \ v_s(p) = \sqrt{E+m}\begin{pmatrix} \frac{\sigma\cdot p}{E+m}\bar{\chi}_s \\ \bar{\chi}_s \end{pmatrix} \ , \tag{1.4.57}$$

the two component spin vector χ_s is an eigenvalue of the spin operator $\mathbf{S} = \sigma/2$, so that for example if we quantize spin in the $+z$ direction ($\mathbf{S} = \sigma_3/2$) then $\chi_\uparrow = (1,0)$ and $\chi_\downarrow = (0,1)$. Since the v-spinors live in the conjugate spin-1/2 representation, $\bar{\chi}_s = \epsilon\chi_s^*$, so that $\bar{\chi}_\uparrow = (0,1)$ and $\bar{\chi}_\downarrow = (1,0)$.

Note that the spin-quantization axis (that defines χ_s and $\bar{\chi}_s$) is independent from the momentum direction, since one can boost into a frame in which the spin along the quantization axis is reversed (i.e. helicity is not Lorentz invariant). It is simplest

to quantize along the z-axis so that $\chi_{1/2} = (1,0)$, $\chi_{-1/2} = (0,1)$ and similarly for $\bar{\chi}_s$. If we now choose momentum in the $+z$ direction, the spin states and helicity states should coincide;

$$u_+(p) = \begin{pmatrix} \sqrt{E+m} \\ 0 \\ \sqrt{E-m} \\ 0 \end{pmatrix} \ , \ u_-(p) = \begin{pmatrix} 0 \\ \sqrt{E+m} \\ 0 \\ -\sqrt{E-m} \end{pmatrix} , \ v_+(p) = \begin{pmatrix} 0 \\ -\sqrt{E-m} \\ 0 \\ \sqrt{E+m} \end{pmatrix} \ , \ v_-(p) = \begin{pmatrix} \sqrt{E-m} \\ 0 \\ \sqrt{E+m} \\ 0 \end{pmatrix} ,$$

then we can transform these to the Weyl basis using the standard unitary transformation (see Sec.A.6),

$$u_+(p) = \begin{pmatrix} \sqrt{E+p} \\ 0 \\ \sqrt{E-p} \\ 0 \end{pmatrix} \ , \ u_-(p) = \begin{pmatrix} 0 \\ \sqrt{E-p} \\ 0 \\ \sqrt{E+p} \end{pmatrix} , v_+(p) = \begin{pmatrix} 0 \\ \sqrt{E-p} \\ 0 \\ -\sqrt{E+p} \end{pmatrix} \ , \ v_-(p) = \begin{pmatrix} \sqrt{E+p} \\ 0 \\ -\sqrt{E-p} \\ 0 \end{pmatrix} , \tag{1.4.58}$$

thus, physically, $u_{1/2}$ ($u_{-1/2}$) describes a fermion travelling in the $+z$ direction with spin up (down). Similarly $v_{1/2}$ ($v_{-1/2}$) describe anti-fermions travelling in the $+z$ direction with spin up (down).

The helicity spinors may be written generally in the Weyl basis choice defined by Eq.(1.6.106)[7]

$$u_\lambda(p) = \begin{pmatrix} \sqrt{E-\lambda|p|}\chi_\lambda(\hat{p}) \\ \sqrt{E+\lambda|p|}\chi_\lambda(\hat{p}) \end{pmatrix} \ , \ v_\lambda(p) = \begin{pmatrix} -\lambda\sqrt{E+\lambda|p|}\chi_{-\lambda}(\hat{p}) \\ \lambda\sqrt{E-\lambda|p|}\chi_{-\lambda}(\hat{p}) \end{pmatrix} \tag{1.4.60}$$

where in this case $\chi_\lambda(p)$ are interpreted as two-component helicity spinors, solutions to the equation,

$$(\sigma \cdot \hat{p})\chi_\pm(p) = \pm\chi_\pm(p) \ . \tag{1.4.61}$$

so then $\chi_+(+z) = (1,0)$, $\chi_-(+z) = (0,1)$, $\chi_+(-z) = (0,1)$, $\chi_-(-z) = (-1,0)$ and this recovers Eq.(1.4.58).

[7]Note the following identity,

$$\sqrt{E \pm p} = \frac{1}{\sqrt{2}}\left(\sqrt{E+m} \pm \sqrt{E-m}\right) . \tag{1.4.59}$$

A.5 Perturbtive Unitarity Violations

For any process $i \to f$, the unitarity bound can be phrased as [12, 72, 392–394],

$$\sum_f \beta_i \beta_f |T^j_{i\to f}|^2 \leq 1, \tag{1.5.62}$$

in our models both i and f are 2-particle states[8], and the amplitude T has definite helicity assignments (there is no interference between different helicity contributions, but one adds all the relevant helicity combinations in the sum). where

$$\beta_i = \frac{1}{S}\sqrt{(S-(m_1+m_2)^2)(S-(m_1-m_2)^2)}, \tag{1.5.63}$$

is a kinematic factor, and T^j is the jth partial wave of the amplitude, found by projecting the usual amplitude[9],

$$T^j_{i\to f,\mu\mu'}(S) = \frac{1}{32\pi}\int_{-1}^{1} d\cos\theta \; d^J_{\mu\mu'}(\theta)\mathcal{M}_{if}(S,\theta), \tag{1.5.64}$$

where $d^J_{\mu\mu'}(\theta)$ are the Wigner d functions, and μ, μ' represent the total helicity of the initial/final state.

Unitarity violations at tree level are present mostly within models which contain massive spin-1 particles due to the longitudinal modes which scale with CM energy as $\sqrt{S}/m$. Naively, the more vectors present in the process the larger the dependence on S. We therefore restrict to models containing spin-1 vectors, which nonetheless are most of the simplified models under study.

Since the violations stem from the longitudinal modes we will ignore the transverse polarizations and then initial (final) state boson pairs have $\mu = 0$ ($\mu' = 0$). This leaves the possibility of a final (initial) state with $\mu = 0, 1$. The $\mu = 1$ state can only occur for spin-1/2 fermion pairs with opposite helicity. In such cases the total

[8] For identical particles in the initial state or final state a factor of 1/2 is applied to β in Eq.(1.5.62).

[9] We will use the notation $T^j_{\mu\mu'}$ where $\mu, \mu' = 0, ++, --$ for scalar/vector and fermion fields respectively.

helicity change by one unit leads to a mass insertion (which will cause a suppression if the fermions are light).

The relevant Wigner d functions for the restricted set of amplitudes we consider are,

$$\begin{aligned} J=0 \ &: \ d^0_{00}=1 \ , \\ J=1 \ &: \ d^1_{00}=\cos\theta, \ d^1_{-10}=-d^1_{10}=\frac{1}{\sqrt{2}}\sin\theta \ , \\ J=1 \ &: \ d^1_{00}=\cos\theta, \ d^1_{01}=-d^1_{0-1}=\frac{1}{\sqrt{2}}\sin\theta \ . \end{aligned} \tag{1.5.65}$$

We now consider each model in turn to quantify the extent of unitarity violation. In our analysis, several models include vectors; $1/2-V$ and $1/2-V^{\pm}$ for fermionic DM; $0-V$ for scalar DM and $1-S$, $1-V$, $1-F^{\pm}$ for vector DM. We will present expressions to leading order in the CM energy S.

Fermionic DM : 1/2-V, 1/2*-V

The relevant processes are (1) $\bar{\chi}\chi\to\bar{\chi}\chi$ (equivalently $\chi\chi\to\chi\chi$), (2) $\bar{q}q\to\bar{q}q$, (3) $\bar{q}q\to\bar{\chi}\chi$, (4) $\bar{\chi}\chi\to VV$ and (5) $\bar{q}q\to VV$.

(1), (2) : Firstly, we can consider DM and quark self-scattering, with an s-channel mediator exchange. The zero helicity combinations of four fermions are $(++,++)$,$(--,--)$,$(++,--)$ and $(--,++)$. For $\chi\chi\to\chi\chi$[10],

$$T^0_{++,--}=T^0_{--,++}=\frac{g^2_{\chi,a}m^2_{\chi}}{\pi m^2_V} \tag{1.5.66}$$

with $T^0_{++,++}=T^0_{--,--}=0$ leading to,

$$\beta_i\beta_f\left(|T^0_{++,--}|^2+|T^0_{--,++}|^2\right)=\left[\frac{2g^4_{\chi,a}m^4_{\chi}}{\pi^2 m^4_V}\right]\leq 1 \ . \tag{1.5.67}$$

The process $\bar{\chi}\chi\to\bar{\chi}\chi$ leads to

$$T^0_{++,--}=T^0_{--,++}\approx\frac{g^2_{\chi,a}m^2_{\chi}}{\pi m^2_V}, \ T^0_{++,++}=T^0_{--,--}\approx\frac{g^2_{\chi,a}m^2_{\chi}}{2\pi m^2_V}, \tag{1.5.68}$$

[10]The process $\chi\chi\to\chi\chi$ and $\chi\bar{\chi}\to\chi\bar{\chi}$ give the same result in the $S\to\infty$ limit.

Model	Process	$\lvert T^0\rvert^2$
0*-V	$\chi\chi^\dagger \to VV, \bar{q}q \to VV$	S^2
	$\chi\chi^\dagger \to \chi\chi^\dagger$	S^0
	$\bar{q}q \to \chi\chi^\dagger$	0
1/2-V, 1/2*-V	$\bar{\chi}\chi \to VV, \bar{q}q \to VV$	S^1
	$\bar{\chi}\chi \to \bar{\chi}\chi, \bar{q}q \to \bar{q}q$	S^0
	$\bar{q}q \to \bar{\chi}\chi$	S^0
1/2-$V^\pm$, 1/2*-$V^\pm$	$\bar{\chi}\chi \to V^\dagger V, \bar{q}q \to V^\dagger V$	S^1
	$\bar{q}q \to \bar{\chi}\chi$	S^0
1-S; 1*-S	$\chi\chi^\dagger \to \chi\chi^\dagger, SS \to \chi\chi^\dagger$	S^2
	$\bar{q}q \to \chi^\dagger\chi$	S^1
1-F, 1*-F	$\bar{q}q \to \chi^\dagger\chi, \bar{F}F \to \chi^\dagger\chi$	S^1
	$\bar{q}q \to \bar{F}F$	S^0
1-V ($\mathcal{V}_{1,2,3}$)	All	S^3

Table A.2: The simplified models containing a vector field, along with the tree-level $2 \to 2$ scattering processes containing at least one vector field. Assuming all vectors to be longitudinally polarized and restricting to the dominant $J = 0$ partial wave, the leading dependence on S is shown when $S \to \infty$ is the largest scale.

and for Majorana DM the extra u-channel diagram increases the leading term by a factor of 5/2. Including only the longitudinal modes:

$$T^0_{++,--} = T^0_{--,++} \approx \frac{3g^2_{\chi,a}m^2_\chi}{2\pi m^2_V},\ T^0_{++,++} = T^0_{--,--} \approx \frac{g^2_{\chi,a}m^2_\chi}{2\pi m^2_V}. \tag{1.5.69}$$

The quark self scattering results in the same bound as for Dirac DM, but with the coupling and mass changed appropriately.

(3) : Next we consider quark-DM scattering which is not tremendously different to the self-scattering since the dominant s-channel diagram is the same; only the axial couplings are present and the result is helicity suppressed,

$$T^0_{++,++} = T^0_{--,--} = T^0_{++,--} = T^0_{--,++} \approx \frac{g_{\chi,a}g_{f,a}m_f m_\chi}{2\pi m^2_V}, \tag{1.5.70}$$

leading to,

$$\beta_i\beta_f \sum_{\mu=\mu'=0} |T^0_{\mu\mu'}|^2 \approx \left[\frac{m^2_f m^2_\chi g^2_{\chi,a}g^2_{f,a}}{\pi^2 m^4_V}\right] \leq 1 \tag{1.5.71}$$

the results are identical for Majorana DM.

(4), (5) : Lastly we consider quark or DM scattering to vector $(\bar{q}q, \bar{\chi}\chi) \to VV$. Once again finds that only the axial couplings are present, alongside a helicity mass factor,

$$T^0_{++} = -T^0_{--} = -\frac{g^2_{\chi,a}\sqrt{S}m_\chi}{8\pi m^2_V}\left(2 + \log\left(\frac{S}{m^2_\chi}\right)\right) \tag{1.5.72}$$

and the resulting bound,

$$\beta_i\beta_f(|T^0_{++}|^2 + |T^0_{--}|^2) = \left[\frac{g^4_{\chi,a}m^2_\chi S}{2\pi^2 m^4_V}\right] \leq 1. \tag{1.5.73}$$

The result is identical for Majorana DM, and for quark initial states with the couplings and mass changed appropriately.

The two S independent bounds lead to,

$$m_V \gtrsim m_X g_{X,a}\sqrt{\frac{\pi}{2^{1/2}}}, \tag{1.5.74}$$

where $X = \chi, f$ (similar expressions arise for Majorana DM). Eq.(1.5.73) combines several parameters, but can be written as a lower bound on the mediator mass for fixed $m_\chi, g_{\chi,a}$

$$m_V \gtrsim 2^{9/4}\sqrt{\pi}\sqrt{m_\chi E}\left(\frac{g_{\chi,a}}{4\pi}\right) \tag{1.5.75}$$

which can be as high as $\sim$ few TeV for LHC energies and heavy DM. This bound is easily evaded at low energies.

Fermionic DM : 1/2-$V^\pm$

Three processes are relevant : (1) $\chi\bar{\chi} \to V^\dagger V$ (2) $q\bar{q} \to V^\dagger V$ and (3) $\bar{\chi}\chi \to \bar{q}q$. With the conventional factor of 1/2 in front of the Lagrangian couplings, the results are identical between Majorana and Dirac DM.

(1) : With mediators in the final state, we can have a $J = 0$ annihilation for the process $\chi\bar{\chi} \to V^\dagger V$ with a t-channel quark. The final state vector are longitudinally polarized and so only the $++, --$ initial state helicities are relevant [392],

$$\begin{aligned} T^0_{++} &= -\frac{\sqrt{S}}{8\pi m_V^2}\left(|g_a|^2(m_f + m_\chi) + m_f(g_a g_v^\dagger - g_v g_a^\dagger) + |g_v|^2(m_\chi - m_f)\right) \ , \\ T^0_{--} &= \frac{\sqrt{S}}{8\pi m_V^2}\left(|g_a|^2(m_f + m_\chi) + m_f(g_v g_a^\dagger - g_a g_v^\dagger) + |g_v|^2(m_\chi - m_f)\right) \ , \end{aligned} \tag{1.5.76}$$

leading to a bound

$$\beta_i\beta_f(|T^0_{++}|^2 + |T^0_{--}|^2) \approx \left[\frac{S m_\chi^2}{32\pi^2 m_V^4}\left(|g_a|^2 + |g_v|^2\right)^2\right] \leq 1. \tag{1.5.77}$$

(2) : The t-channel $\bar{q}q \to V^\dagger V$ process is almost identical (differing only in the replacement of $m_q \leftrightarrow m_\chi$ in Eq.(1.5.76), in the $m_q \to 0$ limit) and results in

$$\beta_i\beta_f(|T^0_{++}|^2 + |T^0_{--}|^2) \approx \left[\frac{S m_\chi^2}{32\pi^2 m_V^4}\left(|g_a|^2 - |g_v|^2\right)^2\right] \leq 1 \ . \tag{1.5.78}$$

(3) : The quark scattering to DM, $q\bar{q} \to \chi\bar{\chi}$ involves the t-channel exchange of the mediator, the restriction to longitudinal modes is accomplished via the replacement of the propagator

$$\frac{1}{t - m_V^2}\left(g^{\mu\nu} - \frac{k^\mu k^\nu}{m_V^2}\right) \to -\frac{k^\mu k^\nu}{m_V^2(t - m_V^2)} \tag{1.5.79}$$

assuming that the initial state mass in negligible then only the $++, --$ and $--, ++$ helicity amplitudes are non-zero in the $S \to \infty$ limit (up to logarithmic terms $\log(S/m_V^2)$ from the non-longitudinal propagator),

$$T^0_{++,--} = T^0_{--,++} = \frac{m_\chi^2\left(|g_a|^2 - |g_v|^2\right)}{8\pi m_V^2} + \mathcal{O}(S^{-1}), \tag{1.5.80}$$

from which the bound is,

$$\left[\frac{\left((m_f + m_\chi)^2|g_a|^2 - (m_f - m_\chi)^2|g_v|^2\right)^2}{32\pi^2 m_V^4}\right] \leq 1\ . \tag{1.5.81}$$

a factor of four is applied to the above expression for initial or final state Majorana fermions to to an extra u-channel diagram, but this is cancelled by the conventional factor of $1/2$ applied to the interaction term.

This provides an energy independent bound on the mediator mass,

$$m_V \gtrsim m_\chi \left(\left(\frac{|g_a|}{4\pi}\right)^2 - \left(\frac{|g_v|}{4\pi}\right)^2\right)^{1/2} \tag{1.5.82}$$

with chiral couplings, the bound is weaker and easily evaded. Since for this model $m_V \gtrsim m_\chi$ for stability of the DM this bound is redundant. Not so easily evaded is Eq.(1.5.77),

$$m_V \gtrsim \sqrt{m_\chi E}\left(\left(\frac{|g_a|}{4\pi}\right)^2 + \left(\frac{|g_v|}{4\pi}\right)^2\right)^{1/2} \tag{1.5.83}$$

which is far more constraining since $E > m_\chi$.

Scalar DM : 0*-V

There are several processes : (1) $\chi\chi \to \chi\chi$ (2) $\bar{q}q \to \chi^\dagger\chi$ (3) $\chi^\dagger\chi \to VV$ and (4) $\bar{q}q \to VV$. This model does not permit real scalar DM, and so χ is a complex field throughout.

(1) : The simplest process is DM self-scattering, $\chi\chi \to \chi\chi$ (or equivalently $\chi^\dagger\chi \to \chi^\dagger\chi$ which is four times smaller), since the scalar DM pair must have $\mu = \mu' = 0$; there are both s and t-channel vector exchanges, dominated by the s-channel.

The longitudinal modes contribute a factor of S on the numerator; thus overall the S dependence cancels in the $S \to \infty$ limit,

$$T^0_{00} = \frac{|g_\chi|^2}{4\pi}\left(1 - 2\log\left(\frac{S}{m_V^2}\right)\right) + \mathcal{O}(S^{-1}), \tag{1.5.84}$$

the logarithmic term causes very light mediators to violate unitarity for

$$\beta_i\beta_f|T^0_{00}|^2 \approx \frac{|g_\chi|^4}{16\pi^2}\left(1 - 2\log\left(\frac{S}{m_V^2}\right)\right)^2 \leq 1\ . \tag{1.5.85}$$

(2) : Next we can consider the $\bar{q}q \to \chi^\dagger\chi$ scattering. The DM final state has $\mu' = 0$. The $J = 0$ partial wave is absent since the quark bilinear couples only to $J = 1$ states; then we can have helicity $0, \pm 1$ in the initial state,

$$\begin{aligned}
T^0_{++} &= T^0_{--} = 0 \\
T^1_{++} &= -T^1_{--} = \frac{g_\chi g_v}{6\pi}\frac{m_q\sqrt{S-4m_\chi^2}}{S-m_V^2} \\
T^1_{+-} &= -T^1_{-+} = \frac{\sqrt{2}}{12\pi}\frac{g_\chi\sqrt{S-4m_\chi^2}}{S-m_V^2}\left(g_v\sqrt{S} + g_a\sqrt{S-4m_q^2}\right)
\end{aligned}$$

The S dependence cancels and leaves a bound on couplings which is negligible unless the couplings are near to their non-perturbative values.

(3) : Lastly, the vector mediator may appear in the final state. For $\chi^\dagger\chi \to VV$ via a t,u-channel diagram with an exchanged DM. The amplitude depends only on the DM parameters. In this case unitary can easily be violated since $\mathcal{M} \propto S$, for LHC energies only very heavy mediators can give a sensible model,

$$T^0_{00} = \frac{g_\chi^2}{4\pi}\left(1 - \frac{S}{2m_V^2}\right) + \mathcal{O}(S^{-1})\ , \tag{1.5.86}$$

leading to,

$$\beta_i\beta_f|T^0_{00}|^2 \approx \left[\frac{g_\chi^2}{4\pi}\left(1 - \frac{S}{2m_V^2}\right)\right]^2 \leq 1\ . \tag{1.5.87}$$

(4) : For the process $\bar{q}q \to VV$ the strong S dependence from the external vectors is compensated by a helicity suppression in the quark state,

$$T^0_{++} = T^0_{--} = \frac{g_a^2 m_q\sqrt{S}}{8\pi m_V^2}\left(2 + \log\left(\frac{S}{m_q^2}\right)\right)\ , \tag{1.5.88}$$

leading to

$$\beta_i\beta_f\left(|T^0_{++}|^2+|T^0_{--}|^2\right)\approx\left[\frac{g_a^4 S m_q^2}{2\pi^2 m_V^4}\right]\leq 1, \tag{1.5.89}$$

the $J=1$ amplitudes are zero at the same order in S.

The first bound, (1), gives $g_\chi \lesssim \sqrt{4\pi}$ which is below the conventional perturbative limit of 4π below which any loop expansion becomes meaningless. Process (3) bounds the mediator mass,

$$m_V \gtrsim 2\sqrt{2\pi}\left(\frac{g_\chi}{4\pi}\right)E \tag{1.5.90}$$

which requires an extremely heavy mediator to evade collider bounds. The last bound from (4),

$$m_V \gtrsim 2^{9/4}\pi^{1/2}\sqrt{m_f E}\left(\frac{g_a}{4\pi}\right) \tag{1.5.91}$$

is safely evaded due to the small quark mass, and weaker E dependence. For indirect searches of the highly nonrelativistic DM, $E\sim m_\chi$ and we bound $m_V \gtrsim m_\chi$ for couplings of $\mathcal{O}(1)$.

Vector DM : 1-S

There are three relevant processes involving the vector DM (1) $\chi\chi\to\chi\chi$ (2) $SS\to\chi^\dagger\chi$ and (3) $\bar{q}q\to\chi^\dagger\chi$.

(1) : The DM self scattering process contains four external vectors and the amplitude should scale as $\mathcal{M}\propto S$ if all four are longitudinally polarized, then only the $\mu=\mu'=0$ combination appears leading to a bound (this result is twice as large as $\chi^\dagger\chi\to\chi^\dagger\chi$)

$$T^0_{00}=\frac{g_\chi^2}{32\pi m_\chi^2}\left(4(m_\chi^2-m_S^2)-S\right),\ \beta_i\beta_f|T^0_{00}|^2\approx\frac{S^2}{m_\chi^4}\left(\frac{|g_\chi|^4}{1024\pi^2}\right)\leq 1, \tag{1.5.92}$$

if the DM is real, then the extra u-channel diagram leads to a cancellation of the dominant term, and

$$T^0_{00}=\frac{3g_\chi^2 m_V^2}{8\pi m_\chi^2},\ \beta_i\beta_f|T^0_{00}|^2\approx\left[\frac{9g_\chi^4 m_V^4}{64\pi^2 m_\chi^4}\right]\leq 1\ . \tag{1.5.93}$$

(2) : The mediator S may scatter with the DM, via a u,t-channel DM exchange (identical between real or complex DM), and ends up scaling in the same way as DM self-scattering due to the longitudinal modes of the mediating DM. This amplitude is very similar to DM self-scattering and thus also bounds only the DM mass,

$$T^0_{00} = -\frac{g_\chi^2 S}{32\pi m_\chi^2} + \mathcal{O}(\log S), \quad \beta_i\beta_f|T^0_{00}|^2 \approx \frac{S^2}{m_\chi^4}\left(\frac{|g_\chi|^4}{1024\pi^2}\right) \leq 1. \tag{1.5.94}$$

(3) : Lastly, quark-DM scattering with an s-channel scalar has a weaker dependence on S due to only two vectors in the process. Nonetheless, it provides a bounds which includes the quark scalar and pseudo-scalar couplings. Only the $++, --$ helicity combinations are necessary

$$T^0_{++} = -T^0_{--} = -\frac{\sqrt{S}}{16\pi m_\chi}\left(g_s + i g_p\right) \tag{1.5.95}$$

leading to,

$$\beta_i\beta_f(|T^0_{++}|^2 + |T^0_{--}|^2) \approx \left[\frac{S}{m_\chi^2}\left(\frac{|g_\chi|^2(g_s^2+g_p^2)}{128\pi^2}\right)\right] \leq 1 \tag{1.5.96}$$

there are no other tree-level, $2 \to 2$ processes containing the vector DM.

The strongest bound from process (1) or (2) leads to a lower DM mass

$$m_\chi \gtrsim 4\sqrt{2\pi}\left(\frac{g_\chi}{4\pi}\right)E \tag{1.5.97}$$

and so unless the couplings are very small, the DM mass must be large to compensate. The third bound may also be written as a lower limit on the DM mass,

$$m_\chi \gtrsim 2\sqrt{2}\pi E\left(\frac{g_\chi}{4\pi}\right)\left(\left(\frac{g_s}{4\pi}\right)^2 + \left(\frac{g_p}{4\pi}\right)^2\right)^{1/2} \tag{1.5.98}$$

which is slightly weaker than the previous bound if the quark couplings are below the perturbative limit. Thus, for low energy searches the model will evade unitarity as long as the DM mass exceeds the energy scale of the experiment.

Vector DM : 1-$F^\pm$, 1^*-$F^\pm$

The 1-$F^\pm$ model is an analogue to $1/2^*$-V with the roles of mediator and DM swapped (for complex vector DM the analogy is not possible). There are three processes (1) $\bar{q}q \to \chi\chi$, (2) $\bar{F}F \to \chi\chi$ and (3) $\bar{q}q \to \bar{F}F$.

(1) : For the $\bar{F}F \to \chi\chi$ process, $T^0_{++} = T^0_{--}$ and :

$$\beta_i\beta_f(|T^0_{++}|^2 + |T^0_{--}|^2) = \left[\frac{S\left((m_F+m_q)|g_a|^2 + (m_F-m_q)|g_v|^2\right)^2}{8\pi^2 m_\chi^4} + \mathcal{O}(S^0)\right] \leq 1 \ . \tag{1.5.99}$$

For complex DM, the result is four times smaller than above.

(2) : The process $\bar{q}q \to \chi\chi$ is identical to (1) under the replacement $m_q \leftrightarrow m_F$:

$$\beta_i\beta_f(|T^0_{++}|^2 + |T^0_{--}|^2) = \left[\frac{S\left((m_F+m_q)|g_a|^2 + (m_q-m_F)|g_v|^2\right)^2}{8\pi^2 m_\chi^4} + \mathcal{O}(S^0)\right] \leq 1 \ , \tag{1.5.100}$$

if the DM is complex the result is again a factor of 4 smaller.

(3) : Lastly, the process $\bar{q}q \to \bar{F}F$ is essentially identical to the quark-DM scattering in the 1/2-$V^\pm$ with appropriate mass replacements,

$$\begin{aligned} T^0_{++,++} &= T^0_{--,--} = \frac{|g_a|^2 - |g_v|^2}{4\pi}\log\left(\frac{S}{m_V^2}\right), \\ T^0_{++,--} &= T^0_{--,++} = \frac{(|g_a|^2(m_f+m_F)^2 - |g_v|^2(m_f-m_F)^2)}{8\pi m_V^2}, \end{aligned} \tag{1.5.101}$$

leading to,

$$\beta_i\beta_f|T^0_{00}|^2 \approx \left[\frac{(|g_a|^2(m_f+m_F^2)^2 - |g_v|^2(m_f-m_F)^2)^2}{32\pi^2 m_\chi^4}\right] \leq 1. \tag{1.5.102}$$

The dominant constraints comes from processes (1) and (2),

$$m_\chi \gtrsim 2^{7/4}\pi^{1/2}\sqrt{m_F E}\left(\left(\frac{|g_a|}{4\pi}\right)^2 + \left(\frac{|g_v|}{4\pi}\right)^2\right)^{1/2} \tag{1.5.103}$$

requiring heavy DM. For low energies when $E \sim m_\chi$ this requires the DM to be heavier than the mediator (unless very small couplings are present). The third bound leads to

$$m_\chi \gtrsim m_F\left(\left(\frac{|g_a|}{4\pi}\right)^2 + \left(\frac{|g_v|}{4\pi}\right)^2\right)^{1/2} \tag{1.5.104}$$

which is weaker than the first since by assumption $E > m_F$. Eq.(1.5.103) removes all the interesting parameter space at LHC energies since $m_\chi < m_F$ for stability of the DM; even at low energies Eq.(1.5.104) leaves only a small window of parameters at $m_\chi \sim m_F$, opening up as the couplings decrease.

Vector DM : 1-V

Quark self-scattering, $q\bar{q} \to q\bar{q}$, and $q\bar{q} \to VV$ are both present and identical to the 0-V and 1/2-V cases respectively, however the largest violations of unitarity come from processes where the external and internal states are all vectors, $\chi^\dagger\chi \to VV$ and $\chi^\dagger\chi \to \chi^\dagger\chi$. With the external vectors longitudinally polarized, $\mathcal{M} \propto S^2$, and this may be further enhanced by the mediating vector to $\mathcal{M} \propto S^3$, leading to unitarity violation over almost all of the phenomenologically interesting phase space.

It is likely that the massive states required to alleviate the violation of unitarity are light enough to impact the DD and ID signals. This model cannot be considered as a sensible approximation until such new physics is added. Thus the LHC bounds on the EFT [12] which appear in several of our plots should be treated with caution. The EFT operators would appear alongside other operators which alleviate the unitarity violation, and in doing so remove the dominant contribution to the signal, reducing the contraint.

These amplitudes are familiar in the SM, as massive gauge boson scattering; in those cases diagrams involving Higgs exchange cancel the unitarity violating amplitudes. This is enforced essentially by relations between SM couplings derived from spontaneous symmetry breaking; if a form of SSB is employed to give the DM and mediator their masses this could prevent unitary violation.

A.6 Conventions

The Dirac basis is defined as,

$$\gamma^0 = \begin{pmatrix} 1 & 0 \\ 0 & -1 \end{pmatrix} \ , \ \gamma^i = \begin{pmatrix} 0 & \sigma^i \\ -\sigma^i & 0 \end{pmatrix} \ , \ \gamma^5 = \begin{pmatrix} 0 & 1 \\ 1 & 0 \end{pmatrix} . \tag{1.6.105}$$

The Weyl basis is defined as,

$$\gamma^0 = \begin{pmatrix} 0 & 1 \\ 1 & 0 \end{pmatrix} \ , \ \gamma^i = \begin{pmatrix} 0 & -\sigma^i \\ \sigma^i & 0 \end{pmatrix} \ , \ \gamma^5 = \begin{pmatrix} 1 & 0 \\ 0 & -1 \end{pmatrix} . \tag{1.6.106}$$

One may transform between these bases (in terms of spinors χ and Dirac matrices γ) according to,

$$\gamma_{\rm D} = U\gamma_{\rm W}U^{-1}\ ,\ \chi_{\rm D} = U\chi_{\rm W},\quad U = \frac{1}{\sqrt{2}}\begin{pmatrix}1 & 1\\ 1 & -1\end{pmatrix}. \tag{1.6.107}$$

There is a further convention often used for which the γ^i and γ^5 pick up a global minus sign relative to the definitions given above, to implement this we can use the unitary matrix UU' where

$$U' = \begin{pmatrix}0 & 1\\ 1 & 0\end{pmatrix}. \tag{1.6.108}$$

A.7 Statistics

The central function in parameter inference is the Likelihood $\mathcal{L}(\theta_i)$ for an n-dimensional parameter space θ_i. In the frequentist approach $\mathcal{L} \in (0, 1)$ represents the probability of finding values θ_i, given the data, in an infinite ensemble of experiments. In the Bayesian approach, the likelihood is multiplied by *prior probability densities* or 'priors' $\pi(\theta_i)$ which represent the probability for a particular set of parameters in the absence of data (in other words they quantify our prior beliefs about the parameters), the resulting probability density function is called the *posterior pdf*, and represents the probability that measured parameters θ_i are equal to their true value.

The full posterior pdf can be reduced to a smaller number of dimensions, treating the unwanted dimensions as *nuisance parameters*. These are called *marginal posteriors*, for example the two dimensional posterior, integrated over all $n-2$ remaining parameters, would be given by

$$p(\theta_{n-1}, \theta_n) = \int \prod_i^n \mathcal{L}(\theta_i)\pi(\theta_i)d\theta_1 \cdots d\theta_{n-2}. \tag{1.7.109}$$

In our results, we restrict to 1D and 2D marginalized posteriors for visual clarity. The result of parameter inference may be to find a best fit value, or more generally to find a *credible region*, which as the name suggests is a region of phase space which has a particular probability of containing the true values of the parameters.

To calculate it one looks for the region R which contains a fixed $1-\alpha$ fraction of the total probability (assuming $p(x,y)$ is normalized to 1). This can be computed following [373] by finding a value of $p(x,y)$, $p_{\rm crit}$ such that

$$\int_{p>p_{\rm crit}} p(x,y)dxdy = 1-\alpha \ . \tag{1.7.110}$$

To work in the frequentist philosophy one requires the *profile likelihood*, this is the likelihood reduced in dimension by setting the value of the nuisance parameters equal to their maximum likelihood value, rather than marginalizing over them. This is done on a bin-by-bin basis, taking the maximum likelihood across all points within the bin. Then the frequentist confidence intervals can be found according to a maximum likelihood analysis (where the maximum likelihood is across all bins), then for each bin the log-likelihood must obey,

$$\log\left(\mathcal{L}\right) \geq \log\left(\mathcal{L}_{\rm max}\right) - \Delta\log\left(\mathcal{L}\right) \tag{1.7.111}$$

where $\Delta\log\left(\mathcal{L}\right)$ is a constant, which depends on the desired level of confidence. This method can have problems when the errors are not Gaussian[395].

The frequentist confidence regions are significantly larger in our MCMC results. This is because there are large regions of allowed parameter space which are equally likely with $\mathcal{L}\sim 1$ (this is expected from an analysis which does not aim to precisely fit the parameters); therefore any bins with allowed points in them become accepted, and not biased by whether they have few or many points. The resulting $1,2,3-\sigma$ contours are roughly equal (with containment probabilities around $\gtrsim 90\%$), and these confidence intervals approach the naive hit-or-miss treatment.

Then Bayesian credible regions are much more useful for understanding the allowed parameter space, taking into account the most probable regions. However, these regions are inevitably biased by the subjective choice of prior. There is no reason a priori to select a log-uniform distribution other than that it is as agnostic as possible[11]. Uniform priors are also taken to be agnostic, however both uniform and

[11] This is not quite true, since the Jeffry's prior is rigorously defined as the prior of most ignorance on a particular parameter. This is computationally expensive and not implemented in MultiNest.

log-uniform are not invariant under transformations, and transforming one into the other demonstrates that the log-uniform is biased towards lower values compared with uniform. Ideally, the choice of priors should have no effect on the result when there is no reason to prefer any particular value. In our results this is not the case, and the two priors can lead to dramatically different results. Fortunately, the log-uniform priors are consistently more conservative (uniform priors generally favour higher values across all variables), and we present all results with these. When parameters are most well constrained, we find much closer agreement between the prior choices. This discussion is visualized in Fig.A.1.

Credible Region in 1D : One simple way to find the credible interval is to look for an interval for which the mean lies in the centre (although in practice this may not be possible for very skewed distributions), this works for highly symmetric distributions, but not so well for the mixing angles and coupling posteriors which tend to be very peaked and asymmetrical. Another possibility is to look for the smallest possible interval, which contains the mode of the distribution if highly peaked. This gives more sensible results in our case, although one should bear in mind that these numbers can be subject to modification up to factor of 2, since the distributions are often rather flat.

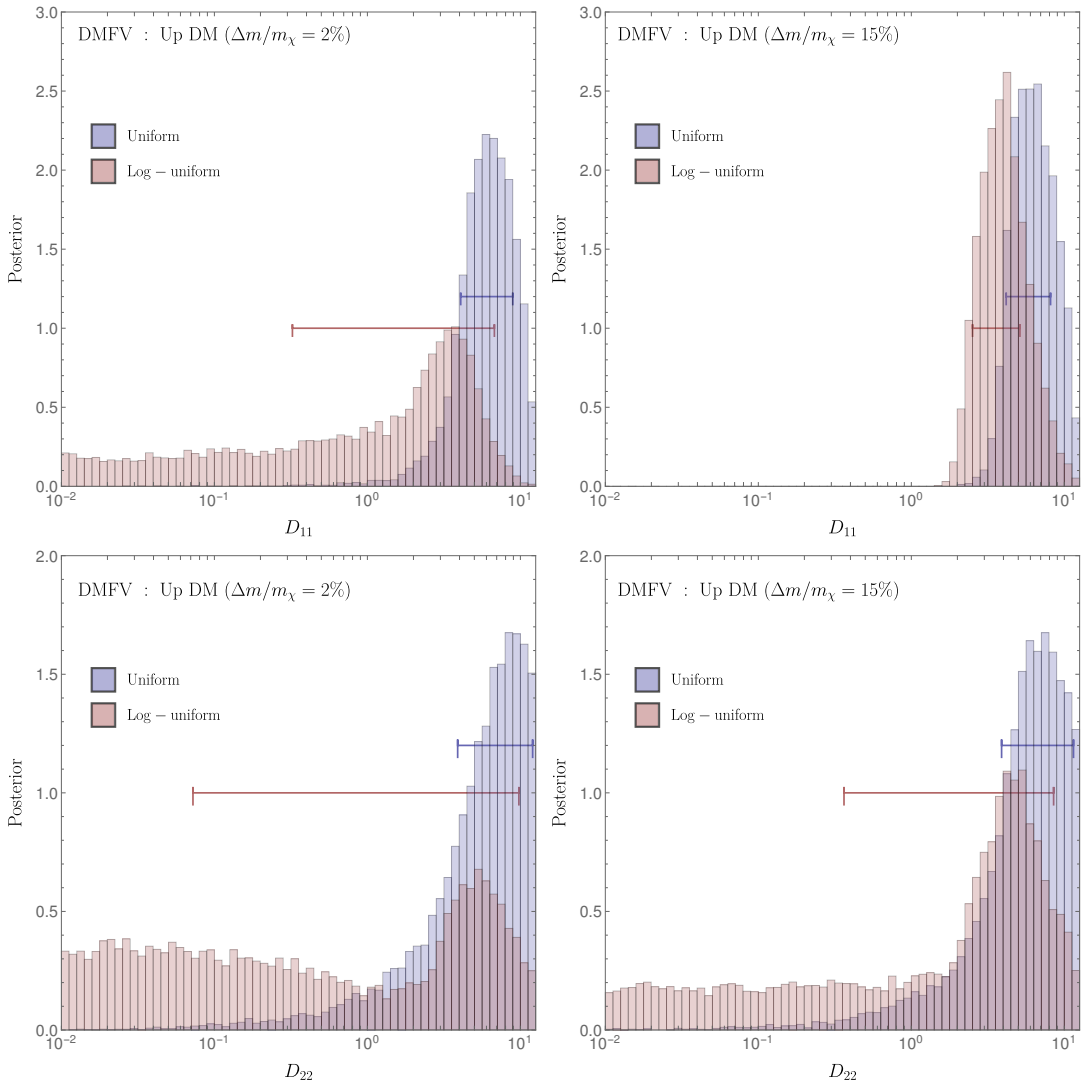

Figure A.1: The posterior distributions for D_{11}, D_{22} for both uniform and log-uniform priors, showing the credible 68% region (1σ). The log-uniform distribution favours low values compared to the uniform, and this can affect the results significantly. See Sec.7.9 for more details.

Appendix B

Annihilation Cross Sections

Within Chapter 5 the thermally averaged annihilation cross section, $\langle \sigma v \rangle$, of DM into fermion pairs is presented in simplified form. Here we present the complete expressions with full mass dependence, expanded up to $\mathcal{O}(v^2)$ in the DM velocity.

We present the expression in a manner appropriate for implementation numerically. To improve the readability we write the cross sections in the schematic form,

$$\sigma v = N_1 \frac{\sqrt{1 - m_f^2/m_\chi^2}}{P^2} \left(\sum_{i,j} g_i g_j S_{ij}(x,y) + N_2 v^2 \sum_{i,j} g_i g_j P_{ij}(x,y) \right), \tag{2.0.1}$$

where S_{ij} and P_{ij} are some polynomials in the dimensionless variables $x = m_f/m_{\rm MED}$ and $y = m_\chi/m_{\rm MED}$, $g_{i,j}$ are the couplings of the model in question, N_1, N_2, P are mass dependent functions. The EFT limit is thus given by $x, y \to 0$. Kinematically $y > x$, and for charged mediator models the DM is stabilized if $y < 1$, and this implies also $x < 1$. However, for neutral mediators x and y can take any values. For this reason we provide complete expressions for s-wave and p-wave annihilation[1].

Since all of the coloured mediators are colour triplets, the colour factor for the

[1] These expressions may be checked against those in [168]. We include several additional models, and for each model we allow complex couplings where possible; several operators in [168] are not hermitian, and one must be careful to take the correct limit to match our expressions.

cross section is extremely simple, in each case given by

$$\sum_{i,j} \delta_{ij} = N_c,$$

where i, j are the colour indices of the external quarks. The spin-averaging produces a factor of 1/4, 1/9 in the cross section for fermionic or vector DM respectively.

Writing amplitudes by hand for Majorana particles requires modified Feynman rules, which can be found in [396].

B.0.1 Fermionic DM

Dirac DM : Neutral Scalar Mediator

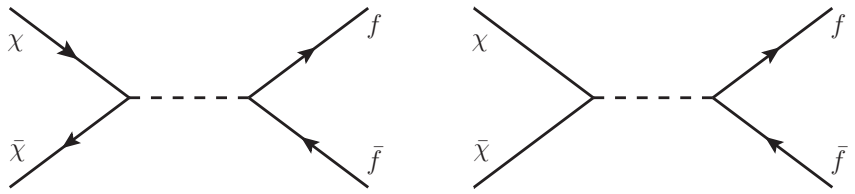

Figure B.1: Dirac (left) or Majorana (right) annihilation into fermions via a neutral scalar mediator ϕ.

A Dirac or Majorana fermion DM candidate annihilates via the diagram in Fig.B.1, giving a matrix element,

$$\mathcal{M} = \frac{1}{s - m_\phi^2} \bar{u}(p_3) \left[g_{f,s} + i g_{f,p} \gamma^5 \right] v(p_4) \; \bar{v}(p_2) \left[g_{\chi,s} + i g_{\chi,p} \gamma^5 \right] u(p_1). \tag{2.0.2}$$

Using this matrix element gives a cross section,

$$\sigma v = \frac{\sqrt{1 - x^2/y^2}}{2\pi m_\phi^2 \left(1 - 4y^2\right)^2} \Bigg[g_{f,p}^2 g_{\chi,p}^2 S_{p,p} + g_{f,s}^2 g_{\chi,p}^2 S_{s,p} + g_{f,p}^2 g_{\chi,s}^2 S_{p,s} + g_{f,s}^2 g_{\chi,s}^2 S_{s,s} - \frac{v^2}{8(1 - 4y^2)(y^2 - x^2)} \left(g_{f,p}^2 g_{\chi,p}^2 P_{p,p} + g_{f,s}^2 g_{\chi,p}^2 P_{s,p} + g_{f,p}^2 g_{\chi,s}^2 P_{p,s} + g_{f,s}^2 g_{\chi,s}^2 P_{s,s} \right) \Bigg], \tag{2.0.3}$$

where the s-wave terms are

$$S_{\mathrm{s,s}} = S_{\mathrm{p,s}} = 0 \; , \; S_{\mathrm{s,p}} = y^2 - x^2 \; , \; S_{\mathrm{p,p}} = y^2 \; , \tag{2.0.4}$$

and the p-wave terms are

$$\begin{aligned} P_{\rm s,s} &= 2(y^2-x^2)^2(4y^2-1)\ , \\ P_{\rm p,s} &= -2y^2(4y^2-1)\ , \\ P_{\rm s,p} &= \left(x^4(1-20y^2)+x^2(y^2+28y^4)-2y^4-8y^6\right)\ , \\ P_{\rm p,p} &= \left(x^2(y^2+12y^4)-2y^4-8y^6\right)\ . \end{aligned} \tag{2.0.5}$$

Dirac DM : Neutral Vector Mediator

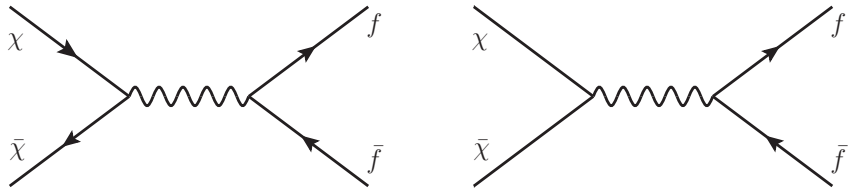

Figure B.2: Dirac (left) or Majorana (right) annihilation via a neutral vector mediator V.

A Dirac or Majorana fermion may annihilate via the exchange of a massive neutral vector boson as shown in Fig.B.2, this gives a matrix element,

$$\begin{aligned} \mathcal{M} = &\frac{1}{s-m_V^2}\bar{u}(p_3)\gamma^\mu\left[g_{f,v}+g_{f,a}\gamma^5\right]v(p_4)\ \bar{v}(p_2)\gamma^\nu\left[g_{\chi,v}+g_{\chi,a}\gamma^5\right]u(p_1) \\ &\times\left(g^{\mu\nu}-\frac{1}{m_V^2}(p_1+p_2)^\mu(p_1+p_2)^\nu\right)\ . \end{aligned} \tag{2.0.6}$$

The cross section may be written,

$$\begin{aligned} \sigma v = \frac{\sqrt{1-x^2/y^2}}{4\pi m_V^2\left(1-4y^2\right)^2}\Big[&g_{f,a}^2g_{\chi,a}^2S_{a,a}+g_{f,v}^2g_{\chi,a}^2S_{v,a}+g_{f,a}^2g_{\chi,v}^2S_{a,v}+g_{f,v}^2g_{\chi,v}^2S_{v,v} \\ &-\frac{v^2}{6(1-4y^2)(y^2-x^2)}\left(g_{f,a}^2g_{\chi,a}^2P_{a,a}+g_{f,v}^2g_{\chi,a}^2P_{v,a}+g_{f,a}^2g_{\chi,v}^2P_{a,v}+g_{f,v}^2g_{\chi,v}^2P_{v,v}\right)\Big]\ , \end{aligned} \tag{2.0.7}$$

where the s-wave terms are

$$S_{\rm v,v}=x^2+2y^2\ ,\ S_{\rm a,v}=2(y^2-x^2)\ ,\ S_{\rm a,a}=x^2(1-4y^2)^2, \tag{2.0.8}$$

and the p-wave terms are

$$
\begin{aligned}
P_{\mathrm{v,v}} &= -(x^4(68y^2-5)+4x^2(8y^4+y^2)-8(8y^6+y^4)) \ , \\
P_{\mathrm{v,a}} &= 4(4y^2-1)(x^4+x^2y^2-2y^4) \ , \\
P_{\mathrm{a,v}} &= 2(x^2-y^2)(x^2(68y^2-5)-4(8y^4+y^2)) \ , \\
P_{\mathrm{a,a}} &= -(4y^2-1)(x^4(144y^4-72y^2+17)+x^2(-96y^6+48y^4-22y^2)+8y^4) \ .
\end{aligned}
\tag{2.0.9}
$$

Dirac DM : Charged Scalar Mediator

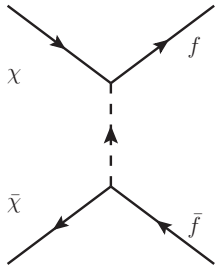

Figure B.3: Dirac DM exchanging a charged scalar mediator, ϕ. Majorana DM includes an extra u-channel diagram.

The matrix element is,

$$
\mathcal{M} = \frac{1}{t-m_{\mathrm{MED}}^2}\bar{u}(p_3)\left[g_s^\dagger + ig_p^\dagger\gamma^5\right]u(p_1)\ \bar{v}(p_2)\left[g_s+ig_p\gamma^5\right]v(p_4) \ , \tag{2.0.10}
$$

which leads to a cross section,

$$
\begin{aligned}
\sigma v = \frac{\sqrt{1-x^2/y^2}}{8\pi m_\phi^2\left(1-x^2+y^2\right)^2}\Bigg[&|g_p|^4S_{p,p}+|g_s|^4S_{s,s}+2|g_s|^2|g_p|^2S_{s,p} \\
&+\frac{v^2}{24(y^2-x^2)(1-x^2+y^2)^2}\left(|g_p|^4P_{p,p}+|g_s|^4P_{s,s}+2|g_s|^2|g_p|^2P_{s,p}\right)\Bigg],
\end{aligned}
\tag{2.0.11}
$$

where the s-wave terms are,

$$
S_{\mathrm{s,s}} = (x+y)^2, S_{\mathrm{s,p}} = (y^2-x^2) \ , \tag{2.0.12}
$$

and the p-wave terms are,

$$P_{\mathrm{s,s}} = (x+y)^2\Big(11x^6 - 2x^4\left(15y^2+11\right) + 16x^3y + x^2\left(27y^4+46y^2+11\right) - 16x\left(y^3+y\right) - 8y^2\left(y^4+3y^2-1\right)\Big),$$
$$P_{\mathrm{s,p}} = 2(y^2-x^2)\Big(7x^6 - 2x^4\left(11y^2+7\right) + x^2\left(23y^4+38y^2+7\right) - 8y^2\left(y^4+3y^2-1\right)\Big), \tag{2.0.13}$$

finally, note that $S_{\mathrm{p,p}}(x,y) = S_{\mathrm{s,s}}(x,-y)$ and $P_{\mathrm{p,p}}(x,y) = P_{\mathrm{s,s}}(x,-y)$.

Dirac DM : Charged Vector Mediator

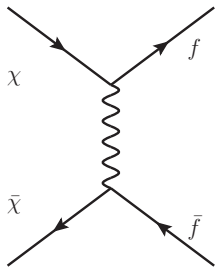

Figure B.4: Dirac DM exchanging a charged vector mediator, V^μ. Majorana DM includes an extra u-channel diagram.

If the vector mediator is exchanged in the t-channel as in Fig.B.4 the matrix element is

$$\mathcal{M} = \frac{1}{t-m_{\mathrm{MED}}^2}\bar{u}(p_3)\gamma_\mu\left[g_v^\dagger + g_a^\dagger\gamma^5\right]u(p_1)\;\bar{v}(p_2)\gamma_\nu\left[g_v + g_a\gamma^5\right]v(p_4) \times\left(g^{\mu\nu} - \frac{1}{m_V^2}(p_1-p_3)^\mu(p_1-p_3)^\nu\right). \tag{2.0.14}$$

The cross section, σv, can be written as Eq.(2.0.11),

$$\sigma v = \frac{N_c\sqrt{1-x^2/y^2}}{8\pi m_V^2\left(1-x^2+y^2\right)^2}\Big[|g_a|^4S_{a,a} + |g_v|^4S_{v,v} + 2|g_v|^2|g_a|^2S_{a,v} + \frac{v^2}{192(y^2-x^2)(1-x^2+y^2)^2}\left(|g_a|^4P_{a,a} + |g_v|^4P_{v,v} + 2|g_v|^2|g_a|^2P_{a,v}\right)\Big], \tag{2.0.15}$$

with,

$$
\begin{aligned}
S_{\mathrm{v,v}} = \Big(& x^6 - 2x^5 y - x^4 y^2 + 4x^3 \left(y^3 + y\right) - x^2 \left(y^4 + 4y^2 - 2\right) \\
& - 2xy \left(y^4 + 2y^2 + 2\right) + y^2 \left(y^4 + 4y^2 + 6\right) \Big), \qquad (2.0.16) \\
S_{\mathrm{a,v}} = & -(x^2 - y^2)\Big(x^4 - 2x^2(y^2 + 2) + 4y^2 + y^4 + 2\Big), \\
P_{\mathrm{v,v}} = \Big(& 11x^{12} - 22x^{11} y - x^{10} \left(41y^2 + 46\right) + 8x^9 y \left(13y^2 + 11\right) \\
& + x^8 \left(46y^4 + 136y^2 + 105\right) - 2x^7 y \left(98y^4 + 164y^2 + 85\right) \\
& + x^6 \left(6y^6 - 108y^4 - 269y^2 - 116\right) + 4x^5 y \left(46y^6 + 114y^4 + 117y^2 + 29\right) \\
& + x^4 \left(-49y^8 - 32y^6 + 231y^4 + 332y^2 + 46\right) \\
& - 2x^3 y \left(43y^8 + 140y^6 + 213y^4 + 122y^2 + 6\right) \\
& + x^2 y^2 \left(35y^8 + 74y^6 - 75y^4 - 232y^2 - 86\right) + 16xy^5 \left(y^6 + 4y^4 + 8y^2 + 8\right) \\
& - 8y^4 \left(y^8 + 3y^6 - y^4 - 2y^2 - 8\right) \Big), \\
P_{\mathrm{a,v}} = \Big(& - 7x^{12} + x^{10}(26 + 43y^2) - x^8(61 + 128y^2 + 110y^4) \\
& - 8y^6(-6 - y^2 + 3y^4 + y^6) + x^6(72 + 175y^2 + 252y^4 + 150y^6) \\
& + x^2 y^2(30 - 24y^2 + 37y^4 + 122y^6 + 47y^8) - x^4(30 + 96y^2 + 159y^4 + 248y^6 + 115y^8) \Big),
\end{aligned}
$$

where $S_{\mathrm{a,a}}(x, y) = S_{\mathrm{v,v}}(x, -y)$ and $P_{\mathrm{a,a}}(x, y) = P_{\mathrm{v,v}}(x, -y)$.

Majorana DM : Charged Scalar Mediator

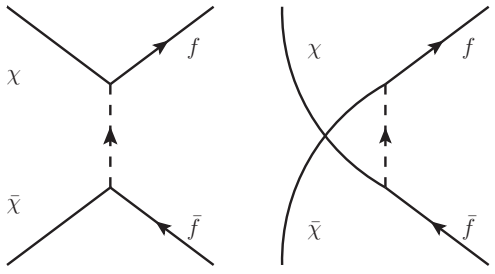

Figure B.5: Majorana DM and charged scalar mediator annihilation involving both t-channel and u-channel

The matrix element is,

$$\mathcal{M} = \frac{1}{t - m_{\rm MED}^2}\bar{u}(p_3)\left[g_s^\dagger + ig_p^\dagger\gamma^5\right]u(p_1)\;\bar{v}(p_2)\left[g_s + ig_p\gamma^5\right]v(p_4) - \frac{1}{u - m_{\rm MED}^2}\bar{u}(p_3)\left[g_s^\dagger + ig_p^\dagger\gamma^5\right]u(p_2)\;\bar{v}(p_1)\left[g_s + ig_p\gamma^5\right]v(p_4), \tag{2.0.17}$$

the cross section can be written as Eq.(2.0.11) with,

$$\sigma v = \frac{\sqrt{1 - x^2/y^2}}{8\pi m_\phi^2\left(1 - x^2 + y^2\right)^2}\Bigg[|g_p|^4 S_p + |g_s|^4 S_s + \left((g_p^\dagger)^2 g_s^2 + (g_s^\dagger)^2 g_p^2\right) S_{sp} + \frac{v^2}{24(y^2 - x^2)(1 - x^2 + y^2)^2}\left(|g_p|^4 P_p + |g_s|^4 P_s + \left((g_p^\dagger)^2 g_s^2 + (g_s^\dagger)^2 g_p^2\right) P_{sp} + |g_s|^2|g_p|^2 P'_{sp}\right)\Bigg], \tag{2.0.18}$$

where,

$$S_{\rm s} = (x+y)^2,\;\; S_{\rm sp} = (y^2 - x^2), \tag{2.0.19}$$

$$P_{\rm s} = (x+y)^2\Big(23x^6 - 8x^5 y - 2x^4\left(21y^2 + 23\right) + 16x^3 y\left(y^2 + 3\right) + x^2\left(15y^4 + 62y^2 + 23\right) - 8xy\left(y^4 + 6y^2 + 5\right) + 4y^2\left(y^4 - 4y^2 + 5\right)\Big),$$

$$P_{\rm sp} = \Big(x^8 + x^6\left(9y^2 - 2\right) + x^4\left(-33y^4 - 12y^2 + 1\right) + 5x^2y^2\left(7y^4 + 6y^2 - 1\right) - 4y^4\left(3y^4 + 4y^2 - 1\right)\Big),$$

$$P'_{\rm sp} = 8\Big(x^8 - x^6(7y^2 + 2) + x^4(15y^4 + 4y^2 + 1) - x^2y^2(13y^4 + 2y^2 + 5) + 4(y^8 + y^4)\Big),$$

finally $S_p(x,y) = S_s(x,-y)$ and $P_p(x,y) = P_s(x,-y)$.

Majorana DM : Charged Vector Mediator

Majorana DM can annihilate via a t-channel charged vector mediator, as in Fig.B.6, and picks up a u-channel term from the crossing of the DM legs,

$$\mathcal{M} = \frac{1}{t - m_{\rm MED}^2}\bar{u}(p_3)\gamma_\mu\left[g_v^\dagger + g_a^\dagger\gamma^5\right]u(p_1)\;\bar{v}(p_2)\gamma_\nu\left[g_v + g_a\gamma^5\right]v(p_4) \times\left(g^{\mu\nu} - \frac{1}{m_{\rm MED}^2}(p_1 - p_3)^\mu(p_1 - p_3)^\nu\right) - \frac{1}{u - m_{\rm MED}^2}\bar{u}(p_3)\gamma_\mu\left[g_v^\dagger + g_a^\dagger\gamma^5\right]u(p_2)\;\bar{v}(p_1)\gamma_\nu\left[g_v + g_a\gamma^5\right]v(p_4) \times\left(g^{\mu\nu} - \frac{1}{m_{\rm MED}^2}(p_2 - p_3)^\mu(p_2 - p_3)^\nu\right). \tag{2.0.20}$$

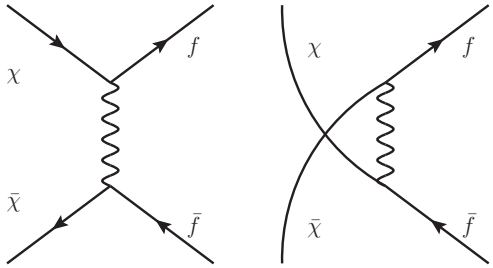

Figure B.6: Majorana DM and charged vector mediator, V^μ, annihilation involving both t-channel and u-channel.

The cross section can be written as Eq.(2.0.15) with

$$S_{\mathrm{v,v}} = \left(x^3 - x^2 y - x\left(y^2+2\right) + y\left(y^2+4\right)\right)^2, \tag{2.0.21}$$

$$S_{\mathrm{a,v}} = \left(x^6 - x^4\left(3y^2+4\right) + x^2\left(3y^4+12y^2+4\right) - y^2\left(y^2+4\right)^2\right),$$

$$\begin{aligned} P_{\mathrm{a,a}} = \Big(& 23x^{12} + 54x^{11}y - x^{10}\left(49y^2+162\right) - 40x^9 y\left(5y^2+8\right) \\ & + x^8\left(-30y^4+456y^2+419\right) + 2x^7 y\left(130y^4+568y^2+311\right) \\ & + x^6\left(150y^6-348y^4-1139y^2-444\right) - 4x^5 y\left(30y^6+372y^4+459y^2+101\right) \\ & + x^4\left(-125y^8-72y^6+1009y^4+1164y^2+164\right) \\ & + 2x^3 y\left(-5y^8+424y^6+903y^4+458y^2+24\right) \\ & + x^2y^2\left(27y^8+174y^6-277y^4-816y^2-328\right) + 16xy^5\left(y^6-11y^4-37y^2-32\right) \\ & + 4y^4\left(y^8-12y^6-3y^4+24y^2+56\right)\Big), \end{aligned}$$

$$\begin{aligned} P_{\mathrm{a,v}} = \Big(& 3x^{12} - x^{10}\left(43y^2+58\right) + x^8\left(170y^4+404y^2+47\right) \\ & - x^6\left(310y^6+1040y^4+437y^2-68\right) + x^4\left(295y^8+1276y^6+1161y^4-4y^2-60\right) \\ & - x^2y^2\left(143y^8+758y^6+1199y^4+352y^2-120\right) \\ & + 4y^4\left(7y^8+44y^6+107y^4+72y^2-24\right)\Big), \end{aligned}$$

where $S_{\mathrm{a,a}}(x,y) = S_{\mathrm{v,v}}(x,-y)$ and $P_{\mathrm{a,a}}(x,y) = P_{\mathrm{v,v}}(x,-y)$.

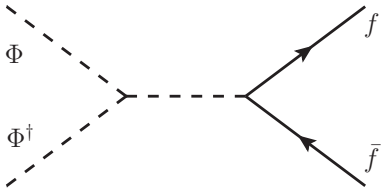

Figure B.7: Scalar DM exchanging a scalar mediator.

B.0.2 Scalar DM

Scalar DM : Scalar Mediator

A real or complex scalar can exchange a neutral scalar mediator with a pair of fermions as shown in Fig.B.7. The matrix element is very simple,

$$\mathcal{M} = \frac{1}{s - m_{\rm MED}^2} \Lambda g_\chi \bar{u}(p_3)(g_s + i g_p \gamma^5) v(p_4), \tag{2.0.22}$$

then the cross section may be written as,

$$\sigma v = \frac{g_\chi^2 \Lambda^2 \sqrt{1 - x^2/y^2}}{4\pi m_\phi^4 (1 - 4y^2)^2} \left[g_s^2 S_{ss} + g_p^2 S_{pp} + \frac{v^2}{8(1 - 4y^2)} \left(g_s^2 P_{ss} + g_p^2 P_{pp} \right) \right]. \tag{2.0.23}$$

The interference terms $\propto g_s g_p$ are zero, the remaining functions are,

$$S_{ss} = 1 - x^2/y^2, \;\; S_{pp} = 1, \tag{2.0.24}$$

and for the p-wave contributions

$$\begin{aligned} P_{ss} &= \frac{1}{y^2} \left(x^2(3 - 28y^2) + 16y^4 \right), \\ P_{pp} &= \frac{1}{y^2 - x^2} \left(x^2(1 - 20y^2) + 16y^4 \right). \end{aligned} \tag{2.0.25}$$

Scalar DM : Vector Mediator

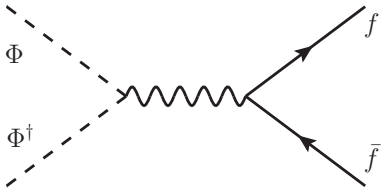

Figure B.8: Scalar DM exchanging a neutral vector mediator.

Scalar (both real and complex) DM can annihilate to fermions via a neutral vector mediator, as shown in Fig.B.8, which leads to a matrix element,

$$\mathcal{M} = \frac{g_\chi}{s - m^2_{\rm MED}} \bar{u}(p_3)\gamma_\mu(g_v + g_a\gamma^5)v(p_4)\,(p_1^\nu - p_2^\nu) \times \left(g^{\mu\nu} - \frac{(p_1+p_2)^\mu(p_1+p_2)^\nu}{m^2_{\rm MED}}\right). \tag{2.0.26}$$

The cross section is purely p-wave and can be written,

$$\sigma v = v^2 g_\chi^2 \frac{\sqrt{1-x^2/y^2}}{6\pi m^2_{\rm MED}(1-4y^2)^2}\left(g_v^2 P_v + g_a^2 P_a\right), \tag{2.0.27}$$

with

$$P_v = x^2 + 2y^2,\ P_a = 2(y^2 - x^2). \tag{2.0.28}$$

Scalar DM : Fermion Mediator

A real scalar DM annihilates via both t and u channel diagrams, whereas a complex DM annihilate only via t-channel, as shown in Fig.B.9

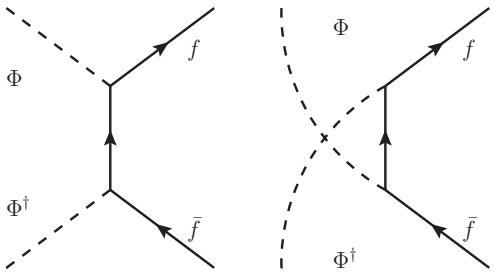

Figure B.9: A scalar DM exchanging a charged fermion mediator in the t or u-channel. Complex scalar annihilate via t-channel, real scalar annihilate via both t and u-channels.

Complex DM

$$\mathcal{M} = \frac{1}{t - m^2_{\rm MED}}\bar{u}(p_3)\left[\left(g_s^\dagger + ig_p^\dagger\gamma^5\right)\left(\not{p}_3 - \not{p}_1 + m_{\rm MED}\right)\left(g_s + ig_p\gamma^5\right)\right]v(p_4). \tag{2.0.29}$$

The cross section is written,

$$\sigma v = \frac{\sqrt{1-x^2/y^2}}{4\pi m_\chi^2(1-x^2+y^2)^2}\Big[\left(|g_s|^4 S_{\rm ss} + 2|g_s|^2|g_p|^2 S_{\rm sp} + |g_p|^4 S_{\rm pp} + ((g_a^\dagger)^2 g_v^2 + (g_v^\dagger)^2 g_a^2)S'_{sp}\right) + \frac{v^2}{24(1-x^2+y^2)^2}\left(|g_s|^4 P_{\rm ss} + 2|g_s|^2|g_p|^2 P_{\rm sp} + |g_p|^4 P_{\rm pp} + ((g_a^\dagger)^2 g_v^2 + (g_v^\dagger)^2 g_a^2)P'_{sp}\right)\Big], \tag{2.0.30}$$

with,

$$S_{\rm ss} = (x+1)^2(y^2-x^2), \tag{2.0.31}$$

$$S_{\rm sp} = x^2(1+y^2-x^2),$$

$$S'_{\rm sp} = y^2, \tag{2.0.32}$$

$$\begin{aligned}
P_{\rm pp} = \Big[&9x^8 - 18x^7 - x^6\left(32y^2+9\right) + 4x^5\left(13y^2+9\right) + x^4\left(41y^4+36y^2-9\right) \\
&- 2x^3\left(25y^4+50y^2+9\right) + x^2\left(-22y^6-35y^4+44y^2+9\right) \\
&+ 16xy^4\left(y^2+4\right) + 4y^4\left(y^4+2y^2-5\right)\Big], \\
P_{\rm sp} = \frac{1+y^2-x^2}{x^2-y^2}\Big[&9x^8 - 18x^6\left(2y^2+1\right) + x^4\left(53y^4+50y^2+9\right) \\
&- 2x^2y^2\left(17y^4+20y^2+3\right) + 8\left(y^8+y^6\right)\Big], \\
P'_{\rm sp} = -\frac{y^2}{x^2-y^2}\Big[&4x^8 - x^6(16y^2+11) + 2x^4(12y^4+15y^2+5) \\
&- x^2(16y^6+27y^4+38y^2+2) + 4y^4(y^4+2y^2+7)\Big],
\end{aligned} \tag{2.0.33}$$

with $S_{\rm pp}(x,y) = S_{\rm ss}(-x,y)$ and $P_{\rm pp}(x,y) = P_{\rm ss}(-x,y)$.

Real DM

$$\begin{aligned}
\mathcal{M} = &\frac{1}{t-m^2_{\rm MED}}\bar{u}(p_3)\left[\left(g_s^\dagger + ig_p^\dagger\gamma^5\right)\left(\not{p}_3 - \not{p}_1 + m_{\rm MED}\right)\left(g_s + ig_p\gamma^5\right)\right]v(p_4) \\
&+ \frac{1}{u-m^2_{\rm MED}}\bar{u}(p_3)\left[\left(g_s^\dagger + ig_p^\dagger\gamma^5\right)\left(\not{p}_3 - \not{p}_2 + m_{\rm MED}\right)\left(g_s + ig_p\gamma^5\right)\right]v(p_4),
\end{aligned} \tag{2.0.34}$$

and cross section,

$$\begin{aligned}
\sigma v = &\frac{\sqrt{1-x^2/y^2}}{\pi m_\chi^2(1-x^2+y^2)^2}\Big[\left(|g_s|^4 S_{\rm ss} + 2|g_s|^2|g_p|^2 S_{\rm sp} + |g_p|^4 S_{\rm pp} + ((g_a^\dagger)^2 g_v^2 + (g_v^\dagger)^2 g_a^2)S'_{sp}\right) \\
&+ \frac{v^2}{24(1-x^2+y^2)^2}\left(|g_s|^4 P_{\rm ss} + 2|g_s|^2|g_p|^2 P_{\rm sp} + |g_p|^4 P_{\rm pp} + ((g_a^\dagger)^2 g_v^2 + (g_v^\dagger)^2 g_a^2)P'_{sp}\right)\Big],
\end{aligned} \tag{2.0.35}$$

the S are identical to the complex scalar

$$P_{\rm ss} = (x+1)\Big[9x^7 + 9x^6 - 2x^5\left(17y^2+9\right) - 2x^4\left(13y^2+9\right) + x^3\left(41y^4+50y^2+9\right) + x^2\left(25y^4+42y^2+9\right) - 16xy^4\left(y^2+2\right) - 8y^4(y^2+3)\Big],$$

$$P_{\rm sp} = \frac{x^2}{x^2-y^2}\Big[9x^8 - x^6\left(43y^2+27\right) + x^4\left(75y^4+100y^2+27\right) - x^2\left(57y^6+119y^4+63y^2+9\right) + 2y^2(8y^6+23y^4+18y^2+3)\Big],$$

$$P'_{\rm sp} = \frac{y^2}{y^2-x^2}\Big[3x^6 - 2x^4(7y^2+3) + x^2(19y^4+30y^2+2) - 8y^4(y^2+3)\Big], \quad (2.0.36)$$

with $S_{\rm pp}(x,y) = S_{\rm ss}(-x,y)$ and $P_{\rm pp}(x,y) = P_{\rm ss}(-x,y)$.

B.0.3 Vector DM

Vector DM : Scalar Mediator

Vector DM can annihilate through a scalar mediator, as in Fig.B.10, with matrix element,

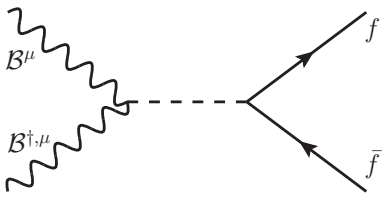

Figure B.10: Vector DM exchanging a neutral scalar mediator.

$$\mathcal{M} = \frac{g_\chi \Lambda}{s - m^2_{\rm MED}} \bar{u}(p_3)(g_s + i g_p \gamma^5) v(p_4) \varepsilon(p_1)\cdot\varepsilon(p_2), \quad (2.0.37)$$

and cross section,

$$\sigma v = \frac{g_\chi^2 \Lambda^2 \sqrt{1-x^2/y^2}}{12\pi m^4_{\rm MED} y^2 (1-4y^2)^2}\left[\left(g_s^2 S_{\rm ss} + g_p^2 S_{\rm pp}\right) - \frac{v^2}{24(1-4y^2)(y^2-x^2)}\left(g_s^2 P_{\rm ss} + g_p^2 P_{\rm pp}\right)\right], \quad (2.0.38)$$

where Λ is the mass scale associated to the DM-mediator vertex, $S_{\rm ss} = y^2 - x^2$, $S_{\rm pp} = y^2$ and,

$$P_{\rm ss} = (y^2 - x^2)\left[x^2(52y^2 - 1) - 8(2y^4 + y^2)\right],$$
$$P_{\rm pp} = y^2\left[x^2(5 + 28y^2) - 8y^2(1 + 2y^2)\right] \ . \tag{2.0.39}$$

The interference terms are both zero $P_{\rm sp} = S_{\rm sp} = 0$.

Vector DM : Vector Mediator

The three possible Lorentz contractions of the triple vector vertex all lead to amplitudes as in Fig.B.11,

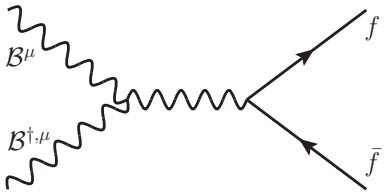

Figure B.11: Vector DM exchanging a neutral vector mediator.

The coupling structure $B^{\mu,\dagger}\partial_\mu B^\nu$ leads to,

$$\mathcal{M} = \frac{1}{s - m^2_{\rm MED}}\bar{u}(p_3)\gamma^\mu(g_v + g_a\gamma^5)v(p_4)\left(g^{\mu\nu} - \frac{1}{m^2_{\rm MED}}(p_1 + p_2)^\mu(p_1 + p_2)^\nu\right)\varepsilon_\sigma(p_1)\varepsilon_\rho(p_2)$$
$$\times\left((\mathrm{Re}(g_\chi) + i\mathrm{Im}(g_\chi))g^{\nu\sigma}p_1^\rho + (\mathrm{Re}(g_\chi) - i\mathrm{Im}(g_\chi))g^{\nu\rho}p_2^\sigma\right). \tag{2.0.40}$$

In this case there is no s-wave term, the p-wave term is,

$$\sigma v = v^2(\mathrm{Re}(g_\chi)^2 + 2\mathrm{Im}(g_\chi)^2)\frac{\sqrt{1 - x^2/y^2}}{27\pi m_V^2(1 - 4y^2)^2}\left(g_v^2 P_{\rm vv} + g_a^2 P_{\rm aa}\right), \tag{2.0.41}$$

with,

$$P_{\rm vv} = 2y^2 + x^2,\ P_{\rm aa} = 2y^2 - 2x^2. \tag{2.0.42}$$

The coupling structure $B^\mu\partial^\nu B^\dagger_\mu$ leads to,

$$\mathcal{M} = \frac{1}{s - m^2_{\rm MED}}\bar{u}(p_3)\gamma^\mu(g_v + g_a\gamma^5)v(p_4)\left(g^{\mu\nu} - \frac{1}{m^2_{\rm MED}}(p_1 + p_2)^\mu(p_1 + p_2)^\nu\right)$$
$$\times\left(\mathrm{Re}(g_\chi)(p_1 + p_2) + i\mathrm{Im}(g_\chi)(p_1 - p_2)\right)^\nu\varepsilon(p_1)\cdot\varepsilon(p_2). \tag{2.0.43}$$

In this case there is no s-wave term, the p-wave term is

$$\sigma v = \frac{\sqrt{1-x^2/y^2}}{3\pi m_V^2}\Bigg[\mathrm{Re}(g_\chi)^2 g_a^2(x^2) \tag{2.0.44}$$

$$+ \frac{v^2}{12(1-4y^2)^2(y^2-x^2)}\left(\mathrm{Re}(g_\chi)^2 g_a^2 P_{r,a} + \mathrm{Im}(g_\chi)^2 g_v^2 P_{i,v} + \mathrm{Im}(g_\chi)^2 g_a^2 P_{i,a}\right)\Bigg], \tag{2.0.45}$$

with,

$$\begin{aligned} P_{\mathrm{r,v}} &= 0, \\ P_{\mathrm{r,a}} &= \frac{1}{2}x^2(8y^2-5x^2)(1-4y^2)^2, \\ P_{\mathrm{i,v}} &= (2y^4 - x^2y^2 - x^4), \\ P_{\mathrm{i,a}} &= 2(x^2-y^2)^2. \end{aligned} \tag{2.0.46}$$

Finally, the coupling structure $\epsilon^{\mu\nu\sigma\rho}B_\mu^\dagger \partial_\nu B_\sigma$ leads to,

$$\mathcal{M} = \frac{1}{s-m_{\mathrm{MED}}^2}\bar{u}(p_3)\gamma^\tau(g_v+g_a\gamma^5)v(p_4)\left(g^{\tau\mu} - \frac{1}{m_{\mathrm{MED}}^2}(p_1+p_2)^\tau(p_1+p_2)^\mu\right)$$

$$\times\, \epsilon_{\mu\nu\sigma\rho}\left(\mathrm{Re}(g_\chi)(p_1+p_2)^\nu + i\mathrm{Im}(g_\chi)(p_1-p_2)^\nu\right)\varepsilon^\sigma(p_1).\varepsilon^\rho(p_2). \tag{2.0.47}$$

The s-wave term appears only for imaginary couplings

$$\sigma v = \frac{2\sqrt{1-x^2/y^2}}{9\pi m_{\mathrm{MED}}^2(1-4y^2)^2}\Bigg[\mathrm{Im}(g_\chi)^2\left(g_v^2 S_{i,v} + g_a^2 S_{i,a}\right)$$

$$+ \frac{v^2}{24(1-4y^2)(y^2-x^2)}\left(\mathrm{Re}(g_\chi)^2 g_a^2 P_{r,a} + \mathrm{Im}(g_\chi)^2 g_v^2 P_{i,v} + \mathrm{Im}(g_\chi)^2 g_a^2 P_{i,a}\right)\Bigg], \tag{2.0.48}$$

with,

$$\begin{aligned} S_{\mathrm{i,v}} &= x^2 + 2y^2, \\ S_{\mathrm{i,a}} &= 2(y^2-x^2), \\ P_{\mathrm{r,a}} &= 6(x^2-y^2)x^2(4y^2-1)^3, \\ P_{\mathrm{i,v}} &= -(x^4(44y^2+1) + 2x^2y^2(4y^2+5) - 4y^4(4y^2+5)), \\ P_{\mathrm{i,a}} &= 2(x^2-y^2)(x^2(1+44y^2) - 2y^2(4y^2+5)). \end{aligned} \tag{2.0.49}$$

Vector DM : Fermion Mediator

When the mediator is a charged fermion, it matters whether the DM is real or complex, as shown in Fig.B.12, since a real DM has an extra diagram. We consider these two cases separately.

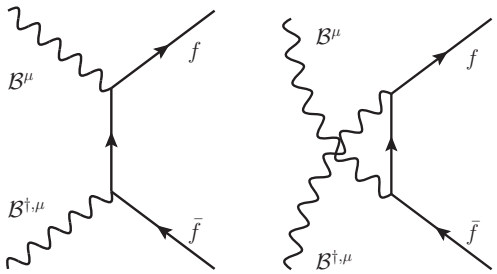

Figure B.12: A vector DM exchanging a charged fermion mediator in the t or u-channel. Complex vector annihilate via t-channel, real vectors annihilate via both t and u-channels.

Complex DM

Complex vector DM scatters through either a t-channel or u-channel diagram,

$$\mathcal{M} = \frac{1}{t - m_{\text{MED}}^2}\bar{u}(p_3)\left[\gamma^\mu\left(g_v^\dagger + g_a^d a g\gamma^5\right)\left(\not{p}_3 - \not{p}_1 + m_{\text{MED}}\right)\gamma^\nu\left(g_v + g_a\gamma^5\right)\right]v(p_4)\;\varepsilon_\mu(p_1)\varepsilon_\nu(p_2). \tag{2.0.50}$$

We will assume for simplicity that $g_{a,v}$ are both real, or both imaginary. Then the cross section may be written,

$$\sigma v = \frac{\sqrt{1 - x^2/y^2}}{36\pi m_\chi^2(1 - x^2 + y^2)^2}\Bigg[\left(|g_v|^4 S_{\text{vv}} + 2|g_v|^2|g_a|^2 S_{\text{av}} + |g_a|^4 S_{\text{aa}} + ((g_a^\dagger)^2 g_v^2 + (g_v^\dagger)g_a^2)S'_{av}\right) + \frac{v^2}{24(1 - x^2 + y^2)^2}\left(|g_v|^4 P_{\text{vv}} + 2|g_v|^2|g_a|^2 P_{\text{av}} + |g_a|^4 P_{\text{aa}} + ((g_a^\dagger)^2 g_v^2 + (g_v^\dagger)g_a^2)P'_{av}\right)\Bigg], \tag{2.0.51}$$

with

$$
\begin{aligned}
S_{\rm vv} &= (y^2-x^2)(5x^2-6x+4y^2+5), \qquad (2.0.52)\\
S_{\rm av} &= -(x^4+x^2(7y^2-9)-8y^4),\\
S'_{\rm av} &= 4x^4-4x^2(2y^2+1)+y^2(4y^2-5),\\
P_{\rm vv} &= \Big[53x^8-78x^7-x^6\left(188y^2+61\right)+12x^5\left(17y^2+13\right)+x^4\left(237y^4+300y^2-37\right)\\
&\quad -6x^3\left(29y^4+74y^2+13\right)+x^2\left(-122y^6-327y^4+80y^2+45\right)\\
&\quad +48xy^2\left(y^4+6y^2+2\right)+4y^2\left(5y^6+22y^4+23y^2+12\right)\Big],\\
P_{\rm av} &= \frac{1}{x^2-y^2}\Big[25x^{10}-x^8(149y^2+131)+x^6(337y^4+600y^2+187)\\
&\quad -x^4(367y^6+951y^4+697y^2+81)+2x^2y^2(97y^6+313y^4+403y^2+27)\\
&\quad -8y^6(5y^4+18y^2+37)\Big],\\
P'_{\rm av} &= \frac{1}{x^2-y^2}\Big[-28x^{10}+92x^8(y^2+1)-x^6(88y^4+193y^2+100)\\
&\quad +x^4(-8y^6+54y^4+158y^2+36)+x^2y^2(52y^6+103y^4+146y^2-57)\\
&\quad -4y^4(5y^6+14y^4+51y^2-12)\Big],
\end{aligned}
$$

with $S_{\rm aa}(x,y) = S_{\rm vv}(-x,y)$ and $P_{\rm aa}(x,y) = P_{\rm vv}(-x,y)$. It is sufficient to include only the s-wave terms for any choice of coupling[2] .

Real DM

The matrix element for the process is given by contributions from t and u-channel diagrams,

[2]If the couplings are complex, then instead of $|g_v|^2|g_a|^2 S_{a,v}$ we get,

$$-2|g_v|^2|g_a|^2(x^4-8y^4+x^2(-9+7y^2))+((g_v g_a^\dagger)^2+(g_v^\dagger g_a)^2)(4x^4-5y^2+4y^4-4x^2(1+2y^2))$$

$$\mathcal{M} = \frac{1}{t - m_{\text{MED}}^2}\bar{u}(p_3)\left[\gamma^\mu\left(g_v^\dagger + g_a^\dagger\gamma^5\right)\left(\not{p}_3 - \not{p}_1 + m_{\text{MED}}\right)\gamma^\nu\left(g_v + g_a\gamma^5\right)\right]v(p_4)\ \varepsilon_\mu(p_1)\varepsilon_\nu(p_2)$$
$$+ \frac{1}{u - m_{\text{MED}}^2}\bar{u}(p_3)\left[\gamma^\mu\left(g_v^\dagger + g_a^\dagger\gamma^5\right)\left(\not{p}_3 - \not{p}_2 + m_{\text{MED}}\right)\gamma^\nu\left(g_v + g_a\gamma^5\right)\right]v(p_4)\ \varepsilon_\mu(p_2)\varepsilon_\nu(p_1). \tag{2.0.53}$$

This leads to

$$\sigma v = \frac{\sqrt{1 - x^2/y^2}}{36\pi m_\chi^2(1 - x^2 + y^2)^2}\Bigg[\left(|g_v|^4 S_{\text{vv}} + 2|g_v|^2|g_a|^2 S_{\text{av}} + |g_a|^4 S_{\text{aa}} + ((g_a^\dagger)^2 g_v^2 + (g_v^\dagger)g_a^2)S'_{av}\right)$$
$$+ \frac{v^2}{24(1 - x^2 + y^2)^2}\left(|g_v|^4 P_{\text{vv}} + 2|g_v|^2|g_a|^2 P_{\text{av}} + |g_a|^4 P_{\text{aa}} + ((g_a^\dagger)^2 g_v^2 + (g_v^\dagger)g_a^2)P'_{av}\right)\Bigg], \tag{2.0.54}$$

with,

$$S_{ss} = (y^2 - x^2)(3x^2 - 2x + 4y^2 + 3), \tag{2.0.55}$$
$$S_{sp} = x^4 + 3x^2 - 9x^2y^2 + 8y^4,$$
$$S'_{sp} = 4x^4 - 8x^2y^2 + 4y^4 - 3y^2,$$
$$P_{vv} = \Big(11x^8 + 6x^7 - x^6\left(14y^2 + 19\right) - 4x^5\left(19y^2 + 3\right) + x^4\left(-61y^4 + 48y^2 + 5\right)$$
$$+ 2x^3\left(67y^4 + 18y^2 + 3\right) + x^2\left(120y^6 + 51y^4 + 70y^2 + 3\right)$$
$$- 8xy^2\left(8y^4 + 3y^2 + 3\right) - 8y^2\left(7y^6 + 10y^4 - 3\right)\Big),$$
$$P_{av} = \frac{1}{y^2 - x^2}\Big(17x^{10} - x^8(143y^2 + 31) + x^6(439y^4 + 196y^2 + 11)$$
$$+ x^4(-629y^6 - 459y^4 + 37y^2 + 3) + 2x^2y^2(214y^6 + 227y^4 - 64y^2 + 3)$$
$$- 16y^6(7y^4 + 10y^2 - 5)\Big),$$
$$P'_{av} = \frac{1}{y^2 - x^2}\Big(28x^{10} - 56x^8(3y^2 + 1) + x^6(392y^4 + 215y^2 + 28) - 2y^2x^4(224y^4 + 171y^2 + 15)$$
$$+ x^2y^2(252y^6 + 263y^4 - 78y^2 + 15) - 8y^4(7y^6 + 10y^4 - 10y^2 + 3)\Big),$$

with $S_{\text{aa}}(x, y) = S_{\text{vv}}(-x, y)$ and $P_{\text{aa}}(x, y) = P_{\text{vv}}(-x, y)$.

Bibliography

[1] D. G. Cerdeño, M. Fairbairn, T. Jubb, P. A. N. Machado, A. C. Vincent, and C. Bœhm, "Physics from solar neutrinos in dark matter direct detection experiments," JHEP **05** (2016) 118, arXiv:1604.01025 [hep-ph]. [Erratum: JHEP09,048(2016)].

[2] T. Jubb, M. Kirk, and A. Lenz, "Charming Dark Matter," arXiv:1709.01930 [hep-ph].

[3] T. Jubb, M. Kirk, A. Lenz, and G. Tetlalmatzi-Xolocotzi, "On the ultimate precision of meson mixing observables," arXiv:1603.07770 [hep-ph].

[4] K. G. Begeman, A. H. Broeils, and R. H. Sanders, "Extended rotation curves of spiral galaxies - Dark haloes and modified dynamics," Monthly Notices of the RAS **249** (Apr., 1991) 523–537.

[5] D. Clowe, M. Bradac, A. H. Gonzalez, M. Markevitch, S. W. Randall, C. Jones, and D. Zaritsky, "A direct empirical proof of the existence of dark matter," Astrophys. J. **648** (2006) L109–L113, arXiv:astro-ph/0608407 [astro-ph].

[6] **Planck** Collaboration, P. A. R. Ade et al., "Planck 2015 results. XIII. Cosmological parameters," Astron. Astrophys. **594** (2016) A13, arXiv:1502.01589 [astro-ph.CO].

[7] B. D. Fields, P. Molaro, and S. Sarkar, "Big-Bang Nucleosynthesis," Chin. Phys. **C38** (2014) , arXiv:1412.1408 [astro-ph.CO].

[8] P. Gondolo and G. Gelmini, "Cosmic abundances of stable particles: Improved analysis," Nucl. Phys. **B360** (1991) 145–179.

[9] T. Lacroix, C. Boehm, and J. Silk, "Probing a dark matter density spike at the Galactic Center," Phys. Rev. **D89** (2014) 063534, arXiv:1311.0139 [astro-ph.HE].

[10] T. Delahaye, J. Lavalle, R. Lineros, F. Donato, and N. Fornengo, "Galactic electrons and positrons at the Earth:new estimate of the primary and secondary fluxes," Astron. Astrophys. **524** (2010) A51, arXiv:1002.1910 [astro-ph.HE].

[11] C. Gordon and O. Macias, "Dark Matter and Pulsar Model Constraints from Galactic Center Fermi-LAT Gamma Ray Observations," Phys. Rev. **D88** no. 8, (2013) 083521, arXiv:1306.5725 [astro-ph.HE]. [Erratum: Phys. Rev.D89,no.4,049901(2014)].

[12] J. Kumar, D. Marfatia, and D. Yaylali, "Vector dark matter at the LHC," Phys. Rev. **D92** no. 9, (2015) 095027, arXiv:1508.04466 [hep-ph].

[13] W. C. Haxton, R. G. Hamish Robertson, and A. M. Serenelli, "Solar Neutrinos: Status and Prospects," Ann. Rev. Astron. Astrophys. **51** (2013) 21–61, arXiv:1208.5723 [astro-ph.SR].

[14] **Borexino** Collaboration, O. Yu. Smirnov et al., "Measurement of neutrino flux from the primary proton–proton fusion process in the Sun with Borexino detector," arXiv:1507.02432 [hep-ex].

[15] R. Harnik, J. Kopp, and P. A. N. Machado, "Exploring nu Signals in Dark Matter Detectors," JCAP **1207** (2012) 026, arXiv:1202.6073 [hep-ph].

[16] S. Bilmis, I. Turan, T. M. Aliev, M. Deniz, L. Singh, and H. T. Wong, "Constraints on Dark Photon from Neutrino-Electron Scattering Experiments," Phys. Rev. **D92** no. 3, (2015) 033009, arXiv:1502.07763 [hep-ph].

[17] E. Rrapaj and S. Reddy, "Nucleon-nucleon bremsstrahlung of dark gauge bosons and revised supernova constraints," Phys. Rev. **C94** no. 4, (2016) 045805, arXiv:1511.09136 [nucl-th].

[18] S. Fajfer and N. Košnik, "Prospects of discovering new physics in rare charm decays," Eur. Phys. J. **C75** no. 12, (2015) 567, arXiv:1510.00965 [hep-ph].

[19] **H.E.S.S.** Collaboration, V. Lefranc and E. Moulin, "Dark matter search in the inner Galactic halo with H.E.S.S. I and H.E.S.S. II," PoS **ICRC2015** (2016) 1208, arXiv:1509.04123 [astro-ph.HE].

[20] **SuperCDMS** Collaboration, R. Agnese et al., "New Results from the Search for Low-Mass Weakly Interacting Massive Particles with the CDMS Low Ionization Threshold Experiment," Phys. Rev. Lett. **116** no. 7, (2016) 071301, arXiv:1509.02448 [astro-ph.CO].

[21] **ATLAS** Collaboration, G. Aad et al., "Search for new phenomena in final states with an energetic jet and large missing transverse momentum in pp collisions at $\sqrt{s}$ =8 TeV with the ATLAS detector," Eur. Phys. J. **C75** no. 7, (2015) 299, arXiv:1502.01518 [hep-ex]. [Erratum: Eur. Phys. J.C75,no.9,408(2015)].

[22] G. Busoni, A. De Simone, T. Jacques, E. Morgante, and A. Riotto, "On the Validity of the Effective Field Theory for Dark Matter Searches at the LHC Part III: Analysis for the t-channel," JCAP **1409** (2014) 022, arXiv:1405.3101 [hep-ph].

[23] **ATLAS** Collaboration, M. Aaboud et al., "Search for new phenomena in final states with an energetic jet and large missing transverse momentum in pp collisions at $\sqrt{s} = 13$ TeV using the ATLAS detector," Phys. Rev. **D94** no. 3, (2016) 032005, arXiv:1604.07773 [hep-ex].

[24] **CMS** Collaboration, V. Khachatryan et al., "Search for dark matter, extra dimensions, and unparticles in monojet events in proton–proton collisions at

$\sqrt{s} = 8$ TeV," Eur. Phys. J. **C75** no. 5, (2015) 235, arXiv:1408.3583 [hep-ex].

[25] **ATLAS** Collaboration, G. Aad et al., "Search for top squark pair production in final states with one isolated lepton, jets, and missing transverse momentum in $\sqrt{s}$ =8 TeV pp collisions with the ATLAS detector," JHEP **11** (2014) 118, arXiv:1407.0583 [hep-ex].

[26] M. Artuso, G. Borissov, and A. Lenz, "CP violation in the B_s^0 system," Rev. Mod. Phys. **88** no. 4, (2016) 045002, arXiv:1511.09466 [hep-ph].

[27] **LHCb** Collaboration, R. Aaij et al., "Measurement of the CP asymmetry in $B_s^0 - \overline{B}_s^0$ mixing," Phys. Rev. Lett. **117** no. 6, (2016) 061803, arXiv:1605.09768 [hep-ex].

[28] **Heavy Flavor Averaging Group (HFAG)** Collaboration, Y. Amhis et al., "Averages of b-hadron, c-hadron, and τ-lepton properties as of summer 2014," arXiv:1412.7515 [hep-ex].

[29] R. J. Hill and M. P. Solon, "Standard Model anatomy of WIMP dark matter direct detection II: QCD analysis and hadronic matrix elements," Phys.Rev. **D91** (2015) 043505, arXiv:1409.8290 [hep-ph].

[30] **ATLAS** Collaboration, G. Aad et al., "Search for squarks and gluinos with the ATLAS detector in final states with jets and missing transverse momentum using $\sqrt{s} = 8$ TeV proton–proton collision data," JHEP **09** (2014) 176, arXiv:1405.7875 [hep-ex].

[31] **ATLAS** Collaboration, M. Aaboud et al., "Search for squarks and gluinos in final states with jets and missing transverse momentum at $\sqrt{s} = 13$ TeV with the ATLAS detector," Eur. Phys. J. **C76** no. 7, (2016) 392, arXiv:1605.03814 [hep-ex].

[32] F. Zwicky, "On the Masses of Nebulae and of Clusters of Nebulae," Astrophys. J **86** (Oct., 1937) 217.

[33] V. C. Rubin and W. K. Ford, Jr., "Rotation of the Andromeda Nebula from a Spectroscopic Survey of Emission Regions," ApJ **159** (Feb., 1970) 379.

[34] D. S. Davis and R. E. White, III, "Rosat temperatures and abundances for a complete sample of elliptical galaxies," Astrophys. J. **470** (1996) L35, arXiv:astro-ph/9607052 [astro-ph].

[35] S. W. Allen, D. A. Rapetti, R. W. Schmidt, H. Ebeling, G. Morris, and A. C. Fabian, "Improved constraints on dark energy from Chandra X-ray observations of the largest relaxed galaxy clusters," Mon. Not. Roy. Astron. Soc. **383** (2008) 879–896, arXiv:0706.0033 [astro-ph].

[36] R. Massey, T. Kitching, and J. Richard, "The dark matter of gravitational lensing," Rept. Prog. Phys. **73** (2010) 086901, arXiv:1001.1739 [astro-ph.CO].

[37] S. Dodelson, Modern Cosmology. Academic Press, Amsterdam, 2003. http://www.slac.stanford.edu/spires/find/books/www?cl=QB981:D62:2003.

[38] E. W. Kolb and M. S. Turner, "The Early Universe," Front. Phys. **69** (1990) 1–547.

[39] V. S. Alpher, "Ralph A. Alpher, George Antonovich Gamow, and the Prediction of the Cosmic Microwave Background Radiation," arXiv:1411.0172 [physics.hist-ph].

[40] A. A. Penzias and R. W. Wilson, "A Measurement of Excess Antenna Temperature at 4080 Mc/s.," ApJ **142** (July, 1965) 419–421.

[41] **Planck** Collaboration, R. Adam et al., "Planck 2015 results. I. Overview of products and scientific results," arXiv:1502.01582 [astro-ph.CO].

[42] K. A. Olive, G. Steigman, and T. P. Walker, "Primordial nucleosynthesis: Theory and observations," Phys. Rept. **333** (2000) 389–407, arXiv:astro-ph/9905320 [astro-ph].

[43] S. Sarkar, "Big bang nucleosynthesis and physics beyond the standard model," Rept. Prog. Phys. **59** (1996) 1493–1610, arXiv:hep-ph/9602260 [hep-ph].

[44] D. N. Schramm and M. S. Turner, "Big bang nucleosynthesis enters the precision era," Rev. Mod. Phys. **70** (1998) 303–318, arXiv:astro-ph/9706069 [astro-ph].

[45] R. A. Alpher, H. Bethe, and G. Gamow, "The origin of chemical elements," Phys. Rev. **73** (Apr, 1948) 803–804. http://link.aps.org/doi/10.1103/PhysRev.73.803.

[46] R. Ichimasa, R. Nakamura, M. Hashimoto, and K. Arai, "Big-Bang Nucleosynthesis in comparison with observed helium and deuterium abundances: possibility of a nonstandard model," Phys. Rev. **D90** no. 2, (2014) 023527, arXiv:1404.4831 [astro-ph.CO].

[47] R. H. Cyburt, B. D. Fields, K. A. Olive, and T.-H. Yeh, "Big bang nucleosynthesis: Present status," Rev. Mod. Phys. **88** (Feb, 2016) 015004. http://link.aps.org/doi/10.1103/RevModPhys.88.015004.

[48] P. S. Bhupal Dev, A. Mazumdar, and S. Qutub, "Constraining Non-thermal and Thermal properties of Dark Matter," Front. Phys. **2** (2014) 26, arXiv:1311.5297 [hep-ph].

[49] K. Griest and D. Seckel, "Three exceptions in the calculation of relic abundances," Phys. Rev. **D43** (1991) 3191–3203.

[50] M. Cannoni, "Relativistic $< \sigma v_{\rm rel} >$ in the calculation of relics abundances: a closer look," Phys. Rev. **D89** no. 10, (2014) 103533, arXiv:1311.4494 [astro-ph.CO].

[51] K. Griest and M. Kamionkowski, "Unitarity Limits on the Mass and Radius of Dark Matter Particles," Phys. Rev. Lett. **64** (1990) 615.

[52] S. P. Martin, "A Supersymmetry primer," arXiv:hep-ph/9709356 [hep-ph]. [Adv. Ser. Direct. High Energy Phys.18,1(1998)].

[53] A. Signer, "ABC of SUSY," J. Phys. **G36** (2009) 073002, arXiv:0905.4630 [hep-ph].

[54] N. Arkani-Hamed, A. G. Cohen, and H. Georgi, "Electroweak symmetry breaking from dimensional deconstruction," Phys. Lett. **B513** (2001) 232–240, arXiv:hep-ph/0105239 [hep-ph].

[55] T. Appelquist, H.-C. Cheng, and B. A. Dobrescu, "Bounds on universal extra dimensions," Phys. Rev. **D64** (2001) 035002, arXiv:hep-ph/0012100 [hep-ph].

[56] M. Blennow, P. Coloma, E. Fernandez-Martinez, P. A. N. Machado, and B. Zaldivar, "Global constraints on vector-like WIMP effective interactions," JCAP **1604** no. 04, (2016) 015, arXiv:1509.01587 [hep-ph].

[57] S. Liem, G. Bertone, F. Calore, R. Ruiz de Austri, T. M. P. Tait, R. Trotta, and C. Weniger, "Effective field theory of dark matter: a global analysis," JHEP **09** (2016) 077, arXiv:1603.05994 [hep-ph].

[58] J. Abdallah et al., "Simplified Models for Dark Matter and Missing Energy Searches at the LHC," arXiv:1409.2893 [hep-ph].

[59] **LHC New Physics Working Group** Collaboration, D. Alves, "Simplified Models for LHC New Physics Searches," J. Phys. **G39** (2012) 105005, arXiv:1105.2838 [hep-ph].

[60] J. Alwall, P. Schuster, and N. Toro, "Simplified Models for a First Characterization of New Physics at the LHC," Phys. Rev. **D79** (2009) 075020, arXiv:0810.3921 [hep-ph].

[61] **ATLAS** Collaboration, M. Aaboud et al., "Search for new phenomena in events with a photon and missing transverse momentum in pp collisions at $\sqrt{s} = 13$ TeV with the ATLAS detector," JHEP **06** (2016) 059, arXiv:1604.01306 [hep-ex].

[62] A. De Simone and T. Jacques, "Simplified models vs. effective field theory approaches in dark matter searches," Eur. Phys. J. **C76** no. 7, (2016) 367, arXiv:1603.08002 [hep-ph].

[63] J. Goodman and W. Shepherd, "LHC Bounds on UV-Complete Models of Dark Matter," arXiv:1111.2359 [hep-ph].

[64] H. Dreiner, D. Schmeier, and J. Tattersall, "Contact Interactions Probe Effective Dark Matter Models at the LHC," Europhys. Lett. **102** no. 5, (2013) 51001, arXiv:1303.3348 [hep-ph].

[65] G. Busoni, A. De Simone, E. Morgante, and A. Riotto, "On the Validity of the Effective Field Theory for Dark Matter Searches at the LHC," Phys. Lett. **B728** (2014) 412–421, arXiv:1307.2253 [hep-ph].

[66] G. Busoni, A. De Simone, J. Gramling, E. Morgante, and A. Riotto, "On the Validity of the Effective Field Theory for Dark Matter Searches at the LHC, Part II: Complete Analysis for the s-channel," JCAP **1406** (2014) 060, arXiv:1402.1275 [hep-ph].

[67] O. Buchmueller, M. J. Dolan, and C. McCabe, "Beyond Effective Field Theory for Dark Matter Searches at the LHC," JHEP **01** (2014) 025, arXiv:1308.6799 [hep-ph].

[68] P. Harris, V. V. Khoze, M. Spannowsky, and C. Williams, "Constraining Dark Sectors at Colliders: Beyond the Effective Theory Approach," Phys. Rev. **D91** (2015) 055009, arXiv:1411.0535 [hep-ph].

[69] D. Abercrombie et al., "Dark Matter Benchmark Models for Early LHC Run-2 Searches: Report of the ATLAS/CMS Dark Matter Forum," arXiv:1507.00966 [hep-ex].

[70] G. Busoni et al., "Recommendations on presenting LHC searches for missing transverse energy signals using simplified s-channel models of dark matter," arXiv:1603.04156 [hep-ex].

[71] D. Goncalves, P. A. N. Machado, and J. M. No, "Simplified Models for Dark Matter Face their Consistent Completions," arXiv:1611.04593 [hep-ph].

[72] F. Kahlhoefer, K. Schmidt-Hoberg, T. Schwetz, and S. Vogl, "Implications of unitarity and gauge invariance for simplified dark matter models," JHEP **02** (2016) 016, arXiv:1510.02110 [hep-ph].

[73] C. Englert, M. McCullough, and M. Spannowsky, "S-Channel Dark Matter Simplified Models and Unitarity," Phys. Dark Univ. **14** (2016) 48–56, arXiv:1604.07975 [hep-ph].

[74] M. Duerr, F. Kahlhoefer, K. Schmidt-Hoberg, T. Schwetz, and S. Vogl, "How to save the WIMP: global analysis of a dark matter model with two s-channel mediators," JHEP **09** (2016) 042, arXiv:1606.07609 [hep-ph].

[75] J. Abdallah et al., "Simplified Models for Dark Matter Searches at the LHC," Phys. Dark Univ. **9-10** (2015) 8–23, arXiv:1506.03116 [hep-ph].

[76] G. D'Ambrosio, G. F. Giudice, G. Isidori, and A. Strumia, "Minimal flavor violation: An Effective field theory approach," Nucl. Phys. **B645** (2002) 155–187, arXiv:hep-ph/0207036 [hep-ph].

[77] B. Batell, J. Pradler, and M. Spannowsky, "Dark Matter from Minimal Flavor Violation," JHEP **08** (2011) 038, arXiv:1105.1781 [hep-ph].

[78] R. Ding and Y. Liao, "Spin 3/2 Particle as a Dark Matter Candidate: an Effective Field Theory Approach," JHEP **04** (2012) 054, arXiv:1201.0506 [hep-ph].

[79] A. Y. Ignatiev, V. A. Kuzmin, and M. E. Shaposhnikov, "Is the electric charge conserved?," Physics Letters B **84** (July, 1979) 315–318.

[80] B. Holdom, "Two U(1)'s and Epsilon Charge Shifts," Phys. Lett. **B166** (1986) 196–198.

[81] S. A. Abel and B. W. Schofield, "Brane anti-brane kinetic mixing, millicharged particles and SUSY breaking," Nucl. Phys. **B685** (2004) 150–170, arXiv:hep-th/0311051 [hep-th].

[82] B. Batell and T. Gherghetta, "Localized U(1) gauge fields, millicharged particles, and holography," Phys. Rev. **D73** (2006) 045016, arXiv:hep-ph/0512356 [hep-ph].

[83] E. Gabrielli, L. Marzola, M. Raidal, and H. Veermäe, "Dark matter and spin-1 milli-charged particles," JHEP **08** (2015) 150, arXiv:1507.00571 [hep-ph].

[84] A. Choudhury, K. Kowalska, L. Roszkowski, E. M. Sessolo, and A. J. Williams, "Less-simplified models of dark matter for direct detection and the LHC," arXiv:1509.05771 [hep-ph].

[85] G. Jungman, M. Kamionkowski, and K. Griest, "Supersymmetric dark matter," Phys. Rept. **267** (1996) 195–373, arXiv:hep-ph/9506380 [hep-ph].

[86] K.-Y. Choi, L. Covi, J. E. Kim, and L. Roszkowski, "Axino Cold Dark Matter Revisited," JHEP **04** (2012) 106, arXiv:1108.2282 [hep-ph].

[87] L. Covi, L. Roszkowski, R. Ruiz de Austri, and M. Small, "Axino dark matter and the CMSSM," JHEP **06** (2004) 003, arXiv:hep-ph/0402240 [hep-ph].

[88] M. Pospelov, A. Ritz, and M. B. Voloshin, "Secluded WIMP Dark Matter," Phys. Lett. **B662** (2008) 53–61, arXiv:0711.4866 [hep-ph].

[89] G. Belanger, A. Pukhov, and G. Servant, "Dirac Neutrino Dark Matter," JCAP **0801** (2008) 009, arXiv:0706.0526 [hep-ph].

[90] H. M. Lee, M. Park, and V. Sanz, "Gravity-mediated (or Composite) Dark Matter," Eur. Phys. J. **C74** (2014) 2715, arXiv:1306.4107 [hep-ph].

[91] H. M. Lee, M. Park, and V. Sanz, "Gravity-mediated (or Composite) Dark Matter Confronts Astrophysical Data," JHEP **05** (2014) 063, arXiv:1401.5301 [hep-ph].

[92] R. Foot and X.-G. He, "Comment on Z Z-prime mixing in extended gauge theories," Phys. Lett. **B267** (1991) 509–512.

[93] P. Fayet, "Light spin 1/2 or spin 0 dark matter particles," Phys. Rev. **D70** (2004) 023514, arXiv:hep-ph/0403226 [hep-ph].

[94] C. A. Argüelles, X.-G. He, G. Ovanesyan, T. Peng, and M. J. Ramsey-Musolf, "Dark Gauge Bosons: LHC Signatures of Non-Abelian Kinetic Mixing," arXiv:1604.00044 [hep-ph].

[95] L. Basso, Phenomenology of the minimal B-L extension of the Standard Model at the LHC. PhD thesis, Southampton U., 2011. arXiv:1106.4462 [hep-ph]. https://inspirehep.net/record/914502/files/arXiv:1106.4462.pdf.

[96] C. Boehm and P. Fayet, "Scalar dark matter candidates," Nucl. Phys. **B683** (2004) 219–263, arXiv:hep-ph/0305261 [hep-ph].

[97] S. Andreas, T. Hambye, and M. H. G. Tytgat, "WIMP dark matter, Higgs exchange and DAMA," JCAP **0810** (2008) 034, arXiv:0808.0255 [hep-ph].

[98] V. Barger, P. Langacker, M. McCaskey, M. J. Ramsey-Musolf, and G. Shaughnessy, "Cern lhc phenomenology of an extended standard model with a real scalar singlet," Phys. Rev. D **77** (Feb, 2008) 035005. http://link.aps.org/doi/10.1103/PhysRevD.77.035005.

[99] J. McDonald, "Gauge singlet scalars as cold dark matter," Phys. Rev. **D50** (1994) 3637–3649, arXiv:hep-ph/0702143 [HEP-PH].

[100] E. Di Valentino, E. Giusarma, M. Lattanzi, A. Melchiorri, and O. Mena, "Axion cold dark matter: status after Planck and BICEP2," Phys. Rev. **D90** no. 4, (2014) 043534, arXiv:1405.1860 [astro-ph.CO].

[101] Q. Yang, "Axions and Dark Matter," arXiv:1509.00673 [hep-ph].

[102] R. D. Peccei and H. R. Quinn, "CP conservation in the presence of pseudoparticles," Phys. Rev. Lett. **38** (Jun, 1977) 1440–1443. http://link.aps.org/doi/10.1103/PhysRevLett.38.1440.

[103] R. D. Peccei and H. R. Quinn, "Constraints imposed by CP conservation in the presence of pseudoparticles," Phys. Rev. D **16** (Sep, 1977) 1791–1797. http://link.aps.org/doi/10.1103/PhysRevD.16.1791.

[104] S. Andreas, C. Arina, T. Hambye, F.-S. Ling, and M. H. G. Tytgat, "A light scalar WIMP through the Higgs portal and CoGeNT," Phys. Rev. **D82** (2010) 043522, arXiv:1003.2595 [hep-ph].

[105] C. D. Carone and R. Ramos, "Classical scale-invariance, the electroweak scale and vector dark matter," Phys. Rev. **D88** (2013) 055020, arXiv:1307.8428 [hep-ph].

[106] H.-C. Cheng, J. L. Feng, and K. T. Matchev, "Kaluza-Klein dark matter," Phys. Rev. Lett. **89** (2002) 211301, arXiv:hep-ph/0207125 [hep-ph].

[107] G. Servant and T. M. P. Tait, "Elastic scattering and direct detection of Kaluza-Klein dark matter," New J. Phys. **4** (2002) 99, arXiv:hep-ph/0209262 [hep-ph].

[108] L. Randall and R. Sundrum, "A Large mass hierarchy from a small extra dimension," Phys. Rev. Lett. **83** (1999) 3370–3373, arXiv:hep-ph/9905221 [hep-ph].

[109] T. Han, H. E. Logan, B. McElrath, and L.-T. Wang, "Phenomenology of the little Higgs model," Phys. Rev. **D67** (2003) 095004, arXiv:hep-ph/0301040 [hep-ph].

[110] N. Arkani-Hamed, A. G. Cohen, E. Katz, and A. E. Nelson, "The Littlest Higgs," JHEP **07** (2002) 034, arXiv:hep-ph/0206021 [hep-ph].

[111] M. Perelstein, "Little Higgs models and their phenomenology," Prog. Part. Nucl. Phys. **58** (2007) 247–291, arXiv:hep-ph/0512128 [hep-ph].

[112] T. Hambye, "Hidden vector dark matter," JHEP **01** (2009) 028, arXiv:0811.0172 [hep-ph].

[113] Y. Farzan and A. R. Akbarieh, "VDM: A model for Vector Dark Matter," JCAP **1210** (2012) 026, arXiv:1207.4272 [hep-ph].

[114] J.-H. Yu, "Vector Fermion-Portal Dark Matter: Direct Detection and Galactic Center Gamma-Ray Excess," Phys. Rev. **D90** no. 9, (2014) 095010, arXiv:1409.3227 [hep-ph].

[115] V. Barger, W.-Y. Keung, and G. Shaughnessy, "Spin Dependence of Dark Matter Scattering," Phys. Rev. **D78** (2008) 056007, arXiv:0806.1962 [hep-ph].

[116] J. B. Dent, L. M. Krauss, J. L. Newstead, and S. Sabharwal, "A General Analysis of Direct Dark Matter Detection: From Microphysics to Observational Signatures," Phys. Rev. **D92** no. 6, (2015) 063515, arXiv:1505.03117 [hep-ph].

[117] J. Kumar and D. Marfatia, "Matrix element analyses of dark matter scattering and annihilation," Phys.Rev. **D88** no. 1, (2013) 014035, arXiv:1305.1611 [hep-ph].

[118] J. Goodman, M. Ibe, A. Rajaraman, W. Shepherd, T. M. P. Tait, and H.-B. Yu, "Gamma Ray Line Constraints on Effective Theories of Dark Matter," Nucl. Phys. **B844** (2011) 55–68, arXiv:1009.0008 [hep-ph].

[119] S. Profumo, F. S. Queiroz, and C. E. Yaguna, "Extending Fermi-LAT and H.E.S.S. Limits on Gamma-ray Lines from Dark Matter Annihilation," arXiv:1602.08501 [astro-ph.HE].

[120] M. Duerr, P. Fileviez Perez, and J. Smirnov, "Gamma Lines from Majorana Dark Matter," Phys. Rev. **D93** (2016) 023509, arXiv:1508.01425 [hep-ph].

[121] M. Duerr, P. Fileviez Perez, and J. Smirnov, "Simplified Dirac Dark Matter Models and Gamma-Ray Lines," Phys. Rev. **D92** no. 8, (2015) 083521, arXiv:1506.05107 [hep-ph].

[122] **HESS** Collaboration, A. Abramowski et al., "Search for Photon-Linelike Signatures from Dark Matter Annihilations with H.E.S.S.," Phys. Rev. Lett. **110** (2013) 041301, arXiv:1301.1173 [astro-ph.HE].

[123] **Fermi-LAT** Collaboration, M. Ackermann et al., "Search for gamma-ray spectral lines with the Fermi large area telescope and dark matter implications," Phys. Rev. **D88** (2013) 082002, arXiv:1305.5597 [astro-ph.HE].

[124] Y.-F. Liang, Z.-Q. Shen, X. Li, Y.-Z. Fan, X. Huang, S.-J. Lei, L. Feng, E.-W. Liang, and J. Chang, "Search for a gamma-ray line feature from a group of nearby galaxy clusters with Fermi LAT Pass 8 data," Phys. Rev. **D93** no. 10, (2016) 103525, arXiv:1602.06527 [astro-ph.HE].

[125] M. Duerr, P. Fileviez Pérez, and J. Smirnov, "Scalar Dark Matter: Direct vs. Indirect Detection," JHEP **06** (2016) 152, arXiv:1509.04282 [hep-ph].

[126] M. Cirelli, G. Corcella, A. Hektor, G. Hutsi, M. Kadastik, P. Panci, M. Raidal, F. Sala, and A. Strumia, "PPPC 4 DM ID: A Poor Particle Physicist Cookbook for Dark Matter Indirect Detection," JCAP **1103** (2011) 051, arXiv:1012.4515 [hep-ph]. [Erratum: JCAP1210,E01(2012)].

[127] A. Klypin, H. Zhao, and R. S. Somerville, "Lambda CDM-based models for the Milky Way and M31 I: Dynamical models," Astrophys. J. **573** (2002) 597–613, arXiv:astro-ph/0110390 [astro-ph].

[128] J. Vega, G. Yepes, and S. Gottlöber, "On the shape of dark matter halos from MultiDark Planck simulations," arXiv:1603.02256 [astro-ph.CO].

[129] J. F. Navarro, A. Ludlow, V. Springel, J. Wang, M. Vogelsberger, S. D. M. White, A. Jenkins, C. S. Frenk, and A. Helmi, "The Diversity and Similarity

of Cold Dark Matter Halos," Mon. Not. Roy. Astron. Soc. **402** (2010) 21, arXiv:0810.1522 [astro-ph].

[130] J. F. Navarro, C. S. Frenk, and S. D. M. White, "The Structure of cold dark matter halos," Astrophys. J. **462** (1996) 563–575, arXiv:astro-ph/9508025 [astro-ph].

[131] A. W. Graham, D. Merritt, B. Moore, J. Diemand, and B. Terzic, "Empirical models for Dark Matter Halos. I. Nonparametric Construction of Density Profiles and Comparison with Parametric Models," Astron. J. **132** (2006) 2685–2700, arXiv:astro-ph/0509417 [astro-ph].

[132] J. Stadel, D. Potter, B. Moore, J. Diemand, P. Madau, M. Zemp, M. Kuhlen, and V. Quilis, "Quantifying the heart of darkness with GHALO - a multi-billion particle simulation of our galactic halo," Mon. Not. Roy. Astron. Soc. **398** (2009) L21–L25, arXiv:0808.2981 [astro-ph].

[133] P. Salucci, A. Lapi, C. Tonini, G. Gentile, I. Yegorova, and U. Klein, "The Universal Rotation Curve of Spiral Galaxies. 2. The Dark Matter Distribution out to the Virial Radius," Mon. Not. Roy. Astron. Soc. **378** (2007) 41–47, arXiv:astro-ph/0703115 [ASTRO-PH].

[134] A. Burkert, "The Structure of dark matter halos in dwarf galaxies," IAU Symp. **171** (1996) 175, arXiv:astro-ph/9504041 [astro-ph]. [Astrophys. J.447,L25(1995)].

[135] K. N. Abazajian and M. Kaplinghat, "Detection of a Gamma-Ray Source in the Galactic Center Consistent with Extended Emission from Dark Matter Annihilation and Concentrated Astrophysical Emission," Phys. Rev. **D86** (2012) 083511, arXiv:1207.6047 [astro-ph.HE]. [Erratum: Phys. Rev.D87,129902(2013)].

[136] T. Lacroix, "Fitting the Fermi-LAT GeV excess: on the importance of the propagation of electrons from dark matter," PoS **FFP14** (2016) 054, arXiv:1501.07485 [astro-ph.HE].

[137] P. Gondolo and J. Silk, "Dark matter annihilation at the galactic center," Phys. Rev. Lett. **83** (1999) 1719–1722, arXiv:astro-ph/9906391 [astro-ph].

[138] D. Merritt, "Dark matter spikes and indirect detection," in Proceedings, 4th International Workshop on The identification of dark matter (IDM 2002 pp. 96–101. 2003. arXiv:astro-ph/0301365 [astro-ph].

[139] F. Iocco, M. Pato, G. Bertone, and P. Jetzer, "Dark Matter distribution in the Milky Way: microlensing and dynamical constraints," JCAP **1111** (2011) 029, arXiv:1107.5810 [astro-ph.GA].

[140] J. I. Read, "The Local Dark Matter Density," J. Phys. **G41** (2014) 063101, arXiv:1404.1938 [astro-ph.GA].

[141] W. B. Atwood, A. A. Abdo, M. Ackermann, W. Althouse, B. Anderson, M. Axelsson, L. Baldini, J. Ballet, D. L. Band, G. Barbiellini, and et al., "The Large Area Telescope on the Fermi Gamma-Ray Space Telescope Mission," Ap. Phys. J **697** (June, 2009) 1071–1102, arXiv:0902.1089 [astro-ph.IM].

[142] S. D. Hunter, D. L. Bertsch, J. R. Catelli, T. M. Dame, S. W. Digel, B. L. Dingus, J. A. Esposito, C. E. Fichtel, R. C. Hartman, G. Kanbach, D. A. Kniffen, Y. C. Lin, H. A. Mayer-Hasselwander, P. F. Michelson, C. von Montigny, R. Mukherjee, P. L. Nolan, E. Schneid, P. Sreekumar, P. Thaddeus, and D. J. Thompson, "Egret observations of the diffuse gamma-ray emission from the galactic plane," The Astrophysical Journal **481** no. 1, (1997) 205. http://stacks.iop.org/0004-637X/481/i=1/a=205.

[143] L. Bouchet, E. Jourdain, J. P. Roques, A. Strong, R. Diehl, F. Lebrun, and R. Terrier, "INTEGRAL SPI All-Sky View in Soft Gamma Rays: Study of Point Source and Galactic Diffuse Emissions," Astrophys. J. **679** (2008) 1315, arXiv:0801.2086 [astro-ph].

[144] **HESS** Collaboration, A. Abramowski et al., "Search for a Dark Matter

annihilation signal from the Galactic Center halo with H.E.S.S," Phys. Rev. Lett. **106** (2011) 161301, arXiv:1103.3266 [astro-ph.HE].

[145] A. W. Strong, I. V. Moskalenko, and O. Reimer, "Diffuse galactic continuum gamma rays. A Model compatible with EGRET data and cosmic-ray measurements," Astrophys.J. **613** (2004) 962–976, arXiv:astro-ph/0406254 [astro-ph].

[146] S. Kappadath, "," Ph. D. Thesis (1998) , arXiv:astro-ph/0406254 [astro-ph].

[147] T. Delahaye, Propagation of Galactic Cosmic Rays and Dark Matter indirect Detection. PhD thesis, Savoie U., 2010. http://tel.archives-ouvertes.fr/docs/00/53/86/39/PDF/these.pdf.

[148] T. Lacroix, Phenomenology of dark matter particles at the centers of galaxies. Theses, Université Pierre et Marie Curie - Paris VI, July, 2016. https://tel.archives-ouvertes.fr/tel-01369006.

[149] T. Delahaye, J. Lavalle, R. Lineros, F. Donato, and N. Fornengo, "Galactic electrons and positrons at the Earth: new estimate of the primary and secondary fluxes," Astronomy and Astrophysics **524** (Dec., 2010) A51, arXiv:1002.1910 [astro-ph.HE].

[150] N. Fornengo, L. Maccione, and A. Vittino, "Constraints on particle dark matter from cosmic-ray antiprotons," JCAP **1404** no. 04, (2014) 003, arXiv:1312.3579 [hep-ph].

[151] M. Cirelli and G. Giesen, "Antiprotons from Dark Matter: Current constraints and future sensitivities," JCAP **1304** (2013) 015, arXiv:1301.7079 [hep-ph].

[152] L. Bergstrom, T. Bringmann, I. Cholis, D. Hooper, and C. Weniger, "New

limits on dark matter annihilation from AMS cosmic ray positron data," Phys. Rev. Lett. **111** (2013) 171101, arXiv:1306.3983 [astro-ph.HE].

[153] **IceCube** Collaboration, R. Abbasi et al., "Search for Neutrinos from Annihilating Dark Matter in the Direction of the Galactic Center with the 40-String IceCube Neutrino Observatory," arXiv:1210.3557 [hep-ex].

[154] **Super-Kamiokande** Collaboration, S. Desai et al., "Search for dark matter WIMPs using upward through-going muons in Super-Kamiokande," Phys. Rev. **D70** (2004) 083523, arXiv:hep-ex/0404025 [hep-ex]. [Erratum: Phys. Rev.D70,109901(2004)].

[155] T. Delahaye, F. Donato, N. Fornengo, J. Lavalle, R. Lineros, P. Salati, and R. Taillet, "Galactic secondary positron flux at the Earth," Astron. Astrophys. **501** (2009) 821–833, arXiv:0809.5268 [astro-ph].

[156] J. Lavalle, J. Pochon, P. Salati, and R. Taillet, "Clumpiness of dark matter and positron annihilation signal: computing the odds of the galactic lottery," Astron. Astrophys. **462** (2007) 827–848, arXiv:astro-ph/0603796 [astro-ph].

[157] E. A. Baltz and J. Edsjo, "Positron propagation and fluxes from neutralino annihilation in the halo," Phys. Rev. **D59** (1998) 023511, arXiv:astro-ph/9808243 [astro-ph].

[158] G. R. BLUMENTHAL and R. J. GOULD, "Bremsstrahlung, synchrotron radiation, and compton scattering of high-energy electrons traversing dilute gases," Rev. Mod. Phys. **42** (Apr, 1970) 237–270. http://link.aps.org/doi/10.1103/RevModPhys.42.237.

[159] M. Cirelli, P. D. Serpico, and G. Zaharijas, "Bremsstrahlung gamma rays from light Dark Matter," JCAP **1311** (2013) 035, arXiv:1307.7152 [astro-ph.HE].

[160] M. Asplund, N. Grevesse, and J. Sauval, "The Solar chemical composition,"

Nucl. Phys. **A777** (2006) 1–4, arXiv:astro-ph/0410214 [astro-ph]. [ASP Conf. Ser.336,25(2005)].

[161] M. Cirelli and P. Panci, "Inverse Compton constraints on the Dark Matter e+e- excesses," Nucl. Phys. **B821** (2009) 399–416, arXiv:0904.3830 [astro-ph.CO].

[162] G. B. Rybicki and A. P. Lightman, Synchrotron Radiation, pp. 167–194. Wiley-VCH Verlag GmbH, 2007. http://dx.doi.org/10.1002/9783527618170.ch6.

[163] A. W. Strong, I. V. Moskalenko, and O. Reimer, "Diffuse continuum gamma-rays from the galaxy," Astrophys. J. **537** (2000) 763–784, arXiv:astro-ph/9811296 [astro-ph]. [Erratum: Astrophys. J.541,1109(2000)].

[164] M. Wechakama and Y. Ascasibar, "Multimessenger constraints on dark matter annihilation into electron-positron pairs," mnras **439** (Mar., 2014) 566–587, arXiv:1212.2583.

[165] T. Delahaye, R. Lineros, F. Donato, N. Fornengo, and P. Salati, "Positrons from dark matter annihilation in the galactic halo: Theoretical uncertainties," Phys. Rev. **D77** (2008) 063527, arXiv:0712.2312 [astro-ph].

[166] P. Sorensen and C. E. Dahl, "Nuclear recoil energy scale in liquid xenon with application to the direct detection of dark matter," Phys. Rev. **D83** (2011) 063501, arXiv:1101.6080 [astro-ph.IM].

[167] D. Maurin, F. Donato, R. Taillet, and P. Salati, "Cosmic rays below z=30 in a diffusion model: new constraints on propagation parameters," Astrophys. J. **555** (2001) 585–596, arXiv:astro-ph/0101231 [astro-ph].

[168] A. Berlin, D. Hooper, and S. D. McDermott, "Simplified Dark Matter Models for the Galactic Center Gamma-Ray Excess," Phys. Rev. **D89** no. 11, (2014) 115022, arXiv:1404.0022 [hep-ph].

[169] **Fermi-LAT** Collaboration, M. Ackermann et al., "Dark matter constraints from observations of 25 Milky Way satellite galaxies with the Fermi Large Area Telescope," Phys. Rev. **D89** (2014) 042001, arXiv:1310.0828 [astro-ph.HE].

[170] **Fermi-LAT** Collaboration, M. Ackermann et al., "Searching for Dark Matter Annihilation from Milky Way Dwarf Spheroidal Galaxies with Six Years of Fermi Large Area Telescope Data," Phys. Rev. Lett. **115** no. 23, (2015) 231301, arXiv:1503.02641 [astro-ph.HE].

[171] **Fermi-LAT, MAGIC** Collaboration, J. Rico, M. Wood, A. Drlica-Wagner, and J. Aleksić, "Limits to dark matter properties from a combined analysis of MAGIC and Fermi-LAT observations of dwarf satellite galaxies," in Proceedings, 34th International Cosmic Ray Conference (ICRC 2015). 2015. arXiv:1508.05827 [astro-ph.HE]. https://inspirehep.net/record/1389141/files/arXiv:1508.05827.pdf.

[172] A. Geringer-Sameth, S. M. Koushiappas, and M. G. Walker, "Comprehensive search for dark matter annihilation in dwarf galaxies," Phys. Rev. **D91** no. 8, (2015) 083535, arXiv:1410.2242 [astro-ph.CO].

[173] J. Aleksić et al., "Optimized dark matter searches in deep observations of Segue 1 with MAGIC," JCAP **1402** (2014) 008, arXiv:1312.1535 [hep-ph].

[174] **VERITAS** Collaboration, B. Zitzer, "Search for Dark Matter from Dwarf Galaxies using VERITAS," in Proceedings, 34th International Cosmic Ray Conference (ICRC 2015). 2015. arXiv:1509.01105 [astro-ph.HE]. https://inspirehep.net/record/1391628/files/arXiv:1509.01105.pdf.

[175] **HAWC** Collaboration, J. P. Harding and B. Dingus, "Dark Matter Annihilation and Decay Searches with the High Altitude Water Cherenkov (HAWC) Observatory," in Proceedings, 34th International Cosmic Ray Conference (ICRC 2015). 2015.

arXiv:1508.04352 [astro-ph.HE]. https://inspirehep.net/record/1388349/files/arXiv:1508.04352.pdf.

[176] **HESS** Collaboration, A. Abramowski et al., "Search for dark matter annihilation signatures in H.E.S.S. observations of Dwarf Spheroidal Galaxies," Phys. Rev. **D90** (2014) 112012, arXiv:1410.2589 [astro-ph.HE].

[177] **DES, Fermi-LAT** Collaboration, A. Drlica-Wagner et al., "Search for Gamma-Ray Emission from DES Dwarf Spheroidal Galaxy Candidates with Fermi-LAT Data," Astrophys. J. **809** no. 1, (2015) L4, arXiv:1503.02632 [astro-ph.HE].

[178] M. R. Buckley, E. Charles, J. M. Gaskins, A. M. Brooks, A. Drlica-Wagner, P. Martin, and G. Zhao, "Search for Gamma-ray Emission from Dark Matter Annihilation in the Large Magellanic Cloud with the Fermi Large Area Telescope," Phys. Rev. **D91** no. 10, (2015) 102001, arXiv:1502.01020 [astro-ph.HE].

[179] R. Caputo, M. R. Buckley, P. Martin, E. Charles, A. M. Brooks, A. Drlica-Wagner, J. M. Gaskins, and M. Wood, "Search for Gamma-ray Emission from Dark Matter Annihilation in the Small Magellanic Cloud with the Fermi Large Area Telescope," Phys. Rev. **D93** no. 6, (2016) 062004, arXiv:1603.00965 [astro-ph.HE].

[180] B. Siffert, A. Limone, E. Borriello, G. Longo, and G. Miele, "Radio emission from dark matter annihilation in the Large Magellanic Cloud," Monthly Notices of the RAS **410** (Feb., 2011) 2463–2471, arXiv:1006.5325 [astro-ph.HE].

[181] B. Cordier, D. Attie, M. Casse, J. Paul, S. Schanne, P. Sizun, P. Jean, J. P. Roques, and G. Vedrenne, "Search for a light dark matter annihilation signal in the Sagittarius dwarf galaxy," arXiv:astro-ph/0404499 [astro-ph]. [ESA Spec. Publ.552,581(2004)].

[182] M. G. Walker, M. Mateo, E. W. Olszewski, O. Y. Gnedin, X. Wang, B. Sen, and M. Woodroofe, "Velocity Dispersion Profiles of Seven Dwarf Spheroidal Galaxies," Astrophys. J. **667** (2007) L53, arXiv:0708.0010 [astro-ph].

[183] J. e. a. Aleksić, "MAGIC Gamma-ray Telescope Observation of the Perseus Cluster of Galaxies: Implications for Cosmic Rays, Dark Matter, and NGC 1275," ApJ **710** (Feb., 2010) 634–647, arXiv:0909.3267 [astro-ph.HE].

[184] A. e. a. Abramowski, "Search for Dark Matter Annihilation Signals from the Fornax Galaxy Cluster with H.E.S.S.," ApJ **750** (May, 2012) 123, arXiv:1202.5494 [astro-ph.HE].

[185] F. e. a. Aharonian, "Constraints on the multi-TeV particle population in the Coma galaxy cluster with HESS observations," aap **502** (Aug., 2009) 437–443, arXiv:0907.0727.

[186] T. e. a. Arlen, "Constraints on Cosmic Rays, Magnetic Fields, and Dark Matter from Gamma-Ray Observations of the Coma Cluster of Galaxies with VERITAS and Fermi," ApJ **757** (Oct., 2012) 123, arXiv:1208.0676 [astro-ph.HE].

[187] M. e. a. Ackermann, "Constraints on dark matter annihilation in clusters of galaxies with the Fermi large area telescope," Journal of Cosmology and Astroparticle Physics **5** (May, 2010) 025, arXiv:1002.2239 [astro-ph.CO].

[188] X. Huang, G. Vertongen, and C. Weniger, "Probing Dark Matter Decay and Annihilation with Fermi LAT Observations of Nearby Galaxy Clusters," JCAP **1201** (2012) 042, arXiv:1110.1529 [hep-ph].

[189] S. Ando and D. Nagai, "Fermi-LAT constraints on dark matter annihilation cross section from observations of the Fornax cluster," Journal of Cosmology and Astroparticle Physics **7** (July, 2012) 017, arXiv:1201.0753 [astro-ph.HE].

[190] J. Han, C. S. Frenk, V. R. Eke, L. Gao, S. D. M. White, A. Boyarsky, D. Malyshev, and O. Ruchayskiy, "Constraining extended gamma-ray

emission from galaxy clusters," Monthly Notices of the RAS **427** (Dec., 2012) 1651–1665, arXiv:1207.6749 [astro-ph.CO].

[191] **Fermi-LAT** Collaboration, M. Ackermann et al., "Search for extended gamma-ray emission from the Virgo galaxy cluster with Fermi-LAT," Astrophys. J. **812** no. 2, (2015) 159, arXiv:1510.00004 [astro-ph.HE].

[192] E. Storm, T. E. Jeltema, S. Profumo, and L. Rudnick, "Constraints on Dark Matter Annihilation in Clusters of Galaxies from Diffuse Radio Emission," ApJ **768** (May, 2013) 106, arXiv:1210.0872.

[193] A. E. Egorov and E. Pierpaoli, "Constraints on dark matter annihilation by radio observations of M31," Phys. Rev. **D88** no. 2, (2013) 023504, arXiv:1304.0517 [astro-ph.CO].

[194] G. Bertone, M. Cirelli, A. Strumia, and M. Taoso, "Gamma-ray and radio tests of the e+e- excess from DM annihilations," JCAP **0903** (2009) 009, arXiv:0811.3744 [astro-ph].

[195] R. M. Crocker, N. F. Bell, C. Balazs, and D. I. Jones, "Radio and gamma-ray constraints on dark matter annihilation in the Galactic center," Phys. Rev. **D81** (2010) 063516, arXiv:1002.0229 [hep-ph].

[196] N. Fornengo, R. A. Lineros, M. Regis, and M. Taoso, "Galactic synchrotron emission from WIMPs at radio frequencies," Journal of Cosmology and Astroparticle Physics **1** (Jan., 2012) 005, arXiv:1110.4337 [astro-ph.GA].

[197] M. Cirelli and M. Taoso, "Updated galactic radio constraints on Dark Matter," arXiv:1604.06267 [hep-ph].

[198] T. Bringmann, M. Vollmann, and C. Weniger, "Updated cosmic-ray and radio constraints on light dark matter: Implications for the GeV gamma-ray excess at the Galactic center," Phys. Rev. **D90** no. 12, (2014) 123001, arXiv:1406.6027 [astro-ph.HE].

[199] M. Boudaud, "A fussy revisitation of antiprotons as a tool for Dark Matter searches," arXiv:1510.07500 [astro-ph.HE].

[200] H.-B. Jin, Y.-L. Wu, and Y.-F. Zhou, "Implications of the first AMS-02 antiproton data for dark matter," Int. J. Mod. Phys. **A30** no. 28n29, (2015) 1545008, arXiv:1508.06844 [hep-ph].

[201] D. Hooper, T. Linden, and P. Mertsch, "What Does The PAMELA Antiproton Spectrum Tell Us About Dark Matter?," JCAP **1503** no. 03, (2015) 021, arXiv:1410.1527 [astro-ph.HE].

[202] M. Di Mauro and A. Vittino, "AMS-02 electrons and positrons: astrophysical interpretation and Dark Matter constraints," in Proceedings, 34th International Cosmic Ray Conference (ICRC 2015). 2015. arXiv:1507.08680 [astro-ph.HE]. https://inspirehep.net/record/1385851/files/arXiv:1507.08680.pdf.

[203] A. Ibarra, A. S. Lamperstorfer, and J. Silk, "Dark matter annihilations and decays after the AMS-02 positron measurements," Phys. Rev. **D89** no. 6, (2014) 063539, arXiv:1309.2570 [hep-ph].

[204] B.-Q. Lu and H.-S. Zong, "Limits on the Dark Matter from AMS-02 antiproton and positron fraction data," arXiv:1510.04032 [astro-ph.HE].

[205] **IceCube** Collaboration, M. G. Aartsen et al., "All-flavour Search for Neutrinos from Dark Matter Annihilations in the Milky Way with IceCube/DeepCore," Eur. Phys. J. **C76** no. 10, (2016) 531, arXiv:1606.00209 [astro-ph.HE].

[206] J. D. Zornoza and C. Toennis, "Results of dark matter searches with the ANTARES neutrino telescope," in 27th International Conference on Neutrino Physics and Astrophysics (Neutrino 2016) Lon 2016. arXiv:1611.02555 [astro-ph.HE]. https://inspirehep.net/record/1496365/files/arXiv:1611.02555.pdf.

[207] J. Choquette, J. M. Cline, and J. M. Cornell, "p-wave Annihilating Dark Matter from a Decaying Predecessor and the Galactic Center Excess," Phys. Rev. **D94** no. 1, (2016) 015018, arXiv:1604.01039 [hep-ph].

[208] A. E. Vladimirov, S. W. Digel, G. Johannesson, P. F. Michelson, I. V. Moskalenko, P. L. Nolan, E. Orlando, T. A. Porter, and A. W. Strong, "GALPROP WebRun: an internet-based service for calculating galactic cosmic ray propagation and associated photon emissions," Comput. Phys. Commun. **182** (2011) 1156–1161, arXiv:1008.3642 [astro-ph.HE].

[209] M. W. Goodman and E. Witten, "Detectability of Certain Dark Matter Candidates," Phys. Rev. **D31** (1985) 3059.

[210] J. Fan, M. Reece, and L.-T. Wang, "Non-relativistic effective theory of dark matter direct detection," JCAP **1011** (2010) 042, arXiv:1008.1591 [hep-ph].

[211] A. L. Fitzpatrick, W. Haxton, E. Katz, N. Lubbers, and Y. Xu, "The Effective Field Theory of Dark Matter Direct Detection," JCAP **1302** (2013) 004, arXiv:1203.3542 [hep-ph].

[212] R. Catena and B. Schwabe, "Form factors for dark matter capture by the Sun in effective theories," JCAP **1504** no. 04, (2015) 042, arXiv:1501.03729 [hep-ph].

[213] F. Mayet et al., "A review of the discovery reach of directional Dark Matter detection," Phys. Rept. **627** (2016) 1–49, arXiv:1602.03781 [astro-ph.CO].

[214] K. Freese, M. Lisanti, and C. Savage, "Colloquium: Annual modulation of dark matter," Rev. Mod. Phys. **85** (2013) 1561–1581, arXiv:1209.3339 [astro-ph.CO].

[215] R. Essig, A. Manalaysay, J. Mardon, P. Sorensen, and T. Volansky, "First Direct Detection Limits on sub-GeV Dark Matter from XENON10," Phys. Rev. Lett. **109** (2012) 021301, arXiv:1206.2644 [astro-ph.CO].

[216] R. Essig, M. Fernandez-Serra, J. Mardon, A. Soto, T. Volansky, and T.-T. Yu, "Direct Detection of sub-GeV Dark Matter with Semiconductor Targets," arXiv:1509.01598 [hep-ph].

[217] S. K. Lee, M. Lisanti, S. Mishra-Sharma, and B. R. Safdi, "Modulation Effects in Dark Matter-Electron Scattering Experiments," Phys. Rev. **D92** no. 8, (2015) 083517, arXiv:1508.07361 [hep-ph].

[218] V. Novikov, M. A. Shifman, A. Vainshtein, and V. I. Zakharov, "Calculations in External Fields in Quantum Chromodynamics. Technical Review," Fortsch.Phys. **32** (1984) 585.

[219] J. Hisano, R. Nagai, and N. Nagata, "Effective Theories for Dark Matter Nucleon Scattering," arXiv:1502.02244 [hep-ph].

[220] S. Groote and A. Pivovarov, "Heavy quark induced effective action for gauge fields in the SU(N(c)) x U(1) model and the low-energy structure of heavy quark current correlators," Eur.Phys.J. **C21** (2001) 133–143, arXiv:hep-ph/0103313 [hep-ph].

[221] M. T. Frandsen, U. Haisch, F. Kahlhoefer, P. Mertsch, and K. Schmidt-Hoberg, "Loop-induced dark matter direct detection signals from gamma-ray lines," JCAP **1210** (2012) 033, arXiv:1207.3971 [hep-ph].

[222] A. J. Buras, "Asymptotic Freedom in Deep Inelastic Processes in the Leading Order and Beyond," Rev. Mod. Phys. **52** (1980) 199.

[223] J. Hisano, K. Ishiwata, and N. Nagata, "Gluon contribution to the dark matter direct detection," Phys.Rev. **D82** (2010) 115007, arXiv:1007.2601 [hep-ph].

[224] M. Drees and M. Nojiri, "Neutralino - nucleon scattering revisited," Phys. Rev. **D48** (1993) 3483–3501, arXiv:hep-ph/9307208 [hep-ph].

[225] P. B. Pal, "Representation-independent manipulations with Dirac spinors," arXiv:physics/0703214 [physics.ed-ph].

[226] P. Agrawal, Z. Chacko, and C. B. Verhaaren, "Leptophilic Dark Matter and the Anomalous Magnetic Moment of the Muon," JHEP **1408** (2014) 147, arXiv:1402.7369 [hep-ph].

[227] G. Belanger, F. Boudjema, A. Pukhov, and A. Semenov, "Dark matter direct detection rate in a generic model with micrOMEGAs 2.2," Comput. Phys. Commun. **180** (2009) 747–767, arXiv:0803.2360 [hep-ph].

[228] J. Hisano, K. Ishiwata, N. Nagata, and M. Yamanaka, "Direct Detection of Vector Dark Matter," Prog. Theor. Phys. **126** (2011) 435–456, arXiv:1012.5455 [hep-ph].

[229] P. Agrawal, Z. Chacko, C. Kilic, and R. K. Mishra, "A Classification of Dark Matter Candidates with Primarily Spin-Dependent Interactions with Matter," arXiv:1003.1912 [hep-ph].

[230] M. Cirelli, E. Del Nobile, and P. Panci, "Tools for model-independent bounds in direct dark matter searches," JCAP **1310** (2013) 019, arXiv:1307.5955 [hep-ph].

[231] M. A. Shifman, A. I. Vainshtein, and V. I. Zakharov, "Remarks on Higgs Boson Interactions with Nucleons," Phys. Lett. **B78** (1978) 443–446.

[232] H.-Y. Cheng and C.-W. Chiang, "Revisiting Scalar and Pseudoscalar Couplings with Nucleons," JHEP **1207** (2012) 009, arXiv:1202.1292 [hep-ph].

[233] X.-d. Ji and D. Toublan, "Heavy-quark contribution to the proton's magnetic moment," Phys.Lett. **B647** (2007) 361–365, arXiv:hep-ph/0605055 [hep-ph].

[234] G. Belanger, F. Boudjema, A. Pukhov, and A. Semenov, "micrOMEGAs3: A program for calculating dark matter observables," Comput. Phys. Commun. **185** (2014) 960–985, arXiv:1305.0237 [hep-ph].

[235] F. Lyonnet, A. Kusina, T. Ježo, K. Kovarík, F. Olness, I. Schienbein, and J.-Y. Yu, "On the intrinsic bottom content of the nucleon and its impact on heavy new physics at the LHC," JHEP **07** (2015) 141, arXiv:1504.05156 [hep-ph].

[236] M. V. Polyakov, A. Schafer, and O. Teryaev, "The Intrinsic charm contribution to the proton spin," Phys.Rev. **D60** (1999) 051502, arXiv:hep-ph/9812393 [hep-ph].

[237] Greiner, W. Schramm, S. Stein, E., Quantum Chromodynamics. Springer-Verlag, Berlin Heidelberg, 2007. http://www.springer.com/gb/book/9783540485346.

[238] E. Stein, P. Gornicki, L. Mankiewicz, and A. Schafer, "QCD sum rule calculation of twist four corrections to Bjorken and Ellis-Jaffe sum rules," Phys. Lett. **B353** (1995) 107–113, arXiv:hep-ph/9502323 [hep-ph].

[239] N.-Y. Lee, K. Goeke, and C. Weiss, "Spin dependent twist four matrix elements from the instanton vacuum: Flavor singlet and nonsinglet," Phys. Rev. **D65** (2002) 054008, arXiv:hep-ph/0105173 [hep-ph].

[240] K. G. Chetyrkin, B. A. Kniehl, and M. Steinhauser, "Strong coupling constant with flavor thresholds at four loops in the MS scheme," Phys. Rev. Lett. **79** (1997) 2184–2187, arXiv:hep-ph/9706430 [hep-ph].

[241] **Particle Data Group** Collaboration, C. Patrignani et al., "Review of Particle Physics," Chin. Phys. **C40** no. 10, (2016) 100001.

[242] J. M. Alarcon, J. Martin Camalich, and J. A. Oller, "The chiral representation of the πN scattering amplitude and the pion-nucleon sigma term," Phys. Rev. **D85** (2012) 051503, arXiv:1110.3797 [hep-ph].

[243] A. Crivellin, M. Hoferichter, and M. Procura, "Accurate evaluation of hadronic uncertainties in spin-independent WIMP-nucleon scattering: Disentangling two- and three-flavor effects," Phys. Rev. **D89** (2014) 054021, arXiv:1312.4951 [hep-ph].

[244] L. Alvarez-Ruso, T. Ledwig, J. Martin Camalich, and M. J. Vicente Vacas, "Nucleon mass and pion-nucleon sigma term from a chiral analysis of lattice QCD world data," EPJ Web Conf. **73** (2014) 04015.

[245] F. Bishara, J. Brod, B. Grinstein, and J. Zupan, "Chiral Effective Theory of Dark Matter Direct Detection," JCAP **1702** no. 02, (2017) 009, arXiv:1611.00368 [hep-ph].

[246] **Particle Data Group** Collaboration, K. A. Olive et al., "Review of Particle Physics," Chin. Phys. **C38** (2014) 090001.

[247] S. D. Bass, R. J. Crewther, F. M. Steffens, and A. W. Thomas, "Heavy quark axial charges to nonleading order," Phys. Rev. **D66** (2002) 031901, arXiv:hep-ph/0207071 [hep-ph].

[248] S. D. Bass, "Neutrino proton elastic scattering and the spin structure of the proton," Nucl. Phys. **A752** (2005) 34–37, arXiv:hep-ph/0407243 [hep-ph].

[249] J. Collins, F. Wilczek, and A. Zee, "Low-energy manifestations of heavy particles: Application to the neutral current," Phys. Rev. D **18** (Jul, 1978) 242–247. http://link.aps.org/doi/10.1103/PhysRevD.18.242.

[250] D. B. Kaplan and A. Manohar, "Strange Matrix Elements in the Proton from Neutral Current Experiments," Nucl.Phys. **B310** (1988) 527.

[251] J. Li and A. W. Thomas, "Bottom quark contribution to spin-dependent dark matter detection," Nucl. Phys. **B906** (2016) 60–76, arXiv:1506.03560 [hep-ph].

[252] H.-x. He and X.-D. Ji, "The Nucleon's tensor charge," Phys. Rev. **D52** (1995) 2960–2963, arXiv:hep-ph/9412235 [hep-ph].

[253] Z.-B. Kang, A. Prokudin, P. Sun, and F. Yuan, "Extraction of Quark Transversity Distribution and Collins Fragmentation Functions with QCD Evolution," Phys. Rev. **D93** no. 1, (2016) 014009, arXiv:1505.05589 [hep-ph].

[254] **PNDME** Collaboration, T. Bhattacharya, V. Cirigliano, S. Cohen, R. Gupta, A. Joseph, H.-W. Lin, and B. Yoon, "Iso-vector and Iso-scalar

Tensor Charges of the Nucleon from Lattice QCD," Phys. Rev. **D92** no. 9, (2015) 094511, arXiv:1506.06411 [hep-lat].

[255] S. Scopel and H. Yu, "From direct detection to relic abundance: the case of proton-philic spin-dependent inelastic Dark Matter," JCAP **1704** no. 04, (2017) 031, arXiv:1701.02215 [hep-ph].

[256] M. Pitschmann, C.-Y. Seng, C. D. Roberts, and S. M. Schmidt, "Nucleon tensor charges and electric dipole moments," Phys. Rev. **D91** (2015) 074004, arXiv:1411.2052 [nucl-th].

[257] N. Yamanaka, T. M. Doi, S. Imai, and H. Suganuma, "Quark tensor charge and electric dipole moment within the Schwinger-Dyson formalism," Phys. Rev. **D88** (2013) 074036, arXiv:1307.4208 [hep-ph].

[258] F. D'Eramo and M. Procura, "Connecting Dark Matter UV Complete Models to Direct Detection Rates via Effective Field Theory," JHEP **04** (2015) 054, arXiv:1411.3342 [hep-ph].

[259] J. Kopp, L. Michaels, and J. Smirnov, "Loopy Constraints on Leptophilic Dark Matter and Internal Bremsstrahlung," JCAP **1404** (2014) 022, arXiv:1401.6457 [hep-ph].

[260] N. Anand, A. L. Fitzpatrick, and W. C. Haxton, "Weakly interacting massive particle-nucleus elastic scattering response," Phys. Rev. **C89** no. 6, (2014) 065501, arXiv:1308.6288 [hep-ph].

[261] T. Marrodán Undagoitia and L. Rauch, "Dark matter direct-detection experiments," J. Phys. **G43** no. 1, (2016) 013001, arXiv:1509.08767 [physics.ins-det].

[262] **PICASSO** Collaboration, S. Archambault et al., "Constraints on Low-Mass WIMP Interactions on ^{19}F from PICASSO," Phys. Lett. **B711** (2012) 153–161, arXiv:1202.1240 [hep-ex].

[263] **COUPP** Collaboration, E. Behnke et al., "First Dark Matter Search Results from a 4-kg CF_3I Bubble Chamber Operated in a Deep Underground Site,"

Phys. Rev. **D86** no. 5, (2012) 052001, arXiv:1204.3094 [astro-ph.CO]. [Erratum: Phys. Rev.D90,no.7,079902(2014)].

[264] **PICO** Collaboration, C. Amole et al., "Dark Matter Search Results from the PICO-2L C_3F_8 Bubble Chamber," Phys. Rev. Lett. **114** no. 23, (2015) 231302, arXiv:1503.00008 [astro-ph.CO].

[265] **PICO** Collaboration, C. Amole et al., "Dark matter search results from the PICO-60 CF_3I bubble chamber," Phys. Rev. **D93** no. 5, (2016) 052014, arXiv:1510.07754 [hep-ex].

[266] **SuperCDMS** Collaboration, R. Agnese et al., "Search for Low-Mass Weakly Interacting Massive Particles with SuperCDMS," Phys. Rev. Lett. **112** no. 24, (2014) 241302, arXiv:1402.7137 [hep-ex].

[267] **LUX** Collaboration, D. S. Akerib et al., "First results from the LUX dark matter experiment at the Sanford Underground Research Facility," Phys. Rev. Lett. **112** (2014) 091303, arXiv:1310.8214 [astro-ph.CO].

[268] **LUX** Collaboration, D. S. Akerib et al., "Improved WIMP scattering limits from the LUX experiment," arXiv:1512.03506 [astro-ph.CO].

[269] **CRESST** Collaboration, G. Angloher et al., "Results on light dark matter particles with a low-threshold CRESST-II detector," Eur. Phys. J. **C76** no. 1, (2016) 25, arXiv:1509.01515 [astro-ph.CO].

[270] **SuperCDMS** Collaboration, R. Agnese et al., "Search for Low-Mass Weakly Interacting Massive Particles with SuperCDMS," Phys. Rev. Lett. **112** no. 24, (2014) 241302, arXiv:1402.7137 [hep-ex].

[271] T. Saab, "An Introduction to Dark Matter Direct Detection Searches & Techniques," in The Dark Secrets of the Terascale: Proceedings, TASI 2011, Boulder, Colorado, USA, Ju pp. 711–738. 2013. arXiv:1203.2566 [physics.ins-det]. https://inspirehep.net/record/1093524/files/arXiv:1203.2566.pdf.

[272] L. Baudis, "Direct dark matter detection: the next decade," Phys. Dark Univ. **1** (2012) 94–108, arXiv:1211.7222 [astro-ph.IM].

[273] M. Messina, "Status of direct search of WIMP Dark Matter," PoS **NOW2016** (2017) 080.

[274] L. Roszkowski, E. M. Sessolo, and S. Trojanowski, "WIMP dark matter candidates and searches - current issues and future prospects," arXiv:1707.06277 [hep-ph].

[275] J. Conrad, "Statistical Issues in Astrophysical Searches for Particle Dark Matter," Astropart. Phys. **62** (2015) 165–177, arXiv:1407.6617 [astro-ph.CO].

[276] S. Yellin, "Finding an upper limit in the presence of unknown background," Phys. Rev. **D66** (2002) 032005, arXiv:physics/0203002 [physics].

[277] S. Yellin, "Extending the optimum interval method," ArXiv e-prints (Sept., 2007) , arXiv:0709.2701 [physics.data-an].

[278] G. J. Feldman and R. D. Cousins, "A Unified approach to the classical statistical analysis of small signals," Phys. Rev. **D57** (1998) 3873–3889, arXiv:physics/9711021 [physics.data-an].

[279] F. D'Eramo, B. J. Kavanagh, and P. Panci, "Probing Leptophilic Dark Sectors with Hadronic Processes," arXiv:1702.00016 [hep-ph].

[280] S. Malik et al., "Interplay and Characterization of Dark Matter Searches at Colliders and in Direct Detection Experiments," 2014. arXiv:1409.4075 [hep-ex].
http://inspirehep.net/record/1316493/files/arXiv:1409.4075.pdf.

[281] T. J. Weiler, "On the likely dominance of WIMP annihilation to fermion pair+W/Z (and implication for indirect detection)," arXiv:1301.0021 [hep-ph]. [AIP Conf. Proc.1534,165(2012)].

[282] M. D. Schwartz, Quantum Field Theory and the Standard Model. Cambridge University Press, 2014. http://www.cambridge.org/us/academic/subjects/physics/theoretical-physics-and-mathematical-physics/quantum-field-theory-and-standard-model.

[283] K. Cheung, P.-Y. Tseng, Y.-L. S. Tsai, and T.-C. Yuan, "Global Constraints on Effective Dark Matter Interactions: Relic Density, Direct Detection, Indirect Detection, and Collider," JCAP **1205** (2012) 001, arXiv:1201.3402 [hep-ph].

[284] **ATLAS** Collaboration, G. Aad et al., "Search for direct third-generation squark pair production in final states with missing transverse momentum and two b-jets in $\sqrt{s} = 8$ TeV pp collisions with the ATLAS detector," JHEP **10** (2013) 189, arXiv:1308.2631 [hep-ex].

[285] **ATLAS** Collaboration, G. Aad et al., "Summary of the searches for squarks and gluinos using $\sqrt{s} = 8$ TeV pp collisions with the ATLAS experiment at the LHC," JHEP **10** (2015) 054, arXiv:1507.05525 [hep-ex].

[286] R. Davis, Jr., D. S. Harmer, and K. C. Hoffman, "Search for neutrinos from the sun," Phys. Rev. Lett. **20** (1968) 1205–1209.

[287] J. N. Bahcall, N. A. Bahcall, and G. Shaviv, "Present status of the theoretical predictions for the Cl-36 solar neutrino experiment," Phys. Rev. Lett. **20** (1968) 1209–1212.

[288] **Super-Kamiokande** Collaboration, Y. Fukuda et al., "Measurements of the solar neutrino flux from Super-Kamiokande's first 300 days," Phys. Rev. Lett. **81** (1998) 1158–1162, arXiv:hep-ex/9805021 [hep-ex]. [Erratum: Phys. Rev. Lett.81,4279(1998)].

[289] L. Wolfenstein, "Neutrino Oscillations and Stellar Collapse," Phys. Rev. **D20** (1979) 2634–2635.

[290] L. Wolfenstein, "Neutrino Oscillations in Matter," Phys. Rev. **D17** (1978) 2369–2374.

[291] S. P. Mikheev and A. Yu. Smirnov, "Resonance Amplification of Oscillations in Matter and Spectroscopy of Solar Neutrinos," Sov. J. Nucl. Phys. **42** (1985) 913–917. [Yad. Fiz.42,1441(1985)].

[292] S. P. Mikheev and A. Yu. Smirnov, "Resonant amplification of neutrino oscillations in matter and solar neutrino spectroscopy," Nuovo Cim. **C9** (1986) 17–26.

[293] **Borexino** Collaboration, G. Bellini et al., "Final results of Borexino Phase-I on low energy solar neutrino spectroscopy," Phys. Rev. **D89** no. 11, (2014) 112007, arXiv:1308.0443 [hep-ex].

[294] **SNO** Collaboration, B. Aharmim et al., "Determination of the ν_e and total ^{8}B solar neutrino fluxes with the Sudbury neutrino observatory phase I data set," Phys. Rev. **C75** (2007) 045502, arXiv:nucl-ex/0610020 [nucl-ex].

[295] N. Arkani-Hamed, S. Dimopoulos, G. R. Dvali, and J. March-Russell, "Neutrino masses from large extra dimensions," Phys. Rev. **D65** (2001) 024032, arXiv:hep-ph/9811448 [hep-ph].

[296] E. Aprile and XENON1T collaboration, "The XENON1T Dark Matter Search Experiment," ArXiv e-prints (June, 2012) , arXiv:1206.6288 [astro-ph.IM].

[297] B. Cabrera, L. M. Krauss, and F. Wilczek, "Bolometric detection of neutrinos," Phys. Rev. Lett. **55** (Jul, 1985) 25–28. https://link.aps.org/doi/10.1103/PhysRevLett.55.25.

[298] J. Monroe and P. Fisher, "Neutrino Backgrounds to Dark Matter Searches," Phys. Rev. **D76** (2007) 033007, arXiv:0706.3019 [astro-ph].

[299] L. E. Strigari, "Neutrino Coherent Scattering Rates at Direct Dark Matter Detectors," New J. Phys. **11** (2009) 105011, arXiv:0903.3630 [astro-ph.CO].

[300] J. Billard, L. Strigari, and E. Figueroa-Feliciano, "Implication of neutrino backgrounds on the reach of next generation dark matter direct detection experiments," Phys. Rev. **D89** no. 2, (2014) 023524, arXiv:1307.5458 [hep-ph].

[301] D. Z. Freedman, "Coherent effects of a weak neutral current," Phys. Rev. D **9** (Mar, 1974) 1389–1392. https://link.aps.org/doi/10.1103/PhysRevD.9.1389.

[302] D. Z. Freedman, D. N. Schramm, and D. L. Tubbs, "The Weak Neutral Current and Its Effects in Stellar Collapse," Ann. Rev. Nucl. Part. Sci. **27** (1977) 167–207.

[303] R. H. Helm, "Inelastic and elastic scattering of 187-mev electrons from selected even-even nuclei," Phys. Rev. **104** (Dec, 1956) 1466–1475. https://link.aps.org/doi/10.1103/PhysRev.104.1466.

[304] **LUX** Collaboration, D. S. Akerib et al., "Tritium calibration of the LUX dark matter experiment," arXiv:1512.03133 [physics.ins-det].

[305] L. Baudis, "WIMP Dark Matter Direct-Detection Searches in Noble Gases," Phys. Dark Univ. **4** (2014) 50–59, arXiv:1408.4371 [astro-ph.IM].

[306] **LZ** Collaboration, D. S. Akerib et al., "LUX-ZEPLIN (LZ) Conceptual Design Report," arXiv:1509.02910 [physics.ins-det].

[307] **DARWIN Consortium** Collaboration, L. Baudis, "DARWIN: dark matter WIMP search with noble liquids," J. Phys. Conf. Ser. **375** (2012) 012028, arXiv:1201.2402 [astro-ph.IM].

[308] F. S. Queiroz and W. Shepherd, "New Physics Contributions to the Muon Anomalous Magnetic Moment: A Numerical Code," Phys. Rev. **D89** no. 9, (2014) 095024, arXiv:1403.2309 [hep-ph].

[309] D. Hanneke, S. F. Hoogerheide, and G. Gabrielse, "Cavity Control of a Single-Electron Quantum Cyclotron: Measuring the Electron Magnetic

Moment," Phys. Rev. **A83** (2011) 052122, arXiv:1009.4831 [physics.atom-ph].

[310] J. Redondo and G. Raffelt, "Solar constraints on hidden photons re-visited," JCAP **1308** (2013) 034, arXiv:1305.2920 [hep-ph].

[311] D. F. Bartlett and S. Lögl, "Limits on an electromagnetic fifth force," Phys. Rev. Lett. **61** (Nov, 1988) 2285–2287. https://link.aps.org/doi/10.1103/PhysRevLett.61.2285.

[312] J. B. Dent, F. Ferrer, and L. M. Krauss, "Constraints on Light Hidden Sector Gauge Bosons from Supernova Cooling," arXiv:1201.2683 [astro-ph.CO].

[313] J. D. Bjorken, R. Essig, P. Schuster, and N. Toro, "New Fixed-Target Experiments to Search for Dark Gauge Forces," Phys. Rev. **D80** (2009) 075018, arXiv:0906.0580 [hep-ph].

[314] H. Merkel et al., "Search at the Mainz Microtron for Light Massive Gauge Bosons Relevant for the Muon g-2 Anomaly," Phys. Rev. Lett. **112** no. 22, (2014) 221802, arXiv:1404.5502 [hep-ex].

[315] **APEX** Collaboration, S. Abrahamyan et al., "Search for a New Gauge Boson in Electron-Nucleus Fixed-Target Scattering by the APEX Experiment," Phys. Rev. Lett. **107** (2011) 191804, arXiv:1108.2750 [hep-ex].

[316] J. Heeck, "Unbroken B – L symmetry," Phys. Lett. **B739** (2014) 256–262, arXiv:1408.6845 [hep-ph].

[317] **BaBar** Collaboration, J. P. Lees et al., "Search for a Dark Photon in e^+e^- Collisions at BaBar," Phys. Rev. Lett. **113** no. 20, (2014) 201801, arXiv:1406.2980 [hep-ex].

[318] R. Essig, J. Mardon, M. Papucci, T. Volansky, and Y.-M. Zhong, "Constraining Light Dark Matter with Low-Energy e^+e^- Colliders," JHEP **11** (2013) 167, arXiv:1309.5084 [hep-ph].

[319] **BOREXINO** Collaboration, G. Bellini et al., "Neutrinos from the primary proton–proton fusion process in the Sun," Nature **512** no. 7515, (2014) 383–386.

[320] R. Saldanha, Precision Measurement of the 7 Be Solar Neutrino Interaction Rate in Borexino. PhD thesis, Princeton University, January 2012. https://www.princeton.edu/physics/graduate-program/theses/Saldanha-thesis.pdf.

[321] G. Bellini et al., "Precision measurement of the 7Be solar neutrino interaction rate in Borexino," Phys. Rev. Lett. **107** (2011) 141302, arXiv:1104.1816 [hep-ex].

[322] **Super-Kamiokande** Collaboration, K. Abe et al., "Solar neutrino results in Super-Kamiokande-III," Phys. Rev. **D83** (2011) 052010, arXiv:1010.0118 [hep-ex].

[323] **Super-Kamiokande** Collaboration, K. Abe et al., "Solar Neutrino Measurements in Super-Kamiokande-IV," Phys. Rev. **D94** no. 5, (2016) 052010, arXiv:1606.07538 [hep-ex].

[324] T. Yokozawa, Precision solar neutrino measurements with Super-Kamiokande-IV. PhD thesis, U. Tokyo (main), 2012. http://www-sk.icrr.u-tokyo.ac.jp/sk/pub/yokozawa_thesis.pdf.

[325] P. Agrawal, M. Blanke, and K. Gemmler, "Flavored dark matter beyond Minimal Flavor Violation," JHEP **10** (2014) 72, arXiv:1405.6709 [hep-ph].

[326] M. Blanke, "Flavoured Dark Matter Beyond MFV," PoS **FWNP** (2014) 011, arXiv:1412.3589 [hep-ph].

[327] M.-C. Chen, J. Huang, and V. Takhistov, "Beyond Minimal Lepton Flavored Dark Matter," JHEP **02** (2016) 060, arXiv:1510.04694 [hep-ph].

[328] M. Blanke and S. Kast, "Top-Flavoured Dark Matter in Dark Minimal Flavour Violation," arXiv:1702.08457 [hep-ph].

[329] G. Isidori and D. M. Straub, "Minimal Flavour Violation and Beyond," Eur. Phys. J. **C72** (2012) 2103, arXiv:1202.0464 [hep-ph].

[330] M. E. Peskin and D. V. Schroeder, An Introduction to quantum field theory. 1995. http://www.slac.stanford.edu/spires/find/books/www?cl=QC174.45%3AP4.

[331] H. An, X. Ji, and L.-T. Wang, "Light Dark Matter and Z' Dark Force at Colliders," JHEP **07** (2012) 182, arXiv:1202.2894 [hep-ph].

[332] T. Jacques and K. Nordström, "Mapping monojet constraints onto Simplified Dark Matter Models," JHEP **06** (2015) 142, arXiv:1502.05721 [hep-ph].

[333] G. Busoni, A. De Simone, T. Jacques, E. Morgante, and A. Riotto, "Making the Most of the Relic Density for Dark Matter Searches at the LHC 14 TeV Run," JCAP **1503** no. 03, (2015) 022, arXiv:1410.7409 [hep-ph].

[334] G. Bertone, D. Hooper, and J. Silk, "Particle dark matter: Evidence, candidates and constraints," Phys. Rept. **405** (2005) 279–390, arXiv:hep-ph/0404175 [hep-ph].

[335] M. Backovic, K. Kong, and M. McCaskey, "MadDM v.1.0: Computation of Dark Matter Relic Abundance Using MadGraph5," Physics of the Dark Universe **5-6** (2014) 18–28, arXiv:1308.4955 [hep-ph].

[336] G. Bélanger, F. Boudjema, A. Pukhov, and A. Semenov, "micrOMEGAs4.1: two dark matter candidates," Comput. Phys. Commun. **192** (2015) 322–329, arXiv:1407.6129 [hep-ph].

[337] A. Karam and K. Tamvakis, "Dark Matter from a Classically Scale-Invariant $SU(3)_X$," Phys. Rev. **D94** no. 5, (2016) 055004, arXiv:1607.01001 [hep-ph].

[338] M. Bobrowski, A. Lenz, and T. Rauh, "Short distance D-Dbar mixing," in Proceedings, 5th International Workshop on Charm Physics (Charm 2012): Honolulu, Ha 2012. arXiv:1208.6438 [hep-ph]. https://inspirehep.net/record/1184026/files/arXiv:1208.6438.pdf.

[339] A. F. Falk, Y. Grossman, Z. Ligeti, and A. A. Petrov, "SU(3) breaking and D0 - anti-D0 mixing," Phys. Rev. **D65** (2002) 054034, arXiv:hep-ph/0110317 [hep-ph].

[340] A. F. Falk, Y. Grossman, Z. Ligeti, Y. Nir, and A. A. Petrov, "The D0 - anti-D0 mass difference from a dispersion relation," Phys. Rev. **D69** (2004) 114021, arXiv:hep-ph/0402204 [hep-ph].

[341] E. Golowich and A. A. Petrov, "Short distance analysis of D0 - anti-D0 mixing," Phys. Lett. **B625** (2005) 53–62, arXiv:hep-ph/0506185 [hep-ph].

[342] A. Lenz and M. Bobrowski, "Standard Model Predictions for D^0-oscillations and CP-violation," Int. J. Mod. Phys. Conf. Ser. **02** (2011) 117–121, arXiv:1011.5608 [hep-ph].

[343] A. Lenz and T. Rauh, "D-meson lifetimes within the heavy quark expansion," Phys. Rev. **D88** (2013) 034004, arXiv:1305.3588 [hep-ph].

[344] E. Golowich, J. Hewett, S. Pakvasa, and A. A. Petrov, "Implications of D^0 - $\bar{D}^0$ Mixing for New Physics," Phys. Rev. **D76** (2007) 095009, arXiv:0705.3650 [hep-ph].

[345] P. Singer, "Rare decays of heavy quarks: Searching ground for new physics," Acta Phys. Polon. **B30** (1999) 3861–3873, arXiv:hep-ph/9911215 [hep-ph].

[346] H. E. Logan and U. Nierste, "$B_{s,d} \to \ell^+\ell^-$ in a two Higgs doublet model," Nucl. Phys. **B586** (2000) 39–55, arXiv:hep-ph/0004139 [hep-ph].

[347] **Fermi-LAT** Collaboration, M. Ackermann et al., "Updated search for spectral lines from Galactic dark matter interactions with pass 8 data from

the Fermi Large Area Telescope," Phys. Rev. **D91** no. 12, (2015) 122002, arXiv:1506.00013 [astro-ph.HE].

[348] C. B. Jackson, G. Servant, G. Shaughnessy, T. M. P. Tait, and M. Taoso, "Gamma-ray lines and One-Loop Continuum from s-channel Dark Matter Annihilations," JCAP **1307** (2013) 021, arXiv:1302.1802 [hep-ph].

[349] H. H. Patel, "Package-X: A Mathematica package for the analytic calculation of one-loop integrals," Comput. Phys. Commun. **197** (2015) 276–290, arXiv:1503.01469 [hep-ph].

[350] A. Alloul, N. D. Christensen, C. Degrande, C. Duhr, and B. Fuks, "FeynRules 2.0 - A complete toolbox for tree-level phenomenology," Comput. Phys. Commun. **185** (2014) 2250–2300, arXiv:1310.1921 [hep-ph].

[351] T. Hahn, "Generating Feynman diagrams and amplitudes with FeynArts 3," Comput. Phys. Commun. **140** (2001) 418–431, arXiv:hep-ph/0012260 [hep-ph].

[352] T. Hahn and M. Perez-Victoria, "Automatized one loop calculations in four-dimensions and D-dimensions," Comput. Phys. Commun. **118** (1999) 153–165, arXiv:hep-ph/9807565 [hep-ph].

[353] P. Gondolo and S. Scopel, "On the sbottom resonance in dark matter scattering," JCAP **1310** (2013) 032, arXiv:1307.4481.

[354] A. Ibarra and S. Wild, "Dirac dark matter with a charged mediator: a comprehensive one-loop analysis of the direct detection phenomenology," JCAP **1505** no. 05, (2015) 047, arXiv:1503.03382 [hep-ph].

[355] F. Kahlhoefer and S. Wild, "Studying generalised dark matter interactions with extended halo-independent methods," JCAP **1610** no. 10, (2016) 032, arXiv:1607.04418 [hep-ph].

[356] S. Chang, R. Edezhath, J. Hutchinson, and M. Luty, "Leptophilic Effective WIMPs," Phys. Rev. **D90** no. 1, (2014) 015011, arXiv:1402.7358 [hep-ph].

[357] P. Agrawal, S. Blanchet, Z. Chacko, and C. Kilic, "Flavored Dark Matter, and Its Implications for Direct Detection and Colliders," Phys. Rev. **D86** (2012) 055002, arXiv:1109.3516 [hep-ph].

[358] A. L. Fitzpatrick, W. Haxton, E. Katz, N. Lubbers, and Y. Xu, "Model Independent Direct Detection Analyses," arXiv:1211.2818 [hep-ph].

[359] M. Schumann, L. Baudis, L. Bütikofer, A. Kish, and M. Selvi, "Dark matter sensitivity of multi-ton liquid xenon detectors," JCAP **1510** no. 10, (2015) 016, arXiv:1506.08309 [physics.ins-det].

[360] **ATLAS, CMS** Collaboration, A. de Cosa, "LHC results for dark matter from ATLAS and CMS," in Proceedings, 12th Conference on the Intersections of Particle and Nuclear Physics (CIPA 2015. arXiv:1510.01516 [hep-ex]. https://inspirehep.net/record/1396320/files/arXiv:1510.01516.pdf.

[361] S. Y. Hoh, J. Komaragiri, and W. A. T. B. W. Abdullah, "Dark Matter Searches at the Large Hadron Collider," AIP Conf. Proc. **1704** (2016) 020005, arXiv:1512.07376 [hep-ex].

[362] J. Goodman, M. Ibe, A. Rajaraman, W. Shepherd, T. M. P. Tait, and H.-B. Yu, "Constraints on Dark Matter from Colliders," Phys. Rev. **D82** (2010) 116010, arXiv:1008.1783 [hep-ph].

[363] M. Papucci, A. Vichi, and K. M. Zurek, "Monojet versus the rest of the world I: t-channel models," JHEP **11** (2014) 024, arXiv:1402.2285 [hep-ph].

[364] H. An, L.-T. Wang, and H. Zhang, "Dark matter with t-channel mediator: a simple step beyond contact interaction," Phys. Rev. **D89** no. 11, (2014) 115014, arXiv:1308.0592 [hep-ph].

[365] A. Goyal and M. Kumar, "Fermionic Dark Matter in a simple t-channel model," JCAP **1611** no. 11, (2016) 001, arXiv:1609.03364 [hep-ph].

[366] M. E. Peskin and T. Takeuchi, "A New constraint on a strongly interacting Higgs sector," Phys. Rev. Lett. **65** (1990) 964–967.

[367] M. E. Peskin and T. Takeuchi, "Estimation of oblique electroweak corrections," Phys. Rev. **D46** (1992) 381–409.

[368] W. Grimus, L. Lavoura, O. M. Ogreid, and P. Osland, "The Oblique parameters in multi-Higgs-doublet models," Nucl. Phys. **B801** (2008) 81–96, arXiv:0802.4353 [hep-ph].

[369] **Gfitter Group** Collaboration, M. Baak, J. Cúth, J. Haller, A. Hoecker, R. Kogler, K. Mönig, M. Schott, and J. Stelzer, "The global electroweak fit at NNLO and prospects for the LHC and ILC," Eur. Phys. J. **C74** (2014) 3046, arXiv:1407.3792 [hep-ph].

[370] K. Kainulainen, K. Tuominen, and J. Virkajärvi, "A model for dark matter, naturalness and a complete gauge unification," JCAP **1507** (2015) 034, arXiv:1504.07197 [hep-ph].

[371] F. Feroz, M. P. Hobson, E. Cameron, and A. N. Pettitt, "Importance Nested Sampling and the MultiNest Algorithm," ArXiv e-prints (June, 2013) , arXiv:1306.2144 [astro-ph.IM].

[372] F. Feroz, M. P. Hobson, and M. Bridges, "MultiNest: an efficient and robust Bayesian inference tool for cosmology and particle physics," Mon. Not. Roy. Astron. Soc. **398** (2009) 1601–1614, arXiv:0809.3437 [astro-ph].

[373] A. Fowlie and M. H. Bardsley, "Superplot: a graphical interface for plotting and analysing MultiNest output," Eur. Phys. J. Plus **131** no. 11, (2016) 391, arXiv:1603.00555 [physics.data-an].

[374] M. Srednicki, Quantum field theory. Cambridge University Press, 2007.

[375] M. A. Shifman, "Quark hadron duality," in Proceedings, 8th International Symposium on Heavy Flavor Physics (Heavy Flavors 8), p. hf8/013. 2000. arXiv:hep-ph/0009131 [hep-ph]. http://jhep.sissa.it/archive/prhep/preproceeding/hf8/013. [,hf8/013(2000)].

[376] A. Lenz, "Lifetimes and HQE," arXiv:1405.3601 [hep-ph].

[377] I. I. Y. Bigi and N. Uraltsev, "A Vademecum on quark hadron duality," Int. J. Mod. Phys. **A16** (2001) 5201–5248, arXiv:hep-ph/0106346 [hep-ph].

[378] A. Lenz, "Heavy flavour physics and effective field theories," Epiphany, 2015. https://www.ippp.dur.ac.uk/~lenz/Flavour-Notes$_$Lenz$_$2015.pdf.

[379] A. J. Buras, M. Jamin, and P. H. Weisz, "Leading and Next-to-leading QCD Corrections to ϵ Parameter and $B^0 - \bar{B}^0$ Mixing in the Presence of a Heavy Top Quark," Nucl. Phys. **B347** (1990) 491–536.

[380] A. Lenz and U. Nierste, "Theoretical update of $B_s - \bar{B}_s$ mixing," JHEP **06** (2007) 072, arXiv:hep-ph/0612167 [hep-ph].

[381] A. Lenz and U. Nierste, "Numerical Updates of Lifetimes and Mixing Parameters of B Mesons," in CKM unitarity triangle. Proceedings, 6th International Workshop, CKM 2010, Warwick, 2011. arXiv:1102.4274 [hep-ph]. https://inspirehep.net/record/890169/files/arXiv:1102.4274.pdf.

[382] E. Bagan, P. Ball, B. Fiol, and P. Gosdzinsky, "Next-to-leading order radiative corrections to the decay b —¿ c c s," Phys. Lett. **B351** (1995) 546–554, arXiv:hep-ph/9502338 [hep-ph].

[383] E. Bagan, P. Ball, V. M. Braun, and P. Gosdzinsky, "Theoretical update of the semileptonic branching ratio of B mesons," Phys. Lett. **B342** (1995) 362–368, arXiv:hep-ph/9409440 [hep-ph]. [Erratum: Phys. Lett.B374,363(1996)].

[384] I. I. Y. Bigi, N. G. Uraltsev, and A. I. Vainshtein, "Nonperturbative corrections to inclusive beauty and charm decays: QCD versus phenomenological models," Phys. Lett. **B293** (1992) 430–436, arXiv:hep-ph/9207214 [hep-ph]. [Erratum: Phys. Lett.B297,477(1992)].

[385] E. Franco, V. Lubicz, F. Mescia, and C. Tarantino, "Lifetime ratios of beauty hadrons at the next-to-leading order in QCD," Nucl. Phys. **B633** (2002) 212–236, arXiv:hep-ph/0203089 [hep-ph].

[386] F. Krinner, A. Lenz, and T. Rauh, "The inclusive decay $b \to c\bar{c}s$ revisited," Nucl. Phys. **B876** (2013) 31–54, arXiv:1305.5390 [hep-ph].

[387] T. Ohl, G. Ricciardi, and E. H. Simmons, "D - anti-D mixing in heavy quark effective field theory: The Sequel," Nucl. Phys. **B403** (1993) 605–632, arXiv:hep-ph/9301212 [hep-ph].

[388] I. I. Y. Bigi and N. G. Uraltsev, "D0 - anti-D0 oscillations as a probe of quark hadron duality," Nucl. Phys. **B592** (2001) 92–106, arXiv:hep-ph/0005089 [hep-ph].

[389] E. Golowich, S. Pakvasa, and A. A. Petrov, "New Physics contributions to the lifetime difference in D0-anti-D0 mixing," Phys. Rev. Lett. **98** (2007) 181801, arXiv:hep-ph/0610039 [hep-ph].

[390] M. Bobrowski, A. Lenz, J. Riedl, and J. Rohrwild, "How Large Can the SM Contribution to CP Violation in $D^0 - \bar{D}^0$ Mixing Be?," JHEP **03** (2010) 009, arXiv:1002.4794 [hep-ph].

[391] R. Lehnert, "Cpt symmetry and its violation," Symmetry **8** no. 11, (2016) 114.

[392] K. S. Babu, J. Julio, and Y. Zhang, "Perturbative unitarity constraints on general W' models and collider implications," Nucl. Phys. **B858** (2012) 468–487, arXiv:1111.5021 [hep-ph].

[393] M. S. Chanowitz, M. A. Furman, and I. Hinchliffe, "Weak Interactions of Ultraheavy Fermions. 2.," Nucl. Phys. **B153** (1979) 402–430.

[394] M. Endo and Y. Yamamoto, "Unitarity Bounds on Dark Matter Effective Interactions at LHC," JHEP **06** (2014) 126, arXiv:1403.6610 [hep-ph].

[395] J. Hamann, "Evidence for extra radiation? Profile likelihood versus Bayesian posterior," JCAP **3** (Mar., 2012) 021, arXiv:1110.4271.

[396] A. Denner, H. Eck, O. Hahn, and J. Küblbeck, "Feynman rules for fermion-number-violating interactions," Nuclear Physics B **387** no. 2, (1992) 467–481.